SINTEF
PROCEEDINGS
1

Selected papers from 10th International Conference on Computational Fluid Dynamics in the Oil & Gas, Metallurgical and Process Industries

Progress in Applied CFD

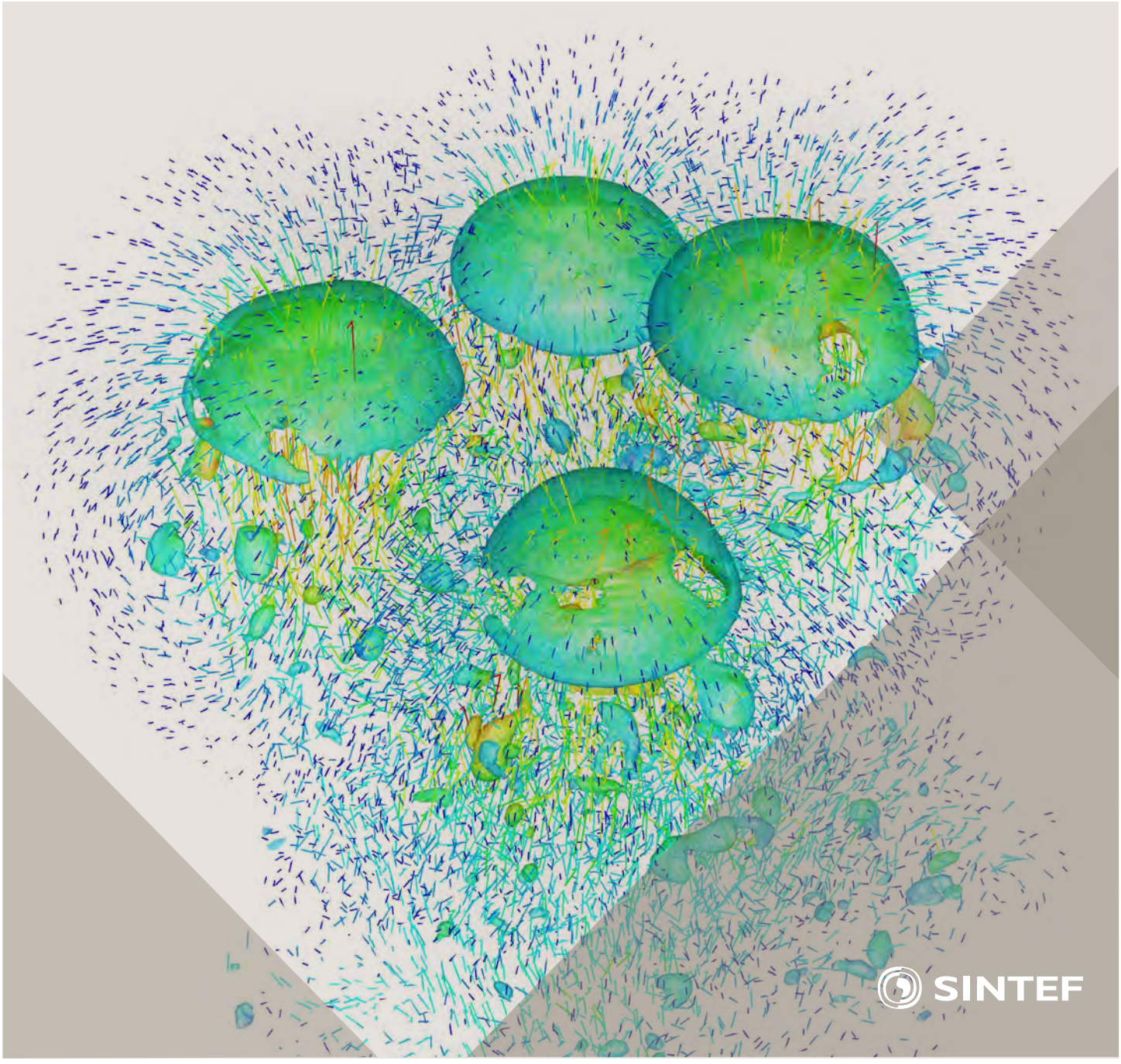

SINTEF Proceedings

Editors:
Jan Erik Olsen and Stein Tore Johansen

Progress in Applied CFD

Selected papers from 10th International Conference on Computational Fluid Dynamics in the Oil & Gas, Metallurgical and Process Industries

SINTEF Academic Press

SINTEF Proceedings no 1
Editors: Jan Erik Olsen and Stein Tore Johansen
Progress in Applied CFD
Selected papers from 10th International Conference on Computational Fluid Dynamics in the Oil & Gas, Metallurgical and Process Industries

Key words:
CFD, Flow, Modelling

Cover, illustration: Rising bubbles by Schalk Cloete

ISSN 2387-4287 (printed)
ISSN 2387-4295 (online)
ISBN 978-82-536-1432-8 (printed)
ISBN 978-82-536-1433-5 (pdf)

60 copies printed by AIT AS e-dit
Content: 100 g munken polar
Cover: 240 g trucard

SINTEF Academic Press
Address: Forskningsveien 3 B
PO Box 124 Blindern
N-0314 OSLO
Tel: +47 22 96 55 55
Fax: +47 22 96 55 08

www.sintef.no/byggforsk
www.sintefbok.no

SINTEF Proceedings
SINTEF Proceedings is a serial publication for peer-reviewed conference proceedings on a variety of scientific topics.
The processes of peer-reviewing of papers published in SINTEF Proceedings are administered by the conference organizers and proceedings editors. Detailed procedures will vary according to custom and practice in each scientific community.

PREFACE

This book contains selected papers from the 10th International Conference on Computational Fluid Dynamics in the Oil & Gas, Metallurgical and Process Industries. The conference was hosted by SINTEF in Trondheim in June 2014 and is also known as CFD2014 for short. The conference series was initiated by CSIRO and Phil Schwarz in 1997. So far the conference has been alternating between CSIRO in Melbourne and SINTEF in Trondheim. The conferences focus on the application of CFD in the oil and gas industries, metal production, mineral processing, power generation, chemicals and other process industries. The papers in the conference proceedings and this book demonstrate the current progress in applied CFD.

The conference papers undergo a review process involving two experts. Only papers accepted by the reviewers are presented in the conference proceedings. More than 100 papers were presented at the conference. Of these papers, 27 were chosen for this book and reviewed once more before being approved. These are well received papers fitting the scope of the book which has a slightly more focused scope than the conference. As many other good papers were presented at the conference, the interested reader is also encouraged to study the proceedings of the conference.

The organizing committee would like to thank everyone who has helped with paper review, those who promoted the conference and all authors who have submitted scientific contributions. We are also grateful for the support from the conference sponsors: FACE (the multiphase flow assurance centre), Total, ANSYS, CD-Adapco, Ascomp, Statoil and Elkem.

Stein Tore Johansen & Jan Erik Olsen

Organizing committee:

Conference chairman: Prof. Stein Tore Johansen
Conference coordinator: Dr. Jan Erik Olsen
Dr. Kristian Etienne Einarsrud
Dr. Shahriar Amini
Dr. Ernst Meese
Dr. Paal Skjetne
Dr. Martin Larsson
Dr. Peter Witt, CSIRO

Scientific committee:

J.A.M.Kuipers, TU Eindhoven
Olivier Simonin, IMFT/INP Toulouse
Akio Tomiyama, Kobe University
Sanjoy Banerjee, City College of New York
Phil Schwarz, CSIRO
Harald Laux, Osram
Josip Zoric, SINTEF
Jos Derksen, University of Aberdeen
Dieter Bothe, TU Darmstadt
Dmitry Eskin, Schlumberger
Djamel Lakehal, ASCOMP
Pär Jonsson, KTH
Ruben Shulkes, Statoil
Chris Thompson, Cranfield University
Jinghai Li, Chinese Academy of Science
Stefan Pirker, Johannes Kepler Univ.
Bernhard Müller, NTNU
Stein Tore Johansen, SINTEF
Markus Braun, ANSYS

CONTENTS

Chapter 1: Pragmatic Industrial Modelling 7
On pragmatism in industrial modeling 9
Pragmatic CFD modelling approaches to complex multiphase processes 25
A six chemical species CFD model of alumina reduction in a Hall-Héroult cell 39
Multi-scale process models to enable the embedding of CFD derived functions:
Curtain drag in flighted rotary dryers 47

Chapter 2: Bubbles and Droplets 57
An enhanced front tracking method featuring volume conservative remeshing and mass transfer 59
Drop breakup modelling in turbulent flows 73
A Baseline model for monodisperse bubbly flows 83

Chapter 3: Fluidized Beds 93
Comparing Euler-Euler and Euler-Lagrange based modelling approaches for gas-particle flows 95
State of the art in mapping schemes for dilute and dense Euler-Lagrange simulations 103
The parametric sensitivity of fluidized bed reactor simulations carried out in different
flow regimes 113
Hydrodynamic investigation into a novel IC-CLC reactor concept for power production
with integrated CO_2 capture 123

Chapter 4: Packed Beds 131
A multi-scale model for oxygen carrier selection and reactor design applied
to packed bed chemical looping combustion 133
CFD simulations of flow in random packed beds of spheres and cylinders:
analysis of the velocity field 143
Numerical model for flow in rocks composed of materials of different permeability 149

Chapter 5: Metallurgical Applications 157
Modelling argon injection in continuous casting of steel by the DPM+VOF technique 159
Modelling thermal effects in the molten iron bath of the HIsmelt reduction vessel 169
Modelling of the Ferrosilicon furnace: effect of boundary conditions and burst 179
Multi-scale modeling of hydrocarbon injection into the blast furnace raceway 189
Prediction of mass transfer between liquid steel and slag at continuous casting mold 197

Chapter 6: Oil & Gas Applications 205
CFD modeling of oil-water separation efficiency in three-phase separators 207
Governing physics of shallow and deep subsea gas release 217
Cool down simulations of subsea equipment 223
Lattice Boltzmann simulations applied to understanding the stability of multiphase interfaces 231

Chapter 7: Pipeflow 239
CFD modelling of gas entrainment at a propagating slug front 241
CFD simulations of the two-phase flow of different mixtures in a closed system flow wheel 251
Modelling of particle transport and bed-formation in pipelines 259
Simulation of two-phase viscous oil flow 267

Chapter 1: Pragmatic Industrial Modelling

Computational Fluid Dynamics is basically the computation of flows using spatially resolved mass, energy and momentum equations. By applying homogenization methods such as volume averaging and ensemble averaging to statistically represent unresolved phenomena as well as temporal system evolution, very complex systems can be described by CFD. The homogenization methods will always involve modeling of non-resolved phenomena. Often multiple temporal and spatial scales must be modeled, involving a multitude of scales which has to be related. At the same time the computational time to calculate a real time unit increases with approximately a factor of 16 by halving the size of grid cells in a single processor dynamic 3D computation. These challenges indicate that CFD often involves complex modeling, involving uncertainties, and sometimes we expect very long computational times.

CFD is a powerful approach to understand phenomena, interpret experimental data but also to make useful predictions. However, if the intension of using CFD is to be able to answer industrially or societal important questions we need to place the role of CFD into the larger context. The role we have decided to take here is not to ask how we can use CFD to solve the problem, but rather:" Where do we have to apply CFD to give the most useful answer to the question". By doing this we focus on responding to the posed challenge and much less of finding another project for applying CFD. If we, as an example, do CFD to solve a problem where good analytical solutions exist, we will discredit not only ourselves but also the entire community of CFD.

The *Pragmatic industrial modelling* sessions on CFD 2014 were created with this intension to see CFD in a greater perspective. The focus must be on the questions to answer, taking into account the available information and methods, the needs for additional information and how fast and accurate new information and methods can be developed or executed. Sometimes the posed questions need fast answers, making on-the-fly CFD impossible, or the requested accuracy tells that approximate analytical solutions is more than good enough. By using CFD where only CFD can provide a solutions, or where CFD is cost effective compared to experiments, it will become evident directions of CFD which has to be developed to make CFD even more successful.

In the lead paper we proposed to develop a standard for *Pragmatic industrial modelling***,** and Phil Schwarz contributed with his life long experience in pragmatic modeling approaches. Strong applications of pragmatic modeling are demonstrated in the papers, not only in this chapter but also in other chapters in this book.

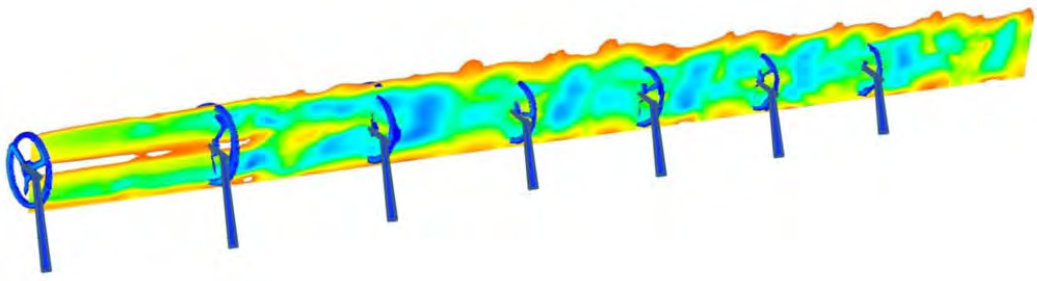

10th International Conference on CFD in Oil & Gas, Metallurgical and Process Industries
SINTEF, Trondheim, Norway *CFD 2014*
17-19 June 2014

ON PRAGMATISM IN INDUSTRIAL MODELING

Josip Zoric[a], Stein Tore Johansen[a,c], Kristian Etienne Einarsrud[a,b], Asbjørn Solheim[a]
[a]SINTEF Materials and Chemistry, Trondheim, Norway
[b]Sør Trøndelag University College (HiST), Trondheim Norway
[c]Norwegian University of Science and Technology, Department of Energy and Process Engineering
(Josip.Zoric; Stein.T.Johansen; Asbjorn.Solheim @sintef.no, kristian.e.einarsrud@hist.no)

ABSTRACT

Many natural or industrial processes are of extreme complexity, and where the time- and length scales range from an atomistic level to years and kilometers. Often the processes or phenomena consist of multiple sub processes in which each comprises its own length and time scales. An example can be production of aluminum by the Hall-Heroult process, where process streams or raw materials, flow dynamics and segregation in silos, with time varying quality, the feeding and operational routines, the reduction cells with numerous sub processes, and the tapping process, all make up a complete process. To optimize such production processes with respect to economic and environmental parameters we will have to develop models which can give the overall picture and at the same time be accurate enough to support the optimization process. As there are many dynamic aspects of an industrial production, the ultimate need will be a model which can compute much faster than real time and which can be used to support current operations and to develop new processes.

In this paper we discuss how this type of pragmatic industrial models can be developed. We will identify and discuss the tools needed for such an analyses, including the analyses process itself and the frameworks needed for such analyses. Key elements in our pragmatic modeling concepts are human knowledge, including capabilities to understand complex phenomena and how these can be modeled in a simplified but "good enough" manner, systematic use of existing information, systematic analyses of what information (model results) is needed and at which accuracy and speed the results must be produced. Another key element is the selection and collection of experimental data, organized and made accessible in an optimal manner to support the predictiveness of the pragmatic model. We propose that all types of data are organized by a "bridge" (modeling middleware) between complex scientific (aspect/phenomenon oriented) physical models, simplified models and process data. We believe that these types of pragmatic industrial models will enable a step change in both operation, operator training and process optimization, as well as design of new processes. Finally, in a case study, we apply our pragmatic modeling concept to the aluminum production process and discuss the implications of our proposed concept.

Keywords: Modeling, framework, pragmatism, industry, process.

INTRODUCTION

Position and Motivation

Many natural or industrial processes are of extreme complexity, and where the time and length scales range from an atomistic level to years and kilometers. Often the processes or phenomena consist of multiple sub processes in which each comprises its own length and time scales. An example can be production of aluminum by the Hall-Heroult process (Thonstad et al., 2001) where process streams or raw materials, flow dynamics and segregation in silos, with time varying quality, the feeding and operational routines, the reduction cells with numerous sub processes, and the tapping process, all make up a complete process. To optimize such production processes with respect to economic and environmental parameters we will have to develop models which can give the overall picture and at the same time be accurate enough to support the optimization process. As there are many dynamic aspects of an industrial production, the ultimate need will be a model which can compute much faster than real time and which can be used both to support current operations and to develop new processes.

It has been stated at a previous CFD conference in Melbourne that no metallurgical process has hitherto been designed based on CFD. At the same time significant CFD work has been done on metallurgical processes. Keeping in mind the extreme complexity in a full process we realize that CFD, applied to optimize a single process step without seeing this as element in a larger system, would not be capable of driving technological-economical step changes. We will therefore have to investigate ways to model a process; ways which are simplified, but fast and sufficiently accurate to serve its purpose. These models should be based on physics, which is critical to ensure predictive power. However, if these types of pragmatic industrial models can be developed, they will enable a step change in both operation, operator

training and process optimization, as well as in the design of new processes.
Over many years SINTEF has been involved in research projects where the costumer's needs have been in focus and scientific excellence may conflict with the need to give the user something which can be applied immediately. Examples of this type of work are illustrated by following two applications:

1) Mitigation of large HF emissions in aluminum plants was studied by CFD. To run a larger parametric study the complex 3D problems were extremely simplified by smaller 2D problems. In this manner it was possible to complete the study and the results gave clear and, as later observed, successful advice.
2) In the second case (Johansen et al., 1998) melt refining of liquid aluminum was predicted and optimized with a simulation tool, which was based on a combination of 1D and 0D transient models, and where sub-scale information (closures) were obtained from experimental studies and 3D CFD simulations. With this approach it was possible to make sufficiently accurate predictions much faster than real time, allowing this to become an operational tool.

In general we have experienced that use of interpolation inside pre-calculated (by CFD or similar) tables is a powerful approach, to be used as part of a model or application. As an example we have made a complete application, which is based on interpolation within data obtained from CFD calculations. However, for design of the "experimental matrix" we see clear needs for scientific experiment planning methods, including high/low analyses and factorial designs, as crucial tools for generating such tables. These observations indicated the need for a more systematic and scientific approach in development of industrial models, and we need to start out from where the scientific community currently stands on these issues.

From scientific to pragmatic

The great efforts of the natural science community ensured that many phenomena can be understood to a high level of details. Of course, in many cases the existing techniques may have to be improved or new techniques developed, to obtain the required information. However, these detailed and accurate studies (numerical or experimental) usually require significant time. In many cases long-time work with detailed phenomena has resulted in engineering correlations such as wall friction in pipe flow. Hence, these correlations can be used to make very fast calculations of pressure drops and flow capacities. If we move to the more complex multiphase pipeline flows, development of accurate correlations becomes much more demanding, e.g. gas may flow as bubbles or a continuous fluid, while liquid flows as droplets and/or a continuous liquid. At the same time, droplets and bubbles are in continuous evolution due to coalescence, breakup, deposition and entrainment. Currently, we have direct simulation techniques that enable simulation of detailed bubbly flows (Lu and Tryggvason, 2007). Such simulations can be performed on volumes containing at most a few liters of fluid, and where the simulations over some seconds of real time may take several days on a high performance computer cluster. In an extreme industrial case like the potential Russian Shtokman pipeline, the volume of the flow line is around 10^{11} liters, and the flow time scales are of the order of weeks (10^6 sec). Accordingly, it is currently infeasible to simulate the transient flow in such a pipeline with a multidimensional approach. Our best hope is to develop simplified 1D models, which by learning from fundamental simulations, such as in Lu & Tryggvason 2007, and experiments, can be made accurate enough to be industrially useful. In the past, this has been done using different pragmatic approaches, although with varying success.

From pragmatic to scientific

As discussed above, we will in many situations need a pragmatic approach to obtain industrially relevant information. For the industrial user the model results must be available within a given time span. If not, the results may have no value. At the same time, the accuracy of the model should be quantified (probably a collaborative effort of the industrial user (case owner) and solution architects (see Figure 1 and Figure 2), such that the user knows the significance of the predicted results and recommendations. The industrial model will have to be built on different building blocks, which will have to be put into system (orchestrated) by a well-defined framework (our view on the elements of the pragmatic analysis and its analytical framework are illustrated in Figure 1). What emerges from this is a need to put all these critical elements into a scientifically founded framework. As has been learned from the past, not every pragmatic approach has been successful, urging that we need to put science into the pragmatism itself.

Structure of this work

This work is organized in the following way. The *Introductory section* of this paper gives our position and motivation for pragmatism in industrial modeling. We continue by discussing how to move from scientific analysis to its industrial counterpart, and vice versa. Both are important for effective and pragmatic contribution to the industry activities.
Section 2 takes a process view on pragmatic industrial analysis, including in addition to the modeling (a primary focus of our work) experimental activity, various theoretical analyses and organizational and management activities. Before focusing on modeling, it is important to enlighten its contribution to the total analytical process, and its

interplay with other, equally important parts of the pragmatic analysis. This interplay of practical, holistically organized and orchestrated methods is the property that makes the pragmatic analysis so important for the industry and different from other scientific and research approaches.

Section 3 narrows our analysis on its modeling part. Our system view on modeling is inspired by software (SW) engineering. We start by discussing modeling frameworks (an effective way to organize modeling functionality and its SW realizations), existing research body and modeling industry trends. We continue by summarizing the research and scientific requirements for a modeling framework, and map them to SW engineering requirements. We suggest the necessary evolution of modeling frameworks, for their more effective industrial use. Thereafter we treat analysis and modeling as workflows, and give a simplified example of interacting models that are orchestrated and give solution/answer on an industry-relevant problem. This introduces section 4, which illustrates the modeling workflow on the example of industrial Al electrolysis.

Section 4 follows the analysis workflow logic suggested above on the example of industrial Al electrolysis (the Hall-Héroult process (Thonstad et al., 2001)). In this practical case the questions to be answered are:

- How does the heat loss from the process vary with the anode-cathode distance for the case when interfacial waves are neglected?
- What is the thickness of the frozen bath crust (side-ledge) as function of the anode-cathode distance?

Section 5 discusses our experiences with this theoretical and practical exercise and suggests future steps and improvements. We try to motivate the reader for future systematic treatment of the field "pragmatic industrial modeling", because the standardization and consolidation in industry and research, as well as SW technology, might lead to much more effective use and reuse of modeling, analyses and results.

For the reader's convenience we offer a list of terms and definitions at the end of the paper, because this multi-disciplinary paper uses many terms coming from SW engineering, system sciences and other research disciplines. We have tried to take over as much standard definitions as possible (from common Web definition sources (Web refs. 5, 9, 19, 20, 21, 23) , and slightly adjust them for our use. In such a way we want to contribute to the spirit of standardization of the research praxis, which this paper strongly advocates.

PROCESS VIEW ON PRAGMATIC INDUSTRIAL ANALYSIS

Pragmatic industrial analyses should be carefully organized, planned and executed. They require a structure not just in models, simulations, experiments, information and data, but also in analytical processes, concluding by well-structured communication of the results and the analytical context in which the results are valid. We see these important elements as parts of the analytical framework (FW), illustrated in Figure 1. Let us shortly discuss some of the important phases, and the results they produce:

1. ***Problem and Context Identification*** - this analytical phase requires discussions between the actors and stakeholders involved in industrial analysis. It includes clarifications of the use case, specification of the industrial/analytical context, agreement on needed accuracy of the solution, specification of necessary input and output information (its data formats etc.), as well as required interaction with other information systems and processes. Explicit simulations and experiments are agreed upon to answer given explicit questions. There are many SW Engineering tools, standards and methodologies available that can help structuring these important specifications (e.g. requirement analysis, use case specifications, pilot and demo exercises etc.). These analyses are grouped in ***step 1*** in Figure 1.
2. ***Analytical Strategy and Plan*** – Many industrial cases are complex and resource demanding and thus require a good analytical strategy and planning. This may be in contrast with the systems that will use their results (e.g. Decision Support Systems), because they might require information, which will be provided in real-time or nearly real-time conditions. Thus, in some cases, it will not be possible to give the answer with sufficient speed and accuracy. In such cases we need to carefully plan the experimental work or numerical experiments. Correct analytical strategy and planning (e.g. including metamodeling techniques) is critical for obtaining the results, which can be properly analyzed and qualified (illustrated as ***step 2*** in Figure 1). Several statistical methods, such as Analysis of variance (ANOVA), are available to analyze how combinations of input parameters may impact the results. Example tools that support executing such analyses are DAKOTA (Web ref. 8) and Mode Frontier (Web ref. 15).
3. ***Architecture of the Analytical Framework*** - The agreed analytical questions will often need models at many different levels to give acceptable answers. As the complexity of a model increases, the organization of the models will require a framework for systemizing and orchestrating its sub models. Such an analytical framework must

be well structured, applying an organized set of models, simulations, experiments and related information/data structures (***step 3*** in Figure 1). An example of such a framework is the volume-averaging technique (Whitaker, 1969 and Soo, 1989). The volume-averaging technique allows the derivation of continuum based conservation equations, based on a continuum model for the underlying materials and fluids. The approach allows multiple layers of averaging, which allows treatment of very complex systems. Such a procedure is also known as multi-scale or multi-level modeling (Ghosh, 2011).

4. ***Execution (Orchestration of Analyses, Simulations and Experiments)*** – by completing the first 3 steps illustrated in Figure 1, the necessary set of models, simulations, experiments and other analytical procedures are prepared, and one can proceed with the ***step 4***, - orchestrating them in a holistic analysis. Such an orchestration might include various modeling and analytical techniques, varying in complexity and heterogeneity, e.g. meta-modeling becomes increasingly important as the complexity of models increases. In the case of multilevel modeling, the volume averaging techniques are critical in analyzing, constructing and developing part of the model framework. The volume averaging technique, when applied to a class of problems, will allow reuse of models, rules and constraints. When the analysis of the problem indicates that the time required to answer a request from a higher level in the model hierarchy is too great, we have to resort to pre-calculations or experiments. This is fully possible if a robust procedure for this is developed.
5. ***Evaluation of the Solution*** - When we are doing experiments or simulations to answer posed questions, it is critical to understand the consequence of modeling results. It is tempting to make one prediction and give a fast feedback. However, we need to have a systematic approach to assessing the results (***step 5*** in Figure 1 – solution analysis). From experience, it is well known that simulation models have many weaknesses, as well as the human limited knowledge. This imperfection is illustrated by giving 10 different, but qualified people, an industrial problem and asking for the solution based on a given code (common to them all). This can result in 10 different answers, owing to differences in understanding of the problem and what it takes to solve the problem. An obvious deficiency is the lack of standards for problem definition, requirements to the accuracy of the results, communication, and interpretation of input and output data. Such challenges illustrate that our systematic approach must try to reduce the uncertainty in predictions and for now primarily by quantifying it. Then we have obvious reasons to apply ANOVA methods on both numerical and experimental data, as well as their combinations. Hence, it will be possible to quantify the accuracy of a given answer to a given question. The knowledge extraction process will often require handling of large data sets or streams. In these cases the productivity will be increased by using script based analysis tools such as MatLab (Web ref. 14) or Octave (Web ref. 16).
6. ***Conclusion and Communication*** **–** it is very important to conclude pragmatic analysis by a communication of the analytical results (step 6 in Figure 1). Usefulness of produced and published modeling and analytical results is often limited, because it is not well related to the analytical context. It is important to relate the analysis to its context, containing among others: (a) important analytical parameters, (b) information about modeling scale, (c) accuracy of the proposed solution, (d) estimates of representability, (e) predictive power, (f) computing and experimental resource consumption, etc.

   Information about analytical context is needed not only for the evaluation of existing models/analyses/experiments, but also for their future use and reuse. One could even require that such information is standardized, and in such a way facilitate efficient and standard interworking (and possibility to combine existing and new analyses in solution of industrial problems).

If we succeed in standardizing, we might even manage to "decouple" the analyses from their context and reuse them in new applicable analytical situations (context). One of the reasons why a given model is not used widely is that it may suffer from lack of analytical transparency.

In the engineering literature there are no clear strategies for how a complex model should be designed, assembled and qualified. Most typical is to build the model based on some specification, or let the model develop organically. However, industrial models very often have clear specification of the needed time response, accuracy, formats for information flow, as well as the rules and the framework for building the entire model system (frequently specified by requirements and/or use cases). To give one example:

The accurate prediction of liquid holdup and pressure drop in multiphase pipelines is of significant industrial value. A 3D model takes typically two orders longer time than a 2D/Q3D model, which typically takes two orders longer time than a 1D flow model. These models are extremely time-consuming compared to a multiphase point model (steady state) which typically can produce results in 1 ms or faster. Still, even such an efficient model has around 15 input parameters (properties, geometry, and velocities). If we want to cover a full matrix with 10 values for each input parameter, simulation of the matrix once will need more than 18 years of CPU

time. This illustrates that we need a scientific approach to all phases of pragmatic industrial modelling, and standardization and systematization of its phases.

SYSTEM VIEW ON INDUSTRIAL ANALYSIS - MODELING FRAMEWORKS

This section focuses on the modeling part of pragmatic industrial analysis (phase 3 and 4 in Figure 1). Our system view on modeling is inspired by SW engineering. We start by discussing requirements for modeling frameworks, comment on existing engineering efforts, research and industry trends. We suggest standardization and development actions for modeling frameworks, which will enhance their effective scientific and industry use. We also analyze the modeling with help of scenario and workflow techniques and give a simplified example that will be used in the practical example in section 4.

Existing research and engineering work

Based on observations from industrially related development work over many years (some referenced below), we see that there is a need for a well-structured, scientifically founded, and highly standardized framework for developing industrial models. Such a framework should be well defined in several perspectives: e.g. domain knowledge (e.g. physics, chemistry, structural mechanics…), mathematical/numerical aspects, and SW engineering perspective.

In this section we discuss the SW engineering perspective, which focus on the modeling frameworks (often called modeling platforms), their modeling elements/modules, and their architecture, topology and implementation technology.

The main purpose of so-called "pragmatic modeling" is to adjust the research models to the realism/world of industrial processes, their scope, perspective and challenges. So-called industrial models have requirements as: (a) industrial scope and perspective, (b) usefulness, (c) required accuracy and predictive-ness, (d) simplicity of use, (e) response time and speed, (f) compatibility with other (industrial) models, etc.

To meet the above-mentioned requirements, the number of the "practical" system and SW engineering requirements have to be realized, e.g.:

- Interactivity with well-established industrial standards,
- Modularity,
- Clear interfaces / API with other models and modeling tool-boxes,
- Compliancy with industrial and SW engineering standards,
- Well-defined "insertion procedures" and interaction rules in calculations (meshing interactions, initial and boundary condition inclusion, libraries of user-defined functions, procedures for solver algorithms changes etc.),
- Inter-model interworking and interoperability,
- Well-structured and standardized raw data and metadata,
- Documentation.

There is currently extensive work on modeling technology, showing variety of approaches, modelling architectures, modeling strategies, modeling technologies, e.g. expert systems based on qualitative reasoning engines and elements of AI (Enemark-Rasmussen et al., 2012), hybrid multi-zonal CFD models (Bezzo et al. 2004), coupling modeling and decision tools (Rossig et al., 2010), model-centric support for manufacturing operations (Rolandi and Romagnoli (2010)), and optimizations by reduced CFD models (Lang et al., 2011).

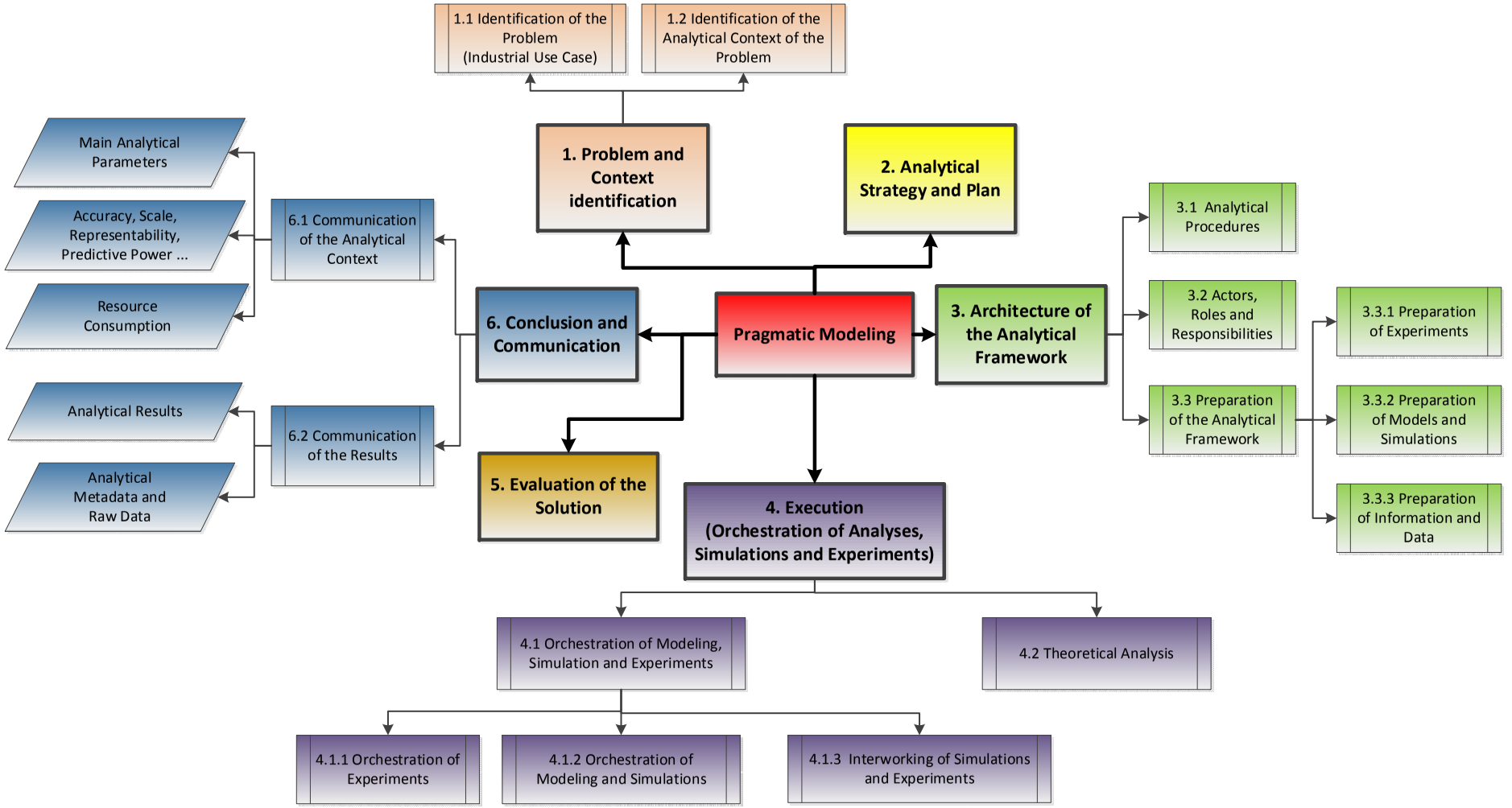

Figure 1. Some of the important phases, processes and results in a typical pragmatic analysis (terms and definitions are given in section 1).

Various model types are being combined in solutions of industrial problems, e.g.: (Rolandi and Romagnoli, 2010), (Chen, 2001), (Malawaki et al, 2005), (Power and Sharda, 2007), Urban et al. 2009). CFD models are used for different purposes. Power and Sharda (2007) discusses embedded quantitative models in Decision Support Systems. Authors emphasize that the nature of interconnected models can vary from algebraic, decision analytic, financial, simulation, optimization and many other types. Power and Sharda (2007) stresses the need for standardization of data structures (XML), protocols and other involved ICT technologies. Lang et al., 2011 discusses the need for standardization of industrial models, with example of computer-aided process engineering (CAPE). Authors emphasize two particular advances the industry can benefit from: (1) general-purpose custom-modeling platforms and (2) standardization of interface specification for component-based process simulations.

Rolandi & Romagnoli 2010, as well as Urban et al. (2009) stress the lack of development of both high-level frameworks and low-level mechanisms to assist the formulation of "models" of process engineering problems for support of process operations.

Rolandi & Romagnoli 2010 divides the framework models in several categories: (a) first-principles process models, (b) high-fidelity process models, (c) plant-wide process models, (d) large-scale process models. They also discusses different modeling framework components, used in various phases of the modeling/analytical process: the data pre-processing environment, the estimation / reconciliation environment, the consistent data etc. They give a schema for typical modeling activities included in a typical framework for integrated model-centric support of process operations.

Lang et al., 2011 describes a use of reduced order CFD models in optimization of IGCC processes. The procedure for development of reduced order models (ROM) is explained in Lang et al., 2011 and Lang et al. 2009. They "wrap" the ROM to fit the modular framework of the simulator. Lang et al., 2011, expects that the future work will continue the improvement of methods to develop accurate and efficient ROMs from CFD models, along with their integration and validation within process optimization environments.

This implementation will also be extended to the CAPE-OPEN software standard (Web ref. 6) and to integration within the APECS system.

Several industrial initiatives (Web ref. 12) and open standards / approaches, such as in (Web ref. 6), are getting momentum; however, at the current time, generic, standardized frameworks for scientific computing are not wide-spread. Several software vendors are instead progressing towards product-centric multiphysics frameworks, such as ANSYS workbench (Web ref. 1) and COMSOL Multiphysics (Web ref. 7). However, a two way connectivity of such software platforms, such as recently realized between MATLAB (Web ref. 14) and MAPLE (Web ref. 13), has still not been fully realized.

Industry makes efforts towards proprietary customizable workbench solutions, which enable connecting external tools to their solutions. Workbench solutions include a combination of standard scripting languages, e.g. Python (Web ref. 1), data standards and interfaces, standardized modeling techniques, with well-defined protocols (Web ref. 1 and Web ref. 2). Such tools combine technologies as: bidirectional CAD connectivity, powerful highly-automated meshing, project-level update mechanisms, pervasive parameter management and various integrated optimization tools. Examples of these customizable modelling technologies include references (Web ref. 6, 8 10, 15, 17, 18).

Several strategies (both centralized and decentralized modeling approaches) to "bridging" scientific and industrial models are used in praxis:

- **Direct inclusion** of new scientific models (or their approximations / simplifications) into industrial models – enrichment of industrial models, (e.g. via libraries of user-defined functions, modification in calculation procedures / algorithms, new modeling modules, new solvers etc.)
- **Building completely new industrial models** – from scratch, based on the newest achievements of scientific models and equation solver strategies.
- **Orchestration** of various model types (e.g. script-based orchestration of models with well-arranged information exchange between models). A combination of extra-model orchestration (middleware-based) and intra-model interventions (by changing user-defined functions (UDFs), boundary conditions etc.), exchange of input/output files etc.

We expect that the future evolution of modeling frameworks for pragmatic modeling will (with respect to the topology) head in two directions:

(1) *Centralized architectures* (main modeling tool controls the modeling/simulation process, including underlying tools and modeling elements) and

(2) *Decentralized architecture*s (middleware for model orchestration: script-based or middleware-based orchestration of various models and modeling tools).

We would like to motivate further development and standardization of the SW engineering related to modeling frameworks, e.g.:

- **Standardization of the modelling middleware including standardization of:**
  - Application Programming Interfaces (APIs) and protocols, and their module-like implementations,

- Scripts for orchestration of models, and related workflow like data exchange,
- Monitoring, logging and control routines and mechanisms.

- **Standardization of data exchange formats (e.g. XML-based)...**
- **Standardization of modelling metadata:**
  - Specifying the analytical context in which industrial problem will be solved.
  - Specifying the accuracy, sensitivity and quality of models and simulations (this can be organized as a part of the analytical context).
  - Ensuring the description of the data entities, models, their modules and processes.

Modeling workflow – a scenario perspective

Pragmatic modeling is often a part of a complex analytical and/or design process (Figure 1). It is a team work, as illustrated by Figure 2, driven by analytical workflows (often structured by usage/analytical scenarios (Figure 2- Figure 4)). It employs a modeling framework / architecture and a set of modeling technologies. The system architects specify a set of data/information exchange standards, protocols and interfaces (to mention just a few SW design artefacts), a number of design tools (e.g. Web ref. 8 and 15) and modeling tools (Web ref. 3 and 14). Designers and analytics verify often the results by various model analyses and fine-tuning techniques (e.g. sensitivity analyses – evaluated against physical elements).

Figure 2 gives a high-level over-simplified illustration of an abstract analysis/design process, which will include modeling support in its decision-making. It illustrates pragmatic modeling roles and scenarios, modelled in unified modeling language (Web ref. 22).

Figure 3 shows the main analysis process as a Sequence Diagram (Web ref. 22). Main Analysis triggers the Analysis 1, the algorithm of which relies upon the Analyses 2 and 3. The interaction of various analyses and their respective models is shown as sequence diagram interactions. One interaction can involve several data/information exchange processes and respective algorithms.

Figure 4 details the interaction between the Analysis 1 and the Analysis 2 (illustrated in Figure 3). In this figure we see the details of the algorithm of the Analysis 2 and the data/information exchanged among its model elements.

These high level diagrams (Figure 2- Figure 4) illustrate the SW engineering view on modeling. We will illustrate it by concrete examples offered in Section 4. We use SW-focused view to discuss the requirements and SW Engineering issues related to model interaction, data/information exchange, interfacing, standardization and other important elements for design of pragmatic models.

PRACTICAL EXAMPLE

Analysis 1 – Aluminum electrolysis

Primary aluminum is manufactured exclusively by the Hall-Héroult process (Thonstad et al., 2001). The process is based on electrolytic decomposition of alumina dissolved in a fluoride mixture serving as electrolyte at 960 ^{o}C, using consumable carbon anodes and horizontal anode configuration. A cross-sectional view through a typical electrolysis cell is shown in Figure 5).

Owing to the high temperature, highly corrosive and opaque environment, the interior of the cell has limited access for inspection and measurement, and the processes taking place are strongly coupled. It is, therefore, necessary to apply models for predicting how the entire system will react on changes in construction or operation. For instance, to optimize the energy consumption in the cell, such changes could be related to the anode topology,

In the Hall-Héroult process, several questions may be asked, which need to be answered by models and modeling frameworks. In the present example the main question to be answered is:

- How does the heat loss from the process vary with the anode-cathode distance for the case when interfacial waves are neglected?
- Additional response requested: What is the thickness of the frozen bath crust (side-ledge) as function of the anode-cathode distance.
- Answering such questions requires some mathematical model, as direct empiric is insufficient for such an extremely complex process. As a result of the complexity and requirements to get fast and at least qualitatively correct answers, a large number of partial process models have been developed in Microsoft Excel (Web ref. 11). Such models are for instance used for predicting the current efficiency, the cell voltage, the energy balances taking into account the enthalpies for the main chemical and electrochemical reactions as well as the distribution of the heat losses, and finally the temperature, pressure, and gas composition inside the cell superstructure and the flue gas scrubbing system. All partial models are based on first principles wherever possible and include fitted experimental and numerical data.
- Considering our posed question above on the overall heat loss, we simplify the heat loss from the central part of the cell bottom by regarding this as a 1D problem, and calculating the heat loss by standard engineering formulas for a layered structure. The heat loss from the sides and ends are calculated by subdivision of these regions into a number of 2D elements connected by thermal resistances depending on the cell geometry and the thermal conductivities of the materials used.

The heat loss through the different parts of the top of the cell (crust, anode, anode stubs) is computed by analytical expressions derived from numerical calculations and real measurements. The cell voltage is based on similar approaches, ranging from standard engineering formulas (ohmic resistances) via thermodynamic and electrochemical data (reversible cell voltage) to fitted laboratory and numerical data (overvoltages).

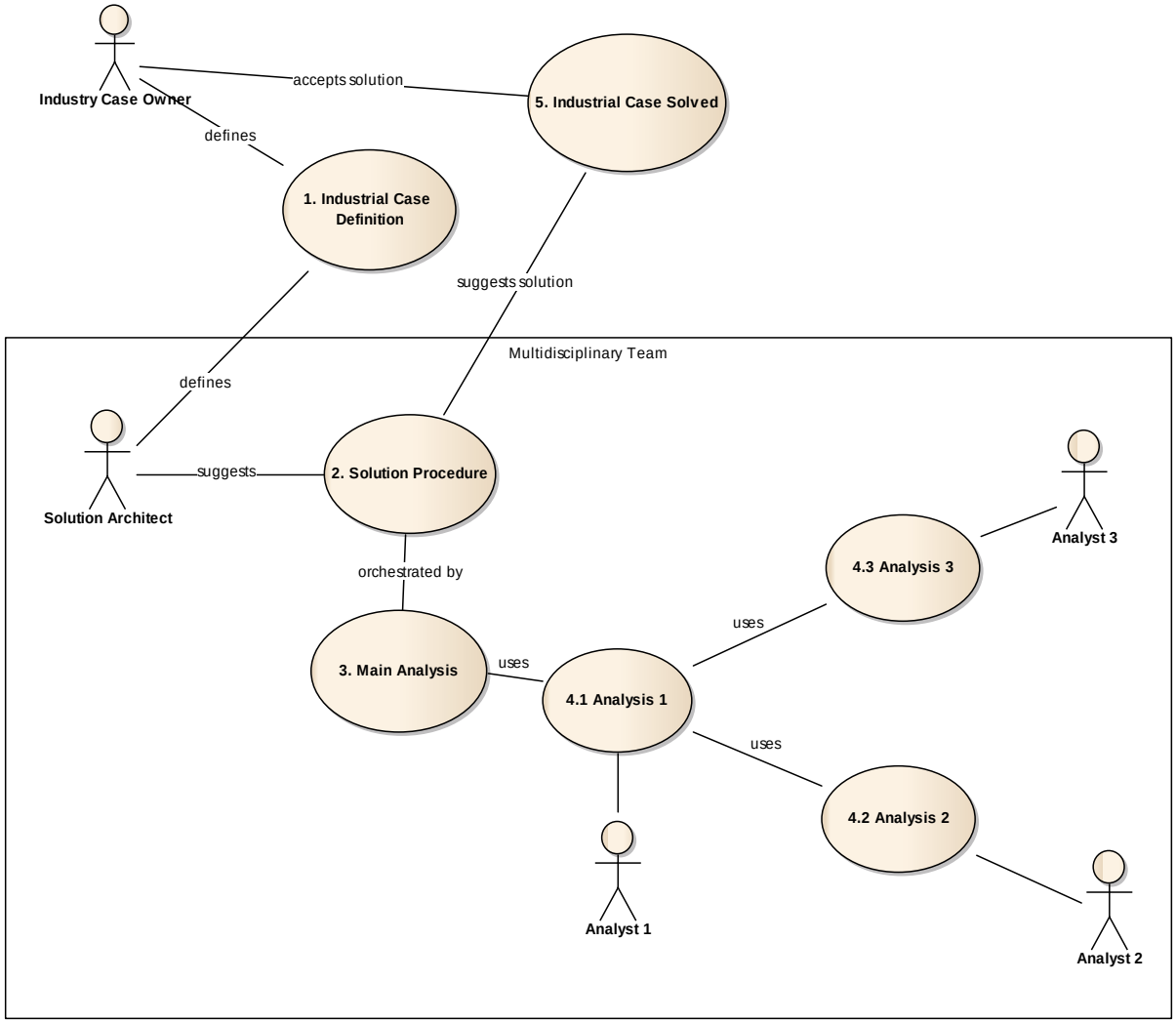

Figure 2. Use case diagram (modelled in Unified Modeling Language (Web ref. 22)). illustrating a simplified collaboration among actors (with their roles and responsibilities) in a pragmatic industrial modeling process.

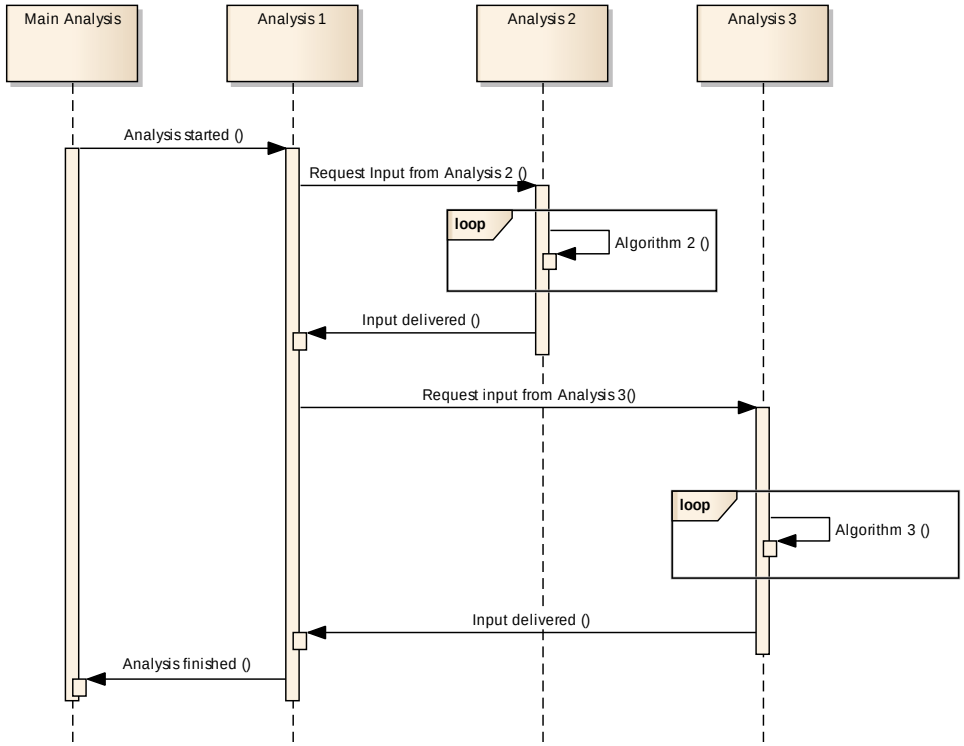

Figure 3. Sequence diagram (in Unified Modeling Language (Web ref. 22)) illustrating the partial realization of the use cases for the Main Analysis (shown in Figure 2).

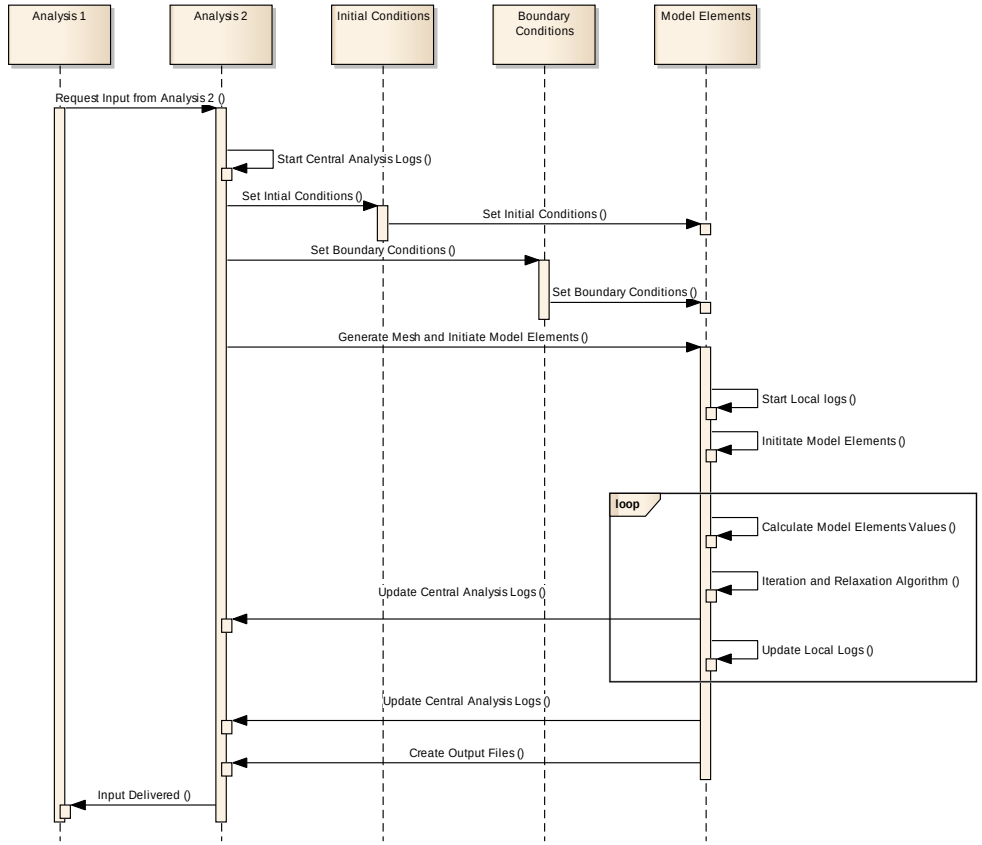

Figure 4. Sequence diagram detailing the realization of the use case "Analysis 2" from Figure 3.

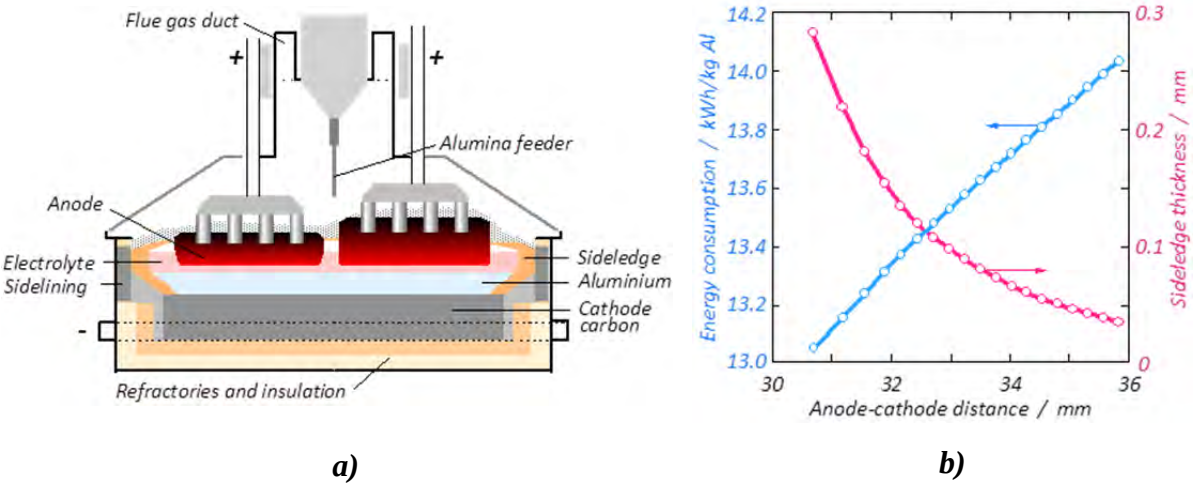

Figure 5. ***a)*** Schematic cross-section through an aluminum electrolysis cell, ***b)*** Predicted energy consumption and side ledge thickness versus anode-cathode distance.

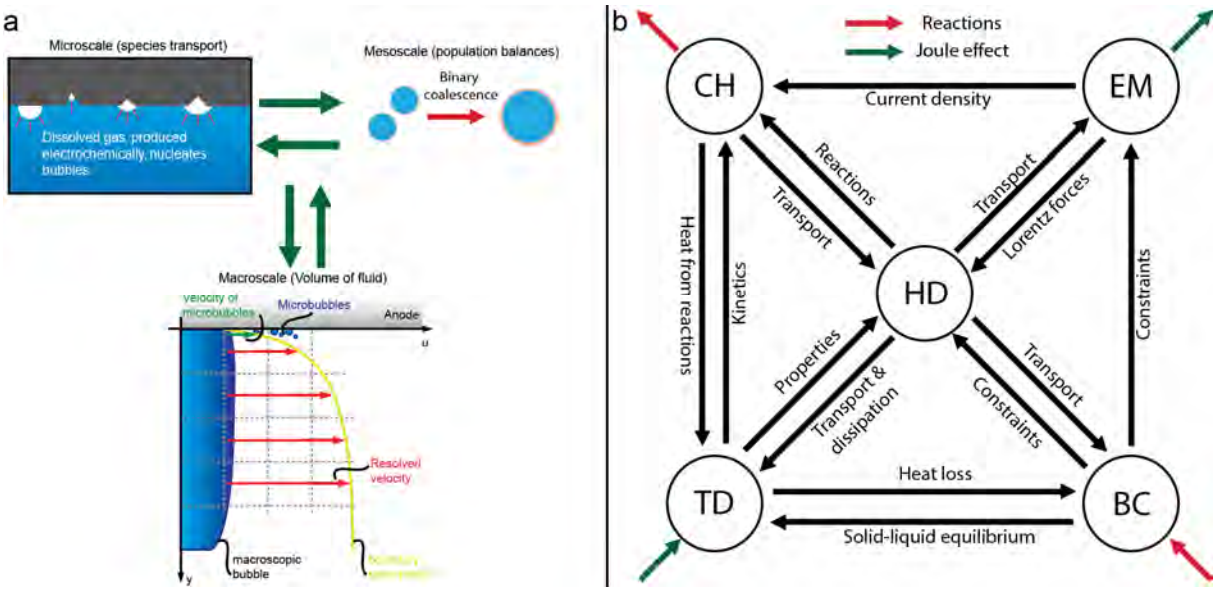

Figure 6. Schematic of multiscale approach a), and principal coupling diagram b), indicating the coupling between different phenomena in an electrolysis cell; chemical reactions (CH), electromagnetism (EM), boundary conditions (BC), thermodynamics (TD) and hydrodynamics (HD).

Some of the partial models can be used as stand-alone models, but they are all included in a total electrolysis cell modelling framework, allowing for coupled calculations and thus a holistic understanding of the overall heat balance of the cell.

The main numerical task in the framework is related to adjusting the anode-cathode distance of each individual anode until the cell voltage and the total current equal the pre-determined values, and the thickness of the side-ledge is varied until the total heat loss exactly balances the difference between the total energy input and the change in enthalpy in the process. Unfortunately, there is no way of measuring the anode-cathode distance accurately, and this parameter must be calculated from the bath voltage. The bath voltage is the difference between the total cell voltage and the remaining voltage terms, which can be either measured or modelled. The electrochemical overvoltage and the extra voltage drop due to the shielding effect of the gas bubbles ("bubble overvoltage"), which both are significant, are however difficult to measure. Presently, the calculation of the "bubble overvoltage" is based on a water model. Today, it is within reach to use CFD modelling to obtain better data on the extra resistance due to bubble shielding resulting from different complicated anode geometries , and being a function of the gas evolution rate and flow conditions. As

response to the questions posed above, a typical answer (prediction) from the model is seen in Figure 5b).
If the required correlations for bubble overvoltage are not available for the current configuration, for instance due to a novel anode design, the current analysis will ask for specific input (for instance a correlation between bubble overvoltage, anode topology and current density) from an analysis performed by a separate model framework. The calculation of such a correlation is exemplified in the following section.

Analysis 2 – Gas Evolution in Al Electrolysis

A simulation framework allowing for the description of bubble evolution on a single anode has recently been developed (Einarsrud, 2012), based on a multiscale coupled population balance / Volume of Fluid approach, as sketched in Figure 6 a): On a (micro) species level, gas is produced electrochemically by the presence of an electrical current. Following saturation, mesoscale bubbles are formed, treated by population balance modeling. As small bubbles evolve due to coalescence and mass transfer, macro-scale bubbles are formed, treated by the Volume of Fluid method. Owing to low electrical conductivity, the presence of bubbles alters the current density, consequently altering the distribution of gas on the microlevel, and thus also future nucleation events. Evidently, such a framework involves coupled phenomena spanning several disciplines, as indicated in Figure 6 b).

The *simulation* framework is fully orchestrated within the user-defined-function (UDF) functionality available in ANSYS FLUENT (Web ref. 3), allowing a user to add and couple additional models to the solver, based on specific macros supplied by the solver. The execution order of the conservation equations (i.e. mass, momentum, turbulence and scalar fields) is fixed by the solver, while the additional required UDFs can be executed either following each iteration or each time step. Currently, resulting source terms, for instance Lorentz forces, are calculated based on converged values of the fields at the previous time step, i.e. a time-splitting scheme is adopted. As the UDFs can be used to specify only specific terms used (although choices are vast) and that the overall execution order is dictated by the solver, this is an example of a product specific orchestration.
Considering the calculation of bubble induced voltage drop, several values must be given initially, for instance the nominal current density, system temperature, fluid properties and sought anode position in the cell, all of which can be supplied from the main analysis described above. Moreover, the anode shape and surface structure (i.e. porosity distribution) are required for realistic simulations. These properties can be obtained by other modelling approaches or material databases. The conditions supplied from other models and databases serve as initial and boundary conditions for the bubble flow simulation, as sketched in Figure 6 for a general analysis.
Following meshing, on a coarse or fine level, depending upon sought accuracy and time constraints set by Analysis 1, and initialization, the bubble simulation loop is initiated and run following a specific order, based on source terms and material properties obtained at the previous time step:

1) Flow, mass and turbulence equations are solved.
2) Electrical potential is solved, and current densities are determined.
3) Additional scalar fields are solved, representing chemical species and bubble number densities (population balance model)
4) New source terms are calculated based on converged fields, initiating the next time step.

After reaching a statistically steady state, the bubble induced voltage component is monitored and averaged for a given amount of time, finally yielding the output sought by Analysis 1, which in this specific example is a correlation between bubble overvoltage, anode topology, current density and electrolyte composition. This correlation can now be returned to the model in Chapter 4.1, yielding the required output, using the requested data format.

Our experiences with this practical modeling exercise (where we have tried to follow the modeling and analytical framework mindset (section 0)) show that significant energy has been used to establish a common view on the problem, understanding of the analytical context, the common knowledge base and the common problem dictionary. When those obstacles have been removed, the orchestration of various analyses towards the final solution was reduced to a manageable problem.

With respect to SW engineering technology, our modeling FW was based on a combination of "in-house" developed models (Excel (Web ref. 11) – based macro development (Analysis 1), with a customized workbench solution – based on ANSYS FLUENT product portfolio (Web ref. 1 and 3). We preferred to work as close as possible to industry standards, and the closest available approach was the customization of the widely-accepted SW products.

With respect to standardized processes for pragmatic industrial analyzes we have not found available and wide-spread methodologies. Therefore we have proposed the approach illustrated in Figure 1 and described in sections 2 and 3.

DISCUSSION AND CONCLUSION

In many situations a pragmatic analytical and modeling approach is needed to obtain industrially relevant information. For the industrial user the model result should be available within a given time span. If not, the results may have no value. At the same time, the accuracy of the model should be quantified, such that the user knows the significance of the predicted results and resulting recommendations. The industrial model will have to be built on different building blocks, which will have to be put into system (orchestrated) by a well-defined analytical and modeling framework.

Our view on the elements of the pragmatic analysis and its analytical framework is illustrated in Figure 1. What emerges from this is a need to put all these critical elements into a scientifically founded framework. As has been learned from the past, not every pragmatic approach has been successful, urging that we need to put science into the pragmatism itself. We believe that all of the six phases in a typical industrial (pragmatic) analytical process illustrated in Figure 1 can be to some extent standardized, e.g.: (1) problem and context identification, (2) standardized strategy and planning, (3) architecture of the analytical framework, (4) standardized orchestration and execution, (5) standard ways and criteria to evaluate the solution, and (6) standards for communicating the results and analytical context (for which they are valid, and usable). We can standardize the structure of the processes, the tools that are used, the quality assurance methods, as well as establish standards for how the results and analytical context are presented and described.

We would like to motivate the establishment of a scientific discipline that will focus on pragmatic industrial analyses and modeling frameworks. The effort of transforming the scientific results to industrial praxis is not just a methodological approach, but also a strategic activity. We hope that this paper and our technical opinion will contribute to establishing such a knowledge body.

REFERENCES

BEZZO, F., MACCHIETTO S. and PANTELIDES C.C, (2004), "A general methodology for hybrid multizonal/CFD models, Part I. Theoretical Framework", *Computers and Chemical Engineering*, 28, 501-511.

CHEN, J., (2001), "A predictive system for blast furnaces by integrating a neural network with qualitative analysis", *Engineering Applications of Artificial Intelligence*, 14 , 77-85.

EINARSRUD, K.E., (2012), "A Treatise on Interpolar Transport Phenomena", Ph.D. Thesis 2012:201, Norwegian University of Science and Technology (NTNU).

ENEMARK-RASMUSSEN, R., et al., (2012), "A simulation based engineering method to support HAZOP studies", *Proceedings of the 11th International Symposium on Process Systems Engineering*. R. Srinivasan, Elsevier Science, 1271-1275.

GHOSH, S., (2011), "Micromechanical Analysis and Multi-Scale Modeling Using the Voronoi Cell Finite Element Method", CRC Press.

JOHANSEN. S.T., GRAADAHL, S., TETLIE, P., RASCH, B., and MYRBOSTAD, E., (1998), "Can Rotor-Based Refining Units Be Developed and Optimised Based on Water Model Experiments?", *Light Metals*, Edited by Barry Welch, TMS, 805-810.

LANG, Y., ZITNEY, S.E. and BIEGLER, L.T., (2011), "Optimization of IGCC processes with reduced order CFD models", *Computers and Chemical Engineering*, 35, 1705-1717.

LANG, Y.-D., MALACINA, A., BIEGLER, L. T., MUNTEANU, S., MADSEN, J. I., and ZITNEY, S. E., (2009), "Reduced order model based on principal component analysis for process simulation and optimization", *Energy and Fuels*, 23, 1695–1706.

LU, J. and G. TRYGGVASON, (2007), "Effect of bubble size in turbulent bubbly downflow in a vertical channel." *Chemical Engineering Science*, 62, 3008-3018.

MALKAWI, A. M. et al., (2005) ,"Decision support and design evolution: integrating genetic algorithms, CFD and visualization", *Automation in Construction*, 14, 33-44.

POWER, D.J. and SHARDA, R., (2007), "Model-driven decision support systems: Concepts and research directions", *Decision Support Systems*, 43, 1044-1061.

ROLANDI, P.A and ROMAGNOLI, J.A., (2010), "Integrated model-centric framework for support of manufacturing operations. Part I: The framework", *Computers and Chemical Engineering*, 34 , 17-35.

ROSSING, N.L. et. al., (2010), "A functional HAZOP methodology", *Computers and Chemical Engineering*, 34, 244-253.

SOO, S.L., (1989), "Particulates and continuum: Multiphase Fluid Dynamics", Hemisphere Publishing, New York.

THONSTAD, J. , FELLNER, P., HAARBERG, G.M., HIVES, J. , KVANDE, H. and STERTEN, A., (2001), Aluminium Electrolysis – Fundamentals of the Hall-Héroult process, 3rd Ed., Aluminium Verlag.

URBAN, Z., CHENG, Y-S. and PANTELIDES, C.C., (2009), "High-fidelity modelling and detailed design of PEM fuel cell stacks", *Conference Proceedings - 2009 AIChE Annual Meeting, 09AIChE*

Web ref. 1: ANSYS Workbench Integrated Environment, http://www.ansys.com/Products/Workflow+Technology/ANSYS+Workbench+Platform.

Web ref. 2: ANSYS DesignXplorer®, http://www.ansys.com/Products/Workflow+Technology/ANSYS+Workbench+Platform/ANSYS+DesignXplorer

Web ref. 3: Ansys, Fluent, http://www.ansys.com/Products/Simulation+Technology/Fluid+Dynamics/Fluid+Dynamics+Products/ANSYS+Fluent

Web ref. 4: Aspen Custom Modeler, https://www.aspentech.com/products/aspen-custom-modeler.aspx

Web ref. 5: http://www.businessdictionary.com/definition/

Web ref. 6: The CAPE-OPEN Laboratories Network, www.colan.org.

Web ref. 7: COMSOL Mulitiphysics, http://www.comsol.com

Web ref. 8: Dakota, http://www.dakota.sandia.gov/about.html

Web ref. 9: http://www.dictionary.reference.com

Web ref. 10: Dymola, Dynamic Modeling Laboratory, http://www.3ds.com/products-services/catia/capabilities/systems-engineering/modelica-systems-simulation/dymola

Web ref. 11: http://office.microsoft.com/en-us/excel/

Web ref. 12: IMS, Intelligent Manufacturing Systems, www.ims.org.

Web ref. 13: Maple, http://www.maplesoft.com/products/Maple/professional/

Web ref. 14: Matlab, http://www.mathworks.se/products/matlab/.

Web ref. 15: Model Frontier, http://www.esteco.com/modefrontier.

Web ref. 16: Octave, http://wiki.octave.org/

Web ref. 17: Open Modelica, https://www.openmodelica.org/

Web ref. 18: SIMULIA V6 Overview, http://www.3ds.com/products-services/simulia/portfolio/simulia-v6/overview.

Web ref. 19: http://whatis.techtarget.com/definition/

Web ref. 20: http://searchsoa.techtarget.com/definition/

Web ref. 21: http://www.thefreedictionary.com

Web ref. 22: Unified Modeling Language, www.uml.org

Web ref. 23: http://wikipedia.org

WHITAKER, S., (1969), "Advances in Theory of Fluid Motion in Porous Media", *Ind. Eng. Chem.*, 61, 14-28.

1. TERMS AND DEFINITIONS

Table 1. List of terms and definitions.

(To offer as standard approach as possible (with respect to industry, SW engineering and usual modeling and simulation praxis), all the definitions in the paper are taken over from the common Web definition sources (Web ref. 5, 9, 19, 20, 21, 23) and sometimes slightly adjusted for the use in this paper.)

Term	Definition (Definitions are taken over from the following Web definition sources - references (Web ref. 5, 9, 19, 20, 21, 23), and sometimes slightly adjusted for the use in this paper.)
Analytical Process	• A method of studying the nature of something or of determining its essential features and their relations (Web ref. 9). • In this work – a chosen method for studying an industrial problem, containing a number of well-defined steps, and results, with clear roles and responsibilities for participating actors (see also FIGURE 2).
Framework (FW)	• A skeletal structure designed to support or enclose something (Web ref. 9). A frame or structure composed of parts fitted together (Web ref. 21), the manner of construction of something and the arrangement of its parts (Web ref. 21). The underlying structure; "providing a factual framework for future research" (Web ref. 21). • In general, a framework is a real or conceptual structure intended to serve as a support or guide for the building of something that expands the structure into something useful (Web ref. 19). • In computer systems, (definition used in Web ref. 19) a framework is often a layered structure indicating what kind of programs can or should be built and how they would interrelate. Some computer system frameworks also include actual programs, specify programming interfaces, or offer programming tools for using the frameworks. A framework may be for a set of functions within a system and how they interrelate; the layers of an operating system; the layers of an application subsystem; how communication should be standardized at some level of a network; and so forth. A framework is generally more comprehensive than a protocol and more prescriptive than a structure (Web ref. 19). • In this work – we will mostly use the definition taken from computer system sciences (Web ref. 19).
Analytical FW	• In this work – a conceptual structure of various analytical methods (experiments, modeling, simulations, theoretical analyses), incorporated and orchestrated in an analytical process.
Modeling FW	• In this work – we take over the definition taken from computer system sciences (Web ref. 19), and use it in modeling, simulations and related SW engineering activities.
Orchestration	• Orchestration describes the automated arrangement, coordination, and management of complex computer systems, middleware, and services (Web ref. 23). • In this work we discuss orchestration of modeling, simulation and analytical processes in general.
Unified Modeling Language (UML)	• The Unified Modeling Language (UML) is a general-purpose modeling language in the field of software engineering. The basic level provides a set of graphic notation techniques to create visual models of object-oriented software-intensive systems. Higher levels cover process-oriented views of a system (Web ref. 22 and 23).
Use Case	• In software and systems engineering, a use case is a list of steps, typically defining interactions between a role (known in UML as an "actor") and a system, to achieve a goal. The actor can be a human or an external system. In systems engineering, use cases are used at a higher level than within software engineering, often representing missions or stakeholder goals (Web ref. 22 and 23).
Scenario	• A predicted or postulated sequence of possible events (Web ref. 21), an outline of the plot of dramatic work, giving particulars of the scenes, characters etc. (Web ref. 21). (We can talk of modeling scenarios, simulation scenarios, usage scenarios, analytical scenarios etc.)
Workflow	• The set of relationships between all the activities in a project, from start to finish. Activities are related by different types of trigger relation. Activities may be triggered by external events or by other activities (Web ref. 9).
Sequence Diagram	• A sequence diagram is an interaction diagram that shows how processes operate with one another and in what order. A sequence diagram shows object interactions arranged in time sequence. It depicts the objects and classes involved in the scenario and the sequence of messages exchanged between the objects needed to carry out the functionality of the scenario. Sequence diagrams are typically associated with use case realizations in the Logical View of the system under development (Web ref. 22 and 23).

Interface	• In computer science, an interface is the point of interaction with software, or computer hardware. Some computer interfaces can send and receive data, while others can only send data (Web ref. 23). The types of access that interfaces provide between software components can include: constants, data types, types of procedures, exception specifications and method signatures (Web ref. 23). The interface of a software module is deliberately kept separate from the implementation of that module. The latter contains the actual code of the procedures and methods described in the interface, as well as other "private" variables, procedures, etc. (Web ref. 23).
Application Programing Interface (API)	• In computer programming, an application programming interface (API) specifies how some software components should interact with each other (Web ref. 23). An API specification can take many forms, including an International Standard such as POSIX, vendor documentation such as the Microsoft Windows API, the libraries of a programming language, e.g., Standard Template Library in C++ or Java API. Web APIs are also a vital component of today's web fabric. An API differs from an application binary interface (ABI) in that an API is source code based while an ABI is a binary interface (Web ref. 23).
Middleware	• In the computer industry, middleware is a general term for any programming that serves to "glue together" or mediate between two separate and often already existing programs. A common application of middleware is to allow programs written for access to a particular database to access other databases. Typically, middleware programs provide messaging services so that different applications can communicate. The systematic tying together of disparate applications, often through the use of middleware, is known as enterprise application integration (EAI) (Web ref. 20).
Raw data	• Raw data (also known as primary data) is a term for data collected from a source. Raw data has not been subjected to processing or any other manipulation, and are also referred to as primary data. Raw data is a relative term (see data). Raw data can be input to a computer program or used in manual procedures such as analyzing statistics from a survey. The term can refer to the binary data on electronic storage devices such as hard disk drives (also referred to as low-level data) (Web ref. 23).
Metadata	• Metadata is "data about data". Structural metadata is about the design and specification of data structures and is more properly called "data about the containers of data"; descriptive metadata, on the other hand, is about individual instances of application data, the data content (Web ref. 23). As information has become increasingly digital, metadata are also used to describe digital data using metadata standards specific to a particular discipline. By describing the contents and context of data files, the quality of the original data/files is greatly increased (Web ref. 23).
Context	• Background, environment, framework, setting, or situation surrounding an event or occurrence (Web ref. 5). • In computer science, a task context (process, thread ...) is the minimal set of data used by this task that must be saved to allow a task interruption at a given date, and a continuation of this task at the point it has been interrupted and at an arbitrary future date (Web ref. 23).
Analytical Context	• In this work the analytical context is a minimal set of data and metadata, needed to describe, define the analytical procedure (and if necessary reproduce it).

PRAGMATIC CFD MODELLING APPROACHES TO COMPLEX MULTIPHASE PROCESSES

M. Philip SCHWARZ[1], Yuqing FENG[1]
[1] CSIRO Mineral Resources Flagship, Clayton, AUSTRALIA

* E-mail: Phil.Schwarz@csiro.au

ABSTRACT

Modelling of complex multiphase processes in the minerals and energy resources industries requires a balance between the pursuit for detail and recognition of computational resource limitations, if it is to lead to effective and productive outcomes. Computational fluid dynamics (CFD) modelling can be a powerful tool to assist in improving these processes or designing new processes and equipment, since flow-related operations such as mixing, reaction or separation very often limit effectiveness. However, highly detailed CFD models for such complex and large-scale processes generally require such enormous amounts of computer resources that their effectiveness for actual process improvement can be limited. High level expertise is required to ensure that proper account is taken for multi-phase interactions, multi-scale effects, and additional non-flow physics and chemistry critical to the process while allowing outcomes to be obtained on industrially useful timescales. This may be termed the pragmatic approach.

Keywords: CFD, multiphase flow, chemical reactors, flow modelling, multi-scale, pragmatic modelling.

NOMENCLATURE

Greek Symbols

α Volume fraction, [-].
ρ Mass density, [kg/m^3].
μ Dynamic viscosity, [kg/m.s].

Latin Symbols

$\mathbf{M}$ Source term (interphase interactions), [kg/m^2.s^2].
p Pressure, [Pa].
$\mathbf{S}$ Source term (body forces), [kg/m^2.s^2].
t Time, [s].
$\mathbf{u}$ Velocity, [m/s].

Sub/superscripts

i Phase.

INTRODUCTION

Processing in the resources industries generally involves large flow rates and reactor volumes, and must be performed at minimal cost given the products are bulk commodities. Small improvements in energy efficiency or product recovery efficiency can thus make a significant difference to economics of the overall operation. Such improvements can be difficult to identify and risky to realize through trial-and-error at the plant. Similarly, radical improvements are hard to test at full-scale and involve substantial risk to the operating company during implementation. Computer simulation is the obvious tool to assist process optimisation while minimising risk (Schwarz, 1994).

Processing of mineral resources to extract valuable metals or chemicals involves unit operations that are designed to achieve mixing, reaction or separation, or a combination of these, often in the same unit (Schwarz, 1991). To achieve these ends in the most efficient way, achieving the greatest product yield, requires careful design of the flow field within the reactor.

A critically important characteristic of the flow field is the intensity of turbulence. Mixing and reaction are usually achieved most rapidly and with minimum energy requirement in a highly turbulent field. On the other hand, separation requires either careful control of the turbulence field, or ideally a laminar flow. These principles are further complicated for multi-phase situations. For example the desirability of high turbulence for mixing and reaction can sometimes be tempered by the need to avoid breakage of droplets into a fine dispersion (this can reduce the efficiency of subsequent separation steps) or the breakage of particles such as catalysts. On the other hand, separation of droplets may be improved by moderate turbulence to enhance coalescence, and hence settling speeds. Clearly the design of reactors, particularly multiphase reactors, requires nuanced consideration of the optimal conditions - all the more so if two or three functions (such as reaction and separation) are being carried out in the same vessel, in which case different flow zones may be desirable.

To achieve such particular and specific conditions in a vessel which must be large to accommodate bulk flows is a demanding task unlikely to be accomplished by a

trial-and-error approach. In the past, room temperature physical modelling has been used to attempt this task, but only general information can normally be obtained because of the impossibility of exact similitude in situations with complex multiphase effects, reactions, high temperatures, etc. As an alternative, computational fluid dynamics (CFD) modelling provides a powerful tool to assist in improving these processes or designing new processes and equipment by simulating actual reactor conditions.

While there has been welcome development of powerful and versatile commercial CFD solvers (eg ANSYS CFX, 2002), the degree of difficulty in obtaining realistic yet practical models of processes in the minerals and energy domains should not be underestimated. The challenge is to represent the critical multi-phase flow physics and chemistry sufficiently realistically that factors limiting performance can be analysed, yet at the same time design the model so that it can be run in industrially-useful timescales. This may be called the pragmatic modelling approach. It requires the highest level of expertise in fluid dynamics modelling and numerical analysis, as well as the ability to interface effectively at all stages of the modelling process with process expertise, engineering requirements and experimental programs.

Pragmatic modelling generally seeks to answer a limited range of specific questions about a system to assist in design or process improvement, rather than seeking to build a "virtual reality" that would mimic every aspect of a system exactly. While this latter type of model is the ultimate aspiration, industrial-scale multiphase systems are too complex to achieve anything of this sort at present. This means that some aspects of such systems must be modelled, rather than relying on brute-force simulation to produce a virtual reality. (Modelling here means invoking physical and chemical laws to approximate a system by equations of lower order; as opposed to simulation, which implies computing the behaviour of a complex system simply by performing a huge number of basic calculations at an element level. Pragmatic CFD inevitably involves a mix of modelling, in this sense, and simulation.) Though perhaps counter-intuitive, well-designed pragmatic modelling of this kind requires far greater expertise than brute-force simulation.

Staging can be a valuable aspect of modelling. A pragmatic staged approach is schematically represented in Figure 1. Staging of CFD model development is advisable to ensure that model results are reliable as each new degree of complexity is introduced. The approach shown above integrates this procedure into a feedback loop where the results at each stage are interrogated to determine implications for process improvement. In this regard, the modeller should heed the maxim expressed by Glasscock and Hale (1994), that 80% of the benefit comes with the first 20% of model complexity! Such staging can lead to a productive cycle of innovation, whereby both process productivity and modelling development benefit.

In this paper we will consider several of the complexities involved in reacting multi-phase processes, and how to pragmatically deal with these, using examples from the resources industries as illustrations of the approach.

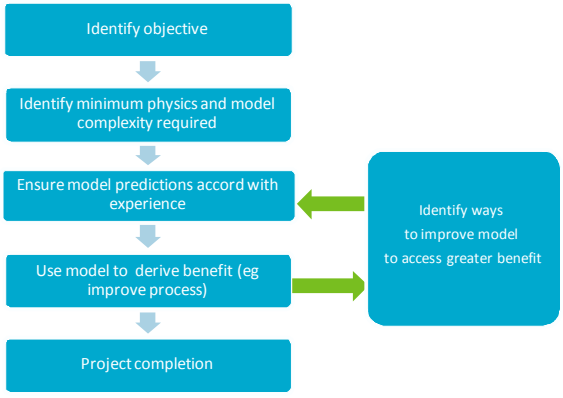

Figure 1: Flow diagram representation of a pragmatic staged approach to CFD modelling.

MULTIPHASE INTERACTIONS

Modelling Techniques

There is a vast literature on modelling techniques for multiphase flows which can be classified as dispersed or separated. The focus here is on dispersed flows, that is, flows in which an ensemble of many bubbles, droplets or particles moves within a bulk, continuum fluid; techniques for separated flow, while certainly non-trivial, tend to be more straightforward to develop and implement.

The continuum is almost always modelled by Eulerian flow equations solved using finite volume or finite element techniques over a discretised mesh (one exception being Smoothed Particle Hydrodynamics, see Monaghan, 2012).

Techniques for the dispersed phase could be conveniently categorised into three types:

- Particle tracking (Lagrangian)
- Multi-fluid (Eulerian)
- Direct simulation

Particle tracking is in principle straightforward, and is ideal for low dispersed phase loadings: most techniques of this kind do not account for the volume of the phase, nor intra-phase interactions, though particle-particle collisions are now being allowed for in coupled CFD-DEM models (Feng and Yu, 2007) and versions of the Particle-in-Cell method such as Barracuda (Snider, 2001). These limitations mean that most practical industrial modelling of large-scale dispersed systems uses the multi-fluid method as the pragmatic approach.

Multi-fluid techniques are however substantially more complex, both conceptually and in practice. The equations can be derived rigorously by averaging the

exact equations for multiple phases (by ensemble-, time- or space- averaging; see the work by Drew and co-authors, Drew, 1983, Arnold et al., 1988, Kashiwa and VanDerHeyden, 2000), giving:

Continuity equation

$$\frac{\partial \alpha_i \rho_i}{\partial t} + \nabla \cdot \left(\alpha_i \rho_i \mathbf{u}_i \right) = 0 \qquad (1)$$

Momentum equation

$$\frac{\partial \alpha_i \rho_i \mathbf{u}_i}{\partial t} + \nabla \cdot \left(\alpha_i \rho_i \mathbf{u}_i \mathbf{u}_i \right) = -\alpha_i \nabla p + \nabla . \alpha_i \mu_i \nabla \mathbf{u}_i + \mathbf{S}_i + \mathbf{M}_i \qquad (2)$$

However, terms appear in the averaged equations that cannot be evaluated and must be modelled, and the usual way of proceeding is to heuristically relate these terms to physical forces (eg drag, lift, virtual mass, etc.) and then replace them by expressions obtained from experiment or a combination of experiment and theory (e.g. Ishii and Zuber, 1979). The rigorous averaging step is important because the form of some of these terms can be non-intuitive (e.g. the terms to account for turbulent diffusion when using Favre averaging, Burns et al., 2004). In general, terms other than drag are often poorly known, particularly when turbulence is involved. For example, the classical Saffman and Magnus lift forces are known for isolated rigid particles under limiting Reynolds number conditions, but bubbly flows allow no accurate theoretical description (Sokolichin et al., 2004).

The pragmatic approach is to determine constants in expressions for interphase interaction terms from experiment: simple experiments that seek to isolate the specific interaction and/or simplified archetypes of the process conditions involved. The important aspect of the approach is that the form of the expressions used should be based on sound multiphase physics (and chemistry where appropriate). This then maximises the range of applicability of the fitted expressions.

The third category of multi-phase model, direct simulation, attempts to solve the exact equations at the particle/bubble/drop scale for a large ensemble. DEM methods are used for particles (though even here modelling must be invoked for the inter-particle forces), moving embedded grid and immersed body grid techniques can be used for particles or non-deformable drops or bubbles, while free-surface methods must be employed for deformable drops or bubbles. In general direct simulation is still not possible for most industrial scale systems, but it can be valuable for sub-domains, (see the discussion in the Multi-scale Interactions section of this paper). This approach is only now beginning to be used to determine more reliable expressions for multi-scale interactions for use in multi-fluid simulations.

Turbulence

Derivation of the multi-fluid equations for turbulent multi-phase equations involves double averaging (either explicitly or implicitly) – over turbulence (Reynolds averaging) and over phase structure (Elghobashi and AbouArab, 1983, Kataoka and Serizawa, 1989). This results in terms that contain correlations between turbulence fluctuations and phase fluctuations, evaluation of which cannot be done heuristically. Resolution of this complexity requires more detailed modelling (e.g. Large Eddy Simulation, LES, or Direct Simulation) backed by careful and detailed experimental measurements. An example is the work on stirred tanks by Tabib and Schwarz (2011) and Tabib et al. (2012). A thorough analysis of LES techniques for multi-phase flows has been given by Fox (2012). As he has pointed out, the probability density function formalism for deriving the multi-fluid equations (Pai and Subramanian, 2009) may be more suitable than averaging for determining closures, particularly for determinations based on meso- and micro- scale simulation "experiments".

Of most importance is the effect of particles and bubbles on turbulence. It is found from experimental studies that large particles and bubbles generate additional turbulence whereas small particles have the effect of damping turbulence (Crowe, 2000). Turbulence is generated in the wakes of large particles and bubbles, and various expressions have been proposed to account for this effect, with parameters that need to be derived from experiment. Unfortunately, there is no general agreement on a definitive expression at this stage. The damping effect caused by small particles results from the lag in response of a particle to random eddy movements. Expressions have been derived for this effect dependent on the ratio of particle size to turbulence length scale (Crowe, 2000), Stokes number, or force considerations (Kataoka and Serizawa, 1989).

Diffusion (dispersion) of a particulate or bubble phase can be problematic to model. Diffusion of a bubble plume in an industrial application was first introduced by Boysan and Johansen (1985) and Johansen et al. (1987) in Euler-Lagrangian simulation, and by Schwarz and Turner (1988) in Euler-Euler simulation; they showed it could have a substantial effect on predicted plume velocity. In the case of bubble plume, diffusion is caused both by turbulent dispersion and bubble-wake interactions, which in the simplest case of a single spherical bubble is described as the "lift force", but in the case of a swarm of bubbles, some of which are highly distorted and wobbling, is rather more complex. Moraga et al. (2003) discuss some of these complexities in more detail.

Unexpected particle-turbulence interaction effects also occur. Brucato et al. (1998) found that the slip velocity of particles/bubbles decreases as the particle size increases relative to the turbulence scale, and Lane et al. (2005) showed that local voidage values could not be correctly predicted for a stirred tank with air sparging,

unless this effect is taken into account in the multi-phase CFD model. Further data was obtained by Doroodchi et al. (2009), but the effect is still not well understood. It may be that it reflects varying degrees of centrifuging of particles/bubbles to the edges/centres of turbulent eddies.

As with the multi-phase closures discussed in the previous section, the pragmatic approach seeks to use the best physics knowledge available together with empirical constants obtained from available experimental data to develop expressions for the turbulent multi-phase closures. Pragmatism demands a high level of understanding of the flow physics involved, together with the ability to design and interrogate experiments to develop the sub-models required for the CFD simulations.

Transient Flows

Turbulent flows are of course time-dependent, but this dependence is generally removed by Reynolds averaging, resulting in effectively steady-state equations. When unsteadiness is forced by impellers or pulsing, it is found that U-RANS (Unsteady Reynolds Averaged Navier-Stokes) models such as k-ε perform well: good agreement has been found for stirred tanks (Lane et al., 2000) and for periodic variation in a pulsed column (Bujalski et al., 2006).

However flows can also be subject to internally generated large-scale instabilities that are not properly described as turbulence, and this is particularly so for multi-phase flows. Straightforward application of U-RANS can result in damping of the large-scale unsteadiness that one wishes to capture, and one approach to overcome this is to use LES.

An important example of an industrial reactor in which such phase-driven unsteadiness is a major characteristic of the flow is the fluidised bed, models of which were pioneered by Gidaspow (1994) and implemented first in CFX by Witt et al. (1998). In bubbling beds, it is believed that damping due to the high solids loading prevents any shear-related turbulence, so the continuum is modelled with a laminar assumption. The same assumption is used to model fast fluidisation and circulating fluidised beds, although its validity is likely to be questionable in the lean regions.

A pragmatic compromise between U-RANS and LES, (dubbed Very Large Scale Eddy Simulation, VLES) was used by Schwarz (2001) and Davis et al., (1998) to simulate gas-agitated baths. This technique has been placed on a firmer footing for certain single phase flows by Labois and Lakehal (2011) (see also Johansen et al., 2004).

In some cases capturing the transient behaviour fully in a CFD simulation may be beyond what can be achieved in an industrially-relevant time-frame. Other modelling techniques can then be called upon to complement the steady-state CFD simulations. An example is the coupling between bubble plume dynamics and surface wave motion in a system such as ladle refining. Schwarz (1990, 1995) developed a mathematical model for the coupling that could be used in a pragmatic way together with a steady-state multi-fluid model of the bubble plume to provide a more complete picture of the flow dynamics in the system.

Example of a Gravity Thickener

Gravity thickeners are large tanks used to separate fine solids from slurries by flocculating them into aggregates. The solids then settle more readily to a bed which can be readily removed via an underflow. Modelling of thickeners was conventionally confined to one-dimensional modelling of bed consolidation until CSIRO researchers recognized that upstream conditions and flocculation performance would substantially control the effectiveness and extent of bed consolidation. This together with the introduction of three-dimensional multiphase CFD modelling revolutionized the understanding of thickeners. This research has been conducted at CSIRO through a long-running series of projects (labeled P266), substantially funded by the mining industry through its research broking organization, AMIRA International.

One of the first important findings was that density currents, flows generated by differences in effective slurry density from one part of the tank to another, can be remarkably strong. The density differences arise from differences in solids concentration, and are most pronounced when the feed has a reasonably high solids concentration, say more than 5%. In such situations, the feed stream can sink quite rapidly out of the feedwell, without mixing into the dilution streams being entrained into the well, as illustrated in Figure 2 (Johnston et al., 1996). The most serious situation arises when the feed-stream leaves before mixing with flocculant, as this results in both poor flocculation and waste of expensive flocculant. Kahane et al. (1997) showed that use of CFD could ensure that flocculant sparges were optimally placed for mixing into the feed, and that shelves could be used to reduce the short-circuiting induced by density currents. In fact, in one case (at Worsley Alumina) such design changes were so successful that the throughput could be doubled with no degradation in performance, saving the company millions of dollars in capital and operating costs (Kahane et al., 2002).

Perhaps the most remarkable aspect of the CFD modeling behind this initial research is that it incorporated very little of the flocculation mechanisms themselves, and did not include the presence of the bed. This highlights an aspect of pragmatic modeling – that a model does not need to incorporate all the detail of a process to be valuable.

To guide more refined design changes, the CSIRO model has been extended in stages to include aspects of the flocculation process. Schwarz and Johnston devised a model for flocculant mixing and adsorption onto particles (Kahane et al., 1997) which has been used

extensively to assist many sponsor companies improve their thickener design and performance (Kahane et al., 2002). More recently, Heath and Koh (2003) have incorporated a full population balance model for aggregate size within the CFD model, and the model has been extended to further enhance the diagnostic capability (Nguyen et al., 2006).

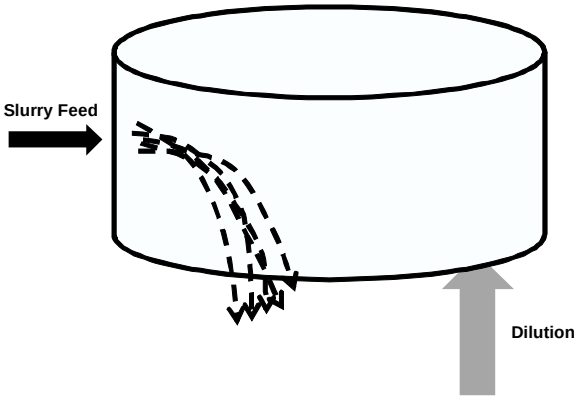

Figure 2: General behaviour of slurry feed in thickener feedwells found from CFD modelling (after Kahane et al., 1997).

COMPLEX PHYSICS AND CHEMISTRY

Additional variables that must commonly be solved for in CFD simulations are temperature and species concentration, as expected for applications involving heat and mass transfer. In the simplest situation, this is done by solving the standard advection-diffusion equation. However the situation quickly becomes more complex when reactions, solidification, melting, etc., are involved. Techniques are well established for homogeneous turbulent reacting systems (e.g. gas phase reactions), but when reactions involve particles, drops or bubbles, care must be taken to properly account for boundary layer diffusion, chemical kinetics and surface effects. These are all very situation dependent.

One of the most prevalent reaction systems in industry is combustion, and coal combustion is a multi-phase system for which there has been some effort developing CFD modelling techniques (Stopford, 2002), but the wide variety of properties of coal used and the complex fluid dynamics of multiple interacting industrial-scale jets mean that these are still challenging systems (see, e.g., Tian et al., 2010).

Other physical effects that can be important include particle attrition, surface erosion, droplet and bubble coalescence and breakup, effects due to magnetic and electric fields, Marangoni effects, and so on.

Bath Smelting Model

The HIsmelt Process is an iron-making process based on molten iron bath smelt-reduction (Davis et al., 1998). Iron ore fines and coal are injected into the iron bath through submerged inclined lances. Coal is devolatilised and carbonises the iron bath; iron ore reacts with the carbon to generate large volumes of CO gas, which, together with the volatiles, throw iron and slag drops and streamers into the topspace of the smelting vessel. The CO and H_2 gases are burnt in the topspace in a swirled flame, and the heat returned to the bath by slag droplets. It is important that iron drops are not oxidised in the oxidising atmosphere of the topspace. Designing and scaling-up the process thus involved many challenges, and CFD modelling was applied extensively to assist using a staged pragmatic process, as suggested in the Introduction.

Development of a CFD model of the smelting bath (Schwarz, 2001, Schwarz and Davis, 2011, Stephens et al., 2012) required linking together multi-phase techniques with considerable physics and chemistry that required experimental inputs. The two liquid phases (slag and metal) are agitated extremely vigorously by very large rates of submerged gas generation. The first pragmatic decision made was to split the problem into a "bath model", which involves considerable transient multi-phase complexity, and a "topspace model", which focuses on gas-phase combustion with heat and mass transfer to droplets. The splitting allowed faster development of each model, and, since the latter is steady-state, more rapid evaluation of design options.

The two models are coupled primarily by means of the fountain of droplets generated by the bath – fountain characteristics (mass, height, etc) determined by the bath model were fed into the topspace model. Because of the long run-times for the bath model, a "correlation", based on semi-theoretical derivation and fitted to "data" from a limited number of CFD simulations, was used to interpolate fountain characteristics for design investigations. Surrogate modelling of this sort can be a successful feature of a pragmatic approach.

The bath was initially modelled using a two-phase model of gas injection into a molten iron bath (Schwarz et al., 1987, Schwarz, 1995), with an "instantaneous-reaction rate" model i.e. gasses generated instantly from coal devolatilisation and ore reduction. Data from water, molten tin and molten iron baths were used for validation.

A slag phase was later added, with the three phases treated by the multi-fluid (Eulerian) technique, and the interaction between the two liquids was treated with the algebraic slip (or mixture) model. Coal and ore particle tracking was also added using the Lagrangian technique, with the particles able to penetrate into the liquid phases, where they then react, generating gases. Simplified reaction kinetics were designed to capture important timescales of both coal devolatilisation and ore reduction, without attempting to simulate all the details of what are extremely complex interaction phenomena at the particle scale.

A considerable amount of experimental work, both in the laboratory and from pilot plant, was done to assist

the development and validation of the model at various stages of its advance (Schwarz, 2001, Schwarz et al., 2011).

Keys to the success of the pragmatic approach were: staging of the development, with the model assisting design and scale-up along the way; close-coupling of modelling with plant trials and experimental work, with modelling suggesting further experimental work and engineering considerations driving modelling developments; and an objective-driven team approach.

An example of the computed liquid distribution on one plane through the reactor at one instant of time is shown in Figure 3. Gas (red) generated near the tips of the lances throws splash in the form of drops and streamers up into the topspace of the vessel. The positioning of the lances is critical to ensuring that gas is generated in appropriate locations to drive the required amount of splash to the required height in the vessel. The fountain of slag splash must be positioned so as to enable transfer of heat back to the iron bath, but also to ensure that iron is not re-oxidised by the topspace atmosphere.

Figure 4 shows typical computed trajectories of ore particles in the CFD model of HIsmelt reactor. The red tracks show the jets from the lances, while the orange tracks show particles at various degrees of reaction. Results of such models were used to determine fountain characteristics such as height, mass, and position relative to the top jet flame, and hence assist design of injection configuration and lance positioning. CFD modelling was a critical component of the process development which resulted in successful operation of a demonstration-scale plant (nominally 0.75 Mt/yr).

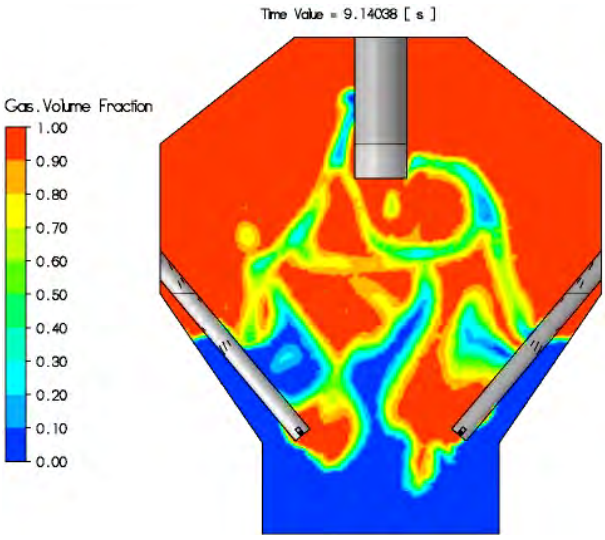

Figure 3: Gas volume fraction contours and splashing of liquid at one instant of time in CFD model of HIsmelt reactor. From Stephens et al. (2012).

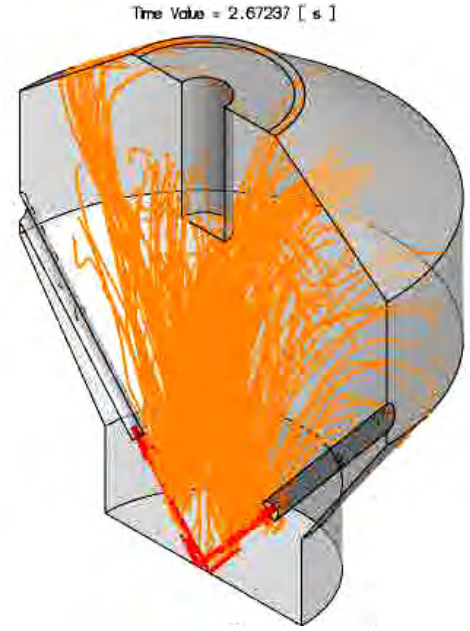

Figure 4: Typical computed trajectories of ore particles in CFD model of HIsmelt reactor. From Stephens et al. (2012).

FCC Regenerator Model

The FCC (Fluidised Catalytic Cracker) regenerator is a turbulent fluidised bed in which catalyst is regenerated by burning off the coke deposited during cracking. In the facility at the BP Bulwer Island refinery, air and oxygen enriched air is injected through distributor rings near the base of the bed and as carrier gas for catalyst being returned from a cooler (Schwarz and Lee, 2007). Prior to 2006, there had been some indications that the regenerator performance could be improved, for example, measurements showed temperature differences from one side of the vessel to the other. Catalyst performance is sensitive to overheating, so optimum performance of the regenerator would be obtained with a uniform internal temperature.

As mentioned previously, fluidised beds can be modelled using the two-fluid approach in which the solids phase is treated as a quasi-fluid. This is a sensible pragmatic approach, but it must be remembered that interaction terms such as drag, solids pressure and solids viscosity can be quite complicated. Particles tend to cluster in turbulent (and fast) fluidisation, but the small-scale structures (i.e. clusters) are too small to be captured in industrial simulations. As a result, drag is far too high if the single-particle drag formulation is used. While techniques are being developed to overcome this problem (e.g. Li et al., 2010), no entirely satisfactory solution exists. In this work, a pragmatic approach was adopted, in which effective cluster size was determined from experimental pressure drop.

A pragmatic approach was also applied to modelling combustion, with reactions limited to four species, and kinetics determined from experimental work. One additional element needed to be added to the modelling strategy: the fluidised bed model requires a very short

timestep (of order ms) for stability, yet the thermal timescale is of order many hours. To address this issue, a specialised averaging technique was developed (Schwarz and Lee, 2007): a smart pragmatic approach as opposed to brute-force integration which would not have been possible in a realistic time-frame.

A relatively sophisticated multi-phase reacting model of the regenerator could then be developed: analysis using the model together with plant experience identified likely by-passing by some oxygen through the bed. The model was then used to trial possible modifications to the catalyst return distributor, identifying one which was likely to improve the situation. When implemented in the plant, the modified distributor resulted in improved oxygen utilisation and increased temperature uniformity (Schwarz and Lee, 2007).

Figures 5 and 6 illustrate the computed gas distribution and catalyst flow field on one plane through the regenerator before the modifications were made.

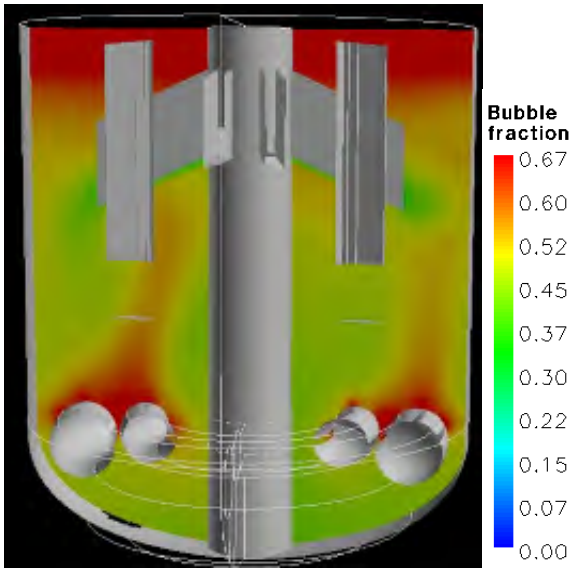

Figure 5. Computed time-averaged bubble fraction plotted on a vertical plane bisecting the regenerator for the original configuration. From Schwarz and Lee (2007).

MULTI-SCALE INTERACTIONS

Techniques

Techniques for multi-scale modelling have been pursued with enthusiasm and some success in the field of materials science. However, attempts to develop a methodology for CFD simulations of complex process applications have not progressed far, though some mathematical methodologies have been formulated for single phase flows and for porous media applications in the oil and gas industries where the technique is known as up-scaling.

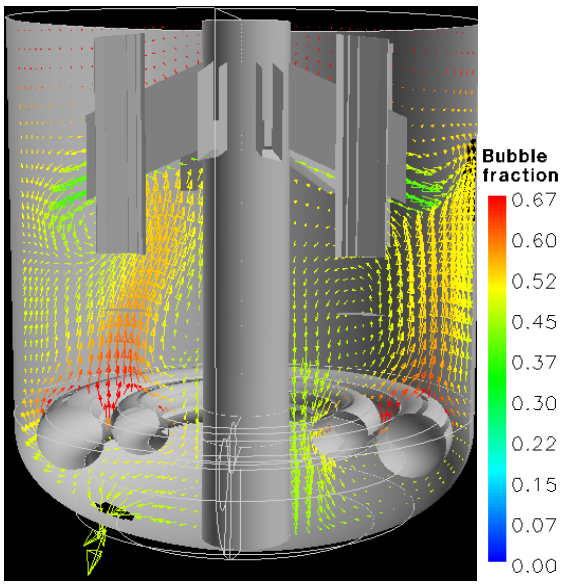

Figure 6. Computed time-averaged vector velocities plotted on a vertical plane bisecting the regenerator for the original configuration. Vectors are coloured by bubble fraction. From Schwarz and Lee (2007).

Multi-phase processing-related flows are often rich in phenomena occurring at a wide range of length and time scales. Of course turbulence itself is a multi-scale phenomenon, where the length scales are widely separated in the case of high Reynolds number, and well developed techniques exist, supported by a huge experimental data base.

Many of the characteristic scales in processing applications are defined by the length-scales of phase structures, e.g., bubbles, particles, drops, etc., and although multi-phase modelling techniques can be used to simulate a wide range of related effects, many of the terms remain uncertain, and more complex interactions are simply beyond standard methods.

E (2011) has summarised and categorised multi-scale modelling methodologies. Some researchers define multiscale modelling narrowly as simulation at various scales simultaneously (termed concurrent by E): the quantities needed in the macroscale model are computed *on-the-fly* from the microscale models as the computation proceeds. Development of computer algorithms and programming necessarily plays a large part in this approach. On the other hand for complex processing applications, sequential multiscale modelling has been found to a more fruitful approach at CSIRO. E defines this method to be one in which some details of the constitutive relations in a macroscale model are precomputed using microscale models. This is a more efficient approach when the microscale simulations are time-consuming, and the macro-scale simulations require results from many points of the micro-scale parameter space (in the case of CFD models, results are typically required at many spatial points, at many times, and at many stages during the convergence procedure).

Such multi-scale modelling has the characteristics of pragmatic modelling, since it aims to use smart techniques to avoid the pit-falls of a straightforward brute-force approach.

An intrinsically multi-scale system of importance in process engineering is the fluidised bed. As mentioned, hydrodynamic instability leads to the formation of particle clusters, particularly in turbulent and fast fluidisation, and these cannot normally be fully resolved in simulations of very large systems such as industrial-scale circulating fluidised beds (CFB). Multi-fluid models of CFB risers in which gas-solids drag is given by the single particle value predict incorrect solids velocity. One approach to solve this issue is the EMMS (energy minimization multi-scale) model (Li et al., 2010), in which an equation based on energy minimisation is effectively solved for cluster size as a function of position in the riser; this diameter is then used in a multi-fluid simulation.

On the other hand, Igci and Sundaresan (2011) have used the sequential multiscale modelling approach as defined by E (2011): they present a methodology where computational results, obtained through highly resolved micro-scale simulations of gas-particle flows, are used to improve macro-scale models. Results from microscopic models are filtered to deduce models for the residual correlations (or closures) appearing in the corresponding filtered two-fluid model (TFM) equations that are appropriate for coarse grid simulations (their so-called coarse grained equations). Using the kinetic theory-based TFM, they obtained computational data on the filtered drag coefficient, the filtered particle phase pressure, and the filtered particle phase viscosity, which they reduce to the form of correlations that can readily be employed in coarse-grid simulations.

This sequential approach has been taken at CSIRO for the complex multi-phase system involved in mineral flotation. Detailed models of particles in a turbulent stream flowing past a single rising bubble (Liu and Schwarz, 2009) have led to improved expressions for collision rates and hence particle-bubble attachment rates. These can be used to improve macro-scale models of the entire flotation cell (Koh and Schwarz, 2008) in which statistical techniques must be used to quantify attachment rates. With such a complex process with length scales of importance ranging from metres down to the nano-scale, experiment inevitably plays an important role. Verrelli et al. (2014) have designed a well-controlled experiment to study the attachment process with interactions occurring in a realistic way, as in industrial flotation. In the following sub-section, we summarise a similar approach being taken for a smelting process.

Aluminium reduction cell modelling

Aluminium is produced industrially by electrolysis in the Hall-Heroult process: an electrical current is passed between carbon anodes partially submerged in a bath of molten cryolite electrolyte and a cathode on which a pool of molten aluminium forms. Alumina is dissolved in the cryolite and CO_2 bubbles are evolved on the bottom surface of the anodes as a result of the reduction. The bubbles slide along the anode until they reach channels in which they can rise to the electrolyte surface. As they rise, they drive recirculating flows in the cryolite that are critical to the process: the flows assist in the dissolution and mixing of alumina normally fed at a small number of discrete points in the cell, and they are critical to the maintenance of a stable frozen cryolite layer (or “ledge”) on the side walls of the cell which protects the walls from chemical attack by the molten cryolite.

Feng et al. (2010) have developed a two-fluid model of bubble driven flow in the cell to investigate issues such as alumina dissolution, heat transfer to the ledge, and minimisation of the bubble-related component of electrical resistance by reducing the hold-up of bubbles under anodes. The model was validated using PIV (Particle Image Velocimetry) measurements of velocity in an air-water physical model of a cell built at industrial scale and comprising three anodes. Figure 7 compares the water velocity distribution over a horizontal plane just below the anodes obtained with a two-fluid CFD simulation with that measured by PIV. The measurement plane is halfway between the base of the anodes and the bottom of the water bath; since water is used to simulate the electrolyte, the bottom of the water bath represents the boundary between cryolite and molten aluminium.

The agreement between model and measured flows found in Figure 7 is remarkable given the complexity of the pattern, and the sensitivity of the flow to minor perturbations – the lower faces of the anodes are all flat and horizontal, so bubbles do not *a priori* have any preferred direction of travel along the faces. In reality the bottoms of the anodes wear to a somewhat rounded shape, which then biases the movement of bubbles in the direction dictated by buoyancy.

It is believed that bubbles initially form in the fine sub-millimeter size range and coalesce as they move under the anodes. The complexity of bubble shape, contact angle issues at the surface of anode, bubble coalescence (and breakage in the vertical channels), and other such phenomena cannot be accounted for in the two-fluid model with standard sub-models. The approach being pursued is to use a VOF (Volume of Fluid) approach to simulate individual bubbles to determine constitutive relationships for the multi-fluid macro-model (Zhang et al., 2013).

Figure 8 illustrates bubble shapes calculated with such a VOF model by Zhang et al. (2013). Three different bubble sizes are shown sliding under an anode base inclined at 1.5° to the horizontal. The shapes and thicknesses calculated for an air-water system (Figure 8(a)) are in good agreement with experimental observations in such physical models. Figure 8(b) shows the corresponding computed bubble shapes for a

CO_2-cryolite system. The shapes are very similar, lending support to the use of air-water models to study electrolyte dynamics, though the thickness of the bubbles is less for the real CO_2-cryolite system.

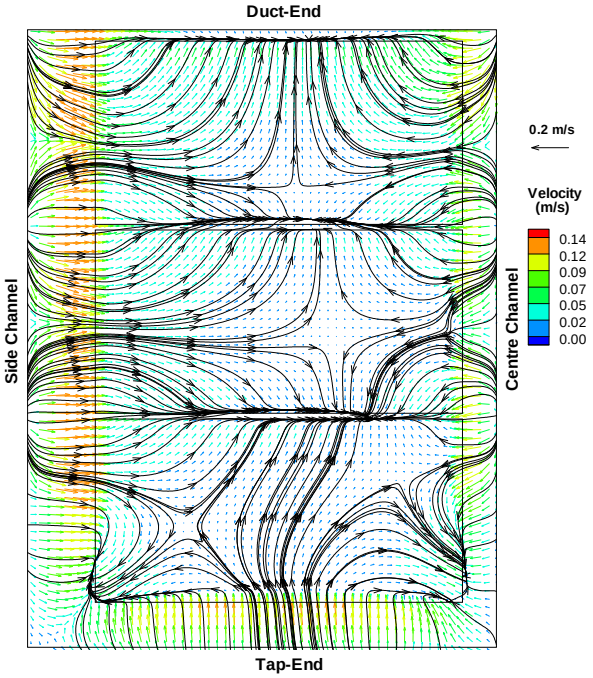

(a) CFD

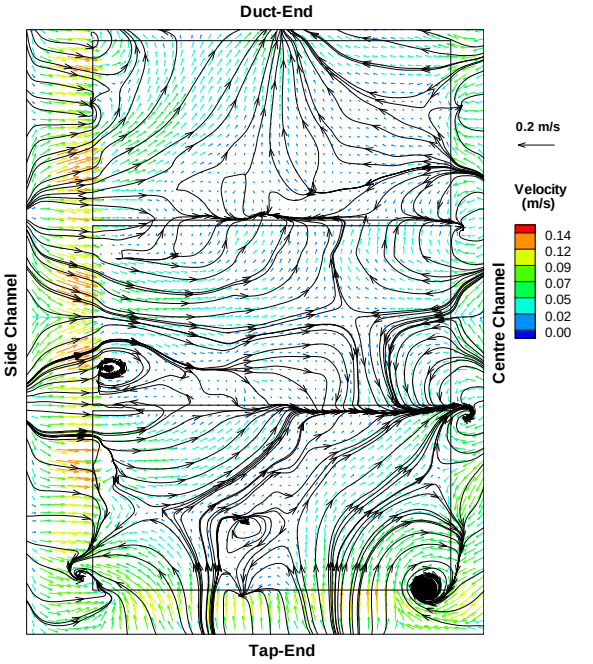

(b) PIV

Figure 7: Water velocity distribution over a horizontal plane in the middle of anode-cathode gap: (a) CFD simulation; (b) PIV measurement. From Feng et al. (2010).

Standard closure relationships for drag and other interphase interactions do not exist for the unusual bubble shapes shown in Figure 8, and indeed the motion of those bubbles along the bottom surface of the anodes also invalidates the use of standard closures. The multi-scale approach adopted here aims to determine the closures from such micro-scale simulations by treating them as numerical "experiments". Examples of quantities that can be readily determined are bubble size, shape and drag coefficient, and the results can also be interrogated for more complex characteristics such as bubble-turbulence interactions.

VALIDATION AND UNCERTAINTY

It is important that CFD models are validated so that they can be applied with confidence. There are two quite different processes involved in ensuring that a CFD model is reliable. The first entails ensuring that the intended algorithm for solving the discretised equations has been properly coded, that the solution converges to the actual solution as the mesh and time-step are refined. When using a commercial code, much of this process has already been done, but given the necessity to incorporate process specific physics and chemistry, it is important that additional checks are done by the user. For multi-phase flows, this checking process should be conducted against behaviour expected by analysis of the equations (usually for simplified cases), not against experimental data, which is always subject to uncertainties.

The second process of model validation entails ensuring that the equations, and especially the terms for complex physics and chemistry, correctly represent the actual physics and chemistry. This is a much more complex process because, as mentioned, constitutive closures for complex multiphase situations are generally poorly known. Development and validation of a CFD model is often undertaken in a stage-wise fashion, with targeted laboratory experiments designed to assist specific aspects of the physics and chemistry implementation. Finally, the model is preferably checked against some measurements taken from the actual plant: often these will be more integral in nature (e.g. pressure drop or overall reaction rate), or a limited number of point measurements of quantities such as velocity, temperature, and concentration. By their nature, these data are intrinsically less useful for model development or improvement than for assessment of model reliability.

Detailed flow measurements are always difficult to make in complex multi-phase flows because of issues such as lack of transparency to visible light, high levels of turbulence, other sources of variability, and biasing effects whereby average measurements are often weighted to either high or low levels of dispersed phase volume fraction. Additionally, detailed measurements are usually constrained to room temperature non-reactive physical models of the actual system, whereas reaction and temperature effects can interact in a significant way with flow behaviour. To overcome this limitation, one can use a multi-scale modelling approach, whereby constitutive relationships are derived on the basis of micro-scale computational models which can capture the actual physics and chemistry more exactly than a macro-scale model of the entire process. This approach has been described in the section Multi-scale Interactions, with an example of the aluminium reduction cell: micro-scale models can capture the movement of CO_2 bubbles in molten

cryolite under an anode with more reliability than air-water physical models.

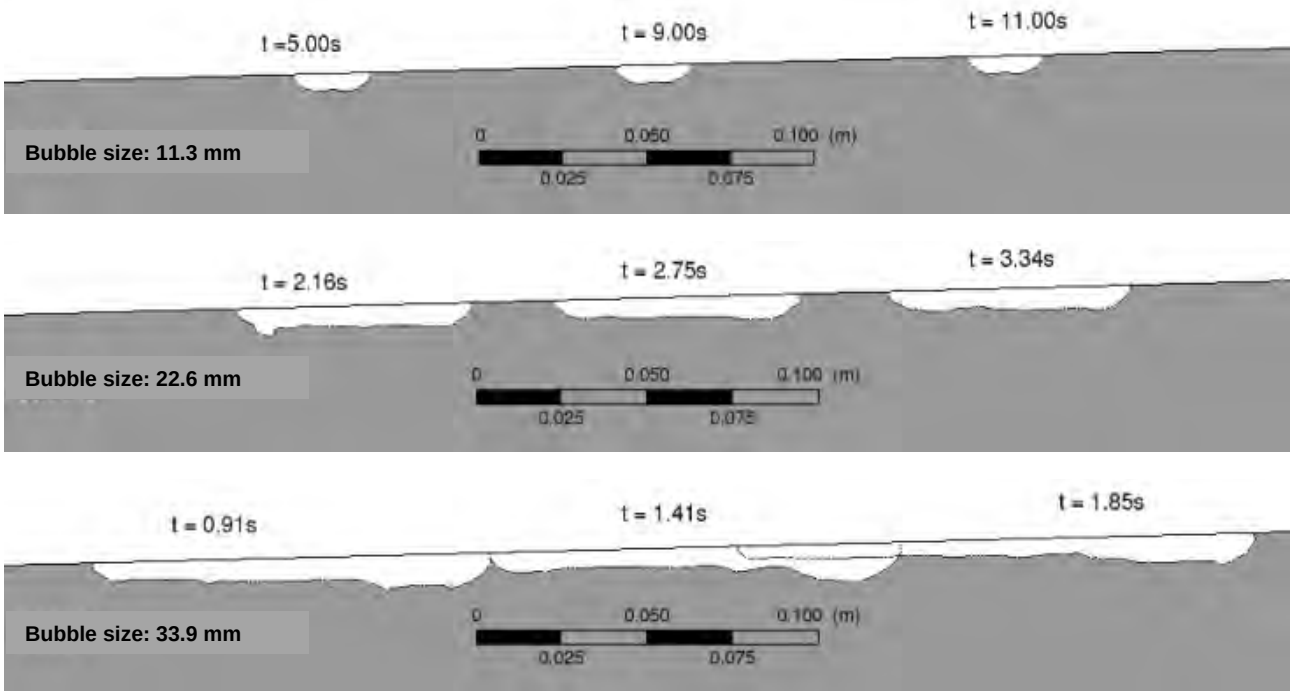

(a) Air-water system

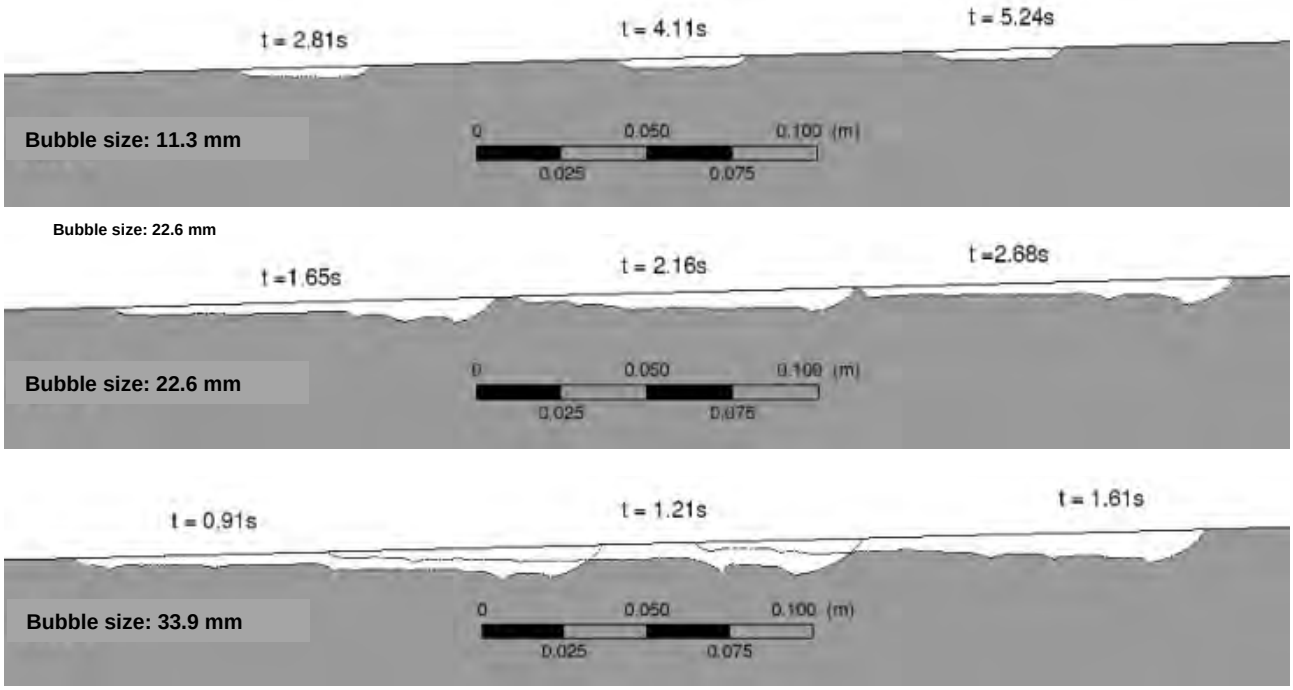

(b) CO_2-cryolite system

Figure 8: Computed bubble shapes for bubbles of three sizes sliding along the bottom surface of an anode in (a) an air-water system, and (b) a CO_2-cryolite system.

The reality of financial pressure in industry means that CFD modelling will often be carried out using standard constitutive relationships together with minimal checking of model behaviour against plant experience. While this is less than ideal for complex processes, modelling results using this approach can still indicate likely paths for process improvement.

As CFD modelling becomes more mainstream, there are increasing demands for uncertainty (or error bounds) to be provided with results. While this is possible for simpler single phase flow situations where uncertainties are dominated by numerical considerations (Karimi et al., 2012), it is much more challenging for multi-phase process applications, where uncertainties are typically dominated by uncertainties in constitutive closures and the representation of the multi-phase physical and chemical interactions. No general procedure exists for assessing uncertainty in such situations, though parameter sensitivity tests can certainly be valuable.

Such an assessment carried out thoroughly is expensive and requires some knowledge of possible ranges in values for parameters from correlations used to describe physics and chemistry. Drzewiecki et al. (2012) were able to carry out such an assessment for a well defined benchmark case because of the limited run times needed for the two-dimensional model used. Gel et al. (2013) avoid the high cost by utilising a surrogate model to propagate uncertainties in inputs through to the end results. Another approach involves comparison of predictions with measurements from plant if available. Care must be taken here however, since experimental uncertainty is rarely properly assessed for plant measurements, plagued as they are by factors such as variability and uncertainty in feed rates and characteristics: measurement error is often not the major source of uncertainty.

Though it will be far from straightforward, research should be conducted on methods of uncertainty assessment for complex multi-phase flows. Furthermore, canonical flows involving reasonably complex but well-defined multi-phase situations should be identified and characterised with a high degree of accuracy as a platform for model validation and uncertainty.

CONCLUSION

Resource processing operations are complex, involving multi-phase and multi-scale effects as well as other physical and chemical phenomena. Detailed flow-based computer models incorporating these effects are the obvious design and optimisation tool, but must be developed with care to ensure they are realistic, predictive and applicable on industrially-relevant time-frames. Expert pragmatic modelling employs suitable approximations to achieve this aim.

Multi-fluid techniques are presently the most versatile and well-developed methods for modelling complex industrial-scale multi-phase processes, and have been shown to be valuable in improving the efficiency of existing processes and equipment such as gravity thickeners and in assisting the development of new processes such as the HIsmelt Process. This approach does not seek to simulate every individual bubble, particle, or droplet, but uses physical, chemical and engineering expertise to model their interactions.

The following guidelines should be followed to ensure optimal outcomes:

1. Staging of model development, with process implications being sought at each stage and feedback from plant to model, results in faster industrial application, and can lead to a productive innovation cycle.
2. Close coupling with process engineers during staged development ensures that the model is designed to address critical issues, and that it reflects observed plant trends.
3. Constitutive closures for interphase interactions necessarily involve empirical input for moderate-to-high dispersed phase loadings in turbulent flow regimes. Expressions for interphase interactions should however be based on sound physical and chemical principles, albeit with fitting parameters.
4. RANS methods appear to be satisfactory for transient flows resulting from imposed forcing, but processes with internally generated flow instabilities may be better tackled with multi-fluid large eddy simulation (LES) methods.
5. Sequential multi-scale modelling using meso- and micro-scale models is a powerful tool for determining constitutive closures and improving macro-scale models of micro-scale physical and chemical processes.
6. Effort needs to be undertaken to refine validation methodologies and to identify ways to assess prediction uncertainty.
7. Teamwork is often a hallmark of successful process design and optimisation using CFD, since sophisticated interfacing with experimental, plant, process engineering and chemistry expertise may be needed.

ACKNOWLEDGEMENTS

The authors wish to thank CSIRO for permission to publish this paper, and all our colleagues and collaborators for their contributions.

REFERENCES

ANSYS CFX 10 User manual, ANSYS Inc. (2002)

ARNOLD, G.S., DREW, D.A. and LAHEY, R.T., (1988), "Derivation of constitutive equations for interfacial force and Reynolds stress for a suspension of spheres using ensemble averaging," *J. of Chem. Eng. Comm.*, **86,** 43-54.

BOYSAN, F. and JOHANSEN, S.T., (1985), "Mathematical modelling of gas-stirred reactors", *International Seminar on Refining and Alloying of Liquid Aluminium and Ferro-Alloys*, Trondheim, Norway, Aluminium-Verlag GmbH, Dusseldorf , 1985, pp. 267-288.

BRUCATO, A., GRISAFI, F., and MONTANTE, G., (1998), "Particle drag coefficients in turbulent fluids", *Chem. Eng. Sci.*, **53**, 3295-3314.

BUJALSKI, J.M., YANG, W., NIKOLOV, J., SOLNORDAL, C.B., and SCHWARZ, M.P., (2006), "Measurement and CFD simulation of single-phase flow in solvent extraction pulsed column", *Chem. Eng. Sci.*, **61**, 2930-2938.

BURNS, A.D., FRANK, T., HAMILL, I., and SHI, J.-M., (2004), "The Favre averaged drag model for turbulent dispersion in Eulerian multi-phase flows", *5th Inter. Conf. on Multiphase Flow, ICMF'04*, Yokohama, Japan, May 30–June 4, 2004, Paper No. 392.

CROWE, C.T., (2000), "On models for turbulence modulation in fluid-particle flows", *Int. J. Multiphase Flow*, **26**, 719-727.

DAVIS, M.P., PERICLEOUS, K., CROSS, M. and SCHWARZ, M.P., (1998), "Mathematical modelling tools for the optimization of direct smelting processes", *Appl. Math. Modelling*, **22**, 921-940.

DOROODCHI, E., EVANS, G.M., SCHWARZ, M.P., LANE, G.L., SHAH, N., NGUYEN, A., (2008),

"Influence of turbulence intensity on particle drag coefficients", *Chem. Eng. J.*, **135**, 129-134.

DREW, D. A., (1983), "Mathematical modeling of two-phase flow", *Ann. Rev. Fluid Mech.* **15**, 261-291.

DRZEWIECKI, T.J., ASHER, I.M., GRUNLOH, T.P., PETROV, V.E., FIDKOWSKI, K.J., MANERA, A. and DOWNAR, T.J., (2012), "Parameter sensitivity study of boiling and two-phase flow models in CFD", *J. Comput. Multiphase Flows*, **4**, 411-425.

E, W., (2011), "Principles of multiscale modeling", Cambridge University Press, Cambridge.

ELGHOBASHI, S.E. and ABOU-ARAB, T.W., (1983), "**A** two-equation turbulence model for two-phase flows", *Physics Fluids***, 26**, 931-938.

FENG, Y.Q. and YU, A.B., (2007), "Microdynamic modelling and analysis of the fluidisation and segregation of binary mixtures of particles", *Chem. Eng. Sci.*, **62**, 256-268.

FENG, Y.Q., YANG, W., COOKSEY, M.A. and SCHWARZ, M.P., (2010), "Development of whole cell CFD model of bath flow and alumina mixing", *J. Comput. Multiphase Flows*, **2**, 179-188.

FOX, R.O., (2012), "Large-eddy-simulation tools for multiphase flows", *Ann. Rev. Fluid Mech*., **44**, 47–76.

GEL, A., LI, T., GOPOLAN, B., SHAHNAM, M., SYAMLAL, M., (2013), "Validation and uncertainty quantification of a multiphase computational fluid dynamics model", *Ind. & Eng. Chem. Res.*, **52**, 11424-11435.

GIDASPOW, D., (1994), "Multiphase flow and fluidization: continuum and kinetic theory descriptions", Academic Press Inc., Boston.

GLASSCOCK, D.A. and HALE, J.C., (1994) "Process Simulation: the art and science of modelling", *Chem. Eng.*, **101**, 82-89.

HEATH, A.R. and KOH, P.T.L., (2003), "Combined population balance and CFD modelling of particle aggregation by polymeric flocculant", *3rd Inter. Conf. CFD in the Minerals and Process Industries.* P Witt and MP Schwarz (Eds), CSIRO Minerals, Melbourne, Australia, 2003, 339-344.

IGCI, Y. and SUNDARESAN, S., (2011), "Constitutive models for filtered two-fluid models of fluidized gas-particle flows", *Ind. Eng. Chem. Res.*, **50**, 13190–13201.

ISHII, M. and ZUBER, N., (1979), "Drag coefficient and relative velocity in bubbly, droplet or particulate flows", *AIChE J*., **25**, 843-855.

JOHANSEN, S.T., BOYSAN, F. and AYERS, W.H., (1987), "Mathematical modelling of bubble driven flows in metallurgical processes", *Appl. Sci. Res*., **44**, 197-207.

JOHANSEN, S.T., and BOYSAN, F., (1988), "Fluid dynamics in bubble stirred ladles; Part II: Mathematical modelling", *Met. Trans. B*, **19**, 755-764.

JOHANSEN, S.T., WU, J., and SHYY, W., (2004) "Filter-based unsteady RANS computations", *Int. J. Heat and Fluid Flow*, **25**, 10–21.

JOHNSTON, R.R.M., NGUYEN, T., SCHWARZ, M.P. and SIMIC, K., (1996), "Fluid flow and natural dilution in open-type thickener feedwells", *4th Inter. Alumina Quality Workshop*, Darwin, June 1996, pp. 467-475.

KAHANE, R., SCHWARZ, M.P. and JOHNSTON, R.R.M., (1997), "Residue thickener modeling at Worsley Alumina", *Proc. Inter. Conf. on CFD in Minerals, Metals Processing and Power Generation*, Melbourne, CSIRO Minerals, pp. 109-118.

KAHANE, R., NGUYEN, T.V., and SCHWARZ, M.P., (2002), "CFD modelling of thickeners at Worsley Alumina Pty Ltd.", *Appl. Math. Modelling*, **26**, 281-296.

KARIMI, M., AKDOGAN, G., DELLIMORE, K.H., BRADSHAW, S.M. (2012), "Quantification of numerical and model uncertainties in the CFD simulation of the gas holdup and flow dynamics in a laboratory scale Rushton-turbine flotation tank", *9th Inter. Conf. CFD in Minerals and Process Industries, CSIRO, Melbourne, Australia 10-12 Dec. 2012.*

KASHIWA, B.A., and VAN DER HEYDEN, W.B., (2000), "Toward a general theory for multiphase turbulence Part I: development and gauging of the model equations", Los Alamos National Laboratory Report LA-13773-MS.

KATAOKA, I. and SERIZAWA, A., (1989), "Basic equations of turbulence in gas-liquid two-phase flow", *Int. J. Multiphase Flow*, **15**, 843-855.

KOH, P.T.L. and SCHWARZ, M.P., (2008), "Modelling attachment rates of multi-sized bubbles with particles in a flotation cell", *Minerals Engineering*, **21**, 989-993.

LABOIS, M. and LAKEHAL, D., (2011), "Very-Large Eddy Simulation (V-LES) of the flow across a tube bundle", *Nuc. Eng. & Des.*, **241**, 2075–2085.

LANE, G.L., SCHWARZ, M.P., EVANS, G.M., (2000), "Comparison of CFD methods for modelling of stirred tanks", *Proc. 10th European Conf. on Mixing*, 2–5 July, 2000, Delft, The Netherlands, pp. 273–280.

LANE, G.L., SCHWARZ, M.P., and EVANS, G.M., (2005), "Numerical modelling of gas-liquid flow in stirred tanks", *Chem. Eng. Sci.*, **60**, 2203-2214.

LI, J.H., GE, W., WANG, W. and YANG, N., (2010), "Focusing on the meso-scales of multi-scale phenomena – In search for a new paradigm in chemical engineering", *Chem. Eng. Sci.*, **66**, 4426–4458.

LIU, T.Y. and SCHWARZ, M.P., (2009), "CFD based multiscale modelling of bubble–particle collision efficiency in a turbulent flotation cell", *Chem. Eng. Sci.*, **64**, 5287–5301.

MONAGHAN, J., (2012), "Smooth particle hydrodynamics and its diverse applications", *Ann. Rev. Fluid Mech.*, **44**, 323-346.

MORAGA, J.F., LARRELEGUY, A.E., DREW, D.A. and LAHEY, R.T., (2003), "Assessment of turbulent dispersion models for bubbly flows in the low Stokes number limit", *Int. J. Multiphase Flow***, 29**, 655-673.

NGUYEN, T., HEATH, A. and WITT, P., (2006), "Population balance - CFD modelling of fluid flows, solids distribution and flocculation in thickener feedwells", In: *Proc. Fifth Inter. Conf. on CFD in the Process Industries*, P.J. Witt & M.P. Schwarz (eds.), CSIRO, Melbourne, Australia, 13-15 Dec.

PAI, M.G. and SUBRAMANIAM, S., (2009), "A comprehensive probability density function formalism for multiphase flows", *J. Fluid Mech.*., **628**, 181–228.

SCHWARZ, M.P., WRIGHT, J.K., and B.R. BALDOCK, B.R., (1987), "Measurement and simulation of the flow in an iron bath stirred with bottom-injected nitrogen". In: *Mathematical Modelling of Materials Processing Operations*, J. Szekely et al, (eds), pp 565-579. TMS.

SCHWARZ, M.P., (1990), "Sloshing waves formed in gas-agitated baths", *Chem. Eng. Sci.*, **45**, 1765-1777.

SCHWARZ, M.P., (1991), "Flow simulation in minerals engineering". *Minerals Engineering*, **4**, 717-732.

SCHWARZ, M.P., (1994), "The role of computational fluid dynamics in process modelling", *6th AusIMM Extractive Metallurgy Conf.*, pp. 31-36.

SCHWARZ, M.P., (1995), "Simulation of gas injection into liquid melts", *Appl. Math. Modelling*, **20**, 41-51.

SCHWARZ, M.P., (2001), "Computational modelling of metals reduction processes", *Computational Modelling of Materials, Minerals and Metals Processing*, M. Cross, J.W. Evans, and C. Bailey, eds., San Diego, USA, September 23-26, 2001, TMS (Warrandale), pp. 23-40.

SCHWARZ, M.P. and TURNER, W.J., (1988), "Applicability of the standard k-ε turbulence model to gas-stirred baths", *Appl. Math. Modelling*, **12,** 273-279.

SCHWARZ, M.P. and LEE, J., (2007), "Reactive CFD simulation of an FCC regenerator", *Asia-Pacific J. of Chem. Eng.*, **2**, 347-354.

SCHWARZ, M.P., and DAVIS, M.P., (2011), "Use of CFD modelling in the development and scale-up of the HIsmelt Process", *Roderick Guthrie Symposium on Process Metallurgy*, 6-9 June 2011, McGill Univ. Metals Processing Centre, Ed. M. Isac, pp. 343-350.

SCHWARZ, M.P., LEE, J, and WITT, P.J., (2006), "CFD modelling of turbulent fluidisation in FCC unit strippers", *5th World Congress on Particle Technology*, Orlando, 23-27 April, 2006, Paper 157c, AIChE.

SNIDER, D.M., (2001), "An incompressible three dimensional multiphase Particle-in-Cell model for dense particle flows", *J. of Comput. Physics*, **170,** 523–549.

SOKOLICHIN, A., EIGENBERGER, G. and LAPIN, A., (2004), "Simulation of buoyancy driven bubbly flow: established simplifications and open questions", *A.I.Ch.E. J.*, **50**, 24-44.

STEPHENS, D, TABIB, M. DAVIS, M. and SCHWARZ, M.P., (2012), "CFD Simulation of bath dynamics in the HIsmelt smelt reduction vessel for iron production", *Progress in Computational Fluid Dynamics*, **12**, 196-206.

STOPFORD, P.J., (2002), "Recent applications of CFD modelling in the power generation and combustion industries", *Appl. Math. Model*., 26, 351–374.

TABIB, M. and SCHWARZ, M.P., (2011), "Quantifying sub-grid scale (SGS) turbulent dispersion force and its effect using one-equation SGS large eddy simulation (LES) model in a gas–liquid and a liquid–liquid system", *Chem. Eng. Sci*., **66**, 3071-3086.

TABIB, M., LANE, G., YANG, W. and SCHWARZ, M.P., (2012), "Quantifying sub-grid scale (SGS) turbulent dispersion force and its effect using one-equation SGS large eddy simulation (LES) model in a gas–liquid and a liquid–liquid system", *Chem. Eng. Sci.*, **80**, 55–69.

TIAN, Z.F., WITT, P.J., SCHWARZ, M.P. and YANG, W., (2010), "Numerical Modeling of Victorian Brown Coal Combustion in a Tangentially Fired Furnace", *Energy and Fuels*, **24**, 4971–4979.

VERRELLI, D.I., BRUCKARD, W.J., KOH, P.T.L., SCHWARZ, M.P., FOLLINK, B., "Particle shape effects in flotation. Part 1: Microscale experimental observations", *Minerals Engineering*, **58**, 80–89.

WITT, P.J., PERRY, J.H., and SCHWARZ, M.P., (1998), "A Numerical Model for Predicting Bubble Formation in a 3D Fluidized Bed", *Appl. Math. Modelling*, **22**, 1071-1080.

ZHANG, K., FENG, Y., SCHWARZ, M.P., WANG, Z., and COOKSEY, M., (2013), "Computational fluid dynamics (CFD) modeling of bubble dynamics in the aluminum smelting process", *Ind. Eng. Chem. Res.*, **52**, 11378−11390.

A SIX CHEMICAL SPECIES CFD MODEL OF ALUMINA REDUCTION IN A HALL-HÉROULT CELL

Peter J. WITT[1*], Yuqing FENG[1], Graeme A. SNOOK[1], Ingo EICK[2] and Mark COOKSEY[1]
[1] CSIRO Mineral Resources Flagship, Melbourne 3169, AUSTRALIA
[2] Hydro Aluminium Deutschland GmbH, Neuss, GERMANY

* E-mail: peter.witt@csiro.au

ABSTRACT

The industrial process for producing primary aluminium metal is the reduction of powdered alumina in a Hall-Héroult reduction cell. These cells operate at temperatures above 940 °C with a highly corrosive electrolyte making physical measurement of the process difficult or nearly impossible. Computational models of the electro-magnetic fields and heat transfer are widely used in industry to design cells. Only recently (Feng et al., 2010b, Witt et al., 2012) have detailed computational models of the molten liquid-gas bath become available. Alumina distribution within the cells is important for cell efficiency and preventing anode effects. Using the bath flow information and an assumption of uniform reduction, a single scalar transport equation has been used to track the time variation of alumina within cells (Feng et al., 2011).

In this work the previous single species model is extended to include six chemical species and four chemical reactions. The reaction pathway developed for the model is that solid alumina particles are fed to the bath surface, where they mix and submerge into the liquid bath, and then undergo dissolution from solid particles to the liquid species $Na_2Al_2O_2F_4$. Within the bath $Na_2Al_2O_2F_4$ converts to $Na_2Al_2OF_6$, which is involved in an oxidation reaction with carbon to produce carbon dioxide and AlF_3 at the anode surface. At the metal pad a cathodic reaction occurs with AlF_3 converting to aluminium metal. Species solubility rates are based on the work of Solheim et al. (1995).

A CFD model of a single anode in a bubbly cryolite bath was built based on a corner anode from an industrial cell. Steady state bath flows were calculated and used to transport the six chemical species in the new bath chemistry model. Results were obtained for 20,000 seconds of real time for species distributions in the anode to cathode distance (ACD), change in mass of species in the bath with time, rates for the four reactions at locations in the bath and change in the species mass fraction with time at various locations during a feeding cycle.

Keywords: CFD, Process metallurgy, Alumina reduction chemistry, Hall-Héroult aluminium cell, Multiphase chemistry.

NOMENCLATURE

Symbols

A_{Anode} Anode surface area, [m^2]
$A_{Cathode}$ Cathode surface area, [m^2]
F Faradays constant = 96 485 [A s mol^{-1}]
J_{Anode} Current density at anode, [A m^{-2}]
$J_{Cathode}$ Current density at cathode, [A m^{-2}]
k_1 Reaction rate equation (1), [mol s^{-1}]
k_2 Reaction rate equation (2), [mol s^{-1}]
k_3 Reaction rate equation (3), [mol s^{-1}]
k_4 Reaction rate equation (4), [mol s^{-1}]
r Cryolite ratio (molar ratio of NaF and AlF_3)
x_1 Molar fraction of $Na_2Al_2OF_6$
x_2 Molar fraction of $Na_2Al_2O_2F_4$
Y_i Mass fraction for species *i*

Sub/superscripts

a Anode
c Cathode
i Index *i.*

INTRODUCTION

The Hall-Héroult process is the dominant industrial scale technology for reducing alumina powder to primary aluminium metal. Reduction cell performance is dependent on a mix of complex physical processes that occur in the cell and includes electrochemical, electro-magnetic, heat transfer and hydrodynamic processes.

Alumina particles are periodically feed on to the top of this molten cryolite bath; these particles then dissolve into the bath. Electrical current is supplied to the cell through anodes that are partially immersed into the top of the bath. Through an electrochemical reaction this electrical current reduces alumina in the presence of carbon anode to aluminium metal and carbon dioxide. Evolved carbon dioxide gas forms bubbles under the anodes where buoyancy forces cause these bubbles to

travel along the anode's base, before they rise to the surface beside the anode. A strong internal flow of liquid bath is established by the bubble motion and this acts to transport alumina and heat through the bath. Aluminium metal, reduced by the reaction, forms a layer of molten metal in the bottom of the cell.

Aluminium reduction cells operate in a harsh environment as the bath is molten cryolite, known to dissolve most engineering materials, and at a temperature of approximately 940°C. Electrical currents in the range of 100 to 450 kA are typical in reduction cells. Such currents induce strong magnetic fields, which act on conducting liquid metal and the molten bath, inducing secondary flows by Lorentz forces. These conditions along with restricted access make measurements on operating cells very difficult and greatly limit the amount of information that can be obtained.

To develop new cells and to improve the economic and environmental performance of existing cells, new tools are needed. Moxnes et al. (2009) described how optimised alumina feeding through experimentation can improve performance. However, experimentation is very costly and time consuming. Mathematical models can provide a tool to understand and explore how changes to cell geometry and operation affect performance (Gusberti et al. 2012). Thus validated mathematical models can provide a more efficient means of achieving improved cell performance than through experimentation.

The above description of the alumina reduction process is vastly simplified but has been successfully used previously to develop a computational fluid dynamics (CFD) model of alumina distribution in these cells. Feng *et al.* (2010a) and Feng *et al.* (2011) tracked an alumina species using a predicted bath flow field and assumed that uniform reduction occurred throughout the anode to cathode distance (ACD) under the anodes. Alumina distribution within the cell and feeding policies were able to be investigated; such an investigation was reported by Feng et al. (2010a).

In practice the bath consists of a number of ionic species that undergo a series of complex reactions. Work such as those by Gagnon *et al.* (2011), Kvande (1986) Mandin *et al.* (2009) and Solheim (2012) among others have proposed reaction models and bath species. All have assumed species transport by diffusion or simple hydrodynamic models.

In this work we extend the earlier alumina distribution model of Feng *et al.* (2011) to include six chemical species so as to more accurately represent the underlying electro-chemistry occurring in Hall-Héroult cells.

MODEL DESCRIPTION

The CFD modelling approach used in this work is to solve a steady-state model for the bath and bubble flow within a cell. Then by holding the bath flow fixed a transient model of species transport, alumina feeding and reactions is used to predict the time varying species concentration in the cell.

Details of the CFD model physics, approach and implementation in ANSYS/Fluent (ANSYS, 2013) have been previously documented in previous works Feng *et al.* (2010a, 2010b, 2011) and Witt *et al.* (2012). For brevity only an overview of the bath flow model is presented here.

The bath flow model describes the steady state flow of both gas and liquid phases based on a time averaged method. Key features of the bath flow model are:

- Gas and liquid flow are modelled using the Eulerian-Eulerian or two-fluid approach,
- Small-scale structures such as bubbles and turbulent structures are averaged in time and space,
- Drag from the bubbles is modelled using the Ishii and Zuber (1979) drag law,
- Turbulent effects are modelled using the k-ε turbulence model with modifications for multiphase flow to include, turbulent dispersion Lopez de Bertodano (1991), bubble induced turbulence (Smith, 1998 and Olmos *et al.*, 2003) and enhanced turbulent viscosity,
- Electro-magnetic effects are included through the Lorentz force, which is calculated from magnetic and electric fields for a typical pot line.

The alumina distribution model describes the transient distribution of alumina and other chemical species within the liquid bath. Transport of alumina and other chemical species is based on the steady state bath flow model.

The key stages in reduction of alumina to aluminium metal are:

- **Feeding** of alumina to the bath surface, this can occur at various times and at a number of locations,
- **Initial breakup, mixing** and submersion of particles from the surface into the liquid bath, assumed to occur over 10 seconds, this is used to set a boundary condition for the alumina such that the mass from a feed event is averaged over a 10 second period,
- **Dissolution** of alumina particles into the bath through the reaction:

$$Al_2O_{3(sol)} + 3\,NaF + AlF_3 \overset{k1}{\Rightarrow} \frac{3}{2}\,Na_2Al_2O_2F_4 \qquad (1)$$

- **Equilibrium** bath reaction:

$$Na_2Al_2O_2F_4 + 2\,NaF + 2\,AlF_3 \overset{k2}{\Leftrightarrow} 2\,Na_2Al_2OF_6 \qquad (2)$$

- **Anode** boundary layer reaction:

$$2\,Na_2Al_2OF_6 + C \overset{k3}{\Rightarrow} 4e^- + 4\,AlF_3 + 4\,Na^+ + CO_2 \qquad (3)$$

- **Cathode** or metal pad boundary layer reaction:

$$AlF_3 + 3\,Na^+ + 3e^- \overset{k4}{\Rightarrow} Al + 3\,NaF \qquad (4)$$

Reactions rates are required for equations (1) to (4).

The rate for alumina dissolution into the bath is based on the work of Frolov *et al.* (2007) who observed

alumina dissolution in both an industrial bath and a modified bath with fast dissolution properties. By fitting two straight lines to their data for the industrial cell, as shown in Figure 1, the following rate equation can be obtained:

$$k_1 = \max(0, 0.35 - \frac{0.35}{0.03} Y_{Al2O3dis}, 0.164 - \frac{0.164}{0.07} Y_{Al2O3dis}) \quad (5)$$

To limit the reaction in areas of low undissolved alumina the equation is modified to:

$$k_1 = (1.0 - e^{-500 Y_{Al2O3Und}}) \max(0, 0.35 - \frac{0.35}{0.03} Y_{Al2O3dis}, 0.164 - \frac{0.164}{0.07} Y_{Al2O3dis}) \quad (6)$$

Where $Y_{Al2O3dis}$ is the mass fraction of dissolved alumina in the bath and $Y_{Al2O3Und}$ the undissolved alumina in the bath. In this work the dissolved alumina species are $Na_2Al_2O_2F_4$ and $Na_2Al_2OF_6$.

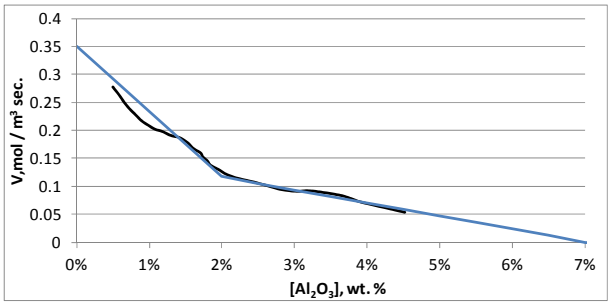

Figure 1: Dissolution rate of alumina in industrial baths at temperature 960 °C from Frolov *et al.* (2007) – black line and the model of equation (5) – blue line.

For equation (2), data from Solheim and Sterten (1999) was used to derive the equilibrium condition that was reported in Solheim (2013) as:

$$\frac{x_1^2}{x_2} = 11.3e^{-2.63r} \quad (7)$$

where x_1 and x_2 are the molar fractions of $Na_2Al_2OF_6$ and $Na_2Al_2O_2F_4$ respectively, and r is the molar ratio (Cryolite Ratio) of NaF and AlF_3. From the equilibrium condition in equation (7), the reaction rate, k_2, needed to bring the two species into equilibrium in that time step is determined.

Reaction rates for the anode and cathode reactions (equations (3) and (4)) are based on the current density such that:

$$k_3 = \frac{J_{Anode} dA_a}{4F} \quad (8)$$

and

$$k_4 = \frac{J_{Cathode} dA_c}{3F} \quad (9)$$

where J_{Anode} is the current density at the anode, $J_{Cathode}$ is the current density at the cathode, F is Faradays constant and dA_a is surface area of the anode and cathode.

Since the current density is not solved in the model, a fixed value at the anode of 0.9 [A cm^{-2}] is used and then, assuming conservation of charge, the cathode current density is $J_{Cathode} = J_{Anode} \frac{A_{anode}}{A_{cathode}}$.

GEOMETRY AND BOUNDARY CONDITIONS

Geometry for the single anode model was based on a Hydro Aluminium HAL300 cell and is shown in Figure 2. The full industrial cell has 30 anodes, to simplify the model for this work a corner anode from the full cell was built, including a typical ledge profile, and meshed using ANSYS/ICEM to give 124,000 hexahedral cells. The anode had two slots; the centreline of the full cell is treated using a symmetry plane while the inter-anode gap is considered to be a vertical wall.

Details of the physics and boundary conditions used are as per the full cell model reported in Witt *et al.* (2012). Gas enters the model through the anode base coloured red in Figure 2. Gas leaves the domain through the free surface coloured green via a degassing boundary condition. Alumina feeding could be varied to different positions in the cell and in this work was to the top of the side channel of the cell through the purple region shown in Figure 2. Each feed was chosen to be 0.15 kg of alumina uniformly added over a 10 second period and was added every 80 seconds.

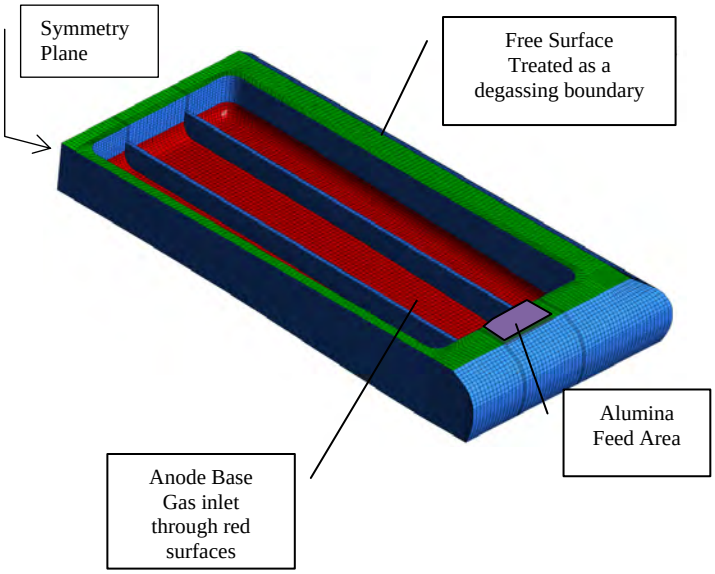

Figure 2: Single Anode Model Geometry.

Initial concentrations for the mass fractions are given in Table 1, which gives a cryolite ratio of 2.2, from which the equilibrium condition for $Na_2Al_2OF_6$ and $Na_2Al_2O_2F_4$ can be determined. The model was run for a time of 20,000 seconds with 1 second time steps.

Table 1: Initial Species mass fraction in the Single Anode Model.

Al_2O_3	$Na_2Al_2O_2F_4$	$Na_2Al_2OF_6$	Na	NaF	AlF_3
0.025[1]	0.044[2]	0.084[2]	0.070[2]	0.420[2]	0.382[2]

[1] Mass fraction of total liquid phase
[2] Mass fractions of dissolved species

RESULTS

For the single anode model the steady state bath flow model was first run to calculate the bath flow field. Results for the bath flow are shown by the streamlines plotted in Figure 3, velocity vectors in the ACD plotted in Figure 4 and the gas volume fraction plotted on two vertical slices near the centre of the anode in Figure 5. These plots show that the model predicts a thin gas layer under the anode that drives a strong bath flow under the anode towards the centre channel. Liquid bath then flows to the end channel, along the end channel and back to the side channel.

Using PIV measurements the bath flow model formulation used in this work was validated for a three anode water model by Feng *et al.* (2010b), thus we expect that the current model should also predict reasonable results. Geometry used by Feng *et al.* (2010b) differs from the current geometry in a number of keys areas: a single anode rather than three anodes, a narrower centre channel, shaped external cell walls due to ledge formation rather than vertical walls, slotted rather than unslotted anodes and an anode slope of nearly 2° upward at the centre channel compared to the flat anodes in the earlier work. These changes prevent direct comparison and have an effect on the flow field. Measurements reported by Feng *et al.* (2010b) show the velocity in the ACD can exceed 0.12 m s^{-1} with a complex flow field. Due to the sloping base of the current anode, which will create stronger and more directional buoyancy forces, flow is directed along the anode length to the centre channel and velocity in the ACD is higher with predicated values up to 0.2 m s^{-1}.

Analysis of streamlines indicates that the travel time for the bath from the side channel under the anode to the centre channel and back along the end channel is approximately 50 seconds.

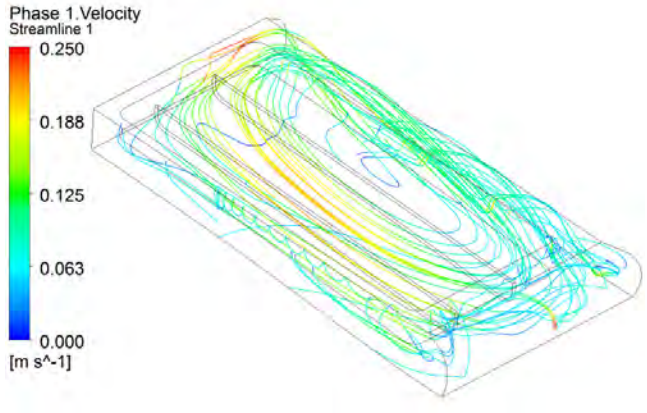

Figure 3: Streamlines showing the bath flow in the Single Anode Model.

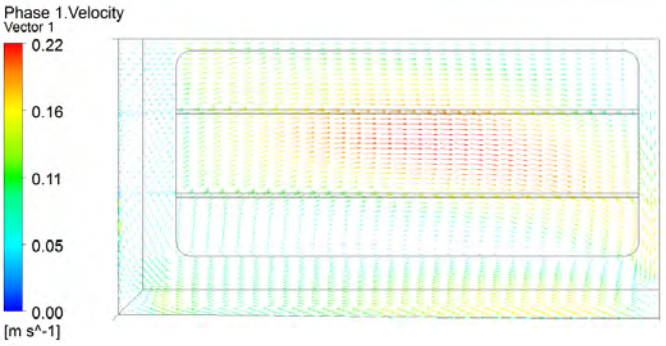

Figure 4: Liquid velocity vectors on a plane through the ACD showing the bath flow in the Single Anode Model.

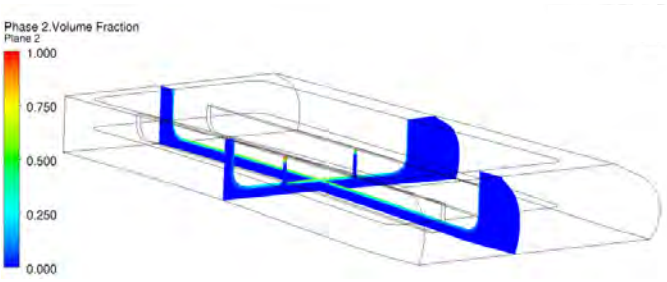

Figure 5: Gas volume fraction on two vertical planes in the Single Anode Model.

Mass fractions for the undissolved and dissolved alumina species considered in the single anode model are plotted on two vertical planes in Figures 6 to 8 after 20,000 seconds (5 hrs 33 minutes). This time instant was selected as it is just before a feed of alumina is about to occur and thus is likely to be close to the point of minimum alumina concentration under the anode. Low alumina concentration in the ACD is one potential cause of anode effects. As alumina is fed to the top of the side channel, undissolved alumina mass fraction is highest in the side channel but lowest in the inter-anode gap and centre channel. The dissolved alumina species in Figures 7 and 8 have a similar concentration distribution to the alumina but note that the plot range is very narrow to highlight the distribution within the cell.

The reaction rate for the dissolution reaction is shown in Figure 9 and indicates that the rate is constant through the cell. The equilibrium reaction rate is plotted in Figure 10 and shows that the reaction proceeds strongly under the anode and reverses in parts of the side and end channels. Figure 11 plots the reaction rate for the anode reaction, and shows the reaction has a slightly lower rate in the centre of the anode due to the gas holdup. The cathode reaction rate is not shown as it is uniform across the metal pad surface.

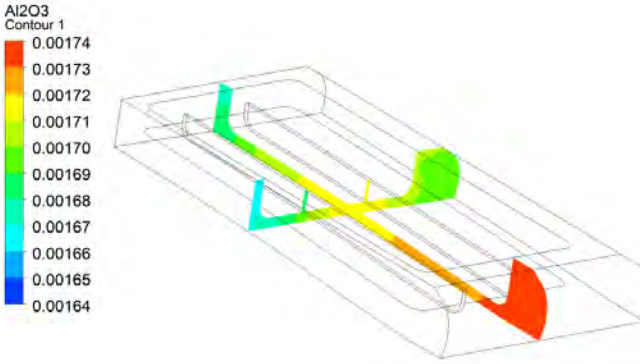

Figure 6: Undissolved alumina mass fraction on two vertical planes in the Single Anode Model at 20,000 [s].

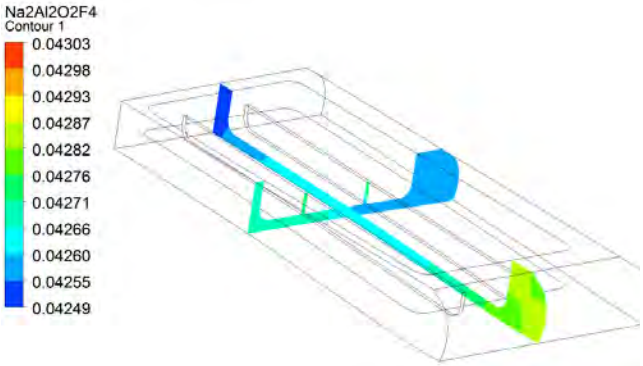

Figure 7: $Na_2Al_2O_2F_4$ mass fraction on two vertical planes in the Single Anode Model at 20,000 [s].

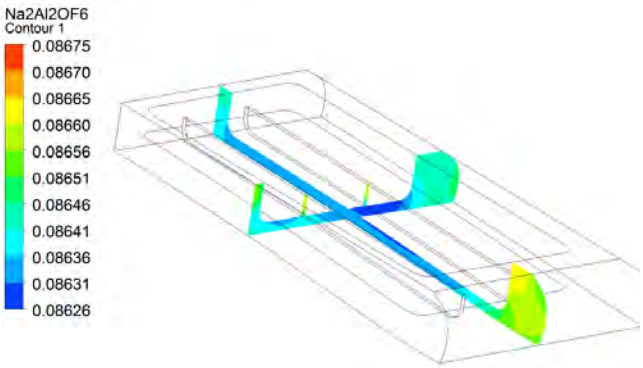

Figure 8: $Na_2Al_2OF_6$ mass fraction on two vertical planes in the Single Anode Model at 20,000 [s].

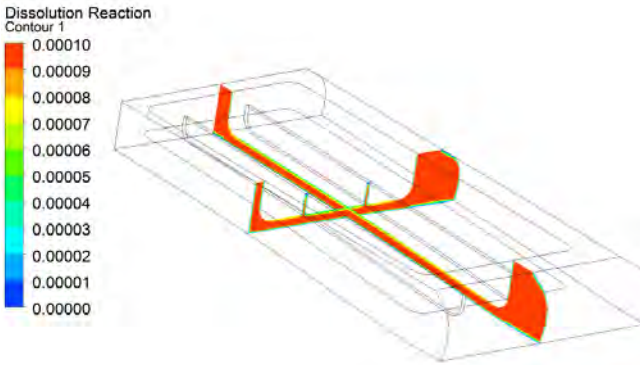

Figure 9: Dissolution reaction rate on two vertical planes in the Single Anode Model at 20,000 [s].

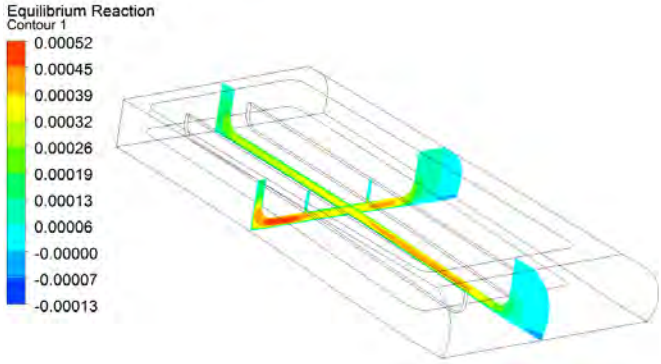

Figure 10: Equilibrium reaction rate on two vertical planes in the Single Anode Model at 20,000 [s].

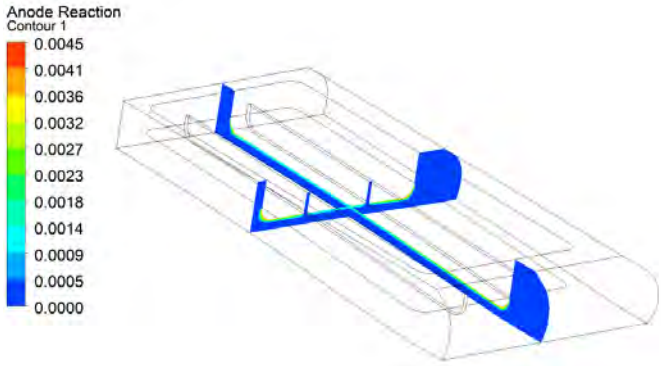

Figure 11: Anode reduction reaction rate on two vertical planes in the Single Anode Model at 20,000 [s].

Figure 12 shows the variation in undissolved alumina on a plane through the centre of the ACD at 20,000 seconds. The magnitude of the variation in species mass fraction is not great but results indicate regions of higher and lower concentrations. Figure 13 plots the equilibrium reaction rate on a plane through the ACD. The equilibrium reaction rate is the fastest under the one-third of the anode near the inter-anode gap and the reaction is predicted to reverse in the side and end channels.

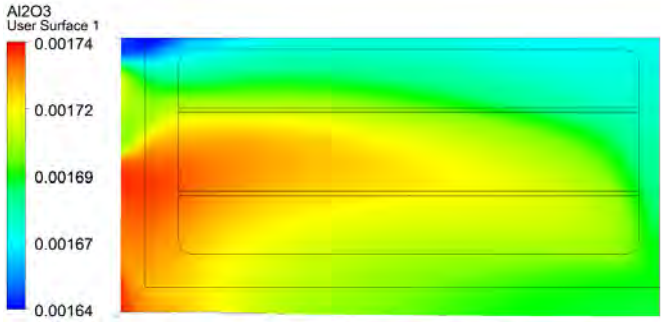

Figure 12: Undissolved alumina mass fraction on a plane through the ACD in the Single Anode Model at 20,000 [s].

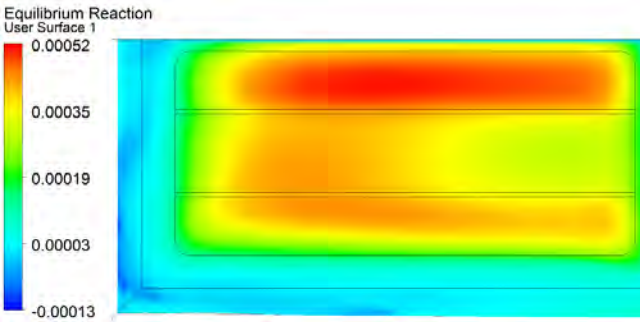

Figure 13: Equilibrium reaction rate on a plane through the ACD in the Single Anode Model at 20,000 [s].

The total mass of the chemical species in the bath and how they change with time is plotted in Figures 14 to 16. In Figure 14 the mass of alumina in the bath varies due to periodic feeding, as shown by the inset; this results in what appears as a wide band for the alumina mass at any time instant. The initial condition for this run was an undissolved alumina mass of 0.984 kg; this reduced rapidly to between 0.7 and 0.8 kg after about 5,000 seconds. After this time the mass is reducing slightly indicating the bath has not completely reached a steady operating condition, but is close to a steady condition. Two other preliminary calculations were run; one with a zero initial undissolved alumina concentration and one with the initial mass set to 4 kg. Both of these showed significant changes in the mass of alumina but would require significantly more than 20,000 seconds before reaching a steady condition. From these preliminary calculations the initial value of 0.984 kg was identified as being close to the steady condition. Mass of the other bath species are plotted in Figures 15 and 16 and show slight changes in their mass with time.

Based on the above results it was concluded that the model was at close to stable operating species concentrations and conditions at 20,000 seconds. To assess the magnitude of the change in bath chemistry between feed additions the results at 20,000 seconds were used to restart the model, from which time it was run for a further 100 seconds. During this short run species mass fractions at nine monitoring points were stored at each time step. The locations of the points are shown in Figure 17. Points 1 to 4 are located on the top of the bath with point 1 being at the feed location. The remaining 5 points are located in the ACD with point 6 being near the centre of the anode and the other four located near the anode edge.

Figure 18 plots the change in undissolved alumina at these locations. The mass fraction at the feeding location, Point 1, initially increases from 0.002 to 0.007 during feeding and the initial 10 second immersion. After feeding it drops rapidly back to the steady state condition, indicating that convective transport rapidly disperses the alumina particles. Points 2 and 8 show nearly a 50% rise in concentration approximately 20 seconds after feeding commences. The streamline in Figure 3 and velocity vectors in Figure 4 show the bath flows from the feed location towards the inter-anode gap and then along the anode to the centre channel, which transports the alumina through the cell and results in the increase in alumina concentration at points 2 and 8.

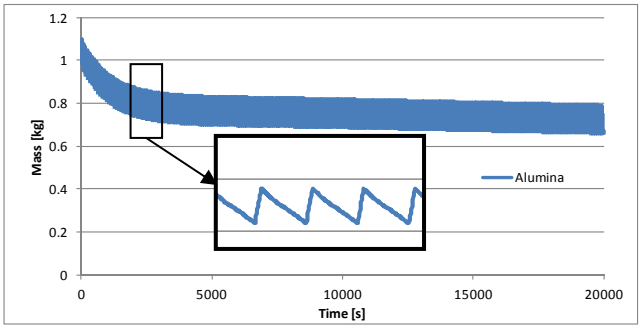

Figure 14: Change in Undissolved Alumina Mass with time for the Single Anode Model.

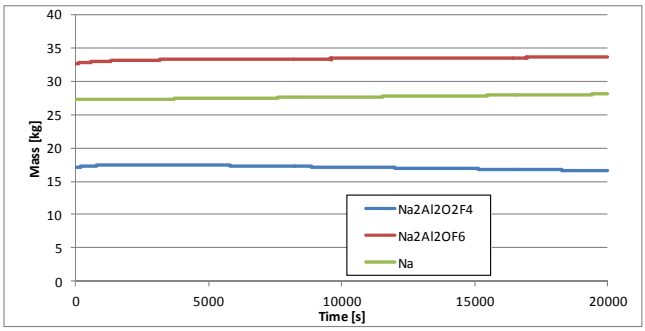

Figure 15: Change in species mass with time for the Single Anode Model.

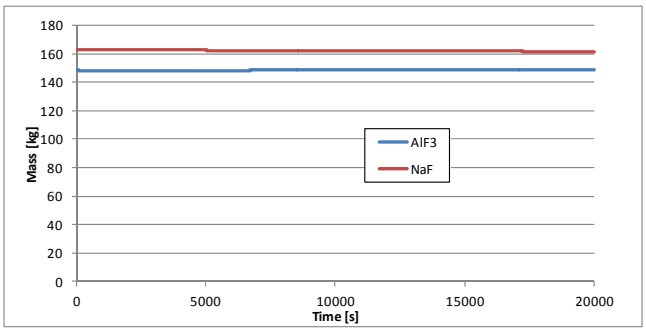

Figure 16: Change in AlF_3 and NaF mass with time for the Single Anode Model.

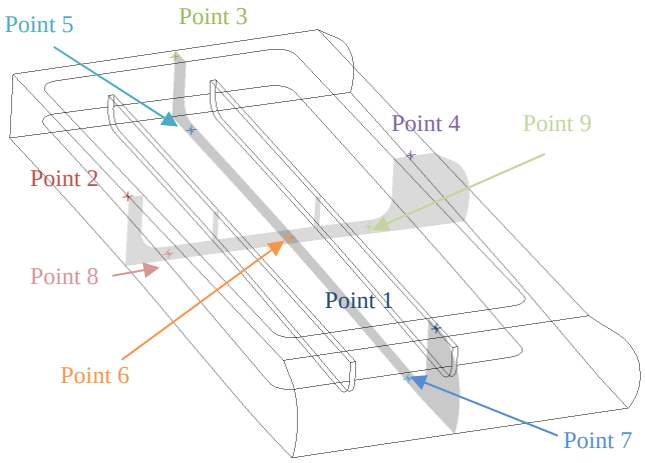

Figure 17: Location of monitoring points in the Single Anode Model.

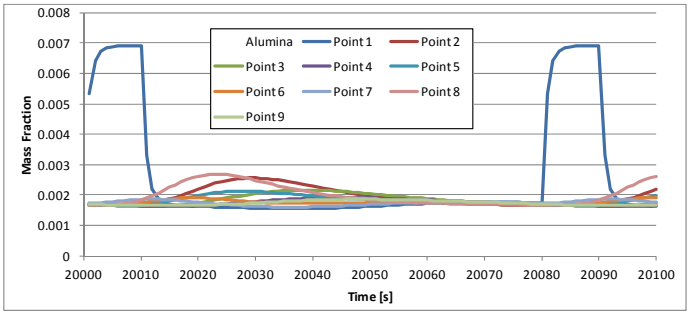

Figure 18: Change in undissolved Alumina mass fraction with time at various locations in the Single Anode Model.

DISCUSSION

The complex reactions, high temperature and harsh chemical environment make direct validation of the single anode model extremely difficult. Based on our past work (Feng *et al.*, 2010a, 2010b and Witt *et al.* 2012) we have a reasonable level of confidence in the bath flow and alumina distribution predictions. Further work using a water model with tracers could be used to improve confidence in the model. Moxnes *et al.* (2009) have used AlF_3 addition to change bath conductivity and measure changes in anode currents. In future work it may be possible to apply this approach to validate the model on a full cell.

For simplicity at the present stage of model development we assume a uniform current distribution across the anode base. This leads to uniform gas generation rate and uniform anode and cathode reaction rates. Clearly this is a simplification as current distribution is non-uniform and a function of gas generated through the anodic reaction. Our plan in future work is to include current distribution in the model and to link the anode and cathode reactions to the local current density. A further complication is our present use of a steady-state bath flow. We propose to iterate between the bath flow and transient chemical reaction models to couple the effects of anode reaction, gas generation, bubble flow and species distribution to overcome limitations in the present approach.

CONCLUSION

We have proposed a new alumina reduction model for the Hall-Héroult process that consists of six chemical species and four reactions. The reaction pathway developed for the model is that solid alumina particles are feed to the bath surface; they take a short time to mix and submerge into the liquid bath, where they undergo dissolution from solid particles to the liquid species $Na_2Al_2O_2F_4$. Within the bath a reaction reduces $Na_2Al_2O_2F_4$ to $Na_2Al_2OF_6$, which is further reduced to carbon dioxide and AlF_3 at the anode surface. At the metal pad a cathodic reaction reacts AlF_3 to form aluminium metal.

A previously published CFD model is used to transport chemical species within the bath based on bubble and MHD driven flow. Reaction for the new bath chemistry model were included in a CFD model and tested on the geometry for a single anode that was run for 20,000 seconds of real time.

Key findings from the model are:

- Preliminary calculations show that if the initial undissolved alumina mass fraction is significantly different from the steady operating state then real times of over 20,000 seconds maybe be required to reach steady conditions.
- Alumina was fed to the top of the side channel and because of this the highest concentration of undissolved alumina was found in the side channel. This location was also where the undissolved alumina mass fraction increased from 0.002 to 0.007 during feeding.
- At a location near the inter-anode gap and midway along the anode the undissolved alumina mass fraction increased by approximately 50% about 20 seconds after feeding commenced.
- Other species showed only a small variation in mass fraction both across the cell and with time.
- Reaction rate for the dissolution reaction was found to be reasonably constant throughout the cell.
- The equilibrium reaction rate was high in the ACD under the anode and highest for the part of the anode near the inter-anode gap. In some parts of the side and end channels the equilibrium reaction was predicted to go in the reverse direction.

ACKNOWLEDGMENTS

The present work was supported by the project “Gas and Alumina Distribution and Transport” (GADT), financed by the Research Council of Norway and Hydro Primary Metal Technology. Permission to publish the results is gratefully acknowledged.

The authors wish to acknowledge the valuable discussions and advice provided by Asbjorn Solheim on the electro-chemical reactions, rates and processes in aluminium reductions cells.

REFERENCES

ANSYS Workbench / Fluent 14.5, ANSYS Inc., USA. 2013.

FENG, Y.Q., COOKSEY, M. and SCHWARZ, M.P., (2010a), “CFD Modelling of alumina mixing in aluminium reduction cells”, *Light Metals 2010*, 455-460.

FENG, Y.Q., YANG, W., COOKSEY, M. and SCHWARZ, M.P., (2010b), “Development of Bubble Driven Flow CFD Model Applied for Aluminium Smelting Cells”, J. Comp. Multiphase Flows, 2(3), 179-188.

FENG, Y.Q., COOKSEY, M. and SCHWARZ, M.P., (2011), “CFD Modelling of alumina mixing in aluminium reduction cells”, *Light Metals 2011*, 543-548.

FROLOV, A.V., GUSEV, A.O., ZAIKOV, Y.P., KHRAMOV, A.P., SHUROV, N.I., TKACHEVA, O.Y., APISAROV, A.P. and KOVROV, V.A. (2007), “Modified alumina-cryolite bath with high electrical conductivity and dissolution rate of alumina”, *Light Metals 2007*, 571-576.

GAGNON, F., ZIEGLER, D. and FAFARD, M., (2011), "A preliminary finite element electrochemical model for modelling ionic species transport in the cathode block of a Hall-Héroult cell"**,** *Light Metals*, 537-542.

GUSBERTI, V., SEVERO, D.S., WELCH, B.J., and SKYLLAS-KAZACOS, M., (2012), "Modeling the mass and energy balance of different aluminium smelting cell technologies", *Light Metals 2012*, 929-934.

ISHII, M. and ZUBER, N., (1979), *AIChE J.*, **25**, 843-855.

LOPEZ DE BERTODANO, M., (1991), *Turbulent bubbly flow in a triangular duct*, Ph.D. Thesis, Rensselaer Polytechnic Institute, New York.

KVANDE, H. (1986), "The structure of alumina dissolved in cryolite melts", *Light Metals*, 451-459.

MANDIN, P., WATHRICH, R. and ROUSTAN, H. (2009) "Industrial Aluminium Production: the Hall-Heroult Process Modelling" in *ECS Transactions*, p. 1, Industrial Electrochemistry and Electrochemical Engineering General Session - 215th ECS Meeting, San Francisco, CA.

MOXNES, B., SOLHEIM, A., LIANE, M., SVINSÅS, E. and HALKJELSVIK, A., (2009), *Light Metal*, 461-466.

OLMOS, E., GENTRIC, C. and MIDOUX, N., (2003) "Numerical description of flow regime transitions in bubble column reactors by a multiple gas phase model", Chemical Engineering Science, **58**, 2113-2121.

SMITH, B.L., (1998) "On the modelling of bubble plumes in a liquid pool", *Applied Mathematical Modelling*, **22**, 773-797.

SOLHEIM, A. (2012), "Concentration gradients of individual anion species in the cathode boundary layer of aluminium reduction cells", *Light Metals*, 665-670.

SOLHEIM, A., (2013), Personal Correspondence.

SOLHEIM, A. and STERTEN, A., (1999) "Activity of Alumina in the System NaF-AlF_3-Al_2O_3 at NaF/AlF_3 Molar rations ranging from 1.4 to 3", *Light Metals 1999*, 445-452.

SOLHEIM, A. ROLSETH, S., SKYBAKMOEN, E. STØEN, L. STERTEN Å. and STØRE, T. (1995) "Liquidus Temperature and Alumina Solubility in the System Na_3AlF_6-AlF_3-LiF-CaF_2-MgF_2", Light Metals 1995, 451-460.

WITT, P.J., FENG, Y.Q., EICK, I. and SCHWARZ, M.P., (2012), "Modelling bubble flow with CFX and Fluent for aluminium reductions cells", *9th Int. Conference on CFD in the Mineral and Process Industries*, CSIRO, Melbourne, Australia, 10-12 Dec.

10th International Conference on CFD in Oil & Gas, Metallurgical and Process Industries
SINTEF, Trondheim, Norway *CFD 2014*
17-19 June 2014

MULTI-SCALE PROCESS MODELS TO ENABLE THE EMBEDDING OF CFD DERIVED FUNCTIONS: CURTAIN DRAG IN FLIGHTED ROTARY DRYERS

Andrew LEE[2], Madoc SHEEHAN[1] , Philip SCHNEIDER[1]
[1] James Cook University, 4812 Townsville, AUSTRALIA
[2] University of Melbourne, 3010 Melbourne, AUSTRALIA

Email: madoc.sheehan@jcu.edu.au

ABSTRACT

Flighted rotary dryers are large industrial devices which are commonly used to dry mineral ores and mineral concentrates, as well as other valuable commodity products. They are high capital cost units as well as large consumers of energy. Solids movement and energy exchanges within these devices occurs via a range of complex mechanisms that involve rolling and bouncing in a dense bed of solids, as well as the falling through a cross-flowing gas stream in lean particle curtains. Although a fundamental approach is attractive, full CFD simulations of such devices would be prohibitively expensive. The complexity of such a model would preclude its use for design and control applications, which are the most prevalent concerns to industry. Pseudo-physical compartment modelling is a powerful alternative technique that can be used to reproduce, in a physically meaningful way, the important characteristics of dryers such as residence time distributions and loading states. This scalable modelling approach also provides a convenient multi-scale structure that facilitates the representation of a system (in this case a flighted rotary dryer) as a series of smaller, distinctive, interacting phases. It is these smaller phase structures, such as the air-borne phase, that are suitable for modelling with either CFD or DEM type approaches. In this paper CFD modelling of single particle curtains and multiple side-by-side particle curtains is presented, with particular emphasis on quantifying gas induced drag and gas penetration into the curtain phase. The results are discussed in terms of their suitability to integrate CFD derived phase information within the broad process model. The simulations described in this paper provide valuable insights into the dryer design considerations such as flight serrations and axial flight staggering. The methodology presented in this paper provides an example that could be adapted to enable the evaporation, convection and radiation heat transfer in curtains to be accounted for.

Keywords: CFD, compartment model, particle curtain, drag, multi-scale, dryers

INTRODUCTION

Flighted rotary dryers (FRD's) are used extensively in a range of industries for control of the temperature and moisture content of free flowing, particulate solids, such as grains, sugar, and mineral ores as shown in cross-section, in Fig.1. FRDs range from small bench scale apparatus in pharmaceutical manufacturing, to 30m long, 6m diameter, industrial ore dryers. FRDs offer simplicity, low operating costs, and handle a wide range of throughputs and feed-stocks. Due to their size, rotary dryers often represent a significant capital expense. Thus it is necessary to have a good understanding of dryer operations and design features to ensure that the unit meets desired operational requirements.

Many different types of flighted rotary dryers exist, including multi-pass units and units with centre fills. However the simplest and most common flighted rotary dryers consist of a rotating, inclined drum with lifters or flights fitted to the internal walls. Moist solids are fed into the dryer at one end where they are collected in the flights. The flights carry the solids into the upper half of the drum, where they are released in a series of continuous curtains across the width of the dryer (see Figure 1). These particles fall under the influence of gravity and return to the floor of the dryer where they are collected once again by the flights. Axial transport of solids within the dryer is caused by the slope of the drum, and occurs via both the cascading of solids off flights and rolling/kilning motion of solids along the drum base. Drying gasses, commonly air or combustion gasses, are fed through the dryer either co- or counter-currently. These gases interact with the falling curtains of solids, removing heat and moisture and creating drag forces that will influence the curtains of falling particles, causing dispersion of the solids within the dryer. The rolling solids also interact with the drying gasses, but to a lesser extent.

Whilst flighted rotary dryers are widely used and have been widely studied, their complex solids transport behaviour and the difficulty in integrating solids transport and heat and mass transfer phenomena have proved to be significant stumbling blocks to modelling. As a rotary dryer and the behaviour of its contents are three-dimensional and vary with time, a comprehensive first principles dynamic model of a dryer would need to be multi-dimensional in order to capture the full detail of the solids transport. Furthermore, both granular flow (flight-borne and kilning solids) and pneumatic flow (curtaining solids) occur within these devices. Whilst a combined CFD and DEM model can be conceptualised, the particle numbers and mesh nodes necessary to model a full scale unit would be enormous. Even ignoring the uncertainties in first principles modelling of granular flow, the numerical demands of such a model would preclude its practical use for either design or control purposes. Clearly, a rigorous fluid dynamic or discrete element model of an entire dryer is not feasible, and a more pragmatic modelling approach is necessary for guiding the development of industry-scale process models. In what follows we have been guided by the principles of pragmatism, attempting to use as simple a model as possible while still capturing important influences on system behaviour.

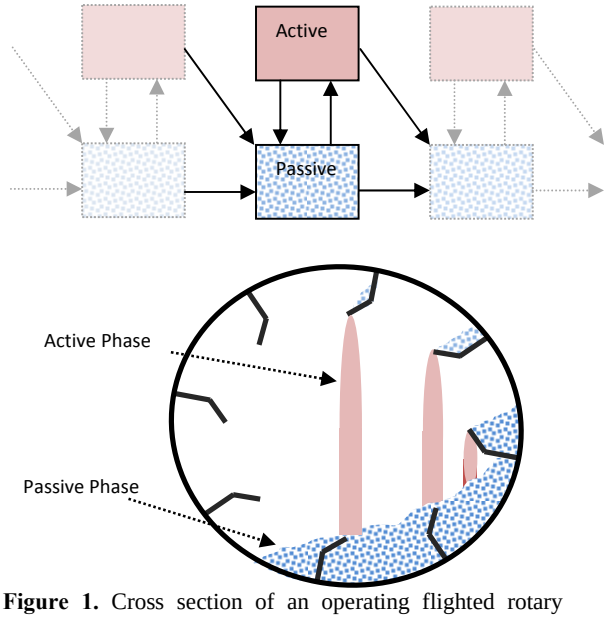

Figure 1. Cross section of an operating flighted rotary dryer (below) and the corresponding pseudo-physical compartment model (above). The light-shaded solids are the airborne solids (curtains) and the patterned solids are the flight and drum borne solids.

Unfortunately simple empirical models have also been unable to predict the full behaviour of the dryer systems (Cao and Langrish (1999), Lee *et al*. (2009)). In particular, the influence of the flights on system performance has proven difficult to capture with empirical techniques. Early semi-empirical applications of compartment modelling of FRD's by both Matchett and Baker (1987), and Duchesne *et al* (1996) led to the development of more realistic representations of solids transport in flighted rotary dryers. The model structures they suggested were capable of reproducing typical dryer experimental observations such as residence time distributions. The important model features developed in these works were the use of a twin tanks in series model structure, where one tank represented the flight and drum borne solids and the other tank represented the airborne solids (see Figure 1). In these models, the exchange rates moderating solids flows between the tanks, such as the flow of airborne solids off the flights and onto the base of the drum, were parameter estimated. Sheehan *et al.* (2005) and Britton *et al.* (2006) extended this work by developing a multi-scale flighted rotary dryer model, which integrated physically-derived (i.e. mechanistic) model parameters, instead of statistically estimated parameters, into the twin-tanks in series compartment model structure. They called this approach pseudo-physical compartment modelling (PPCM). The PPCM is an adaptable pragmatic model framework, and it has been successfully used to model industrial sugar drying (Britton *et al.* (2006), a full-scale zinc concentrate dryer with both flighted and unflighted sections (Ajayi, 2011) and a fluidised drum granulator (Rojas *et al.*, 2010). In the PPCM approach, scalable dynamic models are derived which are capable of reproducing experimentally observable features (such as the residence time distribution and holdup profiles). Furthermore, the effects of internal geometry, operating conditions and solids flow properties on dryer performance could also be accurately predicted and integrated into the model equations in a meaningful way.

Similar to the network of zones approach in CFD, each well-mixed tank in the PPCM has a distinct physical representation. Each tank is defined by its corresponding dynamic mass and energy conservation equations, as well as geometrically defined capacity constraints. For example, an active phase tank in the model physically represents (within a distinct slice of the dryer) the curtains of particles that cascade off the flight tips as the drum rotates. The corresponding passive phase tank physically represents the solids in the flights and on the floor of the drum. Capacity constraints, exchange rates between these tanks and between adjacent tanks are described using mechanistic arguments, based solely on solids flow properties and drum and flight geometry. A separate unloading flight geometry model was used to generate the model parameters controlling the exchange rates in and out of each tank or phase.

Considering the exchange rate characterising the flow between the passive and active tanks (i.e. flight

discharge), Lee and Sheehan (2010) showed that for a free flowing material which discharges continuously from the flights, the discharging behaviour of a flight as it travels around the circumference of the dryer can be calculated solely from the geometry of the flight and drum, the amount of solids present in the flight, and the solids dynamic angle of repose. Thus, an unloading profile of a flight (mass flow versus time) can be calculated as a function of the drum loading.

In the discussion that follows, we describe aspects of the PPCM process model structure that help to outline the potential to utilise CFD outputs to regress model parameters within the PPCM. In particular, we emphasise the model parameters that moderate active phase flows (i.e. the curtains of particles that cascade off the flights) that are currently predicted using the geometry model, but could instead be generated using CFD simulations. It important to note that because of the scaling associated with the compartmentalisation of the full scale unit, these simulations would be of a more tractable size and reduced level of complexity compared to a first principles simulation.

Two key parameters utilised in the PPCM are the airborne solids residence time, and the horizontal drag experienced by the curtains due to cross-flowing gas. For a specific example, the solids flow rates out of each compartment in the model are calculated using the relation $F_i = m_i / \overline{t}_i$ where F_i is the flow rate of solids leaving compartment i and m_i and $\overline{t_i}$ are the solids holdup and average residence time in compartment i, respectively. Currently, to evaluate drag and residence time correlations used within the PPCM, the unloading flight geometry sub-model is used as boundary conditions for solving Newtons equations of motion for a isolated particle. The bulk curtain behaviour is estimated by calculating the path or trajectory of a single spherical falling particle, including displacement due to cross flowing gas induced drag. The critical assumption inherent in this approach is that the bulk curtain behaviour can be assumed to be adequately represented by the motion of an isolated sphere. Furthermore, heat transfer in the curtains is also approximated by assuming correlations (such as the Ranz Marshall correlation) based on an assembly of isolated spheres.

Unfortunately there is strong evidence that curtains of particles behave significantly differently to isolated spheres (Wardjamin *et al.* (2008, 2009) and Hruby *et al.* (1988)). Because of gas entrainment, curtains exhibit reduced residence times and reduced drag in comparison to isolated spheres. Although simplifying the modelling, the assumption that an isolated sphere adequately represents the airborne solids can be improved upon, through the use of CFD. For example, CFD can be used as a tool to progressively improve the prediction of drag and residence time (and also heat transfer) by modelling either a single (i.e. average) particle curtain or for an increased level of sophistication, modelling a series of particle curtains corresponding to the discharging flights. It is worth noting here that the potential to utilise CFD sub-modelling to improve overall model predictions is only made possible by the enforced physical realism inherent in the pragmatic compartment-model structure. In this way the PPCM methodology facilitates varying degrees of pragmatism to be used to incrementally and systematically improve representation of the underlying phenomena.

In this paper we use the case study of a flighted rotary dryer as context for describing new CFD modelling of drag within particle curtains. We describe the CFD modelling of a single cascading curtain as well as multiple cascading curtains and also discuss the potential for embedding CFD derived information within multi-scale process compartment models.

CFD curtain modelling

A number of researchers have studied the effects of the gas-solids interactions in the active phase on the solids transport operations within a rotary dryer. Obviously, the moving stream of drying gasses will result in a displacement of the falling solids due to drag effects. Previous research has demonstrated that the gas-solids interactions within a rotary dryer are complicated. Simplifications of the system, such as the extremes of assuming isolated spherical particles (maximum drag) or flat-plate behaviour (minimum drag) (Baker, 1992), are generally insufficient. However, modelling the gas-solids interactions within a single curtain of falling solids is well within the capabilities of current CFD packages.

In order to model the gas-solids interactions influencing the active phase, a multi-phase CFD approach was implemented in Ansys CFX® 5.7.1. Due to the large number of solid particles present a Lagrangian method was not feasible, whilst the solid curtain was not considered dense enough to warrant the use of a granular model for the solids. Thus an Eulerian-Eulerian approach was used with a full buoyancy model and a k-ε model for turbulence. Although the k-ε model remains the industry standard, and has been widely used to model gas-solid systems (Du *et al.* (2006) for example), it's accuracy has been noted to depend on the use of sufficiently fine mesh and time step (Fletcher *et al.* (2006)). Uncertainty in the choice of turbulence modelling emphasizes the importance of experimental data to validate model predictions. In this work we draw confidence in our model choices and the resulting simulation results, from prior studies comparing experimental (isothermal) curtain profiles to the simulated curtain profiles that were

determined using the same model approach, but for a scaled-down system. In those wind tunnel studies (Wardjiman *et al.* (2008, 2009)), both free falling curtains in still air and free falling curtains exposed to cross flowing gas were examined. Good agreement between the experimental and simulated results was obtained under both scenarios. Wardjiman *et al.* (2008, 2009) found that a cutoff solids volume fraction of 5.6×10^{-4} corresponded well with the experimentally observed curtain boundaries, and a similar threshold of 4.3×10^{-4} has been used in this work. However, to ensure complete confidence in the results presented in this paper, a comprehensive set of experimental data for curtain profiles would be required.

Gas-solids interactions occurring within a full rotary dryer are complex, with multiple flights unloading solids at different locations. Each of these individual curtains will have different mass flow rates, particle velocities and solids volume fractions, and the presence of the curtains will affect the flow of gas through the dryer. In this work, two series of simulations were conducted. The first studied a single curtain of solids falling perpendicular to a moving gas stream (i.e. a single curtain in isolation) and the second examined multiple parallel curtains to determine whether the presence of multiple curtains affected the displacement of solids and extent of gas penetration.

Single Curtain Studies

In order to achieve meaningful results from the single curtain simulations, it was necessary to determine a set of initial conditions that would represent the average gas-solids interactions for the falling curtain in a typical industrial dryer. The curtain conditions for the average fall path of a particle were used, based on the predictions of the geometric unloading model of Lee and Sheehan (2010) and experimental observations (Lee, 2008). These gave an initial curtain width of 18 mm with an initial vertical particle velocity of 1 m/s and a mass flow rate per metre of flight length of 5.18 kg/m·s. The single curtain studies were simulated in a tunnel 0.8 m long, 0.52 m wide and 2 m tall. Solids were introduced through an 18 mm wide variable length inlet along the centreline of the tunnel, allowing a 0.1m entry zone for the gas stream. Turbulence was modelled using the k-ε model and a full buoyancy model was used. Drag forces were modelled using the Schiller-Naumann (Schiller and Naumann, 1935) equation assuming a particle size of 850 µm.

The numerical domain was discretised with a 9 mm tetrahedral mesh applied to the region occupied by the particle curtain and extended for a minimum of 50 mm beyond the expected curtain boundaries. The remainder of the tunnel was discretised using a maximum mesh size of 35mm, resulting in a total mesh of 136,000 nodes. The system was solved using the inbuilt Automatic Timescale calculator in CFX 5.7.1 (Ansys CFX (2006)) until all residuals were less than 10^{-4}, or 100 iterations had been performed. The gas velocity at the inlet to the duct was specified at the experimental conditions and at the solids inlet, the mass flow rate, velocity and initial solids volume fraction were specified. The inlet solids volume fraction of solids, r_{p0} , was calculated based on experimental data using the following equation $r_{p0} = \frac{\dot{M}_p}{\rho_p U_0 A}$, where $\dot{M}_p$ is the mass flow rate of solids entering the system, U_0 is the initial velocity of the solids entering the duct, and A is the cross-sectional area of the solids inlet. At the downstream end of the duct, the boundary was defined as an outlet boundary, such that material can only exit the system through this boundary. In the absence of experimental data, the gas and solids inlets were given a turbulence intensity of 5% (Ansys CFX (2006)). The remaining boundary conditions were governed by the no-slip condition.

In order to test the influence of gas velocity on the curtain displacement, simulations were conducted with a curtain length of 0.5m, and gas velocities of 0.5 m/s (slow), 1 m/s (normal gas velocity for rotary dryers) and 2 m/s (fast). Although not presented here, simulations were also conducted with 5 different curtain lengths (i.e. axial distances) to study how far the moving gas stream penetrated the falling curtain, and how solids displacement varied with curtain length.

Figure 2 shows the simulated results for the curtain profile measured at the centreline of the tunnel, for a 0.5 m long curtain at different gas velocities. It can be clearly seen that the gas velocity has a significant effect on the leading edge of the curtain, with increasing gas velocities causing greater displacement of the solids. At the trailing edge however, the profile is very similar at both 0.5 m/s and 1 m/s, with the solids falling almost vertically under these conditions. It is only with a gas velocity of 2 m/s that the gas is able to fully penetrate and the trailing edge of the curtain is displaced.

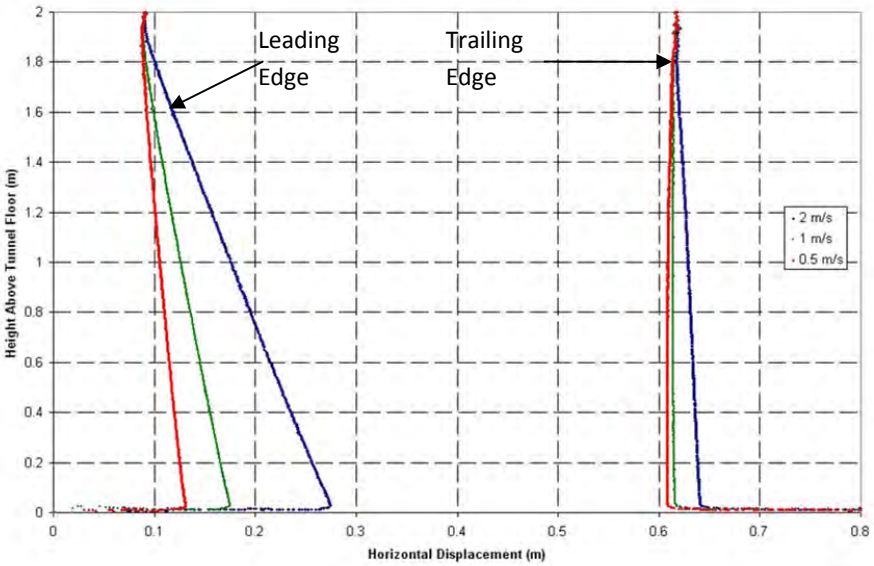

Figure 2. Solids curtain profile at different gas velocities (0.5 - 2m/s).

Figure 3 shows a colour map of the horizontal component of the gas velocity for the 1 m/s simulation. These measurements were taken in the horizontal plane at a height of 1 m above the tunnel floor (arbitrarily chosen to illustrate the behaviour of the system), with the gas being introduced from the bottom of the figure. The black line indicates the edge of the particle curtain (defined as a solids volume fraction of 0.43×10^{-3}). Figure 3 clearly shows the gas being channelled around the solids curtain, with increases of up to 25% in the gas velocity being observed around the curtain. It can also be seen that the moving gas only penetrates a short distance into the solid curtain, producing an area of negligible horizontal velocity throughout large portions of the curtain. Figure 4 shows the same measurement as Figure 3 for an initial gas velocity of 2 m/s, and again gas velocities up to 25% greater than the initial velocity can be observed. Clearly, the increased gas velocity has a significant impact on the leading edge of the curtain, causing appreciable curtain displacement and compression. It can also be seen that the moving gas penetrates deeper into the curtain than in the 1 m/s simulation, however there is still an area of negligible horizontal gas velocity throughout large portions of the curtain. Given that flights are often staggered to maximise gas-solid interactions, these results provide useful guides to appropriate spacing. In industry flights are typically staggered at around 1-2 m intervals, yet this study suggests that staggering of between 10 and 20 cm would be more effective in promoting gas penetration.

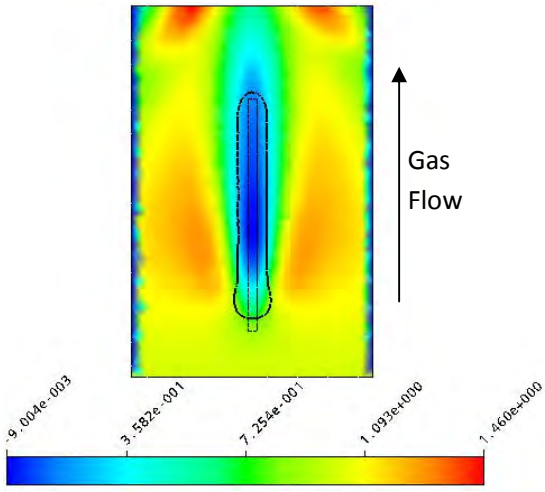

Figure 3. Horizontal gas velocity colour map at 1 m above tunnel floor (1 m/s initial gas velocity, 0.5 m inlet, 5.18 kg/m.s solids flow rate). Units are m/s.

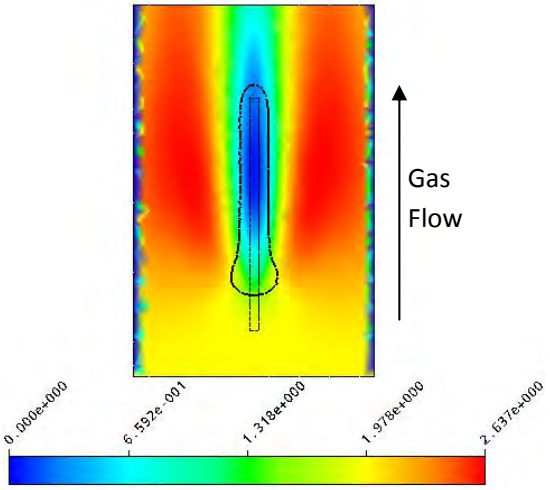

Figure 4. Horizontal gas velocity colour map at 1 m above tunnel floor (2 m/s initial gas velocity, 0.5 m inlet, 5.18 kg/m.s solids flow rate). Units are m/s.

From the simulation results, it is possible to assess curtain displacement resulting from changes in gas velocity. Figure 5 shows the trend in the displacement of the curtains leading edge over a fall of 2 metres at the gas velocities studied. The curtain displacement is well represented by a second order polynomial, which reconciles with fact that drag is proportional to velocity squared.

Simulations such as this provide an example whereby CFD can be used to regress correlations that can be embedded in the PPCM of a industrial flighted rotary dryer. In this case, PPCM parameters (e.g. curtain displacement) become functions of operating variables such as gas velocity. Extensions could include developing CFD derived regressions that also account for the effects of solids flow rates and/or particle size distribution. Furthermore, using averaged CFD curtain properties such as the fall time (i.e. mean residence time in the active phase), can be used to replace isolated sphere model predictions. This would be advantageous because it is well known that drag in curtains is different to that experienced by isolated single particles (Hurby *et al.* (1988)).

The predicted displacement of the solids due to gas-solids interactions appears small in comparison to those reported by Baker (1992), which is likely due to different initial conditions of the curtain. In these simulations, the initial conditions were taken using experimental data from a flight unloading apparatus with an un-serrated flight (Lee and Sheehan, 2010). However, most industrial dryer use serrated flights, which create a broader, less dense curtain. This reduced density allows greater gas-solids interaction and thus greater displacement of solids. Another possible factor affecting the results is the interactions between curtains. In a system with multiple curtains there will not be as much space available for channelling around the curtains, which may cause greater interactions between the gas and solids.

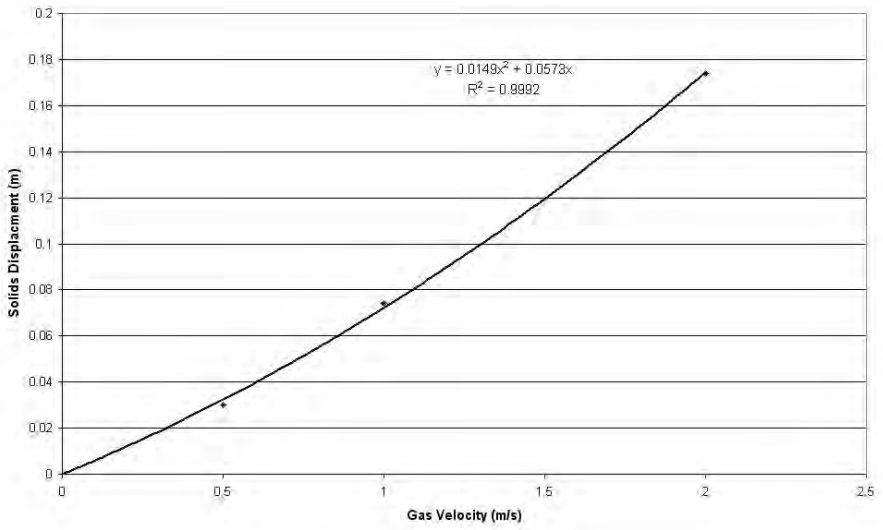

Figure 5. Simulated single curtain displacement over 2 metres at different gas velocities.

Multiple Curtain Studies

The phenomenon of channelling of the gas flow around the falling curtains in a rotary dryer was first considered by Baker (1992) as part of his studies into the gas-solids interactions. In a system with multiple curtains, the gas flow should channel between curtains, resulting in channels of high gas velocity that may influence solid particles at the curtain edges. In order to understand channelling behaviour, a series of simulations were conducted using multiple curtains with different spacing between curtains.

CFD simulations were conducted using the average particle curtain properties used for the single curtain simulations for all curtains, which is a reasonable approximation for the middle of the unloading profile where the unloading rate is reasonably constant. The simulations were conducted using a tunnel 500 mm high, 340 mm across and 800 mm long. A smaller system geometry (compared to the single curtain simulations) was used due to the greater mesh requirements to resolve the gas-solids interactions for the multiple curtains. Solids were introduced along the top of the tunnel starting 100 mm from the gas inlet, and allowing 200 mm between the end of the inlet and the end of the tunnel. The tunnel was discretised with an 8.4 mm tetrahedral mesh across the entire tunnel, resulting in 368,780 nodes. Four simulations were run with curtain spacing varying between 50 mm and 80mm. Curtains were equally spaced across the tunnel, with the two outermost curtains extended to reach the wall to prevent gas for being channelled along the wall without affecting the curtain. Due to the fixed size of the tunnel, the constant curtain spacing meant that the number of curtains present in the simulations also varied with curtain spacing, making extrapolations based on total curtain numbers difficult.

Figures 6 to 7 show the simulated solids volume fraction at a horizontal cross-section 0.25 m above the floor of the tunnel (halfway through the fall) for the different curtain spacing, with gas entering from the right hand side at 1m/s. The black boxes show the location of the solid inlets. As can be seen, with a curtain spacing of 50 mm, the curtains have merged to form a single broad curtain, but as the curtain spacing increases to 80mm, individual curtains begin to become apparent. This agrees well with the results reported by Wardjiman *et al.* (2009). In these experiments, it was observed that falling curtains of solids with high solids volume fractions tended to expand until a stable state was reached. They proposed that this was due to the difference in pressure inside the curtain compared to outside, causing the curtain to expand until the pressures equalised. This explains the expansion of the curtains observed in the multiple curtain simulations, resulting in the merging of the curtains into a uniform phase when the curtain spacing is small enough.

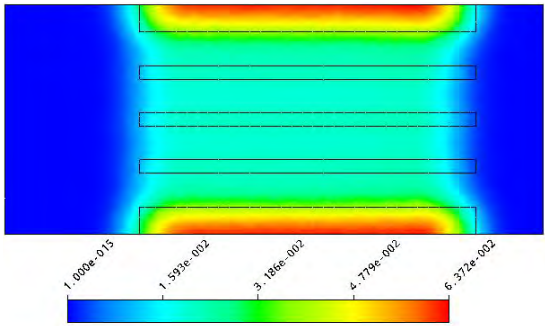

Figure 6. Solids volume fraction colour map at 0.25 m above tunnel floor with 50 mm curtain spacing.

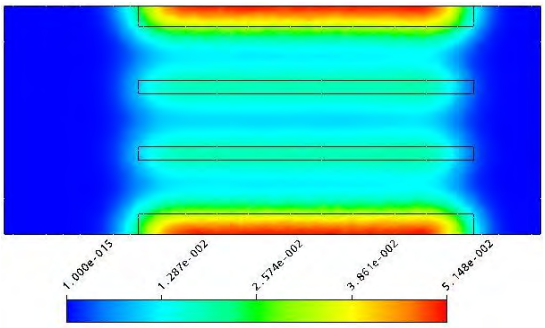

Figure 7. Solids volume fraction colour map at 0.25 m above tunnel floor with 80 mm curtain spacing.

This means that at low curtain spacing, where the curtains have merged into a single uniform phase, the gas flow through the curtain should also be uniform, as there are no regions of reduced solids volume fraction through which the gas will channel. As the curtain spacing increases, and individual curtains become distinct, and the regions of lower solids volume fraction between the curtains will allow for the gas to be channelled. This effect is seen in Figures 8 and 9, which show the gas velocity profile through the same cross-section of the tunnel. The thick black line indicates the contour of a solids volume fraction of 4.3×10^{-3}.

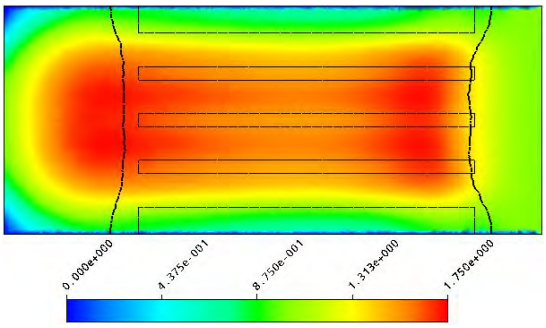

Figure 8. Horizontal gas velocity colour map at 0.25 m above tunnel floor with 50 mm curtain spacing. Units are m/s and the inlet gas velocity is 1m/s.

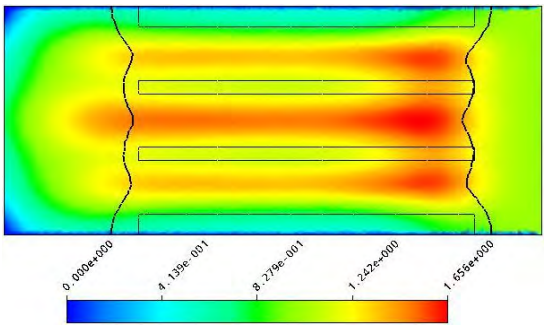

Figure 9. Horizontal gas velocity colour map at 0.25 m above tunnel floor with 80 mm curtain spacing. Units are m/s and the inlet gas velocity is 1m/s.

As can be seen, the channelling of gas flow between the curtains increases with increasing curtain spacing. At a curtain spacing of 50 mm and a fall height of 0.25 m, the gas velocity through the combined curtains is close to uniform, whilst at a curtain spacing of 80 mm significant channelling of the gas flow can be seen. Larger velocity differences between the cross-flowing gas and falling solids within the curtains would lead to enhanced heat and mass transfer. Clearly CFD simulations involving heat and/or mass transfer would be an important step defining these potential enhancements, and would have significant repercussions for flight design, and selecting the appropriate number of flights/curtains. In these simulations, it can be seen that there is significant gas velocity within the curtains, unlike the single curtain experiments where the gas velocity within the curtain could be considered negligible in comparison. This increased gas velocity within the falling curtain of solids would result in an increased displacement of the solids compared to the single curtain simulations, as was shown in Figure 10. Figure 10 shows the profile of the falling curtain, defined by a solids volume fraction of 4.3×10^{-3}, for the different simulations compared to the single curtain simulation with the same initial conditions. The curtain profile was measured along the centreline of one of the solid inlets.

It can be clearly seen that the single curtain simulation predicts less displacement of the solids curtain, due to the channelling of the gas around the curtain. It can be seen that the effects of the gas-solids interactions occur primarily at the leading edge of the curtain, with a significant displacement of solids being observed.

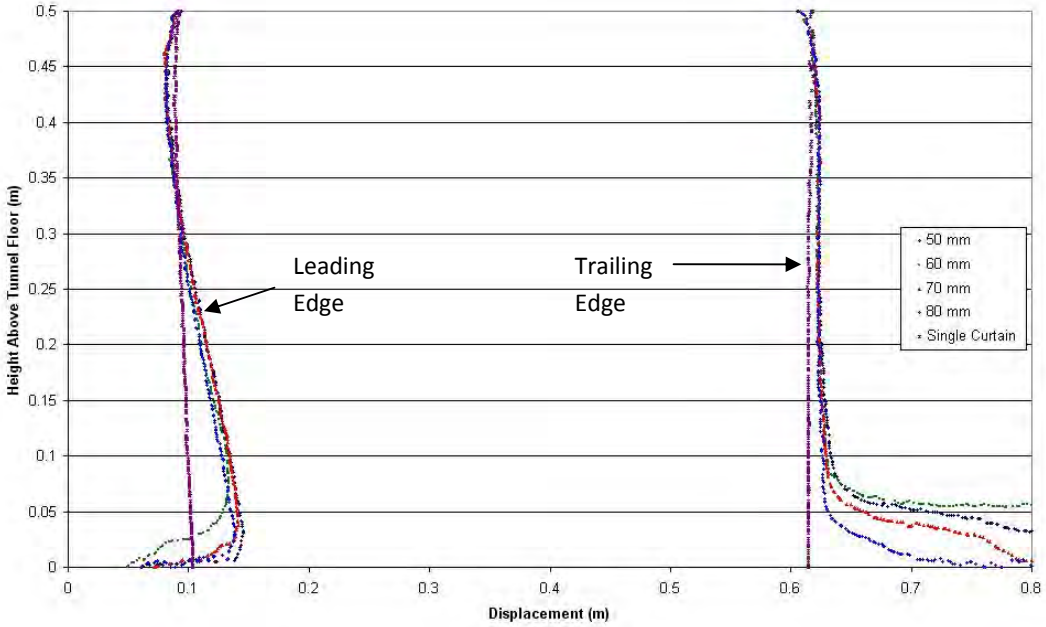

Figure 10. Curtain profiles for different curtain spacing and cross flowing gas at 1m/s.

CONCLUSIONS

The pseudo-physical compartment model (PPCM) is presented as a convenient structure to reduce the size and scale of modelled phenomena whist maintaining physical realism. In this case, a flighted rotary dryer is modelled in such a way that the behaviour of falling curtains of particles can be compartmentalised and emphasised. Eularian-Eularian CFD simulations of gas induced drag on the curtain phase within a flighted rotary dryer are described. Both single curtain simulations and multiple curtain simulations are presented. Examples illustrating the use of CFD results to develop correlations suitable for use within the PPCM are described.

Single curtain simulations show substantial channelling of gas around the sides of the particle curtain, leading to reduced particle drag (except at the leading edge) and low levels of gas penetration (20cm or less at 2m/s gas velocity). However, simulation of multiple curtains lead to more significant gas penetration that is dependent on the curtain to curtain separation. In terms of particle drag, the displacements of solids in the single curtain simulations with 850 μm particles are less than expected. The simulations conducted in this study used data measured from unserrated flights, resulting in thinner, denser curtains, that potentially under-predict solids displacement that would be observed when using serrated flights. An experimental study of the unloading behaviour of serrated flights is necessary in order to develop a better model for the gas-solids interactions in flighted rotary dryers.

REFERENCES

AJAYI OO (2011) Multiscale modelling of industrial flighted rotary dryers. PhD thesis, School of Engineering and Physical Sciences, James Cook University, Townsville.

Ansys CFX Solver Modelling Guide, (2006), Ansys Inc., Canonsburg

BAKER, C.G.J., (1992), “Air-Solids Drag in Cascading Rotary Dryers”, *Drying Technology*, **10**, 365-393

BRITTON P.F., SHEEHAN M.E. and SCHNEIDER P.A., (2006) A physical description of solids transport in flighted rotary dryers. *Powder Technology* **165**, 153-160.

CAO, W.F. and LANGRISH, T.A.G., (1999) Comparison of residence time models for cascading rotary dryers. *Drying Technology*, **17** (4&5), 825-836.

DU, W., BAO, X., XU, J. and WEI, W., (2006) “Computational fluid dynamics modelling of spouted bed: assessment of drag coefficient correlations”, *Chem. Eng. Science*, **61**, 1401-1420

DUCHESNE, C., THIBAULT, J. and BAZIN, C., (1996) “Modelling of the Solids Transportation within an Industrial Rotary Dryer: A Simple Model”, *Ind. Eng. Chem. Research*, **35**, 2334-2341

FLETCHER, D.F., GUO, B., HARVIE, D., LANGRISH, T.A.G., NIJDAM, J.J. and WILLIAMS, J., (2006) “What is important in the simulation of spray dryer performance and how do current CFD models perform? ”, *App. Math. Modelling*, **30**, 1281-1292

HURBY, J., STEEPER, R. EVANS, G. and CROWE, C., (1988) An experimental and numerical study of flow and convective heat transfer in freely falling curtain of particles. *Journal of Fluid Engineering - Trans ASME*, **110**, 172-181.

LEE A (2009) Modelling the solids transport phenomena within flighted rotary dryers. PhD thesis, School of Engineering and Physical Sciences, James Cook University, Townsville.

LEE, A. and SHEEHAN, M.E., (2010), “Development of a Geometric Flight Unloading Model for Flighted Rotary Dryers”, *Powder Technology*, **198**, 395-403

MATCHETT, A.J. and BAKER, C.G.J. (1987) Particle residence times in cascading rotary dryers Part 1 - Derivation of the two-stream model. *Journal of Separation Process Technology*, **8**, 11-17.

ROJAS, R., PIÑA, J., BUCALA, V., (2010), "Solids transport modeling in a fluidised drum granulator", *Ind. Eng. Chem. Res.*, **49**, 6986-6997

SCHILLER, L. and NAUMANN, Z., (1935), “A Drag Coefficient Correlation”, *Zeitschrift des Vereines Deutscher Ingenieure*, **77**, 318-320

SHEEHAN, M.E., BRITTON, P. and SCHNEIDER, P.A., (2005), “A Model for Solids Transport in Flighted Rotary Dryers Based on Physical Considerations”, *Chem. Eng. Science*, **60**, 4171-4182

WARDJIMAN, C., LEE, A., SHEEHAN, M. and RHODES, M., (2008), “Behaviour of a Curtain of Particles Falling Through a Horizontal Gas Stream”, *Powder Technology*, **188(2)**, 110-118

WARDJIMAN, C., LEE, A., SHEEHAN, M. and RHODES, M., (2009), “Shape of a Particle Curtain Falling in Stagnant Air”, *Powder Technology*, **192(3)**, 384-388

Chapter 2: Bubbles and Droplets

Bubbles and droplets have fascinated scientists for centuries. However, the list of unresolved questions is long which is confirmed by the number of scientists currently working on the topic. Technological developments the last decades within photography, lasers and computers have advanced our ability to quantitatively describe the motion and behavior of bubbles and droplets. This is important for understanding many phenomena in nature and industry. These dispersed particles are present in rainfall, chemical and metallurgical reactors, champagne and beer, in oil and gas pipelines and many other contexts. They play an important role in mixing and separation, and in heat and mass transfer.

Bubbles and droplets can be studied by CFD as individual particles, as a small or limited number of particles or as an infinite amount of particles in a large reactor. Since the number of bubbles and/or droplets varies greatly between the different phenomena of interest, the modelling techniques will also vary due to the pragmatic choice of resolution and computational time versus sufficient accuracy. The following papers illustrate this nicely as 3 different approaches to the topic are presented.

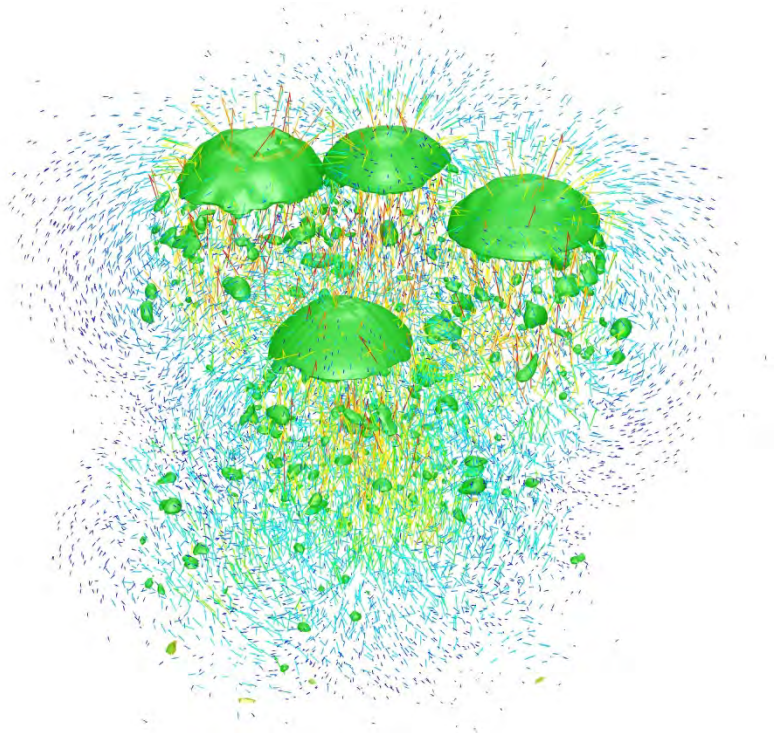

AN ENHANCED FRONT TRACKING METHOD FEATURING VOLUME CONSERVATIVE REMESHING AND MASS TRANSFER

Ivo ROGHAIR[1]*, **Martin VAN SINT ANNALAND**[1]†, **Hans KUIPERS**[2]‡

[1]Chemical Process Intensification, Multiphase Reactors Group, Eindhoven University of Technology, The Netherlands

[2]Multiscale Modeling of Multiphase Flows, Multiphase Reactors Group, Eindhoven University of Technology, The Netherlands

* E-mail: i.roghair@tue.nl
† E-mail: m.v.sintannaland@tue.nl
‡ E-mail: j.a.m.kuipers@tue.nl

ABSTRACT

A chemical species transport model is developed and coupled to an improved Front-Tracking model, enabling dynamic simulation of gas-liquid mass transfer processes in dense bubbly flows. Front-Tracking (FT) is a multiphase computational fluid dynamics technique where the location of a fluid-fluid interface is tracked via the advection of interface marker points, which make up a triangular mesh. A common drawback of FT implementations is that the volume enclosed by a mesh is not conservative during transient simulations. A remeshing technique is adopted to counteract these volume defects while keeping all physical undulations unharmed. The new remeshing procedures have been verified by comparison with results from the literature.

Species transport is modelled by a convection-diffusion equation which is discretized on a Eulerian grid, superimposed and possibly refined with respect to the grid used for the solution of the fluid flow equations. The velocity components have been interpolated to the refined grid using a higher-order solenoidal method. Enforcement of the Dirichlet condition for the concentration at the gas-liquid interface is achieved with an immersed boundary method, enabling the description of gas to liquid mass transfer. Careful validation of the newly implemented model, using synthetic benchmarks (exact solutions) and a comparison with correlations from the literature, has shown satisfactory results.

The model is used for a variety of hydrodynamic studies. In particular, the model is very suited to simulate (dense) bubbly flows due to the absence of artificial coalescence. A number of results, such as a closure of the drag force for bubbles rising in a bubble swarm and simulations of the bubble-induced turbulent energy spectra will be outlined.

The liquid side mass transfer coefficient in dense bubble swarms, with gas fractions between 4% and 40%, has been investigated using the new model. The simulations have been performed in a 3D domain with periodic boundaries, mimicking an infinite swarm of bubbles. To prevent the liquid phase to become saturated with chemical species (with the consequence of a vanishing chemical species flux due to saturation of the liquid bulk), simulations have been performed using either artificial fresh liquid inflow, or a first order chemical reaction in the liquid phase. The results indicate that the liquid-side mass transfer coefficient rises slightly with increasing gas fraction.

Keywords: CFD, hydrodynamics, bubbly flows, turbulence, mass transfer .

NOMENCLATURE

Greek Symbols

α	Gas hold-up, [-].
Γ	Solution grid, [-].
ϕ	Volume fraction, [-].
ρ	Mass density, [kg/m^3].
μ	Dynamic viscosity, [Pa s].
σ	Surface tension, [N/m].
χ	Aspect ratio, [-].

Latin Symbols

A,S	Surface, [m^2].
$\mathbf{c}$	Centroid, [m].
c	Concentration, [mol/L].
C_D	Drag coefficient, [-].
d	Diameter, [m].
$\mathscr{D}$	Diffusion coefficient, [m^2/s].
Eo	Eötvös numer Eo $= \frac{gd^2\rho}{\sigma}$, [-].
F	Force, [N].
g	Gravity constant, [m/s^2].
H	Henry's constant, [-].
k_L	Mass transfer coefficient, [m/s].
p	Pressure, [Pa].
Pe	Péclet number Pe $= \frac{v_\infty d}{\mathscr{D}}$, [-].
Re	Reynolds number Re $= \frac{\rho\|\mathbf{u}\|d}{\mu}$, [-].
Sh	Sherwood number Sh $= \frac{k_L d}{\mathscr{D}}$, [-].
$\mathbf{n}$	Normal, [-].
$\mathbf{t}$	Tangent, [-].
t	Time, [s].
$\mathbf{u}$	Velocity, [m/s].
V	Volume, [m^3].

Sub/superscripts

a,b,c,i,m	Marker indicator.
h,s	Hydrodynamic/Species mesh.
b	Bubble.
$n,*,n+1$	Previous, intermediate, next (time step).
∞	Single rising bubble in a quiescent liquid.

INTRODUCTION

In the chemical industry, many processes involve the exchange of (possibly reacting) components between a gas and liquid phase, for instance in oxidation or hydrogenation processes (Deen *et al.*, 2010). Such processes are typically per-

formed in bubble column (slurry) reactors, a column filled with liquid (and possibly a solid catalyst) in which gaseous reactants are introduced at the bottom or via immersed spargers. The gas flow rate is usually large so that dense bubble swarms rise through the liquid.

In order to understand and optimize these processes, it is important to gain insight in the the hydrodynamic and mass transfer characteristics of bubbles rising in a swarm. In recent work, we have used direct numerical simulations (DNS) to study the drag acting on bubbles rising in a swarm (Roghair *et al.*, 2011b), and the resulting closure relations have successfully been applied in a (larger scale) discrete bubble model (Lau *et al.*, 2011). The use of DNS, as opposed to detailed experiments, has advantages, as it provides full insight in the dynamics of the flow, including the deformation of the interface and the micro-structure of the flow field. Besides studying the drag acting on rising bubbles, the method can be used to describe bubble clustering and bubble induced turbulence, but when a suitable extension with mass transfer equations is provided, it can be used to study the overall mass transfer coefficient k_L in dense bubble swarms.

The current work presents a number of hydrodynamic studies that have been performed with the Front Tracking model as well as our recent achievements to obtain the gas-to-liquid mass transfer coefficient for bubbles rising in a swarm. We outline the implementation of the numerical model (hydrodynamics and mass transfer), provide validation of the implementation and evaluate the results.

MODEL DESCRIPTION

The front tracking model used in this work has been in development in our group for about 9 years. The hydrodynamics discretisation and implementation using the Finite Volume Method is also described in detail in Dijkhuizen *et al.* (2010b). In the sections below, the basic routines of the algorithm are described. We want to highlight the renewed remeshing procedures and the incorporation of the mass transfer module.

Hydrodynamics modeling

The governing equations of the fluid flow field are given by the incompressible Navier-Stokes equation and the continuity equation, discretized on a Cartesian coordinate system using a one-fluid formulation:

$$\rho\frac{\partial \mathbf{u}}{\partial t}+\rho\nabla\cdot(\mathbf{uu})=-\nabla p+\rho\mathbf{g}+\nabla\cdot\mu\left[\nabla\mathbf{u}+(\nabla\mathbf{u})^T\right]+\mathbf{F}_\sigma \tag{1a}$$

$$\nabla\cdot\mathbf{u}=0 \tag{1b}$$

where $\mathbf{u}$ is the fluid velocity and $\mathbf{F}_\sigma$ representing a singular source-term for the surface tension force at the interface. The velocity field is continuous even across interfaces, so a one-fluid formulation has been used. The equations are solved with a finite volume technique using a staggered discretisation (see Figure 1). The flow field is solved using a two-stage projection-correction method. After solving the momentum balance for each velocity component separately, a pressure-correction step is taken to satisfy the continuity equation. These steps use an incomplete Cholesky conjugate gradient (ICCG) method to solve the linearized equations. The boundary conditions can be adjusted between free-slip, no-slip and periodic, but only the latter is used in this work.

Surface mesh

The interface is parameterized by Lagrangian tracking (control) points. The connectivity of the points build up a mesh with triangular cells, called markers (Figure 1). The positions of the control points are updated each time step. After the fluid flow has been calculated, the Lagrangian control points are moved with the interpolated velocity to their new locations (a cubic spline method is used for interpolation). The actual movement is performed using a 4$^{\text{th}}$ order Runge-Kutta time stepping scheme.

Surface tension force and pressure jump

In Eq. 1a, $\mathbf{F}_\sigma$ represents the surface tension force, a vector quantity that can be directly calculated from the positions of the interface markers. The individual pull-force of neighbouring marker i acting on marker m can be computed from their normal vectors and joint tangent as illustrated in Figure 2:

$$\mathbf{F}_{\sigma,i\to m}=\sigma\left(\mathbf{t}_{mi}\times\mathbf{n}_{mi}\right) \tag{2a}$$

The shared tangent $\mathbf{t}_{mi}$ is known from the control point locations, and the shared normal vector $\mathbf{n}_{mi}$ is obtained by averaging, from which we can discard one term due to orthogonality:

$$\mathbf{t}_{mi}\times\mathbf{n}_{mi}=\frac{1}{2}\left(\underbrace{(\mathbf{t}_{mi}\times\mathbf{n}_m)}_{=0}+(\mathbf{t}_{mi}\times\mathbf{n}_i)\right) \tag{2b}$$

Hence, the total surface tension force on a marker m is obtained by summing Eq. 2a for all three neighbouring markers:

$$\mathbf{F}_{\sigma,m}=\tfrac{1}{2}\sigma\sum_{i=a,b,c}(\mathbf{t}_{mi}\times\mathbf{n}_i)=\tfrac{1}{2}\sum_{i=a,b,c}\mathbf{F}_{\sigma,i\to m} \tag{2c}$$

As a result, three pull forces on each marker are defined which yield a net force inward, opposing the pressure jump.

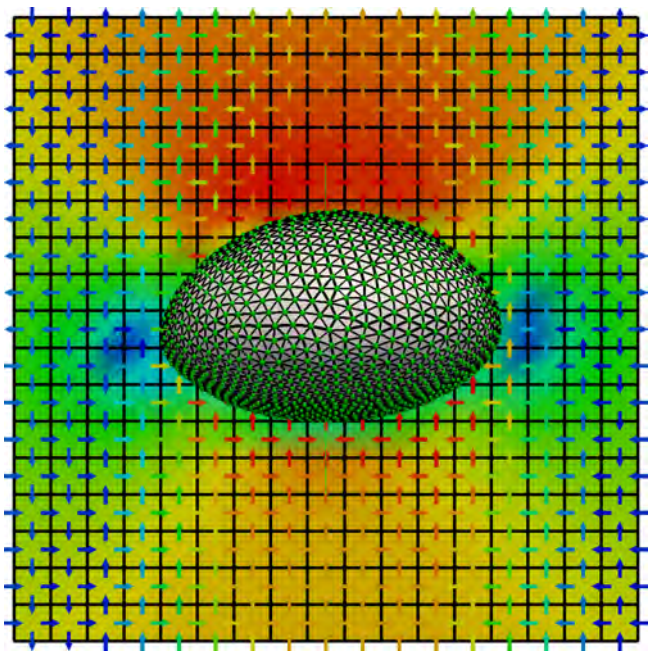

Figure 1: A zoomed snapshot of a rising FT bubble (at a very low resolution for illustration purposes), showing the tracking points and surface mesh, and the background grid with staggered velocity vectors. The colors of the background grid indicate the pressure profile, and the colors of the velocity vectors represent the magnitude.

For a closed surface, the net surface tension force on the entire object will be zero. This force $\mathbf{F}_\sigma$ is then mapped to the Eulerian cells closest to marker m using mass-weighing (Deen *et al.*, 2004) (regularized Dirac function). An important aspect of DNS involving small bubbles (e.g. $d_b \leq 1.0$ mm air bubbles in water) is the large pressure jump at the gas-liquid interface, which may cause parasitic currents that may affect the final solution significantly. While these artificial currents are decreased by the mass weighing implementation (explained above), Popinet and Zaleski (1999) demonstrated that the coupling between the surface forces and the pressure jump is crucial to further minimize them. Our approach is outlined in Dijkhuizen *et al.* (2010b). The Front-Tracking model uses a method similar to Renardy and Renardy (2002) and Francois *et al.* (2006), where the pressure forces will be extracted from the surface forces at the interface, only mapping the resulting net force.

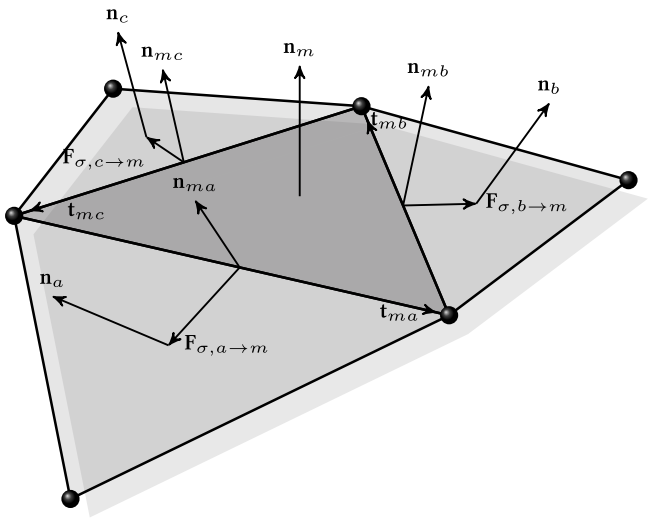

Figure 2: The surface tension calculation on marker involves the calculation of three pull-forces using the tangent and normal vectors shared with the neighbouring marker.

First note that the partial pressure drop (i.e. the pressure jump $[p]$ resulting from the surface tension force on a single marker), can be calculated using Eq. 3, if the shear stress in the normal direction is neglected.

$$\int_{\partial S} [p]\, dS = \int_{\partial S} \mathbf{F}_\sigma \cdot \mathbf{n}$$
$$[p] = \frac{\int_{\partial S} \mathbf{F}_\sigma \cdot \mathbf{n}}{\int_{\partial S} dS} = \frac{\sum_m \mathbf{F}_{\sigma,m} \cdot \mathbf{n}_m}{\sum_m S_m} \tag{3}$$

The sum of the surface forces of all markers yields the pressure jump of the bubble as a whole. By distributing the total pressure jump equally back to the Eulerian mesh, the pressure jump is incorporated in the right-hand side of the momentum equations. For interfaces with a constant curvature (i.e. a sphere), the pressure jump and surface tension cancel each other out exactly, and if the curvature varies over the interface, only a relatively small nett force will be transmitted to the Euler grid.

Phase fraction and physical properties

Since the marker positions are exactly known, the phase fraction ϕ in each Eulerian cell can be computed exactly using geometric analysis. With the phase fraction, the density of each Eulerian cell is calculated by weighted averaging. The viscosity is obtained by harmonic averaging of the kinematic viscosities (Prosperetti, 2002):

$$\rho(\mathbf{x}) = \sum_{p=0}^{n_{\text{phase}}-1} \phi_p(\mathbf{x})\, \rho_p \tag{4a}$$

$$\frac{\rho(\mathbf{x})}{\mu(\mathbf{x})} = \sum_{p=0}^{n_{\text{phase}}-1} \phi_p(\mathbf{x})\, \frac{\rho_p}{\mu_p} \tag{4b}$$

The bubble properties *viz.* total surface area, volume and centroid position, can be efficiently obtained by summing over all triangular markers of an interface n_m. A scale factor s_m is defined, equal to twice the surface area of a marker obtained by the magnitude of the cross product of two marker edges $\mathbf{t}_{ma}$ and $\mathbf{t}_{mb}$:

$$s_m = |\mathbf{t}_{ma} \times \mathbf{t}_{mb}| \tag{5}$$

The total surface area of bubble b is computed with:

$$A_b = \frac{1}{2} \sum_{m=1}^{n_m} s_m \tag{6}$$

The volume of a bubble is obtained using:

$$V_b = \frac{1}{6} \sum_{m=1}^{n_m} s_m (\mathbf{c}_m \cdot \mathbf{n}_m) \tag{7}$$

with $\mathbf{c}_m$ the geometric centre of the marker and $\mathbf{n}_m$ the unit normal vector of the marker. Finally, the bubble centroid follows directly from the centroids of the triangular markers weighted with the surface area:

$$\mathbf{c}_b = \frac{\sum_{m=1}^{n_m} s_m \mathbf{c}_m}{\sum_{m=1}^{n_m} s_m} \tag{8}$$

The bubble velocity is computed from the displacement of the bubble centroid. Also, the bubble diameter along the Cartesian directions can be obtained from the minimum and maximum location of the marker points.

Remeshing

The remeshing procedure is an essential part of the Front-Tracking technique. Due to interface advection, velocity gradients induce surface grid distortion and marker elements become too large or too small, leading to a poor grid quality and in its turn decreased accuracy in the surface tension force computation. To overcome this, the remeshing procedure takes care of local relocation of the points and marker connectivity (topology changes), without "ironing out" physical undulations.

Volume changes

In the Front-Tracking method, the volume enclosed by an interface mesh may change. Although the volume changes per time step are very small, these volume changes may accumulate significantly during a simulation due to the very large number of time steps required (Figure 3) and hence must be prevented (Pivello *et al.*, 2013). Especially for the simulation of bubble swarms, where simulations should last for a longer time than for single rising bubbles, it is essential to prevent such effects. The change in volume can be caused by remeshing operations, such as edge splitting, collapsing, smoothing and swapping and due to the advection of the interface.
Bunner and Tryggvason (2002) have proposed to solve this problem by displacing the points with respect to the bubble centroid every 100 time steps in such a way that the volume

of the bubble is identical to the original bubble volume. This might cause problems when the centroid lies outside the actual enclosed volume (*viz.* skirted bubbles). In this work, a remeshing technique was implemented to prevent bubble volume changes, with a minimal impact on the bubble shape.

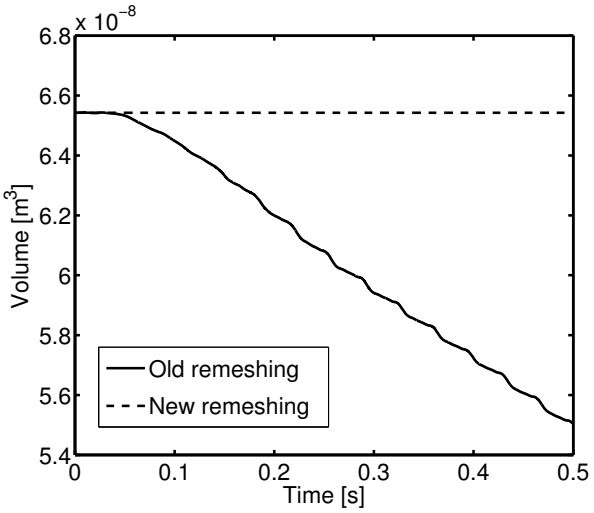

Figure 3: Volume changes may accumulate significantly during a simulation, due to advection of the interface and by using traditional, non volume-conservative remeshing methods. Using a volume-conservative remeshing technique, these effects can be prevented. The figure shows a volume vs time plot of a $d_b = 5.0$ mm air bubble in water, using both the old and new remeshing techniques.

Elementary remeshing operations

The traditional remeshing approach involves edge splitting, collapsing and swapping. In the remeshing technique presented here, these common procedures have been extended with volume conservative smoothing (regularization of the interface markers) as discussed below. Additionally, procedures are required to prevent the occurrence of rare but catastrophic mesh configurations, such as pyramids (tetraeders connected to the mesh by only a single point) or double folded marker cells.

Edge splitting and collapsing An edge is splitted (node addition) or collapsed (node removal) based on the edge length criterium which relates the edge length ℓ_m to the Eulerian cell size h according to $\frac{1}{5}h \leq \ell_m \leq \frac{1}{2}h$. In order to obtain a higher resolution in more deformed regions of the mesh, the local mesh roughness (defined as the minimum dot product of any two adjacent normals of markers connected to a node) is used to shift the balance in this algorithm towards node addition or removal.

Edge swapping In some cases, it is preferable to swap an edge rather than deleting or adding a node to the mesh. Whether or not an edge needs to be swapped depends on the number of connections of the nodes involved. This procedure ensures that equilateral marker cells are preferred.

Smoothing By distributing the control points over the interface, the grid quality can be enhanced and the required frequency of applying the other remeshing algorithms can be strongly decreased. In our algorithm, we have opted for edge-relaxation as explained by (Kuprat *et al.*, 2001).

Volume restoring/conservation

We have implemented a volume restoration/conservation method as described by Kuprat *et al.* (2001) in the Front-Tracking model. Here we present the general idea of the algorithm, the referred work provides more details on its implementation.

Whenever a node is displaced, a volume defect can be obtained by considering the volume for the situation before and after remeshing. The volume is obtained by selecting all marker cells that are connected to that node, and creating several tetrahedra using the three nodes of each marker and the bubble centroid using a scalar triple product. This volume defect can be corrected by shifting edges such that the original volume is restored, while the impact on the actual geometry of the mesh is minimized.

While this technique resolves volume changes due to prescribed point removal, edge swapping or smoothing, any volume changes that may have occurred during mesh advection, however, still need to be restored. Therefore, after the mesh restructuring, the algorithm sweeps over an entire interface mesh at once, distributing any additional volume corrections over the entire interface. This may cause the interfaces of different dispersed elements in very close proximity to cross each other, hence yield non-physical results. If such a situation occurs, the points crossing another interface are moved back and the volume difference is again distributed over all nodes of the interface, excluding those that have been moved back. We use a k-dimensional tree (kdtree, Tsiombikas (2009)) to efficiently find any points that may overlap with another interface.

Performance of the new remeshing technique

The complete revision of a cornerstone element such as the remeshing must be thoroughly validated before the code can be used for production runs. We have simulated a $d_b = 4.0$ mm air bubble in water using the old and new technique and compared the interface mesh (Figure 4) and the rise velocity profile as a function of time (Figure 5).

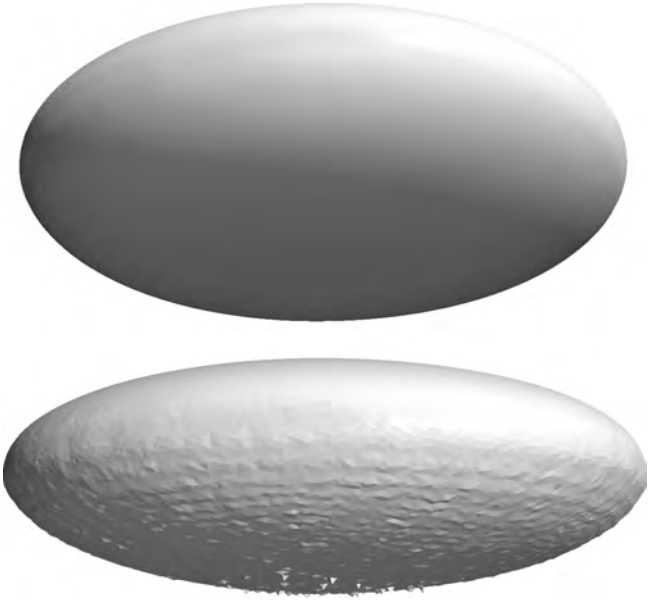

Figure 4: The mesh structure compared for the old and new remeshing techniques. It can be seen that the bubble interface using the old remeshing technique shows profound undulations and artefacts.

The interface mesh is, as expected, much smoother compared to the old remeshing technique. The rise velocity shows a slightly different profile; although both techniques show the onset of the velocity oscillations at the same time (due to the wobbling behaviour of the bubble), the velocity profiles are out of phase. The new remeshing makes the bubble rise velocity oscillate with a slightly larger amplitude (due to stronger shape deformations), resulting in a slightly lower frequency. Partly, this is due to the volume conservative properties of the new remeshing method, but also the enhanced mesh topology may be of importance. The time-averaged rise velocities do not differ significantly after discarding the transient period of the first 0.2 s, the new remeshing yields 2.82 m/s, whereas the old remeshing gives 2.88 m/s.

The Front-Tracking model with the traditional remeshing technique was used to derive a drag closure for single rising bubbles in an infinite quiescent liquid (Dijkhuizen *et al.*, 2010a). These results were validated against experimental data, and therefore these results provide a good benchmark to assess the performance of the new remeshing implementation. The drag closure that was derived combines a Reynolds dependent part and an Eötvös dependent part:

$$C_D = \sqrt{C_D(\mathrm{Re})^2 + C_D(\mathrm{Eo})^2} \tag{9a}$$

using an empirically derived correlation for the Eötvös dependent part, and the correlation by Mei *et al.* (1994) for the Reynolds dependent part:

$$C_D(\mathrm{Eo}) = \frac{4\mathrm{Eo}}{\mathrm{Eo}+9.5} \tag{9b}$$

$$C_D(\mathrm{Re}) = \frac{16}{\mathrm{Re}}\left(1+\frac{2}{1+\frac{16}{\mathrm{Re}}+\frac{3.315}{\sqrt{\mathrm{Re}}}}\right) \tag{9c}$$

Further details are omitted here, since they are discussed in more detail in Dijkhuizen *et al.* (2010a). The new remeshing technique has also been used to perform simulations using air bubbles in water, and air bubbles in a viscous liquid ($\mu_l = 0.1$ Pa s), using bubble diameters varying from $d_b = 0.1$ mm and 7.0 mm. The extracted drag coefficients for all these cases have been checked to match very well with the previously derived correlation.

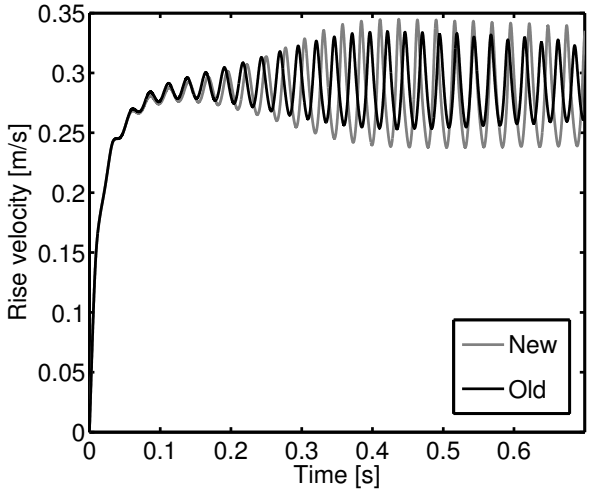

Figure 5: Comparison of the bubble rise velocity vs. time for a 4 mm bubble. While the average rise velocity is consistent in both techniques, the oscillations of the bubble occur at a slightly different frequency.

Mass transfer

In order to investigate the mass exchange between the gas and liquid phase in a bubble swarm in full detail, a mass transport model was implemented and coupled to the flow field of the Front-Tracking model. The mass transfer model accounts for convection, diffusion, species transfer from the gas to the liquid through the interface, and first-order chemical reaction. This section describes the implementation of the species transport equations into the Front-Tracking framework.

Convection-diffusion equation and boundary conditions

The mass transport equations are solved on a regular Cartesian grid, Γ_s, which is a possibly refined Eulerian mesh directly superimposed onto and aligned with the hydrodynamics grid Γ_h. A refinement factor $\mathscr{R} \in \mathbb{N}$ is used to set the relative mesh size, hence a "parent" hydrodynamics cell contains $\mathscr{R}^3$ "daughter" cells in 3D for solving the mass transfer equations. This technique allows a detailed calculation of the species balance, while keeping the computational time required for the flow solver (especially the expensive pressure-Poisson equation) within limits. Due to the deforming bubble interface and changing flow field properties emerging from the hydrodynamics part of the model, the mass transfer equations must be solved at every time step. The mass balance is given by the convection-diffusion equation on Γ_s as:

$$\frac{\partial c}{\partial t} + \nabla\cdot(\mathbf{u}c) = \mathscr{D}\nabla^2 c - k_1 c + F_s \tag{10}$$

Here c denotes the concentration in mol/L, $\mathbf{u}$ the velocity, $\mathscr{D}$ the diffusion coefficient in m^2/s, and F_s the source term to enforce the boundary condition at the interface. The diffusion and first order chemical reaction terms are treated implicitly, while the other terms are treated explicitly. The convection term is discretized using the Van Leer scheme.

The solution method uses a projection-correction algorithm to accurately enforce the interface condition, i.e. $c_{\text{interface}} = c_{\text{saturation}}$. First, the equations are solved without a source term F_s^* (Eq. 11) to obtain an intermediate concentration field c^*. The appropriate forcing term can then be calculated after which the correction step follows (Eq. 12).

$$\frac{c^* - c^n}{\Delta t} = -\nabla\cdot(\mathbf{u}^n c^n) + \mathscr{D}\nabla^2(c^*) - k_1 c^* \tag{11}$$

$$\frac{c^{n+1} - c^*}{\Delta t} = -\nabla\cdot(\mathbf{u}^n c^n) + \mathscr{D}\nabla^2\left(c^{n+1}\right) - k_1 c^{n+1} + F_s^* \tag{12}$$

The ICCG matrix solver used to solve the momentum and pressure-Poisson equations in the hydrodynamics part of the code, was also employed here.

Immersed boundary method

An immersed boundary method (IBM) is employed to enfore the interface condition. The species volumetric forcing term F_s^* is determined by calculating the forcing terms for a cell i using the intermediate solution:

$$f_i^* = \frac{Hc_0 - c_i^*}{\Delta t} \tag{13}$$

where H is Henry's constant (dimensionless) and c_0 is the concentration inside the bubble. The forcing term should

only be accounted for near the interface. The regularization of the forcing term is achieved by using a weighing factor (Eq. 14) from a mapping function (Eq 15), typically using volume weighing (Deen *et al.*, 2004).

$$F^*_{s,i} = w_i \cdot f^*_i \tag{14}$$

$$w_i = \sum_m D\left(\bar{x}_i - \bar{x}_m\right) \frac{V_m}{V_{\text{cell}}} \tag{15}$$

where V_m is the volume associated with a marker m, defined as the marker area A_m multiplied with the characteristic grid cell size:

$$V_m = A_m \sqrt[3]{V_{\text{cell}}} \tag{16}$$

Velocity interpolation

The velocity, required to calculate the convective fluxes of the species, is only known on Γ_h. For $\mathscr{R} > 1$, however, the velocity is required on the refined mesh as well, and an interpolation method is required. It is important to make sure that the resulting velocity field on Γ_s is also divergence free (solenoidal), to prevent local sources or sinks for the concentration and assure that the overall mass balance is intrinsically conserved. Two interpolation techniques that have this property have been implemented:

Piecewise linear interpolation This method, where each direction is interpolated individually, is based on the work of Rudman (1998), who initially described it to perform advection of a colour function on a refined grid. For mass transfer, the method has already been applied in the work of Darmana (2006).

Higher order solenoidal interpolation This method also takes into account the orthogonal translation of the velocity components on the interpolated mesh, describing the velocities on refined cell faces using multiple (one for each direction) second-order polynomials. Details are found in the work of Balsara (2001).

For both methods it has been verified that the initial divergence-free velocity field on Γ_h can be interpolated to Γ_s while maintaining the divergence-free criterium. The latter method shows somewhat smaller errors in our evaluation using synthetic benchmarks, and it will be used as the default interpolation technique.

Initial conditions and boundary conditions

The initial concentration is typically set to zero for cells that contain only liquid, while the concentration inside the bubble is set to the saturation concentration (gas concentration c_0 multiplied by the dimensionless Henry's constant.) To account for cells containing partially gas, the following condition is applied:

$$c_g = c^* = \begin{cases} Hc_0 & \text{if } \phi_{g,i} \geq 0.99 \\ 0 & \text{if } \phi_{g,i} < 0.99 \end{cases} \tag{17}$$

where $i \in \Gamma_s$ denotes the cell on the species grid and $\phi_{g,i}$ the gas fraction in that cell.
Robin (mixed) boundary conditions have been implemented fully implicitly, which can be tuned by setting (α, β, γ) to appropriate values:

$$\alpha c_{\text{wall}} + \beta \left.\frac{\partial c}{\partial x}\right|_{\text{wall}} = \gamma \tag{18}$$

Mass transfer coefficients

The mass transfer between the phases is quantified by calculating the mass transfer coefficient k_L, which can be defined in two different ways;

- Global mass transfer coefficient, integrated over the entire domain. This mass transfer coefficient is calculated using the change of species concentration in the domain before and after the forcing step:

$$k_{L,\text{domain}} = \frac{V_{\text{cell}}}{A_{\text{total}} \Delta t \left(Hc_0 - \langle c \rangle\right)} \sum_{i=0}^{i=n_{\text{cells}}} \left(c_i^{n+1} - c_i^n\right) \tag{19}$$

- Bubble wise, by summing the mass forcing for each marker on a bubble ($F^*_{s,i}$, see Eq. 14), followed by summing the mass transfer for all bubbles. The advantage of this approach is that the mass forcing can be plotted per-marker (for visualisation purposes), and for bubbles rising in swarms, the mass transfer for each bubble can be inspected separately. For a given bubble i, this mass transfer coefficient is given by:

$$k_{L,\text{bubble}} = \frac{V_{\text{cell}}}{A_b \Delta t \left(Hc_0 - \langle c \rangle\right)} F^*_{s,i} \tag{20}$$

Note that the average liquid concentration, $\langle c \rangle$, vanishes for single bubbles rising in a clean, "infinite" liquid. It has been varified that the average of $k_{L,\text{bubble}}$ over all bubbles yields $k_{L,\text{domain}}$.

Validation

Simulations of mass transfer of single rising bubbles have been performed to allow for comparison with correlations from the literature. Many correlations to predict the Sherwood number Sh for single rising bubbles can be found in literature, which are often applicable to a specific regime. An experimentally derived correlation was proposed by Takemura and Yabe (1998) for spherical gas bubbles with a Reynolds number less than 100, and Péclet numbers $\text{Pe} > 1$:

$$\text{Sh} = \frac{2}{\sqrt{\pi}} \left(1 - \tfrac{2}{3} \frac{1}{\left(1 + 0.09\text{Re}^{\frac{2}{3}}\right)^{\frac{3}{4}}}\right)^{\frac{1}{2}} \left(2.5 + \sqrt{\text{Pe}}\right) \tag{21}$$

Lochiel and Calderbank (1964) present Eq 22a to account for the Sherwood number of oblate spheroidal bubbles:

$$\text{Sh} = \frac{2}{\sqrt{\pi}} \sqrt{\text{Pe}} \left\{ \frac{2}{3} \left(1 + - \left(\frac{e\chi^2 - \chi \sin^{-1} e}{e - \chi \sin^{-1} e}\right)\right)\right\}^{1/2} \times \frac{2\chi^{1/3} \left(\chi^2 - 1\right)^{1/2}}{\chi \left(\chi^2 - 1\right)^{1/2} + \ln\left[\chi + \sqrt{\chi^2 - 1}\right]} \tag{22a}$$

where $\chi = \frac{\text{major axis}}{\text{minor axis}}$ is the bubble aspect ratio and e the corresponding eccentricity given by:

$$e = \sqrt{(1 - \chi^2)} \tag{22b}$$

Simulations of a single rising bubble in an infinite liquid, including mass transfer from the gas to the liquid phase, have been performed. The performance of all aspects of the mass

transfer model (diffusion, convection, immersed boundary method) have been verified.
The comparison of these results with the correlations is presented in Figure 6. We have determined that the simulations describe the results within 12% of the literature values.

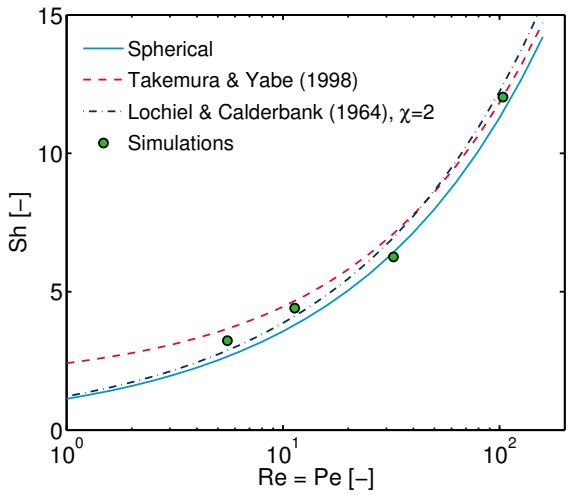

Figure 6: The Sherwood number of a single rising bubble in an infinite, initially quiescent liquid is compared to the exact correlation for flow around a sphere (potential flow) and the correlations of Takemura and Yabe (1998) and Lochiel and Calderbank (1964), the latter plotted for $\chi = 2$

RESULTS

Drag correlation

Simulations have been performed to derive a drag correlation for bubbles rising in a swarm as a function of the gas hold-up (Roghair *et al.*, 2011b).

Simulation settings

The simulation settings (physical parameters) to derive the drag closure are given in this section. Initially, the bubbles are placed randomly throughout the periodic domain. The physical properties of the gas and liquid phases are, for the base case, set up using the values for air bubbles in water. These properties have been varied to investigate the influence of the Eötvös and Morton number. These properties and the resulting Morton and Eötvös numbers are shown in Table 1. For each case, multiple simulations were performed to account for different gas fractions, varying between 5 and 45%. The cases 1–5 were selected to study the influence of the Eötvös number, whilst keeping the Morton number constant. Cases 6–8 are used to study the influence of the Morton number, so we have chosen a set of three Eötvös numbers to which we should compare the results of these cases. For all cases described, the bubble Reynolds number is typically between 150 and 1200.
Although it depends on the exact conditions (viscosity of the liquid phase, bubble diameter, gas fraction), the simulation time is typically about 1.0 s, using a time step of $1 \cdot 10^{-5}$ s. The time-averaged slip-velocity (excluding the initial 0.2 seconds to omit start-up effects) has been used to derive the drag coefficient for each bubble, which is then again averaged to deliver a single drag coefficient.

A drag correlation for bubbles rising in swarms

The relative drag coefficient resulting from the simulations were sorted into series with identical Eötvös numbers. Plotting the drag coefficients, normalised with the drag coefficient on a single rising bubble (Eq. 9a, $C_{D,\infty}$), vs the gas fraction reveals a linear relation with the gas fraction, which starts at $C_D/C_{D,\infty} = 1$ for single rising bubbles, i.e. $\alpha = 0$. The slope of the linear relation varies significantly with the Eötvös number, as shown in Figure 7. A correlation that predicts the drag coefficient of a bubble in a swarm taking into account the Eötvös number and the gas hold-up α can be written as Eq. 23, where the function g incorporating Eo determines the slope of the drag coefficient vs. α.

$$\frac{C_D}{C_{D,\infty}(1-\alpha)} = f(\alpha) = 1 + g(\mathrm{Eo})\alpha \tag{23}$$

A least squares fit has yielded:

$$\frac{C_D}{C_{D,\infty}(1-\alpha)} = 1 + \left(\frac{18}{\mathrm{Eo}}\right)\alpha \tag{24}$$

In the range of $1 \leq \mathrm{Eo} \leq 5$ the correlation performs particularly well, describing the drag coefficient found in the simulations within, on average, 1.5% accuracy, while the maximum deviation was found to be 21%. Note that the limit of Eo $\to 0$ yields an infinitely large drag coefficient, however, it can be expected that at such low Eötvös numbers, a Reynolds number dependency will be found rather than an Eötvös number dependency.

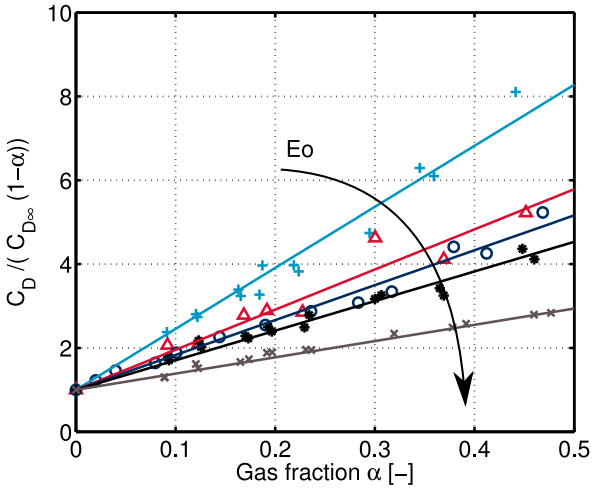

Figure 7: The drag coefficient of a bubble in a swarm, normalized with the drag on a single rising bubbles as a function of the gas fraction, for series of different Eötvös numbers. Legend: +: Eo = 1.21; △: Eo = 1.92; ○: Eo = 2.15; ∗: Eo = 2.58; ×: Eo = 4.83. Reprinted from Roghair *et al.* (2011b) with permission from Elsevier.

The simulation results shown in Figure 7 have been lumped into data series with identical Eötvös numbers, disregarding the fact that they may have different Morton numbers.
The cases that are lumped together are (see Table 1): 1 with 8 (Eo = 1.21), 4 with 6 (Eo = 2.58) and 5 with 7 (Eo = 4.83). It can be observed in Figure 7, that for all cases, no different trends or otherwise distinctive features due to differences in the Morton numbers can be discerned. In the relatively small range of Morton numbers used in the simulations (between

Table 1: Physical properties for the air-water (base case) simulations. Reprinted from Roghair *et al.* (2011b) with permission from Elsevier.

Case	d_b [mm]	μ_l [Pa s]	ρ_l [kg/m^3]	σ [N/m]	-log(Mo)	Eo	Comment
1	3.0	$1.0\cdot10^{-3}$	1000	0.073	10.6	1.21	Air-water
2	6.0	$1.5\cdot10^{-3}$	750	0.138	10.6	1.92	
3	4.0	$1.0\cdot10^{-3}$	1000	0.073	10.6	2.15	Air-water
4	6.0	$2.0\cdot10^{-3}$	1250	0.171	10.6	2.58	
5	6.0	$1.0\cdot10^{-3}$	1000	0.073	10.6	4.83	Air-water
6	4.5	$1.5\cdot10^{-3}$	950	0.073	9.87	2.58	
7	4.5	$2.0\cdot10^{-3}$	1025	0.042	8.67	4.83	
8	4.5	$1.0\cdot10^{-3}$	840	0.138	11.35	1.21	

Mo $= 2\cdot10^{-9}$ and Mo $= 4\cdot10^{-12}$), the Morton number does not affect the drag coefficient.

The derived drag closure, Eq. 24, has been implemented in a discrete bubble model and its performance has been evaluated in Lau *et al.* (2011). The proposed correlation was found to significantly improve the description of the hydrodynamics of bubble columns in comparison to drag coefficients that have been derived using single rising bubbles only. Especially the description of the velocity profiles in the centre part of the column in higher regions has improved with the newly derived correlation.

Bubble induced turbulence

Apart from bubble rise velocities and hence drag coefficients, the front tracking model can also yield information on the liquid characteristics. As bubbles rise, they induce liquid fluctuations which are referred to as pseudo-turbulence. A correct understanding of the pseudo-turbulence is critical for the simulation of bubbly flows, since it influences momentum, heat, and mass transfer rates. The Front Tracking model has been used to study these turbulent fluctuations (Roghair *et al.*, 2011a).

The characteristics of these turbulent fluctuations in the liquid are reflected in the energy spectrum. It has been shown that the energy cascade of pseudo-turbulence behaves differently from homogeneous single-phase turbulence, and hence deserves special attention in large-scale models. Lance and Bataille (1991) studied bubbles rising through an imposed turbulent flow. They measured the energy spectrum of the fluctuations and found a power law scaling with a slope of about $-8/3$, in contrast to the classical $-5/3$ for homogeneous single-phase turbulence.

In the numerical work on pseudo-turbulence by Mazzitelli and Lohse (2009) a slope of $-5/3$ of the energy spectrum was observed. However, in those simulations bubbles were approximated as point-like particles, thus disregarding finite-size effects and capillary phenomena. As Mazzitelli and Lohse (2009) mentioned in their paper, the "wrong" $-5/3$ scaling cannot be the signature of real (experimental) bubble columns.

Indeed, the experimental work of Martínez Mercado *et al.* (2010) found a scaling of the energy spectrum close to -3 for various gas fractions in the very dilute regime. These results were obtained by single-point measurements in flows with gas fractions ranging from $\alpha = 0.8$ to 2.2%, using a phase-sensitive constant-temperature anemometry (CTA) probe.

Simulation settings

Analogue to the experiments due to Martínez Mercado *et al.* (2010), simulations have been performed with the Front Tracking model, hence using finite size bubbles in contrast to the numerics due to Mazzitelli and Lohse (2009). A number of $N_b = 16$ air bubbles in water have been simulated in a fully periodic domain. The bubble Reynolds number is of order O(1000), and the Eötvös number is 2.15.

The simulation time is 4.0 s and we use a time step of $5\cdot10^{-5}$ s. Similar to the previous section, transient effects of the initially quiescent liquid and bubbles are excluded by discarding the interval of 0.0—0.2 s for the analysis. Numerical probes have been implemented to record the liquid velocity at different points in the simulation domain. These probes register the phase fraction and the fluid velocity vector in a computational cell at each time step, providing a signal very similar to the signal from the experiments. Hence, these probes are the numerical equivalent to the experimental phase sensitive CTA probe. An array of $3\times3\times3$ probes has been set up throughout the computational domain.

Turbulent energy spectrum

For the calculation of the energy spectra of liquid fluctuations we follow the method described in Martínez Mercado *et al.* (2010). Since the liquid velocity can only be used if the probe resides in a liquid-filled cell, the velocity signal becomes segmented in time due to passing bubbles. For each probe we calculate the power spectrum density of the segments larger than 256 data points and average over all segments. Finally, an ensemble average over all the 27 probes is done to obtain the final power spectrum.

Figure 8 shows the averaged spectrum of all 27 numerical probes of an $\alpha = 5\%$ simulation together with the experimental data by Martínez Mercado *et al.* (2010). The simulation shows a good agreement, having a slope close to -3 in the frequency range of 20—200 Hz. The scaling frequency range for the simulations is shorter as compared to the experimental case due to the difference in simulation and measurement time. Risso and Ellingsen (2002) pointed out that the power spectra are not influenced by α, based on their experimental findings. In spite of a shorter simulation time and the above discussed convergence problems, in figure 8 we also show the spectra for a case with $\alpha = 15\%$. Due to the smaller signal segments, caused by the smaller distance between the bubbles at higher gas loadings, the -3 scaling range decreases to less than a decade.

Our finding gives additional support to the idea that this particular power law scaling in pseudo-turbulence is related to the wake of the finite-size bubbles. Whether the actual mechanism is dissipiation or transfer should be further investigated. This conclusion lies in line with experiments by Roig and de Tournemine (2007); Risso *et al.* (2008), and theoretical arguments by Lance and Bataille (1991); Risso (2011), who have also indicated the importance of bubbles' wake phenomena.

Mass transfer in bubble swarms

In this section, mass transfer from the gas phase to the liquid phase in a rising bubble swarm is studied using direct numerical simulations. We focus on the industrially relevant case of wobbling air bubbles rising in water. The chemical species that is dissolving has a dimensionless Henry constant of $H = 0.8371$ and a diffusion coefficient of $\mathscr{D} = 10^{-6}$ m/s^2.

Preventing solute accumulation

To prevent the accumulation of species in the domain, and hence to allow for simulation of an indefinite time, the top and bottom boundaries of Γ_s are treated such that the concentration of any inflowing liquid is set to zero, whereas the concentration gradient in the normal direction is gradient free for outflowing fluid. Note that the hydrodynamic equations will still be solved in a regular periodic domain. This way,the domain can be considered as a continuously stirred tank reactor (CSTR), from which the mass transfer coefficient $k_{L,\mathrm{CSTR}}$ can be determined:

$$k_{L,\mathrm{CSTR}} = \frac{\phi_v c_{\mathrm{out}}}{A_{\mathrm{lg}}\left(c^* - c_{\mathrm{out}}\right)} = \frac{\phi_v \left\langle c \right\rangle}{A_{\mathrm{lg}}\left(c^* - \left\langle c \right\rangle\right)} \tag{25}$$

Another method of limiting the liquid concentration below the saturation concentration is to incorporate a reaction term into the species balance, so mass transfer to the liquid phase will eventually balance the chemical consumption. In contrast to the method described above, the boundaries are fully periodic, hence there is no inflow or outflow to be considered. When it is assumed that the domain can be represented as a well stirred tank, the domain can be described as an integral mass balance for a batch reactor with mass transfer and reaction in steady state, and the mass transfer coefficient can be determined after rearranging the integral balance:

$$k_{L,\mathrm{batch}} = \frac{k_1 \left\langle c \right\rangle}{A_{\mathrm{lg}}\left(c^* - \left\langle c \right\rangle\right)} \tag{26}$$

Snapshots of the simulations at $\alpha = 8\%$ and $\alpha = 30\%$, using the CSTR approach and fast and slow chemical reactions, have been provided in the appendix, Figures 11 and 12.

Determining the mass transfer coefficient

The two methods described above have been used to determine the evolution of the mass transfer coefficient for bubbles rising in a swarm as a function of the gas hold-up. For the CSTR case, the time averaged mass transfer coefficient $k_{L,\mathrm{CSTR}}$ as a function of the gas hold-up is given in Figure 9. It is calculated using the forcing terms acting on the interface markers, and using Eq. 25 using both $\langle c \rangle$ and c_{out}. A marginal increase of $k_{L,\mathrm{CSTR}}$ can be discerned when increasing the gas hold-up from 4% to 40%. Extrapolating the trend towards $\alpha = 0.0$ approaches $k_L = 0.016$ m/s, the result for a single rising bubble in an infinite, quiescent liquid. The accuracy of the results strongly decreases for lower gas hold-up ($\alpha < 0.1$), since the number of bubbles, and thus statistics, is limited.

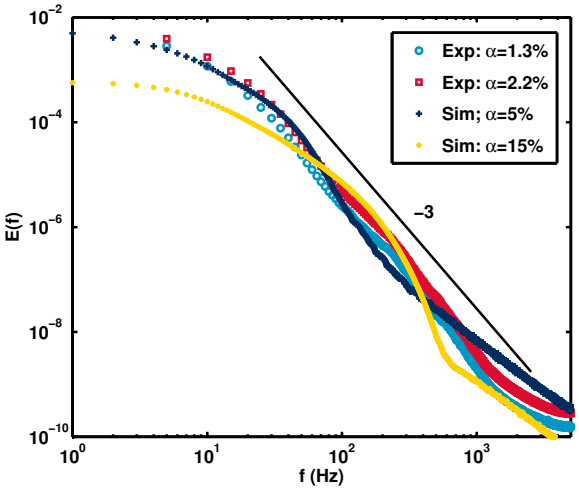

Figure 8: The energy spectra of the simulation is compared to experimental results. For the simulation with $\alpha = 5\%$, a power law close to -3 is observed for nearly one decade starting for frequencies of about 20 Hz till 200 Hz. We also show the simulation case with $\alpha = 15\%$ and with 2 s simulation time, which is not yet fully converged. Reprinted from Roghair *et al.* (2011a) with permission from Elsevier.

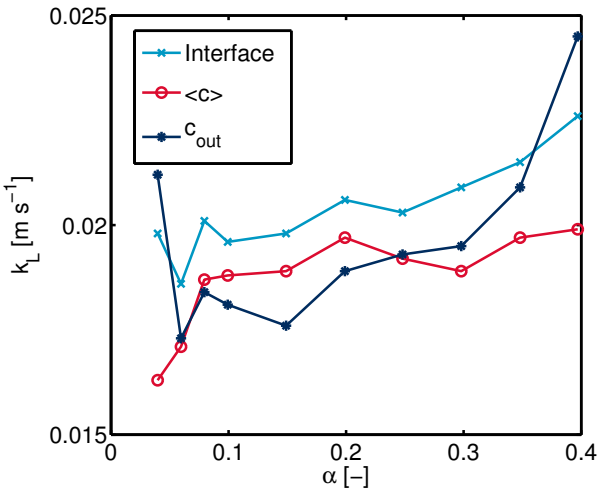

Figure 9: The mass transfer coefficient k_L of bubbles rising in a swarm plotted as a function of the gas hold-up α, determined using fresh inflow boundaries on the top and bottom walls.

The difference between the interface derived mass transfer coefficient and that using the integral balance, is explained by the large fluctuations in the concentration throughout the domain; a closer examination of the liquid concentration in the domain revealed that the standard deviation is of the same order of magnitude as the average concentration. Hence, despite the thorough mixing induced by the bubbles, high and low concentration zones exist throughout the domain, whereas the integral balance assumes a uniform bulk concentration. Rising bubbles encounter both high concentration zones, in the wakes of preceding bubbles, and low concentration zones due to the fresh inflow. The largest portion of the mass transferred through the interface, originates from

the top of the bubble. If this part is surrounded by a high concentration wake of another bubble, the mass transfer rate suddenly decreases.

For the batch reactor approach, two reaction rates have been selected; $k_1 = 50$ s^{-1} and $k_1 = 5$ s^{-1}. The mass transfer coefficient for both cases is shown in Figure 10, using both the integral mass balance (Eq. 26) and the interface forcing terms.

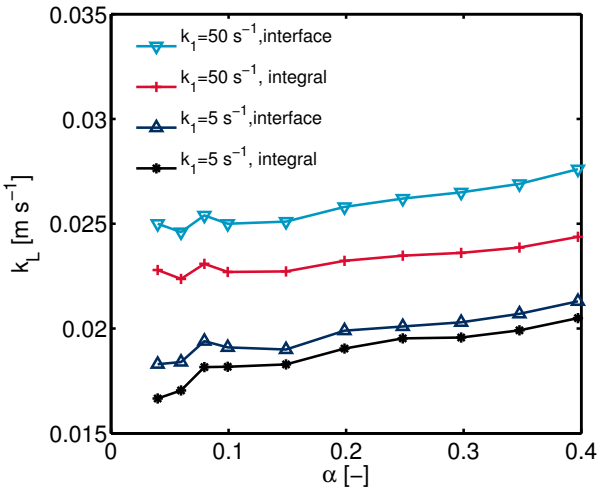

Figure 10: The mass transfer coefficient k_L of bubbles rising in a swarm plotted as a function of the gas hold-up α, determined using a first-order chemical reaction in the liquid phase.

It is observed that the mass transfer coefficient derived from the interface forcing terms is slightly higher than the mass transfer coefficient from the integral balance. The reason for this is similar to that given in the previous section; the concentration field that a bubble actually surrounds, may be quite different from the domain average concentration.

CONCLUDING REMARKS

This work has outlined the implementation of a volume-conserving remeshing technique for the Front Tracking method, and the incorporation of chemical species transport equations. The versatility of the model has been shown by studies focusing on the drag coefficient, bubble induced turbulence and mass transfer for bubbles rising in a swarm.

REFERENCES

BALSARA, D. (2001). "Divergence-free adaptive mesh refinement for magneto-hydrodynamics". *J. Comp. Phys.*, **174**, 614–648.

BUNNER, B. and TRYGGVASON, G. (2002). "Dynamics of homogeneous bubbly flows part . rise velocity and microstructure of the bubbles". *J. Fluid Mech.*, **466**, 17–52.

DARMANA, D. (2006). *On the multiscale modelling of hydrodynamics, mass transfer and chemical reactions in bubble columns*. Ph.D. thesis, University of Twente.

DEEN, N. *et al.* (2004). "Multi-scale modeling of dispersed gas-liquid two-phase flow". *Chem. Eng. Sci.*, **59(8-9)**, 1853–1861.

DEEN, N. *et al.* (2010). *Ullmann's Encyclopedia of Industrial Chemistry*, chap. Bubble Columns. Wiley-VCH Verlag GmbH & Co. KGaA, Weinheim.

DIJKHUIZEN, W. *et al.* (2010a). "DNS of gas bubbles behaviour using an improved 3D front tracking model–drag force on isolated bubbles and comparison with experiments". *Chem. Eng. Sci.*, **65(4)**, 1415–1426.

DIJKHUIZEN, W. *et al.* (2010b). "DNS of gas bubbles behaviour using an improved 3D front tracking model–model development". *Chem. Eng. Sci.*, **65(4)**, 1427–1437.

FRANCOIS, M. *et al.* (2006). "A balanced-force algorithm for continuous and sharp interfacial surface tension models within a volume tracking framework". *J. Comp. Phys.*, **213(1)**, 141–173.

KUPRAT, A. *et al.* (2001). "Volume conserving smoothing for piecewise linear curves, surfaces, and triple lines". *J. Comp. Phys.*, **172**, 99–118.

LANCE, M. and BATAILLE, J. (1991). "Turbulence in the liquid phase of a uniform bubbly air–water flow". *J. Fluid Mech.*, **222**, 95–118.

LAU, Y. *et al.* (2011). "Numerical investigation of the drag closure for bubbles in bubble swarms". *Chem. Eng. Sci.*, **66**, 3309–3316.

LOCHIEL, A. and CALDERBANK, P. (1964). "Mass transfer in the continuous phase around axisymmetric bodies of revolution". *Chem. Eng. Sci.*, **19**, 471–484.

MARTÍNEZ MERCADO, J. *et al.* (2010). "On bubble clustering and energy spectra in pseudo-turbulence". *J. Fluid Mech.*, **650**, 287–306.

MAZZITELLI, I. and LOHSE, D. (2009). "Evolution of energy in flow driven by rising bubbles". *Phys. Rev. E*, **79(6)**, 066317.

MEI, R. *et al.* (1994). "A note on the history force on a spherical bubble at finite Reynolds number". *Phys. Fluids*, **6**, 418–420.

PIVELLO, M. *et al.* (2013). "A fully adaptive front tracking method for the simulation of two phase flows". *International Journal of Multiphase Flow*.

POPINET, S. and ZALESKI, S. (1999). "A front-tracking algorithm for the accurate representation of surface tension". *Int. J. Numer. Meth. Fluids*, **30**, 775–793.

PROSPERETTI, A. (2002). "Navier-stokes numerical algorithms for free-surface flow computations: an overview". *Drop-surface interaction*, **237**.

RENARDY, Y. and RENARDY, M. (2002). "Prost: A parabolic reconstruction of surface tension for the volume-of-fluid method". *J. Comp. Phys.*, **183(2)**, 400–421.

RISSO, F. (2011). "Theoretical model for k^{-3} spectra in dispersed multiphase flows". *Phys. Fluids*.

RISSO, F. and ELLINGSEN, K. (2002). "Velocity fluctuations in a homogeneous dilute dispersion of high-Reynolds-number rising bubbles". *J. Fluid Mech.*, **453**, 395–410.

RISSO, F. *et al.* (2008). "Wake attenuation in large Reynolds number dispersed two-phase flows". *Phil. Trans. R. Soc. A*, **366**, 2177–2190.

ROGHAIR, I. *et al.* (2011a). "Energy spectra and bubble velocity distributions in pseudo-turbulence: Numerical simulations vs. experiments". *Int. J. Multiphase Flow*, **37(9)**, 1093–1098.

ROGHAIR, I. *et al.* (2011b). "On the drag force of bubbles in bubble swarms at intermediate and high Reynolds numbers". *Chem. Eng. Sci.*, **66**, 3204–3211.

ROIG, V. and DE TOURNEMINE, L. (2007). "Measurement of interstitial velocity of homogeneous bubbly flows at low to moderate void fraction". *J. Fluid Mech.*, **572**, 87–110.

RUDMAN, M. (1998). "A volume-tracking method for incompressible multifluid flows with large density variations". *Int. J. Numer. Meth. Fl.*, **28(2)**, 357–378.

TAKEMURA, F. and YABE, A. (1998). "Gas dissolution process of spherical rising gas bubbles". *Chem. Eng. Sci.*,

53(15), 2691–2699.

TSIOMBIKAS, J. (2009). "kdtree: A simple C library for working with KD-trees `http://code.google.com/p/kdtree/`".

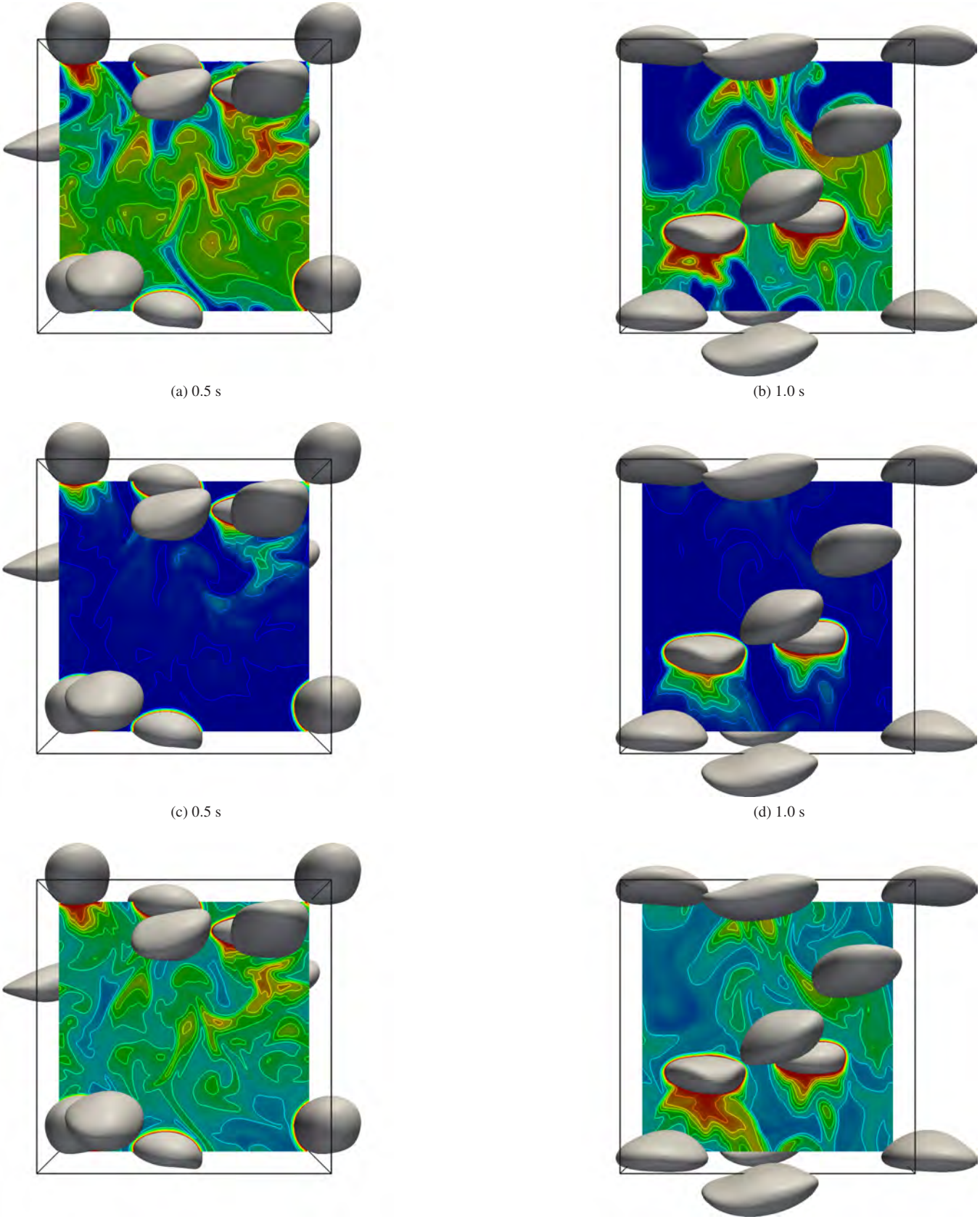

(a) 0.5 s

(b) 1.0 s

(c) 0.5 s

(d) 1.0 s

(e) 0.5 s

(f) 1.0 s

Figure 11: Snapshots of the $\alpha \approx 0.08$ simulations showing the concentration profile in a bubble swarm. From top to bottom, the CSTR approximation, fast reaction and slow reaction are displayed at 0.5 sand 1.0 s. Bubbles on the foreground have been removed for visibility reasons.

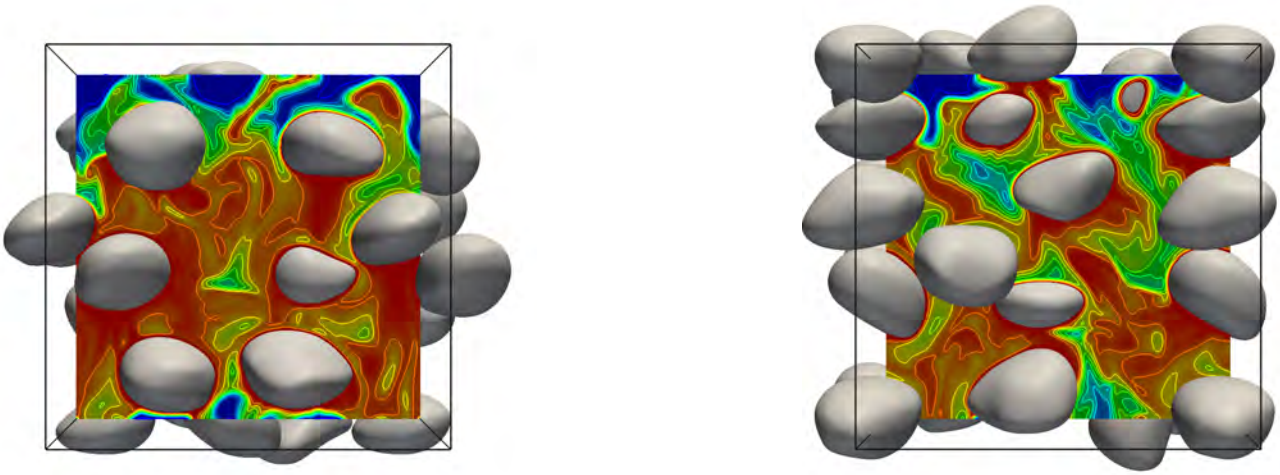

(a) 1.0 s

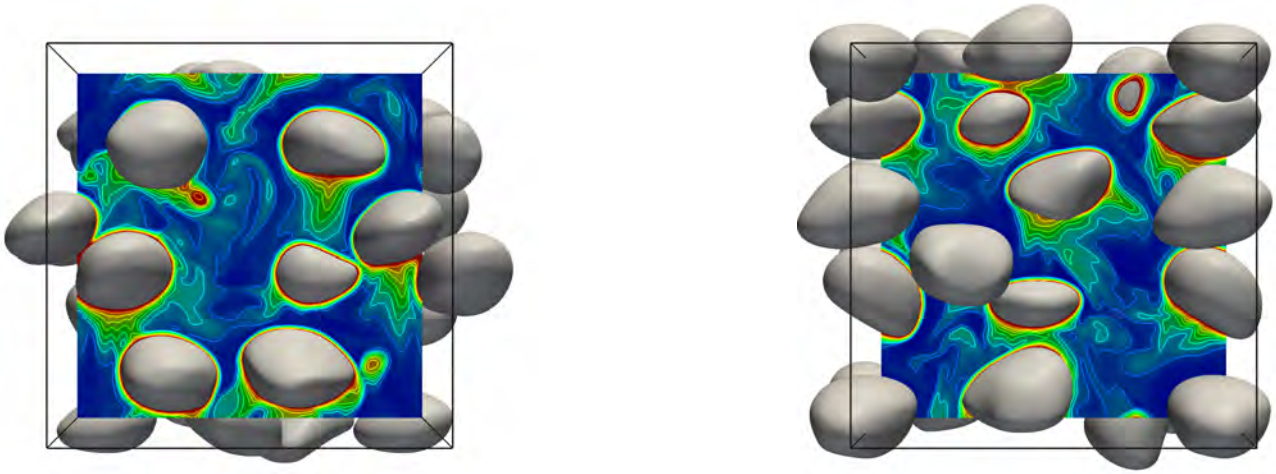

(b) 0.5 s

(c) 1.0 s

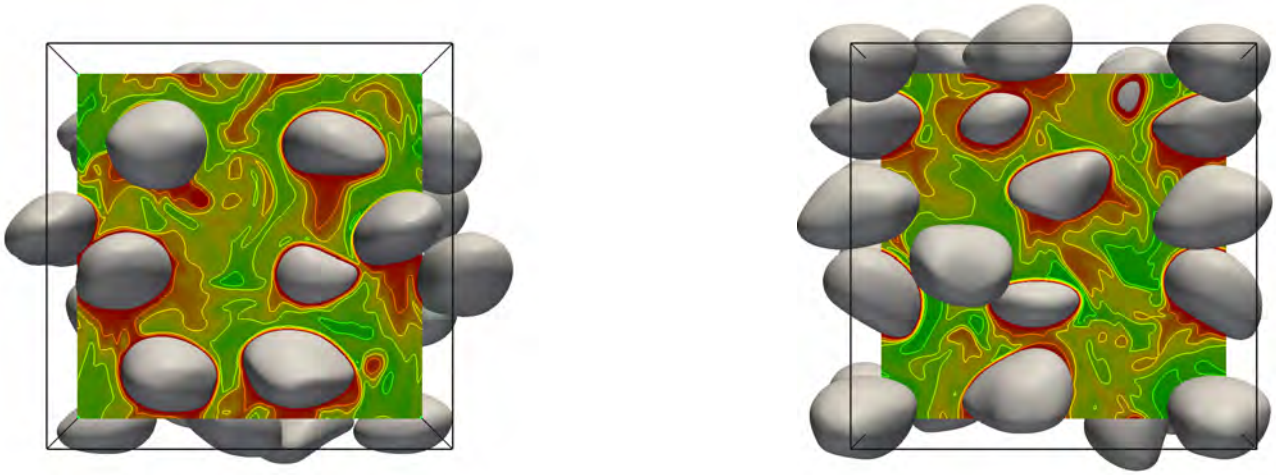

(d) 0.5 s

(e) 1.0 s

Figure 12: Snapshots of the $\alpha \approx 0.30$ simulations showing the concentration profile in a bubble swarm. From top to bottom, the CSTR approximation, fast reaction and slow reaction are displayed at 0.5 sand 1.0 s. Bubbles on the foreground have been removed for visibility reasons.

DROP BREAKUP MODELLING IN TURBULENT FLOWS

Benjamin LALANNE[1,4*], Sébastien TANGUY[2,4], Jiří VEJRAZKA[3], Olivier MASBERNAT[1,4], Frédéric RISSO[2,4]

[1] Laboratoire de Génie Chimique, TOULOUSE

[2] Institut de Mécanique des Fluides de TOULOUSE

[3] Institute of Chemical Process Fundamentals, PRAGUE

[4] Fédération de recherche FERMAT, TOULOUSE

* E-mail: Benjamin.Lalanne@ensiacet.fr

ABSTRACT

This paper deals with drop and bubble break-up modelling in turbulent flows. We consider the case where the drop/bubble slip velocity is smaller than or of the order of the turbulent velocity scales, or when the drop/bubble deformation is mainly caused by the turbulent stress (atomisation is not addressed here).
The deformation of a drop is caused by continuous interactions with turbulent vortices; the drop responds to these interactions by performing shape-oscillations and breaks up when its deformation reaches a critical value. Following these observations, we use a model of forced oscillator that describes the drop deformation dynamics in the flow to predict its break-up probability. Such a model requires a characterization of the shape-oscillation dynamics of the drop. As this dynamics is theoretically known only under restrictive conditions (without gravity, surfactants), CFD two-phase flow simulations, based on the *Level-Set* and *Ghost Fluid* methods, are used to determine the interface dynamics in more complex situations: deformation of a drop in the presence of gravity, bubble-vortex interactions. Results are compared with experimental data.
The perspectives to apply this model to breakup in emulsification processes are also discussed.

Keywords: Bubble and droplet dynamics, DNS, breakup modelling, turbulent flows, emulsions.

NOMENCLATURE

Greek Symbols

ρ Mass density, [kg/m^3].
μ Dynamic viscosity, [Pa.s].
$\hat{\rho}$ Ratio of densities: $\hat{\rho} = {\rho_d}/{\rho_c}$, [-].
$\hat{\mu}$ Ratio of viscosities: $\hat{\mu} = {\mu_d}/{\mu_c}$, [-].
ω Frequency of oscillation, [rad/s]
β Damping rate of the oscillations, [s^{-1}].
∂u Fluctuation of velocity, [m/s].
σ Surface tension, [N/m].
ϕ Level-Set function, [m].
θ Colatitude angle of spherical coordinates, [rad].
κ Interface curvature, [m^{-1}].

Latin Symbols

d Diameter of the drop or bubble, [m].
D Pipe diameter, [m].
R Radius of the drop or bubble, [m].
t Time, [s].
$\tilde{t}$ Normalized time, [-].
r Radial position in spherical coordinates, [m].
K Constant of the model, [-].
P Pressure, [Pa].
$\boldsymbol{U}$ Velocity, [m/s].
$\boldsymbol{g}$ Acceleration of gravity, [m/s^2].
$\boldsymbol{D}$ Rate of deformation tensor, [s^{-1}].
a_2 Amplitude of deformation of harmonic 2, [m].
$\widetilde{a_2}$ Normalized amplitude $\widetilde{a_2} = a_2/d$, [-].
We Weber number, [-].
Re Reynolds number, [-].
Bo Bond number, [-].
F Non-dimensional function, [-].
G Non-dimensional function, [-].
P Legendre polynomial.
V_v Vortex velocity, [m/s].
a Length of large axis of an ellipsoid, [m].
b Length of mean axis of an ellipsoid, [m].
c Length of short axis of an ellipsoid, [m].
d_0 Initial distance, [m].

Sub/superscripts

$\overline{\ }$ Mean value notation.
c Continuous phase.
d Dispersed phase.
l Number of a mode of oscillation.
$crit$ Critical value that indicates breakup.
th Values predicted by a theory.
$_{ASC}$ Used to characterise rising motion.
$_{OSC}$ Used to characterise oscillating motion.
∞ Used to characterise a value in steady state.
[ ] Jump notation at the interface.

INTRODUCTION

In industrial chemical processes, turbulent flows with dispersed deformable media (drops, bubbles) are commonly encountered and a better control of the size of the drops is desired for transport, separation issues, and maximization of interfacial area. Examples include oil industry with problems of separation of oil and water, health and food industry with the need to produce emulsions of very fine droplets in high-pressure homogenizers, nuclear energy industry with pulsed extraction columns for treatment of irradiated nuclear fuel or chemical industry for enhancement of mass transfers in gas-liquid reactors.

In CFD Eulerian codes, population-balance approaches are often used to calculate the drop (or bubble) size distribution. These approaches require closure models for coalescence and breakup phenomena.

The present study focuses on breakup phenomena occurring in turbulent flows. A recent review by Liao and Lucas (2009) has shown that several models have been derived to predict breakup probability, breakup frequency, daughter-drop size distribution after breakup. Most of these existing models use a breakup criterion based on a critical Weber number We_{crit}: it consists in a static force balance between the hydrodynamic forces responsible for deformation (turbulent stresses at the scale of the drop) and the force of surface tension that resists to shape deformations. Performing a comparison of these models, Liao and Lucas have shown that they can predict very different breakup frequencies and daughter drop size distributions when applied to a process that is not the one for which they have been calibrated. The conclusion of their paper is that physical improvements are needed for breakup modelling.

We are currently developing a new approach by modelling the deformation process of a drop in a turbulent flow using a scalar parameter $\widetilde{a_2}$ that describes its deformation. In such an approach, the breakup criterion is based on a critical deformation $\widetilde{a_{2\,crit}}$. This new model calculates the dynamic response of drops that are excited by turbulent fluctuations of the continuous phase. As shown in Galinat *et al*. (2007) or in Maniero *et al*. (2012), it gives better predictions of breakup probability than models based on a We_{crit} when compared to experimental breakup statistics.

Section 1 of this article presents our new approach and the physics on which it is based. Then, predictions of the breakup probability with our new model are compared with experimental statistics on heptane drops in a turbulent pipe flow downstream of a restriction. This section will show that our model requires a description of the drop interface dynamics, which lies on two key-parameters: the frequency of oscillation ω_2 and their damping rate β_2. Nevertheless, these parameters are known only in a limited number of situations: in case of deformations of low amplitudes, in the absence of gravity effects and without surfactants adsorbed at the interfaces.

The objective of the present paper is to show how Direct Numerical Simulations can be used to calculate ω_2 and β_2 in situations of practical interest. To achieve this goal, two-phase flow simulations using the *Level-Set* method are performed. Section 2 describes the numerical methods.

Then, after validation of the code, three examples of interface dynamics are emphasized in section 3: (a) the study of influence of gravity on ω_2 and β_2 for drops, (b) first results on the effect of surface contamination on the shape-oscillations and (c) the study of the interaction between a rising bubble and a single strong vortex.

Finally, the conclusion will introduce several perspectives of development of this model.

A DYNAMIC MODEL OF DROP DEFORMATION

As example of turbulent flow, let us consider a water pipe flow downstream of a restriction at a Reynolds number of 2100 (based on the orifice diameter), where turbulence is generated after the orifice, like in Galinat *et al*. (2007). Fig. 1 shows experimental pictures of a colored heptane drop travelling through this flow. The velocity field has been measured by PIV. From the results, we calculate a local and instantaneous turbulent Weber number *We* based on the square of the fluctuating velocity $\boldsymbol{\partial u^2(d)}$ between two points distant of the drop diameter $\boldsymbol{d}$ (taking the maximum of the difference between vertical, transversal and diagonal components): $\boldsymbol{We = \rho\, \partial u^2(d) d/\sigma}$. By averaging $\boldsymbol{\partial u^2(d)}$ in time, we obtain a map of the mean turbulent Weber number $\boldsymbol{\overline{We} = \rho\, \overline{\partial u^2(d)} d/\sigma}$, shown in fig. 1. It has been found that $\boldsymbol{\overline{We}}$ is always one order of magnitude higher than other Weber numbers that characterize the inertial drop deformation due to its mean slip velocity or due to the mean flow deceleration in the flow direction after the orifice, indicating that the turbulent fluctuations are the dominant breakup cause in this flow. Nevertheless, breakup locations do not always correspond to locations of maximum values of $\boldsymbol{\overline{We}}$.

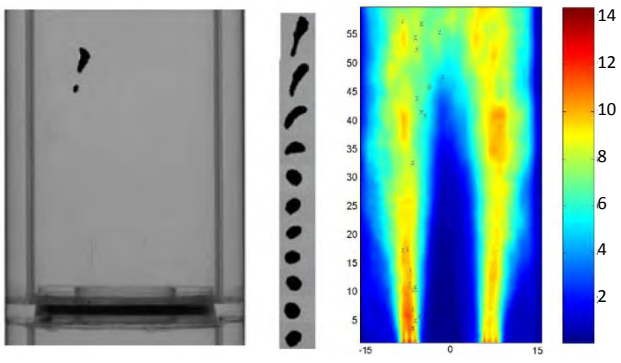

Figure 1: Breakup of a heptane drop downstream of a pipe restriction: deformation of the drop and map of $\boldsymbol{\overline{We}}$ (crosses indicate breakup locations). Figure from Galinat *et al*. (2007).

Fig. 1 illustrates also the deformation process of a drop leading to its breakup. As mentioned by Risso and Fabre (1998), the time evolution of the surface area of the drop shows the existence of a characteristic angular frequency ω_2 which is the frequency of oscillation of its shape. The time scale $t_2 = 2\pi/\omega_2$ is thus characteristic

of the response of an interface submitted to perturbations of its shape, in a similar way to what occurs in turbulent flows.

The problem of the oscillations of a drop submitted to low-amplitude shape deformations has been mathematically studied by Lamb (1932), Miller and Scriven (1968) and Prosperetti (1980). They have theoretically calculated the modes of the oscillations, which are described by means of series of spherical harmonics. A frequency ω_l and a damping rate β_l (due to the dissipation of energy ensured by viscous effects) is associated to the dynamics of each mode of order *l*. Generally, the mode *l=2,* that represents the oscillation between a prolate and an oblate shape for a drop, is enough to describe the drop or bubble shape in first approximation. Thus, the theoretical expressions given in their papers for ω_2^{th} and β_2^{th} constitute accurate predictions of the characteristic time scales of drop or bubble dynamics.

In order to take into account the interface dynamics in a deformation model, we propose to represent the drop as an oscillator, forced by the turbulent fluctuations experienced by the drop when travelling the flow. If the residence time t_r of the drop in the turbulent field is short compared to its response time t_2, breakup can occur only if the turbulent fluctuations are intense enough, as predicted by a static force balance approach. Nevertheless, if t_r is of same order or larger than t_2, the dynamic response of the drop cannot be ignored. Indeed, in that case, the drop filters the turbulent fluctuations at its own time scale t_2, and its deformation results from a coupling between turbulence and the interface dynamics.
We define a scalar parameter – amplitude of mode 2 of oscillation $\widetilde{a_2}$, normalized by d – to characterize the drop deformation, which is the solution of the following forced oscillator:

$$\frac{d^2\widetilde{a_2}}{d\tilde{t}^2} + 2\frac{\beta_2}{\omega_2}\frac{d\widetilde{a_2}}{d\tilde{t}} + \widetilde{a_2} = K\,We(\tilde{t}) \qquad (1)$$

$\tilde{t} = t/t_2$, and K is a constant parameter of the model that can be identified using experimental data. Breakup occurrence criterion is based on a threshold value of $\widetilde{a_2}$ denoted $\widetilde{a_{2\,crit}}$.Experiments show that the maximum extension of a drop prior to breakup is about twice its diameter, giving an estimation of $\widetilde{a_{2\,crit}} \cong 1/2$, but this value can vary depending on the fluids and the process considered.

Note that a similar approach that describes oscillating and distorting droplets, known as the TAB model (Taylor Analogy Breakup), is commonly used by engineers to calculate breakup in low Weber number sprays (O'Rourke and Amsden (1987)).

The 1D model of eq. (1) requires the knowledge of (i) the time evolution of the turbulent fluctuations $We(\tilde{t})$ experienced by the drop along its trajectory and (ii) the eigenfrequency of oscillation of the drop ω_2 and damping rate β_2. Note that $We(\tilde{t})$ can be obtained either from PIV measurements (Galinat *et al*. (2007)) or DNS of the single phase carrier flow (Maniero *et al.* (2012)).
As an example, fig. 2 illustrates the computation of the response $\widetilde{a_2}$ of a drop by eq. (1) to a turbulent signal $We(\tilde{t})$ from the experiment of fig. 1. On this signal, $\widetilde{a_2}$ overheads its critical value after 3 periods of oscillation: breakup does not result from a single interaction of the drop with one eddy but from a resonant interaction between the drop and several moderate vortices that allow the drop to accumulate energy of deformation in time. It is clear from this example that a model based on a critical Weber number is not accurate to predict this breakup event. To confirm this, fig. 3 compares the experimental break-up probability to the model (1) predictions for a large number of droplets and using either a critical deformation or a critical Weber number.

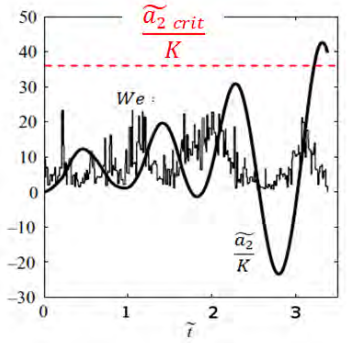

Figure 2: Computation of the deformation of a drop from model (1) using measurements of the turbulence at the scale of the drop We (Galinat *et al*. (2007)).

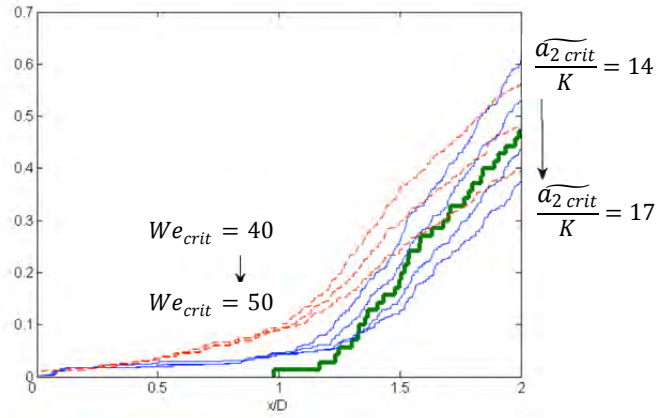

Figure 3: Breakup probability *versus* the distance from the orifice in the pipe. Thick continuous line: experiment. Thin continuous lines: prediction of model (1) assuming different values of $\widetilde{a_{2\,crit}}$. Dotted lines: predictions of model (1) assuming different We_{crit}. Figure from Maniero *et al*. (2012).

It is observed that an approach based on We_{crit} overestimates the breakup probability in the interval $0.5 < x/D < 1.5$ whereas our model based on $\widetilde{a_{2\,crit}}$ well reproduces the experimental data (the best criterion value being $\widetilde{a_{2\,crit}}/K = 16$ for this experiment). That explains why breakup locations do not necessary match with locations of high $\overline{We}$ in fig. 1.

In order to apply our model, one needs to be able to know the times scales $1/\omega_2$ and $1/\beta_2$ describing the

interface dynamics. As already mentioned, theoretical expressions ω_2^{th} and β_2^{th} for these parameters have been derived by several authors; for example, Miller and Scriven (1968) gave

$$\boldsymbol{\omega_2^{th} = \omega_2^* - \frac{\mu_d}{\rho_d R^2} F\sqrt{Re_d}} \quad (2)$$

$$\boldsymbol{\beta_2^{th} = \frac{\mu_d}{\rho_d R^2}\left[-2F^2 + G + F\sqrt{Re_d}\right]}. \quad (3)$$

F and G are functions of the density and viscosity ratios given in appendix A, $\boldsymbol{Re_d = \rho_d \omega_2^* R^2/\mu_d}$, $\boldsymbol{\text{and } \omega_2^* = (24\sigma/((3\rho_d + 2\rho_c)\, R^3))^{0.5}}$. Expressions (2) and (3) result from an asymptotic development of the solution at large Reynolds number of oscillation $\boldsymbol{Re_d}$. They are valid in the linear regime of oscillation (*i.e* for low amplitudes of deformation), disregard the effect of gravity, and are restricted to the case of pure fluids. Thus, it is requested to model the interface dynamics in more complex configurations such as in concentrated emulsions with surfactants. One way to reach this goal is to perform Direct Numerical Simulations in order to include complexity progressively.
Next section describes the numerical methods used in our CFD two-phase flow code.

NUMERICAL METHODS FOR TWO-PHASE FLOW SIMULATIONS

Configurations which are studied in the context of interface dynamics include axisymmetric and three-dimensional simulations of shape-oscillations of rising drops and bubbles, interaction between a bubble and a vortex, and breakup of bubbles/drops in turbulent flows. Direct Numerical Simulations based on the *Level-Set* and *Ghost-Fluid* methods are performed, their outlines are briefly described in this section.

In the *Level-Set* method, the interface is numerically represented by the zero-level curve of a continuous function ϕ which is defined as the algebraic distance to the interface. Its displacement in a velocity field $\boldsymbol{U}$ is computed by solving an advection equation:

$$\boldsymbol{\frac{\partial \phi}{\partial t} + U.\nabla\phi = 0} \quad (4)$$

In the framework of a one-fluid approach, the fluid motion is calculated by solving the incompressible Navier-Stokes equations by means of a projection method:

$$\begin{cases} \nabla.\boldsymbol{U} = 0 \\ \dfrac{\partial \boldsymbol{U}}{\partial t} + (\boldsymbol{U}.\boldsymbol{\nabla})\boldsymbol{U} + \dfrac{\nabla P}{\rho(\phi)} = \dfrac{\nabla.(2\mu(\phi)\boldsymbol{D})}{\rho(\phi)} + \boldsymbol{g} \end{cases} \quad (5)$$

where P is the pressure, μ the dynamic viscosity, ρ the density, $\boldsymbol{g}$ the acceleration of the gravity and $\boldsymbol{D}$ the rate of deformation tensor. I
n these equations, ρ, μ and P are discontinuous across the interface. The normal stress balance at the interface assumes that

$$[P] = \sigma\kappa + 2\,[\mu\, \partial U_n/\partial n], \quad (6)$$

where U_n is the velocity normal to the interface, n is the coordinate in the direction normal to the interface, σ the surface tension and κ the interface curvature.

To handle the discontinuity of the pressure at the interface and calculate accurately its derivatives, a *Ghost Fluid method* has been implemented: the jump condition is extrapolated in one ghost cell on each side of the interface. The numerical formulation for the viscous term and the pressure jump at the interface follows the method detailed in Sussman *et al*. (2007).
An algorithm of redistanciation is used to ensure that ϕ remains a distance function at each time step, as described in Tanguy and Berlemont (2005).

These partial differential equations are discretized using the finite volume technique on staggered grids. Spatial derivatives are estimated with a second order central scheme while a fifth order *WENO* scheme is used for the convective terms, which ensures that the solution is robust. Temporal derivatives are approximated with a second-order Runge-Kutta scheme.

DNS OF INTERFACE DYNAMICS

This section illustrates how CFD is used to calculate interface dynamics in several configurations. First, the shape-oscillations of drops and bubbles are calculated and the results used to validate our numerical code. Then, the linear shape-oscillations of rising drops are simulated in order to assess the influence of gravity on the oscillations and to extend the theoretical results in that case. Thirdly, another configuration of interaction between a rising bubble and a single vortex is studied in order to characterise the interface dynamics for non-linear deformations as those occurring in a turbulent flow.

Validation for interface dynamics problems

The numerical methods previously presented are applied to the calculation of shape-oscillations of deformed drops and bubbles. The results obtained are validated against the linear theory of oscillation, or experiments.

Comparison with theory and mesh convergence

Axisymmetric simulations of the shape-oscillations of an initially deformed drop in the absence of gravity are performed. The imposed deformation corresponds to the mode l=2 of oscillation with a low initial amplitude $a_2(0)/R = 0.1$. In order to characterise the oscillations, we define a Reynolds number of oscillation, that compares the inertial effects of deformation over the viscous damping: $Re_{OSC} = \rho_C\,(\sigma/(\rho_C R^3))^{1/2}\, R^2/\mu_C$. Three values of Re_{OSC} are investigated: 50, 100, 200. Calculations are performed on a regular mesh of 16, 32 and 64 grid points per drop radius so as to study mesh convergence of the results.

Thanks to the Level-Set function ϕ, the drop contour in spherical coordinates, $r(\theta,t)$ is extracted from the simulation at each time step, and the interface is decomposed into spherical harmonics, reading:

$$r(\theta,t) = R + a_2(t)P_2(\cos\theta), \quad (7)$$

P_2 being the Legendre polynomial of order *l*=2.

From the time evolution of a_2, the frequency ω_2 and damping rate β_2 of the oscillations can be obtained and compared against the predictions of the linear theory ω_2^{th} and β_2^{th}:

$$a_2(t) = a_2(0)\cos(\omega_2 t)\, e^{-\beta_2 t}. \quad (8)$$

	Mesh : N grid points on R	$Re_{OSC} = 50$	$Re_{OSC} = 100$	$Re_{OSC} = 200$
Error on ω_2^{th}	16	-0.07%	-0.51%	-0.43%
	32	0.06%	0.07%	-0.27%
	64	0.19%	0.01%	-0.09%
Error on β_2^{th}	16	0.18%	0.91%	5.67%
	32	-0.68%	-0.45%	-0.07%
	64	-1.15%	-1.07%	-0.76%

Table 1: Validation of the axisymmetric calculation of the shape-oscillations of non-rising drops.

Relative errors are reported in table 1 for the three Re_{OSC}. Results show that the numerical code gives very accurate results on both frequency and damping rates in this range of Re_{OSC}, for grids containing 32 or 64 points in a radius. Spatial convergence of the simulations is also proved by the tests.

Thus, these results provide a good validation of our axisymmetric numerical code to deal with interface dynamics problems. In order to validate also the Cartesian version of the code, a 3D simulation of the shape-oscillations of a bubble is carried out at $Re_{OSC} = 50$ on a grid containing 16 cells in a radius. Results obtained are superimposed on fig. 4 with the curves given by the axisymmetric version of the code with 8, 16, 32 and 64 grid points in a radius.

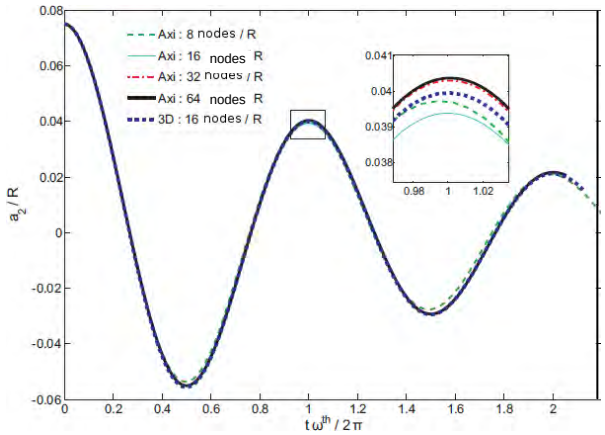

Figure 4: Validation of the 3D Cartesian calculation of the shape-oscillations of a non-rising bubble at $\boldsymbol{Re_{OSC} = 50}$. Figure from Lalanne (2012).

Fig. 4 proves again the mesh convergence of the numerical simulations for the axisymmetric calculations, and shows that the accuracy of the oscillations calculated by the 3D Cartesian version of the code is comparable to that of the axisymmetric calculation with the same number of grid points.

We can then conclude that a calculation with 16 points per bubble radius at $Re_{OSC} = 50$, either in an axisymmetric cylindrical or in a 3D Cartesian domain, gives accurate results in accordance with the theory.

Comparison with an experiment

The code is then validated by comparison with experimental measurements of the shape-oscillations of a slow-rising bubble thanks to a high-speed camera. In the experiment, the bubble is initially attached to a capillary; its sudden translation causes the detachment of the bubble that rises in still water while performing shape-oscillations. The experiment was carried out in ultra-pure conditions in order to avoid contamination due to surfactants. The oscillations, characterized by $Re_{OSC} = 164$, are described using the first ten modes and the initial amplitudes, obtained from the experimental shape at the instant of detachment, are larger than in the previous case ($a_2(0)/R = 0.18$). The Bond number $Bo = (\rho_c - \rho_d)gd^2/\sigma$ is very low ($Bo = 0.08$) to ensure that gravity has negligible effects on both the oscillations and the mean shape of the bubble (which remains spherical during the rising motion).

The shape of the interface is decomposed in spherical harmonics (until order 10):

$$r(\theta,t) = \sum_{l=0}^{10} a_l(t)P_l(\cos\theta). \quad (9)$$

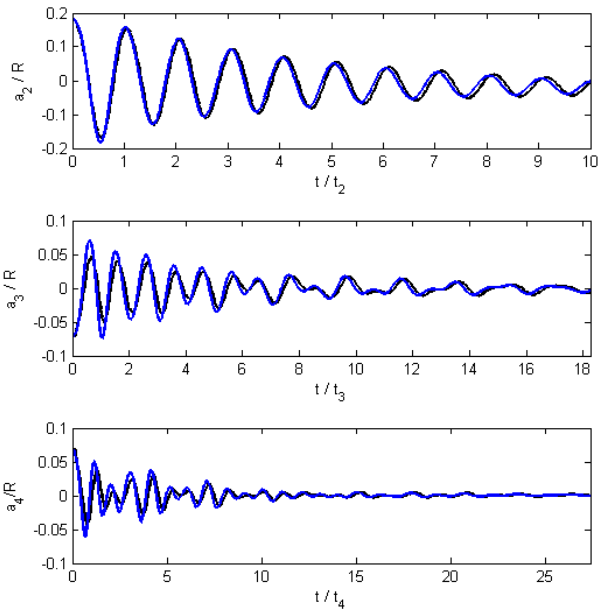

Figure 5: Time evolution of a_2, a_3 and a_4: experiments (black lines) and simulations (blue lines).

Fig. 5 compares the time evolution of a_2, a_3 and a_4 between the experiment and a simulation on a mesh with 32 nodes per bubble radius.

Results show an excellent agreement between the numerical simulations and the experiment for the different modes of oscillation, with a very good accuracy even for strongly damped oscillations (amplitudes less than 0.005R), validating again the use of the present code to capture bubble or drop interface dynamics.

Shape-oscillations of rising drops

We have achieved axisymmetric simulations of a drop rising in a quiescent liquid, its shape being initially elongated in the vertical direction. Thus, while rising, the drop performs shape-oscillations.
The objective is here to understand the effect of the rising motion on the shape-oscillation dynamics, by comparing the frequency and damping rates values with those predicted by the linear theory of oscillation, ω_2^{th} and β_2^{th}, in the absence of gravity.

The problem can be parameterized by four non-dimensional numbers: ratios of density and viscosity $\hat{\rho}$ and $\hat{\mu}$, a Reynolds number of translation $Re_\infty = \rho_C V_\infty d/\mu_C$ based on the rising drop velocity V_∞, and a Reynolds number of oscillation Re_{OSC} based on the oscillating velocity. For these simulations, $\hat{\rho}$=0.99 and $\hat{\mu} = 1$ (liquid-liquid configuration), Re_{OSC} is varied between 50 and 200, and Re_∞ ranges from 60 to 600.
The initial deformation of the drop is set to $a_2/R = 0.1$: it is low enough to ensure a linear regime of oscillation.
The regular grid used for the simulation is composed of 32 nodes per drop radius.

Let us examine the shape-oscillations of this rising drop. At $Re_{OSC} = 100$, fig. 6 presents the time evolution of the Reynolds number of rising $Re_{ASC}(t) = \rho_C V(t) d/\mu_C$ for four different values of Re_∞, and fig. 7 displays the corresponding time evolution of the second harmonic amplitude.

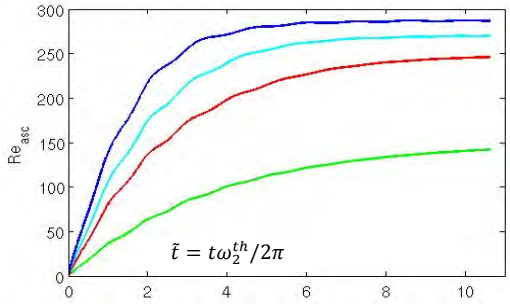

Figure 6: Time evolution of Reynolds number of rising for four drops at $\boldsymbol{Re_{OSC} = 100}$, **and** $\boldsymbol{Re_\infty}$ = 150, 200, 270, 290. Figure from Lalanne (2012).

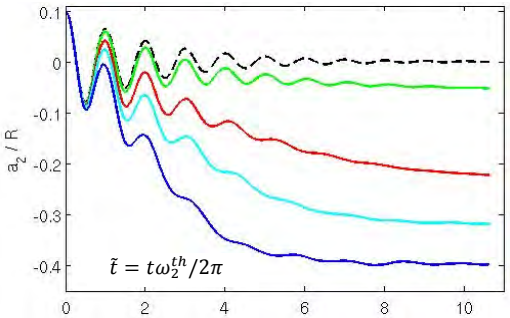

Figure 7: Time evolution of amplitude of harmonic 2 for four rising drops at $\boldsymbol{Re_{OSC} = 100}$, and $\boldsymbol{Re_\infty}$ = 150, 200, 270, 290. Dotted line: calculation for a non-rising drop. Figure from Lalanne (2012).

For each drop, the rising velocity increases until the steady state is reached. The translational velocity is very slightly affected by the presence of the shape oscillations. The evolution of the drop shape with time shows that a_2 globally decreases during the acceleration stage since the drop becomes an oblate spheroid due to the rising motion. On this curve, the shape-oscillations due to the initial perturbation are also visible. In order to analyse them and conclude about the effect of the rising motion (*i.e* the effect of Re_∞), we apply a high-pass filter at frequency ω_2^{th} to the time evolution of a_2 in order to separate the evolution of the drop mean shape (which flattens with time) from that of the shape-oscillations. Then, we measure frequency and damping rate of the oscillations on the filtered signal. We observe that the frequency of oscillation is maximum for the non-rising drop and decreases slightly (-10%) when the rising velocity increases. On the contrary, we note a strong increase of the damping rate (until +300%) of the oscillations for the cases at high Re_∞. It is interesting to note that ω_2 and β_2 do not keep constant values for a given set of parameters (Re_{OSC}, Re_∞) but instead they evolve monotonically with time.

This observation leads us to relate the decrease of the eigenfrequency and the increase of the damping rate with the drop instantaneous velocity, which increases with time. Fig. 8 and 9 display the results for drops at Re_{OSC} = 50, 100, 200 and several Re_∞: ω_2 and β_2 are presented as a function of an instantaneous Weber number $We(t) = 0.5\,(Re_{ASC}(t)/Re_{OSC})^2$ that compares the magnitudes of rising and oscillatory motions. Doing so, time evolutions of both frequency and damping rate seem to collapse on single master curves. Despite a certain scattering of the results that indicates that other factors may play a role on the oscillations (drop acceleration for example), these plots tend to show that the deviation from the theory is mainly controlled by the instantaneous velocity.

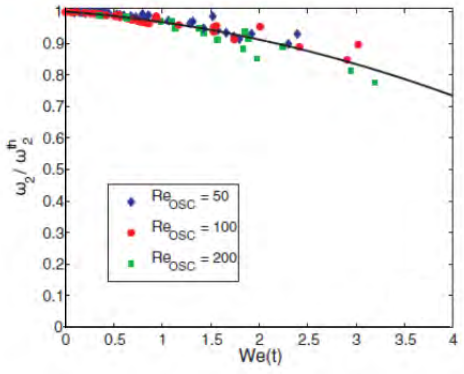

Figure 8: Frequency of oscillation of a rising drop normalized by the theoretical frequency for a non-rising drop, *versus* $\boldsymbol{We(t)}$. Figure from Lalanne *et al.* (2013).

Thus, the main effect of the rising motion on the shape-oscillations of drops is to increase the rate of dissipation of oscillation energy, provided that the rising velocity is large enough compared to the oscillating velocity.

For non-rising drops, the linear theory of oscillation (Miller and Scriven (1968)) shows that the dissipation takes place in boundary layers located on both sides of the interface, as illustrated in fig. 10, which represents the vorticity field of an oscillating drop.

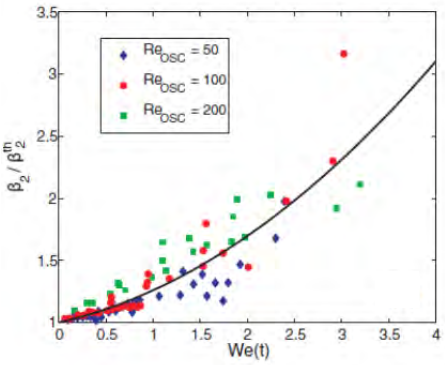

Figure 9: Damping rate of oscillation of a rising drop, normalized by the theoretical damping rate for a non-rising drop, *versus* $\boldsymbol{We(t)}$. Figure from Lalanne *et al*. (2013).

From our numerical simulations, we extract the vorticity field. For slow-rising and oscillating drops, *i.e* when the damping rate of the oscillations is not found to be affected by the translating motion, we observe that the vorticity of the flow is the sum of the vorticity involved in the motion of the same slow-rising drop which does not oscillate (called "pure rising flow"), and of the vorticity involved in the motion of the same oscillating drop that does not rise (called "pure oscillation flow"). Hence, pure rising and pure oscillation flows do not interact in the case of a slow-rising and oscillating drop, explaining why β_2 remains close to β_2^{th}. However, for rapidly rising and oscillating drops, this is not the case: we observe that vorticity contributions of rising and oscillatory motions interact, leading to an increase of the oscillation energy dissipation (*cf* Lalanne *et al*. (2013)).

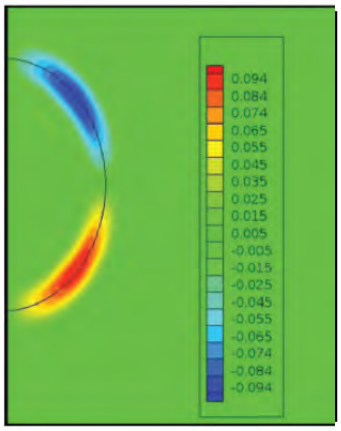

Figure 10: Vorticity field (normalized by $\boldsymbol{\omega_2^{th}}$) of an oscillating and non-rising drop at $\boldsymbol{Re_{OSC} = 100}$. The boundary layers of oscillation visible in this figure are the main location of the dissipation of the energy of oscillation. Figure from Lalanne *et al*. (2013).

Consequently, the effect of the rising motion on the damping rate of oscillation can be explained by looking at the vorticity field during the oscillating motion of the droplets.

For micrometer or millimeter-sized droplets like those commonly involved in many industrial flows, the Weber number based on the rising velocity – as defined here - can hardly be larger than unity. Therefore, the present results (fig. 8 and 9) show that the predictions of the linear theory of oscillation, which do not include the effect of gravity, provide good estimations of ω_2 and β_2 (less than 5% of discrepancy for ω_2 and less than 30% of discrepancy for β_2). This is a practical conclusion, useful to know the limits where the linear theory of oscillation remains valid in order to predict the time scales of the interface dynamics.

Oscillations of contaminated rising drops

Let us consider now the experimental investigation of a shape-oscillating heptane drop which is rising in non ultra-pure water, carried out by Abi Chebel *et al.* (2012). For different drop diameters (millimeter-sized droplets), the authors have measured the damping rates of the oscillations. Results are displayed in table 2 for two contrasted drop diameters. The experimental measurements show that β_2 overestimates by 200% or 300% the theoretical prediction of β_2^{th}, which does not consider either the rising motion or any surface contamination. Using numerical results of fig. 9, we can predict what should be the damping rate of the oscillations in the case of pure fluids and clean interfaces for these rising drops. It is found that the measured damping rates in the experiment are twice these values. Thus, another mechanism is involved: the strong increase of β_2 can be related to the presence of contaminants adsorbed at the liquid-liquid interface. Indeed, it is extremely difficult to carry out experiments with pure fluids in liquid-liquid dispersions. In that experiment, the contamination of the interfaces has been proved by calculating the experimental drag coefficient of the drops, which is found to match that of a solid sphere and not that of a drop with clean interface. We conclude from table 2 that the presence of surface-active contaminants alters significantly the shape-oscillation dynamics. This is probably related to additional tangential stresses that appear close to the interface because of contamination, which may increase strongly the dissipation within the boundary layers of oscillation.

d (mm)	Re_{OSC}	Re_∞	We at steady state	Measured β_2 / β_2^{th}	Prediction of β_2 / β_2^{th} for pure fluids
0.59	120	17	0.01	2.0	1.0
3.52	293	480	1.34	2.7	1.4

Table 2: Experimental results for oscillating and rising heptane drops in non ultra-pure water. From Abi Chebel *et al.* (2012).

Further studies are required to characterise completely the interface dynamics of drops in the presence of surfactants, which depends on the transport properties of these adsorbed contaminants at the interfaces.

Bubble-vortex interaction

In turbulent flows, bubble (or drop) breakup can result from either an interaction with a single intense vortex or with a series of moderate vortices that make the bubble accumulate energy of deformation until breakup (Risso and Fabre (1998)). Therefore, the elementary key mechanism responsible of the deformation of a bubble (or a drop) is its interaction with a vortex. An experimental study of breakup of a rising bubble in a turbulent flow, carried out by Ravelet *et al*. (2011), has shown that large bubble deformations caused by the turbulent fluctuations of the flow are quickly damped, and the authors have not observed shape-oscillations of the bubbles after interaction with strong vortices, contrary to what has been previously reported in microgravity conditions (Risso and Fabre 1998).
In order to investigate this open question of interface dynamics in a turbulent flow in the presence of gravity, three-dimensional simulations of the interaction between a rising bubble and a single vortex have been carried out. The objective of the simulations was to study the response of the bubble after large deformations of its shape.

The non-dimensional parameters that describe the rising bubble are: the ratio of density $\hat{\rho}$=0.001, the ratio of viscosity $\hat{\mu} = 0.016$, the Reynolds number of oscillation Re_{OSC}= 50, the Reynolds number of rising Re_∞= 89 or 142. A Hill's vortex of same dimension than the diameter of the bubble has been chosen in order to provoke bubble large scale deformations. Indeed, it is admitted since the pioneering works of Hinze and Kolmogorov that vortices of same size as the bubble diameter are the most efficient for breakup.
The initial condition of the calculation is illustrated in fig. 11. It is the superimposition of the velocity field induced by a Hill's vortex - known analytically, involving a potential flow of characteristic velocity V_{v0}, which is the initial velocity of the Hill's vortex (*cf* Morton (2004)) - and of the flow corresponding to a rising bubble at terminal velocity and characterized by Re_∞(calculated through a preliminary simulation). To avoid singular conditions, the vortex and the bubble are off-centered from a distance $d_0 = \sqrt{2}/2\ R$.
The mesh is Cartesian but non uniform far from the bubble. The bubble dynamics is captured thanks to the use of 16 grid points per bubble radius.
The intensity of the interaction between the vortex and the bubble is scaled by a Weber number based on the velocity V_v of the vortex at the instant it encounters the bubble: $We_v = \rho_C {V_v}^2\ d/\sigma$.

Fig. 12 displays pictures of the simulation in the case of a very intense interaction: $We_v = 16.5$ and Re_∞= 142. Before the interaction, the bubble is flattened with an aspect ratio of 1.84 because of its rising motion. During the interaction, we do not observe bubble breakup but large and non-axisymmetric deformations. To obtain an accurate description of the global shape of the bubble (large scales), we calculate its equivalent ellipsoid.

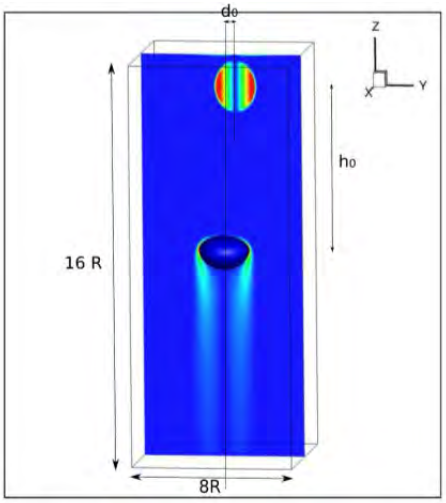

Figure 11: Initial condition (vorticity field) for a 3D-calculation of the interaction of a rising bubble and a Hill's vortex. Figure from Lalanne (2012).

It is defined as the ellipsoid of same inertia matrix as the bubble. In the following, we note *a* the length of the major semi-axis of the ellipsoid, *b* the length of the intermediate semi-axis, and *c* the length of the shorter semi-axis. Fig. 13 displays the evolution of *a*, *b* and *c* in the simulation that corresponds to fig. 12.

The bubble shape is initially symmetric around a vertical axis (see picture 1 of fig. 12) and its rising motion is steady. When the vortex arrives at the bubble location, it causes a large elongation of the bubble and consequently a strong increase of the length of its major axis. In the same time, its medium axis is slightly reduced, leading to a shape close to a cylinder with a large major axis and two small other axes. The maximum deformation can be seen in picture 3 of fig. 12. It is remarkable that the symmetry of the bubble has changed from an axisymmetric oblate shape before the interaction to an axisymmetric prolate shape at the maximum of deformation. Finally, the vortex leaves the bubble, which relaxes towards its equilibrium shape (pictures 4-7 of fig. 12). Its rising motion becomes unsteady and follows a *zig-zag* path.

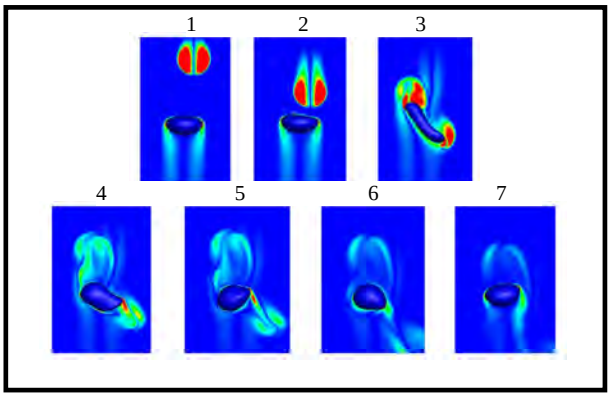

Figure 12: Bubble-vortex interaction at $\boldsymbol{We_v = 16.5}$ and $\boldsymbol{Re_\infty}$= 142. Colors correspond to vorticity levels. Time increases with the picture numbers. Note that picture 1 is the initial condition where the bubble has an oblate shape, and picture 3 is that of maximum deformation where the bubble has a prolate shape (close to a cylinder).

It can be observed in fig. 13 that the major part of the large perturbation induced by the vortex is quickly attenuated. The residual departure from the initial shape leads to slowly damped shape oscillations of low amplitudes.

Consequently, the bubble-vortex interaction can be described in two phases: the first one corresponds to a large deformation of the bubble, which is quickly damped; the second one corresponds to the relaxation of the bubble through linear oscillations.

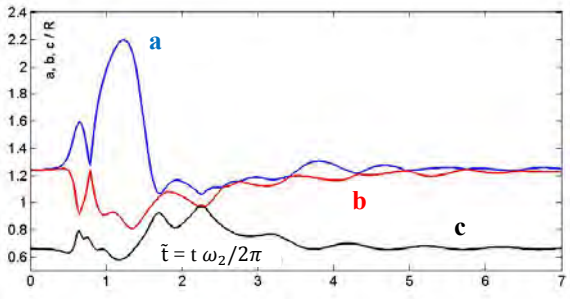

Figure 13: Time evolution of bubble semi-axes during its deformation by a vortex at $\boldsymbol{We_v = 16.5}$ and $\boldsymbol{Re_\infty}$= 142.

Various simulations have been carried out from different sets of parameters (different rising bubble velocities and vortex intensities). The decomposition of the interaction into two phases is relevant for every case.

During the first phase of large deformation, it is observed that the length of the major axis of the bubble is proportional to We_v. Fig. 14 shows the time evolution of the length of the major axis for different cases, the time being normalized by the frequency of oscillation of the rising bubble given by the theory of Meiron (1989). The duration of the large deformation phase is found to be very close to one period of oscillation.

These conclusions are in agreement with the experimental observations of Ravelet *et al.* (2011), who have also noticed that: (1) large deformations correspond to prolate bubble shapes, (2) the duration of the large deformation is equal to one period of oscillation, and (3) statistics of large bubble deformations are proportional to statistics of large turbulent fluctuations.

Hence, in case where the turbulent intensity is weak like in the experiment of Ravelet *et al.* (velocity fluctuations of about 20% of the mean velocity components), the bubble can be considered as a strongly damped oscillator, breakup is rare and occurs only during the interaction with a strong vortex characterized by a large We_v.

Note that, in the simulations, breakup is observed when the bubble elongation (compare to its initial length) is about one diameter, scaling the maximum amplitude a bubble can reach before breaking up.

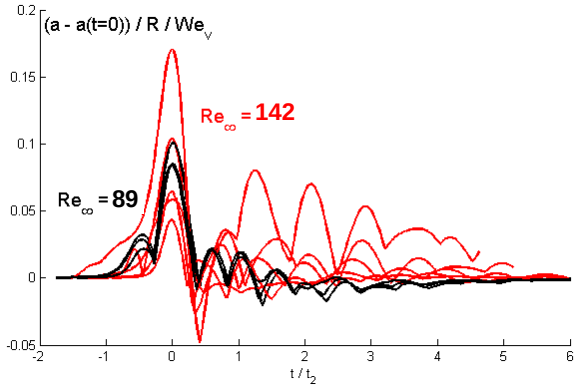

Figure 14: Time evolution the bubble elongation defined as $(a - a(t{=}0))/R$ and normalized by $\boldsymbol{We_v}$, for several bubble-vortex interactions at $\boldsymbol{Re_\infty}$= 89 or 142, and $\boldsymbol{1.5 \leq We_v \leq 16.5}$.

CONCLUSION

A new dynamic 1D approach to predict breakup probability of drops or bubbles in turbulent flows has been presented. This approach uses a scalar to describe the dynamics of deformation of a bubble/drop in a turbulent flow and predicts breakup occurrences on the basis of a critical value of deformation, contrary to most of the other existing approaches that consider a critical Weber number. The deformation dynamics is modelled as a linear oscillator forced by the turbulent fluctuations experienced by the particle along its trajectory in the flow. Two time scales are used to characterize the drop-oscillator: its frequency of oscillation ω_2 and the damping rate β_2.

These parameters are theoretically known in limited cases: in the absence of gravity, for low-amplitude oscillations and in the absence of surfactants. The purpose of this paper was to show how CFD simulations (but also complementary experiments) can be used to determine these parameters which are characteristics of the interface dynamics.

In this way, we have studied the influence of gravity on ω_2 and β_2. For liquid-liquid flows, this influence is generally low due to low density differences. In return, for gas-liquid flows, buoyancy effects have to be accounted for. Hence, simulations of the interaction between a rising bubble and a Hill's vortex reveals overdamped oscillations after a large deformation caused by the vortex. This example of simple configuration is a first step towards a better description of the complexity of breakup phenomenology in turbulent flows, where interactions between a bubble (or a drop) and vortices occur continuously and randomly.

With the aim of handling practical situations like those involved in chemical processes, other effects have to be considered, like those related to the presence of surfactants adsorbed at the interfaces, which provide them additional properties of elasticity and viscosity.

Thanks to comparisons between experimental and numerical measurements of the damping rate of oscillating drops, it has been shown in this paper that the presence of contaminants can modify drastically the interface dynamics. Further studies, combining experimental and numerical tools, are required to tackle more accurately the effect of surfactants on the shape-oscillations dynamics. Moreover, to deal with breakup in concentrated emulsions (e.g. of breakup in high-pressure homogenizers or in static mixers), we should also be able to determine how drop interactions alter the droplet dynamics with respect to the case of an isolated drop, following the work of Galinat et al (2007) where break-up statistics in concentrated emulsions up to 40% have been analysed.

Currently, the proposed model can predict breakup probability of a single drop (with clean interface) travelling in a turbulent inhomogeneous flow.
One objective is to extend this model to turbulent bubbly flows or emulsions with surfactants, after numerical and experimental elementary studies of the interface dynamics.
Another objective is to use the calculated deformation of a drop at the instant of breakup in order to quantify its excess surface energy, and to predict the number and size of daughter drops that will be formed after breakup. We are currently focusing on the validation of such an approach to predict daughter-drop size distribution against experimental data, including cases of binary breakup and breakage into several droplets.
A longer term goal is to develop new breakup kernels that could be implemented in balance population models.

REFERENCES

ABI CHEBEL N., VEJRAZKA J., MASBERNAT O., RISSO F. (2012). Shape oscillation of an oil drop rising in water: Effect of surface contamination. *Journal of Fluid Mechanics*, **702**, 533-542.

GALINAT S., RISSO F., MASBERNAT O., GUIRAUD P. (2007). Dynamics of drop breakup in inhomogeneous turbulence at various volume fractions. *Journal of Fluid Mechanics*, **578**, 85–94.

LALANNE B. (2012) Simulation numérique directe des oscillations, de la déformation et de la rupture d'une bulle en ascension dans un écoulement instationnaire. *Thèse INPT*, Institut de Mécanique des Fluides de Toulouse.

LALANNE B., TANGUY S., RISSO F. (2013). Effect of rising motion on the damped shape oscillations of drops and bubbles. *Physics of Fluids*, **25**, 112107.

LAMB (1932). *Hydrodynamics*. Cambridge University Press.

LIAO, Y., LUCAS, D. (2009). A literature review of theoretical models for drop and bubble breakup in turbulent dispersions. *Chemical Engineering Science*, **64**, 3389-3406.

MANIERO R., MASBERNAT O., CLIMENT E., RISSO F. (2012). Modelling and simulation of inertial drop break-up in a turbulent pipe flow downstream of a restriction. *International Journal of Multiphase Flow*, **42**, 1-8.

MEIRON D.I. (1989). On the stability of gas bubbles rising in an inviscid fluid, *Journal of Fluid Mechanics,* **198**, *101-114.*

MILLER C.A., SCRIVN L.E. (1968). The oscillations of a fluid droplet immersed in another fluid, *Journal of Fluid Mechanics*, **32**, 417-435.

MORTON T. S. (2004). The velocity field within a vortex ring with a large elliptical cross-section, *Journal of Fluid Mechanics,* **503**, *247-271.*

O'ROURKEP. J., AMSDEN A. A. (1987). The TAB method for numerical calculation of spray droplet, SAE Technical Paper, **218**, 872089.

PROSPERETTI A. (1980). Normal mode analysis for the oscillations of a viscous liquid drop in an immiscible liquid. *Journal de Mécanique*, 19, 149-182.

RAVELET F., COLIN C., RISSO F. (2011). On the dynamics and breakup of a bubble immersed in a turbulent flow. *Physics of Fluids*, **23**, 103301.

RISSO F., FABRE J. (1998). Oscillations and breakup of a bubble immersed in a turbulent field. *Journal of Fluid Mechanics*, **372**, 323-355.

SUSSMAN M., SMITH K.M., HUSSAINI M.Y., OHTA M., ZHI-WEI R. (2007) A sharp interface method for incompressible two-phase flows*, Journal of Computational Physics*, **221**, 469-505.

TANGUY S., BERLEMONT A. (2005). Application of a Level-Set method for simulation of droplet collisions. *International Journal of Multiphase Flow*, **31**, 1015-1035.

APPENDIX A

We give here the *F* and *G* functions, associated with eq. (2) and (3), corresponding to the theoretical calculation of Miller and Scriven (1968) for frequency and damping rate of the axisymmetric shape-oscillations of mode $l = 2$, valid for low viscous oscillations of a drop or a bubble (*i.e* at large Reynolds number of oscillation Re_d), in the case of low deformations, in zero-gravity conditions and without surfactants:

$$F = \frac{25\ (\hat{\rho}\hat{\mu})^{1/2}}{2\sqrt{2}(2\hat{\rho}+3)(1+\ (\hat{\rho}\hat{\mu})^{1/2})}$$

$$G = \frac{5\ (\ 6+4\hat{\mu}-\hat{\rho}\hat{\mu}+\ 16\ \hat{\rho}\hat{\mu}^2\ )}{2\ (2\hat{\rho}+3)(1+\ (\hat{\rho}\hat{\mu})^{1/2})}.$$

A BASELINE MODEL FOR MONODISPERSE BUBBLY FLOWS

Roland Rzehak[1*] , Eckhard Krepper[1] , Thomas Ziegenhein[1] , Dirk Lucas[1]

[1] Helmholtz-Zentrum Dresden - Rossendorf, P.O. Box 510119, 01314 Dresden, Germany

* E-mail: r.rzehak@hzdr.de

ABSTRACT

For practical applications the Euler-Euler two-fluid model relies on suitable closure relations describing interfacial exchange processes. The quest for models with a broad range of applicability allowing predictive simulations is an ongoing venture. A set of closure relations for adiabatic bubbly flow has been collected that represents the best available knowledge and may serve as a baseline for further improvements and extensions. In order to allow for predictive simulations the model must work for a certain range of applications without any adjustments. This is shown here for flows that allow to impose a fixed bubble size distribution which bypasses the need to model coalescence and breakup processes.

Keywords: Dispersed gas-liquid multiphase flow, Euler-Euler two-fluid model, closure relations, CFD simulation, model validation.

NOMENCLATURE

Greek Symbols

α	volume fraction [-]
ε	turbulent dissipation [$m^2\ s^{-3}$]
μ	viscosity [Pa s]
ρ	density [$kg\ m^{-3}$]
σ	surface tension [$N\ m^{-1}$]
τ	bubble-induced turbulence time scale [s]
ω	shear-induced turbulence time scale [s]

Latin Symbols

C	constant [-]
d	bubble diameter [m]
D	pipe / column diameter or width [m]
Eo	Eötvös number [-]
F	force [$N\ m^{-3}$]
g	gravitational constant [$m\ s^{-2}$]
J	superficial velocity [$m\ s^{-1}$]
k	turbulent kinetic energy [$m^2\ s^{-2}$]
ℓ	shear-induced turbulence length scale [m]
L	pipe / column length [m]
Mo	Morton number [-]
r	radial coordinate [m]
R	pipe / column radius or halfwidth [m]
Re	Reynolds number [-]
S	source term
u	axial component of mean velocity [$m\ s^{-1}$]
u'	axial component of fluctuating velocity [$m\ s^{-1}$]
y	coordinate normal to wall [m]

Sub/superscripts

B	bubble
eff	effective
G	gas
L	liquid
$turb$	turbulent
$\perp$	perpendicular to main motion

INTRODUCTION

CFD simulations of dispersed bubbly flow on the scale of technical equipment are feasible within the Eulerian two-fluid framework of interpenetrating continua. However, accurate numerical predictions rely on suitable closure models. A large body of work using different closure relations of varying degree of sophistication exists, but no complete, reliable, and robust formulation has been achieved so far.

An attempt has been made to collect the best available description for the aspects known to be relevant for adiabatic monodisperse bubbly flows (Rzehak and Krepper 2013), where closure is required for (i) the exchange of momentum between liquid and gas phases, and (ii) the effects of the dispersed bubbles on the turbulence of the liquid carrier phase. Apart from interest in its own right, results obtained for this restricted problem also provide a good starting point for the investigation of more complex situations including bubble coalescence and breakup, heat and mass transport, and possibly phase change or chemical reactions.

Predictive simulation requires a model that works without any adjustments within a certain domain of applicability. The purpose of the present contribution therefore is to validate this baseline model for a number of experimental data sets taken from the literature. These comprise flows in flat and round bubble columns as well as flows in vertical pipes of different diameter and length. A range of gas and liquid superficial velocities, gas volume fractions, and bubble sizes is covered. In all cases a fixed, but not necessarily

monodisperse distribution of bubble sizes is assumed as taken from the measurements.

The results show that reasonable agreement is obtained for all different data with the exact same model. This demonstration is the main new achievement that goes beyond previous individual consideration of some of the tests (Rzehak and Krepper 2013, Rzehak et al. 2013, Ziegenhein et al. 2013).

Restriction to situations where a fixed distribution of bubble sizes may be imposed excludes the additional complexity of modelling bubble coalescence and breakup processes and thus facilitates a step-by-step validation procedure. Expanding the range of applicability as well as the achieved accuracy is a continuously ongoing development effort.

DATA

Four test cases have been selected for the present investigation as described below. A summary of the setups is given in Table 1.

Table 1: Experimental conditions.

name	D mm	J_L m/s	J_G m/s	$\langle d_B \rangle$ mm	$\langle \alpha_G \rangle$ %
bin Mohd Akbar et al. (2012): flat bubble column					
A1	240	-	0.003	4.3	1.4
A2	240	-	0.013	5.5	6.2
Mudde et al. (2009): round bubble column					
M1	150	-	0.015	4.02	6.1
M2	150	-	0.017	4.06	7.6
M3	150	-	0.025	4.25	11
M4	150	-	0.032	4.47	16
M5	150	-	0.039	4.53	20
M6	150	-	0.049	4.44	25
Liu (1998): round pipe					
L21B	57.2	1.0	0.14	3.03	10.6
L21C	57.2	1.0	0.13	4.22	9.6
L22A	57.2	1.0	0.22	3.89	15.7
L11A	57.2	0.5	0.12	2.94	15.2
TOPFLOW: round pipe					
TL12-041	195.3	1.017	0.0096	4.99	1.1

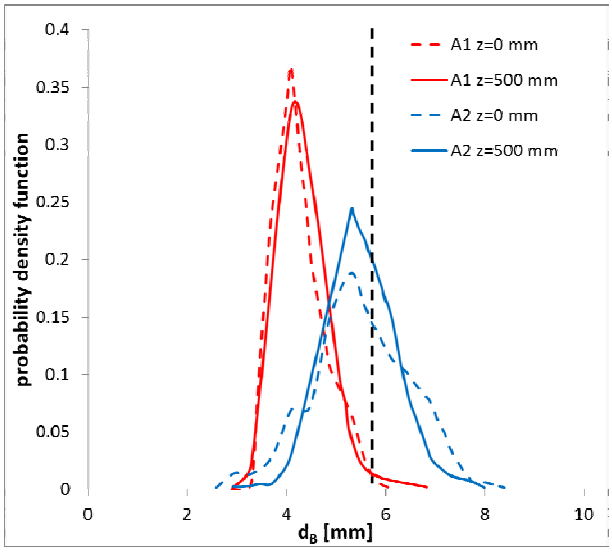

Figure 1: Measured bubble size distributions for tests A1 and A2.

Tests of bin Mohd Akbar et al. (2012)

The experiments of bin Mohd Akbar et al. (2012) were conducted in a flat bubble column of width D = 240 mm using air and water at ambient conditions. Without gas supply the water level was at 0.7 m. Profiles of gas volume fraction, axial liquid velocity, and axial turbulence intensity as well as the bubble size distribution were measured at a plane 0.5 m above the inlet. The bubble size distribution in addition was measured also near the inlet. As shown in Fig. 1 no significant change occurs over the column height. Two values of superficial gas velocities are available.

Tests of Mudde et al. (2009)

The setup of Mudde et al. (2009) consists of a round bubble column with diameter D = 150 mm again operated with air and water at ambient conditions. The ungassed fill-height was 1.3 m. Measurements of gas volume fraction and axial liquid velocity profiles were taken at different levels of which the one at 0.6 m above the inlet has been chosen for the comparison here. The sparger was designed specifically to provide highly uniform inlet conditions. Several values of the gas superficial velocity are available reaching rather large values of gas volume fraction. The mean bubble size and variation around it have been measured at two locations close to the inlet and close to the top water level. Since a slight increase is observed the average value of both measurements corresponding to the middle level has been used in the simulations.

Tests of Liu (1998)

The system studied by Liu (1998) is vertical upflow of water and air in a round pipe with inner diameter D = 57.2 mm, presumably at ambient conditions as well. The total length of the flow section was 3.43 m. A special gas injector was used that allowed to adjust the bubble size independently of liquid and gas superficial velocities. A variety of combinations of these three parameters are available. Radial profiles of void-fraction, mean bubble-size, axial liquid velocity, and axial liquid turbulence intensity were measured at an axial position $L / D = 60$ corresponding to fully developed conditions.

TOPFLOW tests

The TOPFLOW facility operated at HZDR has been specifically designed to obtain high quality data for the validation of CFD models. The tests used here (Lucas et al. 2010) have been run for cocurrent vertical upward flow of air and water in a round pipe with an inner diameter of D = 195.3 mm. Measurements were made by a wire mesh sensor at the top end of the pipe while gas injection occurs at different levels below. The operating conditions were set to a temperature of 30 °C and a pressure of 0.25 MPa at the location of the active gas injection. In this way the flow development can be studied as it would be observed for gas injection at a fixed position and measurements taken at different levels above. Distances L between the injection devices and the sensor are given in Table 2 for the different levels. The values of mean bubble size and average gas

Table 2: Length of test section for different levels of gas injection.

level		A	C	F	I	L	O	R
L	[mm]	221	335	608	1552	2595	4531	7802
L/D	[-]	1.1	1.7	3.1	7.9	13.3	23.2	39.9

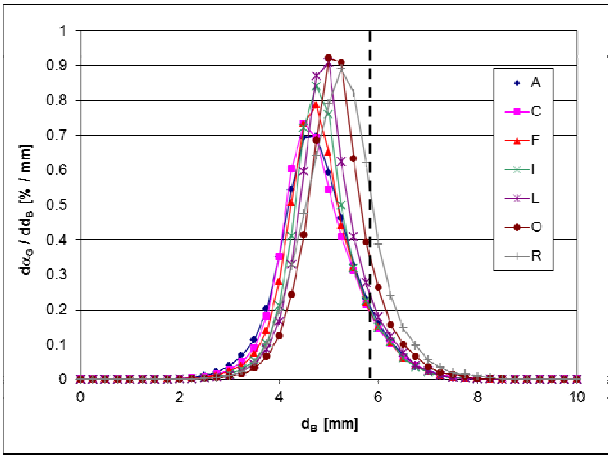

Figure 2: Distributions of bubble size for test TL12-041 at levels A to R.

volume fraction given in Table 1 correspond to the highest measurement level R.

Instrumentation with a wire mesh sensor allows collection of data on radial profiles of gas-fraction and gas-velocity as well as distributions of bubble size. A large range of liquid and gas superficial velocities was investigated in which all flow regimes from bubbly to annular occur. In the detailed report (Beyer et al. 2008) it has been noted that for bubbly flows the gas volume fluxes calculated from the measured profiles by integrating the product of volume fraction and velocity were systematically larger than those measured by the flow meter controlling the inlet. This deviation is likely to be caused by the distance between the sending and receiving wire planes, which leads to an increased value of void fraction, but a detailed explanation is not available yet. The ratio of the values calculated from the profiles (cf. Eq. (19)) to the values measured directly at the inlet has an approximately constant value of 1.2 over the bubbly flow regime (Beyer et al. 2008, Fig. 1-19). In the simulations the values measured by the flow meter will be used to set the inlet boundary condition. To get the same integral value of this conserved quantity for each cross-sectional plane, all measured void fractions are divided by 1.2 throughout this work.

A selection of tests in the bubbly flow regime has been made based on an examination of the measured bubble size distributions as shown in Fig. 2. It may be seen that a significant polydispersity is present as evidenced by a significant width of the measured bubble size distributions. The increase of average bubble size from level A to R is due to the decrease in hydrostatic pressure with height which in turn results in a proportionally decreasing gas density according to the ideal gas law. By transforming the distribution to the bubble mass as the independent variable this pressure effect may be eliminated. Apparently, for this test the opposing processes of bubble coalescence and -breakup are in a dynamic equilibrium where the net effect of both cancels. Therefore these processes need not be modeled explicitly, but the measured bubble mass distribution may be imposed in the simulations.

MODELING

The conservation equations of the Euler-Euler two-fluid model have been discussed at length in a number of books (e.g. Drew and Passman 1998, Yeoh and Tu 2010, Ishii and Hibiki 2011), while the extension to treat multiple bubble size and velocity classes (inhomogeneous MUSIG model) have been presented in research papers (e.g. Krepper et al. 2008). A broad consensus has been reached, so this general framework will not be repeated here.

Closure relations required to complete the model, in contrast, are still subject to considerable variation between researchers. Therefore, the specific correlations used here are given following (Rzehak and Krepper 2013) with the inclusion of a virtual mass force.

Bubble Forces

The closures used for the bubble forces are largely based on experiments on single bubbles in laminar flows. These are highly idealized conditions with respect to the applications intended to cover by Euler-Euler simulations, i.e. turbulent flows with void fractions up to ~25%. Nevertheless as will be shown, useful results may be obtained with this approach although improvements are obviously desirable.

Drag Force

The drag force reflects the resistance opposing bubble motion relative to the surrounding liquid. The corresponding gas-phase momentum source is given by

$$\mathbf{F}^{drag} = -\frac{3}{4d_B} C_D \rho_L \alpha_G |\mathbf{u}_G - \mathbf{u}_L| \, (\mathbf{u}_G - \mathbf{u}_L) \,. \quad (1)$$

The drag coefficient C_D depends strongly on the Reynolds number and for deformable bubbles also on the Eötvös number, but turns out to be independent of Morton number. A correlation distinguishing different shape regimes has been suggested by Ishii and Zuber (1979), namely

$$C_D = \max\left(C_{D,sphere}, \min\left(C_{D,ellipse}, C_{D,cap}\right)\right), \quad (2)$$

where

$$C_{D,sphere} = \frac{24}{\mathrm{Re}}\left(1 + 0.1\ \mathrm{Re}^{0.75}\right)$$
$$C_{D,ellipse} = \frac{2}{3}\sqrt{\mathrm{Eo}} \quad . \quad (3)$$
$$C_{D,cap} = \frac{8}{3}$$

This correlation was compared with an extensive data set on the terminal velocity of bubbles rising in quiescent liquids covering several orders of magnitude for each of *Re*, *Eo* and *Mo* in (Tomiyama et al. 1998) with good agreement except at high values of *Eo*.

Lift Force

A bubble moving in an unbounded shear flow experiences a force perpendicular to the direction of its motion. The momentum source corresponding to this shear lift force, often simply referred to as lift force, can be calculated as (Zun 1980):

$$\mathbf{F}^{lift} = -C_L \rho_L \alpha_G (\mathbf{u}_G - \mathbf{u}_L) \times rot(\mathbf{u}_L) \,. \qquad (4)$$

For a spherical bubble the shear lift coefficient C_L is positive so that the lift force acts in the direction of decreasing liquid velocity, i.e. in case of co-current pipe flow in the direction towards the pipe wall. Experimental (Tomiyama et al. 2002) and numerical (Schmidtke 2008) investigations showed, that the direction of the lift force changes its sign if a substantial deformation of the bubble occurs. From the observation of the trajectories of single air bubbles rising in simple shear flow of a glycerol water solution the following correlation for the lift coefficient was derived:

$$C_L = \begin{cases} \min[0.288 \tanh(0.121 \mathrm{Re}), f(Eo_\perp)] & Eo_\perp < 4 \\ f(Eo_\perp) & for \quad 4 < Eo_\perp < 10 \\ -0.27 & 10 < Eo_\perp \end{cases}$$

with (5)

$$f(Eo_\perp) = 0.00105 Eo_\perp^3 - 0.0159 Eo_\perp^2 - 0.0204 Eo_\perp + 0.474 \,.$$

This coefficient depends on the modified Eötvös number given by

$$Eo_\perp = \frac{g(\rho_L - \rho_G) d_\perp^2}{\sigma} \,, \qquad (6)$$

where $d_\perp$ is the maximum horizontal dimension of the bubble. It is calculated using an empirical correlation for the aspect ratio by Wellek et al. (1966) with the following equation:

$$d_\perp = d_B \sqrt[3]{1 + 0.163 \; Eo^{0.757}} \,, \qquad (7)$$

where *Eo* is the usual Eötvös number.

The experimental conditions on which Eq. (5) is based, were limited to the range $-5.5 \le log_{10} Mo \le -2.8$, $1.39 \le Eo \le 5.74$ and values of the Reynolds number based on bubble diameter and shear rate $0 \le Re \le 10$. The water-air system at normal conditions has a Morton number $Mo = 2.63e\text{-}11$ which is quite different, but good results have nevertheless been reported for this case (Lucas and Tomiyama 2011).

For the water-air system the sign change of C_L occurs at a bubble diameter of $d_B = 5.8$ *mm.*

Wall Force

A bubble translating next to a wall in an otherwise quiescent liquid also experiences a lift force. This wall lift force, often simply referred to as wall force, has the general form

$$\mathbf{F}^{wall} = \frac{2}{d_B} C_W \rho_L \alpha_G |\mathbf{u}_G - \mathbf{u}_L|^2 \hat{\mathbf{y}} \,, \qquad (8)$$

where $\hat{\mathbf{y}}$ is the unit normal perpendicular to the wall pointing into the fluid. The dimensionless wall force coefficient C_W depends on the distance to the wall *y* and is expected to be positive so the bubble is driven away from the wall.

Based on the observation of single bubble trajectories in simple shear flow of a glycerol water solution Tomiyama et al. (1995) and later Hosokawa et al. (2002) concluded a different functional dependence

$$C_W(y) = f(Eo) \left(\frac{d_B}{2y} \right)^2 \,. \qquad (9)$$

In the limit of small Morton number the correlation

$$f(Eo) = 0.0217 \;\; Eo \qquad (10)$$

can be derived from the data of Hosokawa et al. (2002). The experimental conditions on which Eq. (10) is based are $2.2 \le Eo \le 22$ and log10 Mo = -2.5 … -6.0 which is still different from the water-air system with Mo = 2.63e-11, but a recent investigation (Rzehak et al. 2012) has nonetheless shown that good predictions are obtained also for air bubbles in water.

Turbulent Dispersion Force

The turbulent dispersion force describes the effect of the turbulent fluctuations of liquid velocity on the bubbles. Burns et al. (2004) derived an explicit expression by Favre averaging the drag force as:

$$\mathbf{F}^{disp} = -\frac{3}{4} C_D \frac{\alpha_G}{d_B} |\mathbf{u}_G - \mathbf{u}_L| \frac{\mu_L^{turb}}{\sigma_{TD}} \left(\frac{1}{\alpha_L} + \frac{1}{\alpha_G} \right) \mathrm{grad}\, \alpha_G \,. \qquad (11)$$

In analogy to molecular diffusion, σ_{TD} is referred to as a Schmidt number. In principle it should be possible to obtain its value from single bubble experiments also for this force by evaluating the statistics of bubble trajectories in well characterized turbulent flows, but to our knowledge this has not been done yet. A value of $\sigma_{TD} = 0.9$ is typically used.

In the same work the expression for the so-called Favre averaged drag (FAD) model has also been compared with other suggestions from the literature and it was shown that all agree at least in the limit of low void fraction.

Virtual Mass Force

When a bubble is accelerated, a certain amount of liquid has to be set into motion as well. This may be expressed as a force acting on the bubble as

$$\mathbf{F}^{VM} = -C_{VM} \rho_L \alpha_G \left(\frac{D_G \mathbf{u}_G}{Dt} - \frac{D_L \mathbf{u}_L}{Dt} \right), \qquad (12)$$

where D_G / Dt and D_L / Dt denote material derivatives with respect to the velocity of the indicated phase. For the virtual mass coefficient a value of 0.5 has been derived for isolated spherical bubbles in both inviscid and creeping flows by Auton et al. (1988) and Maxey and Riley (1983), respectively. Results of direct simulations of a single bubble by Magnaudet et al. (1995) suggest that this value also holds for intermediate values of *Re*. For steady parallel flows this force vanishes and can be excluded from the calculations**.**

Bubble-induced Turbulence

Due to the low density and small spatial scales of the dispersed gas it suffices to consider turbulence only in the

continuous liquid phase. We adopt a two equation turbulence model for the liquid phase with additional source terms describing bubble induced turbulence. The formulation given is equally applicable to either k-ε, k-ω or SST model, but the latter (Menter 2009) will be used presently.

Concerning the source term describing bubble effects in the k-equation there is large agreement in the literature. A plausible approximation is provided by the assumption that all energy lost by the bubble due to drag is converted to turbulent kinetic energy in the wake of the bubble. Hence, the k-source becomes

$$S_L^k = \mathbf{F}_L^{drag} \cdot (\mathbf{u}_G - \mathbf{u}_L). \quad (13)$$

For the ε-source a similar heuristic is used as for the single phase model, namely the k-source is divided by some time scale τ so that

$$S_L^\varepsilon = C_{\varepsilon B} \frac{S_L^k}{\tau}. \quad (14)$$

Further modeling then focuses on the time scale τ proceeding largely based on dimensional analysis. This follows the same line as the standard modeling of shear-induced turbulence in single phase flows (Wilcox 1998), where production terms in the ε-equation are obtained by multiplying corresponding terms in the k-equation by an appropriate time scale which represents the life-time of a turbulent eddy before it breaks up into smaller structures. In single phase turbulence the relevant variables are obviously k and ε from which only a single time scale $\tau = k_L / \varepsilon_L$ can be formed. For the bubble-induced turbulence in two-phase flows the situation is more complex. There are now two length and two velocity scales in the problem, where one of each is related to the bubble and the other to the turbulent eddies. From these a total of four different time scales can be formed. In the absence of theoretical arguments to decide which of these is the most relevant one, a comparison of all four alternatives (Rzehak and Krepper 2013, 2013a) has shown the best performance for the choice

$$\tau = \frac{d_B}{\sqrt{k_L}}. \quad (15)$$

For the coefficient $C_{\varepsilon B}$ a value of 1.0 to was found to give reasonable results.

For use with the SST model, the ε-source is transformed to an equivalent ω-source which gives

$$S_L^\omega = \frac{1}{C_\mu k_L} S_L^\varepsilon - \frac{\omega_L}{k_L} S_L^k \quad . \quad (16)$$

This ω-source is used independently of the blending function in the SST model since it should be effective throughout the fluid domain.

Since bubble-induced effects are included in k and ε / ω due to the respective source terms, the turbulent viscosity is evaluated from the standard formula

$$\mu_L^{turb} = C_\mu \rho_L \frac{k_L^{\,2}}{\varepsilon_L} \quad (17)$$

and the effective viscosity is simply

$$\mu_L^{eff} = \mu_L^{mol} + \mu_L^{turb}. \quad (18)$$

Boundary conditions on k and ε / ω are taken the same as for single phase flow, which is consistent with the view that the full wall shear stress is exerted by the liquid phase which contacts the full wall area. A single phase wall function is employed to avoid the need to resolve the viscous sublayer.

All turbulence model parameters take their usual single phase values.

RESULTS

Simulations were performed by a customized version of ANSYS CFX. Depending on the test under investigation different setups were used as listed in Table 3. The calculations were made either in stationary mode imposing plane / axisymmetric conditions by considering only a thin slice / sector of the domain together with symmetry conditions or in transient mode with subsequent averaging of the results and fully 3D on the same domain as the experiments. The reason to choose the stationary or quasi-2D approximation whenever applicable is that it drastically reduces the computation time. For the transient simulations the reported quantities are averages over the statistically steady state.

At the inlet a uniform distribution of gas throughout the cross-section was assumed or the injection nozzles or needles were modelled as CFX point sources. For the liquid, fully developed single phase velocity and turbulence profiles were assumed in the pipe flow cases.

At the top a pressure boundary condition was set for the pipe flow cases while the CFX degassing condition was employed for the bubble column cases. On the walls a no-slip condition was used for the liquid phase and a free-slip condition for the gas phase assuming that direct contacts between the bubbles and the walls are negligible. To avoid the need to resolve the viscous sublayer, the automatic wall function treatment of CFX was applied.

Concerning bubble size a monodisperse approximation was used whenever the bubbles are smaller than the critical diameter of 5.8 mm where the lift force changes its sign. In the other cases an inhomogeneous MUSIG model with two velocity groups corresponding to bubbles smaller and larger than 5.8 mm was applied.

Table 3: Simulation setup summary.

tests	domain	solution	MUSIG size groups	MUSIG velocity groups	inlet
bin Mohd Akbar et al. (2012): flat bubble column					
A1	3D	transient	1	1	needles
A2	3D	transient	2	2	needles
Mudde et al. (2009): round bubble column					
M1	3D	transient	1	1	uniform
M2	3D	transient	1	1	uniform
M3	3D	transient	1	1	uniform
M4	3D	transient	1	1	uniform
M5	3D	transient	1	1	uniform
M6	3D	transient	1	1	uniform
Liu (1998): round pipe					
L21B	2D sector	stationary	1	1	uniform
L21C	2D sector	stationary	1	1	uniform
L22A	2D sector	stationary	1	1	uniform
L11A	2D sector	stationary	1	1	uniform
TOPFLOW: round pipe					
TL12-041	3D	stationary	10	2	nozzles

If there is a significant variation of pressure within the domain, the gas density will change according to the ideal gas law and consequently the bubble size changes since mass is conserved. Yet the flow of both gas and liquid remains incompressible to a good approximation. To keep the computational advantage of treating both gas and liquid as incompressible fluids with constant material properties in a fully developed flow, as discussed in Rzehak et al. (2012), the gas flux at the inlet is adjusted to the value obtained by evaluating

$$J_G = 2\pi \int_0^{D/2} \alpha_G(r)\, u_G(r)\, r\, dr \qquad (19)$$

using the data at the measurement location. In cases where only $\mathbf{u}_L$ but not $\mathbf{u}_G$ has been measured, an estimate of the latter may be obtained from the former and α_G based on the assumption of fully developed stationary flow. Where this procedure has been applied the adjusted values are given in Table 1.

Turbulence data frequently give the axial intensity of turbulent fluctuations while in the simulations based on two-equation models only the turbulent kinetic energy is available. For a comparison it has to be considered that wall-bounded turbulence is anisotropic with the axial component of fluctuating velocity being larger than those in radial and azimuthal directions. The ratio $\sqrt{k}$ / *u'* is bounded between $\sqrt{(1/2)} \approx 0.71$ and $\sqrt{(3/2)} \approx 1.22$ corresponding to unidirectional and isotropic limiting cases. Taking *u'* as an estimate for $\sqrt{k}$ thus provides an estimate that is accurate to within ~20%.

Tests of bin Mohd Akbar et al. (2012)

For the tests of bin Mohd Akbar et al. (2012) transient 3D simulations were performed using a gas inlet configuration that represents the experimental needle sparger. Due to the small column height the pressure effect is negligible. For the lower value of gas volume flux a monodisperse bubble size distribution was imposed, for the higher value two MUSIG size and velocity groups were used with diameters of 5.3 mm and 6.3 mm and relative amounts of 63 % and 37 %. For the evaluation of *k*, the axial component of the resolved transient fluctuations has been added to the unresolved part obtained from the turbulence model.

A comparison between simulation results and measured data is shown in Fig. 3. As may be seen the agreement between both is quite good for gas volume fraction and axial liquid velocity. Slight differences are that the predicted gas volume fraction profile is a little bit too peaked near the wall and there is a small dip in the predicted liquid velocity in the center of the column. The turbulent kinetic energy in the column center is somewhat underpredicted by the simulations and the peak in *k* near the wall is not reproduced by the simulations.

Tests of Mudde et al. (2009)

For the tests of Mudde et al. (2009), transient 3D simulations were performed assuming a uniform distribution of gas at the inlet. For the column height of 1.3 m the pressure effect is still small enough to be neglected. A monodisperse bubble size distribution corresponding to the measured values was used.

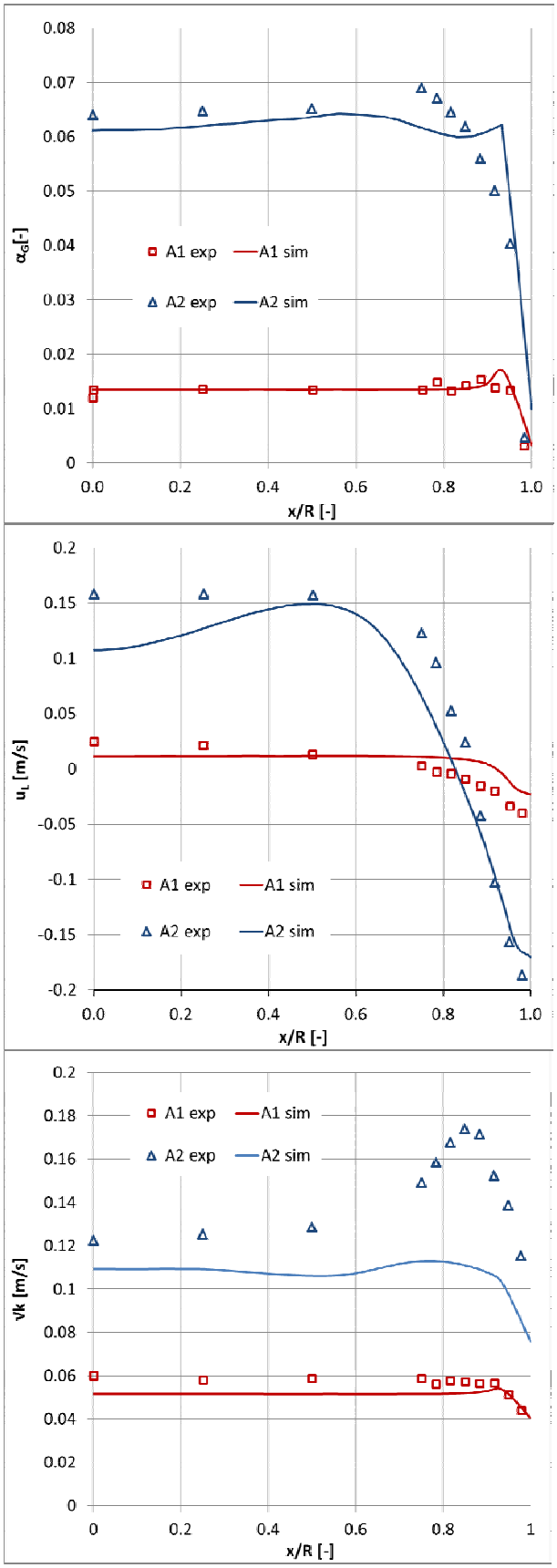

Figure 3: Gas volume fraction (top), axial liquid velocity (middle), and turbulent kinetic energy (bottom) for the tests of bin Mohd Akbar et al. (2012). Solid lines: simulation results, symbols: measured values. Only half of the column is shown.

Measured and calculated values are compared in Fig. 4. Clearly the gas volume fractions are predicted within the experimental errors. The calculated liquid velocity profiles do not depend on the total gas hold-up. Since the measured profiles do not show any systematic trend as a function of this variable, their variation is most likely an indication of the measurement errors.

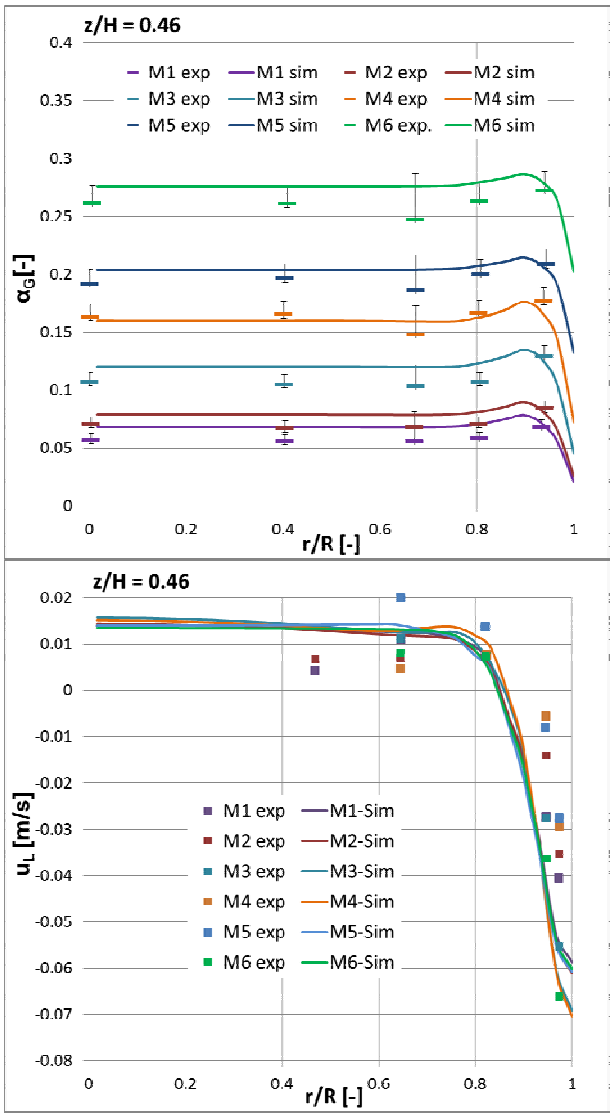

Figure 4: Gas volume fraction (top) and axial liquid velocity (bottom) for the tests of Mudde et al. (2009). Solid lines: simulation results, symbols: measured values.

Tests of Liu (1998)

For the tests of Liu (1998) stationary axisymmetric simulations were done assuming a uniform distribution of gas at the inlet. Since the pressure effect is significant for the 3.43 m long pipe, gas volume fluxes were adjusted to allow treating the gas as incompressible. A monodisperse bubble size distribution was imposed with the bubble size set equal to the average of the measured profiles.

The comparison of calculated and measured profiles in Fig. 5 shows reasonable agreement for the gas volume fraction and the axial liquid velocity. Notable deviations occur in the region close to the wall where the simulations predict the peak in the gas fraction too high and the gradient of the liquid velocity too steep. For the

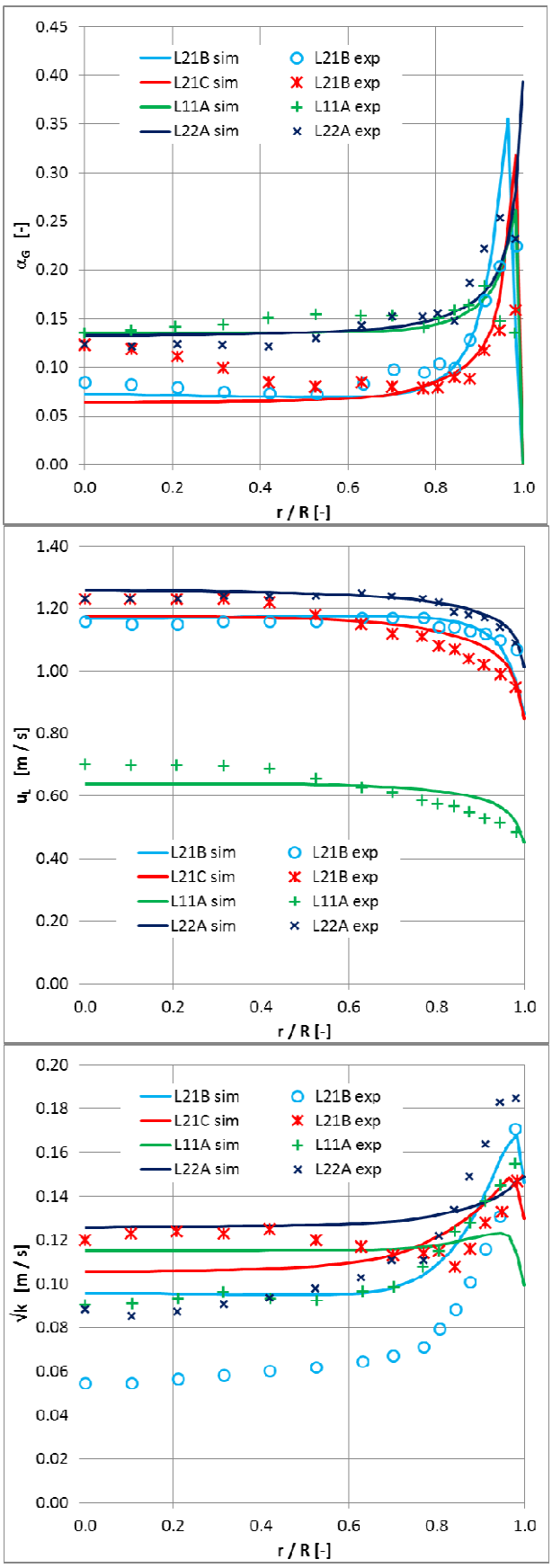

Figure 5: Gas volume fraction (top), axial liquid velocity (middle), and turbulent kinetic energy (bottom) for the tests of Liu (1998). Solid lines: simulation, symbols: experiment.

turbulent kinetic energy the agreement between simulation and measurement is not as good, but possibly to a large extent due to the isotropic approximation.

TOPFLOW tests

For the TOPFLOW test stationary axisymmetric simulations were done with the gas inlet modeled as individual nozzles. The pressure effect is included in the calculation using the MUSIG model since the implementation in CFX is based on classes of bubble mass and a transformation to / from bubble size occurs only as part of the pre- / post-processing. Two velocity groups were used as described above. For the size groups a width Δd_B = 1.0 mm was set and as many groups as needed to cover the range of the measured distributions from inlet to outlet were used.

Results for the development of gas volume fraction profiles are shown in Fig. 6. It can be seen that near the inlet the wall peak is underestimated by the simulation, but at the higher levels it is overpredicted. Likewise the initial width of the peak comes out too broad in the simulations, but the shoulder that develops subsequently has a narrower range than in the experiments.

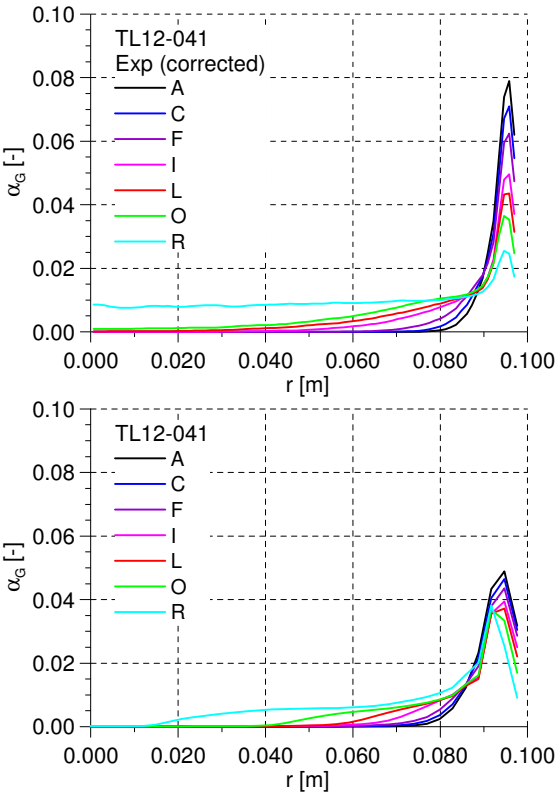

Figure 6: Gas volume fraction at different levels for the TOPFLOW test case TL12-041. Top: experimental data corrected as described in the text, bottom: simulation results.

CONCLUSION

A single model for bubbly two-phase flow has been applied to a range of diverse conditions. Reasonable agreement between data and simulations has been found for all investigated tests. Meaningful numbers quantifying the accuracy of the simulations are not readily given since experimental errors are rarely specified. As a rough guide it may be said that typical deviations between measured and simulated data are in the range of 15-20% for the void fraction and mean liquid velocity and 30-40% for the turbulent fluctuations. Maximum deviations tend to occur close to the wall where in the pipe flow cases the height of the void fraction peak is off by up to a factor of two whereas in the bubble column cases the point of zero liquid velocity is shifted which also results in a relative deviation up to a factor of two. This is encouraging for this first version of a baseline model although clearly there is still a need to expand its range of validated applicability as well as the quantitative agreement with the data.

To improve the model correlations for the bubble forces terms including effects of shear, turbulence and multiple bubbles should be derived from experiment of direct numerical simulations. The dependence of the turbulence source terms on additional dimensionless parameters like the ratio of bubble- and shear-induced length- and velocity scales could be obtained from direct numerical simulations as well.

REFERENCES

AUTON, T., HUNT, J. and PRUD'HOMME, M., (1988), "The force exerted on a body in inviscid unsteady non-uniform rotational flow", *J. Fluid Mech.,* **197**, 241.

BEYER, M., LUCAS, D., KUSIN, J. and SCHÜTZ, P., (2008), "Air-water experiments in a vertical DN200-pipe", *Helmholtz-Zentrum Dresden - Rossendorf* technical report FZD-505.

BURNS, A.D., FRANK, T., HAMILL, I. and SHI, J.-M., (2004), "The Favre averaged drag model for turbulence dispersion in Eulerian multi-phase flows", *5th Int. Conf. on Multiphase Flow*, ICMF2004, Yokohama, Japan.

DREW, D. A. and PASSMAN, S. L., (1998), "Theory of Multicomponent Fluids", *Springer*.

HOSOKAWA, S., TOMIYAMA, A., MISAKI, S. and HAMADA, T., (2002), "Lateral Migration of Single Bubbles Due to the Presence of Wall", *ASME Joint U.S.-European Fluids Engineering Division Conference*, FEDSM 2002, Montreal, Canada.

ISHII, M. and HIBIKI, T., (2011), "Thermo-fluid dynamics of two-phase flow", *Springer*, 2nd ed.

ISHII, M. and ZUBER, N., (1979), "Drag coefficient and relative velocity in bubbly, droplet or particulate flows", *AIChE J.,* **25**, 843.

KREPPER, E., LUCAS, D., FRANK, T., PRASSER, H.-M. and ZWART, P., (2008), "The inhomogeneous MUSIG model for the simulation of polydispersed flows", *Nucl. Eng. Des.,* **238**, 1690.

LIU, T. J., (1998), "The role of bubble size on liquid phase turbulent structure in two-phase bubbly flow", *3rd Int. Conf. on Multiphase Flow*, ICMF1998, Lyon, France.

LUCAS, D., BEYER, M., KUSSIN, J. and SCHÜTZ, P., (2010), "Benchmark database on the evolution of two-phase flows in a vertical pipe", *Nucl. Eng. Des.,* **240**, 2338.

LUCAS, D. and TOMIYAMA, A., (2011), "On the role of the lateral lift force in poly-dispersed bubbly flows", *Int. J. Multiphase Flow,* **37**, 1178.

MAGNAUDET, J., RIVERO, M. and FABRE, J., (1995), "Accelerated flows past a rigid sphere or a spherical bubble Part 1: Steady straining flow", *J. Fluid Mech.,* **284**, 97.

MAXEY, M. R. and RILEY, J. J., (1983), "Equation of motion for a small rigid sphere in a nonuniform flow", *Phys. Fluids,* **26**, 883.

MENTER, F.R. (2009). "Review of the shear-stress transport turbulence model experience from an industrial perspective", *Int. J. of Comput. Fluid Dyn.*, **23**, 305.

bin MOHD AKBAR, M.H., HAYASHI, K., HOSOKAWA, S. and TOMIYAMA, A., (2012), "Bubble tracking simulation of bubble-induced pseudo turbulence", *Multiphase Sci. Tech.*, **24**, 197.

MUDDE, R. F., HARTEVELD, W. K. and VAN DEN AKKER, H. E. A. (2009), "Uniform Flow in Bubble Columns", *Ind. Eng. Chem. Res.,* **48**, 148.

RZEHAK, R., KREPPER, E. and LIFANTE, C., (2012), "Comparative study of wall-force models for the simulation of bubbly flows", *Nucl. Eng. Des.,* **253**, 41.

RZEHAK, R. and KREPPER, E., (2013), "Closure Models for turbulent bubbly flows: A CFD study", *Nucl. Eng. Des.,* **265**, 701.

RZEHAK, R. and KREPPER, E., (2013a), "CFD modeling of bubble-induced turbulence", *Int. J. Multiphase Flow,* **55**, 138.

RZEHAK, R., LIAO, Y., LUCAS, D. and KREPPER, E., (2013), "Baseline model for CFD of dispersed bubbly flow", *15th International Topical Meeting on Nuclear Reactor Thermal-hydraulics*, NURETH-15, Pisa, Italy.

SCHMIDTKE, M., (2008), "Investigation of the dynamics of fluid particles using the Volume of Fluid Method", *University Paderborn*, PhD-Thesis (in German).

TOMIYAMA, A., SOU, A., ZUN, I., KANAMI, N. and SAKAGUCHI, (1995), "Effects of Eötvös number and dimensionless liquid volumetric flux on lateral motion of a bubble in a laminar duct flow", *2nd Int. Conf. on Multiphase Flow*, ICMF1995, Kyoto, Japan.

TOMIYAMA, A., KATAOKA, I., ZUN, I. and SAKAGUCHI, T., (1998), "Drag Coefficients of Single Bubbles under Normal and Micro Gravity Conditions", *JSME Int. J. B,* **41**, 472.

TOMIYAMA, A., TAMAI, H., ZUN, I. and HOSOKAWA, S., (2002), "Transverse migration of single bubbles in simple shear flows", *Chem. Eng. Sci.,* **57**, 1849.

WELLEK, R.M., AGRAWAL, A.K. and SKELLAND, A.H.P., (1966), "Shapes of liquid drops moving in liquid media", *AIChE J.,* **12**, 854.

WILCOX, D. C., (1998), "Turbulence Modeling for CFD", *DCW-Industries*.

YEOH, G. H. and TU, J. Y., (2010), "Computational Techniques for Multiphase Flows — Basics and Applications", *Butterworth-Heinemann*.

ZIEGENHEIN, T., LUCAS, D., RZEHAK, R. and KREPPER, E., (2013), "Closure relations for CFD simulation of bubble columns", *8th Int. Conf. on Multiphase Flow,* ICMF2013, Jeju, Korea.

ZUN, I., (1980), "The transverse migration of bubbles influenced by walls in vertical bubbly flow", *Int. J. Multiphase Flow,* **6**, 583.

Chapter 3: Fluidized beds

Fluidized bed reactors find application in a wide range of process industries thanks to the excellent mixing and good contact between the fluidized particles and the carrier phase. Due to the strong coupling between the multiphase hydrodynamics, heat and mass transfer, and reactions in fluidized bed reactors, CFD has an important role to play in developing a proper understanding of these processes.

The hydrodynamics of fluidized bed reactors is especially complex with the flow typically characterized by the formation of transient small-scale particle clusters. These clusters of particles require fine grids and small timesteps to resolve the physics accurately, thus making well resolved fluidized bed reactor simulations highly computationally expensive. However, the large influence of clustering on overall reactor behaviour makes adequate representation of this phenomenon mandatory for sufficiently accurate results.

CFD modelling of fluidized beds has been explored since the 1980s with most work being focused on the resolved Eulerian-Eulerian approach often referred to as the Two Fluid Model. This approach represents the solids phase as a fluid with a variable viscosity which accounts for the effect of particle collisions and translations according to the Kinetic Theory of Granular Flows. More recently, Eulerian-Lagrangian approaches as well as filtered Eulerian-Eulerian approaches have emerged to address some of the weaknesses of the Two Fluid Model such as the large computational expense and the difficulty in representing particle size distributions. Both the Eulerian and Lagrangian approaches are represented in the papers that follow this introduction.

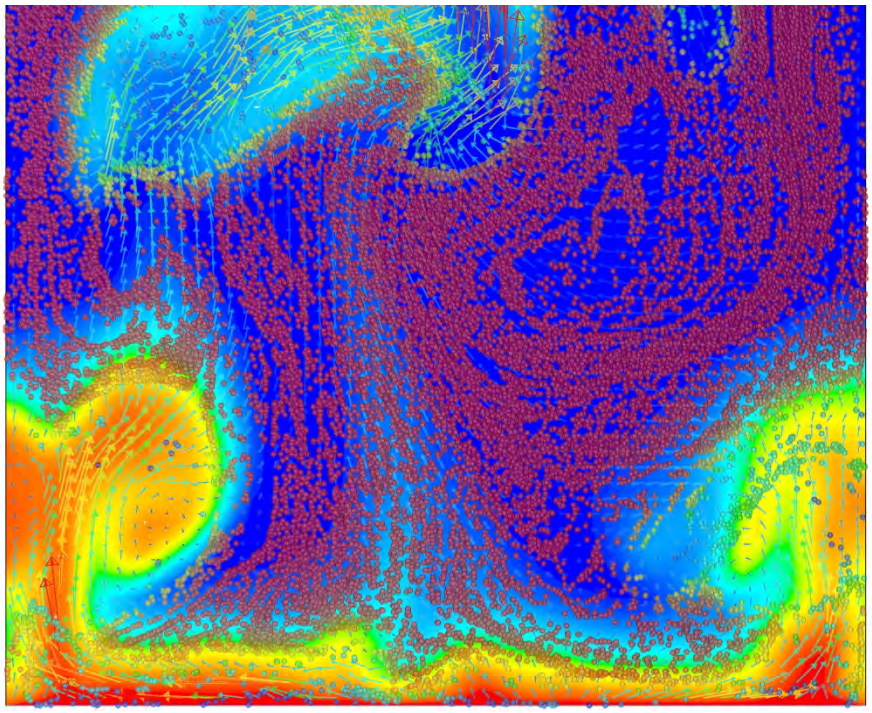

COMPARING EULER-EULER AND EULER-LAGRANGE BASED MODELLING APPROACHES FOR GAS-PARTICLE FLOWS

Markus BRAUN[1], Markus LAMBERT[1], Shailesh OZARKAR[2]*, Jay SANYAL[2]

[1] ANSYS Germany GmbH, Birkenweg 14a, D-64295 Darmstadt, Germany

[2] ANSYS Inc., 275 Technology Drive, Canonsburg, PA, 15317, US

* E-mail: shailesh.ozarkar@ansys.com

ABSTRACT

Comparative assessment of Euler-Euler and Euler-Lagrange modelling approaches for gas-particle flows is performed by comparing their predictions against experimental data of two fluidization challenge problems put forth by National Energy Technology Laboratory (NETL), Morgantown, WV, USA. The first fluidization challenge problem is based on a laboratory scale fluidized bed while the second fluidization challenge problem is based on a pilot scale circulating fluidized bed. It is found that both computational models predict comparable results and those results are in qualitative agreement with the experimental data.

Keywords: Euler-Euler, Euler-Lagrange, Gas-Particle flows, Fluidized bed.

NOMENCLATURE

Greek Symbols

ϕ	Volume fraction of particles.
δ	Normal overlap, [m].
γ	Damping coefficient, [kg/s].
μ	Coefficient of friction.
η	Coefficient of restitution.

Latin Symbols

$\vec{u}_p$	Velocity of a particle p, [m/s].
$\vec{F}$	Various forces acting on a particle, [N].
$\vec{F}_1$	Normal contact force acting on particle 1, [N].
Re_m	Mean flow Reynolds number.
d_p	Diameter of a particle, [m].
m_i	Mass of a particle i, [kg].
m_{12}	Reduced mass, [kg].
K	Normal spring constant, [N/m].
$\vec{e}_{12}$	Unit vector defined from particle 1 to particle 2.
$\vec{v}_{12}$	Relative velocity, [m/s].
t_{coll}	Time scale of collision, [s].

INTRODUCTION

Simulations of gas-particle flows in commercial scale devices such as fluidized beds are of interest to many industries including chemical processing, oil and gas, and energy. For these simulations, traditional Euler-Euler models based on kinetic theory of granular flow (KTGF) along with classical or refined form of gas-particle drag law are routinely used, (Gidaspow et al, 1992; Igci and Sundaresan, 2011; Li and Kwauk, 1994; Milioli et al, 2013; Parmentier et al, 2012; Wen and Yu, 1966). With recent advances in computing power and computational algorithms, there is a growing interest in using Euler-Lagrange models since these models are well suited for accounting for particle size distributions in comparison to Euler-Euler KTGF models.

In this computational study, a comparative assessment of Euler-Euler KTGF and Euler-Lagrange models is performed using small (laboratory) scale fluidized bed (SSFB) and pilot scale circulating fluidized bed (CFB) challenge problems designed for validation. Both problems are particularly suited for modelling using Euler-Euler KTGF and Euler-Lagrange models and for their comparative assessment since the particles considered in both problems are nearly monodisperse (Geldart Group D in SSFB and Group B based cases in CFB). The advantage with monodisperse particle system based comparative assessment of models is that the system remains free of size or density based segregation effects and polydisperse gas-particle drag force related effects. Furthermore, for gas-particle systems, drag force is the most dominant interaction force and it can easily be accounted in an equivalent manner in both models. In SSFB, inventory of particles corresponds to about 93000 particles. Therefore, Euler-Lagrange simulations with Discrete Element Method (DEM) to resolve collisions based on individual particles can be performed in affordable manner. In CFB problem, time-averaged inventory of particles in main riser section is such that the Euler-Lagrange with DEM simulations can only be performed by tracking

trajectories and collisions of group of particles or parcels.

This paper is organized as follows. We begin with a brief description of experimental facilities, flow conditions and experimental measurements. Next, we give an overview of models along with geometry simplification, grid resolutions and boundary conditions considered in simulations. After that, results from SSFB and CFB simulations are presented with the conclusion in the end.

EXPERIMENTAL FACILITY

On NETL website both challenge problems (NETL CFB 2010, NETL SSFB 2013) are well documented including information on test units, geometrical dimensions, instrumentation, and experimental measurements. Here we provide only brief description.

NETL Small Scale Fluidized Bed

A schematic of the rectangular fluidized bed test unit is shown in Figure 1. Physical properties of gas (air) and particles (Geldart Group D) are given in Table 1. Experimental flow conditions are given in Table 2. Gas entering the test unit at the bottom first gets distributed by bottom distributor and then gets redistributed by top distributor above which fluidized bed particles are present. The diameter of each orifice on the top distributor is slightly smaller than the diameter of a particle.

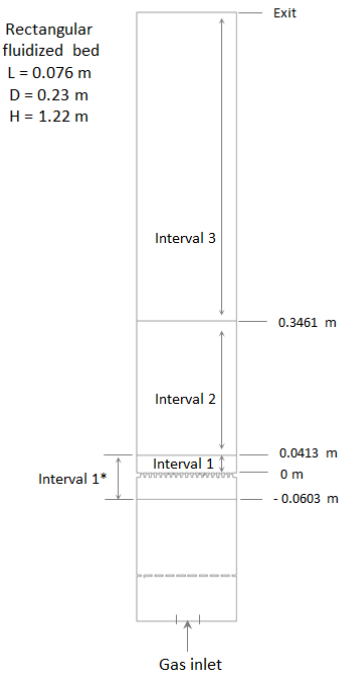

Figure 1: Schematic of small scale fluidized bed test unit.

Table 1: Physical properties of gas and particles

Particle diameter	3.256×10^{-3} m
Particle density	1131 kg/m^3
Gas density	1.2 kg/m^3
Gas viscosity	1.8×10^{-5} kg/m s

Experimental data have been reported in the form of mean and standard deviation of differential pressure (DP) across Interval 1*, Interval 2 and Interval 3; mean and additional statistical quantities of vertical and horizontal velocities of the particles; and granular temperature. The DP across Interval 1* includes DP across distributor and DP across interval 0 m to 0.0413 m which henceforth referred to as Interval 1. Since DP data across Interval 1 are not provided in the experimental data set, we extracted DP data across this interval by subtracting DPs across Intervals 2 and 3 from DP estimated based on total inventory of particles. Such extracted DP data across Interval 1 were used for comparison with simulation predictions.

Table 2: Flow conditions

Case	Solid Weight (Kg)	Gas Superficial Velocity (m/s)
1	1.9	2.19
2	1.9	3.28
3	1.9	4.38

NETL Circulating Fluidized Bed

The NETL circulating fluidized bed test unit is shown in Figure 2. Gas (air) enters the test unit from axial inlet located at the bottom of riser and solids returning from standpipe are recirculated back into the riser from a side inlet. The CFB was operated at five different flow conditions out of which only Case 3 is considered in this study. Case 3[1] corresponds to Group B particles with mean diameter 748 μm and density 863.3 kg/m^3. Superficial velocity of gas and solids circulation rate are 5.71 m/s and 5.54 kg/s, respectively.

MODEL DESCRIPTION

Simulations of both SSFB and CFB were performed using Euler-Euler KTGF model and Euler-Lagrange model with DEM to account for particle or parcel collisions.

Euler-Euler KTGF model

In this modelling approach, gas and particle phases are treated in an Eulerian frame and a set of conservation equations is solved for each phase. The governing equations of this model are well documented (Crowe et

[1] "Case 3" as outlined in https://mfix.netl.doe.gov/challenge/CFB_Challenge_Problem.xls, not Case 3 in Table 2.

al. 1998) and hence will not be repeated here. Gas-particle drag force that couples the motion of phases is the most dominant interaction force for gas-particle system since the Stokes number based on particle is typically large. In this computational study, we explored two drag force formulations.

First one is the widely used Gidaspow drag force formulation (Gidaspow et al., 1992). Second one is the drag force formulation put forth by Tenneti et al. (2011) based on DNS study of flow past fixed random assemblies of monodisperse spheres with finite fluid inertia using immersed boundary method. This drag

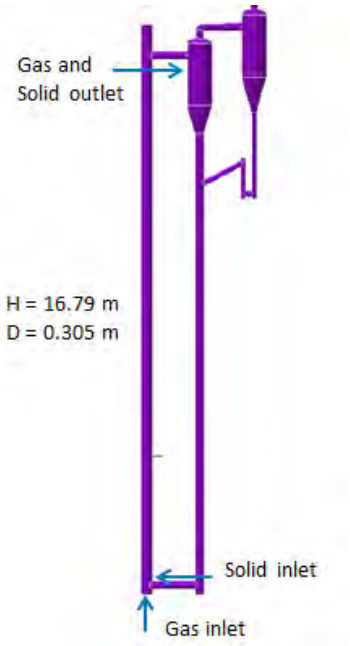

Figure 2: Pilot scale circulating fluidized bed test unit.

force formulation is given as a function of particle volume fraction $\phi\ (0.1 \le \phi \le 0.5)$, and mean flow Reynolds number $\mathrm{Re}_m\ (0.01 \le \mathrm{Re}_m \le 300)$ which is calculated based on particle diameter and magnitude of slip velocity between two phases. In that study, it is shown that the values obtained from Gidaspow drag force formulation begin to differ quite significantly from DNS results in the limits of higher volume fraction $(\phi > 0.2)$ and mean flow Reynolds number. Since both limits are being satisfied in the SSFB problem, for its simulation the use of second drag force formulation is essential. In the CFB problem, average volume fraction of particles remains below 0.2 where Gidaspow drag force formulation does not differ significantly from DNS results over the range of Re_m and thus usage of Gidaspow drag force formulation is adequate.

Euler-Lagrange model

In this modelling approach, the gas phase is treated in Eulerian frame and for the solution of its conservation equations particle volume fraction and velocity information is needed at the centre of each cell in fixed Eulerian grid. This information is provided by averaging over particle field data and then mapping it to Eulerian grid. The particle phase is treated in Lagrangian frame by tracking discrete particles or groups of particles or parcels with their trajectories described by

$$m_p \frac{d\vec{u}_p}{dt} = \vec{F}_d + \vec{F}_p + \vec{F}_{vm} + \vec{F}_g + \vec{F}_{other} + \vec{F}_{contact} \qquad (1)$$

In this equation, terms on right hand side represent drag force, pressure force, virtual mass force, gravitational force, any other forces acting on particle, and particle-particle contact force. The last term is calculated using Discrete Element Method (DEM) based on work of Cundall and Strack (1979). Briefly, the normal contact force on particle 1 which is in contact with particle 2 is calculated using a spring-dashpot model:

$$\vec{F}_1 = \left(K\delta + \gamma\left(\vec{v}_{12} \cdot \vec{e}_{12}\right)\right)\vec{e}_{12} \qquad (2)$$

In tangential direction only sliding contact between particles is considered in this study and tangential contact force is calculated using the equation for Coulomb friction:

$$\vec{F}_{friction} = \mu \vec{F}_{normal} \qquad (3)$$

In simulations involving parcels, the contact force is calculated based on parcel mass and its diameter. The parcel mass is calculated as sum of mass of all particles in a parcel and the parcel diameter is calculated from mass of a parcel and density assumed to be the same as the particle density.

SIMULATIONS

In this computational study, all simulations were carried out using ANSYS Fluent 15.0.

SSFB simulations

First, series of Euler-Euler KTGF model based simulations of Case 1 (considered as a test-bed) were performed to check the effects of drag force formulations and gas-inlet configurations. After these simulations, simulations of Case 2 and Case 3 were performed with one selected gas-inlet configuration and without making any changes to the model. For Case 1 simulations, we considered three different types of gas-inlet configurations. In first type of configuration, only a portion of geometry above top distributor was considered, and without resolving nozzles in geometry, gas mass flow rate corresponding to the superficial velocity given in Table 2 was specified on the whole inlet surface. This configuration is referred to as Uniform Inlet. In the second type of configuration referred to as Distributor Inlet, we kept the geometry as in first configuration but resolved all of the nozzles on the top distributor. In the third type of configuration referred to as Complete Geometry, we considered the whole geometry shown in Figure 1. In all of the configurations, the cell size in the main part of the fluidized bed (above inlet regions) was kept approximately as 3.9 times particle diameter. Total

number of cells in the grids with Uniform Inlet, Distributor Inlet and Complete Geometry were 10000, 48000 and 244000, respectively. For both gas and particle phases, wall boundary condition was set to no-slip.

Euler-Lagrange model simulations require the cell size in the grid to be bigger than the size of particle or parcel. The grid with Uniform Inlet configuration can easily satisfy this requirement but the grids with Distributor Inlet and Complete Geometry configurations cannot. Therefore for these simulations, instead of accurately resolving nozzles, we considered simplified rectangular shaped nozzles as shown in Figure 3 and generated a grid with cell size of about 3.5 times particle diameter. For particle-particle and particle-wall collision calculations, spring constant, coefficient of restitution and coefficient of friction were arbitrarily set to 500 N/m, 0.9 and 0.1, respectively. Particle time step was set to $t_{coll}/5$ where t_{coll} is the collisional time scale that is given by

$$t_{coll} = \left(\frac{m_{12}}{K} \left(\pi^2 + (\ln \eta)^2 \right) \right)^{\frac{1}{2}} \qquad (4)$$

where, reduced mass is calculated from masses of particle 1 and 2: $m_{12} = (m_1 m_2 / (m_1 + m_2))$. All simulations of SSFB were run up to at least 15 sec of flow time calculations and next 10 sec of flow time data were used for time-averaging. Data gathering frequency was set to 1000 Hz.

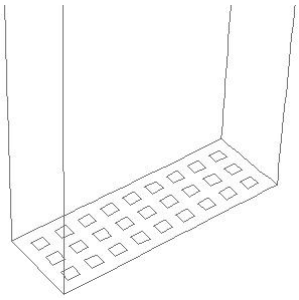

Figure 3: Gas-inlet configuration considered for Euler-Lagrange model based simulations.

CFB simulations

Agrawal et al. (2001) showed that for realistic predictions of gas-particle flows, grid resolution must be of the order of few particle diameters in order to resolve fine scale structures (clusters and streamers) that are shown to further reduce gas-particle drag. For understanding the change in simulation predictions with successive grid refinements and for comparative assessment study, we performed CFB simulations using Euler-Euler KTGF model with three different grid resolutions – coarse, intermediate and refined grids consisting of 65000, 1.67 million and 3 million cells, respectively. The various parameters of these grids are shown in Table 3.

Recently we started CFB simulations using Euler-Lagrange model. Since it is nearly impractical to perform individual particles based simulations, for CFB study, we took parcel based approach. Here we present results from a preliminary simulation run that was performed using 96000 hexahedral cells and 0.47 million parcels with 1826 particles per parcel. Parcel-Parcel collisions were accounted using DEM with spring constant, coefficient of restitution and friction coefficient arbitrarily set to 1000 N/m, 0.7 and 0.25, respectively. Subsequent simulations with lesser number of particles per parcel will need to be performed to understand its effect on simulation predictions. All CFB simulations were run for sufficiently longer time to allow cases to reach statistical steady state before gathering data for time-averaging.

Table 3: The various parameters of grids considered in CFB simulations using Euler-Euler KTGF model.

	Approximate cell lengths			
	Along circumference	Across diameter	Along axis	Grid Size
Coarse	90* d_p	31*d_p	40*d_p	65000
Intermediate	22* d_p	10*d_p	10*d_p	1.67M
Fine	10* d_p	10*d_p	10*d_p	3 M

RESULTS AND DISCUSSIONS

SSFB simulation results

Mean DP values across Interval 2 from experiments and simulations of Case 1 are given in Table 4. Several points emerge from this table after we compare these values. Overall, simulations slightly over predict mean DP values compared to experiments. As expected, the values obtained from simulations using Tenneti et al. drag law are lower compared to those obtained using Gidaspow drag law and closer to experimental data. By comparing the values for three different gas-inlet configurations obtained from Euler-Euler KTGF simulations with Gidaspow or Tenneti et al. drag law, we see that Uniform Inlet always leads to higher solids hold up in that interval compared to other two gas-inlet configurations which give almost same mean DP values. Mean DP values predicted by Euler-Lagrange model with Tenneti et al. drag law for two different gas-inlet configurations do not differ much indicating that assumed size of each rectangular shaped nozzle in Distributor Inlet configuration is too coarse and overall gas-particle flow distribution is same with both inlet configurations. By comparing mean DP values from Euler-Lagrange and Euler-Euler KTGF models, it can be said that predictions from both models are comparable.

Figure 4 shows snapshots of volume fraction of particle- phase obtained from simulations using Euler-Euler KTGF model with Tenneti et al. drag law for three different inlet configurations. In case of Uniform Inlet, we see constant presence of thin uniform layer consisting of lower volume fraction of particle-phase

next to inlet surface. This forces more particles into Interval 2 and hence leads to higher hold up predictions in that interval. With other two inlet configurations, gas streams emerging from nozzles merge together and periodically generate bubbles that rise upward and eventually burst into free board region. We see that the particles flow upward in centre region and downward adjacent to walls. Since there is no significant difference between Distributor Inlet and Complete Geometry results, we performed simulations of Case 2 and Case 3 using Distributor Inlet configuration and Tenneti et al. drag law with Euler-Euler KTGF as well as Euler-Lagrange model. In simulations of Case 2 and 3, fluidization behaviour looked significantly different from Case 1. At higher superficial velocities both models predict vigorous fluidization as opposed to periodic generation of bubbles seen in Case 1.

Table 4: Mean DP across Interval 2 from experiments and simulations of Case 1.

Case 1	Mean DP across Interval 2 (kPa)
Experiments	0.686
Euler-Euler KTGF model with Gidaspow drag law	
Uniform Inlet	0.916
Distributor Inlet	0.862
Complete Geometry	0.857
Euler-Euler KTGF model with drag law proposed by Tenneti et al.	
Uniform Inlet	0.844
Distributor Inlet	0.783
Complete Geometry	0.794
Euler-Lagrange model with drag law proposed by Tenneti et al.	
Uniform Inlet	0.856
Distributor Inlet - Square nozzles	0.873

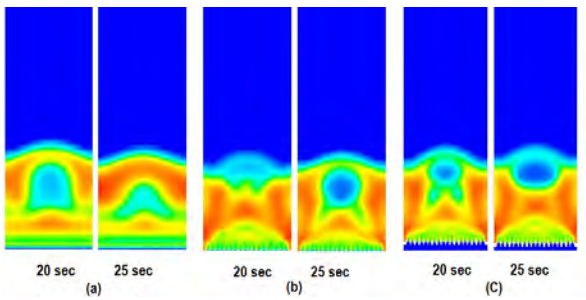

Figure 4: Snapshots of particle-phase volume fraction at 20 and 25 sec of flow time from simulations using Euler-Euler KTGF model with Tenneti et al. drag law. (a) Uniform Inlet. (b) Distributor Inlet. (c) Complete Geometry (bottom portion not shown).

Figure 5 shows comparison of mean DP predictions obtained from Euler-Euler KTGF model based simulations of three cases (listed in Table 2) with the experimental data. In this figure, filled symbols represent experimental data and open symbols with lines represent simulations. Circles are for mean DP across Interval 1, squares are for Interval 2 and triangles are for Interval 3. In experiments, with increase in superficial velocity, mean DP increases across Intervals 1 and 3, and decreases across Interval 2. Euler-Euler KTGF model qualitatively captures the trends for the Intervals 1 and 3 but does not predict significant decrease in mean DP across Interval 2 as seen with experimental data.

Figure 6 shows predictions from Euler-Lagrange model simulations. These simulations do predict decrease in mean DP across Interval 2 with the increase in superficial velocity. From last two figures, we see that both Euler-Euler KTGF and Euler-Lagrange models predict comparable mean DP values for all three intervals but when compared with experimental data, quantitative

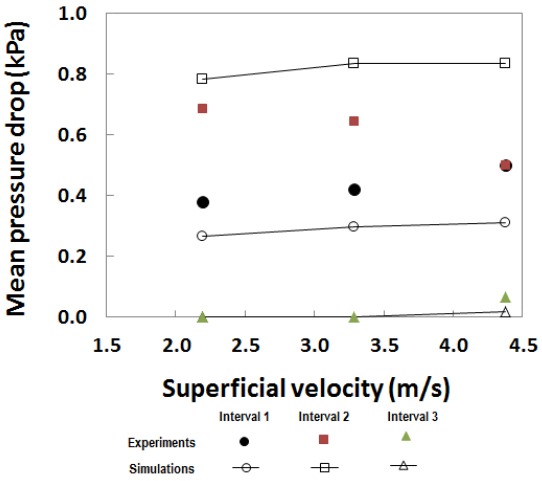

Figure 5: Effect of superficial velocity on mean DP across three intervals. Simulation predictions are from Euler-Euler KTGF model.

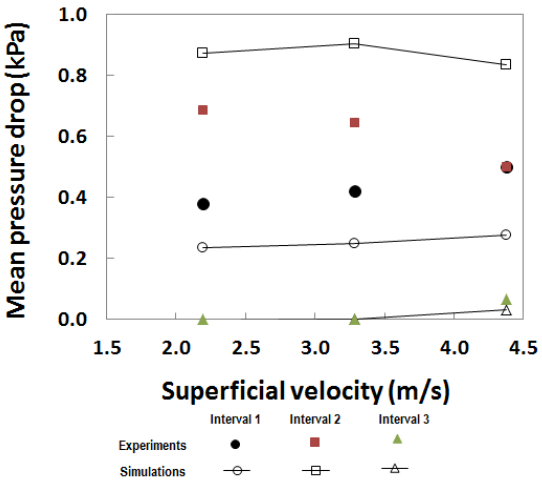

Figure 6: Effect of superficial velocity on mean DP across three intervals. Simulation predictions are from Euler-Lagrange model.

differences are clearly visible. We have not yet explored the effect of wall boundary conditions as well as Euler-Euler KTGF model parameters such as coefficient of restitution, which might play some role in the model

predictions. Similar study with Euler-Lagrange approach is also needed.

Figure 7 shows comparison of standard deviation of DP across Interval 2 obtained from Euler-Euler KTGF and Euler-Lagrange models with experimental data. Predictions from both models are in good agreement with experimental data at smallest and largest superficial velocities but not at intermediate superficial velocity.

We now compare time-averaged particle-phase vertical velocity predictions obtained from Euler-Euler KTGF and Euler-Lagrange models with the experimental data. In experiments, particle-phase velocity measurements were performed using high speed PIV that traced particles appearing in cells (0.0457 m X 0.0457 m X 0.003 m)

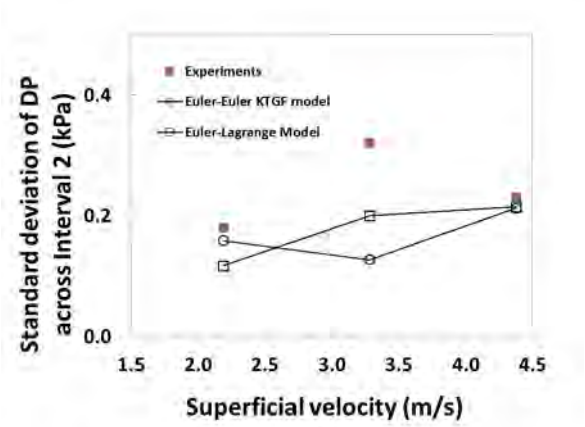

Figure 7: Effect of superficial velocity on standard deviation of DP across Interval 2.

located adjacent to the wall and at the mid-point elevation of 0.0762 m measured from top distributor. Since these measurements were performed within a particle diameter distance from the wall, the measurements were expected to be strongly influenced by particle-wall interactions.

Figure 8 shows comparison of time-averaged particle-phase vertical velocity profiles obtained from Euler-Euler KTGF model based simulations with the experimental data. Since these profiles are from near wall regions and in simulations we used no-slip boundary condition for both phases, as expected, we see under prediction of velocities at all lateral locations. Since in Euler-Lagrange simulations particles were allowed to slip with specified particle-wall collision parameters, we see visible improvements in velocity predictions in Figure 9. Slight asymmetry in velocity profiles indicates that the considered time interval for simulation data gathering was not long enough.

CFB simulation results

To understand the change in simulation predictions with successive grid refinements and for comparative assessment of the models, we performed a set of simulations using Euler-Euler KTGF model with coarse, intermediate and refined grids consisting of 65000, 1.67 million and 3 million cells, respectively. Figure 10 shows time-averaged gas-phase axial pressure gradient profiles obtained from these simulations. In this figure, experimental data is also shown for comparison. With successive global grid refinements we see improvements in pressure gradient predictions, however even with refined grid where cell size is about ten times particle diameter, the model under predicts the hold up.

Predictions from Euler-Lagrange model are also given in Figure 10. The Euler-Lagrange simulations were performed on a coarse grid consisting of 96000 cells and

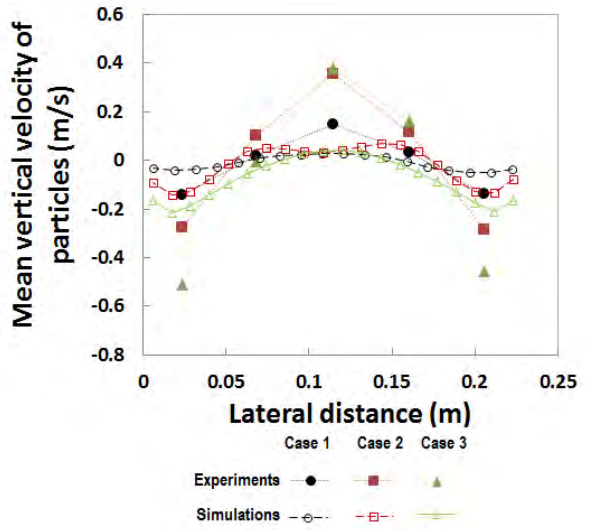

Figure 8: Comparison of time-averaged particle-phase vertical velocity profiles obtained from Euler-Euler KTGF simulations with experimental data. Profiles are from regions adjacent to the wall.

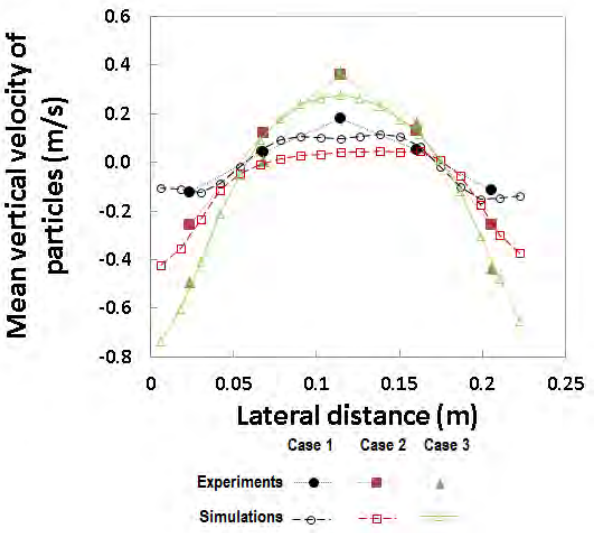

Figure 9: Comparison of time-averaged particle-phase vertical velocity profiles obtained from Euler-Lagrange simulations with experimental data. Profiles are from regions adjacent to the wall.

0.47 million parcels. We see that the predictions from Euler-Lagrange model are comparable to those obtained

from Euler-Euler KTGF model using coarse grid. Comparison of time-averaged particle-phase axial velocity profiles obtained at 8.88 m elevation is shown in Figure 11. These preliminary results indicate that further studies with Euler-Lagrange model are also needed to understand the effects of grid and boundary layer resolution along with the number of parcels on model predictions.

SUMMARY

Euler-Euler KTGF and Euler-Lagrange models gave similar results for gas-particle flows in small scale fluidized bed (SSFB) and pilot scale circulating fluidized bed (CFB). In SSFB study, the results were found to be in qualitative agreement with the experimental data. Resolving nozzles on gas distributor and using DNS based drag law proposed by Tenneti et al. (2011) led to further improvement in results. In CFB study, both models gave similar results with coarse grid resolution. Euler-Euler KTGF model predictions improved with successive global grid refinements; however additional elaborate study is needed to understand the effects of various parameters including resolution of boundary layer cells. Similar CFB study with Euler-Lagrange model is needed to understand the effects of grid and boundary layer resolution, number of parcels, and parameters used in DEM calculations.

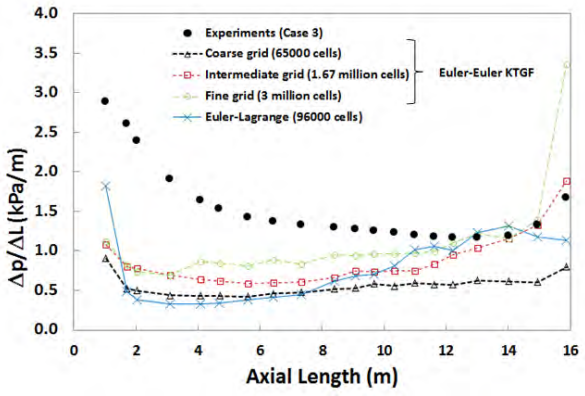

Figure 10: Predictions of time-averaged gas-phase axial pressure gradient from Euler-Euler KTGF and Euler-Lagrange simulations. Experimental data is also shown for comparison.

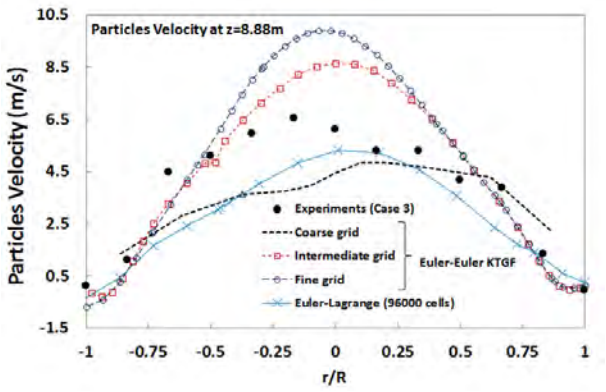

Figure 11: Predictions of time-averaged particle-phase axial velocity from Euler-Euler KTGF and Euler-Lagrange simulations. Experimental data is also shown for comparison.

REFERENCES

AGRAWAL, K., LOEZOS, P. N., SYAMLAL, M. and SUNDARESAN, S., (2001), "The role of mesoscale structures in rapid gas-solid flows", *J. Fluid Mech.*, **445,** 151-185.

CROWE, C., SOMMERFELD, M. and TSUJI, Y., (1998), "Multiphase Flows with Droplets and Particles", CRC Press.

CUNDALL, P.A. and STRACK, O.D.L., (1979), "A discrete numerical model for granular assemblies. *Geotechnique*, **29,** 47-65.

GIDASPOW, D., BEZBURUAH, R. and DING, J., (1992), "Hydrodynamics of circulating fluidized beds, kinetic theory approach", *In Fluidization VII, Proceedings of the 7th Engineering Foundation Conference on Fluidization*, 75–82.

IGCI, Y. and SUNDARESAN, S.,(2011), "Constitutive models for filtered two-fluid models of fluidized gas-particle flows", *Ind Eng Chem Res.*, **50,** 13190-13201.

LI, J. and KWAUK, M., (1994), "Particle-Fluid two-phase flow: Energy-Minimization Multiscale Method", Beijing, P. R. China, Metallurgical Industry Press.

MILIOLI, C., MILIOLI, F., HOLLOWAY, W., AGRAWAL, K. and SUNDARESAN, S., (2013), "Filtered two-fluid models of fluidized gas-particle flows: New constitutive relations", *AIChE J.*, **59,** 3265-3275.

NETL CFB 2010 challenge problem https://mfix.netl.doe.gov/challenge/index_2010.php

NETL SSFB 2013 challenge problem https://mfix.netl.doe.gov/challenge/index.php

PARMENTIER, J-F., SIMONIN, O. and DELSARTK, O., (2012), "A functional subgrid drift velocity model for filtered drag prediction in dense fluidized bed", *AIChE J.*, **58**, 1084-1098.

TENNETI, S., GARG, R. and SUBRAMANIAM, S., (2011), "Drag law for monodisperse gas-solid systems using particle-resolved direct numerical simulation of flow past fixed assemblies of spheres", *Int. J. Multiphase Flow*, **37,** 1072-1092.

WEN, C.-Y. and YU, Y. H., (1966), "Mechanics of fluidization", *Chem. Eng. Prog. Symp. Series.*, **62**, 100–111.

STATE OF THE ART IN MAPPING SCHEMES FOR DILUTE AND DENSE EULER-LAGRANGE SIMULATIONS

Stefan RADL,[1*] Begona C. GONZALES,[1] Christoph GONIVA,[2,3] Stefan PIRKER[3]

[1] Institute of Process and Particle Engineering, TU Graz, AUSTRIA

[2] DCS Computing GmbH, Linz, AUSTRIA

[3] Department of Particulate Flow Modelling, JKU Linz, AUSTRIA

* E-mail: radl@tugraz.at

ABSTRACT

Euler-Lagrange (EL) simulations are an extremely important tool for academia and industry to better understand gas-particle flows. We present simulation results for various gas-particle flow configurations using a variety of Lagrangian-to-Euler coupling schemes. Specifically, we have combined the idea of smoothing the exchange fields (as proposed by Pirker et al. (2011), as well as Capecelatro and Desjardins (2013)) to design a new generation of robust mapping schemes that allow implicit, explicit or a hybrid implicit/explicit time marching. Our schemes enable EL simulations of highly loaded gas-particle flows in which particles have a broad size distribution. We demonstrate the performance of our mapping schemes for the case of (i) a bubbling bi-disperse fluidized bed, (ii) a freely sedimenting suspension, as well as (iii) particle injection in turbulent cross flow configurations.

Keywords: Euler-Lagrange, numerical schemes, gas-particle flow.

NOMENCLATURE

Greek Symbols

β	Friction coefficient, [kg/m³/s]
ϕ	Mass density, [kg/m^3]
γ	Transported quantity (scalar or vectorial)
κ	Indicator function
η	Dynamic viscosity, [Pa·s]
μ	Mass loading, [kg/kg]
μ_{pp}	Inter-particle friction coefficient
ρ	Mass density, [kg/m^3]
τ	Characteristic time scale, [s]
$\boldsymbol{\tau}$	Stress, [Pa]
$\boldsymbol{\Phi}$	Volumetric coupling force, [N/m³]

Latin Symbols

$\mathbf{a}$	Acceleration, [m/s²]
d	Diameter, [m]
e	Coefficient of restitution
$\mathbf{f}$	Force, [N]
$\mathbf{g}$	Gravity, [m/s²]
l	Length, [m]
m	Mass flow rate, [kg/s]
p	Pressure, [Pa]
t	Time, [s]
$\mathbf{u}$	Fluid velocity, [m/s]
$\mathbf{v}$	Particle velocity, [m/s]
w	Weighting function
x,y,z	Cartesian coordinate, [m]
CG	Coarse graining ratio, ($CG = d_{parcel}/d_p$)
Co	Courant number
D	Diffusion coefficient, [m²/s]
L,H,W	Channel length, height, width, [m]
N	Number of particles
S	Source term (scalar or vectorial)
U	Characteristic velocity, [m/s]
V	Volume, [m³]
X,Y,Z	Overall extension of simulation domain, [m]

Sub/superscripts

*	Dimensionless quantity
$\langle\rangle$	Domain-averaged quantity
c	Cell centered value
d	Drag
f	Fluid
i	Particle index
inlet	At the inlet
j	Fluid cell index
jet	Jet property
m	Sub-time stepping index
n	Time index
p	Particle (primary)
parcel	Parcel (computational)
s	Superficial
t	Terminal
slip	Relative between the two phases
orig	Original (unsmoothed) variable

INTRODUCTION

EL simulations are of key importance to simulate the flow in (i) gas-particle separation devices, (ii) reactive fluidized beds with changing particle properties (e.g., size, porosity, or chemical composition), or (iii) particle

classification equipment. In case the particle population is polydisperse and particles are non-spherical, EL (or hybrid EL-Euler) simulations are currently the only reliable tool to investigate cluster formation, mixing or segregation effects. However, EL simulations are computationally expensive, and this work aims on providing some guidance for selecting appropriate numerical schemes that alleviate challenges associated with the maximum allowable computation time.

One important class of numerical schemes used in EL simulations is the coupling scheme that is used to transfer information from the particle phase to the Eulerian phase (i.e., "two-way" or "back-coupling"). For the coupling scheme a variety of strategies are available in literature. For example, the group of Sommerfeld (Lain and Sommerfeld, 2008; Sommerfeld and Lain, 2012) used an under-relaxation technique in which particle-phase properties are pre-averaged (in time) before the back-coupling is performed. Despite the great success of this technique in predicting experimental data, this approach cannot be used for a time-resolved simulation, and also cannot strictly guarantee Newton's Third Law (i.e., "action et reactio") in an instantaneous sense. Another approach (called "EUgran+poly") has been chosen by the group of Pirker (Schellander et al., 2013), in which a transient simulation (based on an Euler-Euler approach and a mean particle diameter of the particle cloud) is performed first. Then, tracer particles are used to predict individual particle trajectories in a polydisperse particulate flow. Finally, the mean particle diameter of the granular (Euler) phase is updated, and the transient Euler-Euler simulation is continued. While both strategies have proven to be very efficient in terms of computation time, they are not fully transient in the sense that both phases are updated in a time-resolved fashion. Furthermore, these two approaches are limited to moderately dense flows, because their collision models rely on closures from kinetic theory.

In this work we focus on a fully transient approach, which is based on the classical CFD-DEM (Zhou et al., 2010). This approach allows simulations of fluid-particulate flows from the dilute to very dense regimes (i.e., near or above the close-packing limit), which is its key advantage. Specifically, we have chosen the implementation CFDEMcoupling (www.cfdem.com) as the basis of our work, which relies on a parallel implementation of a finite-volume fluid solver (N.N., 2013), and the DEM (Kloss et al., 2012).

In the next chapter we briefly explain the underlying model equations, and the coupling algorithms we have implemented in CFDEMcoupling. We then analyse the time-step restrictions immanent to phase coupling, and finally consider a variety of test cases in order to benchmark the coupling algorithms. By considering a wide range of numerical parameters, we highlight the effect of these parameters on the predictions and the implications in terms of the computation time step required to ensure a stable integration. This allows us to give recommendations for numerical parameters that yield predictions with acceptable accuracy at a minimal computational cost.

MODEL DESCRIPTION

CFD-DEM Approach

The well-known CFD-DEM approach (Zhou et al., 2010) relies on the solution of the filtered Navier-Stokes equations, i.e.,

$$\frac{\partial\left(\rho_f \phi_f\right)}{\partial t} + \nabla\cdot\left(\rho_f \phi_f \mathbf{u}\right) = 0\,, \qquad (1)$$

$$\frac{\partial\left(\rho_f \phi_f \mathbf{u}\right)}{\partial \mathrm{t}} + \nabla\cdot\left(\rho_f \phi_f \mathbf{u}\mathbf{u}\right) = -\phi_f \nabla p_f - \phi_f \nabla\cdot\boldsymbol{\tau}_f + \boldsymbol{\Phi}_d + \rho_f \phi_f \mathbf{g}\,, \qquad (2)$$

and the integration of Newton's equation of (translational and rotational) motion for each individual particle. Here $\boldsymbol{\Phi}_d$ is a volumetric coupling force (excluding buoyancy effects), i.e., the force exerted by the particle phase on the fluid phase per unit volume of the gas-particle mixture.

Assuming a fixed particle mass, Newton's equation of translational motion yields an equation for the acceleration of each individual particle. Taking into account (i) contact, (ii) drag, (iii) fluid-stress, and (iv) gravitational forces, this equation is:

$$\mathbf{a}_i = \frac{\mathbf{f}_{cont,i}}{\rho_p V_{p,i}} + \frac{\beta_{p,i}}{\rho_p}\left(\mathbf{u}_i - \mathbf{v}_i\right) - \frac{1}{\rho_p}\nabla\cdot\boldsymbol{\tau}_f + \mathbf{g}\cdot \qquad (3)$$

The integration of the above equations is straight forward once each force component has been computed based on particle and fluid data available at time t^m and t^n, respectively. Note, that in this work we have considered only contact forces to integrate the equations of rotational motion, and have neglected hydrodynamic torque.

The above equation requires closures for the contact forces, the fluid-particle friction coefficient, and the fluid stress. We use a standard linear spring-dashpot model for the contact forces, the model proposed by Beetstra et al. (2010) for the friction coefficient, and a laminar fluid stress model.

CFD-DPM Approach

In order to simulate systems of industrial scale, the CFD-DEM approach cannot be used because of the excessively large number of (physical) particles. Instead, various flavours of "parcel methods", in which computational parcels are used to represent multiple physical particles, have been documented in literature during the last fifteen years. In CFDEMcoupling, both the MP-PIC method introduced by Snider (2001), as well as the DPM approach by Patankar and Joseph (2001) is available. While the MP-PIC approach does not require direct tracking of (parcel) collisions, DPM relies on a detection of collisions of spheres that represent a typical collision volume of each parcel. In parcel-based approaches, fluid-particle interaction forces are based on the physical diameter of the particles that are represented by each parcel. In such a way, fluid-particle momentum transfer can be modelled correctly.

We find that for situations involving dense granular flows the DPM results in much more robust simulation compared to the MP-PIC method. Consequently, we

have used the DPM approach in all the simulations presented in this paper.

Coupling Algorithm

The overall flow chart for the coupling algorithm implemented in CFDEMcoupling is illustrated in Figure 1. Starting with the known fluid and particle velocities, Eulerian quantities (e.g., the fluid velocity, or the voidage) are interpolated at the particle location to allow the computation of forces acting on each particle. Particle properties (i.e., velocity and position) are then updated with sub-time stepping (time index m), either in an implicit or an explicit fashion. Note, that for implicit time marching of the particles, the fluid velocity at the particle position and the drag coefficient must be known. In this work, we have used explicit time marching for the particle phase.

Updating the fluid flow field is more involved, and is detailed in the following paragraphs.

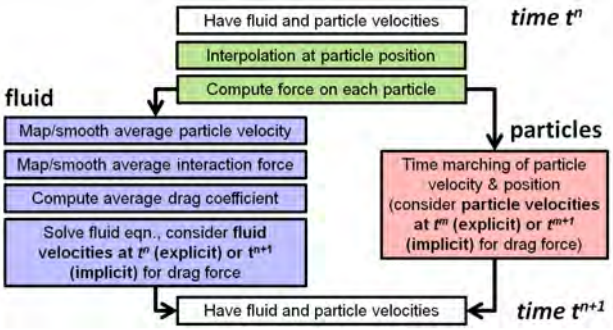

Figure 1: Flow chart of the coupling algorithm.

Mapping Algorithm

A mapping algorithm is used to calculate the weights w_{ij} that determine the contribution of the properties of particle i to cell j. The algorithm used in this work is based on a simple search algorithm that uses 29 satellite points (located inside the particle or parcel volume). Specifically, w_{ij} is determined by the number of satellite points of particle i that are located in cell j, divided by the total number of satellite points (of particle i) that are located in the fluid domain. This simple algorithm is very robust, conserves particle properties, can be used for any polyhedral mesh, and naturally handles situations in which particles are located near walls. Note that each particle (or parcel) only contributes to cells which are physically overlapping with the particle. This situation is unsatisfactory in case the typical size of a fluid cell is in the order of, or smaller than the particle (or parcel) diameter. In the following, we discuss an approach to overcome this limitation.

Smoothing

After the mapping algorithm has been executed, filtered Eulerian quantities (with a filter length equal to the grid spacing Δx) of the particle properties are available at the fluid grid. These quantities can now be smoothed over a length l_{smooth}. The physical meaning of this smoothing length is that each particle (or parcel in case of the DPM) will influence the fluid around it over a certain distance. Naturally, this distance will be some multiple of the particle (or parcel) radius. Typically, we have chosen $l_{smooth} = 3d_p$ in this work. Note that such a smoothing procedure is only relevant for small $\Delta x/d_p$ ratios. In case this ratio is large, however, the smoothing inherent to the mapping algorithm yields satisfactory exchange fields, and smoothing has no effect.

The smoothing operation is realized by (implicit) solution of a diffusion equation for each transferred quantity γ (e.g., the coupling force $\mathbf{\Phi}$):

$$\frac{\partial \gamma}{\partial t} = D\nabla^2\gamma \,. \qquad (4)$$

Here the diffusion coefficient is computed as $D = l_{smooth}^2/\Delta t$. Note that this smoothing operation is conservative, and has been used in previous work (Capecelatro and Desjardins, 2013; Pirker et al., 2011).

In case an implicit time marching for the fluid phase is used (see next section), a smoothed mean particle velocity field must be available. When performing the smoothing operation, the mean particle velocity field must be fixed in cells where particles are present ("filled cells"), and smoothing must be applied only to neighbour cells (of these filled cells). This can be realized by adding a source term S in the diffusion equation, i.e.,

$$S_\alpha = \frac{\kappa}{\Delta t}\left(\gamma_{orig} - \gamma\right), \text{ with}$$
$$\kappa = \begin{cases} 10^5 \;\; if\, \gamma_{orig} \neq 0 \\ 0 \;\; otherwise \end{cases}, \qquad (5)$$

that forces the original values (γ_{orig}) in filled cells to remain unchanged during the smoothing operation (Pirker et al., 2011).

Implicit/Explicit Time Marching for the Fluid Phase

At this point it is important to note that the volumetric coupling force $\mathbf{\Phi}$ can dominate Eqn. 2 in dense gas-particle flows involving small (i.e., d_p < ca. 100 µm) particles. In such a situation, this term is balanced (to a first approximation) with the pressure gradient term (i.e., the first term on the right hand side of Eqn. 2). Consequently, an implicit treatment of the coupling force $\mathbf{\Phi}$ would be desirable when updating the fluid's velocity and pressure field, because it would improve the stability of the integration. Indeed, we find that an implicit handling allows us to take 5 to 15 times larger fluid time steps, critically reducing the computation time in situations in which the load from the fluid solver is substantial compared to the particle solver.

In most gas-particulate flows, the drag force is the key force component, hence $\mathbf{\Phi} \approx \mathbf{\Phi}_d$. $\mathbf{\Phi}_d$ is a function of the local fluid and particle velocity, as well as the fluid-particle friction coefficient β experienced by each individual particle. The total coupling force available at the new time t^{n+1} (but before updating the fluid velocity) is:

$$\mathbf{\Phi}_{d,j}{}^{n+1} = -\frac{1}{V_j}\sum_i w_{ij} V_{p,i} \beta_{p,i} \left(\mathbf{u}_i{}^n - \mathbf{v}_i{}^{n+1}\right) \qquad (6)$$

Note that it is not possible to consider the new fluid velocity $\mathbf{u}_i{}^{n+1}$ in the calculation of the total coupling force given by Eqn. 6, since particle velocities are advanced with sub-time stepping. To realize an implicit coupling, i.e., consider the new fluid velocity $\mathbf{u}_c{}^{n+1}$ (located at the cell centres), it is necessary to recast the coupling force in an expression that involves an average

fluid-particle friction coefficient, as well as an average relative particle velocity. Thus,

$$\mathbf{\Phi}_{d,j}^{\,n+1} = -\frac{\left\langle w_{ij} V_{p,i} \beta_{p,i} \right\rangle}{V_j} \left(\mathbf{u}_c^{\,n} - \left\langle \mathbf{v}_i^{\,n+1} \right\rangle \right) \cdot \qquad (7)$$

One can now easily calculate the average friction coefficient $\langle w_{ij} V_{p,i} \beta_{p,i} \rangle$ from Eqn. 7 based on (the known) value for $\mathbf{\Phi}_d$. In case an implicit handling of the coupling force is performed, the new fluid velocity appears in the expression for the coupling force, leading to a slightly different version of Eqn. 7:

$$\mathbf{\Phi}_{d,j}^{\,n+1'} = -\frac{\left\langle w_{ij} V_{p,i} \beta_{p,i} \right\rangle}{V_j} \left(\mathbf{u}_c^{\,n+1} - \left\langle \mathbf{v}_i^{\,n+1} \right\rangle \right) \cdot \qquad (8)$$

Note, that such an implicit handling of the coupling force has two important consequences: (i) Newton's Third Law is not strictly enforced (because $\mathbf{\Phi}_{d,j}^{\,n+1} \neq \mathbf{\Phi}_{d,j}^{\,n+1'}$), and (ii) the effect of particle velocity fluctuations (which might affect $\beta_{p,i}$) is not accounted for. While the latter is thought to be of minor importance for typical gas-particle flows involving particles with d_p < 100 µm, the former is of concern in case an exact conservation of the system's momentum is required. We will discuss this point in our results for the freely sedimenting suspensions.

The interested reader might have observed another subtle difference between Eqns. 6, 7 and 8: particle-based quantities (index *i*) have been replaced by cell-based quantities (index *c*) when solving the fluid's governing equations. This is a problem when using an implicit scheme, i.e., one employs Eqn. 8, because the drag force on a particle is related to $\mathbf{u}_i$ and $\mathbf{v}_i$ (and not $\mathbf{u}_c$ and $\langle \mathbf{v}_i \rangle$). We have previously proposed a force splitting scheme (see Radl et al., 2012) that accounts for this discrepancy by splitting-off an explicit force component. Tests show that in dense flows (e.g., packed beds) this splitting increases the stability of the fluid solver (data not shown). We have indicated results obtained by such an improved method by "split impl./expl." in the current work. Furthermore, we have considered a variant of the coupling algorithm in which we treat the coupling force in cells that are void of particles (and hence no average particle velocity can be estimated) explicitly. In the remaining fluid cells the coupling force was treated implicitly. Such an approach avoids the need for smoothing the (average) particle velocity field, which we find to be problematic in regions with high particle velocity gradients.

THEORETICAL CONSIDERATIONS

Relaxation Times

A key physical time scale in a gas-particle flow is the particle relaxation time τ_p defined as (assuming Stokes drag law):

$$\tau_p = \frac{d_p^{\,2} \rho_p}{18 \eta_f} . \qquad (9)$$

This time scale sets an upper bound for the numerical integration of the particles' equation of motion (note that the particle-particle interaction force model might impose an additional limitation on the time step). Physically, this time scale can be interpreted as the time needed to accelerate the particle to a certain fluid velocity *U* by means of drag forces. The time step used for the integration of the particle equations must be smaller than the particle relaxation time in order to ensure an accurate and stable (in case of a simple forward Euler integration) numerical simulation.

Similarly, one can define a fluid relaxation time τ_f as:

$$\tau_f = \frac{U}{a_f} = \frac{\tau_p}{\mu} = \frac{d_p^{\,2} \rho_f}{18 \eta_f} \frac{1-\phi_p}{\phi_p} . \qquad (10)$$

Here a_f is a typical acceleration of the fluid due to drag forces. This time scale can be interpreted as the time it takes for the fluid to accelerate to a certain particle velocity *U* under the action of drag forces. This time scale sets an upper bound for the numerical integration of the equations that govern fluid flow. Clearly, the time step used for the integration of the Navier-Stokes equations must be smaller than the fluid relaxation time. In typical gas-particle flows with moderate to large particle volume fractions, and particles in the µm size-range, this fluid relaxation time is $O(10^{-5})$ seconds or smaller, depending on the mass loading.

Time Step Restrictions

In addition to the above characteristic relaxation times, the Courant number *Co* must be kept sufficiently low (typically less than 0.5) in order to ensure a stable numerical solution. Thus, the characteristic time scale

$$\tau_{Co} = \frac{\Delta x}{U} Co \qquad (11)$$

limits the fluid time step.

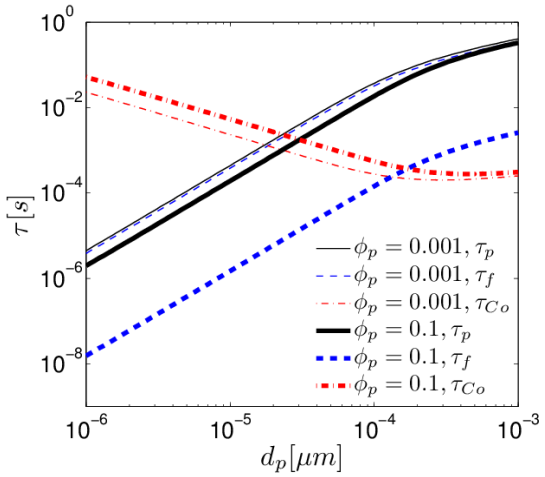

Figure 2: Characteristic time scales relevant for the simulation of a freely-sedimenting gas-particle suspension (ρ_p = 1500 [kg/m³], $\eta_f = 1.8 \cdot 10^{-5}$ [Pa·s], ρ_f = 1.3 [kg/m³], Beetstra et al. drag law).

The time step restrictions for integrating the Navier-Stokes equations are summarized in Figure 2 for a freely sedimenting gas-particle suspension. Note that in this figure the particle and fluid relaxation time for dense suspensions at non-zero Reynolds numbers have been computed using the drag model of Beetstra et al. (2010). As can be seen, for a dilute suspension (i.e., ϕ_p = 0.001), the particle relaxation time becomes the limiting time scale in case particles are smaller than ca. 15 µm, and τ_f

$\approx \tau_p$. However, for moderately dense suspensions (i.e., $\phi_p = 0.1$) the largest possible time step is set by the fluid relaxation time τ_f for particle diameters smaller than ca. 200 µm. For particles with a diameter of ca. 20 µm or smaller, the largest possible time step becomes $O(10^{-6})$ seconds or smaller. Thus, an integration of the Navier-Stokes equations for these systems requires very small time steps, or a robust (implicit) coupling algorithm, such as the one we have outlined above.

RESULTS

Bi-Disperse Bubbling Fluidized Bed (CFD-DEM)

To illustrate that our proposed methodology can handle systems near close packing, we have simulated the bubbling fluidized originally studied by Goldschmidt et al. (2003), and simulated recently by Capecelatro and Desjardins (2013). Key system parameters are summarized in Table 1. In these simulations an implicit time marching for the fluid phase was performed, and no smoothing of exchange fields was performed.

Predictions both from the current work and from literature are summarized in Figure 3. As can be seen, there is reasonable agreement in the predicted particle distribution. However, the shape of the interface between the two particle species is different, especially for longer simulation times. A possible explanation of this difference is the different drag law used in the simulations. Specifically, our comparison of particle velocities (see Figure 4) might hint to differences in the particle flow pattern caused by bubbling. Unfortunately, we could not find reference results for the particle flow pattern in literature. Hence, we can only speculate about the effect of bubbling, and have included snapshots of the particle velocity distribution in Figure 4.

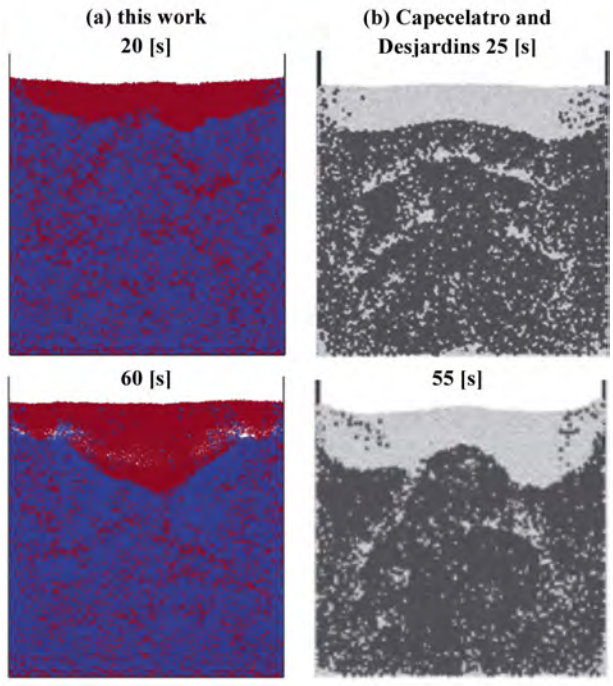

Figure 3: Snapshots of the spatial distribution of particles in a bubbling fluidized bed (a: this work, small particles are colored red and large particles are colored blue; b: literature data from Capecelatro and Desjardins, 2013, using the Tenneti et al., 2011, drag model).

Our results indicate that there is noticeable particle motion only near the free interface of the particle bed, and distinct bubbles do not form. Also, we found that even for moderate diameter ratios (i.e., 1.67 as in the current presentation), the drag formulation had a significant impact on the predicted bed expansion (i.e., bubbles occurred for other drag models) and on the segregation profile. Surprisingly, we found that the standard (i.e., mono-disperse) formulation of the drag model provided by Beetstra et al. (2010) gave the best agreement with the experimental data of Goldschmidt et al. (2003). Interestingly, also Capecelatro and Desjardins (2013) used a drag law that has been designed for mono-disperse particle beds. Thus, more research is needed to explain why a mono-disperse drag formulation gives better predictions for bi-disperse bubbling bed compared to more elaborate drag models.

Table 1: Physical parameters of the bubbling fluidized bed test case.

Parameter	*Value*
Domain (X x Y x Z)	0.15 x 0.015 x 0.45 [m]
Particle density (ρ_p)	2525 [kg/m³]
Particle diameter (d_p)	1.5 … 2.5 [mm]
Gas density (ρ_f)	1.13 [kg/m³]
Gas dynamic viscosity (η_f)	$1.77 \cdot 10^{-5}$ [Pa·s]
$N_{p,1}$ / $N_{p,2}$	17,940 / 27,720
U_s	1.3 [m/s]
e_p / μ_{pp}	0.9 / 0.1

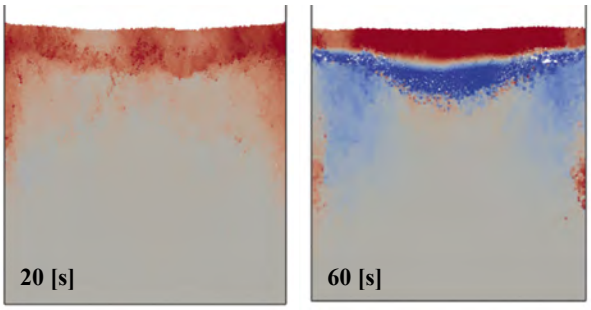

Figure 4: Snapshots of the vertical (i.e., z-) particle velocity in a bubbling fluidized bed (colors indicate velocities between -0.06, blue, and +0.06 [m/s], red, t = 60 [s]).

Freely Sedimenting Suspension (CFD-DPM)

A critical test for an EL code is its ability to predict the fluid-particle slip velocity during the sedimentation in a fully periodic box. In such a configuration no external forces act on the fluid-particle system (the weight of the system must be balanced by pressure gradient, though). Hence the total momentum of the system should remain unchanged. We have performed simulations of a sedimenting gas-particle mixture (d_p = 150 µm, ρ_p = 1500 kg/m³, $\langle\phi_p\rangle$ = 0.10, the gas phase was air at ambient conditions) using implicit and explicit time marching for the fluid phase. Results for the domain-averaged slip velocity (i.e., the difference between the momentum-averaged velocity of the two phases) for several choices of the dimensionless fluid time step Δt^*

$= \Delta t/t_f$ are summarized in Figure 5. Our simulations using an explicit time marching were performed with a time step of Δt^*=0.025 - larger simulations were impossible due to stability reasons. As can be seen, the results of the implicit time marching are in good agreement with the results for the explicit procedure (fluid grid size effects are typically larger, see blue and black symbols in Figure 5; note that these fluid grid size effects arise naturally due to non-resolved fluid velocity fluctuations, see Radl et al., 2012). The advantage of the implicit procedure is that it allows a time step up to 17.5 times larger than the one used for an explicit procedure.
As mentioned in the previous chapter, an implicit procedure does not perfectly enforce Newton's Third Law, and hence leads to a drift of the system's momentum. In order to control the drift velocity, it is necessary to add a correction force that is in the order of 5 to 15% of the total system weight (the correction in case of the explicit procedure is much smaller, i.e., 0.4%; splitting the coupling force into an implicit and explicit part reduces the necessary correction force to ca. 1% of the system weight). This correction force reflects the integral error due to the violation of Newton's Third Law. Furthermore, we find that the correction force depends on the fluid grid size (smaller grid size lead to a smaller correction), i.e., the correction is proportional to the number of particles per fluid grid cell. In summary, one should carefully evaluate whether implicit time marching yields accurate results, especially in case comparably coarse fluid grid cells are used. Our simulation results indicate that this is typically the case for moderately dense to dense gas-particle suspensions. In dilute flows (for which τ_f is close to, or larger than τ_p), we suggest using an explicit procedure, or an algorithm based on implicit/explicit force splitting because of a more precise conservation of the system's momentum.

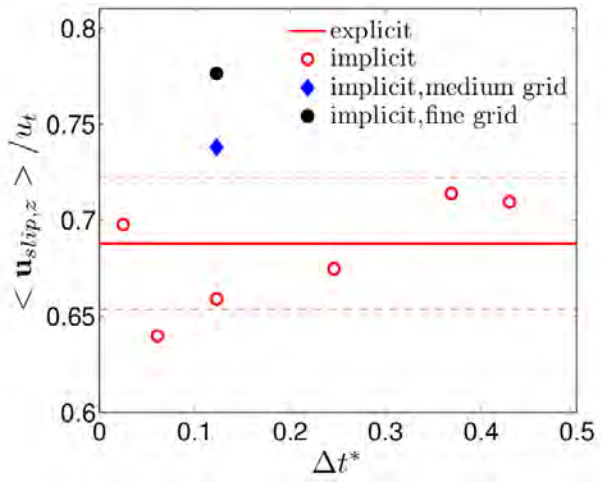

Figure 5: Predicted slip velocity of a freely-sedimenting gas-particle suspension for various dimensionless fluid time steps (the red dashed lines indicate ± 5% of the results using the explicit coupling procedure).

2D Bi-Disperse Jet in Cross Flow (CFD-DPM)

Setup

To investigate the performance of the mapping and smoothing schemes to model comparably dilute flows, we consider the injection of a particle jet in a turbulent cross flow (JICF). Specifically, we consider a synthetic configuration, in which a bi-disperse particle population is injected into a (pseudo) two-dimensional fluid flow field (i.e., air at ambient conditions). The physical parameters of the JICF configuration are summarized in Table 2. The fluid mesh resolution was Δx = 0.01 [m], and the time resolution of the base case was $\Delta t = 10^{-5}$ [s] to advance the fluid's governing equations.

Table 2: Physical parameters of the 2D JICF test case.

Parameter	*Value*
Domain (X x Y x Z)	1.8 x 0.7 x 0.002 [m]
Particle density (ρ_p)	2500 [kg/m³]
Particle diameter (d_p)	5 … 20 [µm]
Gas density (ρ_f)	1.1 [kg/m³]
Gas dynamic viscosity (η_f)	$1.91 \cdot 10^{-5}$ [Pa·s]
Mass loading ($\mu = m_p/m_f$)	0.5
Rel. particle injection velocity ($\mathbf{v}_y/\mathbf{u}_{inlet,x}$)	0.591
Crossflow velocity ($\mathbf{u}_{inlet,x}$)	25.4 [m/s]

Particle Penetration

Maps of the time-averaged magnitude of the gas velocity, as well as the particle positions are shown in Figure 6. Again, we have attempted to assess the effect of an implicit vs. an explicit time marching procedure on key flow features. As can be seen, explicit time marching leads to a more pronounced particle penetration into the cross flow compared to the implicit procedure (cp. Figure 6a and b). However, the recirculation behind the injection point has a similar extension in the main flow direction whether the implicit or the explicit procedure is employed. The advantage of implicit time marching is that we were able to use a substantially (i.e., 4.9 times) larger time step. Such a large time step could not be realized with explicit time marching, highlighting the robustness of the implicit procedure. Furthermore, we show results for the implicit/explicit coupling force splitting in Figure 6c (in Figure 7 the splitting of the coupling force is illustrated). As we will show in the next paragraph, this force splitting approach yields results that are practically indistinguishable from that obtained with an explicit procedure, but require less computational resources.

Velocity Profiles

A more quantitative comparison of the 2D JICF results is provided in Figure 8, where we have plotted profiles of the time-averaged streamwise (i.e., x-) fluid velocity component. As can be seen, the results for various flavours of the implicit time marching are essentially indistinguishable from each other. Same as for the particle penetration illustrated in Figure 6, the explicit procedure leads almost identical predictions for the velocity distribution when compared to the implicit/explicit mapping approaches. For the time being, we accept our results obtained with the explicit

and implicit/explicit mapping approach as the most accurate predictions (in these simulations Newton's third law is satisfied with an error of less than 1%; experimental validation was addressed to future work). In contrast, and as can be seen in Figure 8, a purely implicit procedure leads to an underprediction of the fluid velocity, especially near the bottom wall. Inspection of the error due to the implicit handling of the coupling force indicates that this error indeed can be substantial (data not shown). This is especially true for the uppermost layer of particles that experiences the highest acceleration, and hence also exerts the largest force onto the fluid.

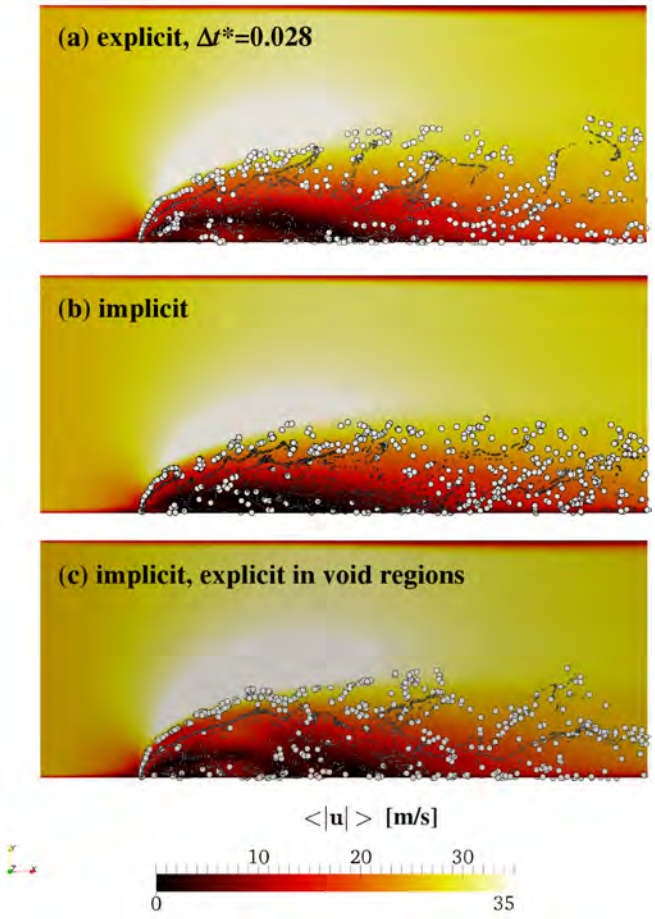

Figure 6: Time-averaged magnitude of the fluid velocity (contours), and particle distribution in the 2D JICF test case (Δt^*=0.138; the simulations in panel c employed impl./expl. force splitting; smoothing based on the local particle diameter was applied; particles are scaled according their primary particle diameter).

Finally, we note that whether smoothing is employed or not results in minimal differences in the predicted flow pattern. This is because of the comparably large fluid grid to parcel diameter ratio that results in a sufficient smoothing inherent to the grid size.

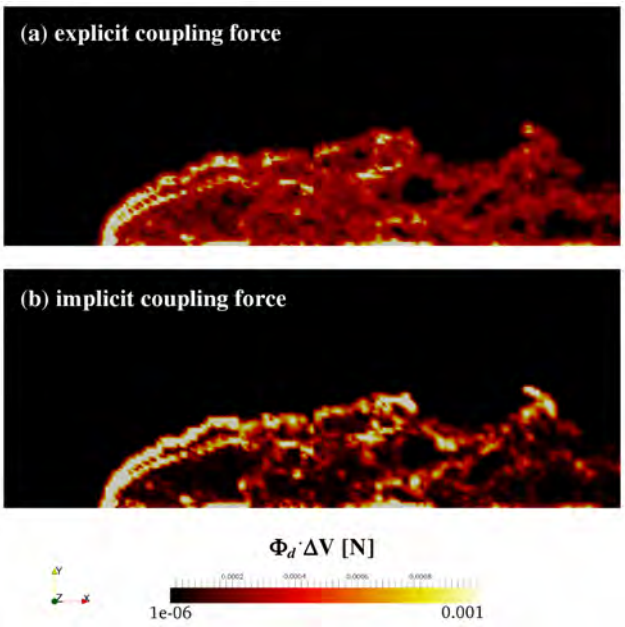

Figure 7: Local coupling force obtained from simulations with implicit force coupling in dense regions, and explicit force treatment in regions void of particles (data from Figure 6c; impl./expl. force splitting was performed).

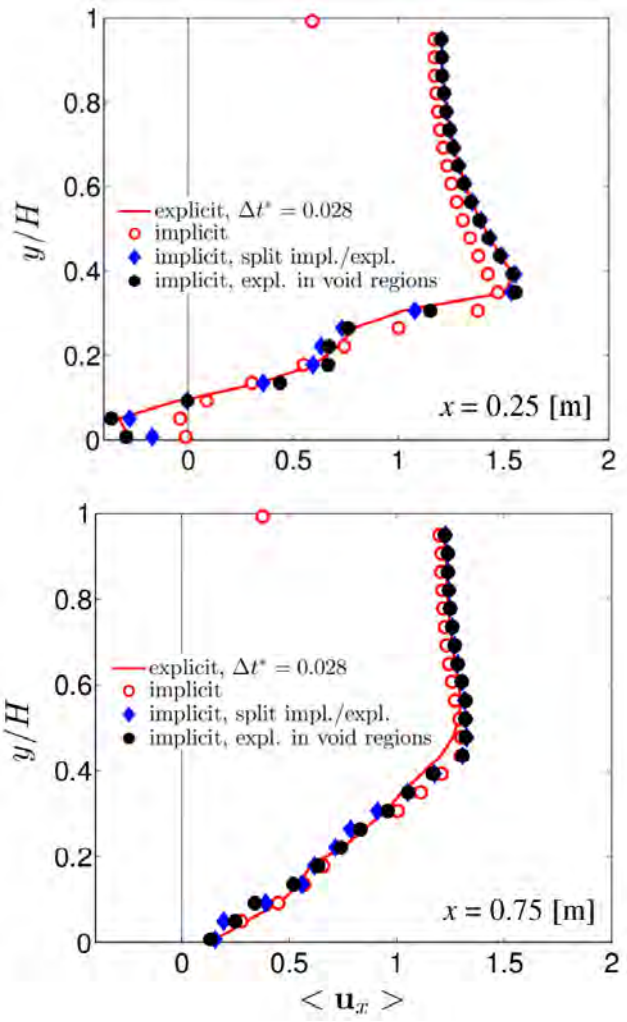

Figure 8: Sensitivity of the fluid velocity profiles in the JICF configuration to the coupling procedure and the fluid time step.

The Salzman 3D JICF Configuration (CFD-DPM)

To investigate whether the developed coupling algorithm can give results independent of parcel size and fluid grid resolution, the (three-dimensional) JICF configuration of Salzman and Schwarz was simulated. The physical parameters are summarized in Table 3, and the geometrical details are shown in Figure 9.

The Salzman configuration has been analysed numerically by Li and Lin (2010), as well as Han and Chung (1992). Only a limited amount of reliable reference data is available for this setup. Therefore, in this work we have used a highly-resolved CFD-DPM simulation with approximately 12.7 Mio. fluid cells to provide reference data for the subsequent analysis. A sub-grid-scale stress model for unresolved fluid velocity fluctuations has been used in this reference simulation. Analysis of the resolved and sub-grid-scale velocity fluctuations indicate that the former are roughly three times larger than the latter downstream of the injection point. Thus, we conclude that sub-grid scale (fluid) velocity do not play an essential role for this reference simulation.

Table 3: Physical parameters of the Salzman JICF test case.

Parameter	*Value*
Jet Diameter (d_{jet})	4.62 [mm]
Particle density (ρ_p)	2638 [kg/m³]
Particle diameter (d_p)	15 [µm]
Gas density (ρ_f)	1.1 [kg/m³]
Gas dynamic viscosity (η_f)	$1.91 \cdot 10^{-5}$ [Pa·s]
Jet mass loading ($m_p/m_{f,jet}$)	20.8
Rel. particle injection velocity ($\mathbf{v}_y/\mathbf{u}_y)_{jet}$	1
Rel. jet velocity ($\mathbf{u}_y/\ \mathbf{u}_{inlet,x}$)	1.57
Crossflow velocity ($\mathbf{u}_{inlet,x}$)	16.8 [m/s]

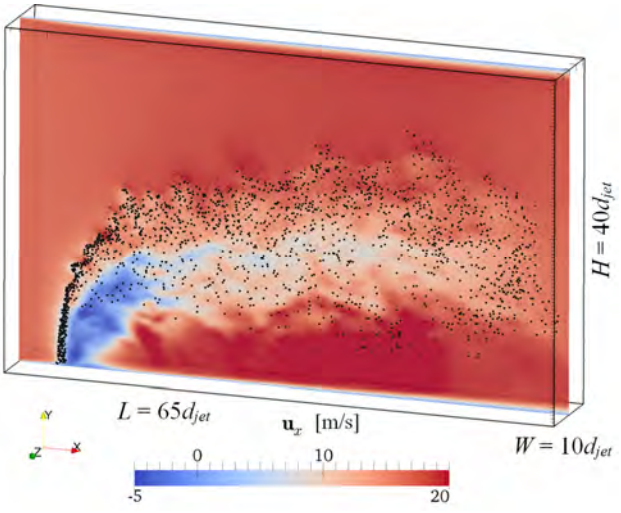

Figure 9: Instantaneous *x*-component of the fluid velocity (contours are shown in a central cut plane), and particle distribution (black dots) in the Salzman JICF configuration.

Particle Penetration

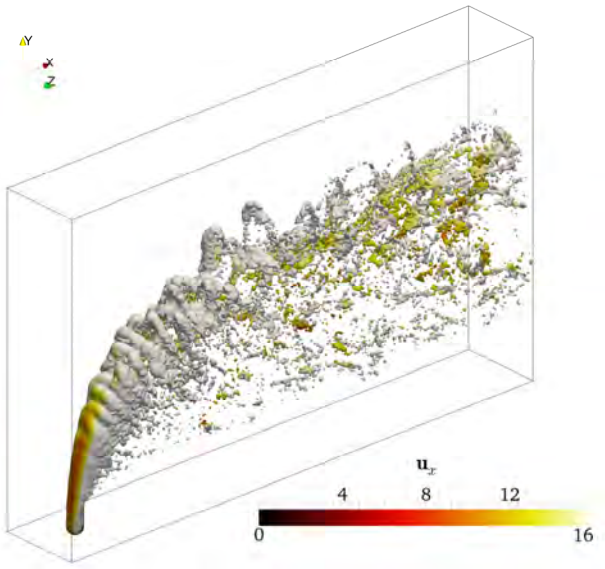

Figure 10: Instantaneous fluid velocity distribution (in [m/s]) on an iso-surface of the particle volume fraction ($\phi_p = 3.5.10^{-4}$) for the Salzman JICF configuration (reference simulation with *CG* = 5, 510 x 314 x 79 grid cells).

Figure 10 and Figure 11 summarize the results for the particle dispersion pattern, as well as the effect of the fluid grid resolution and the coarse graining ratio (*CG*) on our predictions. The reference simulation (see Figure 10) highlights that a complex three-dimensional flow structure develops downstream of the particle injection point. The particle concentration is highest in a U-shaped region that becomes more and more diffuse in the streamwise (i.e., *x*-) direction. Interestingly, the reference simulation predicts a region of comparably low fluid velocity inside this U-shaped region.

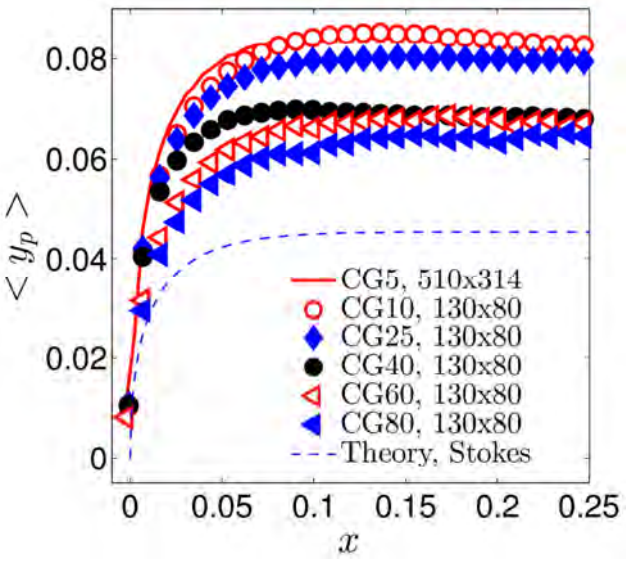

Figure 11: Mean vertical particle position as a function of the streamwise (i.e., *x*-) position to quantify the penetration of the particle jet into the cross flow (dimensions in [m]; all simulations used the smoothing algorithm).

By computing the centre of mass position of the particle population as a function of the streamwise position, we quantify the effect of various numerical settings on the predicted gas-particle flow (see Figure 11). As can be seen, all results with *CG* = 25 (or smaller), show

reasonable agreement with the reference results. For these simulations the smoothing procedure as well as the details of the coupling algorithm had a comparably small effect on the particles' mean trajectory. Results with CG = 40 (or larger) give less satisfactory results, and not employing the smoothing algorithm for CG = 40 (or larger) gave the worst predictions (data not shown). Also, we find that increasing the smoothing length does not improve the predictions for CG = 40 or larger (data not shown). The physical reason for this limitation is the inability to resolve particle and fluid velocity fluctuations when employing extremely large CG ratios. This indicates that (for large parcel sizes) the introduction of a smoothing step can improve the quality of predictions, however, the predictive capabilities are limited by clustering effects not accounted for by the models used by us.

We would like to note that smoothing introduces only an incremental computational cost. Specifically, our simulations indicate that smoothing introduces an additional computational overhead of ca. 18%, but substantially improves the predictions as discussed above.

In summary, we observe that for excessively large CG ratios the jet penetration is underestimated, i.e., a too small disturbance of the flow is predicted. In Figure 11 (blue dashed line) we have also included the theoretical trajectory of an injected particle under the assumption of (i) an undisturbed background flow, as well as (ii) the validity of Stokes' drag relation. As can be seen, all our simulations predict a penetration of the particle jet into the cross flow that is ca. 1.5 to 2 times larger than this theoretical result.

CONCLUSION

We have presented details of numerical schemes implemented in the open-source package CFDEMcoupling, which are relevant for the robust simulation of gas-particle flows involving broad particle size distributions. We made an attempt to estimate relevant time scales that limit the time step in these simulations. We then critically analysed the effect of an implicit time marching procedure for various test cases. Based on our results for a freely sedimenting gas-particle suspension, we conclude that the proposed implicit integration procedure is not strictly conservative, and gives an error between 5% and 15 % depending on the number of particles per computational cell. An improved coupling algorithm that splits the force into an explicit and implicit contribution can alleviate this problem. Clearly, an implicit procedure is essential for a robust simulation in case very small particles need to be modelled. Typically, a time step ca. 15 times larger than that required for an explicit procedure can be used in case an implicit, or a hybrid implicit/explicit procedure is employed.

From our results of the jet-in-cross flow configuration, we conclude that:

1. The implicit integration procedure leads to less particle penetration into the cross flow compared to an explicit procedure. An improved algorithm that splits the coupling force into an implicit and explicit part improves the predictions.
2. Smoothing is key for the correct prediction of particle penetration into the cross flow for the 3D JICF configuration in case large CG ratios must be used. Thus, smoothing becomes essential for CG > 40, which is typically required to simulate industrial-scale problems.
3. A coarse graining ratio of 25 still gives accurate results for the 3D gas-particle JICF configuration with 15 µm primary particles.

Future work might focus on the experimental validation of our JICF simulations to confirm our conclusions.

ACKNOWLEDGEMENTS

The help of Dipl.-Ing. BSc. Stefan Darmann (TU Graz) in setting up the 2D JICF configuration is greatly acknowledged. We acknowledge the support of NAWI Graz by providing access to dcluster.tugraz.at.

REFERENCES

BEETSTRA, R., VAN DER HOEF, M.A., and KUIPERS, J.A.M., (2010), "Drag Force of Intermediate Reynolds Number Flow Past Mono- and Bidisperse Arrays of Spheres", *AIChE J.*, **53,** 489-501.

CAPECELATRO, J., and DESJARDINS, O., (2013), "An Euler–Lagrange Strategy for Simulating Particle-Laden Flows", *J. Comput. Phys.*, **238,** 1-31.

GOLDMISCHDT, M.J.V., LINK, J.M., MELLEMA, S., and KUIPERS, J.A.M., (2003), "Digital image analysis measurements of bed expansion and segregation dynamics in dense gas-fluidised beds", *Powder Technol.*, **138,** 135-159.

HAN, K.S., and CHUNG, M.K., (1992), "Numerical Simulation of Two-Phase Gas-Particle Jet in a Crossflow", *Aerosol Sci. Technol.*, **16**, 126-139.

KLOSS, C., GONIVA, C., HAGER, A., AMBERGER, S., and PIRKER, S., (2012), "Models, Algorithms and Validation for OpenSource DEM and CFD-DEM", *Progr. Comput. Fluid Dyn.*, **12,** 140-152.

LAIN, S. and SOMMERFELD, M., (2008), "Euler/Lagrange computations of pneumatic conveying in a horizontal channel with different wall roughness", *Powder Technol.*, **184,** 76-88.

LI, G., and LIN, J., (2010), "Characteristics of Particle Dispersion in a Jet in Cross-Flow Based on Computational Fluid Dynamics", in: *Asia-Pacific Power and Energy Engineering Conference.*

N.N., (2010), "OpenFOAM 2.2.1 User Manual", www.opencfd.co.uk .

PATANKAR, N.A., and JOSEPH, D.D., (2001), "Modeling and numerical simulation of particulate flows by the Eulerian-Lagrangian approach", *Int. J. Multiphase Flow*, **27**, 1659-1684.

PIRKER, S., KAHRIMANOVIC, D., and GONIVA, C., (2011), "Improving the applicability of discrete phase simulations by smoothening their exchange fields", *Appl. Math. Mod.*, **35,** 2479-2488.

RADL, S., GIRARDI, M. and SUNDARESAN, S., (2012), "Effective Drag Law for Parcel-Based

Approaches - What Can We Learn from CFD-DEM?", in: *ECCOMAS 2012*.

SCHELLANDER, D., SCHNEIDERBAUER, S., and PIRKER, S., (2013), "Numerical study of dilute and dense poly-dispersed gas-solid two-phase flows using an Eulerian and Lagrangian hybrid model", *Chem. Eng. Sci.*, **95,** 107-118.

SNIDER, D.M., (2001), "An incompressible three-dimensional multiphase particle-in-cell model for dense particle flows", *J. Comput. Phys.*, **170,** 523-549.

SOMMERFELD, M., and LAIN, S., (2012), "Analysis of dilute phase pneumatic conveying through pipe systems by the Euler/Lagrange approach", in: *Ninth International Conference on CFD in the Minerals and Process Industries*.

TENNETI, S., GARG, R., and SUBRAMANIAM, S., (2011), "Drag law for monodisperse gas – solid systems using particle-resolved direct numerical simulation of flow past fixed assemblies of spheres", *J. Multiphase Flow*, **37,** 1072-1092.

ZHOU, Z.Y., KUANG, S.B., CHU, K.W., and YU, A.B., (2010), "Discrete particle simulation of particle–fluid flow: model formulations and their applicability", *J. Fluid Mech.*, **661,** 482-510.

10th International Conference on CFD in Oil & Gas, Metallurgical and Process Industries
SINTEF, Trondheim, Norway *CFD 2014*
17-19 June 2014

The parametric sensitivity of fluidized bed reactor simulations carried out in different flow regimes

Schalk CLOETE*, Jan H. CLOETE, Stein Tore JOHANSEN & Shahriar AMINI

[1] SINTEF Materials and Chemistry, 7465 Trondheim, NORWAY

* E-mail: schalk.cloete@sintef.no

ABSTRACT

Fluidized bed simulations carried out within the Kinetic Theory of Granular Flows framework utilize a number of model coefficients which are strongly case dependent and difficult to determine accurately. The most important of these are the specularity coefficient (the degree of friction at the wall) and the particle-particle restitution coefficient (inelasticity of inter-particle collisions). This paper demonstrated that modification of these coefficients can trigger a regime change in very narrow and fast risers, thereby introducing a great amount of uncertainty. For situations sufficiently far from the dilute transport regime, however, sudden regime changes were not observed and the influence of these unknown parameters is more systematic. It was shown that in the case of wide bubbling beds, the effect of these unknown model coefficients can become negligible, making these reactors attractive for simulation studies. Faster and narrower geometries, on the other hand, exhibited greater sensitivity to changes in the specularity coefficient and particle-particle restitution coefficient, thereby introducing ever-increasing quantities of uncertainty stemming from these unknown model coefficients.

Keywords: Fluidized bed reactors, Two Fluid Model, Kinetic Theory of Granular Flows, Specularity coefficient, Restitution coefficient.

NOMENCLATURE

α	Volume fraction
ϕ	Damping of fluctuating motions [kg/(m.s^2)]
γ_{Θ_s}	Collisional dissipation rate [kg/(m.s^2)]
Θ	Granular temperature [m^2/s^2]
ρ	Density [kg/m^3]
$\bar{\bar{\tau}}$	Stress tensor [kg/(m.s^2)]
$\vec{\upsilon}$	Velocity vector [m/s]
∇	Gradient or Del operator [1/m]
C	Species concentration [mol/m^3]
d	Diameter [m]
$\vec{g}$	Gravity vector [m/s^2]
$\bar{\bar{I}}$	Identity tensor
K	Momentum exchange coefficient [kg/(m^3.s)]
k	Reaction rate constant
k_{Θ_s}	Granular temperature conductivity [kg/(m.s)]
p	Pressure [Pa]
Q	Volumetric flow rate [m^3/s]
R	Universal gas constant [kcal/(K.mol)]
R^H	Heterogeneous reaction rate [mol/(m^{3}s)]
S	Source term
T	Temperature [K]
t	Time [s]
V	Volume [m^3]
w	Solids weight [kg]
x	Mass fraction
Y	Species mass fraction

Sub/superscripts

$\vec{\upsilon}$	Momentum
g	Gas
i	Species index
sg	Inter-phase
s	Solids

INTRODUCTION

Fluidized bed reactors find application in a wide range of process industries, primarily due to their excellent gas-solid mass transfer and mixing characteristics. Despite these attractive advantages, however, these reactors are difficult to design and scale up due to the complex hydrodynamics of fluidization. Almost all types of fluidization are characterized by the formation of transient clusters of particles which can dominate transport phenomena inside the reactor. The behaviour of these clusters depends on a wide range of parameters and must be understood to ensure effective reactor design and scale-up.

With the continued exponential increase in computational power and availability, fundamental flow

modelling has emerged as a promising method for improving the understanding of the complex behaviour exhibited by fluidized bed reactors. The foremost of these modelling frameworks, the Two Fluid Model (TFM) closed by the Kinetic Theory of Granular Flows (KTGF) (Jenkins and Savage 1983, Lun, Savage et al. 1984, Gidaspow, Bezburuah et al. 1992, Syamlal, Rogers et al. 1993), has progressed to a high level of maturity over the past three decades of development and can already offer reliable predictions of fluidized bed behaviour (Taghipour, Ellis et al. 2005, Ellis, Xu et al. 2011, Cloete, Zaabout et al. 2014). It therefore holds great potential to support the design and accelerate the scale-up of fluidized bed reactor technology.

The primary challenge facing the TFM is the fine grids required to accurately resolve all of the small scale particle clusters. These fine grids make simulations very computationally expensive and often restrict the TFM to small scale 2D simulations. Alternative modelling approaches such as the Dense Discrete Phase Model (Popoff and Braun 2007) and the filtered Two Fluid Model (Igci, Andrews et al. 2008) are currently under development to also allow for the simulation of cases with fine powders and fast kinetics, but the standard TFM is likely to form the foundation of fluidized bed reactor modelling for many years into the future.

Just like the grid dependence behaviour of the TFM depends greatly on the flow conditions simulated, practical experience has shown other factors such as the wall interactions to also depend strongly on the flow conditions. This is an important observation because fluidized bed reactors can be designed to operate in a wide range of different flow regimes depending on the characteristics of the solid material and the desired reaction. For example, the classic work of Bi and Grace (Bi and Grace 1995) distinguishes between batch operation (typical bubbling or turbulent fluidization) and vertical transport (typical for the riser of a circulating fluidized bed), also identifying different flow regimes within each of these two categories.

TFM simulations of the carbonator in a potassium looping process for post combustion CO_2 capture (more information about this process can be found in (Samanta, Zhao et al. 2011)) will be employed to illustrate one flow regime where simulations are highly sensitive to poorly understood model coefficients (the wall friction and particle restitution coefficient). This will henceforth be termed the "example study". Subsequently, a more generic study of the impact of these two model coefficients under different flow conditions will be made. This will be termed the "generic study".

MODEL DESCRIPTION

The standard TFM equation set is employed with different drag closure laws for the example study (potassium looping) and the generic study (broad study across different flow regimes).

Conservation equations

In all cases, the fundamental conservation equations for mass, momentum and species were solved. Mass was conserved as follows:

$$\frac{\partial}{\partial t}\left(\alpha_g \rho_g\right)+\nabla\cdot\left(\alpha_g \rho_g \vec{v}_g\right)=\alpha_g S_g \quad (1)$$

$$\frac{\partial}{\partial t}\left(\alpha_s \rho_s\right)+\nabla\cdot\left(\alpha_s \rho_s \vec{v}_s\right)=0 \quad (2)$$

The source term for the gas phase equation (right hand term in (**1**) is included to account for mass transfer due to the heterogeneous reaction. Mass changes in the solids phase are neglected because these changes would be insignificant relative to the total mass of the solids.

Momentum conservation for the gas phase is written as

$$\frac{\partial}{\partial t}\left(\alpha_g \rho_g \vec{v}_g\right)+\nabla\cdot\left(\alpha_g \rho_g \vec{v}_g \vec{v}_g\right)=-\alpha_g \nabla p+\nabla\cdot\bar{\bar{\tau}}_g+\alpha_g \rho_g \vec{g}+K_{sg}\left(\vec{v}_s-\vec{v}_g\right)+S_g^{\vec{v}} \quad (3)$$

and for the solids as

$$\frac{\partial}{\partial t}\left(\alpha_s \rho_s \vec{v}_s\right)+\nabla\cdot\left(\alpha_s \rho_s \vec{v}_s \vec{v}_s\right)=-\alpha_s \nabla p-\nabla p_s+\nabla\cdot\bar{\bar{\tau}}_s+\alpha_s \rho_s \vec{g}+K_{gs}\left(\vec{v}_g-\vec{v}_s\right) \quad (4)$$

Species are also conserved for the gas phase.

$$\frac{\partial}{\partial t}\left(\alpha_g \rho_g Y_{g,i}\right)+\nabla\cdot\left(\alpha_g \rho_g \vec{v}_g Y_{g,i}\right)=\nabla\cdot\alpha_g \vec{J}_{g,i}+\alpha_g S_{g,i} \quad (5)$$

No energy conservation was considered under the assumption of isothermal reactor operation.

Closure relations

The conservation equations need to be closed by additional modelling.

Interphase momentum exchange

The drag laws governing the interphase momentum exchange ($K_{gs}=K_{sg}$ in (**3**) and (**4**)) were different for the two studies considered. For the example study, the correlation from Wen and Yu (Wen and Yu 1966) was used, while the more generic Syamlal and O'Brien drag law (Syamlal, Rogers et al. 1993) was implemented for the generic study. These are fairly standard selections in the literature.

Solids stresses

Solids stresses were modelled using the well documented kinetic theory of granular flows (KTGF) (Jenkins and Savage 1983, Lun, Savage et al. 1984, Gidaspow, Bezburuah et al. 1992, Syamlal, Rogers et al. 1993). In the KTGF analogy, the random motion of granular particles is put in analogy to the random motion of gas molecules where the kinetic theory of gasses is applied. This analogy allows the determination of fluid properties for the particulate phase by accounting for the inelasticity of the particles. The granular temperature is a measure of the energy contained in random particle motion and is conserved as follows:

$$\frac{3}{2}\left[\frac{\partial}{\partial t}\left(\alpha_s \rho_s \Theta_s\right)+\nabla\cdot\left(\alpha_s \rho_s \vec{v}_s \Theta_s\right)\right]=\left(-p_s \bar{\bar{I}}+\bar{\bar{\tau}}_s\right):\nabla\vec{v}_s+\nabla\cdot\left(k_{\Theta_s}\nabla\Theta_s\right)-\gamma_{\Theta_s}+\phi_{gs} \quad (6)$$

On the right hand side of the equation, the terms represent the generation of granular temperature via the solids stress tensor, granular temperature conductivity (Gidaspow, Bezburuah et al. 1992), dissipation of energy due to inelastic collisions (Lun, Savage et al. 1984) and the energy exchange between the gas phase and the random motions of the particles (Gidaspow, Bezburuah et al. 1992).

The granular temperature is subsequently used to calculate values of the solids viscosity which is used in the solids stress tensor. Bulk viscosity (Lun, Savage et al. 1984) and the three components of shear viscosity,

collisional (Gidaspow, Bezburuah et al. 1992, Syamlal, Rogers et al. 1993), kinetic (Gidaspow, Bezburuah et al. 1992) and frictional (Schaeffer 1987), were considered in the calculations.

Normal stresses modelled according to the solids pressure are calculated according to (Lun, Savage et al. 1984). The radial distribution function which is a measure of the average distance between particles is a central concept in the KTGF and is calculated according to (Ogawa, Unemura et al. 1980).

Reaction kinetics description

Due to the novelty of the potassium looping CO_2 capture process simulated in the example study, a sufficiently generic description of reaction kinetics specifically formulated for implementation into numerical models is not yet available from a single source. Therefore, the approach used in this paper uses insights from different works studying the kinetics of the carbonation reaction:

$$CO_2 + H_2O + K_2CO_3 \rightarrow 2KHCO_3$$

A simple reaction kinetics description where the rate is dependent only on the CO_2 concentration and the volume fraction of solids was used by (Chalermsinsuwan, Piumsomboon et al. 2010).

$$R^H = k_1 \alpha_s C_{CO_2} \tag{7}$$

This formulation is easy to implement in the code, but the reaction rate constant (taken as $k_1 = 1.95\ \mathrm{s}^{-1}$ in this case) was derived from a parallel plate reactor (not the real fluidized bed application studied here) and it was not expressed as a function of temperature.

Another research group studied the kinetics of the carbonation reaction by collecting CO_2 breakthrough data from a packed reactor and fit a deactivation model to this data (Park, Sung et al. 2006). The deactivation model produced a good fit and described how the material in their study was deactivated over time due to the diffusion resistance from a dense product layer forming on its outside. This deactivation process occurred on a rather long timescale (~1h in the experiments conducted) and will therefore not be significant in real applications where the particle residence time is in the order of seconds or minutes. The deactivation model used was also derived in terms of variables like the gas-solid contact time and the feed rate to the packed bed which is not suitable for implementation into a CFD model.

Therefore, it was assumed that the deactivation caused by the product layer formation is not significant and the rate is exclusively controlled by the kinetics. The aforementioned work (Park, Sung et al. 2006) determined a reaction rate constant as a function of time, but it was expressed in rather unconventional units (m^6/(kg.kmol.min)) as follows:

$$k_b = 1.191 \times 10^5 \exp\left(\frac{-7.544}{RT}\right) \tag{8}$$

Here, R is the universal gas constant expressed in kcal/(K.mol) and T is the temperature in Kelvin. In order to be useful for numerical modelling, however, this reaction rate constant has to be converted to a more standard form with the units of s^{-1}. This was done as follows:

In the experimental work (Park, Sung et al. 2006), this reaction rate constant was used in a 1D species conservation equation through the packed bed:

$$-Q_g \frac{dC_{CO_2}}{dw} = k_b C_{H_2O} C_{CO_2} \tag{9}$$

Here, Q_g is the volumetric flow rate of the feed gas and w is the weight of solids in the bed. In order to be useful for implementation into the CFD model, however, this equation has to be written in a dC_{CO_2}/dt form. This can be done through manipulation using the chain rule:

$$-Q_g \frac{dC_{CO_2}}{dw} = -Q_g \frac{dC_{CO_2}}{dt}\frac{dt}{dw} = -Q_g \frac{dC_{CO_2}}{dt}\frac{dt}{dV}\frac{dV}{dw} = -Q_g \frac{dC_{CO_2}}{dt}\frac{\alpha_g}{Q_g}\frac{1}{\alpha_s \rho_s} \tag{10}$$

(9) can now be rewritten in the desired form:

$$-\frac{dC_{CO_2}}{dt} = \left(\frac{k_b C_{H_2O} \rho_s}{\alpha_g}\right) \alpha_s C_{CO_2} \tag{11}$$

Here, the bracketed term represents the rate constant in the correct form with the units of s^{-1} as written in (7). (7) therefore implicitly assumes that the reaction rate is independent of the water vapour concentration, but this was proven not to be the case in (Park, Sung et al. 2006) where a first order dependency was observed. This work will therefore use a rate equation dependent on both the water vapour and CO_2 molar concentrations.

In addition, another work (Sharonov, Okunev et al. 2004) also observed an inverse proportionality between the reaction rate and the particle diameter. This is a well-known relationship implying that the reaction occurs on the surface of each particle and that smaller particles would present a larger combined surface area per unit volume than larger particles according the ratio between particle surface area and volume $(6/d_s)$.

The final rate equation will therefore be written in the form:

$$-\frac{dC_{CO_2}}{dt} = \frac{6}{d_p} \alpha_s k C_{H_2O} C_{CO_2} \tag{12}$$

In order to arrive at the correct expression for the reaction rate constant, the particle density and particle surface area per volume ratio have to be taken into account:

$$k = \frac{k_b \rho_s d_p}{6 \alpha_g} \tag{13}$$

Taking into account that the particle density was 2394 kg/m^3, the particle diameter was 401.67 µm and the bed void fraction was 0.475 in the experiments (Park, Sung et al. 2006), (13) can be rewritten as follows where the reaction rate constant has the units of (m^3/kmol).(m/s):

$$k = 669.75 \exp\left(\frac{-7.544}{RT}\right) \tag{14}$$

For the generic study, the simple hypothetical reaction rate description given below was used in order to convert species A into species B with a 1:1 stoichiometric ratio. Species A and B had the same material properties in order to ensure that the reaction would not have any influence on the hydrodynamics.

$$-\frac{dC_A}{dt} = 0.25\alpha_s x_A \qquad (15)$$

Geometry and meshing

The riser in the example study was modelled according to the specifications provided in (Yi, Jo et al. 2007). The total length of the riser was 6 m with an inner diameter of 2.5 cm. The lower 0.45 m of the riser was a mixing zone with a wider inner diameter of 3.5 cm which narrowed to 2.5 cm at a height of 0.6 m. 2.5 mm cubical cells were used in the mesh, resulting in a cell size roughly 25 times the particle size. A limited number of computationally expensive simulations were also performed on a mesh with 1.25 mm cells which resulted in 1.7 million cells in the domain.

Simulations for the generic study were carried out on a simple 2D planar geometry meshed with 2.5 mm cells which were also about 13 times the particle size. Five different geometries were studied both under batch (Table 1) and vertical transport (Table 2) operation where the total volume of the domain, the total gas flow through the domain and the total amount of solids within the domain was kept constant between runs as the aspect ratio was varied over a large range.

Table 1: Dimensions and fluidization velocity of the batch operation cases in the generic study.

Width (m)	Height (m)	Fluidization velocity (m/s)
2.4	0.3	0.1
1.2	0.6	0.2
0.6	1.2	0.4
0.3	2.4	0.8
0.15	4.8	1.6

Table 2: Dimensions and fluidization velocity of the vertical transport cases in the generic study.

Width (m)	Height (m)	Fluidization velocity (m/s)
0.600	1.200	1.600
0.424	1.697	2.263
0.300	2.400	3.200
0.212	3.394	4.525
0.150	4.800	6.400

Boundary conditions

The lower face of the geometry in the example study was specified as a velocity inlet, injecting gas at a velocity of 1.02 m/s and solids at a velocity of 0.0209 m/s and a volume fraction of 0.2. The gas stream consisted of 9.72% CO_2, 19% H_2O and the balance N_2 (on a molar basis). These specifications resulted in a gas superficial velocity of 2 m/s in the narrower 2.5 cm top section of the riser and a solids flux of 15 kg/m^{2}s. These were the conditions reported for the 11-17 hour operational period in (Yi, Jo et al. 2007).

For the generic study, the lower face of the geometry was also specified as a velocity inlet, injecting gas at the velocity specified in Table 1. The bed was initialized in such a way that the average solids volume fraction over the entire bed was 0.1. For the vertical transport cases in the generic study (Table 2), solids were also continuously injected over the velocity inlet at a volume fraction of 0.1 and a velocity which was 10% of the gas injection velocity.

The outlets of both geometries were specified as pressure outlets at atmospheric pressure. No-slip wall boundary conditions were specified for the gas phase, while partial slip boundary conditions (Johnson and Jackson 1987) were specified for the solids phase. It must be noted that this model has clear limitations and that improved methods are available (Li and Benyahia 2012, Schneiderbauer, Schellander et al. 2012). However, the Johnson and Jackson model remains the most popular method for accounting for partial slip of solids at walls in fluidized bed simulation studies and therefore merits further investigation. The specularity coefficient (ς in (16) and (17)) and the particle-wall restitution coefficient (e_{sw} in (17)) were varied between the different simulations carried out in this work.

$$\vec{\tau}_s = -\frac{\pi}{6}\sqrt{3}\varsigma\frac{\alpha_s}{\alpha_{s,\max}}\rho_s g_{0,ss}\sqrt{\Theta_s}\vec{U}_{s,\|} \qquad (16)$$

$$q_s = \frac{\pi}{6}\sqrt{3}\varsigma\frac{\alpha_s}{\alpha_{s,\max}}\rho_s g_{0,ss}\sqrt{\Theta_s}\vec{U}_{s,\|}\cdot\vec{U}_{s,\|} - \frac{\pi}{4}\sqrt{3}\frac{\alpha_s}{\alpha_{s,\max}}\left(1-e_{sw}^2\right)\rho_s g_{0,ss}\Theta_s^{3/2} \qquad (17)$$

For the example study, the temperature was fixed as a function of the reactor height in order to reproduce the temperature measurements taken in the experiments (Yi, Jo et al. 2007). The temperature (T) was fixed as a function of the height (h) through the following fourth-order polynomial:

$$T = -0.2073h^4 + 4.4354h^3 - 26.619h^2 + 45.941h + 353.15$$

No energy conservation was included in the bubbling fluidized bed simulations.

Material properties

Material properties for the gas and solids phases are given in Table 3 and Table 4. For the example study, the solids density was calculated from the given bulk density of 1100 kg/m^3 (Yi, Jo et al. 2007) assuming a solids volume fraction of 0.6 under packing.

Table 3: Material properties for the example study.

Gas density:	Ideal gas law
CO_2 viscosity:	4.68E-8T+1.00E-6 kg/(m.s)
H_2O viscosity:	3.42E-8T-3.75E-7 kg/(m.s)
N_2 viscosity:	4.32E-8T+4.94E-6 kg/(m.s)
Solids density:	1833 kg/m^3
Particle size:	98 µm

Table 4: Material properties for the generic study.

Gas density:	0.3 kg/m^3 (species A & B)
Gas viscosity:	4E-5 kg/(m.s) (species A & B)
Solids density:	2500 kg/m^3
Particle size:	200 µm
Minimum fluidization velocity:	0.0184 m/s

RESULTS AND DISCUSSION

This section will be divided in two parts discussing results from the example and generic studies.

Example study

The sensitivity of this narrow riser simulation to unknown model coefficients; the specularity coefficient, the particle-wall restitution coefficient and the particle-particle restitution coefficient, was evaluated by means of a central composite design (Montgomery 2001). This is a form of experimental design (also applicable to simulation experiments) where the response of specific dependent variables to changes in various independent

variables can be easily assessed, accurately quantified and visualized. The three aforementioned model coefficients were taken as the independent variables and simulation behaviour was quantified by means of two dependent variables: the overall pressure drop, which is equivalent to the holdup, and the overall degree of CO_2 absorption.

The central composite design consisted of 16 simulation experiments, filling the three dimensional parameter space with the reactor performance resulting from each specific set of model coefficients. Results will be displayed in two ways: an analysis of variance (ANOVA) and response surfaces of dependent variables to changes in various independent variables. The ANOVA will be used to quantify the significance of the independent variables (i.e. identify the model coefficients which had a statistically significant influence on the simulation behaviour).

The significance of factors will be defined by the p-value which is an indication of the probability of the observed effect to result purely by random chance. If this value becomes small $(p < 0.05)$, the effect is said to be significant because the probability of it arising from pure chance is fairly small. A value of $p < 0.01$ is generally regarded as highly significant. The p-value is calculated from the F-test which weighs the amount of explained variance in the design against the amount of unexplained variance (experimental error, rounding error, averaging error, data not fitting the second order model etc.). This ratio can then be evaluated as a p-value to decide whether the variance is caused by a significant effect or is simply random.

Table 5: ANOVA table summarizing the response of the total pressure drop and the degree of CO_2 absorption to changes in the three unknown model coefficients under investigation: the specularity coefficient (S), the particle-particle restitution coefficient (PP) and the particle-wall restitution coefficient (PW). Significant factors are shown in bold, while highly significant factors are shown in bold italics. The factors are denoted by S (specularity coefficient), H (particle-wall restitution coefficient) and d (particle-particle restitution coefficient). Different effects are indicated by L (linear), Q (quadratic) and by (interaction).

Effect	Pressure drop		CO_2 absorption	
	SS (%)	p-value	SS (%)	p-value
S(L)	***36.12***	***0.0006***	***37.38***	***0.0032***
S(Q)	**5.16**	**0.0453**	3.02	0.2271
PP(L)	***32.29***	***0.0007***	***31.63***	***0.0048***
PP(Q)	4.54	0.0561	2.78	0.2442
PW(L)	4.20	0.0635	6.22	0.1016
PW(Q)	1.26	0.2605	1.71	0.3501
S(L) by PP(L)	***15.56***	***0.0047***	**10.74**	**0.0441**
S(L) by PW(L)	0.11	0.7222	0.00	0.9936
PP(L) by PW(L)	0.13	0.7009	0.02	0.9083
Error	4.88		10.00	
Total	100.00		100.00	

The relative variance explained by each factor will also be given as the percentage of the total sum of squares (SS). The total sum of squares is the sum of all the squared distances between the various data points and the mean. A larger total sum of squares implies that the data are scattered wide around the mean and there is a lot of variance in the design. This measure will give an indication of the importance of significant effects relative to each other. The ANOVA results for the riser simulation are given in Table 5.

It is clear from the data in Table 5 that changes in the specularity coefficient and the particle-particle restitution coefficient had the greatest impact on the results, while the effect of particle-wall restitution coefficient was not statistically significant. This is in line with results from an earlier study on the parametric sensitivity of riser simulations (Cloete, Amini et al. 2011).

However, the most important result from this central composite design is the magnitude of the variations in overall pressure drop and CO_2 absorption caused by changes in the unknown model coefficients. This large variation is shown in Figure 1.

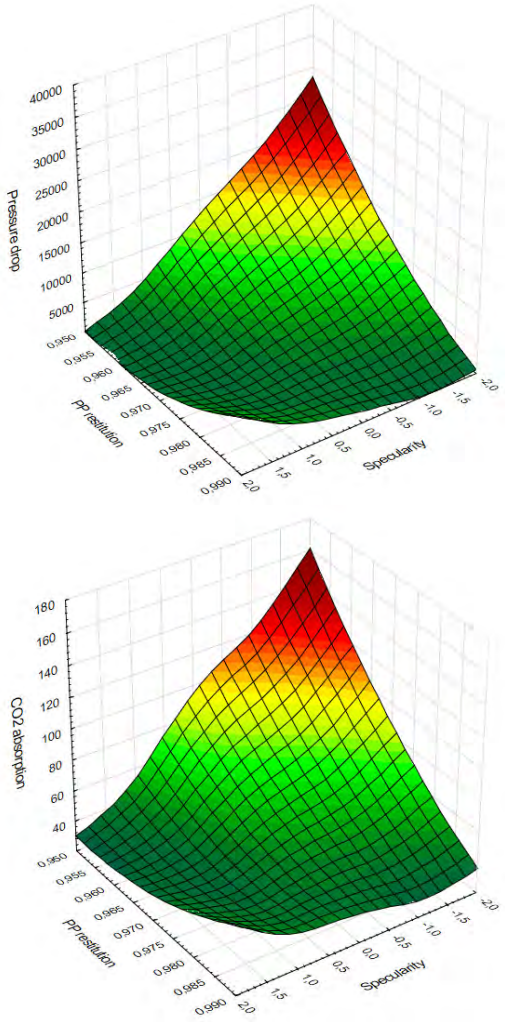

Figure 1: Response of the total pressure drop (Pa) and the CO2 absorption (%) in response to changes in the specularity coefficient and the particle-particle restitution coefficient. Note that the specularity coefficient is given in coded variables (c) where the actual specularity coefficient is given by: $\varsigma = 0.002 \times 2^c$.

Firstly, it must be pointed out that the maximum values in Figure 1 (at the lowest values of the specularity and particle-particle restitution coefficients) can be

misleading because it is an extrapolation of a very sharp gradient. For example, the CO_2 absorption cannot be more than 100%, but the extrapolated value projects an absorption of 160% at the lowest specularity and particle-particle restitution coefficients observed in the simulation.

When looking at results from the simulations, a specularity coefficient of 0.001 (coded variable of -1) and a particle-particle restitution coefficient of 0.96 returned a pressure drop of 12.5 kPa and 89.2% CO_2 absorption, while a specularity coefficient of 0.004 (coded variable of 1) and a particle-particle restitution coefficient of 0.98 returned a pressure drop of 1.3 kPa and 34.7% CO_2 absorption. It is therefore clear that this relatively small variation in model coefficients caused almost an order of magnitude difference in the solids holdup in the riser.

The reason for this large influence is the non-linear influences that cluster formation has on riser performance. Cluster formation can be a self-reinforcing phenomenon since the presence of clusters creates the large velocity gradients necessary to separate free particles from streamlines so that they join into the bulk of the cluster (Cloete, Johansen et al. 2015). This non-linear nature of clustering causes the large difference in riser hydrodynamics shown in Figure 2.

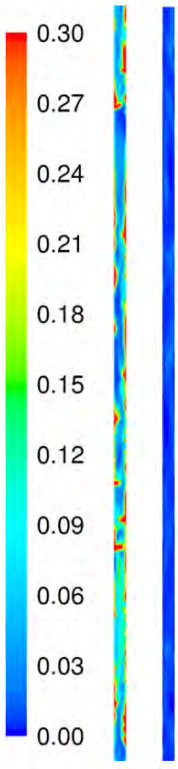

Figure 2: (On the left) Instantaneous volume fraction profiles in identical locations in the riser for the case with a specularity coefficient of 0.001 and a particle-particle restitution coefficient of 0.96 (left) and the case with a specularity coefficient of 0.004 and a particle-particle restitution coefficient of 0.96 (right).

Lower particle-particle restitution coefficients are beneficial to clustering due to the increased dissipation of granular temperature (and the associated reduction in granular pressure) in denser regions. Lower specularity coefficients are beneficial to clustering due to the free slip of denser clusters across smoother walls without being broken up by excessive shear forces. It appears evident that cluster formation is triggered over a very small range of these unknown model coefficients and causes large differences in riser behaviour after being triggered.

In order to assess the influence of the grid size on these phenomena, three computationally expensive simulations were completed on a mesh which was refined via hanging node adaption. Interestingly, the clustering was triggered at significantly lower specularity and particle-particle restitution coefficients than on the coarse mesh. This is counter-intuitive because finer meshes are normally more conducive to clustering. Finer meshes can resolve the high flow gradients around clusters, allowing free-flowing particles to deviate from the streamlines and join in the bulk of the cluster. It is expected that this trend is caused by the larger flow gradients resolved at the walls which can break up clusters more efficiently than on the coarser grid.

The three fine grid simulations were therefore carried out using a particle-particle restitution coefficient of 0.9 and specularity coefficients varying over a wide range of 0.01, 0.001 and 0.0001. The resulting match to pressure drop data from the experiment is given in Figure 3.

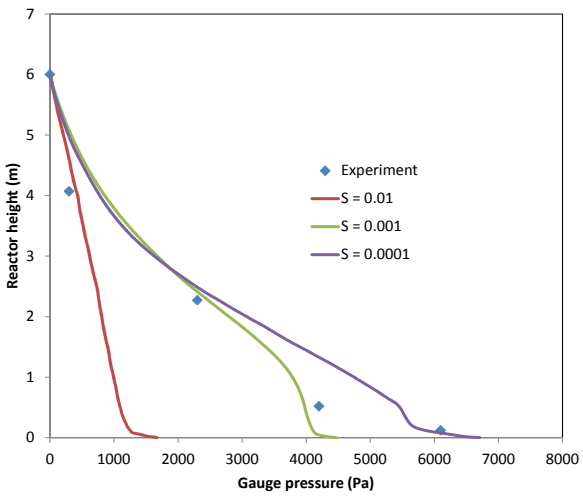

Figure 3: Model comparisons to axial pressure measurements (Yi, Jo et al. 2007) using different specularity coefficients (S) and a particle-particle restitution coefficient of 0.9.

It is shown that the simulations with a low specularity coefficient matched the experimental results well, but a higher specularity coefficient caused a situation where very little cluster formation was simulated and the solids holdup in the reactor was greatly under-predicted.

For the low specularity coefficient cases, a comparison was also made to species measurements at the outlet of the reactor. The simulation returned values around 70% CO2 capture at the outlet while the experimental measurements returned about 50% CO2 capture. This implies that the reaction rate constant in (14) is too high and will need refinement through dedicated experiments.

Generic study

The discussion will be split between the batch operation cases (Table 1) and the vertical transport cases (Table 2).

Batch operation cases

It can be expected that the large influence of unknown model coefficients on important model outputs observed in the previous section for the riser will be significantly reduced for dense fluidization. There are two main reasons for this observation.

Firstly, dense fluidized beds generally have larger diameters due to the fact that they have to employ smaller fluidization velocities. A larger diameter implies a smaller walls/volume ratio and therefore a smaller wall influence. In addition, the slower fluidization in

dense beds will result in smaller wall shear forces and therefore less of an influence on the overall reactor behaviour.

Secondly, dense fluidized beds, if solved on a sufficiently fine grid, will always display clustering or bubbling. The sudden transition from a situation of no clustering to a situation of significant clustering illustrated in Figure 2 can therefore not happen in dense fluidized beds.

As a result of these two factors, it is reasoned that dense fluidization can be simulated with a much larger degree of confidence than riser flow. This assumption was tested via the five cases outlined in Table 1.

Two main variables will be extracted to describe the macroscopic behaviour of the reactor: the pressure drop over the bottom 25% of each domain (an area filled with solids in all cases) and the reactor performance defined as the negative logarithm of the reactant mole fraction exiting the reactor unreacted.

The aim of using the $-\log(x_A)$ measure is to linearize the performance achieved by the reactor running a first order reaction. For example, if all other variables were kept constant, a reactor running a first order reaction would require twice the amount of residence time to achieve 99% conversion than to achieve 90% conversion. Hence, the reactor performance of a reactor achieving 99% conversion is $-\log(0.01)=2$ while the reactor performance of a reactor achieving 90% conversion is $-\log(0.1)=1$.

Firstly, the grid dependency behaviour of the dense fluidized bed cases must be evaluated. As shown in Figure 4 and Figure 5, the influence of different grid sizes on the reactor behaviour was fairly small, especially with regard to the pressure drop. For engineering applications, results derived from the 5 mm grid would be adequate, but the 2.5 mm grid was used in the remainder of this study.

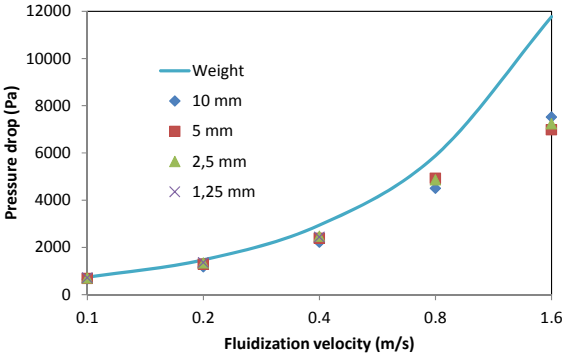

Figure 4: Pressure drop in the lower 25% of the reactor for the five different cases in Table 1 calculated using different cell sizes. The pressure drop related to the weight of the solids is also included for perspective.

The grid dependency effects displayed in Figure 4 and Figure 5 are small in comparison to that observed in the riser case where one refinement could cause a transition from fast fluidization to pneumatic transport, thereby completely changing the behaviour of the reactor.

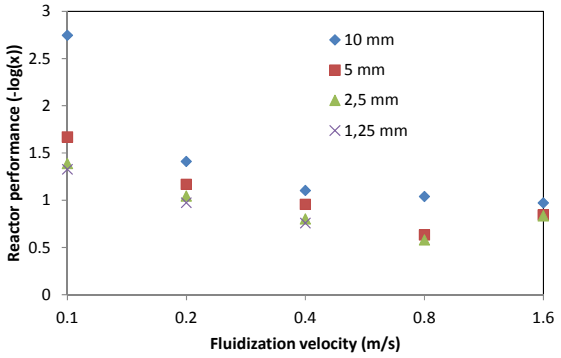

Figure 5: Reactor performance for the five different cases in Table 1 using different cell sizes.

Secondly, the effect of specularity coefficient was assessed with results presented in Figure 6 and Figure 7.

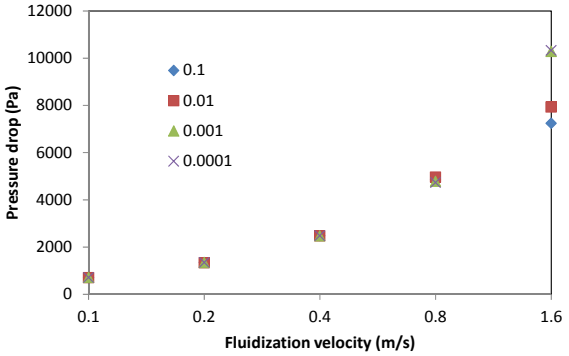

Figure 6: Pressure drop in the lower 25% of the reactor for the five different cases in Table 1 calculated using different specularity coefficients.

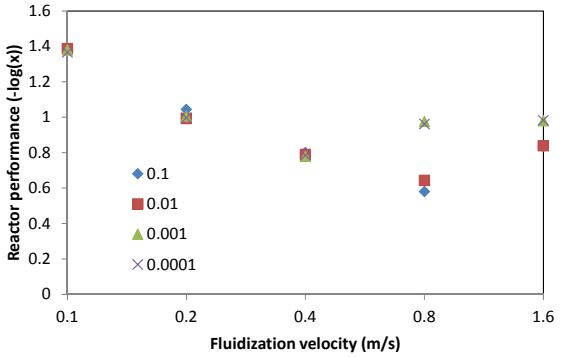

Figure 7: Reactor performance for the five different cases in Table 1 using different specularity coefficients.

It is clear that large changes in the specularity coefficient had no discernible impact on the model results for the cases with a fluidization velocity of 0.4 m/s and below. For the cases with a fluidization velocity of 0.8 m/s and 1.6 m/s, however, a significant difference in rector performance can be observed when transitioning from a specularity coefficient of 0.01 to a specularity coefficient of 0.001.

These geometries were only 30 and 15 cm in diameter respectively and therefore were subject to a significant degree of influence from the walls. As shown in Figure 8, this influence had a significant impact on the nature of the cluster formation in the fluidized bed.

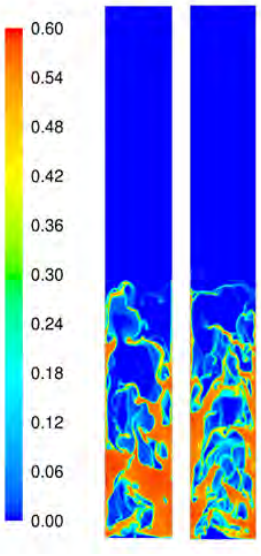

Figure 8: (On the left) Instantaneous volume fraction profiles for the case with a fluidization velocity of 0.8 m/s. The left-hand image is for a specularity coefficient of 0.01 and the right hand image is for a specularity coefficient of 0.001.

The hydrodynamic difference created by a change in the specularity coefficient from 0.01 to 0.001 is evident from Figure 8. When the specularity coefficient is lowered, falling solids near the wall create higher shear forces, leading to finer and more chaotic flow structures. It is clear from Figure 7 that these finer flow structures led to increased gas-solid contact and improved reactor performance (greater conversion).

Figure 6 shows, however, that this improved gas-solid contact was cancelled out to a certain degree in the 1.6 m/s fluidization velocity case by a more compacted bed in the lower reactor regions. This more compact bed reduced the quality of gas/solid contact in this region thereby countered the improved mass transfer effect of the finer flow structures to a certain degree. This is the reason why the specularity coefficient appears to have a larger influence on the reactor performance in the case with 0.8 m/s fluidization velocity than in the case with 1.6 m/s fluidization velocity.

Thirdly, the sensitivity of the dense fluidized bed simulations to changes in the particle-particle restitution coefficient was assessed. As shown in Figure 9 and Figure 10, the impact is again moderate at higher fluidization velocities and negligible at lower fluidization velocities.

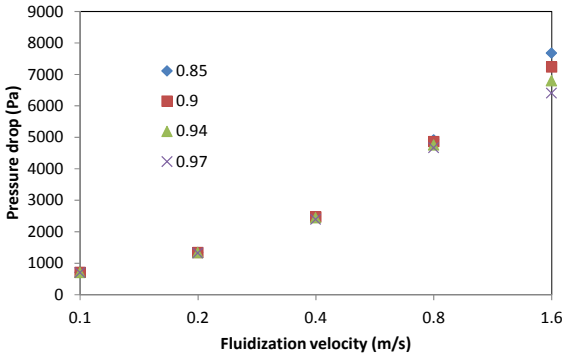

Figure 9: Pressure drop in the lower 25% of the reactor for the five different cases in Table 1 calculated using different particle-particle restitution coefficients.

For the reactor performance (Figure 10) all cases show a discernible impact of the highest particle-particle restitution coefficient (0.97). At this value, cluster formation was sufficiently suppressed to enhance gas-solid contact and thereby increase reactor performance. However, for particle-particle restitution coefficients around values that are usually employed (~0.9), the impact seems to be small.

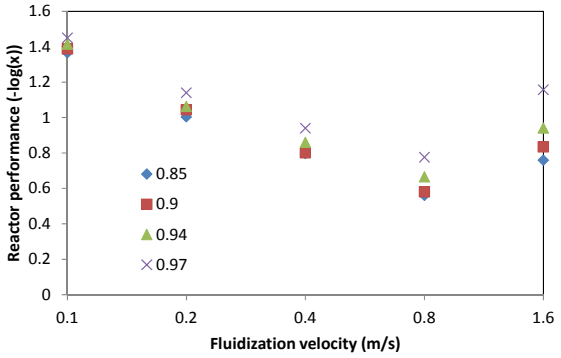

Figure 10: Reactor performance for the five different cases in Table 1 using different particle-particle restitution coefficients.

It is therefore clear that the sensitivity of dense fluidized bed simulations to changes in the two most important unknown model coefficients is much smaller than for the narrow riser case shown in Figure 1.

Vertical transport cases

For the vertical transport cases (Table 2), $-\log(x_A)$ was also used to evaluate the amount of conversion that takes place. However, the average volume fraction of the solids phase within the entire geometry was used as the hydrodynamic performance measure.

When varying the specularity coefficient it is observed (Figure 11) that there is a small effect on solid holdup at all velocities. The overall effect appeared to be too small to distinguish a clear trend on how the specularity coefficient influences the amount of solids in the riser. On the other hand, when evaluating the reactor performance (Figure 12), the effect of the specularity coefficient is highly significant at lower fluidization velocities, but almost disappears for the highest two velocities investigated.

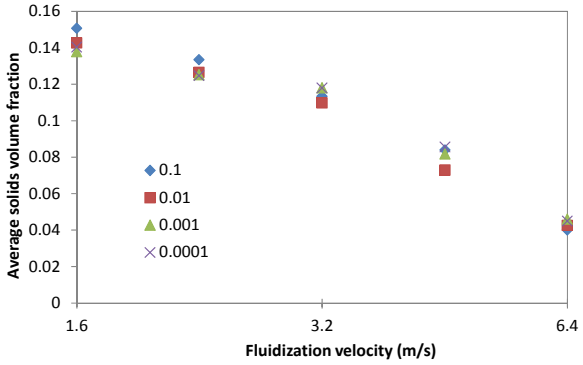

Figure 11: Average solid holdup for five different cases in Table 2 using different specularity coefficients.

Plots of the instantaneous solids volume fraction for different specularity coefficients aid in explaining these trends. Figure 13 shows such plots for the case with a fluidization velocity of 2.26 m/s, where the largest changes in reactor performance were observed. It is shown that at lower specularity coefficients there are streaks of falling solids near the walls. This is similar to what occurred in the dense fluidized bed and the resulting shear stresses cause finer flow structures to form. With an increase in the specularity coefficient, the amount of falling solids decrease and more distinct solids clusters form.

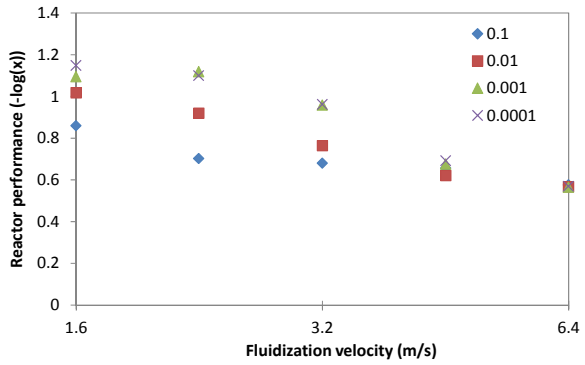

Figure 12: Reactor performance for five different cases in Table 2 using different specularity coefficients.

There are therefore two effects that influence the solid holdup as the specularity coefficient is decreased. Firstly, an increase in falling solids near the walls will tend to keep the solids in the riser column. On the other hand, the finer solid structures will be more easily transported from the column by the gas flow. The relatively small change in solid holdup with specularity coefficient observed in Figure 11 therefore shows that these two effects balance each other out over all fluidization velocities considered.

No sudden regime transitions as seen in the example study were observed. The complete lack of sensitivity of the faster cases to changes in the specularity coefficient is especially surprising considering the large influence of the wall in these cases. This result illustrates that the two effects described above effectively cancel each other out in narrow geometries and that a step change can only be expected when approaching the dilute transport regime where a sudden transition between smooth and clustered flow can be triggered.

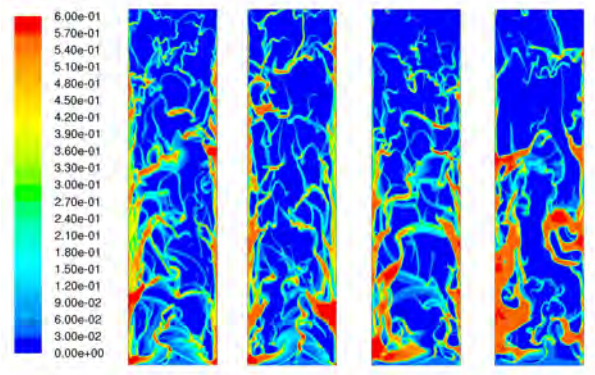

Figure 13: Instantaneous volume fraction profiles for the case with a fluidization velocity of 2.26 m/s. From left to right the specularity coefficients used are: 0.0001, 0,001, 0.01 and 0.1.

In the case of reactor performance, the finer flow structures at low specularity coefficients lead to better gas-solid contact, which explains the increase in conversion with a decrease in specularity coefficient observed in Figure 12.

Analyses of the solid holdup at different particle-particle restitution coefficients shows a clear trend of increased holdup with a decrease in the particle-particle restitution coefficient. This effect changes from moderate (13% increase) at low fluidization velocity to severe (113% increase) at high fluidization velocities. Clusters will form more readily at lower particle-particle restitution coefficients and there will be fewer fine solid structures that can easily be transported from the column.

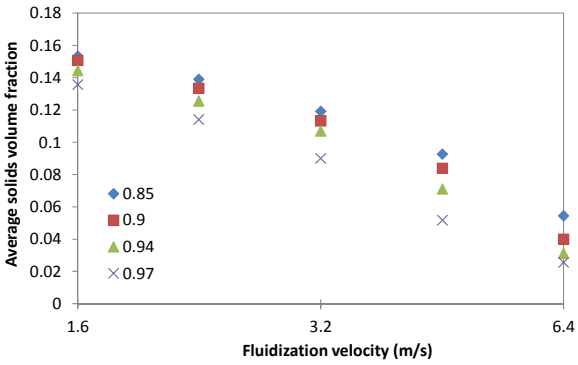

Figure 14: Average solid holdup for five different cases in Table 2 using different particle-particle restitution coefficients.

When assessing the effect on reactor performance (Figure 15), it is seen that, for lower fluidization velocities, the reactor performance increases at higher particle-particle restitution coefficients. This is due to better gas/solid contact in the finer flow structures that form. However, at faster fluidization velocities, the amount of solids present in the riser column decreases significantly at increased particle-particle restitution coefficients, limiting the conversion in the gas phase. Therefore, at fluidization velocities of 4.53 m/s and 6.4 m/s the effect on the reaction rate of increases in solid-gas contact and decreases in the amount of solids cancel each other almost exactly. This explains why changes in the particle-particle restitution coefficient have a negligible impact at faster fluidization velocities.

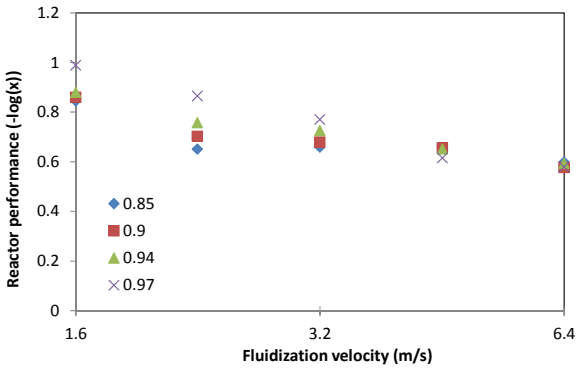

Figure 15: Reactor performance for five different cases in Table 2 using different particle-particle restitution coefficients.

CONCLUSION

The kinetic theory of granular flows commonly used in granular flow simulations involves a number of model coefficients which are difficult to determine accurately and therefore often used as tuning coefficients. These coefficients introduce a significant amount of uncertainty to fluidized bed simulations and can potentially have a large impact on model results.

This study investigated three such model coefficients: the specularity coefficient, the particle-wall restitution coefficient and the particle-particle restitution

coefficient. Of these coefficients, the specularity and particle-particle restitution coefficient were shown to have the greatest impact on model results.

The impact of these unknown model coefficients on simulation results depends strongly on the flow regime under which the simulations were carried out. A very narrow riser case showed large non-linear responses to changes in the specularity and particle-particle restitution coefficients as these coefficients triggered a regime change in the reactor. On the other hand, for bubbling, turbulent and fast fluidization where cluster formation is always present, such rapid regime changes were not observed.

For bubbling fluidization in wide reactors, the effect of these unknown coefficients can become negligible. This, combined with the fact that bubbling beds generally use larger particle sizes and slower reaction rates, makes such reactors much simpler to simulate than faster riser reactors. Even though rapid step changes were not observed for clustered flows in narrower geometries under faster fluidization, the influence of the unknown model coefficients did become increasingly significant, thereby introducing significant amounts of uncertainty into the simulation results.

ACKNOWLEDGEMENTS

The authors gratefully acknowledge the research funding received from the Research Council of Norway as well as the Notur supercomputing facilities used to carry out the expensive riser simulations in this paper.

REFERENCES

Bi, H. T. and J. R. Grace (1995). "Flow regime diagrams for gas-solid fluidization and upward transport." International Journal of Multiphase Flow **21**(6): 1229-1236.

Chalermsinsuwan, B., P. Piumsomboon and D. Gidaspow (2010). "A computational fluid dynamics design of a carbon dioxide sorption circulating fluidized bed." AIChE Journal **56**(11): 2805-2824.

Cloete, S., S. Amini and S. T. Johansen (2011). "A fine resolution parametric study on the numerical simulation of gas-solid flows in a periodic riser section." Powder Technology **205**(1-3): 103-111.

Cloete, S., S. T. Johansen and S. Amini (2015). "Grid independence behaviour of fluidized bed reactor simulations using the Two Fluid Model: Effect of particle size." Powder Technology **269**(0): 153-165.

Cloete, S., A. Zaabout, S. T. Johansen, M. Van Sint Annaland, F. Gallucci and S. Amini (2014). "The effect of frictional pressure, geometry and wall friction on the modelling of a pseudo-2D bubbling fluidized bed reactor." Powder Technology **Under review**.

Ellis, N., M. Xu, C. J. Lim, S. Cloete and S. Amini (2011). "Effect of Change in Fluidizing Gas on Riser Hydrodynamics and Evaluation of Scaling Laws." Industrial & Engineering Chemistry Research **50**(8): 4697-4706.

Gidaspow, D., R. Bezburuah and J. Ding (1992). Hydrodynamics of Circulating Fluidized Beds, Kinetic Theory Approach. 7th Engineering Foundation Conference on Fluidization 75-82.

Igci, Y., A. T. Andrews, S. Sundaresan, S. Pannala and T. O'Brien (2008). "Filtered two-fluid models for fluidized gas-particle suspensions." AIChE Journal **54**(6): 1431-1448.

Jenkins, J. T. and S. B. Savage (1983). "Theory for the rapid flow of identical, smooth, nearly elastic, spherical particles." Journal of Fluid Mechanics **130**: 187-202.

Johnson, P. C. and R. Jackson (1987). "Frictional-Collisional Constitutive Relations for Granular Materials, with Application to Plane Shearing." Journal of Fluid Mechanics **176**: 67-93.

Li, T. and S. Benyahia (2012). "Revisiting Johnson and Jackson boundary conditions for granular flows." AIChE Journal **58**(7): 2058-2068.

Lun, C. K. K., S. B. Savage, D. J. Jeffrey and N. Chepurniy (1984). "Kinetic Theories for Granular Flow: Inelastic Particles in Couette Flow and Slightly Inelastic Particles in a General Flow Field." Journal of Fluid Mechanics **140**: 223-256.

Montgomery, D. (2001). Design and Analysis of Experiments. New York, John Wiley and Sons.

Ogawa, S., A. Unemura and N. Oshima (1980). "On the Equation of Fully Fluidized Granular Materials." Journal of Applied Mathematics and Physics **31**: 483.

Park, S.-W., D.-H. Sung, B.-S. Choi, J.-W. Lee and H. Kumazawa (2006). "Carbonation kinetics of potassium carbonate by carbon dioxide." Journal of industrial and engineering chemistry **12**(4): 522-530.

Popoff, B. and M. Braun (2007). A Lagrangian Approach to Dense Particulate Flows. 6th International Conference on Multiphase Flow. Leipzig, Germany.

Samanta, A., A. Zhao, G. K. H. Shimizu, P. Sarkar and R. Gupta (2011). "Post-Combustion CO2 Capture Using Solid Sorbents: A Review." Industrial & Engineering Chemistry Research **51**(4): 1438-1463.

Schaeffer, D. G. (1987). "Instability in the Evolution Equations Describing Incompressible Granular Flow." Journal of Differential Equations **66**: 19-50.

Schneiderbauer, S., D. Schellander, A. Löderer and S. Pirker (2012). "Non-steady state boundary conditions for collisional granular flows at flat frictional moving walls." International Journal of Multiphase Flow **43**(0): 149-156.

Sharonov, V., A. Okunev and Y. Aristov (2004). "Kinetics of carbon dioxide sorption by the composite material K2CO3 in Al2O3." Reaction Kinetics and Catalysis Letters **82**(2): 363-369.

Syamlal, M., W. Rogers and T. J. O'Brien (1993). MFIX Documentation: Volume 1, Theory Guide. Springfield, National Technical Information Service.

Taghipour, F., N. Ellis and C. Wong (2005). "Experimental and computational study of gas-solid fluidized bed hydrodynamics." Chemical Engineering Science **60**(24): 6857-6867.

Wen, C. Y. and Y. H. Yu (1966). "Mechanics of Fluidization." Chemical Engineering Progress Symposium Series **62**: 100-111.

Yi, C.-K., S.-H. Jo, Y. Seo, J.-B. Lee and C.-K. Ryu (2007). "Continuous operation of the potassium-based dry sorbent CO2 capture process with two fluidized-bed reactors." International Journal of Greenhouse Gas Control **1**(1): 31-36.

HYDRODYNAMIC INVESTIGATION INTO A NOVEL IC-CLC REACTOR CONCEPT FOR POWER PRODUCTION WITH INTEGRATED CO_2 CAPTURE

Abdelghafour Zaabout*, Schalk Cloete, Shahriar Amini
SINTEF Materials and Chemistry, Flow Technology Department, 7034 Trondheim, NORWAY
* E-mail: Abdelghafour.zaabout@sintef.no

ABSTRACT

This paper presents an investigation of the hydrodynamics of a new Chemical Looping Combustion (CLC) reactor concept for power generation with integrated CO_2 capture. This concept consists of an internal circulating fluidized bed (IC-CLC) where a single reactor is divided into two separate sections in a way that oxidation and reduction of the oxygen carrier take place separately. Such a reactor configuration would significantly reduce the costs and solids handling challenges currently hampering the scale-up of CLC technology.

Fundamental multiphase flow models (based on the Kinetic Theory of Granular Flow or KTGF) have been used to investigate the hydrodynamics in different reactor designs in order to identify the most optimized one which maintains minimized leakage between the two reactor sections. The performance of each design has been evaluated through a quantified parameter which is the volumetric gas/solid leakage ratio between the two reactor sections. Reactor designs with narrow connecting ports proved to be the most reliable in minimizing the gas leakage and therefore would maintain high CO_2 purity and CO_2 capture efficiency.

The most optimized reactor design has then been selected for further investigation through a statistical method (central composite design) where the reactor performance response to the change in the bed loading and the air fluidization velocity has been evaluated. Values close to 1 were found for the fuel/solid leakage ratio parameter implying that high CO_2 capture efficiency can be achieved through the chosen design in a wide range of bed loadings and fluidization velocities. In general, the reactor proved to perform best under conditions with high static bed heights and/or high fluidization velocities.

Keywords: Fluidized bed; Chemical Looping Combustion; Simulation-Based Reactor Design.

INTRODUCTION

Carbon capture and storage (CCS) is increasingly seen as a potential environmentally sustainable way for fulfilling world energy needs while minimizing the environmental impact of fossil fuel combustion (Butt, Giddings et al. 2012; IEA 2012). Chemical-looping combustion (CLC) has arisen as a promising technology to carry out CO_2 capture at low energy penalty compared to CO_2 capture technologies, such as pre- and post-combustion technologies (Ekström, Schwendig et al. 2009). CLC is a combustion process which integrates power generation and CO_2 capture. It consists of two interconnected reactors, an air and a fuel reactor. A solid oxygen carrier circulating between them, thereby playing the role of oxygen transporter which transfers the oxygen required for fuel combustion from the air to the fuel. Consequently, any contact between the fuel and the air is inherently avoided in this process, and therefore a pure CO_2 stream, ready for compression and sequestration is produced (Ishida, Zheng et al. 1987).

In addition to development and selection of suitable oxygen carriers materials (Abad, Adanez et al. 2007; Hossain and de Lasa 2008; Adanez, Abad et al. 2012), research on CLC has so far been focused predominantly on the use of dual Circulating Fluidized Beds (CFBs) configuration for the recirculation of the oxygen carrier between the air and the fuel reactors (Abad, Garcia-Labiano et al. 2007; Ekström, Schwendig et al. 2009). Although this configuration has been demonstrated experimentally at lab and pilot scales (Kronberger, Johansson et al. 2004; Linderholm, Abad et al. 2008; Ding, Wang et al. 2012), the dual CFB-based CLC process is still facing many technical and operational complexities which arise mainly from the interconnected reactors configuration. Aside from the design and operational complexity created by the need to manage the solids exchange so that mass and heat balances within the closed loop are fulfilled, the exchange of solids itself brings additional costs and complexity. This circulation between the two reactors requires efficient and costly particles separation system such as a cyclone. This particle separation is particularly difficult due to the extremely harsh reactive and high temperature conditions.

Attempts have followed in recent years to address these issues where reactor concepts with no external solid circulation have been proposed (Noorman, van Sint Annaland et al. 2007; Hamers, Gallucci et al. 2013; Zaabout, Cloete et al. 2013). Following this philosophy, this paper will present a new CLC reactor concept with no external solids circulation. The proposed IC-CLC concept consists of a single reactor divided into two sections, the air and fuel sections, with an oxygen carrier circulating internally between them. This concept is expected to bring large benefits in terms of process simplification through avoiding external solids circulation and process intensification by direct heat integration and ability of operation under pressurized conditions. A large flexibility in the solids circulation rate is also granted due to the ability to operate the air section in a wide range of gas velocities between the bubbling and fast fluidization regime. The fuel section is operated under bubbling regime conditions.

All of these advantages make the IC-CLC concept the most practical solution by which the most important advantages of the interconnected configuration can be

maintained, while alleviating the most important challenges encountered in this configuration.
This paper will use fundamental flow modelling approach for a virtual proof of concept. Fundamental CFD modelling is ideal for this kind of virtual prototyping application because it can be used to quickly and economically evaluate a range of new process ideas and reactor configurations before any expensive and time-consuming physical experiments are conducted. This paper presents a numerical investigation of the hydrodynamics in different reactor designs of the IC-CLC concept. The most optimized design is selected for further hydrodynamic investigation with a dedicated central composite design.

NEW CONCEPT

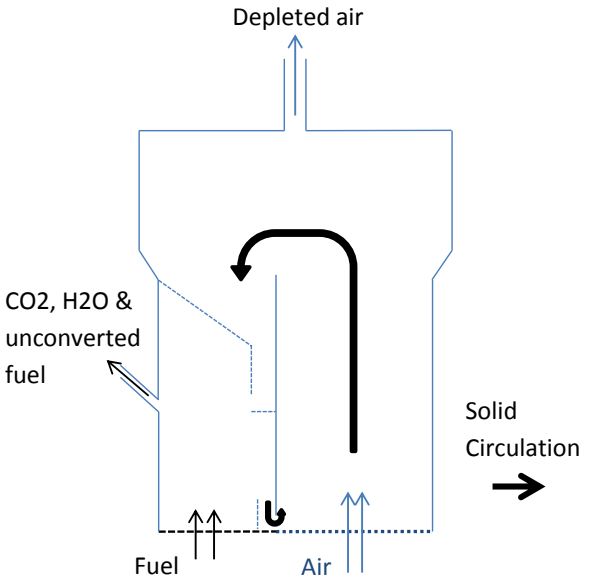

Figure 1: Internal circulating CLC concept IC-CLC

The proposed IC-CLC concept consists of a single reactor with internal physical partitions creating two reactor sections as shown in Figure 1. Air is injected in one section of the reactor (the fast region) for oxidation of the oxygen carrier while a gaseous fuel is injected to the second reactor section (the slow region) where oxygen carrier reduction takes place. An expanding freeboard region is added where the depleted air transporting oxygen carriers slows down before it leaves the reactor from the outlet at the top while the oxygen carriers fall down into the fuel region. To complete the cycle the oxygen carriers flow back to the air region through the opening at the bottom of the reactor. Gaseous reduction products leave the reactor from the fuel section outlet on the side of the reactor (Figure 1).
The two reactor sections are connected to each other without any physical separation or seals. This will certainly allow for gas leakage between the two sections in both sides. The viability of this concept will therefore be proved only when the gas leakage between the two sections can be minimized to tolerable quantities.
In order to calculate the amount of gas leakage that will occur, it can be assumed that the gas will leak from one reactor section to the other at a rate proportional to the solids circulation rate. Hence, a new variable for the volumetric ratio of gas to solids transferred from one reactor section to the next can be defined: the gas/solids leakage ratio. At a fixed gas/solids leakage ratio, the gas leakage will therefore be proportional to the solids circulation rate required to react with a given gas stream. If the rate of solids recirculation is very small in relation to the gas feed streams and the gas/solids leakage ratio is kept small by good reactor design, it is possible that gas leakages can become very small.
As an example, the gas/solids leakage ratio can be calculated for a CLC system using a NiO oxygen carrier and methane as fuel. The reaction occurring in the fuel reactor section is as follows (assuming full oxidation of methane):

Equation 1 :

$$4NiO + CH_4 \rightarrow 4Ni + CO_2 + 2H_2O$$

When assuming a solids circulation rate $\left(\dot{m}_{solids}\right)$ of 1 kg/s, a desired degree of solids conversion $\left(c_{NiO}\right)$ of 50% and an active material content in the oxygen carrier $\left(x_{NiO}\right)$ of 40%, the molar flowrate of NiO $\left(\dot{n}_{NiO}\right)$ to be reacted coming into the fuel reactor can be calculated as:

Equation 2:

$$\dot{n}_{NiO} = \frac{\dot{m}_{solids} c_{NiO} x_{NiO}}{M_{NiO}} = \frac{1 \cdot 0.5 \cdot 0.4}{0.0747} = 2.677 \text{ mol/s}$$

According to the stoichiometric ratio of reactants, 0.669 mol/s of methane would be required to achieve 50% conversion of the solids being fed at 1 kg/s. Assuming 99.9% fuel conversion and no side-reactions, the outlet stream of the fuel reactor section would consist of 0.669 mol/s CO_2, 0.00067 mol/s of unreacted CH_4, 1.337 mol/s of H_2O (which will be easily condensed out before compression, transport and storage) and a certain amount of depleted air which leaked from the air reactor.
For an oxygen carrier material density $\left(\rho_{solids}\right)$ of 3400 kg/m^3, a reactor temperature $\left(T\right)$ of 1200 K and atmospheric pressure $\left(P\right)$, the molar flowrate of gas leakage between reactor sections $\left(\dot{n}_{leak}\right)$ can be calculated as a function of the gas/solids leakage ratio $\left(X\right)$.

Equation 3:

$$\dot{n}_{leak} = \frac{\dot{V}_{leak} P}{RT} = \frac{X \frac{\dot{m}_{solids}}{\rho_{solids}} P}{RT} = X \frac{\frac{1}{3400} 101325}{8.314 \cdot 1200} = 0.00299 \cdot X \text{ mol/s}$$

Assuming that the gas leaking from the fuel reactor to the air reactor is fully converted (consisting only of CO_2 and H_2O in a 1:2 molar ratio), the rate of CO_2 leakage to the air reactor will be one third of that calculated in Eq. 3. Using this information, the purity of the CO_2 (after

water condensation) from the fuel reactor and the CO_2 capture efficiency (determined by the CO_2 which leaked to the air reactor) can be plotted as a function of the gas/solids leakage ratio. For this particular example, this plot is given in Figure 2.

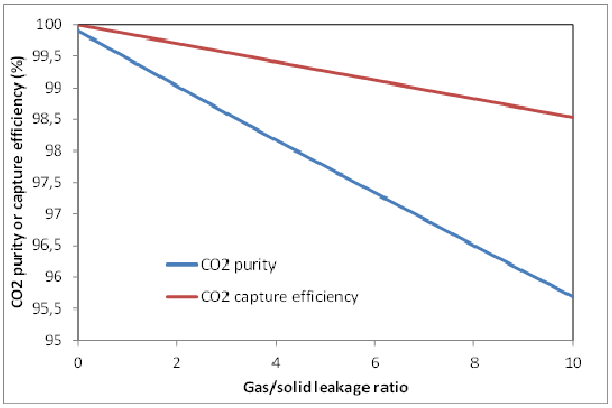

Figure 2: CO_2 purity and CO_2 capture efficiency as a function of gas/solid leakage ratio.

It can be seen that both the CO_2 purity and CO_2 capture efficiency remain high even at high gas/solid leakage ratios. This is a result of the very small volumetric flowrate of solids that is required to react with a given volumetric flowrate of gas and shows that the IC-CLC concept holds great promise for this particular process.
The potential for practically controlling the gas/solids leakage ratio will be further investigated in this work through CFD simulations. This paper will explore options of reactor and connection ports design and operating conditions which would result in minimized gas leakage between the two reactor sections. It is important that the gas leakage is minimized in a way to result in high CO_2 capture efficiency and CO_2 purity. The effect of reducing the contact areas between the two reactor sections by adding physical separation walls (as show the dashed lines in figure 1) close to the connecting opening at the top and the bottom will be investigated using CFD simulations.

SIMULATIONS

Simulations were carried out using the well-established two fluid model (TFM) closed by the kinetic theory of granular flows (KTGF).

Model equations

Conservation equations are solved for each of the two phases present in the simulation. The continuity equations for the gas and solids phases phase are given below:

Equation 4:

$$\frac{\partial}{\partial t}\left(\alpha_g \rho_g\right) + \nabla \cdot \left(\alpha_g \rho_g \vec{v}_g\right) = 0$$

$$\frac{\partial}{\partial t}\left(\alpha_s \rho_s\right) + \nabla \cdot \left(\alpha_s \rho_s \vec{v}_s\right) = 0$$

Momentum conservation for the gas phase is written as

Equation 5:

$$\frac{\partial}{\partial t}\left(\alpha_g \rho_g \vec{v}_g\right) + \nabla \cdot \left(\alpha_g \rho_g \vec{v}_g \vec{v}_g\right) = -\alpha_g \nabla p + \nabla \cdot \bar{\bar{\tau}}_g + \alpha_g \rho_g \vec{g} + K_{sg}\left(\vec{v}_s - \vec{v}_g\right)$$

And for the solids as

$$\frac{\partial}{\partial t}\left(\alpha_s \rho_s \vec{v}_s\right) + \nabla \cdot \left(\alpha_s \rho_s \vec{v}_s \vec{v}_s\right) = -\alpha_s \nabla p - \nabla p_s + \nabla \cdot \bar{\bar{\tau}}_s + \alpha_s \rho_s \vec{g} + K_{gs}\left(\vec{v}_g - \vec{v}_s\right)$$

The inter-phase momentum exchange coefficient $\left(K_{gs} = K_{sg}\right)$ was modelled according to the formulation of Syamlal and O'Brian (Syamlal, Rogers et al. 1993).
Solids phase stresses were determined according to the KTGF analogy. The conservation equation for granular temperature is given below:

Equation 6:

$$\frac{3}{2}\left[\frac{\partial}{\partial t}\left(\alpha_s \rho_s \Theta_s\right) + \nabla \cdot \left(\alpha_s \rho_s \vec{v}_s \Theta_s\right)\right] = \left(-p_s \bar{\bar{I}} + \bar{\bar{\tau}}_s\right) : \nabla \vec{v}_s + \nabla \cdot \left(k_{\Theta_s} \nabla \Theta_s\right) - \gamma_{\Theta_s} + \phi_{gs}$$

This partial differential equation was simplified to an algebraic equation by neglecting the convection and diffusion terms (Van Wachem, Schouten et al. 2001). The two final terms in Eq. 6 are the collisional dissipation of energy (Lun, Savage et al. 1984) and the interphase exchange between the particle fluctuations and the gas phase (Gidaspow, Bezburuah et al. 1992). Solids stresses are calculated according to shear and bulk (Lun, Savage et al. 1984) viscosities. The shear viscosity consists of three parts: collisional (Gidaspow, Bezburuah et al. 1992; Syamlal, Rogers et al. 1993), kinetic (Syamlal, Rogers et al. 1993) and frictional (Schaeffer 1987). The solids pressure formulation by Lun et al. (Lun, Savage et al. 1984) was enhanced by the frictional pressure formulation by Johnson and Jackson (Johnson and Jackson 1987). The radial distribution function of Ogawa and Oshima (Ogawa, Unemura et al. 1980) was employed.

Boundary conditions

A simple no-slip wall boundary condition was set for the gas phase. The Johnson and Jackson (Johnson and Jackson 1987) boundary condition was used for the granular phase with a specularity coefficient of 0.25.

Equation 7:

$$\vec{\tau}_s = -\frac{\pi}{6}\sqrt{3}\varsigma \frac{\alpha_s}{\alpha_{s,\max}} \rho_s g_{0,ss} \sqrt{\Theta_s} \vec{U}_{s,\|}$$

The inlet condition was specified as a velocity inlet injecting air at a flow rate of 0.6 m/s. CO_2 was injected through a velocity inlet on the back wall to mimic the experiment. In the 2D simulation, CO_2 was injected via a source term. The outlet was designated as a pressure outlet at atmospheric pressure.

Flow solver and solver settings

The commercial software package, FLUENT 13.0 was used as the flow solver. The phase coupled SIMPLE scheme (Patankar 1980) was used for pressure-velocity coupling and the higher order QUICK scheme (Leonard and Mokhtari 1990) for the spatial discretization of all remaining equations. First order implicit temporal discretization was used (Cloete, Amini et al. 2011). Unsteady state simulations have been performed with a time step of 0.001s. A restitution coefficient of 0.9 has been used. Further model setting can be found in (Cloete, Zaabout et al. 2013)

RESULTS AND DISCUSSIONS

The IC-CLC concept allows for large flexibility in terms of designing the partitions and connections

between the fuel and the air zones. The resulting reactor design has a direct impact on the reactor performance. A reliable reactor design should be able to maintain minimized leakage between the two reactor sections to ensure high CO2 purity and CO2 capture efficiency. Hence, to reduce the risk, it is highly recommended to use an efficient and quick numerical tool to assess the different reactor design before any expensive and time-consuming experimental demonstration is done. The well-known Two Fluid Model ((TFM) approach closed by the Kinetic Theory of Granular Flows (KTGF)) was used for this purpose as will be shown below.

Reactor design

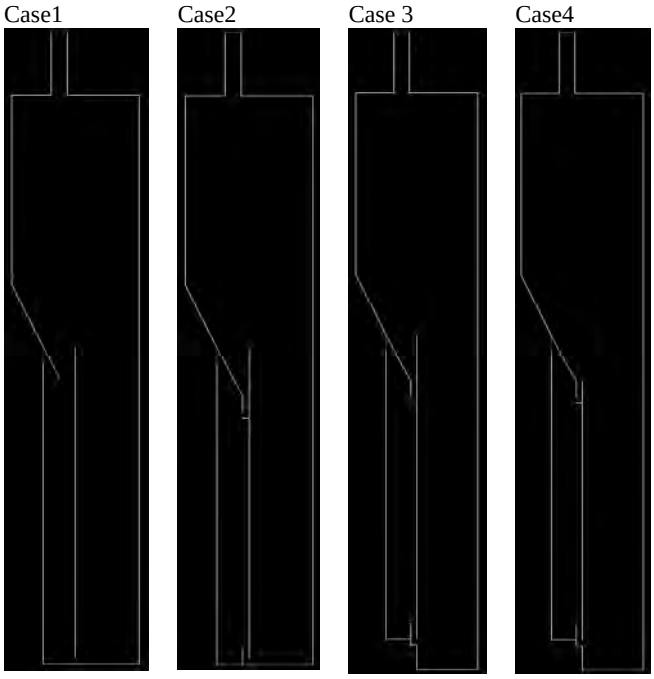

Figure 3: IC-CLC concept: investigated reactor configurations.

Several reactor configurations have been investigated as shown in Figure 3 where the emphasis was put on changing the extent of the connection areas between the two reactor sections (the high of the unit is 2 m in total; the reactor zone is 1 m height and the freeboard region is 1 m. The fuel section width is 0.1 m and the air section width is 0.2 m). Case 1, for example, exhibits large contact areas between the two reactor sections while, for the three other configurations, the contact areas were narrowed to 2 cm width connecting ports; one at the bottom and the other at top. Parameters such as solids circulation rate, air leakage to the fuel section and fuel leakage to the air section have been quantified for each reactor configuration and the performances of each configuration were compared through the previously discussed gas/solid leakage ratio parameter which describes the ratio between the volumetric gas leakage through the port and the volumetric solids circulation rate. Gas feeds to both reactor sections and the static bed height were kept the same for the four reactor configurations during this comparative study: air was used as a feed gas to the air section with 1 m/s fluidization velocity, U, and methane was used as a feed gas to the fuel section with a fluidization velocity of 0.3 m/s. The initial static bed height, H_s, was 0.5 m. Glass beads of 200 µm mean diameter and 2500 kg/m^3 density were used as a bed to be fluidized (The minimum fluidization velocity is 0.0451 m/s).

As shown in Table 1, results from case 1 show high air and fuel leakages through the two connections with a very low solid circulation rate between the two reactor sections. With large connecting areas between the two reactor sections in case 1, gases in both reactor sections find less resistance to flow freely in both sides, causing therefore a large amount of leakage. The resulting air/solid and fuel/solid ratios are very high, implying that this reactor design fails to deliver high CO_2 purity and CO_2 capture efficiency.

Table 1: Effect of reactor design: simulations results. Data have been averaged over 30s real process time.

	Case 1	Case 2	Case 3	Case 4
Air flow rate-bot (m^3/s)	0.00189	2.02E-05	0.00037	1.24 E-5
Air flow rate -top (m^3/s)	0.00857	0.00692	0.00604	0.00541
Fuel flow rate-bot (m^3/s)	0.00837	0.00531	0.00432	0.00781
Fuel flow rate -top (m^3/s)	0.01299	0.00043	0.00092	0.00032
Total-solid flow rate (m^3/s)	0.00022	0.00386	0.00337	0.00530
Fuel flow rate /solid ratio	93.9225	1.4865	1.55856	1.53449
Air flow rate /solid ratio	46.0169	1.795499	1.90612	1.02368

For the three other cases where the connections between the two regions are narrowed, high solids circulation rates were observed. Case 2 and 3 showed comparable values of solids circulation rate although the extension of the air region at the bottom for case 3. Case 4 however showed a 25 % increase in the solids circulation rate compared to case 2 and 3; by shortening the bar separating the two regions in case 4 to the level of the narrow port at the top it becomes easier for more entrained solids to the freeboard to reach the side and fall into the port to circulate to the fuel section. As for the gas leakage between the two reactor sections, the fuel was found to leak mainly through the port at the bottom while the air leaks through the port at the top. It naturally follows the solids circulation path.

The reactor performance with respect to gas leakage was quantified in the form of fuel/solid and air/solids leakage ratio parameters. The three reactor designs with narrow connection ports show values lower than 2 for both fuel/solid and air/solid leakage ratios implying that the three of them have the potential to maintain high CO_2 capture efficiency and CO_2 purity. The port design is therefore the most influential parameter in the gas leakage between the two reactor sections; narrow connection port creates conditions with solids flowing close to maximum packing which make them play the role of a physical plug that restricts the gas freedom to flow through the port.

In the light of the results presented above, the reactor configuration depicted in Figure 4 was selected for further investigation. The top part of the unit was

expanded in both the right and left sides for allowing for larger air flow rate while preventing solids elutriation. Instantaneous solids holdup in the unit shows denser bed conditions in the fuel section due to low gas feed and dilute bed conditions in the air section due to the high fluidization velocity in that region.
Continuous solids circulation between the two reactor sections is established due the difference in the gas feed velocities in each section: solids are first entrained by air to the freeboard then fall into the connecting port at the top, and thereafter flow down to the fuel section. Accumulation of solids in the fuel section leads to hydrostatic pressure build up which drives the solids to flow back to the air section through the connecting port at the bottom.

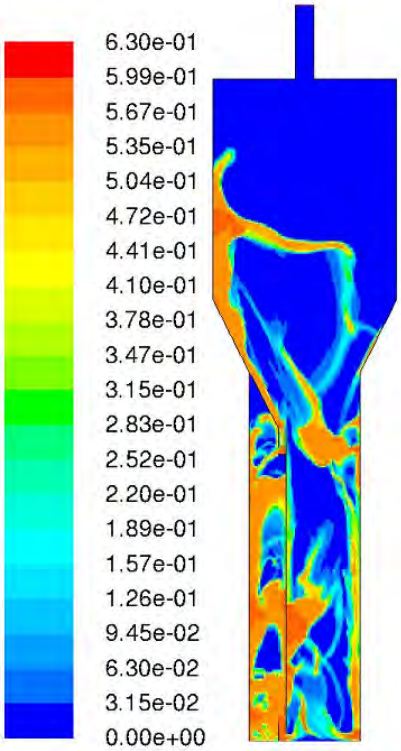

Figure 4: Instantaneous solid holdup in the rig; Hs= 0.6 m and U= 1.25 m/s.

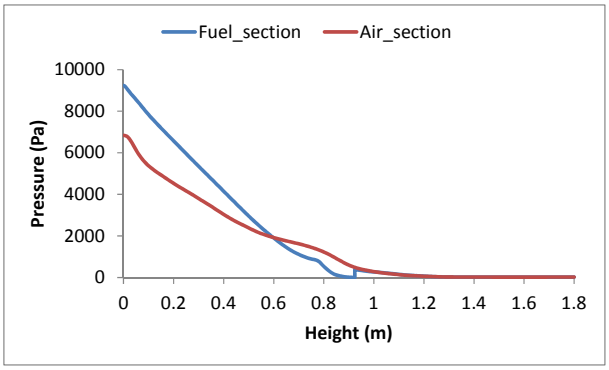

Figure 5: Mean axial pressure plotted along the two reactor sections; Hs= 0.6 m and U= 1.25 m/s.

The axial pressure plotted along the height of the reactor in both the fuel and the air sections (Figure 5) illustrates this solids circulation mechanism where it shows the pressure build up in the fuel section. At the bottom part of the reactor the pressure in the fuel section is higher than in the air section. This forces the solids to flow to the air region through the port at the bottom. At the top part of the reactor the situation is inversed: the pressure in the air section becomes higher than in the fuel one. This pressure difference drives the solids to flow to the fuel section through the port in the top.

More detailed investigation of the reactor configuration

In the light of this good gas leakage performance, the chosen reactor configuration was further investigated by means of a central composite design. A central composite design is a statistical method which allows for the fitting of a second order model through a set of data collected from well-defined experiments (simulation experiments in this case). The relative importance of the different effects in relation to each other can be quantified, together with the accuracy by which the model fits the data. In this case, however, only the response surface is required to gain a better understanding of the performance of this concept as two independent variables were varied:

- The first independent variable was the static bed height (solids loading inside the reactor). Since the mass transfer between reactor sections is driven by hydrostatic pressure differences, the height of the beds in the respective sections are expected to have an influence on the solids recirculation rate and the gas leakage. This factor is expressed as the static bed height with which the simulation was initialized (the initial solids volume fraction was 0.6).
- The velocity at which the air bed section was fluidized was the second factor. A greater difference between the fluidization velocities in the two reactor sections is expected to increase the solids recirculation rate. This factor was expressed as the ratio between the fluidization velocity in the fast section and that in the slow section which was kept constant at 0.3 m/s. As can be seen in **Error! Reference source not found.**, the section at the right was taken as the fast section (air section) and the left section as the slow one (fuel section).

Table 2: Central composite design with varying the fluidization velocity in the air section and the static bed height.

	U (m/s)	H (m)
1	0.8965	0.2586
2	0.8965	0.5414
3	1.6036	0.2586
4	1.6036	0.5414
5	0.7500	0.4000
6	1.7500	0.4000
7	1.2500	0.2000
8	1.2500	0.6000
9 (C)	1.2500	0.4000
10 (C)	1.2500	0.4000

Ten simulations were completed at different values of these two independent variables as specified in Table 2.

The same particles as in the previous section are used for this central composite design study. The response of the following three dependent variables was recorded:

- The solids recirculation rate (m^3/s) quantified as the average volumetric flowrate of the solids through the two connection ports.
- The gas/solid leakage ratio from the air reactor section into the fuel reactor section.
- The gas/solid leakage ratio from the fuel reactor section into the air reactor section.

Reactor performance within the central composite design

As expected, both the fluidization velocity in the air section and the static bed height play a major role in driving solids circulation between the two reactor sections. As can be seen in Figure 6, solid flow rate increases with both the initial static bed height and the fluidization velocity in the air section, although it tends to plateau for higher values. Naturally by increasing either the static bed height or the fluidization velocity larger amount of solids is entrained to the freeboard and falls into the fuel region. Greater solids accumulation in the fuel section leads to greater hydrostatic pressure which builds up and thereby forces a greater amount of solids to circulate back to the air region through the port at the bottom.

This is actually true as along as the port in the top is not completely full of solids. The form of the plateau shown by the response surface is due to the restriction imposed by the size of the connections ports on the solids flow; at high solids entrainment the connections ports get completely filled with solids and therefore restrict further increase in the solids circulation rate. At high static bed heights the unit can also face a loss of solids through the outlet in the fuel section. This explains the decrease in the solids circulation rate shown by the response surface at high static bed heights combined with high fluidization velocity in the air section.

Through this kind of surface response it is also easy to identify the operating conditions under which no solids circulation takes place making it therefore clearer to identify where the process would fail.

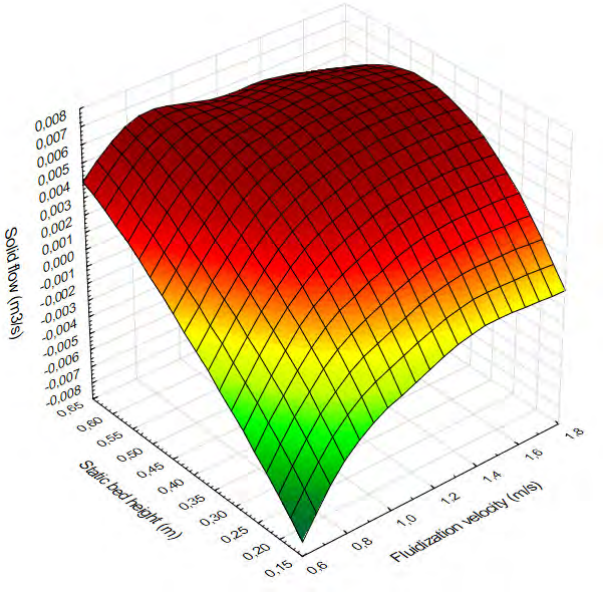

Figure 6: Volumetric solid flow rate response to the change in the fluidization velocity in the air section and the initial static bed height

As for the gas leakage it was found that fuel leakage takes place mainly through the port at the bottom while the air leakage takes place through the port at the top.

The fuel/solid leakage ratio response to the change in the fluidization velocity and the static bed height showed similar shape to that found for the solids flow rate (Figure 7); it increases with the increase in the fluidization velocity and static bed height and then plateaus. As explained previously the plateau forms due to the maximum solids packing conditions which take place in the port during high solids entrainment from the air section. In these conditions any further increase in the solids circulation rate and gas leakage is restricted by the port size.

Values close to 1 were found for the fuel/solid leakage ratio for all operating conditions within the central composite design (the negative values at very low static bed heights and fluidization velocities are simply the result of extrapolation). This means that the chosen reactor configuration is able to maintain very high CO_2 capture efficiency.

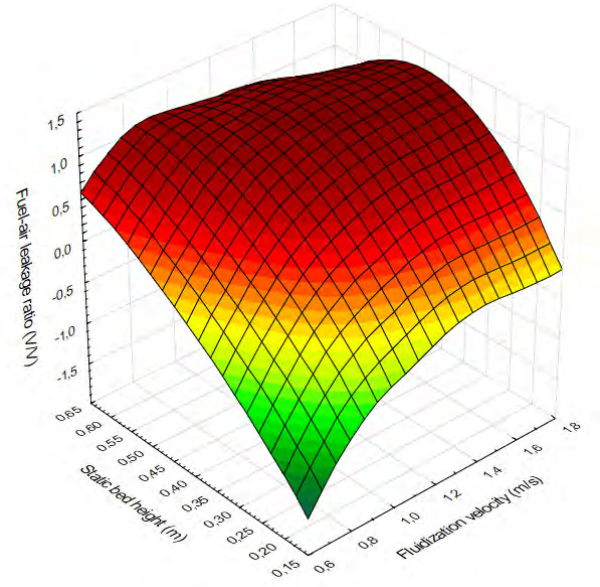

Figure 7: Fuel/solid leakage ratio response to the change in the fluidization velocity in the air section and the initial static bed height

The air/solid leakage ratio responds differently to the change in the air fluidization velocity and the static bed height. Values close to one were found for large fluidization velocities and static bed heights proving the ability of this reactor configuration to maintain very high CO_2 purity within these conditions. However, regions of poor performance were identified where operation of the concept should be avoided; combining low air fluidization velocities with low static bed heights results in very high air/solids leakage ratio and thereby very low CO_2 purity according to the discussion in section 2. The high values of the air/leakage ratio are consequences of the low solids circulation rate between the two reactor sections (Figure 8). As shown earlier, high solids circulation rates are required to create conditions close to maximum solids packing in the port

at the top (from where most of the air leakage takes place), to reduce the freedom of air to leak to the fuel section.

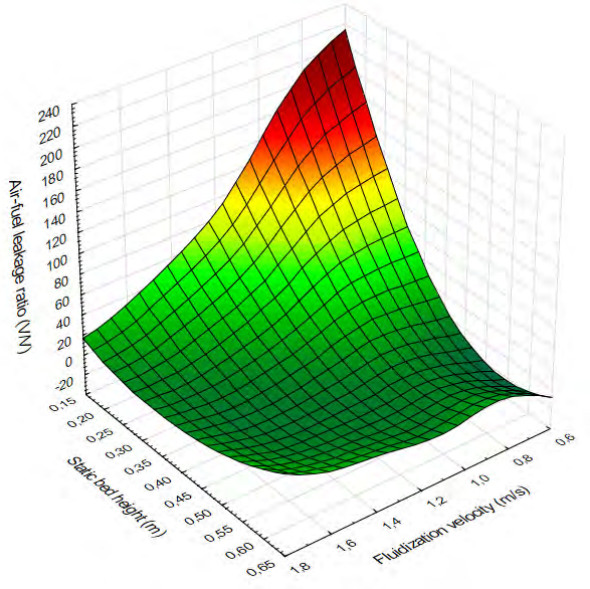

Figure 8: Air/solid leakage ratio response to the change in the fluidization velocity in the air section and the initial static bed height

Experimental unit

In the light of the promising results showed by simulations, a pseudo 2D (1.5 cm depth) experimental unit was constructed and operated in order to study the hydrodynamics of the IC-CLC concept. The bottom part of the unit is 1m height and the freeboard is 80 cm. Narrow connections ports of 2 cm width have been made (

Figure **9**). First tests of the unit with glass particles of 200 µm showed stable operation with continuous solids circulation between the two unit sections. Conditions where solids flow close to maximum packing in the connection ports were also observed (

Figure **9**); no blockage of the ports have been observed to take place in these conditions.

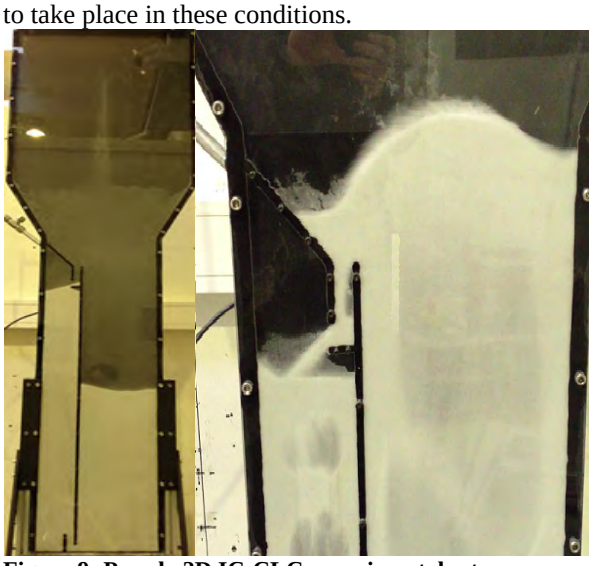

Figure 9: Pseudo 2D IC-CLC experimental setup.

Further testing on this unit is still required to prove experimentally the potential of this concept to maintain minimized leakage between the two unit sections. Parameters such as the solids circulation rate and gas leakages between the two unit sections will be quantified within a wide range of operating conditions.

CONCLUSION

A hydrodynamic investigation of an innovative CLC concept based on internal circulating fluidized bed (IC-CLC) has been carried out. The new concept consists of a single reactor with a physical separation inside dividing it into two sections; the fuel and the air sections. Oxygen carriers circulate between the two sections through two connecting ports, one at the bottom and one at the top. These connections allows for gas leakage in both sides which reduces the concept ability to capture CO_2 and generate high purity CO2. Good reactor design is therefore the key for the IC-CLC concept to succeed in maintaining high CO_2 purity and high CO_2 capture efficiency.

Fundamental multiphase flow models (based on the Kinetic Theory of Granular Flow KTGF) have then been used in this study to investigate the hydrodynamics in different reactor designs in order to identify the most optimized one before any expensive experimental demonstration is made. Reactor designs with narrow connection ports have resulted in the best leakage performance; small port size creates solids packing conditions which play the role of a physical plug that restricts the gas freedom to flow through the ports. The most optimized design has been further investigated in a framework of a central composite design where the bed loading and gas fluidization velocity in the air section are varied. Values close to 1 have been found for the fuel/solid ratio parameter implying that high CO_2 capture efficiency can be achieved through this design in a wide range of operating conditions. Regions of poor performance were also identified where the design would fail to maintain high CO_2 purity. In particular, low bed loadings and low fluidization velocities in the air section should be avoided as they results in high values of the air/solid ratio.

In the light of the promising results found in simulations, an experimental unit designed with narrow connection ports was constructed. The first tests already showed that low gas/solid leakage ratio can be achieved by this design.

REFERENCES

ABAD, A., ADANEZ, J., et al. (2007). "Mapping of the range of operational conditions for Cu-, Fe-, and Ni-based oxygen carriers in chemical-looping combustion." Chemical Engineering Science **62**(1-2): 533-549.

ABAD, A., GARCIA-LABIANO, F., et al. (2007). "Reduction kinetics of Cu-, Ni-, and Fe-based oxygen carriers using syngas (CO + H-2) for chemical-looping combustion." Energy & Fuels **21**(4): 1843-1853.

ADANEZ, J., ABAD, A., et al. (2012). "Progress in Chemical-Looping Combustion and Reforming technologies." Progress in Energy and Combustion Science **38**(2): 215-282.

BUTT, T. E., GIDDINGS, R. D., et al. (2012). "Environmental sustainability and climate change mitigation-CCS technology, better having it than not having it at all!" Environmental Progress & Sustainable Energy **31**(4): 642-649.

CLOETE, S., AMINI, S., et al. (2011). "On the effect of cluster resolution in riser flows on momentum and reaction kinetic interaction." Powder Technology **210**(1): 6-17.

CLOETE, S., ZAABOUT, A., et al. (2013). "The generality of the standard 2D TFM approach in predicting bubbling fluidized bed hydrodynamics." Powder Technology **235**: 735-746.

DING, N., WANG, W. R., et al. (2012). "Development and Testing of an Interconnected Fluidized-Bed System for Chemical Looping Combustion." Chemical Engineering & Technology **35**(3): 532-538.

EKSTRÖM, C., SCHWENDIG, F., et al. (2009). "Techno-Economic Evaluations and Benchmarking of Pre-combustion CO2 Capture and Oxy-fuel Processes Developed in the European ENCAP Project." Energy Procedia **1**(1): 4233-4240.

GIDASPOW, D., BEZBURUAH, R., et al. (1992). Hydrodynamics of Circulating Fluidized Beds, Kinetic Theory Approach. 7th Engineering Foundation Conference on Fluidization 75-82.

HAMERS, H. P., GALLUCCI, F., et al. (2013). "A novel reactor configuration for packed bed chemical-looping combustion of syngas." International Journal of Greenhouse Gas Control **16**(0): 1-12.

HOSSAIN, M. M. and DE LASA, H. I. (2008). "Chemical-looping combustion (CLC) for inherent CO2 separations-a review." Chemical Engineering Science **63**(18): 4433-4451.

IEA (2012). World Energy Outlook 2012, International Energy Agency.

ISHIDA, M., ZHENG, D., et al. (1987). "Evaluation of a chemical-looping-combustion power-generation system by graphic exergy analysis." Energy **12**(2): 147-154.

JOHNSON, P. C. and JACKSON, R. (1987). "Frictional-Collisional Constitutive Relations for Granular Materials, with Application to Plane Shearing." Journal of Fluid Mechanics **176**: 67-93.

KRONBERGER, B., JOHANSSON, E., et al. (2004). "A two-compartment fluidized bed reactor for CO2 capture by chemical-looping combustion." Chemical Engineering & Technology **27**(12): 1318-1326.

LEONARD, B. P. and MOKHTARI, S. (1990). ULTRA-SHARP Nonoscillatory Convection Schemes for High-Speed Steady Multidimensional Flow. NASA TM 1-2568 (ICOMP-90-12), NASA Lewis Research Center.

LINDERHOLM, C., ABAD, A., et al. (2008). "160 h of chemical-looping combustion in a 10 kW reactor system with a NiO-based oxygen carrier." International Journal of Greenhouse Gas Control **2**(4): 520-530.

LUN, C. K. K., SAVAGE, S. B., et al. (1984). "Kinetic Theories for Granular Flow: Inelastic Particles in Couette Flow and Slightly Inelastic Particles in a General Flow Field." Journal of Fluid Mechanics **140**: 223-256.

NOORMAN, S., VAN SINT ANNALAND, M., et al. (2007). "Packed Bed Reactor Technology for Chemical-Looping Combustion." Industrial & Engineering Chemistry Research **46**(12): 4212-4220.

OGAWA, S., UNEMURA, A., et al. (1980). "On the Equation of Fully Fluidized Granular Materials." Journal of Applied Mathematics and Physics **31**: 483.

PATANKAR, S. (1980). Numerical Heat Transfer and Fluid Flow, Hemisphere Publishing Corporation.

SCHAEFFER, D. G. (1987). "Instability in the Evolution Equations Describing Incompressible Granular Flow." Journal of Differential Equations **66**: 19-50.

SYAMLAL, M., ROGERS, W., et al. (1993). MFIX Documentation: Volume 1, Theory Guide. Springfield, National Technical Information Service.

VAN WACHEM, B. G. M., SCHOUTEN, J. C., et al. (2001). "Comparative analysis of CFD models of dense gas-solid systems." AIChE Journal **47**(5): 1035-1051.

ZAABOUT, A., CLOETE, S., et al. (2013). "Experimental Demonstration of a Novel Gas Switching Combustion Reactor for Power Production with Integrated CO2 Capture." Industrial & Engineering Chemistry Research **52**(39): 14241-14250.

Chapter 4: Packed beds

Due to their simplicity and plug-flow nature, packed beds are commonly deployed in various process industries, especially when it comes to catalytic reactions carried out at elevated pressures. The stationary nature of the particle phase can create challenges with regard to temperature distribution and particle handling, but also greatly simplifies the design and operation of these reactors.

Packed beds typically utilize larger particle sizes (order of millimetres) and are manufactured in a wide range of shapes. The nature of these particles strongly influences effects such as the mean packing density, drag coefficient, effective heat and mass diffusion, and effective reaction rate. Accurate information on these effects is essential for the development of reliable closure models used in 1D phenomenological models typically utilized for packed bed reactor design and operation.

For this reason, CFD studies are mostly focused on resolving the transport phenomena around and within particles of various shapes and sizes in order to derive better closures for subsequent use in 1D models. In some cases, the resulting closures are also deployed in multidimensional simulations of the large-scale system. The papers in this chapter give good examples of these applications of CFD.

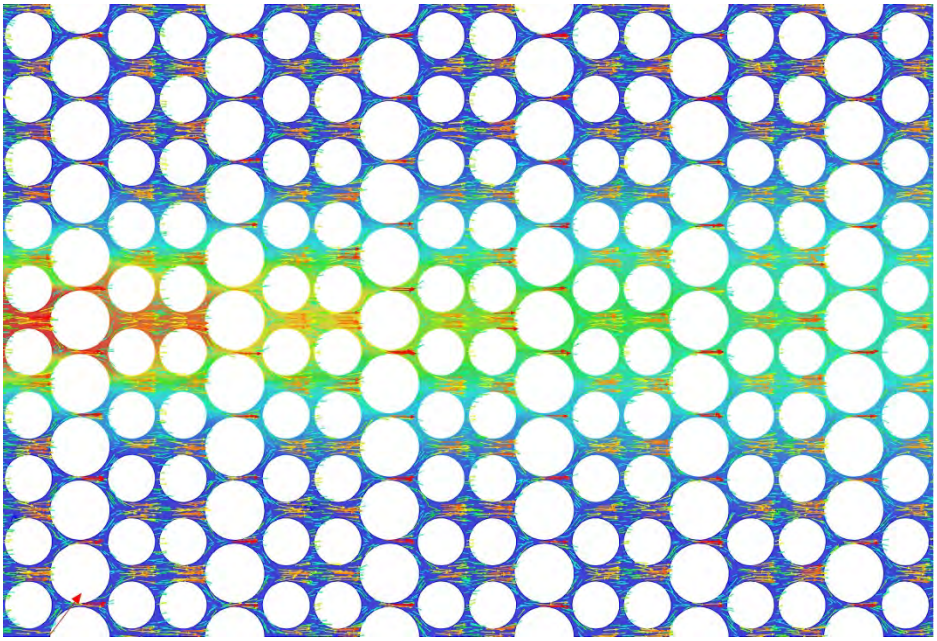

10th International Conference on CFD in Oil & Gas, Metallurgical and Process Industries
SINTEF, Trondheim, Norway *CFD 2014*
17-19 June 2014

A MULTI-SCALE MODEL FOR REACTOR DESIGN AND OXYGEN CARRIER SELECTION APPLIED TO PACKED BED CHEMICAL LOOPING COMBUSTION

Mandar TABIB[1], John MORUD[2], Stein Tore JOHANSEN[1], Shahriar AMINI[1*]

[1] Flow Technology Department, SINTEF Materials and Chemistry, Trondheim, Norway.
[2]Chemical Engineering Department, SINTEF Materials and Chemistry, Trondheim, Norway

* E-mail: Shahriar.Amini@sintef.no

ABSTRACT

Proper selection of a catalyst shape (or a particle shape) can improve the performance of a gas-solid packed bed reactor. The particle shape affects the packing structure and the transport phenomena within the packed bed. This information is not available for many non-spherical particle shapes which limit reactor design options. To enable catalyst and reactor design, a validated 3D Computational Fluid Dynamics (CFD)-Discrete Element Method (DEM) model has been developed to resolve the flow around these particles and to obtain information on the transport phenomena (pressure drop correlation and heat/mass transfer coefficient). The DEM is used to obtain realistic packing structures for different particle shapes, and the CFD is conducted on these DEM generated packing structure. However, the 3D CFD-DEM model cannot be applied on the whole reactor as it is computationally prohibitive. Hence, a multi-scale modelling approach is developed, wherein correlations obtained by the 3D CFD-DEM model from a representative 3D volume of the packed bed are used as closures in a 1D model for reactor design. The validations for all the models have been done. The multi-domain 1D particle-reactor model developed here is a combination of (1) a particle model for radial distribution of chemical species and temperature within a catalyst particle and (2) a 1D reactor model for mass and energy balance along the reactor. This 1D model is able to account for both intra-particle and inter-particle heat and mass transfer phenomena. The proposed multi-scale modelling approach has been applied to select an appropriate oxygen carrier shape for a Chemical Looping Combustion (CLC) packed bed reactor. This work compares the performance of different oxygen carrier shapes (fluted ring shape, cylindrical pellet shape and spherical shape) in terms of reactor operation. The simulations are used to recommend a pellet shape that offers least pressure drop, highest conversion and no early fuel slip for efficient CO_2 capture.

Keywords: Chemical looping combustion, Catalyst design, Packed bed reactor, Multi-scale modelling, CO_2 capture, Discrete Element Modelling, CFD.

NOMENCLATURE

Latin

A	Blake–Kozeny–Carman constant	[ ]
a	Particle surface area per volume of bed	[m^2/m^3]
B	Burke-Plummer constant	[ ]
C	Concentration	[$kmol/m^3$]
Cp	Heat capacity	[J/kg.K]
D_{eff}	Effective diffusivity	[m^2/s]
d_p	Particle diameter	[m]
F_h	Flux of enthalpy	[$J/m^2.s$]
F	Flux	$kmol/m^2.s$
G	Mass flux of gas	[$kg/m^2.s$]
h	Heat transfer coefficient	[$W/m^2.K$]
H	Enthalpy	[J/kmol]
k_g	Mass transfer coefficient	[m/s]
M	Molecular Weight	[Kg/kmol]
P	Pressure	[bar]
R	Particle radius	[m]
Rg	Gas constant	[J/kmol.K]
T	Temperature	[K]
t	Time	[s]
U	Internal energy	[J/m^3]
X_k	Mass fraction of species "k"	[-]
X_i	Conversion of species j	[-]
v_g	Superficial gas velocity	[m/s]
w_f	Fluid mass flow rate	[Kg/s]
w	Weight fraction	[-]
z	Axial position	[m]
r	radial position	[m]
c_∞	Concentration in bulk phase	
r_l	Reaction rate of species "*l*"	[kmol/Kgs]

Greek

$-\Delta H_{rx}$	Heat of reaction	[J/kmol]
ε	Void fraction	[-]
ξ	Ratio of moles of gas to solid needed for the reaction	
Γ_k	Source term for species "k"	[kmol/m3.s]
Γ_u	Source term for enthalpy	[J/m3.s]
λ	Particle thermal conductivity	[W/m.K]
λ_{ax}	Effective bed thermal conductivity	[W/m.K]
μ	Gas viscosity	[kg/m.s]
ρ	Gas density	[kg/m3]
ρ_s	Oxygen carrier density	[kg/m3]
τ	Oxygen carrier tortuosity	[-]

Sub/superscripts

k	*Species "k"*
tot	*Total*
g	*Gas phase*
s	*Solid particle*
l	*Number of Reactions*
kg	*Gas species in gas phase*
ks	*Gas species in particle pores*
j	*Active solid species j*

INTRODUCTION

Significant performance improvements can be obtained in a packed bed reactor by understanding the role of the particle in influencing the intra-particle and inter-particle transport phenomena. The particle can be a catalyst or an oxygen carrier (as in CLC based applications). The physical feature of a particle influences the overall packing structure, pressure drop, heat-transfer, mass-transfer and overall reaction rate in the reactor. Hence, researchers experimentally study different particle shapes (spheres, cylinder, fluted rings, tri-lobe, quadrulobe, monoliths, wagon wheels, hollow extrudates, discs, etc) to identify the most suitable shape/size for a given process. Selecting a suitable particle shape and size involves making compromises between reactivity and pressure drop.

In this regard, development of an accurate modelling approach for enabling catalyst (pellet) shape selection and reactor design will be useful. The packed-bed reactor offers an ideal platform to develop a multi-scale model that can account for the multi-scale phenomena in the packed bed, like: (a) at the pore level within the particle, the reactant gas species diffuses and reacts at the internal pore surface. For processes with high intrapellet Damkohler number (like, for the CLC process under study, it is two orders of magnitude high), the diffusional resistances will play an important role as the species diffusivity is low and intrinsic rate kinetics is fast, (b) at the microscopic boundary layer level formed at external surface of the particles may offer viscous resistance to the flow, and offer external resistance to the transport of gaseous species and heat from bulk gas phase to the particle surface, (c) at the meso-scale (interstitial regions between particles): the wakes behind the particles results in additional form drag and will influence the heat and mass transfer, (d) at the reactor level, the movement of thermal and reaction fronts in the entire bed needs to be captured. The influence of reactor geometry on packing structure and the near wall effects (which is dependent on ratio of particle diameter to reactor diameter) needs to be accounted.

These multi-scale effects can be resolved by accounting and simulating the actual particles in a 3D simulation. But, simulating the whole reactor with particles is prohibitive owing to high mesh grid requirements and computational time. Few multi-scale models have been proposed in literature to overcome this difficulty. Ingram (2004) has showed how three different multi-scale strategies (Multi-domain, Parallel and Embedded) can be applied to simulate a packed bed reactor. From application point of view, the use of simultaneous multi-scale (CFD only) or Parallel multi-scale approach (CFD+1D) are also prohibitive. Here, we propose a novel multi-scale modelling approach that can enable catalyst shape selection and reactor design in an efficient and effective way using a validated 3D-CFD-DEM modelling tool in-conjunction with a validated multi-domain 1D particle-reactor model. The methodology is explained in the next section.

MULTI-SCALE METHODOLOGY

A multi-domain 1D particle-reactor model is an efficient tool for large industrial-scale reactor design, as advanced modelling tools like 3D CFD-DEM will be computationally prohibitive to apply on larger scales. However, the 1D model will need accurate closure information to arrive at precise results. The required closure information involves information on packing structure (porosity, particle surface area per unit reactor volume) and information on transport phenomena (pressure drop correlation, external heat transfer and mass transfer correlation). For many non-spherical particles, such closure information is not available.

In the proposed multi-scale methodology, 3D CFD is applied on a representative volume of a DEM generated packed-bed to obtain the closure information for the 1D model. The use of a representative volume makes the simulations computationally tractable. The Discrete Element Method (DEM) is used to generate a realistic packing structure for spherical/non-spherical particles. In an earlier work (Tabib et. al., 2013), a validated 3D CFD-DEM methodology has been developed to select the dimensions (size) of the bed-segment which can serve as a good representative for the whole packed bed. The 1D model uses the accurate closures derived by the 3D CFD-DEM model to design the large-scale reactor and to study the effect of particle shape/size on the reactor performance. Figure 1 illustrates this multi-scale concept. This form of multi-scale modelling can be termed as a 'Serial by Simplification' multi-scale approach.

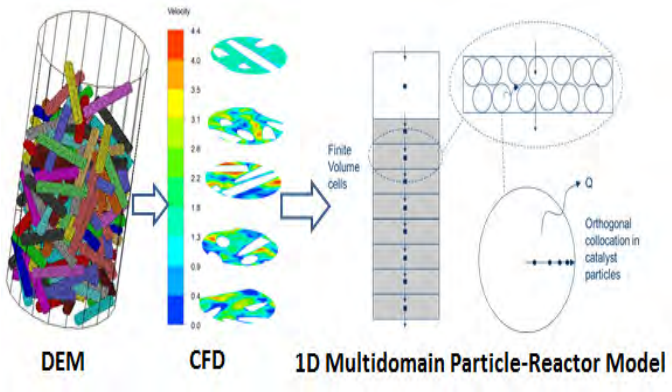

Figure 1 shows schematic representation of Multi-scale formalism. The 3D DEM generates a packed-bed structure, and then 3D CFD is applied on the DEM generated bed-segment to obtain closures for the multi-domain 1D Particle-Reactor model. The 1D model comprises of Finite Volume method on axially discretised reactor space and orthogonal collocation technique on radially discretised particle model.

The devised multi-scale methodology can be described step-wise as:

1. 1. Model the shape of the non-spherical particle using multiple spheres (called multi-sphere approach). For this work, the Fluted ring shape and cylindrical pellet shapes with Aspect ratio 1 (AR1), Aspect ratio 2 (AR2) pellet and Aspect ratio 7 (AR7) pellet have been created. Figure 2 shows the cylindrical pellet (AR7) and the Fluted Ring particle. These shapes are selected to evaluate them for application in a gas-solid non-catalytic Chemical looping combustion unit for power generation integrated with CO_2 capture.

2. Fill a volume (or reactor vessel) with the new catalyst/oxygen carrier shape using Discrete Element

Method. Figure 2 shows the packing structure generated for different particle shapes.

3. Obtain information on bed voidage (or solid porosity profile) and overall particle surface area per unit reactor volume from the DEM generated packing structure. Figure 3 shows the porosity profile obtained for each DEM generated packing and Table 1 shows the particle surface area per unit reactor volume. This information is to be used as closure for the 1D model.

4. Identify the minimum size of the DEM-generated bed-segment that can be a representative of the whole packed bed. The validated methodology to select the cut-segment size is described in Tabib et. al. (2013). The methodology relies on examining the sensitivity of CFD results to varying sample volume size (or to varying dimensions of the cut-segments).

5. The selected cut-segment size is used to simulate flow for wide-range of Reynolds numbers using CFD. Figure 4 shows the 3D CFD-DEM applied on fluted ring and cylindrical pellet. The pressure drop and particle heat transfer coefficient results at different Reynolds number are used to develop an engineering correlation for each of the particle shape.

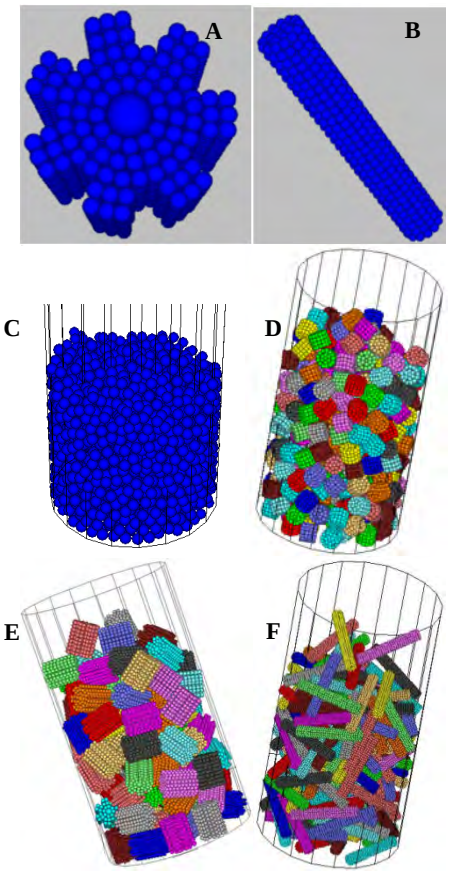

Figure 2 shows (A) Fluted ring particle and (B) cylindrical pellet with aspect ratio 7 generated using multi-sphere approach and the DEM generated packing structure for (C) spherical particle, (D) Aspect ratio 1 particle, (E) Aspect ratio 7 and (F) Fluted Ring.

6. Use the transport phenomena and packing structure information obtained for each packing as closure for the 1D model. The 1D model provides information on conversion profiles, temperature profiles, fuel slip and pressure drop for large scale industrial reactor.

7. Select the catalyst/oxygen carrier shape that provides the lowest pressure and higher reactivity with no fuel slip, and decide the reactor cycle time.

VALIDATION OF MODELS USED IN MULTI-SCALE METHODOLOGY

The 3D DEM-CFD and 1D model developed to implement the proposed multi-scale approach must be validated. The section covers the validation of 3D DEM-CFD model for predicting accurate closures and the validation of 1D model in accurately simulating a CLC operation.

Validation of DEM generated packing and porosity information

Bed voidage and total particle surface area within a reactor volume are important parameters that affect reactivity, pressure drop and cycle-time. Hence, voidage predicted by DEM has been validated with well-established correlations and with the values reported in literature. Figure 2C-2F shows the DEM generated packing for a spherical packing, two cylindrical pellets packing with pellets of aspect ratio 1 and 7, and a fluted ring packing.

The DEM predicted radial variation of bed-voidage (or porosity) for the spherical packing is similar to that predicted by De Klerk (2003) correlation (as seen in Figure 3). Both predict the voidage oscillations to exist up-to a distance of 5 particle-diameters from the wall (see Figure 3A), after which the oscillations settle down to a constant uniform bulk voidage. The constant bulk voidage (bulk porosity) of DEM generated spherical bed packing is around 0.404, which is same as that predicted by Dixon's correlation (1988) and by De Klerk correlation (2003). The amplitude of oscillations predicted by DEM is lower than the De-Klerk prediction. However, the current 1D model requires the constant bulk voidage as an input and not the radial profile. The bulk voidage predictions in DEM are affected by the particle-particle friction coefficient and particle-wall friction coefficient parameters (value of 0.3 used in this work). If the friction coefficient is high, then the particle will get balanced on each other and counteract the gravity. So, a higher friction coefficient would cause a loose packing (leading to higher porosity). Since, the bulk porosity prediction is accurate, so the current DEM parameters can be considered for further studies. The PFC3D software has been used to conduct these DEM simulations and uses the Hertz-Mindlin model to simulate particle collisions and motion.
Figure 3 shows the radial profiles of voidage (porosity) for the spherical particle (Figure 3A), cylindrical pellets with aspect ratio 1 (Figure 3B), aspect ratio 2 (Figure 3C) and aspect ratio 7 (Figure 3D). DEM predicts that as the aspect ratio of pellet increases (or as the non-sphericity increases), the amplitude and frequency of the near-wall radial bed-voidage oscillations decreases and

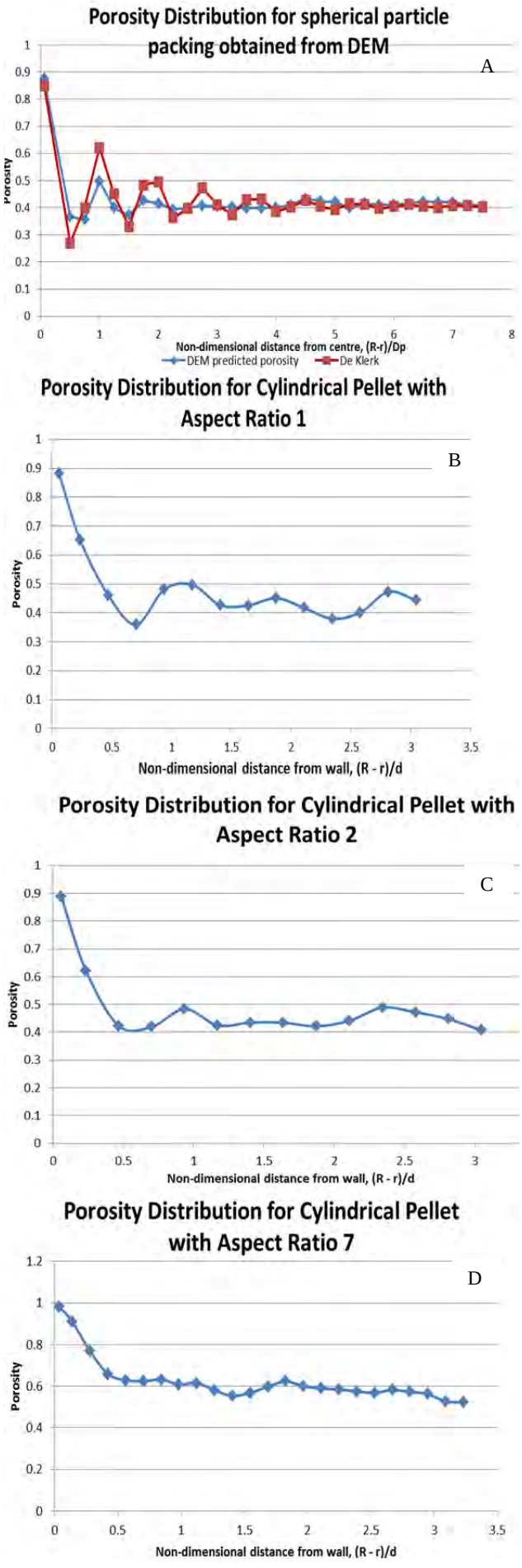

Figure 3 Porosity distribution obtained from DEM generated packing for (A) sphere, (B) AR1, (C) AR2 and (D) AR7.

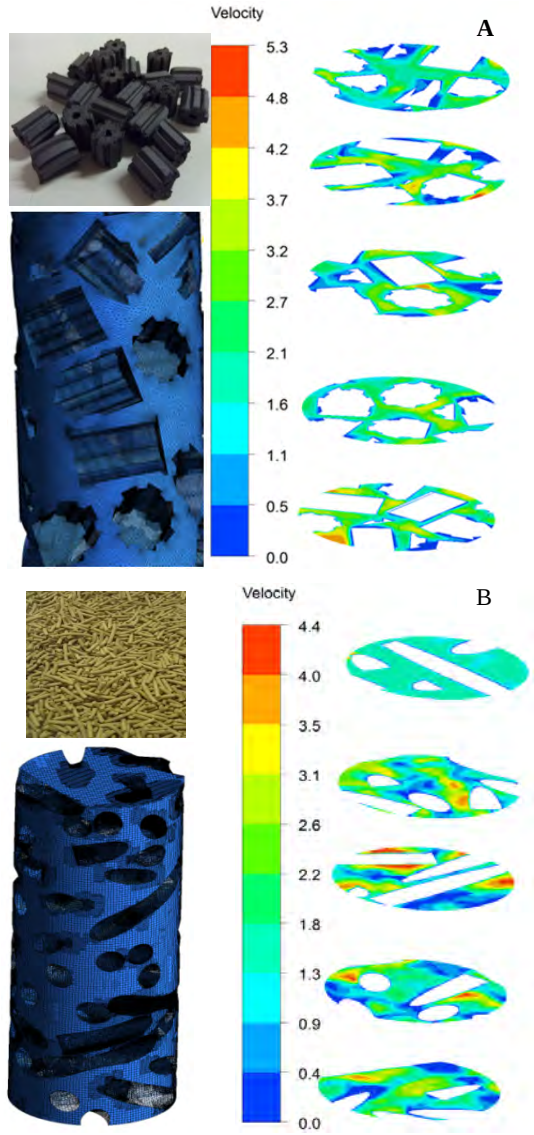

Figure 4 shows 3D CFD-DEM applied on (A) fluted ring and (B) cylindrical pellet.

the wall effect is confined to lesser distance from wall (Figure 3). As seen in Figure 3, there are more oscillations in radial voidage profile for aspect ratio 1 pellet than for aspect ratio 2 pellet. The Aspect ratio 7 pellet shows the least oscillatory behaviour. Comparatively, amongst the three pellets, the radial voidage profile of aspect ratio pellet 1 packing is nearer in behaviour to the spherical packing. The near wall region in Aspect ratio 1 and spherical extends upto five particle-diameters from wall, while for aspect ratio 7 and aspect ratio 2, the near-wall region is limited to two particle diameters from wall. These DEM predictions are quite similar to the observations made by various researchers regarding the variation of bed-voidage with variation of non-sphericity (Roblee (1958), Bey and Eigenberger (1997), Giese et. al. (1998), Caulkin et. al. (2012)). The work done by Nemec and Levec (2005) suggests that with increasing aspect ratio, the bed voidage increases. DEM is also predicting a higher voidage as the aspect ratio of the pellet increases. Thus, DEM predictions for bulk porosity have been validated with well-established correlations for spherical particle and match the observed trends for non-spherical particles.

Validation of 3D CFD-DEM methodology for obtaining closure information

The validation of CFD-DEM methodology to determine the cut-segment size and to obtain the correlations has been presented in Tabib et. al. (2013). Tabib et. al. (2013) conducted CFD simulations on the DEM generated packing segments for a wide particle Reynolds number range (from laminar to turbulent regime) for both the spherical and non-spherical particles. For the spherical particles, the validation was done by comparing the results with well-established correlations, like: Ergun equation (1952) for pressure drop, Wakao correlation (1979) and multi-particle Ranz-Marshal correlation (1952) for particle heat transfer coefficient and Dixon-Lubua (1985) and Colledge-Paterson (1984) correlation for wall heat transfer coefficient. For the non-spherical particles, the correlations obtained for the long cylindrical pellet (aspect ratio 7) packed bed has been compared with the correlation provided by Nemec and Levec (2005) for cylindrical pellet with aspect ratio of 5.77. These comparisons had shown good agreements. This validation gave us the confidence that the proposed CFD-DEM methodology can be used for obtaining useful information on transport phenomena within the bed, which can be used for designing and comparison of performance of large-scale packed bed reactor composed of unique particle shapes. The correlations developed for Aspect ratio 7 pellet and Fluted Ring using this methodology has been used in this work. Table 1 cites the input to be provided to 1D model as closure using the results from 3D CFD – DEM approach.

Validation of 1D model for a chemical looping combustion process (gas-solid non-catalytic reactions)

The 1D model is validated with analytical results for a packed-bed chemical looping combustion (CLC) reactor, which involves cyclic gas-solid non-catalytic reactions. The next section describes the 1D model.

1D model

A software application based on a 1D particle-reactor model has been developed to simulate a packed bed reactor operation. The developed 1D particle-reactor model is a combination of (1) a particle model for simulating radial distribution of chemical species and temperature within a catalyst/oxygen carrier particle and (2) a 1D reactor model for solving mass and energy balance along the reactor. The model accounts for the effect of intra-particle and inter-particle heat and mass transfer on the reactor performance. The reactor model and particle model are coupled together using mass and heat source terms computed at the particle surface. The 1D particle-reactor model can simulate for several different particle shapes (cylindrical pellet, slab and sphere) and offers flexibility in choice of closures (pressure drop correlations, heat-transfer/mass-transfer correlations, voidage and total particle surface area per unit reactor volume). The solution methodology involves a Finite Volume discretization technique for solving gas-phase equations along the reactor and an orthogonal collocation technique for solving the reaction-diffusion equations within the particle. This code is written in Fortran-90, and is easy to use as Microsoft Excel interface has been created. The fortan-90 code has been compiled into a direct link library (dll) form and is linked to the excel sheet using Visual Basic for Application (VBA) programming language. The coded 1D model solves the following equations. All the variables are explained in notation.

Ideal gas equation of state

$$P = C_{tot} R_g T_g \qquad (1)$$

Ergun pressure drop equation

$$\frac{\partial P}{\partial z} = -\frac{G}{\rho d_p}\left(\frac{1-\epsilon_g}{{\epsilon_g}^3}\right)\left(\frac{A(1-\epsilon_g)\mu}{d_p} + BG\right) \qquad (2)$$

Material balance for species "k" in gas phase

$$\varepsilon_g \frac{\partial C_k}{\partial t} + \frac{\partial F_k}{\partial z} = \Gamma_k$$

$$where,\ F_k = F_{tot} X_k - C_{tot} D_{eff,kg} \frac{\partial X_k}{\partial z} \qquad (3)$$

Energy balance for gas phase

$$\varepsilon_g \frac{\partial U}{\partial t} + \frac{\partial F_h}{\partial z} = \Gamma_U$$

$$where,\ F_h = F_{tot} H - \lambda_{ax} \frac{\partial T}{\partial z} \qquad (4)$$

Boundary conditions for gas phase

z=0: mass and energy inlet flux

z=L:

$$\frac{\partial C_k}{\partial z} = 0, \qquad \frac{\partial T}{\partial z} = 0 \qquad (5)$$

Source terms for gas phase mass- and energy balance arising due to mass and heat transfer at the gas-particle interface.

$$\Gamma_k = k_g \ a \ \left(C^s_{k,r=R} - C_k\right)$$

$$\Gamma_U = h \ a \ \left(T^s_{r=R} - T\right) \qquad (6)$$

$$for\ computing\ h,\ \frac{h d_p}{k} = 2.0 + A_c Re_p{}^x Pr^y$$

where, the heat transfer coefficient (*h*) is computed using the Ranz-Marshall equation shown above and k_g is the mass transfer coefficient. The constant A_c for fluted ring and AR7 packed bed system has been obtained by fitting the CFD-DEM heat transfer results to the above Ranz-Marshall correlation (1952) (as described in Tabib. et. al. (2013)).

Solid particle (oxygen carrier or catalyst) model

Mass balance for species "k" inside a catalyst particle volume

$$\varepsilon_s \frac{\partial C^s_k}{\partial t} = \frac{\varepsilon_s D_{eff,ks}}{\tau} \nabla^2 C^s_k + \rho_s r_k \qquad (7)$$

Where, ε_s is the porosity in the particle, $m^3_{pore}/m^3_{particle}$ and C_k^s is Kmol/ m^3_{pore}. $D_{eff,ks}$ is diffusivity of gas species k.

Energy balance for a catalyst particle volume

$$\rho_s C_{ps} \frac{\partial T^s}{\partial t} = \lambda \nabla^2 T^s + \rho_s \sum_l r_l \left(-\Delta H_{rx,l}\right) \quad 8$$

Boundary conditions for catalyst particles
Symmetry at r=0:

$$\frac{\partial C_k^s}{\partial r} = 0 \ \ and \ \ \frac{\partial T^s}{\partial r} = 0 \quad 9$$

Catalyst surface, r=R:

$$-\frac{\varepsilon_s D_{eff,k}}{\tau}\frac{\partial C_k^s}{\partial r} = k_g\left(C_{k,r=R}^s - C_k\right)$$
$$-\lambda\frac{\partial T^s}{\partial r} = h\left(T^s - T\right) \quad 10$$

For each particle configuration, the 3D CFD-DEM and DEM helps to determine the values of voidage (ε), the Blake–Kozeny–Carman constant (A) and Burke–Plummer constant (B) in Ergun Equation (2) , the heat transfer coefficient *h* and surface area per unit reactor volume *a* in Equation 6 (see Table 1). The current 1D model uses the reaction kinetics proposed by Abad et. al. (2011) for ilmenite in all the simulations. The 1D model is able to solve for this stiff reactions scheme as it uses an implicit backward differentiation formula for temporal discretization. The upwind scheme is used for the convective terms. The next section provides a brief description of the packed bed reactive CLC process and the validation result.

Chemical looping combustion and validation

The chemical looping combustion packed bed reactors involves cyclic gas-solid non-catalytic reactions, wherein the fixed packing (made of metal/metal oxide particles) is alternatively exposed to fuel gas stream (reduction cycle) and air stream (oxidation cycle). When exposed to the fuel gas stream (syngas), the metal oxide reduces. This reduction cycle results in production of hot stream of carbon dioxide and super-heated steam, which can be used for energy generation. The CO_2 is isolated by condensing steam. The reduced metal oxide bed is then exposed to the air stream, which re-oxidizes it. This exothermic oxidation cycle produces a stream of hot gas that can also be used for energy production. The reduction-oxidation cycle is then repeated continuously leading to power generation and CO_2 capture. The reaction system studied here is-:

$4FeO + O_2 \rightarrow 2Fe_2O_3$ (Oxidation with air)
$Fe_2O_3 + CO \rightarrow 2FeO + CO_2$ (Reduction with syngas)
$Fe_2O_3 + H_2 \rightarrow 2FeO + H_2O$ (Reduction with syngas)

In the present validation study, ilmenite (FeO-Fe_2O_3-TiO_2) is used as an oxygen carrier. Initially, it is in a fully reduced state (i.e. only FeO-TiO_2 is present and no Fe_2O_3 is present). The system is fed with air at inlet temperature of 650 ^{o}C and the initial bed is considered to be at the same temperature. As the oxygen is exposed to the solid ilmenite particle, the exothermic oxidation reaction takes place. The oxidation reaction continues till the particle is completely oxidized. A reaction front exists as a result of this process. These CLC processes are characterized by the presence of both the reaction front and the thermal front. Both these fronts are identifiable by temperature profile and concentration profile along the reactive bed. The movement of these fronts and the maximum temperature rise predicted by the 1D model is compared to that predicted by an analytical model (Noorman et. al., 2010). The maximum temperature that can be reached in the bed due to the heat liberated by the reaction front and due to the cooling down by incoming gas at the thermal front is obtained using an energy balance, which results in Equation 11. The analytical model provides equation 12 for computing reaction front velocity and Equation 13 for computing thermal front velocity.

$$\Delta T = \frac{\left(-\Delta H_{Rxn,l}\right)}{\frac{C_{p,s}M_s}{w_{sj}X_j\tau} - \frac{C_{p,g}M_g}{w_{g,k}^{in}}} \quad 11$$

$$w_r = \frac{\rho_g w_{g,k}^{in} v_g M_{si}}{\varepsilon_s \rho_s w_{s,j} X_j M_{g,k} \xi} \quad 12$$

$$w_h = \frac{\rho_g v_g C_{p,g}}{\varepsilon_s \rho_s C_{p,s}} \quad 13$$

As per the analytical model, the reaction front velocity is 1.12 x 10^{-2} m/s and the thermal front velocity is 1.43 x 10^{-3} m/s. The reaction front moves about an order of magnitude faster than the thermal front. Figure 5 shows that the 1D model is able to capture the movement of the reaction front and the thermal front quite accurately. The 1D model shows dispersion in reaction and thermal front as compared to the steep front predicted by analytical model. This dispersion is expected owing to the finite heat transfer rate and finite reaction rate in the actual operation (as is considered in the 1D model). The analytical solution assumes infinite reaction rate and infinite heat transfer rate, which is not a realistic condition. Analytically, predicted maximum temperature rise (equation 11) for the oxidation reaction is about 470 ^{o}C. So, the maximum temperature that can be reached in the reactor is about 1120 ^{o}C (Maximum temperature = Inlet air temperature + Max. temperature rise = 650 ^{o}C + 470 ^{o}C).

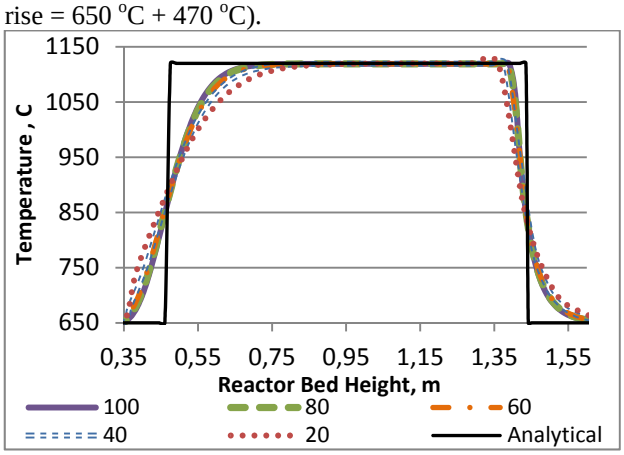

Figure 5 compares 1D model prediction of thermal front movement, reaction front movement and the maximum temperature rise with the analytical result. The results for 1D model are presented at several grid points (20,40,60,80 and 100) to check for grid independence.

Figure 5 shows that the 1D model predicts a maximum temperature of 1120 ^{o}C and the bed region between the thermal and reaction front is at this maximum temperature. Thus, the 1D model is able to capture the movement of the thermal and reaction fronts as well as the maximum temperature rise. This validates the use of the 1D model for the non-catalytic gas-solid operations like chemical looping combustion. The validated models have now been used in conjunction to implement the multi-scale approach for reactor design

APPLICATION OF MULTI-SCALE METHODOLOGY FOR OXYGEN CARRIER SELECTION AND CLC REACTOR DESIGN

Figure 6 and 7 compares the performance of seven different particle shape/size configurations for a 500KW fixed bed CLC reactor operation (height 1.5m and diameter 0.3 m) with air fed at 0.81 Kg/s for oxidation and syn-gas fed at for 0.078 Kg/s (corresponding to 500KW inlet heat) for reduction cycle. The comparisons are made for bed conversion, fuel-slip, pressure drop and cycle-time. The closures obtained for different particle configurations by 3D CFD-DEM has been used (See Table 1) by the 1D model. All the 1D simulations have been done using 80 grid points as the solution becomes grid-independent (see Figure 5). The packing configuration that can provide: (a) lower pressure drop, (b) higher reactivity, (c) Zero or minimal fuel--slip, and (c) lower cycle-time operation should be selected for the chemical looping combustion operation.

Table 1 show that some of the particles being studied have the same particle volume (same effective diameter of 7.5mm) but different shapes (sphere-7.5mm, cylindrical pellet with Aspect ratio (AR) of 1, pellet with Aspect ratio of 2 and pellet with Aspect ratio of 7). This will help to understand the effect of shape for a given size.

Particle Shape and size (effective diameter, actual diameter and height)	**For Ergun Equation (constants A and B in Equation 2).**		**For Ranz-Marshal for *h* in Eqn 6.**	**Voidage and Surface Area per unit Reactor Volume, m^{-1}**
	A	**B**	**A_c**	
Sphere (3mm, 5mm and 7.5mm)	**150**	**1.75**	**1.8**	**0.4 voidage & 1200 m^{-1} (for 3mm), 780 m^{-1} (for 5mm) and 486 m^{-1} (for 7.5mm).**
AR 1 d_{eff} =7.5mm & d_{actual}=6.4mm, h_{actual}= 6.4mm	**310**	**4.56**	**1.8**	**0.42 & 538 m^{-1}**
AR 2 d_{eff} =7.5mm & d_{actual}=10.26mm, h_{actual}= 5.12mm	**180**	**2**	**1.8**	**0.44 & 545 m^{-1}**
AR 7 d_{eff} =7.5mm & d_{actual}=3.4mm, h_{actual}= 23mm	**210**	**2.5**	**1.65**	**0.545 & 577 m^{-1}**
Fluted Ring, AR = 1.4 d_{eff} =14mm & d_{actual}=12.4mm, h_{actual}= 17.3mm	**253**	**2.21**	**1.68**	**0.53 & 560 m^{-1}**

Table 1. Closures for 1D model from DEM & 3D CFD-DEM.

We also study the effect of size by varying the size for a given spherical shape (3mm, 5mm size and 7.5mm) and a fluted ring with 14 mm effective diameter. All the particles are composed of ilmenite and the reaction kinetics proposed by Abad et. al. (2011) has been used in all the cases. Some of these ilmenite based particle shapes/sizes are being considered for the demonstration scale chemical looping combustion operation at Puertollano, Spain under the EU DemoCLOCK project. This scenario offers an ideal platform for developing and implementing the proposed multi-scale approach using validated models. The results are described below.

For reduction cycle, Figure 6A compares the Fe_2O_3 conversion profile along the length of bed after 60 s of reduction cycle operation for 7 different packing, while Figure 6B shows the overall Fe_2O_3 conversion as a function of time. The reaction front moves the fastest for Aspect ratio 7 packing (Figure 6A) and the whole bed is reduced within 74 s (as seen in Figure 6B). In terms of fastest bed conversion (or fastest reaction front), Aspect ratio 7 is followed by Aspect ratio 2, then the spherical pellets, the Aspect ratio 1 pellet and the Fluted ring. Similar trends are observed for oxidation cycle as well (Figure 7A). These trends are because the voidage of the packing structure increases as pellet aspect ratio increases (as predicted by DEM). Higher voidage results in lower amount of solid mass to be converted in the reactor bed. Figure 3 and Table 1 shows that the DEM predicted voidage for Aspect ratio 7 pellet packing is the highest followed by Aspect ratio 2, followed by spherical particles and Aspect ratio 1. The spherical particle and Aspect ratio 1 pellet shape have more compact packing (less voidage and more mass in the reactor) than the high aspect ratio pellets as a result they need more reactor operation time for complete bed conversion (as seen in Figure 6B-7B and Figure 6A-7A for both the oxidation and reduction). Figure 6A-7A shows that reaction fronts of Aspect ratio 1 and spheres (3mm, 5mm and 7.5mm) move with similar velocity, but have varied dispersions along the similar 'mean' front locations. The dispersion in reaction front increases as the size of sphere increases. The slower the effective reaction rate, higher is the dispersion of the reaction front around the mean location. The reason for this dispersion is the mass-transfer limitations accounted by the particle model of 1D particle-reactor model. As the diameter of sphere increases from 3mm to 7.5mm, the mass-transfer diffusional limitations increases and the effective overall rate of reaction decreases, leading to a more dispersed reaction front for higher diameter spheres. Similarly, the Aspect ratio 1 pellet shows more dispersion in reaction front than Aspect ratio 2 and Aspect ratio 7 pellet. This is because for the same particle volume, the actual diameter of pellets increases with decreasing aspect ratio ($diameter_{AR1}$ > $diameter_{AR2}$ >$diameter_{AR7}$). Thus, the Aspect ratio 1 offers higher mass-transfer diffusional resistance to the reactant gaseous species than Aspect ratio 2 and Aspect ratio 7 pellet.

Now, the Fluted Ring packing also has a higher voidage and very less mass within the reactor (equivalent to Aspect ratio 7 pellet), and even the total particle surface area available is comparable to Aspect ratio 7, so one would expect a quick complete bed conversion

(similar to Aspect ratio 7 case). However, as Figures 6B and 7B reveal that at any given time, the Fluted Ring bed is the least converted amongst all and the bed is not completely converted even after 150 s of reactor operation (only 91% conversion). Figure 6A and 7A reveals that Fluted Ring has the most diffused reaction front amongst all the particles (suggesting a very slow effective rate of reaction). The Fluted Ring has the largest particle diameter amongst all the particles and the mass transfer resistances encountered by the gaseous species would reduce the overall effectiveness. The 1D model is able to capture the mass-transfer limitation within the particle. The mass-transfer limitation dominates the faster intrinsic rate kinetics leading to slower conversion of the fluted ring particle.

Thus, a study of conversion profiles reveal that the Aspect ratio 7 pellet and 3 mm sphere particles offer high reaction rates (owing to lower mass-transfer limitations), while Aspect ratio 7 and Aspect ratio 2 packing results in a faster moving reaction front (owing to higher voidages and lower mass). A study of fuel-slip and pressure drop will enable us to make proper choice.

Figure 6C shows the fuel-slip time for the reduction operation. An early fuel-slip of reactant CO and H_2 will disallow any efficient isolation and capture of CO_2 from the exit-gas stream, thus leading to an unsuccessful operation. An early fuel-slip can occur owing to slower effective reaction rate (i.e. diffused reaction front) caused by mass-transfer limitations. The CO fuel-slip is known to occur earlier than hydrogen fuel slip in all the cases (owing to slow effective rate of reaction of CO). Hence we analyze the CO-slip results to compare the different packed beds. A good packing configuration is where the onset of fuel-slip occurs when nearly most of the bed is converted (i.e. when the reaction front reaches the end). Figure 6C and 6B indicate that the onset time of fuel-slip is better for 3mm sphere (75% bed reduced), followed by Aspect ratio 7 (60% bed reduced), 5mm and 7.5mm spherical particles (nearly 60% reduced), Aspect ratio 2 pellet (40% bed reduced) and Aspect ratio 1 pellet (30% bed reduced). This is expected as the reaction rate is higher for 3mm sphere and the Aspect ratio 7 pellet (as indicated by the sharpness of reaction front) than others. Their high reactivity can be explained on the basis of low diffusional resistances (owing to lower particle diameter) and high particle surface area per unit reactor volume.

Amongst the particle of same volume (i.e. same effective diameter of 7.4 mm but different shape, as shown in Table 1), Aspect ratio 7 provides the highest surface area per unit reactor volume (577 m^{-1}) and the lowest diffusional resistance. For both 3mm sphere and Aspect ratio 7 packed bed, by the time the CO exit gas concentration reaches 5%, almost the entire bed is converted.

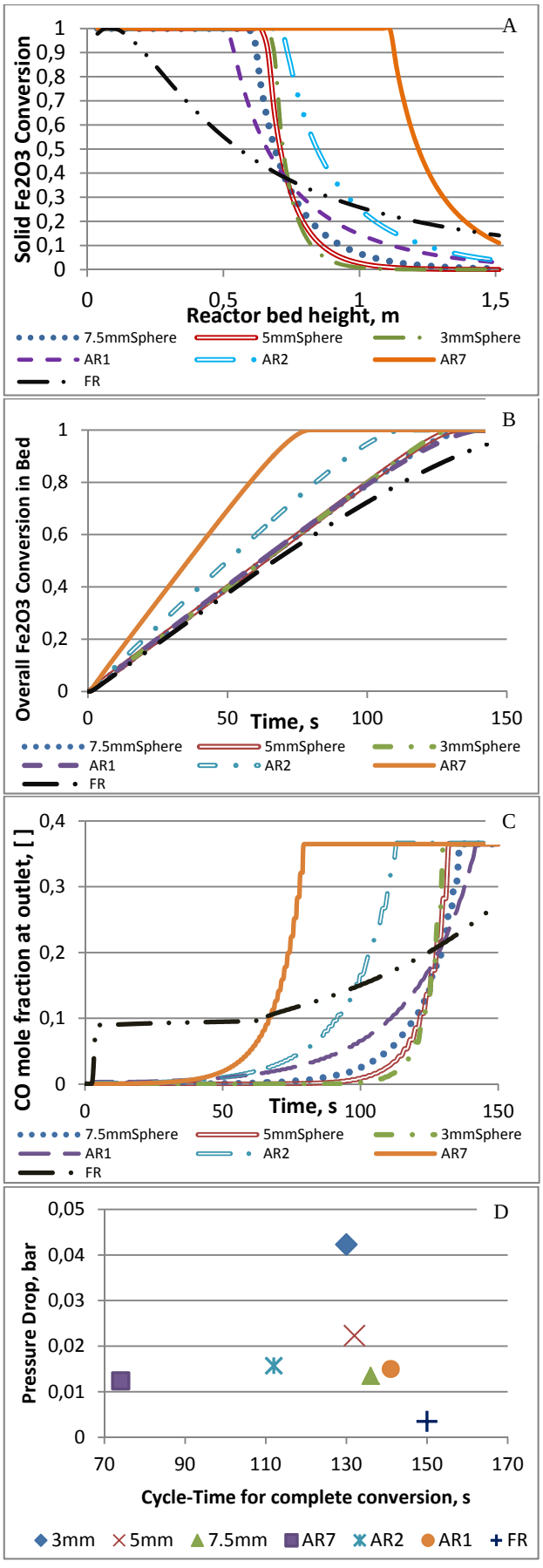

Figure 6 Particle selection for **reduction phase**: comparison of seven different particle configurations : (A) Conversion (Reaction front movement) after 60 s of reactor operation, (B) Overall conversion at a given time, (C) Fuel-slip at reactor exit and (D) Pressure drop and Cycle-time for each particle shape.

With regards to the process, the 14mm Fluted ring can be safely rejected for this CLC application due to a substantial early fuel-slip. This is owing to high mass-transfer limitation that causes a highly diffused reaction front.

Figure 6C and 6B shows that for fluted ring, the fuel slip occurs within first 10 s of reactor start-up and the outlet CO concentration suddenly reaches 10% even though the overall bed is only 5% reduced. Thus, based on the fuel-slip and bed-conversion (reactor bed-utilization) criteria, the Aspect ratio 7 and spherical pellets seem to be good possible choices. However, one needs to look at the pressure drop as well. A higher pressure drop can lower the reaction rate and increase the operating cost. A pressure drop high enough to overcome the weight of the bed can fluidize it or blow it. So, pressure drop is an important criterion.

Figure 6D and 7D shows the pressure drop and cycle-time for packing of each packing configuration for reduction and oxidation, respectively. The figure reveals that the pressure drop is highest for the 3mm sphere followed by 5mm sphere, and is the lowest for the Aspect ratio 7 pellet and fluted ring. The higher particle surface area and lower voidage offered by the 3mm sphere packing ensures that fluid experiences high viscous or skin friction resistance, which results in a higher pressure drop. The pressure drop reduces with increasing sphere size, as is expected. Amongst the particle of same volume, the high voidage in the Aspect ratio 7 packing ensures a lower pressure drop. Though, the pressure drop could have been higher for Aspect ratio 7 and Fluted Ring owing to their higher non-sphericity (which results in higher values of Blake–Kozeny–Carman constant value and the Burke–Plummer constant in the modified Ergun equation, See Table 1) and a higher surface area per unit volume (that can cause higher viscous resistances), but the effect of loose packing (higher voidage) offsets these factors.

From the results of both the oxidation and reduction cycle, it seems that Aspect ratio 7 pellet packed bed can be a good choice as it offers the least pressure drop and high reactivity. In addition, it has a fast moving reaction front that ensures lower cycle-time (thus, lower operating cost) for demonstrating the CLC process. The Aspect ratio 7 pellet performs better than Aspect ratio 2, Aspect ratio 1 and spherical particle of the same particle volume. The alternative can be the 3mm sphere, for which the operating costs could be higher owing to higher pressure drop and higher cycle time (as more mass of catalyst fits in the reactor bed due to low voidage) than the Aspect ratio 7 pellet. However, before finalizing any particle, the ability of the particles to withstand the thermal, chemical and mechanical stress owing to a high temperature-high pressure cyclic operation must be experimentally tested.

Thus, this work has demonstrated the use of a novel multi-scale model in selecting an oxygen carrier for a packed bed chemical looping combustion operation. This methodology can also be applied to create a new catalyst shape and analyze its performance for a catalytic gas-solid reaction.

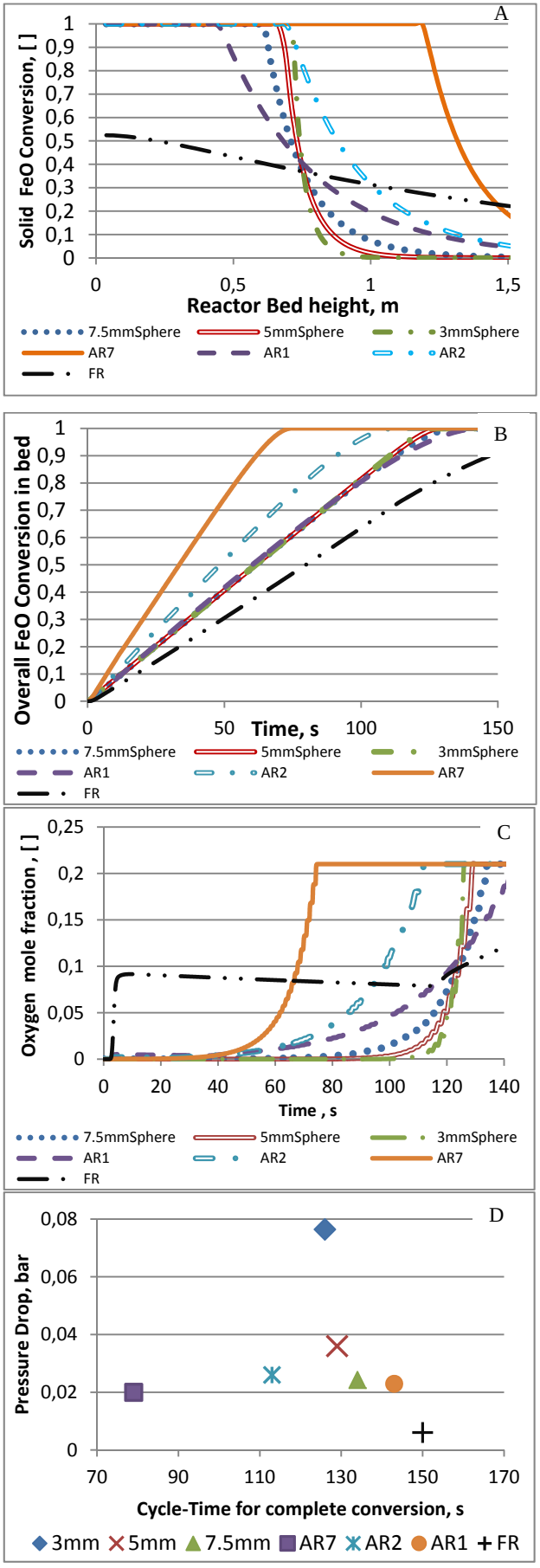

Figure 7 Particle selection for **oxidation phase**: comparison of seven different particle configurations : (A) Conversion (Reaction front movement) after 60 s of reactor operation, (B)

Overall conversion at a given time, (C) Fuel-slip comparison and (D) Pressure drop and Cycle-time for each particle shape.

CONCLUSION

A multi-scale modelling approach is developed for enabling oxygen carrier selection and reactor design. The approach can potentially be used for catalyst design. The multi-scale approach involves a 3D CFD-DEM (Computational Fluid Dynamics and Discrete Element Method) simulation in-combination with a multi-domain 1D particle-reactor model. In this multi-scale approach, a representative segment of the packed bed (generated by DEM) is simulated using CFD to obtain correlation for pressure drop and heat transfer coefficient. These correlations along with the information on packing structure (i.e. porosity and surface area per unit reactor volume obtained from the DEM generated packing) have been used by the 1D particle-reactor model. The 1D model, which includes the inter-particle and intra-particle limitations, is used for simulating the large scale packed bed reactor. The multi-scale approach provides a faster and reasonably accurate means of comparing the effect of oxygen carrier (or catalyst or pellet shape) on reactor performance.

The multi-scale model has been applied to compare performance of different particle configurations (spherical, Aspect ratio 7 pellet, Aspect ratio 2 pellet, Aspect ratio 1 pellet and fluted ring) for a gas-solid non-catalytic chemical looping combustion packed bed reactor. For particles of same equivalent diameter (volume), the Aspect ratio 7 pellet filled reactor offers the least pressure drop, highest reactivity and provides a lower cycle-time operation as compared to spherical pellets and other low aspect ratio cylindrical pellets. The higher voidage created by the aspect ratio 7 packing is the reason for the lower pressure drop. Further, the high surface area per unit reactor volume and lower actual pellet diameter (low diffusional resistance) of aspect ratio 7 packing leads to high catalyst effectiveness, faster reaction rates and avoids early fuel-slip. The 14mm fluted ring offers higher diffusional limitations that results in slower reaction rates and early CO fuel slip is rejected as it will prohibit the isolation and capture of CO_2.

Thus, the work has successfully demonstrated a novel multi-scale modeling approach involving 3D-DEM-CFD-1D model for selecting optimum size/shape of pellets for a packed bed reactor operation. This methodology can be applied to create new particle shapes and analyze their performance (for catalyst design) and for studying pre-existing shapes (like tri-lobe quadrulobe, monoliths, wagon wheels, hollow extrudates, discs etc.).

ACKNOWLEDGEMENT

A POP-SEP funding from SINTEF has been used for the 1D particle-reactor model software development. The multi-scale model development has been carried out as a part of the DemoCLOCK project, which is an EU FP7 funded project under the ENERGY.2010.6.1-1 programme.

REFERENCES

ABAD, A., ADÁNEZ, J., CUADRAT, A., GARCÍA-LABIANO, F., GAYÁN, P., AND DE DIEGO, L. F. (2011), "Kinetics of redox reactions of ilmenite for chemical-looping combustion", *Chemical Engineering Science*, **66**, 92-97.

BEY, O., AND EIGENBERGER, G., (1997) , "Fluid flow through catalyst filled tubes", *Chem Eng Sci*, **52,** 1365-1376.

CAULKIN, R., JIA, X., FAIRWEATHER, AND M.. WILLIAMS, R.A, (2012), "Predictions of porosity and fluid distribution through nonspherical-packed columns", *AIChE Journ*al, **58**, 1503-1512.

COLLEDGE, R.A.P. AND PATTERSON, W. R., (1984) , "Heat Transfer at the Wall of a Packed Bed: A j-Factor Analogy established", *11th Annual Research Meeting; Institution of Chemical Engineers: Bath*, 6 .

DIXON, A.G. AND LABUA, L.A., (1985), Wall-to-fluid coefficients for fixed bed heat and mass transfer, *International Journal of Heat and Mass Transfer*, **28,** 879-881.

DIXON, A.G., (1988), Correlations for wall and particle shape effects on fixed bed bulk voidage, *Canadian Journal of Chemical Engineering*, **66,** 705-708.

DEKLERK, (2003) "Voidage variation in packed beds at small column to particle diameter ratio", *AIChE Journal*, **49,** 2022-2029.

ERGUN, S., Fluid Flow through Packed Columns, *Chem. Eng. Prog*, **48** (1952) 89.

GIESE, M., ROTTSCHÄFER, K., AND VORTMEYER, D., (1998), "Measured and Modeled Superficial Flow Profiles in Packed Beds with Liquid Flow", *AIChE Journal*, **44** , 484-490.

INGRAM, G.D., CAMERON, I.T., AND HANGOS K.M., (2004), "Classification and analysis of integrating frameworks in multiscale modelling", *Chem Eng Sci*, **59** 2171-2187.

NEMEC, D. AND LEVEC, J., (2005), "Flow through packed bed reactors: 1. Single-phase flow", *Chem Eng Sci*, **60** , 6947-6957.

NOORMAN, S., VAN SINT ANNALAND, M., AND KUIPERS, J. A. M, (2010), "Experimental validation of packed bed chemical-looping combustion", *Chemical Engineering Science*, **50**, 1968-1980.

RANZ, W.E. AND MARSHALL, (1952), W.R. "Evaporation from Drops, Part II.", *Chem. Eng. Prog.* , **48,** 173.

ROBLEE, L.H.S., BAIRD, R. M. AND TIERNEY, J. W., (1958) , "Radial porosity variations in packed beds", *A.I.Ch.E.J.*, 460-464.

TABIB, M.V., JOHANSEN, S.T., AND SHAHRIAR, A., (2013), "A 3D CFD-DEM methodology for simulating industrial scale packed bed Chemical Looping Combustion reactors", *Industrial and Engineering Chemistry Research*, **52** (34) 12041–12058.

WAKAO, N., KAGUEI, S., AND FUNAZKRI, T. (1979), "Effect of fluid dispersion coefficients on particle-to-fluid heat transfer coefficients in packed beds: Correlation of nusselt numbers", *Chem. Eng. Sci*., **34**, 325−336.

CFD SIMULATIONS OF FLOW IN RANDOM PACKED BEDS OF SPHERES AND CYLINDERS: ANALYSIS OF THE VELOCITY FIELD

Ferdaous DORAI[1], Matthieu ROLLAND[1*], Anthony WACHS[1], Manuel MARCOUX[2], Eric CLIMENT[2]

[1] IFPEN, Rond-Point de l'Échangeur de Solaize, 69390 Solaize, France

[2] IMFT, 1 Allée du Professeur Camille Soula, 31400 Toulouse, France

* E-mail: matthieu.rolland@ifpen.fr

ABSTRACT

In this work, we aim to better understand the flow patterns in a random arrangement of particles that might affect local mass transfer and effective reactor performance.
Using the DEM code Grains3D, spherical or cylindrical particles are randomly inserted inside a horizontally bi-periodic container and fall under gravity. Hydrodynamic simulations are performed with PeliGRIFF, a Fictitious Domain/Finite Volume numerical model. Simulations parameters are the bed height and particulate Reynolds number. Effect of random packing on the flow field is analysed in terms of the probability distribution function (PDF) of the normalized vertical velocity.
A higher Reynolds number makes more backward flow zones and changes the PDF curves that we interpret as thinner boundary layers.
Unexpectedly, internal variability is independent of bed height. We propose that the probability of occurrence of random structures increases with bed volume in opposition with volume averaging effects.
Internal and external variability are similar for beds of spheres and cylinders of aspect ratio (< 2). However, for longer cylinders (higher aspect ratio), subdomains with same thickness are statistically different from one bed to another. We propose that the subdomain thickness required to average out sources of variability increases with high particle aspect ratio.

Keywords: Chemical Reactors, packed beds, velocity distribution, probability density function.

NOMENCLATURE

Greek Symbols

ρ Fluid density, [kg/m^3].

μ Dynamic viscosity, [kg/m.s].

ε Porosity (void fraction)

Latin Symbols

a Aspect ratio of a cylinder (length /diameter of cylinder)

d Particle equivalent diameter, [m].

l Cylinder length, [m].

P Pressure, [Pa].

U Velocity, [m/s].

Subscripts

c relative to a cylinder

s relative to a sphere

ls liquid, superficial

z vertical direction

INTRODUCTION

In this study, we are interested in small size fixed bed reactors which contain spherical or cylindrical catalysts with a characteristic size of 2-3 mm. These reactors are used to test small amounts of catalyst and are *a priori* more prone to random effects than industrial reactors.
Reactive testing performed inside these reactors involves complex mass transfer interactions between the fluid flow and reaction in the particles. In this paper, we are interested in the flow patterns in random packed beds. In literature, flow distributions are obtained using either an experimental approach (PIV (Particle Image Velocimetry), NMR (Nuclear Magnetic Resonance imaging), MRI (Magnetic Resonance Imaging) ...) or a numerical one. Concerning numerical works in random packing, Maier (1998) performed Lattice-Boltzmann simulations to study viscous fluid flow in a column of glass beads. He found that the velocity distribution is affected by bed porosity and Reynolds number. Rong (2013) performed also Lattice-Boltzmann simulations inside periodic randomly beds of mono-disperse spheres with porosity ranging from 0.37 to 0.8. However, the aforementioned studies do not study and quantify the local variability inside the bed.

The purpose of this work is to give a quantitative information of local velocity field and to link this information to internal and external structural variabilities. Internal variability is defined as variability within a bed, whereas external variability is defined as the difference arising between two random beds.
Numerical simulations for packed beds of spheres and cylinders are performed. We study the effect of Reynolds number, packed bed heights, and local random structure (repeatability) on velocity distributions.

SIMULATIONS DESCRIPTION

In order to examine the flow through packed beds of catalysts, simulations of packed beds of mono-disperse spheres and cylinders were performed in single phase flow in laminar regime (Re<15). The packing is created using the DEM (Discrete Element Method) code Grains3D (Wachs et al. (2012)). Particles are randomly inserted inside a container. They fall from the top under gravity and collide with each other and the bottom of the reactor. The boundary conditions used are periodic in the horizontal directions. Hydrodynamics simulations are performed with PeliGRIFF (Wachs (2010)), using the packing created with Grain3D. The meshing of the fluid domain is based on a cartesian structured grid with a constant grid size in the 3 directions. The CFD boundary conditions are: periodic boundary conditions in the same directions as the DEM simulations, uniform vertical upward velocity in the inlet (bottom wall of the domain) and uniform pressure in the outlet of the domain (top wall of the domain).
The simulations performed for spheres and cylinders are summarised in Table 1.

Table 1: Simulated cases for spheres and cylinders packed beds

Case Label	Particle size (mm)	Reynolds Number	Particles number	Number of repetitions of packing
S1-0.07	$d_s = 3$	0.07	540	1
S1-0.7	$d_s = 3$	0.7	540	1
S1-7	$d_s = 3$	7	540	10
S1-14	$d_s = 3$	14	540	1
S2	$d_s = 3$	7	1000	1
S3	$d_s = 3$	7	1500	1
S4	$d_s = 3$	7	2000	1
C2	$l_c = 2$ $d_c = 1.6$	0.37	380	3
C3	$l_c = 3$ $d_c = 1.6$	0.43	250	3
C4	$l_c = 4$ $d_c = 1.6$	0.47	180	3

Particulate Reynolds number is based on the equivalent diameter (diameter of a sphere of the same volume). It is defined as follows:

$$\mathrm{Re} = \frac{\rho \boldsymbol{U}_{ls} d}{\mu} \qquad (1)$$

In Figure 1-a and b, bed S1 is presented showing the CFD boundary conditions and the mesh used. For S1, the computational domain dimensions are $6d_s*6d_s*17d_s$ (which corresponds to 18 mm*18 mm*51 mm) with entry and exit zones. The spatial resolution used (20 points / particle diameter) gives a computational domain composed of about 5 millions of cells. This resolution has been set after a convergence study toward exact analytic solutions of pressure loss in various packed beds.

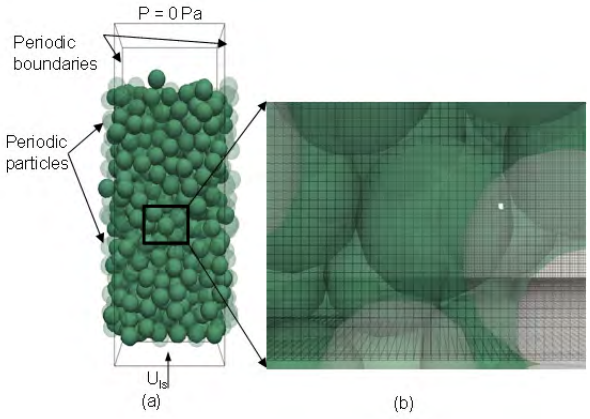

Figure 1: (a) Simulated packed bed of monodisperse spheres (S1) and (b) mesh of the geometry

For packed beds of cylinders, we considered 3 classes of cylinders with the same diameter d_c = 1.6 mm and an increasing length: 2 mm, 3 mm and 4 mm (Table 1). Each case was repeated three times. The bed height is approximately 40mm in all the cases (Figure 2). Particulate Reynolds number is below 0.5. The computational domain dimensions are 8 mm*8 mm*49 mm with entry and exit zones (below and above). The spatial resolution used (32 points / particle diameter) results in a computational domain composed of about 25 millions of cells. It has been chosen after a convergence study that showed that convergence was slower than for spheres Dorai et al. (2014).

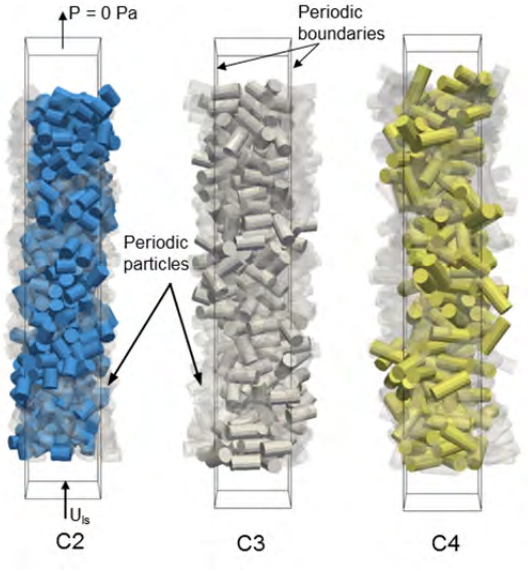

Figure 2: Simulated packed beds of monodisperse cylinders

ANALYSIS METHODOLOGY

Construction of PDF curves

The objective of this work is to compare the spatial velocity distributions for various cases and derive quantitative information for velocity fields in the case of random packed beds with low porosities (around 0.4). The analysis of the results is performed by considering the velocity field as the occurrence of a random variable such as described in Cedenese (1996), Rong (2013). Results are thus presented in the form probability

density functions (PDF) of the normalized vertical velocity (P (U_z / U_{ls})).
The PDF is constructed by first defining velocity classes, then, by counting the number of fluid cells whose velocity belongs to each class. At this step, we obtain a histogram that is converted to a PDF by normalizing the vertical velocity so that it satisfies equation (2).
As we use a large number of velocity classes (400), the information is better presented as a curve.

$$\int P(U_z / U_{ls})dU = 1 \qquad (2)$$

All PDF curves present the same general features (Figure 3): (i) in the left side, the proportion of negative velocity is negligible (about 1% of all occurrences), (ii) sharp peak near U_z /U_{ls}= 0, (iii) gradual decrease for velocities U_z /U_{ls} > 1 (the curve becomes flatter). These observations were also reported by Maier (1998) and Rong et al., (2013) for packed structures (ε~0.36). Rong observed bimodal shapes for loose structures and high Reynolds number.

Effect of entrance and exit regions

By dividing the bed in non-overlapping sub-domains of equal thickness in the vertical direction (= 2*d_s), it is possible to compare the velocity fields within a bed. The PDFs obtained by dividing S1-7 in 7 zones are plotted in Figure 3. Zone 7 (outlet, top of the bed) and the lower extent zone 1 (inlet) have distinct PDF shapes. In zone 7, porosity is much higher as there are some vacancies in the lattice due to lower densification by lack of impacting particles. In zone 1, the rigid flat bottom constraints the packing that is not as random as in the other subdomains. This has been reported and discussed elsewhere (Dorai, 2012). From here on, we will exclude from analysis all subdomains near the top and bottom of the packed beds (excluded zone thickness = 2*d_s for spheres and 2*d_c for cylinders).

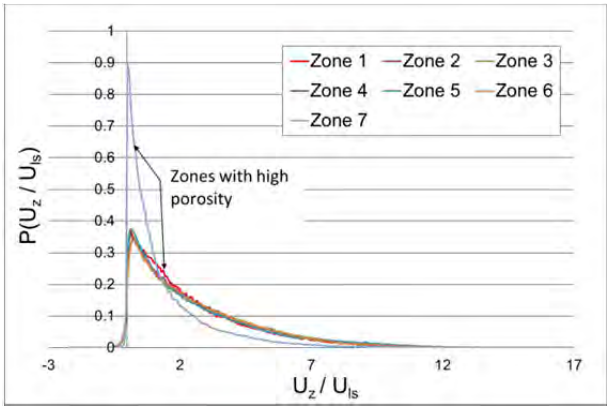

Figure 3: Effect of entrance and exit regions on PDF curves (bed S1-7)

PDFs comparison

Comparison of PDF curves has been performed with two methods: subtraction and statistical. Both methods require to have the same velocity classes for PDF curves. In the subtraction method, we compute the class to class difference between PDFs which is referred to as "PDF deviation" in the rest of the text. If the number of PDFs to compare is larger than 2, it is more convenient to subtract a common reference that should be chosen so as to represent some asymptotic or average case. When studying internal variability, the reference is the PDF of the whole bed (inlet and outlet excluded). If the focus is on external variability, the reference is chosen as the longest bed for length comparison or average of all PDF bed for repeatability. When comparing many PDF curves, after subtracting the reference, we calculate the "Maximum deviation function" that is constructed by choosing for each class the maximum deviation (absolute values) from the reference among all PDFs. Deviation functions are an indicator of the maximum variability within the domain studied. They do not respect equation (2).

Another way to compare PDF functions is to use the statistical "variance test" (Fischer test) that tests the hypothesis H_0 "PDF is identical for all domains". The statistical test is run for each velocity class. The variance test has been used to determine whether domains extracted from different beds present significant differences or not. In other words, can we distinguish a sub domain from another when they do not belong to the same bed.

RESULTS

Simulations with different Reynolds numbers

In this section, the effect of Reynolds number is studied in the same packed bed of spheres in laminar regime (S1, ε = 0.39). PDF curves are presented in Figure 4.

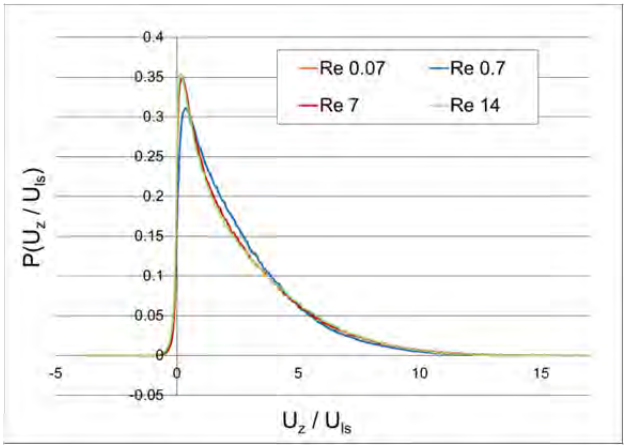

Figure 4: PDFs for different Reynolds numbers, bed S1

At very low Reynolds numbers 0.07 and 0.7 (creeping flow), curves are identical. The peak near 0 is more important for higher Reynolds number, which has also been reported in Rong et al. for ε = 0.5. In all cases, highest velocity can exceed 8*U_{ls}. At higher Reynolds number (7 and 14), there are more fluid cells with important velocity U_z / U_{ls} > 7 and less cells with small velocity (U_z / U_{ls} between 1 and 4) (Figure 5). We propose that increasing the Reynolds number leads to thinner boundary layers and increased number of fluid cells with high velocities.

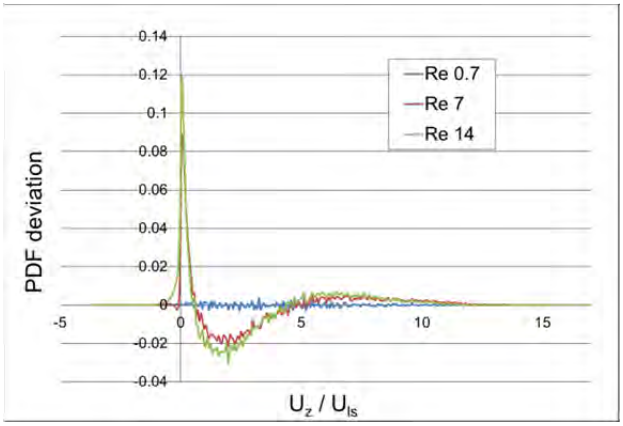

Figure 5: PDFs deviations calculated to PDF of lowest Reynolds number (0.07)

The proportion of negative vertical velocity (backward flow) is higher for higher Reynolds number (Figure 5 and Figure 6). This increase in proportion is more due to an increase in the number of backward flow zones rather than an increase in their size. For S1-14, the backward flow zones are homogeneously distributed in all domains.

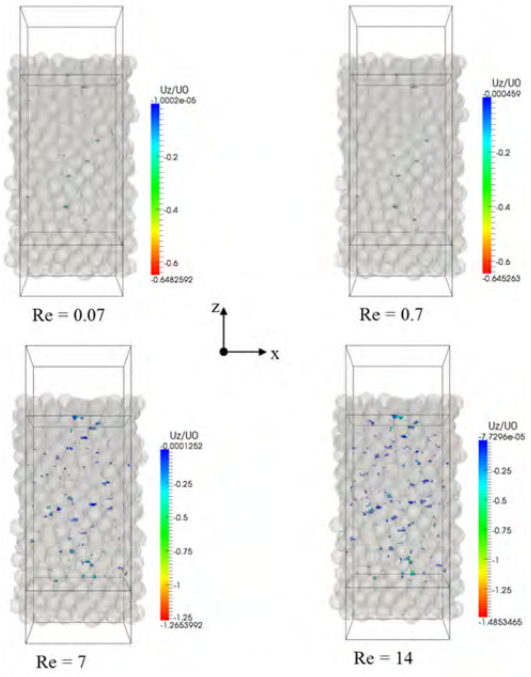

Figure 6: Zones with negative vertical velocity

Comparison of beds with different heights

Four packed beds of spheres (S1, S2, S3 and S4) are divided into regions with equal thickness ($2*d_s$). We calculated the deviation of PDFs in every region to the PDFs of longest packed bed (S4). We expected that maximum PDF variations would be higher for the shortest packed bed and that a longer bed would provide more averaging, which is not the case (Figure 7).
Moreover, the shortest bed (S1) presents less internal variability than the others. An explanation could be that increasing bed length increases the probability of occurrence of sources of variability, may-be from average random structures (tightly packed or loosely packed for example). In conclusion, bi-periodic long beds present the same internal variability as short ones.

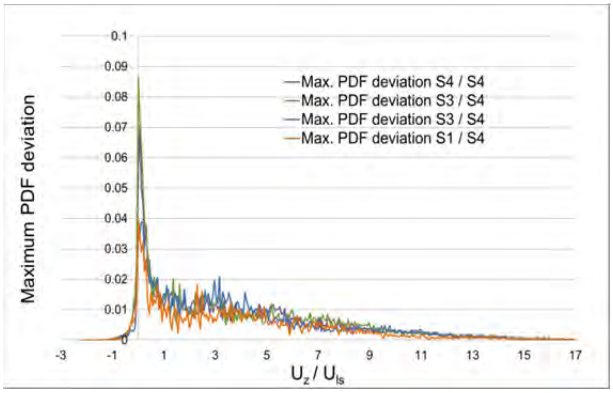

Figure 7: Maximum deviation functions calculated for S1, S2, S3 and S4 to mean PDFs of S4

External and internal variability for spheres

In this section, we want to know if there are any differences in flow structure in random packed beds composed of the same number of spheres (repetition of packing), and if these variations can be compared to the variations inside a given packed bed.
To answer the first question, we performed CFD simulation on 10 randomly packed beds with the same number of spheres; each bed has a different structure from the other. PDF deviation to the average PDF of all repeated cases indicate that some variability between beds is visible (Figure 8), for example “repeat5” bed present less “low velocity” cells and more “high velocity” cells than the average. Except near 0, deviation of all beds remains within a value of 0.003. It would be interesting to compare this value to the internal PDF variations (inside a single packed bed).

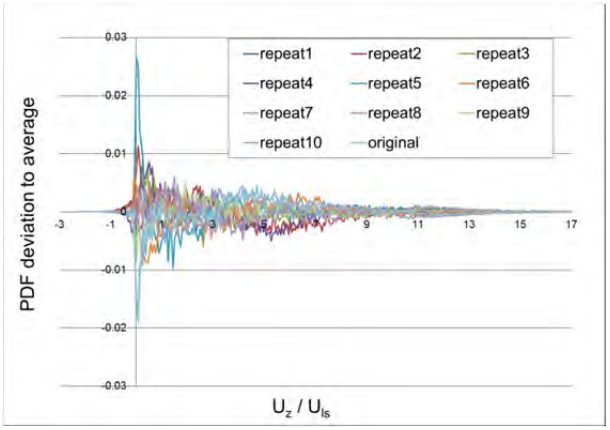

Figure 8: PDFs deviation to the average PDF of all repeated cases

To examine variability inside a bed, S1-7 is divided into domains of equal thickness ($2*d_s$) and PDFs deviations are calculated using the PDF of S1-7 as reference (Figure 9). In this case, except near 0, deviations are within a value of less than 0.01. Before comparing with the variations induced by repetitions (Figure 8), it is worth mentioning that the deviation to the average tends

to decrease linearly with the number of sub-domains used. For example, if we would use two sub-domains instead of five to produce Figure 9, then the deviation would be 2.5 times lower. As the external variability value of 0.003 has been obtained on domains of thickness $10*d_S$, and internal variability value of 0.01 has been estimated of domains of $2*d_S$, the external variability value on 10*ds subdomains in the order of 0.003*5, which is quite similar to the internal variability. We conclude that internal and external variabilities are very similar.

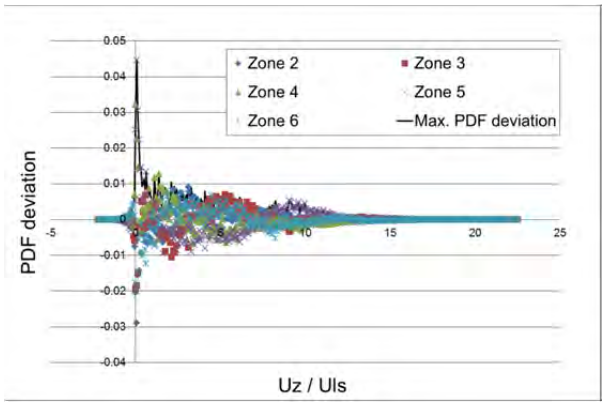

Figure 9: PDFs deviation calculated to the average PDF of all regions in S1

This conclusion is coherent with a variance analysis test performed on 5 sub-domains of S1-7 and 5 sub-domains of S1-7-repeat1. The analysis shows that for 99.5% of classes there is no statistical difference (at 5% risk) between S1-7 and S1-7-repeat1 sub-domains based on flow patterns.

External and internal variability for cylinders

Identical methodology has been applied to packed beds of cylinders with 3 repetitions on each cylinder length case. Variability between repeated beds is similar to that of spheres (Figure 10). Variability inside one bed is also of the same order of magnitude.

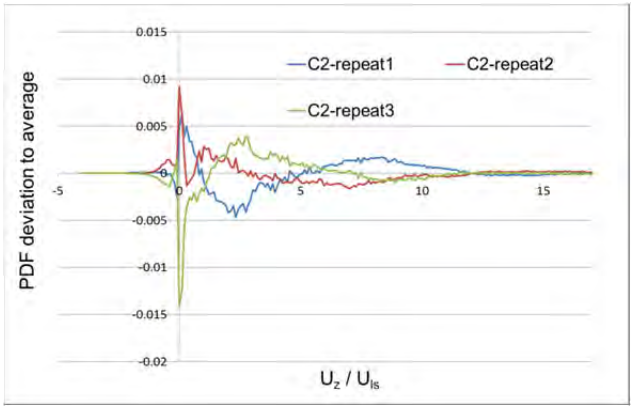

Figure 10: PDF deviation calculated to average PDF of repeated simulations of C2

The variance analysis gives a slightly more precise information. More classes are found to present difference between repetitions: 12.5 % of classes for C4 (a = 2.5), compared to 1.25 % and 0.25 % for C2 (a = 1.25) and C3 (a = 1.875) respectively. C2 and C3 appear to behave like packed beds of spheres: for aspect ratio up to 1.875, subdomains of thickness of $2*d_c$ present the same variability regardless of their origin (any location in any bed). On the opposite, for the highest aspect ratio case, subdomains of the same thickness are statistically different from one bed to another. It may be that higher particle anisotropy increases the minimum volume required to average out the sources of variability, also called Representative Elementary Volume (REV).

CONCLUSION

Simulations of fluid flow in bi-periodic packed beds of mono-disperse spheres and cylinders have been performed using a Fictitious Domain/Finite Volume numerical model. The simulations provide detailed information on the hydrodynamics and local velocity fields. Effect of random packing on the flow field is analysed by considering the velocity field as the occurrence of a random variable characterized by its probability distribution function (PDF).

- Top and bottom part of the packing are excluded from the analysis as they do not present the same flow patterns, due to lack of densification (top) and due to the presence of a flat surface (bottom) that prevents random positioning of particles on a layer of about two particle diameters.
- PDF curves for packed beds of spheres and cylinders have the same overall shape.
- A higher Reynolds number results in the presence of more backward flow zones and change in the PDF curves that we interpret as thinner boundary layers.
- Unexpectedly, internal variability is independent of bed height. We propose that the probability of occurrence of random structures increases with bed volume in opposition with volume averaging effects.
- Internal and external variability are similar for beds of spheres and cylinders of aspect ratio lower than 2. However, for longer cylinders (higher aspect ratio), sub-domains of the same thickness ($2*d_c$) are statistically different from one bed to another. We propose that the subdomain thickness required to average out sources of variability increases with high particles aspect ratio.

Perspectives are: to explore the link between shape and Representative Elementary Volume dimensions, to focus on how the presence of walls may change the results presented in this work and to perform simulations of reactive transport and study the link between structure, flow and reactivity variations in random packed beds.

REFERENCES

CENEDESE A., VIOTTI P., (1996), "Lagrangian analysis of nonreactive pollutant dispersion in porous

media by means of the particle image velocimetry technique", *Water Resources Research*, **32** (8), 2329-2349.

DORAI F., ROLLAND M., WACHS A., MARCOUX M., CLIMENT E., (2012), "Packing Fixed Bed Reactors with Cylinders: Influence of Particle Length Distribution", *Procedia Engineering*, **42**, 1335-1345.

DORAI F., DE MOURA T. C., ROLLAND M., CLIMENT E., MARCOUX M., WACHS A., (2014), "Fully-resolved simulations of the flow through a packed bed of cylinders: effects of size distribution", *under submission in Oil & Gas Science and Technology*.

GUNJAL P.R., RANADE V.V., CHAUDHARI R.V., (2005),"Computational Study of a Single-Phase Flow in Packed Beds of Spheres", *AICHE Journal*, **51** (2), 365-378.

MAIER R.S., KROLL D.M., KUTSOVSKY Y.E., DAVIS, H.T. BERNARD R.S., (1998), "Simulation of flow through bead packs using the lattice Boltzmann method", *Phys. Fluids*, **10** (1), 60-74.

RONG, L.W., DONG, K.J., YU, A.B., (2013), "Lattice Boltzmann simulation of fluid flow through packed beds of uniform spheres: Effect of porosity", *Chemical Engineering Science*, **99**, 44-58.

WACHS A., GIROLAMI L., VINAY G., FERRER G., (2012), "Grains3D, a flexible DEM approach for particles of arbitrary convex shape - Part I: numerical model and validations", Powder *Technology*, **224**, 374-389.

WACHS A., (2010), "PeliGRIFF, a parallel DEM-DLM/FD direct numerical simulation tool for 3D particulate flows", *Journal of Engineering Mathematics*, **71**, 131-155.

NUMERICAL MODEL FOR FLOW IN ROCKS COMPOSED OF MATERIALS OF DIFFERENT PERMEABILITY

R.R. LI[2], Y.S. YANG[1], J. PAN[2], G.G. PEREIRA[1*] ,J.A. TAYLOR[3], M.B. CLENNELL[4], C. ZOU[5]

[1] CSIRO, Private Bag 33, Clayton 3169, AUSTRALIA

[2] North University of China, School of Information and Communication Engineering, Shanxi, 030051, CHINA

[3]CSIRO, G.P.O. Box 664, Canberra, 2601, AUSTRALIA

[4]CSIRO, P.O. Box 1130, Bentley, 6102, AUSTRALIA

[5]Research Institute of Petroleum Exploration and Development (RIPED), PetroChina, Beijing, CHINA

* E-mail: Gerald.Pereira@csiro.au

ABSTRACT

In the oil and gas industry permeability measurements on rock samples give an indication of the capacity to produce the output (oil/gas etc). Permeability of small samples can be derived from x-ray Computed Tomography (CT) scans which yields a three-dimensional (binary) digital image of the sample. Then using suitable numerical tools, one can use this digital data to compute a velocity field and hence the permeability of the sample. Up to now, this has been done on the assumption that fluid can only flow in pores (with no flow in solid regions). However, if the sample is made up of different materials, each material can have a different permeability to fluid flow. Hence, here we consider numerical modelling of flow through such a material. We use the Lattice Boltzmann method to model this flow, but need to change the usual streaming and collision steps to account for the partial permeability of voxels. We first implement this new algorithm on some well-known test cases, with excellent agreement with analytic results and then use our algorithm on some real CT digital data. Our results clearly show the effect of increasing the local fraction of a high permeability material within a sample on the global permeability.

Keywords: Lattice Boltzmann, Computed Tomography scan, digital data, partial permeability.

NOMENCLATURE

Greek Symbols

ρ LB particle density, [dimensionless].
μ LB dynamic viscosity, [dimensionless].
ν LB kinematic viscosity, [dimensionless].

Latin Symbols

n_s solid fraction, [dimensionless].
p_f percolating fraction, [dimensionless].
P LB Pressure, [dimensionless].
f LB particle distribution function, [dimensionless].
$\boldsymbol{u}$ LB Velocity, [dimensionless].
c_s LB speed of sound, [dimensionless].
K LB Permeability [dimensionless].

Sub/superscripts

α LB velocity direction.
x Index x – Cartesian axis.
y Index y – Cartesian axis.
z Index z – Cartesian axis.

INTRODUCTION

Fluid flow in porous media is widely encountered in oil and gas development and production, in addition to various other physical and chemical processes. The Lattice Boltzmann model (LBM) has recently attracted considerable attention in fluid flow simulations in porous media. However, LBM simulations often require an explicit and discrete description of the underlying pore-space geometry. For some applications, such as with unconventional oil and gas reservoirs, the pore sizes encompassing length scales from the nm to mm are relevant. It is technically unfeasible to characterize the pores across such multiple length scales, and computationally unpractical to simulate fluid flow on them with the traditional LBM. As an alternative approach, a partial-bounce-back LBM was suggested by Dardis and McCloskey (1998a, 1998b), which is a meso-scale LBM approach that incorporates the permeability of the medium as a model parameter. Multiple neighboring voxels could be grouped together to form nodes. The LBM simulations were performed on a lattice consisting of such nodes. Rather than a lattice comprising nodes that are either solid or fluid, this is a probabilistic model, where lattice node properties are varied to reflect the local permeability of the material. Their model was inspired by earlier work with lattice gases in which variable permeability materials were simulated by introducing random scatters into the lattice (Balasubramanian *et al.*, 1987; Gao and Sharma, 1994). However, Dardis and McCloskey's (1992a, 1992b) Lattice Boltzmann approach avoided the statistical noise that is inherent in lattice gas models. To date, several different possible models have been proposed for formulating partial-bounce-back LBM approach, described in (Thorne and Sukop, 2004; Walsh *et al.*, 2009; Zhu and Ma, 2013). In all these models, a key parameter n_s, referred to as solid

fraction, is used. It is worth noting that the solid fraction should be regarded as an internal model parameter related to the permeability, rather than a reflection of the actual proportion of solid material at each node. An analytic expression that relates the permeability to solid fraction was derived by Walsh *et al.* (2009). As will be discussed in the next section, an effective percolating fraction p_f (equivalent to 1-n_s) would be a more appropriate notation.

For the existing partial-bounce-back LBM approach, it is required to determine n_s at every lattice node. The discrete internal structure of a node may be characterized approximately using X-ray CT together with an image segmentation method by Desrues *et al* (2006). The permeability of the node is calculated based on its internal structure. When the local permeability of a node was known, and it was homogeneous and isotropic, n_s for the node could be estimated using the equation given in Walsh *et al* (2009). A procedure for estimating the model parameter n_s is proposed in Zhu and Ma (2013). However, a typical sample may contain too many lattice nodes for this to work in practice. Even if the local permeability is estimated at a limited set of selected locations only, it is a non-trivial task to extrapolate them to other locations to obtain all the required n_s values.

It is worth noting that the existing LBM approaches are modeled on binary voxels. That is, a voxel is occupied by either solid or void. If a voxel is partial solid or void, the existing LBM is not applicable. Recently, a data-constrained modeling (DCM) approach has been developed which can generate microscopic partial volume distributions of materials and pores, therefore incorporating the effects of the fine length scale below X-ray CT resolution (Yang *et al*, 2007, Yang *et al*, 2008). In the model, each voxel was represented by partial volumes of various different materials rather than the binary value of only one material present in traditional image segmentation.

In this paper, the partial-bounce-back LBM approach is combined with the DCM partial volume model to simulate fluid flow in porous materials. The partial-bounce-back LBM is extended to incorporate such partial volume voxels at the microscopic length scale on a regular lattice. This enables more accurate permeability simulations for macroscopic samples with fine structures below voxel resolution. The effective percolating fraction p_f introduced in the advanced partial-bounce-back LBM is non-constant through the porous medium. The percolating fraction can be estimated using the volume fractions of the voxels. The advanced approach has been applied to simulate flow between parallel walls and in rectangular duct flow in 2D and 3D respectively. The permeability of two real world sandstone samples is also calculated with the presented method.

Note that we use a single relaxation time (SRT) implementation of the LBM method in this study. However, it is well known (Pereira *et al.*, 2012) that the permeability obtained from an SRT scheme is viscosity dependent. As such, to obtain viscosity independent results, one should use a multi-relaxation time (MRT) scheme. Since we are only demonstrating the feasibility of a new partial bounce-back approach, we implement the simpler SRT scheme in this paper and leave a full MRT scheme to future work.

MODEL DESCRIPTION

Partial-bounce-back Lattice Boltzmann model

The Lattice Boltzmann model is a numerical technique for modeling fluid dynamics. The fluid is represented by discrete fluid particles, with a given mass and velocity, which propagate on a lattice. At each time-step in traditional LBM method, the fluid particles undergo a two-step process:

(1) Streaming step: In this step, the fluid particles are propagated between neighboring nodes. Streaming should be treated as an intermediate step. The result after streaming is denoted by f^*_α:

$$f_\alpha^*(\mathbf{x}+\mathbf{e}_\alpha\Delta t,t) = f_\alpha(\mathbf{x},t), \qquad (1)$$

where, $f_\alpha(\mathbf{x},t)$ is the particle distribution function in the direction α, $\mathbf{x}$ is the centre coordinate of a lattice node and t is time, while Δt is the time increment. $\mathbf{e}_\alpha$ is the unit velocity vector in direction α. In this study, the two-dimensional 9-velocity (D2Q9) and three-dimensional 19-velocity (D3Q19) lattice Boltzmann models were used. That is, the direction α takes 9 and 19 discrete *values* respectively (which include the null vector).

(2) Collision step: In this step, the fluid particles, converging on individual nodes, are redistributed according to a set of predefined rules. Which rule is applied in the collision step depends on whether the node is part of the fluid domain or part of the solid-fluid boundary.

(I) If the node represents part of the fluid domain, then the evolution equation is

$$f_\alpha(\mathbf{x},t+\Delta t) = f_\alpha^*(\mathbf{x},t) + [f_\alpha^{eq}(\mathbf{x},t) - f_\alpha^*(\mathbf{x},t)]/\tau, \quad (2)$$

where, τ is the dimensionless relaxation time. In this study τ is taken to be one. $f_\alpha^{eq}(\mathbf{x},t)$ are the equilibrium distribution functions and selected according to a Maxwell distribution.

(II) If a lattice node is part of a solid-fluid boundary with no-slip conditions, then the fluid particles undergo a bounce-back boundary condition. As the name suggests, at these nodes, the incoming fluid particles are reflected in the opposite direction during the collision step. α' is the opposite direction of α:

$$f_\alpha(\mathbf{x},t+\Delta t) = f_{\alpha'}^*(\mathbf{x},t) \ . \qquad (3)$$

For porous media, the collision step (I) would be considered as a second intermediate step after streaming, and the partial-bounce-back method and collision step (II) were both incorporated into the third process, referred to as porous media step. Denoting f_α^{**} as the result of the collision step (I), at each time-step the fluid particles undergo a three-step process:

(1) streaming step:

$$f_\alpha^*(\mathbf{x}+\mathbf{e}_\alpha\Delta t,t)=f_\alpha(\mathbf{x},t)\ , \qquad (4)$$

(2) collision step:

$$f_\alpha^{**}(\mathbf{x},t+\Delta t)=f_\alpha^*(\mathbf{x},t)+[f_\alpha^{eq}(\mathbf{x},t)-f_\alpha^*(\mathbf{x},t)]/\tau\ , \qquad (5)$$

(3) porous media step:

$$f_\alpha(\mathbf{x},t+\Delta t)=f_\alpha^{**}(\mathbf{x},t+\Delta t)+n_s\cdot\Delta f\ , \qquad (6)$$

where, $n_s(\mathbf{x})$ is the solid fraction mentioned previously per lattice node $\mathbf{x}$. The density per node ρ and the macroscopic flow velocity $\boldsymbol{u}$ are defined in terms of the particle distribution function by (the D2Q9 model)

$$\sum_{\alpha=0}^{8} f_\alpha=\rho\ ,\ \sum_{\alpha=0}^{8} f_\alpha\,\mathbf{e}_\alpha=\rho\,\mathbf{u}\ , \qquad (7)$$

where the pressure is given by $P = c_s^2\rho$, and c_s is the speed of sound with $c_s^2=1/3$.

According to different partially bounce-back models, the term Δf has various forms. The following are three common forms:

(I) first form:

$$\Delta f = f_{\alpha'}(\mathbf{x},t)-f_\alpha(\mathbf{x}-\mathbf{e}_\alpha\Delta t,t)\ . \qquad (8)$$

This form was proposed by Dardis and McCloskey (1998).

(II) second form:

$$\Delta f = f_{\alpha'}^{**}(\mathbf{x}+\mathbf{e}_\alpha\Delta t,t+\Delta t)-f_\alpha^{**}(\mathbf{x},t+\Delta t)\ . \qquad (9)$$

This form was proposed by Thorne and Sukop (2004).

(III) third form:

$$\Delta f = f_{\alpha'}^{*}(\mathbf{x},t)-f_\alpha^{**}(\mathbf{x},t+\Delta t)\ . \qquad (10)$$

This form is proposed by Walsh *et al* (2009). It was demonstrated in this paper that only the third form can conserve mass in heterogeneous media.

Partially percolating Lattice Boltzmann model

In order to incorporate the partial volume effect into the traditional partial-bounce-back LBM, an effective percolating fraction p_f for each voxel is introduced to replace the solid fraction n_s. In the above, the first and second forms both use data from the neighbouring nodes to calculate the term Δf. This would create complications for parallel computation implementation. Significant data exchange and synchronization would be required between processors at each time-step. The third model has the advantage that the collision and porous media step are performed simultaneously without referring to neighbouring nodes. In the following, the third form was used which was named as partially-percolating Lattice Boltzmann model (PP-LBM).

Similar to the LBM approach for porous media, at each time-step in PP-LBM the fluid particles undergo a three-step process: streaming, collision, and porous media steps. The third step could be expressed as:

$$f_\alpha(\mathbf{x},t+\Delta t)=f_\alpha^{**}(\mathbf{x},t+\Delta t)+\left[1-p_f(\mathbf{x})\right]\cdot[f_{\alpha'}^{*}(\mathbf{x},t)-f_\alpha^{**}(\mathbf{x},t+\Delta t)]\ . \qquad (11)$$

SIMULATIONS IN REGULAR GEOMETRIES

Flow between parallel walls

With an incompressible fluid, Poiseuille flow is created between stationary parallel walls (which forms a channel) when a constant pressure difference ΔP is applied between the two openings at the end of the walls. The velocity distribution can be solved analytically. It is parabolic and is given by

$$u(y)=\frac{G\cdot(L-y)\cdot y}{2\mu}\ , \qquad (12)$$

where G is a constant pressure gradient, μ is the dynamic viscosity, L is the perpendicular separation between the two parallel walls so that fluid flows in the channel between $0\le y\le L$.

In order to evaluate the accuracy of the PP-LBM approach as described in Equations (4), (5) and (11), the flow is simulated numerically on a 51×101 square lattice with a D2Q9 model, where $0\le x\le 50$, $0\le y\le 100$, using pressure boundary conditions at the inlet and outlet. To model the impermeable walls, where we have a no slip boundary condition, we simply use $p_f = 0$. The lattice sites between the two walls were assigned the value $p_f = 1$. That is, it is fully void between the walls. For numerical convenience, the simulations were carried out using LBM units where the fluid density is $\rho = 1$, and the dynamic viscosity $\mu = 1/6$. The flow was driven by a constant pressure difference between the inlet and outlet of the flow region, which is generated using a pressure boundary condition in 2D (Zou and He, 1997, Hecht and Harting, 2010). The pressure difference is expressed as $\Delta P=c_s^2\,(\rho_{in}-\rho_{out})$, ρ_{in} is the density of nodes at the inlet with $\rho_{in}=1.00001$ and ρ_{out} is the density of nodes at the outlet with $\rho_{out} = 0.99999$. The value of the pressure difference is $\Delta P = 0.67 \times 10^{-5}$. A relationship between Reynolds number and pressure difference $\mathrm{Re}=\sqrt{(\Delta P/\Delta x)\cdot L^3\cdot\rho}/\mu$ is used to relate the LBM units to physical units. For a fluid with a density $\rho = 10^3$ kg/m^3 and a dynamic viscosity $\mu = 10^{-3}\,\mathrm{kg/m\cdot s}$, the value of constant pressure difference is $\Delta P = 1.5 \times 10^{-5}$ Pa. When the flow reaches a steady-state, the fluid speed depends only on y. The simulation results and the analytic solution are shown in Figure 1. The figure shows an excellent agreement between the analytical solution and the PP-PBM numerical results.

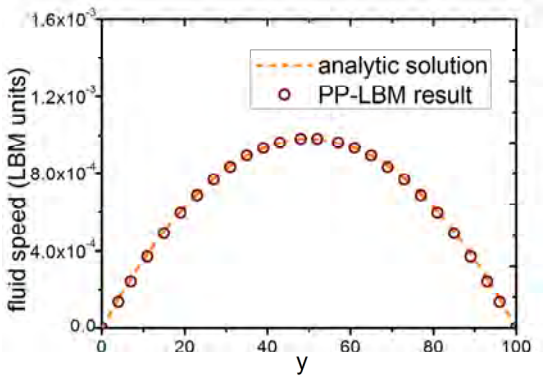

Figure 1. PP-LBM simulation of flow between parallel walls. Analytical solution from Eq. (12) is shown as solid lines and the PP-LBM numerical results at x=25 are shown as circles.

When pixels between the two non-percolating walls are partially percolating with p_f < 1, the fluid velocity distribution is quite different. This problem can also be solved analytically (Balasubramanian, 1987). The solution is expressed as

$$u(y) = -\frac{G}{\varphi\rho}[1-\frac{\cosh[r(y-L/2)]}{\cosh(r\cdot L/2)}] \ , \qquad (13)$$

where φ is a damping coefficient proportional to 1-p_f. φ and r are related through $r=\sqrt{\varphi/\nu}$ and $\nu=\mu/\rho$ is the kinematic viscosity. As $\varphi \to 0$, the solution (13) returns to the standard Poiseuille equation. As additional verifications of the PP-LBM approach, various uniform values of the effective percolating fraction p_f between the non-percolating walls have been simulated from 0.01 to 0.9. Again, the steady-state flow speed depends only on *y*. The simulated speed distributions (symbols) for various uniform values p_f, as a function of *y*, are shown in Figure 2. The analytic results (continuous curves) are also included in Figure 2. Excellent agreement has been obtained between the PP-LBM numerical simulations and analytic solutions. In addition, our numerical results show no abnormal behaviour for all values of p_f in (0, 1). In contrast, the model by Dardis and McCloskey has produced obvious errors near the boundaries for p_f < 0.7 (Chen and Zhu, 2008).

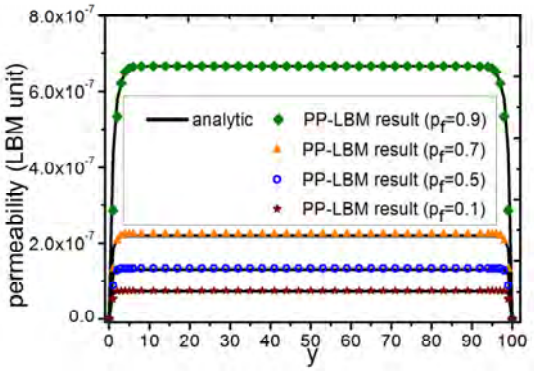

Figure 2. Simulation results when the percolating fraction changed. Analytical solutions from Eq. (13) are shown as solid lines and the PP-LBM numerical results at x=25 are shown as markers.

Flow in a rectangular duct

For a duct with a rectangular cross section, the same pressure difference ΔP creates a quasi-parabolic velocity distribution when the effective percolating fraction is p_f = 1. It can be calculated that the product of the friction coefficient f (a dimensionless variable which quantifies the overall viscous drag) and the Reynolds number Re is a constant. This quantity is given by (Tao and Xu, 2001)

$$f\cdot \mathrm{Re} = \frac{2\cdot\Delta P\cdot de^2}{\mu\cdot L_z\cdot\bar{u}}, \qquad de=\frac{4\cdot L_x\cdot L_y}{2(L_x+L_y)} \ , \ (14)$$

where L_z is the duct length along the *z* axis in the flowing direction, L_x, and L_y are the duct widths in the *x* and *y* directions respectively. $\bar{u}$ is the average velocity of a cross section.

As another validation of the PP-LBM approach, a numerical simulation was implemented on a 101 x 101 x 51 simple cubic lattice with a D3Q19 model, where $0 \le x \le 100$, $0 \le y \le 100$, $0 \le z \le 50$. To model the four impermeable walls, where we have a no-slip boundary condition, we simply use p_f = 0. The lattice sites in the rectangular flow region were assigned the value p_f = 1. The flow is driven by the same pressure difference as the 2D simulation along the *z* axis direction and is generated using the pressure boundary condition in 3D (Zou and He, 1997). All other parameters are the same as given in the previous section. The simulation results are shown in Figure 3. The average velocity $\bar{u}=2.76\times10^{-4}$ was calculated using the velocity profile displayed in Figure 3. Substitution of the simulated average velocity into Equation (14) gives a value of *f*. Re = 56.82. This is in good agreement with the experimentally measured value of 57 (Tao and Xu, 2001).

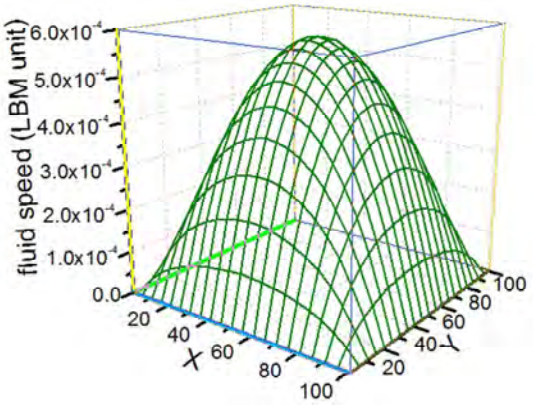

Figure 3. Fluid velocity profile of a cross section at *z*=25 in a rectangular duct.

A number of simulations have also been carried out by sub-dividing the flow region into multiple sub-regions. Different sub-regions have been assigned different constant values of p_f. The model is robust since it does not show any numerical abnormalities.

SIMULATIONS IN REAL ROCKS

The present PP-LBM model is now applied to a real world tight-sandstone sample which consists of quartz, albite, calcite and pyrite. The cylindrical sample, which was drilled from Yaodian area of Yan'an in Erdors Basin, China, has a diameter and height of 3mm and 20mm respectively. The 3D microscopic distribution of mineral phases in the sample is generated with the in-house DCM software in a cubic region of 600 x 600 x 700 voxels (Li *et al.*, 2013). Each voxel represents a size of 3.7 x 3.7 x 3.7 μm^3. An arbitrary sub-domain of 200 x 200 x 50 voxels was selected for the following PP-LBM simulations.

In the sample, pyrite, quartz and albite particles are not permeable. Fluid can flow through void and the partially permeable calcite. Denoting the effective percolating fraction of calcite as p_f^c, the effective percolating fraction of a voxel is approximated as

$$p_f = v_o + p_f^c \cdot v_c \quad , \qquad (15)$$

where v_o and v_c denotes the volume fractions for pore and calcite in the voxel respectively.

The flow is driven by the same pressure difference as the rectangular duct simulation along the *z* axis direction. The pressure difference is implemented numerically in the same way which has been discussed in the previous section. All other parameters are the same as given in the previous section. Various values of p_f^c from 0.0 to 0.2 have been used in the simulation. The typical velocity distributions in the simulated sample region are shown in Figure 4. As shown in Figure 4(a), the high-speed flow occurs only in small regions in the tight sandstone. By comparing Figure 4(b) with 4(c), it was found that just a small proportion of pores participated in the flow. Some pores effectively are not part of the flow path, as has been highlighted by the boxed regions in the figure. Most of the flowing path is occupied by calcite with a low flow speed. There are isolated relatively high-speed regions in the calcite. This indicates the existence of fine flow paths in these regions.

The same method is applied to a CIPS (Calcite In situ Preciptation System) core sandstone sample which consists of quartz and calcite. The 3D microscopic distribution of these mineral phases in this sample is generated with the DCM software in a cubic region of 1450 x 1470 x 340 voxels (Yang *et al*, 2012). Each voxel represents a size of 3.7 x 3.7 x 3.7 μm^3. An arbitrary sub-domain of 200 x 200 x 50 voxels is selected for the following PP-LBM simulations. The flow is driven by the same constant pressure difference as the tight-sandstone in the *z* axis direction and all the other parameters are the same as well. The same method as defined in Equation (15) is used to determine the effective percolating fractions.

In the LBM simulations, once flow is deemed to have reached steady state, the bulk permeability of the medium can be calculated, based on the generated velocity datasets, using Darcy's law as follows:

$$K = \frac{\nu \cdot < \rho u >}{\nabla P} \quad , \qquad (16)$$

where K is the bulk permeability, ∇P is the pressure gradient in a particular direction, ν is the kinematic viscosity of the fluid and u is the component of the velocity in the same direction as the pressure gradient. The quantity $< \rho \cdot u >$ is the average velocity flux over all the flow voxels taken directly from Equation (7).

The simulation is terminated once the following criterion has been reached:

$$\sum_t \frac{\|K(t) - K(t-1)\|}{\|K(t)\|} < 10^{-5} \quad . \qquad (17)$$

The convergence curves of the two samples are shown in Figure 5. The permeability of sandstone converges faster than tight sandstone. For sandstone, it requires 24000 time-steps to reach steady state, while it would need 162000 time-steps for tight sandstone. The code uses OpenMP to implement parallel computation to increase the calculating speed in C++ programs.

The calculated bulk permeability is shown in Figure 6. As anticipated, the bulk permeability increases with the effective percolating fractions of calcite. The bulk permeability of the tight-sandstone is more sensitive to the effective percolating fraction of calcite than for sandstone. That is, fine flow paths in calcite are more important for tight-sandstone than for sandstone. Flow in calcite phase in sandstone makes an insignificant contribution to the bulk permeability. The sandstone has a permeability value up to two orders of magnitude greater than the tight sandstone.

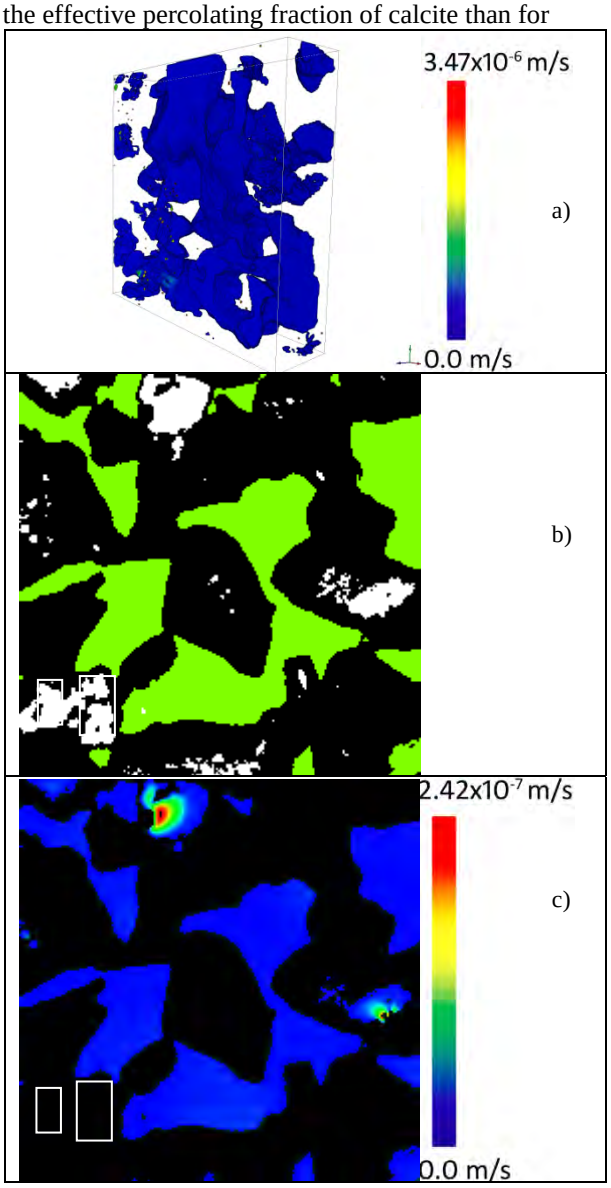

Figure 4. Velocity distribution of a tight sandstone sample where the non-percolating regions voxels are displayed as white and the percolating fraction of calcite is 0.2. (a) 3D velocity distribution image. The high flow speed region is small so it is not visible clearly on the figure. (b) Microstructure composition distribution at slice 20 with pore, calcite and mixture of quartz, albite and pyrite represented by white, green and black. (c) Velocity distribution at slice 20.

In relation to bulk permeability, flow in the calcite phase is essential for tight-sandstone, whereas it could be neglected for sandstone.

CONCLUSIONS

A partially percolating lattice Boltzmann model (PP-LBM) defined on partial volume voxels, rather than binary voxels, is developed. An effective percolating fraction is introduced on each voxel to incorporate the partial volume effect into the partial-bounce-back LBM model. The partial volume effect is related to the fine structures which are smaller than the voxel size, which can be characterized using DCM. The effective percolating fractions of voxels were estimated using the DCM generated volume factions. The PP-LBM is implemented numerically on the square lattice in 2D with square pixels and on the simple cubic lattice in 3D with cubic voxels. In relation to fluid flow, each voxel (pixel) is defined by an effective percolating fraction p_f which is related to the voxel (pixel) permeability, compositional volume fractions and sub-voxel (sub-pixel) fine structures. Fluid flows on regular geometries in 2- and 3-dimentions have been simulated. The numerical results agree with known analytic solutions.

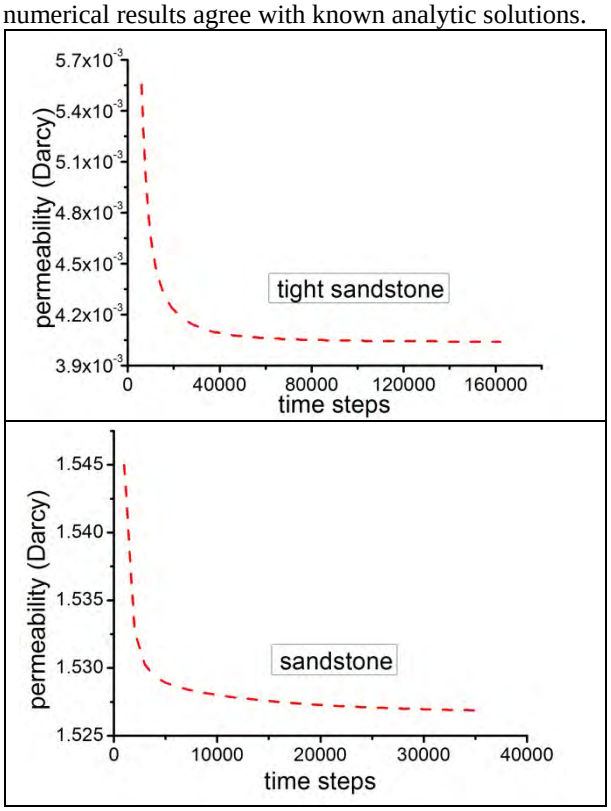

Figure 5. Convergence lines of permeability for tight sandstone and sandstone. The percolating fraction of calcite is 0.0.

The PP-LBM approach has been used to simulate flow in two real-world rock samples – a tight-sandstone and a CIPS sandstone. With the CIPS sandstone, the bulk permeability is insensitive to flow in the calcite phase. Therefore, the conventional LBM flow simulations on image-segmented X-ray CT images would be adequate. However, with the tight-sandstone, the numerical results indicate that the fine flow paths in the calcite phase play a critical role. When the flow paths in the calcite phase are neglected, the sample is essentially non-permeable. That is, the conventional LBM simulation on image-segmented X-ray CT images would produce misleading results. The tight oil & gas resources are going to play an increasingly important role for sustainable energy supply in the world. The PP-LBM and DCM would be useful tools for characterization and modeling of the tight reservoirs.

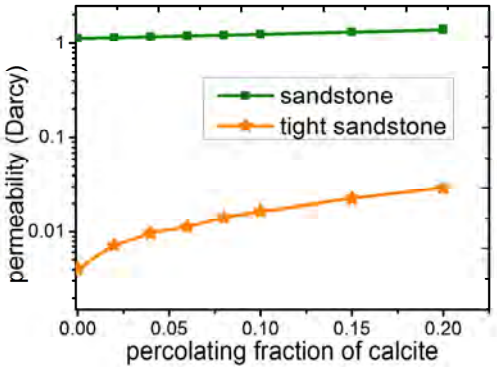

Figure 6. Effect of different percolating fractions of calcite on bulk permeability.

The PP-LBM approach is generic and should be applicable to other types of unconventional reservoirs and advanced materials. Work along this line is in progress.

REFERENCES

BALASUBRAMANIAM, K., HAYOT, F. and SAAM,W.F., (1987) "Darcy's law from lattice- gas hydrodynamics", *Phys. Rev. A*, **36**, 2248–2253.

CHEN, Y. and ZHU, K., (2008) "A study of the upper limit of solid scatters density for gray Lattice Boltzmann Method", *Acta Mech. Sin.*, **24**, 515–522.

DARDIS, O. and McCLOSKEY, J., (1998a) "Lattice Boltzmann scheme with real numbered solid density for the simulation of flow in porous media", *Phys. Rev. E*, **57**, 4834–4837.

DARDIS, O. and McCLOSKEY, J., (1998b) "Permeability porosity relationships from numerical simulations of fluid flow", *Geophys. Res. Letts.*, **25**, 1471–1474.

DESRUES, J., VIGGIANI, G. and BESEUELLE, P. (eds) (2006) "Advances in X-Ray Tomography for Geomaterials", (London: ISTE)

GAO, Y. and SHARMA, M.M., (1994) "A LGA model for fluid flow in heterogeneous porous media", *Transp. in Por. Media*, **17**, 1–17.

HECHT, M. and HARTING, J., (2010), "Implementation of on-site velocity boundary conditions for D3Q19 lattice Boltzmann simulations, J. of Stat. Mech.: Theory and Exp. (http://iopscience.iop.org/1742-5468/2010/01/P01018)

LI, R.R., KONG, H., YANG, S., MAYO, S., ZHU, R., BAI, B., PAN, J. and WANG, H., (2013) *CSIRO Data Collection: Erdors Basin Yanchang Formation Tight Sandstone 3D Microstructures*

PEREIRA, G.G., DUPUY, P.M., CLEARY, P.W., DELANEY, G.W., (2012), "Comparison of permeability of model porous media", *Prog. in Comput. Fluid Dyn.*, **12**, 176-186.

TAO, J., and XU, J., (2001), "The fluid flow rule at laminar flow in rectangle shape channel", *Journal of Huainan Institute of Technology*, **2**,1-10.

THORNE, D. and SUKOP, M., (2004) "Lattice Boltzmann model for the Elder problem" In: Proceedings of the XVth International Conference on Computational Methods in Water Resources (CMWR XV), Chapel Hill, NC, USA, June 13–17. Elsevier, Amsterdam, 2004, pp. 1549–1557

WALSH, S.D.C., BURWINKLE, H. and SAAR, M.O., (2009) "A new partial-bounce back lattice-Boltzmann method for fluid flow through heterogeneous media", *Computers & Geosciences*, **35**, 1186–1193.

YANG, Y.S., TULLOH, A., COLE, I., FURMAN, S. and HUGHES, A., (2007) "A data-constrained computational model for morphology structures", *J. Aust. Ceram. Soc.*, **43**, 159–164.

YANG, Y.S, FURMAN, S and TULLOH, A. "A data-constrained 3D Model for material compositional microstructures", *Adv. Mat. Res.*, **32**, 267-270.

YANG, S, LIU, K, MAYO, S, and TULLOH, A, (2012) *CSIRO Data Collection: CIPS sandstone microstructure*

ZHU, J. and MA, J.S., (2013) "An improved gray lattice Boltzmann model for simulating fluid flow in multi-scale porous media", Adv. in Water Res., **56**, 61–76.

ZOU, Q and HE, H., (1997) "On pressure and velocity boundary conditions for the lattice Boltzmann BGK model", *Phys. Fluids*, **9**, 1591-1598.

Chapter 5: Metallurgical applications

Metal production involves a variety of different processes. In these processes metal often exist in a liquid state which is governed be the laws of fluid dynamics. Thus CFD can be applied to assess metallurgical processes. Processes frequently studied by CFD include metal production in furnaces, electrolysis, casting, refining and more. Although the dominating physics may vary between these processes, most modelling approaches need to account for high temperatures. This can sometimes be challenging, since material properties and validation results can be difficult to obtain at the relevant temperatures.

CFD modelling of metallurgical applications was initiated in the 1980s when computer resources became available at an affordable cost. Since then more and more advanced simulations have been performed. The papers following this introduction indicate how far the CFD technology has come with respect to assessing metallurgical applications. They represent work on casting and furnace operations.

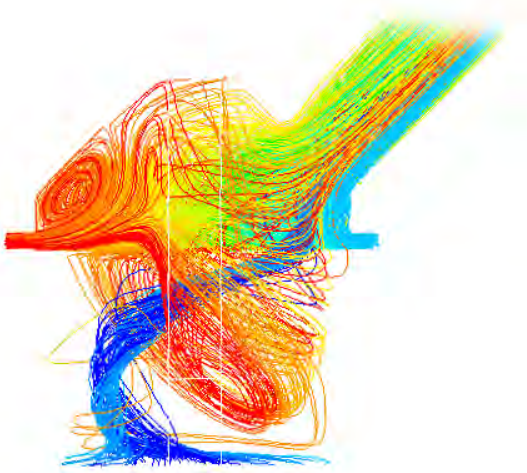

MODELLING ARGON INJECTION IN CONTINUOUS CASTING OF STEEL BY THE DPM+VOF TECHNIQUE

Pavel Ernesto RAMIREZ LOPEZ[1], Pooria Nazem JALALI[1], Ulf SJÖSTRÖM[1] and Christer NILSSON[2]

[1] Swerea MEFOS AB, Box 812, SE-971 25, Luleå, SWEDEN

[2] SSAB EMEA, SE-971 88, Luleå, SWEDEN

* E-mail: pavel.ramirez.lopez@swerea.se

ABSTRACT

An advanced numerical model able to predict transiently the multiphase flow, heat transfer and solidification in a Continuous Casting mould based on the Volume of Fluid Method (VOF) in combination with the tracking of bubble trajectories during argon injection through a Discrete Phase Model (DPM) is presented. This methodology allows studying the effect of Argon injection on process stability; particularly, it investigates the influence of the bubble stream on steel/slag flow dynamics. Thus, different injection parameters such as bubble diameter and gas flow-rate were combined with specific casting practices to emulate industrial cases. As a result, the model makes possible the identification of stable or unstable flows within the mould under a variety of casting conditions (casting speed, nozzle submergence depth, etc.). Application to the industrial practice in a European Research Fund for Coal and Steel project is an ongoing task and preliminary results are illustrated. These results are fully applicable to explain the effect of gas injection on the behaviour of mould level fluctuations in the mould. Moreover, the predicted flow behaviour and bubble trajectories demonstrate good agreement with observed level changes, standing waves and gas departure positions observed on a physical model based on liquid metal and industrial observations. Ultimately, the increased process knowledge is used to optimize gas injection to provide a smooth distribution along the mould that benefits process stability. The robustness of the model combined with physical model observations make possible the description of phenomena difficult to observe in the caster, but critical for its performance and the quality of final products.

Keywords: Bubble dynamics, Argon injection, Discrete Phase Modelling, Volume of Fluid, Multiphase, Casting and solidification.

NOMENCLATURE

Greek Symbols

α Volume fraction
μ Dynamic viscosity
ρ Density
σ Surface tension

Latin Symbols

C Non dimensional coefficient
d Bubble diameter
g Gravity
Eo Eotvos Number
F Force
g Gravitational constant
p Pressure
T Temperature
u Velocity
V Volume

Sub/superscripts

b Bubble
D Drag
L Lift
VM Virtual mass

INTRODUCTION

Argon injection is used during continuous casting to improve the removal of inclusions, which are transported by the argon-bubble stream to the slag bed; to be later assimilated in the liquid slag pool. A good deal of research has been done on this subject in the past 20 years, with mainly 2 numerical approaches to address the gas injection phenomena; namely Euler-Euler approach and Euler-Lagrangian approach (Cross *et al.*, 2006; Díaz *et al.*, 2008; Olmos *et al.*, 2001). The Euler-Euler approach requires tracking of two different sets of equations, one for the *continuum phase* (i.e. steel) and one for the *dispersed phase* (i.e. argon). The phases are solved as non-interpenetrating, immiscible media with their own material properties (density, viscosity, thermal conductivity, etc.) (Zhang *et al.*, 2006); thus, a complete set of flow equations (Navier-Stokes) is solved for each phase. In contrast, in the Euler-Lagrangian approach; the fluid is treated as a continuum by solving the Navier-Stokes equations, while the dispersed phase is solved in a "superimposed" way by tracking the bubbles through the calculated flow field. The dispersed phase can exchange momentum, mass, and energy with the fluid phase; but the trajectories of bubbles or particles are computed individually at specific intervals (i.e. particle or flow time step) during the continuum phase calculation.

Both methods have advantages and limitations. The Euler-Euler method is very accurate and normally favoured for analyzing flow columns with high volumes of gas (i.e. slug or annular flows, where the calculation of individual bubbles cannot be resolved or is not of particular importance, Figure 1).

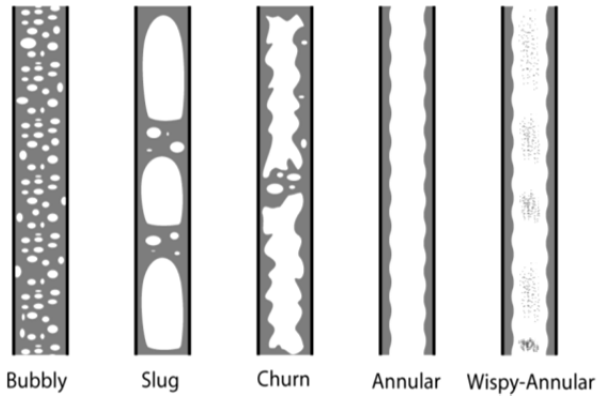

Figure 1: Different flow-gas regimes after Ghajar (Ghajar, 2005).

On the negative side, the Euler-Euler method is already computationally expensive for 2 phases and becomes unrealistically time consuming for a multiphase system such as the continuous casting process where slag, metal and argon are present. In contrast, the Euler-Lagrange method allows individual tracking of the bubbles at lower gas fractions, but former versions of the model used to be inaccurate when the dispersed phase occupied a large volume fraction ($\propto_{gas} > 20\%$). However, improved versions of this approach are readily available in CFD codes such as ANSYS-FLUENT; which make it possible to account for higher gas fractions. These are called Discrete Phase Model (DPM) and Dense DPM model (ANSYS-Inc., 2013).

The DPM model allows more flexibility when coupled to other models such as turbulence, heat transfer and solidification. Moreover, DPM can be efficiently coupled to the Volume of Fluid (VOF) method to track the metal level (free surface) in a transient or steady mode. This VOF approach has been used successfully to track the evolution of the slag/metal interface on a model recently developed by the authors (Ramirez-Lopez *et al.*, 2010; Ramirez Lopez *et al.*, 2010). Nevertheless, the addition of a dispersed phase (argon) to the multiphase system (metal-slag) by DPM has not been tested before in CC modelling. Prior work has been done by Thomas et al. (Thomas *et al.*, 1997) and Pfeifer et al. (Pfeiler *et al.*, 2005) to use the DPM approach to simulate argon injection within the CC mould, but lacks the calculation of the free metal surface. Consequently, it was not possible to directly determine the effect of the gas on metal level stability or initial solidification at the meniscus. Recent application of the DPM technique combined with the VOF method to study metallurgical processes should be attributed to Cloete et al. (Cloete *et al.*, 2009; Olsen *et al.*, 2009) who applied the technique to analyze the stirring of steel ladles with argon. However, the slag phase is absent from the calculations. The use of the DPM+VOF technique in this work is based on such work, but has been extended to account for the slag phase.

The fundamentals behind the DPM model can be found elsewhere and will not be reviewed in this manuscript. Instead, the present text is focused on the description of the modelling technique for adding argon injection to a multiphase-multiscale CC numerical model developed by the authors and validation of these predictions through experiments on a physical model with liquid metal and industrial observations.

BASE CONTINUOUS CASTING MODEL

The "base" CC model developed by the authors couples a multiphase steel-slag approach with heat transfer, mould oscillation and resultant solidification within the mould. The model uses the commercial code ANSYS-FLUENT v.14.5 to solve the Navier-Stokes equations together with the Volume of Fluid (VOF) method for calculation of the phase fractions (steel or slag) and the Continuum Surface Force (CSF) to account for surface tension effects in the meniscus (Brackbill *et al.*, 1992; Liow *et al.*, 2001). The κ-ε RNG turbulence model is used to capture flow turbulence, while heat transfer is solved through the Fourier equation. Heat extracted through the mould is calculated by a constant convection heat transfer coefficient based on the Nusselt number using typical water flow rates measured in the plants and a free stream temperature of 20°C. The heat flow through the slag bed is solved explicitly by addition of casting powder on top of the metal bulk and the calculation of the standard energy equation for a multiphase system in the VOF model. The boundary condition for powder feeding at the mould top depends on the industrial practice, being an air inlet if the slag bed does not fill the mould entirely; otherwise, a powder inlet is used. The slag-bed surface temperature measured with a thermal-camera is used as boundary condition at the mould top. Consequently, the thicknesses of the powdered, sinter and liquid slag layer are determined by the thermal conductivity of the slag as a function of temperature. Full details of the solution method have been published elsewhere (Ramirez-Lopez *et al.*, 2010; Ramirez Lopez *et al.*, 2010) and Figure 2 shows the boundary conditions used for the base model and argon injection.

Predictions include the calculation of the metal flow pattern inside the mould, the metal level height (i.e. metal-slag interface) as well as the behaviour of slag in the bed. The withdrawal of the solidified shell drags liquid slag into the gap to produce a slag film (i.e. lubrication or infiltration). The interfacial resistance between the solid slag and the mould or contact resistance due to the slag film as described by Spitzer et al. (Spitzer *et al.*, 1999) has been computed as a function of the powder's basicity (Ramirez Lopez, 2010). This process is affected by casting conditions such as mould oscillation, powder composition, mould level control, rim formation, etc. Metal flow pattern predictions are shown in Figure 2b. These reveal typical flow structures such as jet and rolls but also the formation of a standing wave at the meniscus resulting from the particular SEN design.

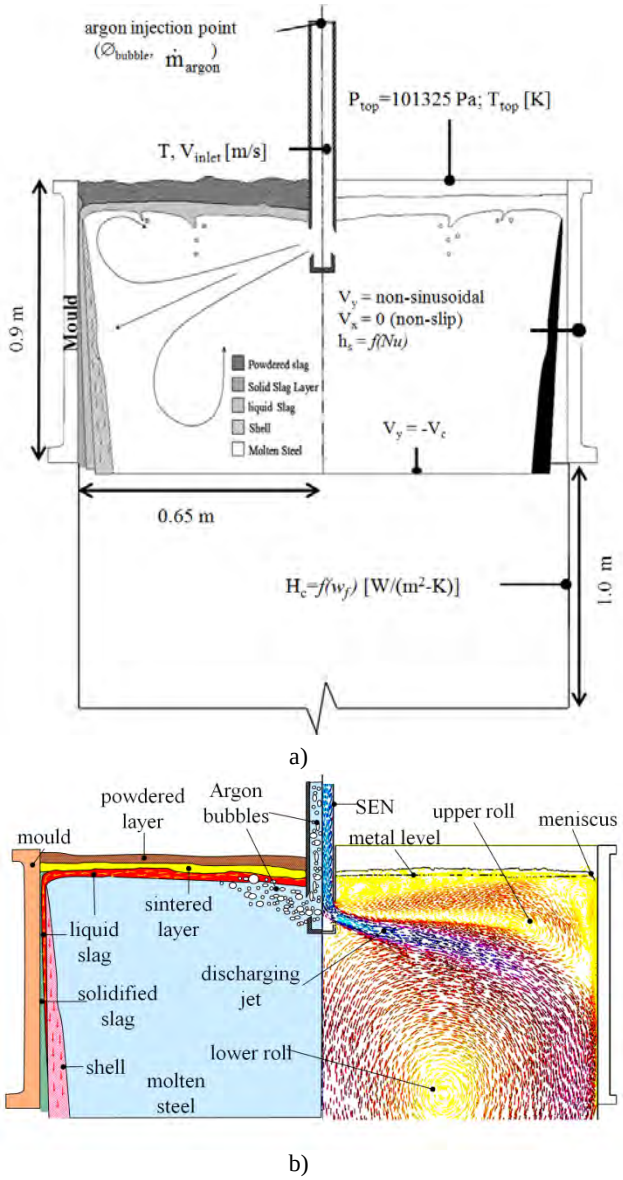

Figure 2: Numerical model for Continuous Casting, a) Boundary conditions used for base model and argon injection and b) Schematics of multiple phases present during casting (left) and typical metal flow predictions (right) after P.E. Ramirez Lopez et al. (Ramirez Lopez *et al.*, 2013)

MODELLING ARGON INJECTION THROUGH THE DPM+VOF APPROACH

Although the fundamentals behind the DPM model can be found in the ANSYS-FLUENT v. 14 theory guide (ANSYS-Inc., 2013), some specific extra source terms (e.g. buoyancy, drag, lift, virtual mass and turbulent dispersion) were added as User Defined Functions (UDF's) (Cloete *et al.*, 2009; Cloete *et al.*, 2009; Olsen *et al.*, 2009). Then, the momentum equation for the DPM model becomes:

$$\frac{du_b}{dt} = \frac{g(\rho_b - \rho)}{\rho_b} + F_D(u - u_b) + F_{VM} + F_L \qquad (1)$$

where u is the velocity in x, y or z axis; ρ and ρ_b are the density of the bulk flow and bubbles and F_D, F_{VM} and F_L are the source terms for drag, virtual mass and lift, respectively.

The drag source term is defined as:

$$F_D = \frac{18\mu}{\rho_b d_b^2}\frac{C_D Re}{24} \qquad (2)$$

where $C_D = 0.666\sqrt{Eo/3}$, which is a function of the Eotvos number. The virtual mass and lift source terms are defined as:

$$F_{VM} = \frac{1}{2}\frac{\rho}{\rho_b}\left(\frac{\partial u}{\partial t} - \frac{\partial u_b}{\partial t}\right) \qquad (3)$$

$$F_L = C_D \rho_l V_b (u_l - u_g) \times (\nabla \times u_l) \qquad (4)$$

Different approaches have been used and a variety of experiments have been performed to determine the evolution of drag and lift for bubble columns and single bubbles (Tomiyama, 2004); however, such discussion is beyond the scope of this work. The present approach is based on a combination of coefficients as suggested by Olsen et al. (Olsen *et al.*, 2009). Regarding turbulence, prior work has highlighted deficiencies on early κ-ε formulations for tracking bubbly flows since turbulence is scaled on mean flow gradients rather than bubble size (Johansen *et al.*, 1988). The *random walk model* was used to address this issue. This approach is a type of "eddy lifetime" model that describes the effects of small-scale turbulent eddies on bubbly flows by using a Gaussian distribution for the turbulent fluctuating velocities and a characteristic timescale for the eddies (ANSYS-Inc., 2013). The bubble size is determined from experiments by Iguchi et al. (Iguchi *et al.*, 1995), where diameter of gas bubbles in liquid iron was proven to depend on the inner diameter of the injection pipe for stagnant flow conditions. The robustness and accuracy of the DPM+VOF technique was validated by comparing to an experimental benchmark (Deen *et al.*, 2001; Zhang *et al.*, 2006). The benchmark consists of a quadrangular base column of water, where air is supplied at the bottom with a given velocity, mass flowrate, bubble size, etc. Details of the benchmark are presented on Figure 3.

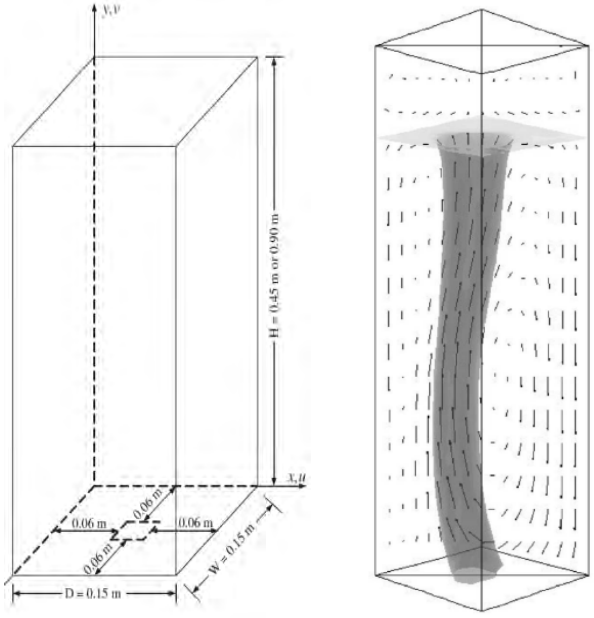

Figure 3: Bubble column experiment after (Deen *et al.*, 2001; Zhang *et al.*, 2006), a) Experiment dimensions, b) schematics of gas plume for experiments and simulations by Zhang et al. (Zhang *et al.*, 2006).

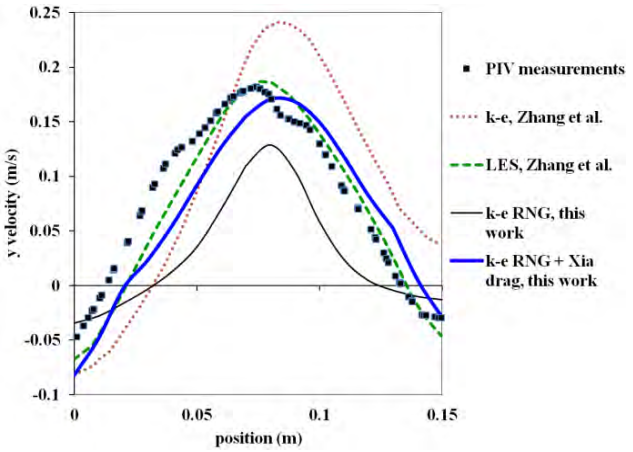

Figure 4: Velocity comparison along a centreline at y=0.25 m and present model with DPM+VOF approach for different drag and turbulence conditions.

The main validation process consisted on predicting flow velocities along a transversal centreline (x axis) at different y positions (height positions); and compare them to the experimental benchmark. The DPM+VOF model showed good overall agreement at a transversal line; y=0.25m, when compared to PIV experiments in the benchmark, with a peak in positive $\boldsymbol{y}$ velocity (upwards) at the centre of the bubble column that decreases towards the exterior and switches to negative $\boldsymbol{y}$ velocity values (downwards) along the walls (Figure 4).

Furthermore, the standard spherical and non-spherical drag functions in FLUENT were compared to the VOF+DPM model with extra source terms added as UDF's. These are shown with the corresponding Figures from the benchmark for a variety of turbulence and flow conditions in Figure 5. The spherical drag law provided closer results to experiments when compared to the non-spherical approach with 0.5 and 0.75 shape factor coefficients. However, native spherical and non-spherical laws still under predict the spreading of the bubble column (Figure 5a-left and centre). The addition of modified drag, lift and virtual mass forces provided a better agreement with the benchmark; with minor differences in velocity magnitude, but capturing satisfactorily the bubble column spread and overall intensity (Figure 5b). This is due to the fact that the built-in spherical and non-spherical drag laws produce a more closely packed column; whereas, the modified drag law provides a more realistic spreading of bubbles. Consequently, the combination of DPM+VOF with modified source terms was used as base to simulate argon injection within the mould during continuous casting.

Once validated, the DPM technique was coupled to the "base" model developed previously by the authors. The model runs in transient mode until a stable flow is achieved (approximately 100-200 seconds after argon injection). This "stable period" is representative of the flow at a constant casting speed, fixed SEN immersion depth and constant cooling conditions (i.e. no casting speed ramping or SEN immersion depth changes).

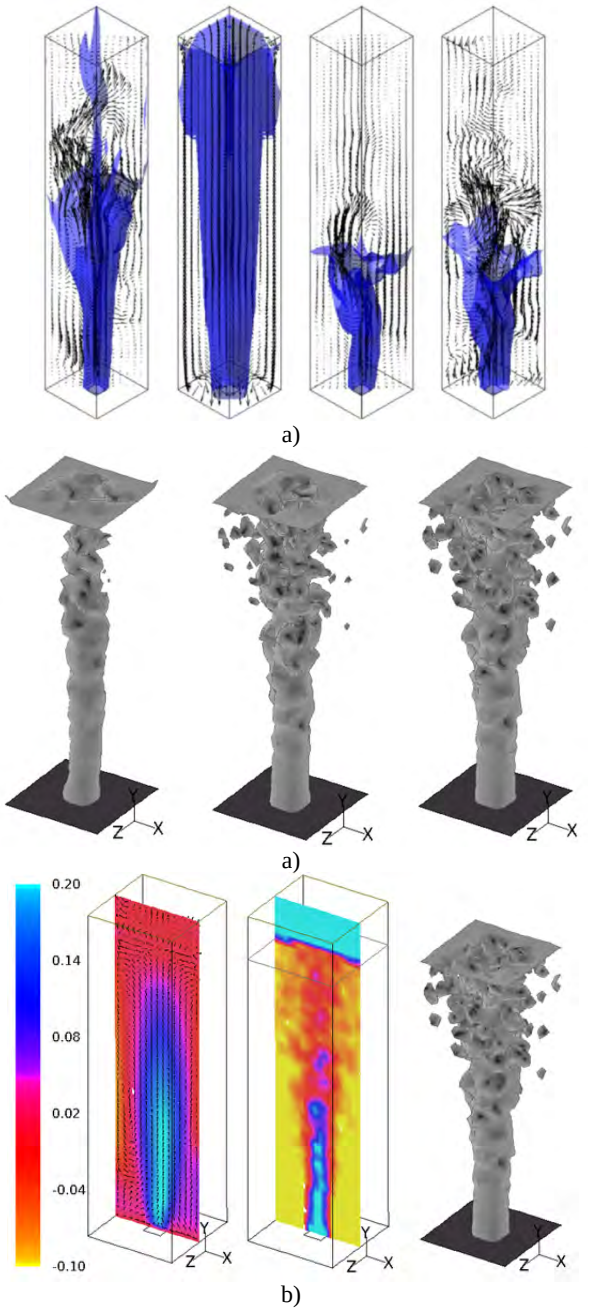

Figure 5: a) Comparison of bubble column spreading for different drag laws: a) Numerical simulations with several turbulence models after (Deen *et al.*, 2001; Zhang *et al.*, 2006) and b-c) Comparison of bubble column spreading for different drag laws: b) This work with standard functions (from left to right): Non-spherical with shape factor=0.5, Spherical and Additional source term; c) Column velocities and spreading for additional terms case.

Boundary conditions for argon injection (DPM model) are as follows:

- Inlet: single point at the nozzle top-centre
- SEN walls and solid surfaces: reflection
- Mould top and outlet of numerical domain: escape
- Metal-slag interface and slag bed: not preconditioned (free transit between boundaries)

PRELIMINARY RESULTS AND VALIDATION

2D Simulations show that injected argon bubbles travel rapidly to reach the SEN ports (~2 s), while the bubble distribution along the SEN bore is considerably irregular along most of the nozzle height. However, before leaving the nozzle, the bubbles accumulate around the upper port and are dragged into the mould by the metal as it leaves the nozzle.

After leaving the port, the bubbles are entrained by the discharging jet for a distance clearly related to the bubble size and argon-flow rate. A variety of tests were carried out to compare FLUENT's built-in drag and numerical schemes (accuracy control, two-way turbulence coupling, tracking scheme selection, etc.). Some of these predictions are shown in Figure 6.

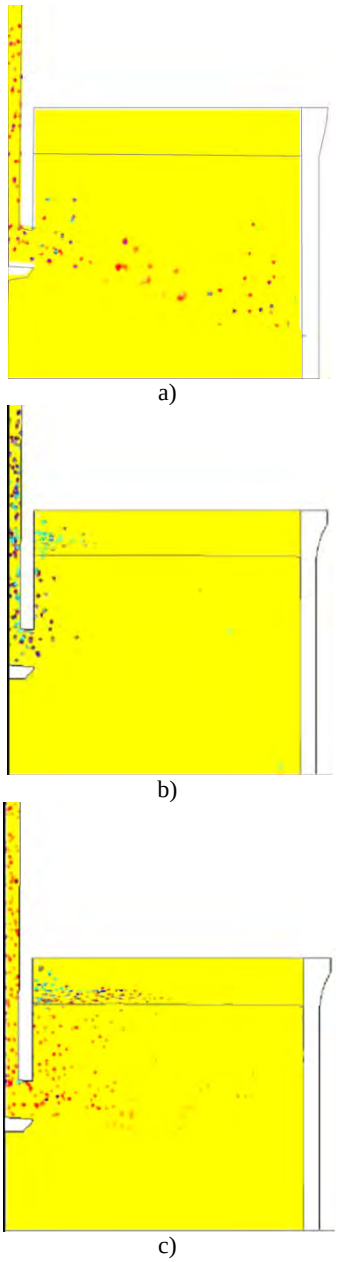

Figure 6: Fully developed bubble distribution for DPM+VOF model: a) DPM+VOF with Non-spherical-drag laws, bubble ∅=2000 μm, b) DPM+VOF with Spherical-drag laws, bubble ∅=2000 μm, and c) DPM+VOF with drag laws via UDFs', bubble ∅=2000 μm.

Results demonstrate clearly that the only approach producing a realistic spreading of bubbles is the DPM+VOF+additional UDF's approach (Figure 6c). In contrast, the non-spherical drag laws cause total entrainment of bubbles along the discharging jet (Figure 6a), whereas the spherical laws cause departure of most bubbles close to the nozzle (Figure 6b). Simulations were performed to explore the influence of bubble size and different gas flow-rates in the calculations. For instance, Figure 7 shows the predicted velocity fields and bubble distribution for 4 and 5 lt/min at constant casting speed; which shows clear differences in bubble departure positions and flow behaviour. The 4 lt/min case produces a more even distribution of bubbles, which are entrained deeper into the melt by the discharging jet (Figure 7a). Thus, lower velocities close to the SEN are observed for the 4 lt/min case. In contrast, the 5 lt/min case leads to bubbles rising closer to the SEN due to coalescence and enhanced buoyancy and drag forces. Hence, bubbles leave "high velocity traces" when escaping the jet and reaching the surface. This creates higher departure velocities close to the SEN (e.g. dark red area adjacent to ports); and weakening of the discharging jet, which is also shorter and more distorted for the higher argon flow-rate (Figure 7b).

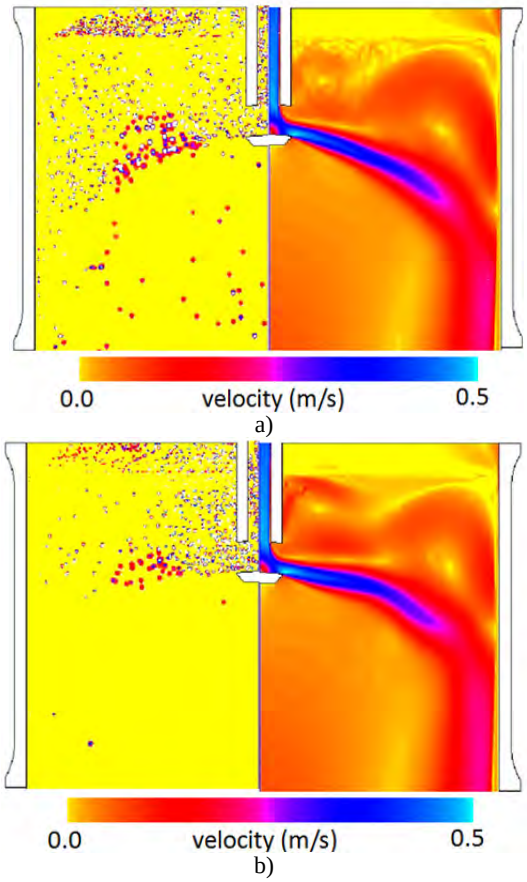

Figure 7: Simulated gas distributions and velocity fields for DPM+VOF model: a) Gas distribution for bubble ∅=4mm and 4 lt/min and b) Gas distribution for bubble ∅=4mm 5 lt/min.

This has deep implications when compared to the industrial praxis. Not incidentally, a transition from stable to unstable flow is detected when increasing the argon flow rate higher than 4.5 lt/min on industrial casters (which is the maximum gas flow rate employed

by operators for this particular case to avoid a "*boiling effect*" at the metal surface). Such *boiling effect* is known to be detrimental to mould level control due to unstable metal flows and produce more surface defects in the final product such as deep oscillation marks and cracks. This effect is a limiting factor since higher argon flow rates are desirable to improve flotation of inclusions but not at the expense of process stability. A key point on the simulations is the use of slag as secondary phase for the VOF model with properties that make it possible to distinguish between the liquid phase (slag pool), sintered layer and loose powder bed. The test runs with the improved model show that argon bubbles can reach the slag-metal interface, travel across it and exit the bed through the powdered layer with a corresponding change in bubble rising velocity through each of the slag layers due to viscosity changes (Figure 8).

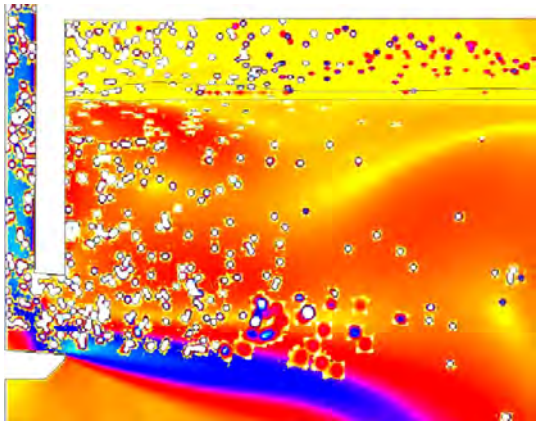

Figure 8: Argon bubble distribution and displacement through the slag-metal interface and through the slag with DPM+VOF embedded into existing CC model.

COMPARISONS WITH CASTING SIMULATOR (CCS-1)

Predictions of the average behaviour of the flow and bubbles once the flow stabilized were taken as basis for comparisons with a Continuous Casting Simulator (CCS-1) at Swerea MEFOS (Ramirez Lopez *et al.*, 2012). Designed and built between 2004-2007 during a RFCS project (Higson *et al.*, 2010), the model is equivalent to a continuous casting machine with tundish, stopper, Submerged Entry Nozzle (SEN) and mould. Hot metal is transported continuously from the tundish to the mould which is connected at the bottom to a heated tank/reservoir. A submerged pump sends the metal back from the tank to the tundish closing the flow loop (Figure **9**). A low melting point alloy (58%Bi-42%Sn), is used as working media to simulate the steel flow, with properties described on Figure 10. The surface tension was defined as a function of temperature after (Aqra *et al.*, 2011; Man, 2000; Yuan *et al.*, 2002). Such alloy was chosen due to its close resemblance on fluid properties to steel and its non-toxicity. Electrical properties of the alloy are also close to liquid steel, which make it an ideal candidate for testing Electro-Magnetic Stirring (EMS) or Electro-magnetic Breaking (EMBr) devices as well as Electromagnetic sensors. The alloy's melting point is approximately 135°C. Hence, temperature in the simulator is maintained within a few degrees to avoid solidification in the pump as well as ensuring a smooth flow control by a stopper, which is controlled through a laser system. The simulator can use replicas in stainless steel of the stopper/SEN or the actual ceramic versions used on real casters. Stable operation for casting speeds between 0.6 to 1.4 m/min for a mould 900 x 200 mm size can be achieved. Higher casting speeds (c.a. 1.5-1.8 m/min) are possible by scaling the mould. Argon is supplied through the stopper tip for testing injection up to 8 lt/min.

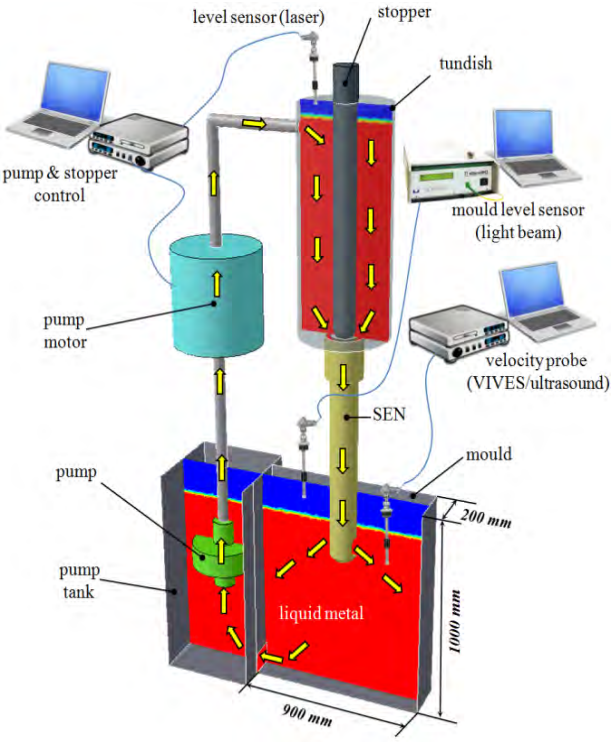

a)

b)

Figure 9: Continuous Casting Simulator CCS-1; a) Sensors and control schematics and b) Actual Continuous Casting Simulator at Swerea MEFOS

Bi-Sn alloy (MCP-137) properties compared to liquid steel				
	viscosity, μ (Pa-s x10^{-3})	density, ρ (kg/m^3)	kinematic viscosity, ν (m^2/s x10^{-6})	electrical conductivity, σ, (1/Ωm x10^6)
Steel (1600 C°)	6.3	7000	0.9	0.7
MCP 137 (150 C°)	10.7	8580	1.25	1.0
MCP 137 (170 C°)	8.6	8580	1	

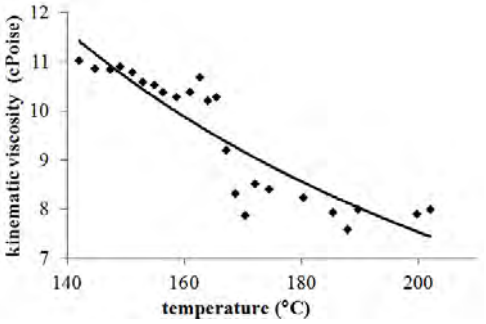

Figure 10: Properties of MCP 137 alloy vs steel and viscosity at operational temperatures

A variety of probes have been tested in order to find the most suitable tools to characterize the flow within the mould. Silicon oil was used to simulate the behaviour of liquid slag on top of the melt, while argon was supplied through the stopper-SEN (Figure 11).

Observations of the metal level in CCS-1 at various flow-rates used typically during casting show that in all cases the bubbles have the following behaviour (Figure 11):

- Bubbles actually leave the metal bulk through the surface (opposite to results in Figure 6a).
- Bubbles are distributed along the whole metal surface (opposite to results in Figure 6b).
- Bubbles exit the metal surface along the whole mould width; with a higher amount bursting close to the SEN (in line with results on Figure 6c).

This demonstrates that the VOF+DPM approach with extra source terms is predicting realistically the behaviour of argon in the Casting Simulator and industrial practice. Furthermore, it is possible to deduct that the effect of higher argon flow-rates (e.g. from 4lt/min to 5lt/min) is an evident increase of instabilities in the mould due to bubble coalescence and augmented drag. In other words, the grouping of bubbles around the nozzle at higher argon loads would favour their collapse into larger bubbles, which offer a higher resistance to the discharging jet and reduce the number of smaller bubbles entrained deeper into the mould. This mechanism was observed by taking video sequences during tests in CCS-1 for the same argon flow rates: 4lt/min and 5 lt/min (Figures 12 and 13).

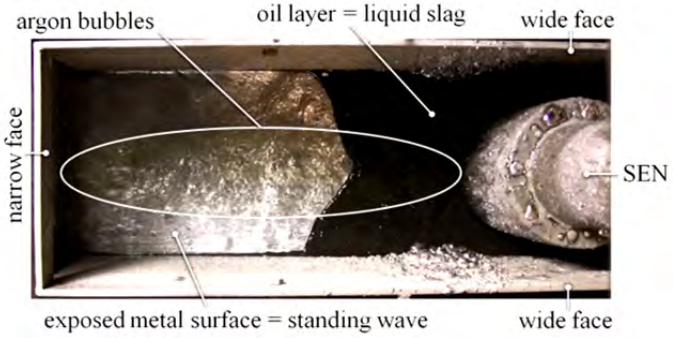

Figure 11: Top view of the metal level and oil simulating slag in CCS-1.

Figure 12: Video snapshots of the metal slag interface during argon injection tests at CCS-1 (taken every 10 seconds for a total time of 1 minute) for an argon mass flow rate=4 lt/min.

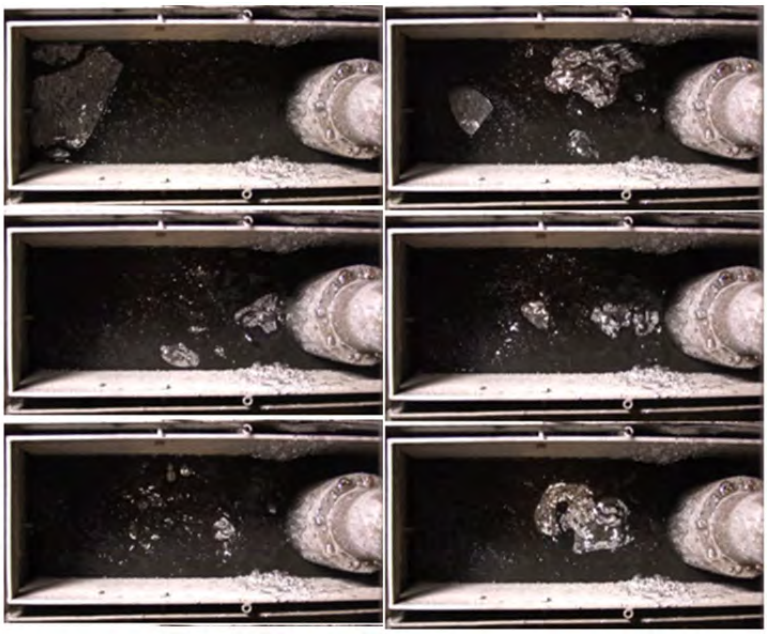

Figure 13: Video snapshots of the metal slag interface during argon injection tests at CCS-1 (taken every 10 seconds for a total time of 1 minute) for an argon mass flow rate=5 lt/min.

Differences in stability of the metal surface are easily noticeable by comparing the image-sequences. Lower argon flow rates produce a more stable flow pattern at the surface, with evidence of the well known "*double roll flow pattern*" (Ramirez-Lopez *et al.*, 2005) (e.g. upper roll pushing constantly the oil layer towards the nozzle).

In this case, argon bubbles depart uniformly along the mould width with smaller bubbles bursting closer to the narrow face; while slightly larger bubbles burst next to the SEN.

In contrast, a higher argon flow rate produces an unstable metal surface (e.g. random oil distribution) with some medium size bubbles bursting at random positions and large bubbles exploding close to the SEN. Comparison between 2D numerical models and CCS-1 are only qualitative. Therefore, 3D runs were performed to analyse the bubble distribution along the metal surface in a full numerical model of CCS-1 (Figures 14 and 15).

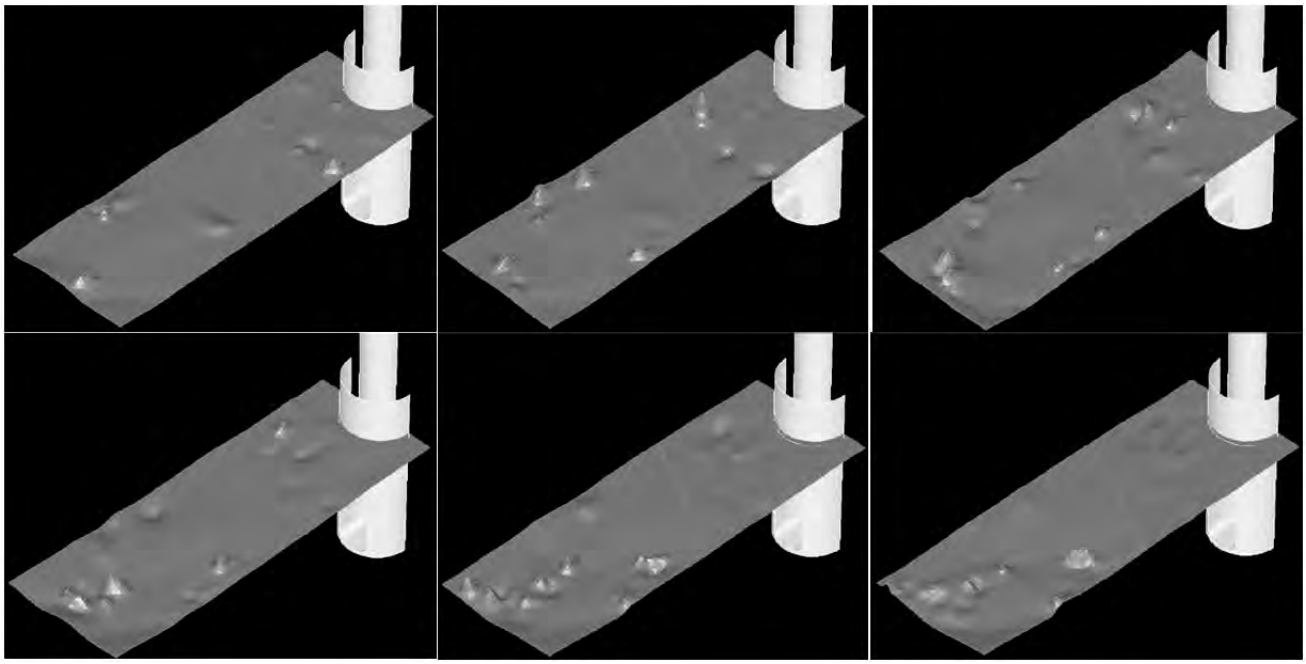

Figure 14: Snapshots every 0.5 s for a total of 3 s for 3D DPM+VOF model at 4lt/min and v_c=1.2 m/min.

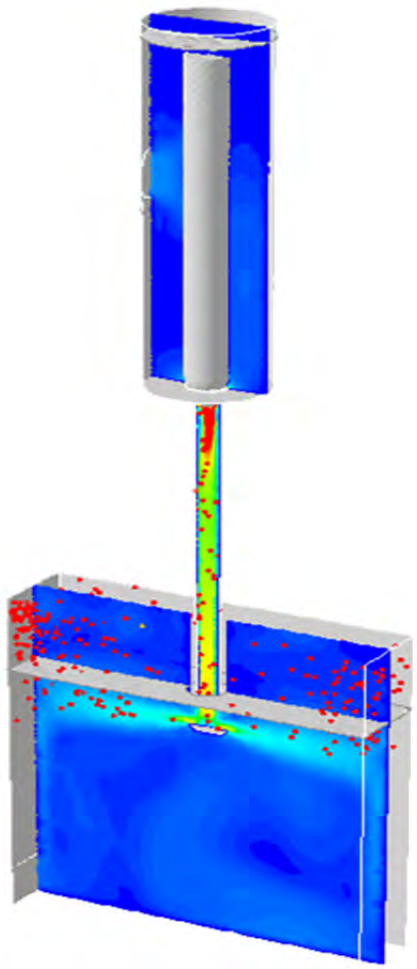

Figure 15: Numerical model of Continuous Casting simulator (CCS-1).

Tracking of the bubbles bursting at the metal surface was performed by counting the number of bubbles departing at different positions along the mould thickness and width (Figure 14). Statistics after 100 seconds show that approximately 60% of the bubbles depart close to a central plane parallel to the wide faces; while the rest burst randomly closer to the mould walls. It was also observed that more than 50% of the bubbles burst close to the SEN. These observations are in line with experiments in CCS-1 and previous plant experiences. This demonstrates that the 2D model is not far from the 3D case as long as slight corrections to the argon flow rate and bubble frequency are performed. This has significant implications for nozzle design and finding optimal argon flow rates for improved process windows. Analysis of these effects are ongoing tasks by means of parametric studies, further tests in CCS-1 and plant trials in a EU funded project (Ramirez Lopez *et al.*, 2013).

CONCLUSIONS

A numerical technique able to predict the multiphase (steel/slag) flow dynamics coupled with argon injection within the CC mould has been presented. The technique is based on the coupling of the DPM Lagrangian approach, which allows individual tracking of gas bubbles in a continuum phase; together with the Volume of Fluid method for calculation of free surfaces on multiphase flows.

The model has been developed with the aim of analysing industrial practices (e.g. argon injection) by comparing results with physical modelling in a Continuous Casting Simulator (CCS-1) and industrial observations. The following conclusions can be drawn from the application of these models:

- The coupling of the DPM technique to an existing CC model based on the multiphase VOF method has proven possible. This includes predictions of the displacement of bubbles across the slag-metal interface and through the slag bed covering the melt.
- The modified DPM+VOF model with additional source terms is capable of describing realistically the distribution of bubbles as seen in the casting simulator and industrial practice.
- Both the numerical and physical models presented are capable of matching phenomena observed in the industrial practice such as the “boiling effect” at excessive argon flow rates and standing waves which are detrimental to process stability as well as the typical double roll pattern seen in most casters.

The combination of predictions with the model developed and observations in CCS-1 allow a deeper understanding of the mechanisms responsible for achieving stable or unstable flows during casting. Findings provide enough evidence to consider the DPM+VOF technique as reliable for analysis of argon injection in the Continuous Casting process.

ACKNOWLEDGEMENTS

PRL would like to thank operators at SSAB for fruitful discussions, Mr. Christer Olofsson for support during CCS-1 trials and Mrs. Pilvi Oksman at Aalto University for proof-reading the manuscript. PJ would like to thank Professor Pär Jonsson at KTH, Stockholm for continuing support during his M.Sc. and Doctoral studies. The research leading to these results has received funding from the European Union's Research Programme of the Research Fund for Coal and Steel (RFCS) under grant agreement n° [RFSR-CT-2011-00005].

REFERENCES

ANSYS-INC.: "ANSYS Fluent v.12 - User's Guide", *ANSYS Inc.*, (2013),

AQRA, F. and AYYAD, A.: "Surface tension of pure liquid bismuth and its temperature dependence: Theoretical calculations", *Materials Letters*, **65** (2011), 760-762.

BRACKBILL, J.U., KOTHE, D.B. and ZEMACH, C.: "A continuum method for modeling surface tension", *Journal of Computational Physics*, **100** (1992), 335-54.

CLOETE, S., OLSEN, J.E. and SKJETNE, P.: "CFD modeling of plume and free surface behavior resulting from a sub-sea gas release", *Applied Ocean Research*, **31** (2009), 220-225.

CLOETE, S.W.P., EKSTEEN, J.J. and BRADSHAW, S.M.: "A mathematical modelling study of fluid flow and mixing in full-scale gas-stirred ladles", *Progress in Computational Fluid Dynamics*, **9** (2009), 345-356.

CROSS, M., CROFT, T.N., DJAMBAZOV, G. and PERICLEOUS, K.: "Computational modelling of bubbles, droplets and particles in metals reduction and refining", *Applied mathematical modelling*, **30** (2006), 1445.

DEEN, N.G., SOLBERG, T. and HJERTAGER, B.H.: "Large eddy simulation of the Gas–Liquid flow in a square cross-sectioned bubble column", *Chemical Engineering Science*, **56** (2001), 6341-6349.

DÍAZ, M.E., IRANZO, A., CUADRA, D., BARBERO, R., MONTES, F.J. and GALÁN, M.A.: "Numerical simulation of the gas–liquid flow in a laboratory scale bubble column: Influence of bubble size distribution and non-drag forces", *Chemical Engineering Journal*, **139** (2008), 363-379.

GHAJAR, A.J.: "Non-boiling heat transfer in gas-liquid flow in pipes: a tutorial", *Journal of the Brazilian Society of Mechanical Sciences and Engineering*, (2005),

HIGSON, S.R., DRAKE, P., LEWUS, M., LAMP, T., KOCHNER, H., VALENTIN, P., BRUCH, C., CIRIZA, J., LARAUDOGOITIA, J., BJÖRKVALL, J. and BERGMAN, L.: "FLOWVIS: measurement, prediction and control of steel flows in the casting nozzle and mould", **EUR 24205** (2010),

IGUCHI, M., CHIHARA, T., TAKANASHI, N., OGAWA, Y., TOKUMITSU, N. and MORITA, Z.-I.: "X-ray fluoroscopic observation of bubble characteristics in a molten iron bath", *ISIJ International*, **35** (1995), 1354-1361.

JOHANSEN, S.T., BOYSAN, F. and AYERS, W.H.: "Mathematical modelling of bubble driven flows in metallurgical processes", *Mathematical and Computer Modelling*, **10** (1988), 798.

LIOW, J.L., RUDMAN, M. and LIOVIC, P.: "A volume of fluid (VOF) method for the simulation of metallurgical flows", *ISIJ international*, **41** (2001), 225-233.

MAN, K.F.: "Surface tension measurements of liquid metals by the quasi-containerless pendant drop method", *International Journal of Thermophysics*, **21** (2000), 793-804.

OLMOS, E., GENTRIC, C., VIAL, C.C. and WILD, G.: "Numerical simulation of multiphase flow in bubble column reactors. Influence of bubble coalescence and break-up", *Chemical engineering science*, **56** (2001), 6359.

OLSEN, J.E. and CLOETE, S.W.P.: "COUPLED DPM AND VOF MODEL FOR ANALYSES OF GAS STIRRED LADLES AT HIGHER GAS RATES", *Seventh International Conference on CFD in the Minerals and Process Industries*, (2009), Melbourne, Australia

PFEILER, C., WU, M. and LUDWIG, A.: "Influence of argon gas bubbles and non-metallic inclusions on the flow behavior in steel continuous casting", *Materials science & engineering. A, Structural materials*, **413-414** (2005), 115-120.

RAMIREZ-LOPEZ, P.E., LEE, P.D., MILLS, K.C. and SANTILLANA, B.: "A new approach for modelling slag infiltration and solidification in a continuous casting mould", *ISIJ International*, **50** (2010), 1797-1804.

RAMIREZ-LOPEZ, P.E., MORALES, R.D., SANCHEZ-PEREZ, R., DEMEDICES, L.G. and DAVILA, P.O.: "Structure of turbulent flow in a slab mold", *Metallurgical and materials transactions. B, Process metallurgy and materials processing science*, **36** (2005), 787-800.

RAMIREZ LOPEZ, P.E.: "Modelling Shell and Oscillation Mark Formation during Continuous Casting via Explicit Incorporation of Slag Infiltration", **PhD Thesis**, Imperial College London (2010), 170.

RAMIREZ LOPEZ, P.E., BJÖRKVALL, J., JONSSON, T., KARAGADDE, S., LEE, P.D., MILLS, K.C., VAN DER PLAS, D., VAN VLIET, E., SHAHBAZIAN, F., ANDERSSON, P., OPPELSTRUP, J., NILSSON, C. and WIKSTRÖM, P.: "Development of a toolbox for direct defect prediction and reduction through the characterisation of the meniscus-slag bed behaviour and initial shell solidification in CC", European-Comission, **RFSR-CT-2011-00005** (2013),

RAMIREZ LOPEZ, P.E., BJÖRKVALL, J., SJÖSTRÖM, U., LEE, P.D., MILLS, K.C., JONSSON, B., JANIS, J., PETÄJÄJÄRVI, M. and PIRINEN, J.: "EXPERIMENTAL VALIDATION AND INDUSTRIAL APPLICATION OF A NOVEL NUMERICAL MODEL FOR CONTINUOUS CASTING OF STEEL",*Ninth International Conference on CFD in the Minerals and Process Industries*, (2012), 1-6.Melbourne, Australia.

RAMIREZ LOPEZ, P.E., JALALI NAZEEM, J., BJÖRKVALL, J., SJÖSTRÖM, U. and JÖNSSON, P.: "Recent Developments of a Numerical Model for Continuous Casting of Steel: Validation and Industrial Application", *3rd International Symposium on Cutting Edge of Computer Simulation of Solidification, Casting and Refining (CSSCR2013). ,* (2013), Stockholm, SWEDEN and Helsinki, FINLAND.

RAMIREZ LOPEZ, P.E., LEE, P.D. and MILLS, K.C.: "Explicit modelling of Slag Infiltration and Shell Formation during Mould Oscillation in Continuous Casting", *ISIJ International*, **50** (2010), 425-434.

SPITZER, K., SCHWERDTFEGER, K. and HOLZHAUSER, J.: "Laboratory study of heat transfer through thin layers of casting slag: Minimization of the slag/probe contact resistance", *Steel research*, **70** (1999), 430-436.

THOMAS, B.G., DENNISOV, A. and BAI, H.: "Behavior of Argon Bubbles during Continuous Casting of Steel", *ISS 80th Steelmaking Conference*, (1997), Chicago, IL.

TOMIYAMA, A.: "Drag, lift and virtual mass forces acting on a single bubble", *Proc.Third Int. Symp.on Two-Phase Flow Modelling and Experimentation*, (2004), Pisa, Italy.

YUAN, Z.F., MUKAI, K., TAKAGI, K., OHTAKA, M., HUANG, W.L. and LIU, Q.S.: "Surface Tension and Its Temperature Coefficient of Molten Tin Determined with the Sessile Drop Method at Different Oxygen Partial Pressures", *Journal of Colloid and Interface Science*, **254** (2002), 338-345.

ZHANG, D., DEEN, N.G. and KUIPERS, J.A.M.: "Numerical simulation of the dynamic flow behavior in a bubble column: A study of closures for turbulence and interface forces", *Chemical Engineering Science*, **61** (2006), 7593-7608.

MODELLING THERMAL EFFECTS IN THE MOLTEN IRON BATH OF THE HISMELT REDUCTION VESSEL

Peter J. WITT[1*], Yuqing FENG[1] and Mark P. DAVIS[2]
[1] CSIRO Mineral Resources Flagship, Melbourne 3169, AUSTRALIA
[2] HIsmelt Corporation Pty Ltd, Kwinana 6966, AUSTRALIA
* E-mail: peter.witt@csiro.au

ABSTRACT

Over a thirty year period the HIsmelt process has been developed as an alternative to the traditional blast furnace for the production of pig iron. This process involves the injection of fine iron ore and non-coking coal particles into a molten iron bath though a number of wall lances. These jets induce substantial mixing and splashing of molten droplets into the top space of the vessel due to the substantial volume of gas generated within the bath. Control of heat transfer, reactions and the complex multiphase fluid dynamics is critical to successful operation of the process. Since inception computational fluid dynamics has played an important role in scale-up and process optimisation (Davis *et al.* 2003, Davis and Dry, 2012).

A "Bath model" has been developed which focuses on the smelt-reduction processes occurring within the bath volume of the HIsmelt vessel (Stephens *et al.* 2011). As this model is a transient multi-component Eulerian-Eulerian model with Lagrangian particle tracking for the coal and ore particles, it requires a substantial computational effort. For this reason (and due to the large thermal inertia of the liquid bath) earlier versions of the model have been isothermal.

Particles enter the molten iron bath at close to ambient temperature. Heating of both the particles and gas stream by the bath will require a finite time and cause local cooling around the particle jet. To investigate this effect the bath model has been extended to include convective heat transfer between the bath, gas and particles, and radiation within the gas cavity.

This paper reports on the incorporation of thermal effects into the model and presents results showing their impact.

Keywords: CFD, Multiphase heat and mass transfer, Process metallurgy, HIsmelt process, Iron Making, Thermal Radiation.

NOMENCLATURE

Greek Symbols
α volume fraction.
ε energy dissipation rate, [m^2 s^{-3}].
λ thermal conductivity, [W m^{-1} K^{-1}].
ρ mass density, [kg m^{-3}].
ϕ_p particle diameter, [m].
τ stress tensor, [Pa].
μ viscosity, [kg m^{-1} s^{-1}].

Latin Symbols
A interfacial area [m^2].
Cp specific heat, [J kg^{-1} K^{-1}].
g gravitational acceleration, [m s^{-2}].
F_D, F_B particle drag and buoyancy force, [N].
h static enthalpy, [J kg^{-1}].
k turbulence kinetic energy, [m^2 s^{-2}].
m_p particle mass, [kg].
$M_{F,r}$ inter-phase drag force, [N m^{-3}].
p pressure, [Pa].
Q_C, $Q_{M,}$, Q_R particle convective, mass transfer and radiation heat sources, [W].
Sc Schmidt number.
T temperature [K].
u_D, u_S drift and slip velocity, [m s^{-1}].
$\mathbf{u}$ velocity, [m s^{-1}].
$\mathbf{v}$ particle velocity, [m s^{-1}].
V_P particle volume [m^3].
$\mathbf{x}$ particle position, [m].
Y species mass fraction.

Sub/superscripts
g gas phase.
i chemical species index.
l liquid bath phase.
p particle phase.
r phase index.

INTRODUCTION

HIsmelt is a direct smelting technology for converting iron ore fines into pig iron. The process has been developed over a number of years and is slowly building into a serious challenge to the blast furnace. It offers the advantages of lower capital and operating costs, and greater raw material flexibility, whilst maintaining a high-quality metal product.

Development of the process has moved through a number of pilot plant designs to a commercial-scale facility of 0.8 Mt/a in Kwinana, Western Australia (2002-2008). All of these plant designs have been aided by the use of physical and CFD models. The plant is

currently being moved to Shandong in China to continue its development.

Scale up of any metallurgical process is problematic due to the increasing scales over which turbulent flow processes operate. Understanding the fluid dynamics involved and the associated heat and mass transfer has been critical to understanding and predicting the behaviour of the process and enabling the progression to larger smelting vessels.

CFD modelling of the HIsmelt Bath has been undertaken at the CSIRO for a number of years and has culminated in the development of the ANSYS/CFX thermal model presented in this paper.

MODEL DESCRIPTION

The domain for the CFD bath model includes the entire volume of the Smelt Reduction Vessel (SRV), illustrated in Figure 1, but the main focus is on ore reduction within the metal bath, coal devolatilisation and dissolution (into the metal), and the mass of liquid splashed into the gas space above the bath. Distinct gas, liquid and solid-particle phases are present in the computational domain and are critical to the smelting process and fluid dynamics behaviour. Each phase is comprised of a number of different components as summarised in Table 1 and Figure 2. There are large regions of continuous gas and similar volumes of continuous liquid; making the multi-fluid Eulerian-Eulerian approach the most appropriate way to model both the liquid bath and gas phases.

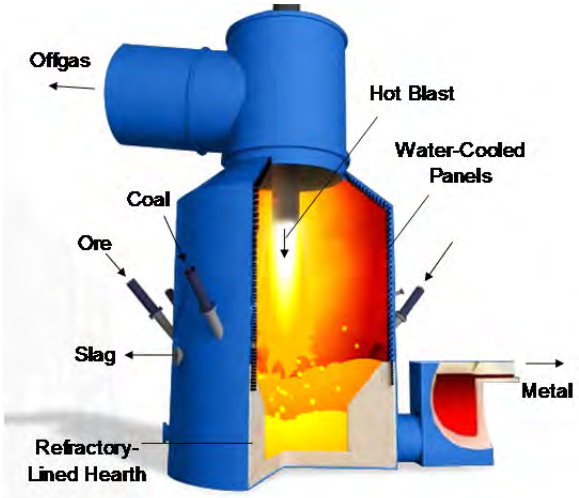

Figure 1: The HIsmelt Smelt Reduction Vessel.

The Eulerian-Eulerian model must simulate both the gas-continuous regions in which the liquid bath phase is assumed to be in dispersed form (splashes of droplets, fingers, sheets, etc in the upper regions of the SRV), as well as the liquid-continuous regions of the bath-proper in which the gas is assumed to be in the form of dispersed bubbles.

Within the gas phase a variable composition mixture is used to account for nitrogen (used as a carrier gas to inject the particles), carbon monoxide (evolved from ore reduction reactions) and hydrogen (evolved from coal devolatilisation). The liquid bath consists of two components, slag and metal. The slag is treated as a constant composition component, while the metal is considered to be a variable composition mixture of iron and carbon. An Algebraic Slip Model (or mixture model in CFX terminology) is used to account for the relative motion of slag and metal (Fe/C melt), as first demonstrated in models of gas injection into a slag/metal bath by Schwarz and Taylor (1998).

Table 1: Phases and their compositions.

Phase	Type	Components
Gas	Eulerian	N_2, CO, H_2
Liquid Bath	Eulerian	Fe, Carbon, Slag
Ore particles	Lagrangian	Fe_2O_3, H_2O
Coal particles	Lagrangian	Coal fixed component, and Coal volatile component.

Iron ore and coal particles are modelled using the Lagrangian particle tracking approach. Iron ore particles are considered to be composed of hematite (Fe_2O_3) and moisture (H_2O). Coal particles are a variable composition mixture of fixed carbon and volatile carbon.

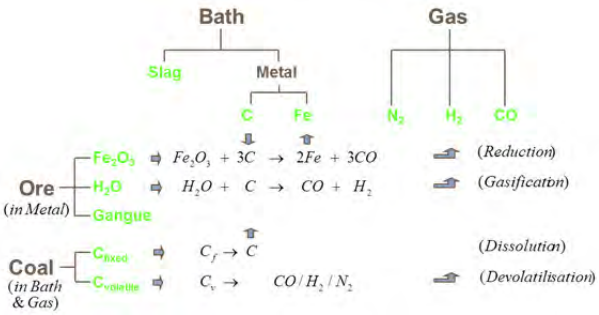

Figure 2: Schematic of the phase and component descriptions and associated reactions.

The reduction process is described by a series of idealised chemical reactions representing coal dissolution (into the molten iron):

$$C_{coal(sol)} \Rightarrow C_{metal} \quad (1)$$

coal devolatilisation (evolution of gaseous volatiles):

$$C_{vol(sol)} \Rightarrow CO + N_2 + H_2 \quad (2)$$

iron ore reduction (by dissolved carbon in the bath to form molten iron and carbon monoxide gas):

$$Fe_2O_{3\,ore} + 3C_{metal} \Rightarrow 2Fe_{metal} + 3CO \quad (3)$$

and gasification (water vapour in the ore particles reacts with dissolved carbon in the metal, generating hydrogen and carbon monoxide gas):

$$C_{metal} + H_2O_{ore} \Rightarrow H_2 + CO \quad (4)$$

Model Equations

For each Eulerian phase (gas and liquid-bath) continuity and momentum equations are solved to calculate the phase velocity, volume fraction and turbulence level. These transport equations can be written as:

Continuity equation with mass transfer

$$\frac{\partial}{\partial t}(\alpha_r \rho_r) + \nabla \cdot (\alpha_r \rho_r \mathbf{u}_r) = S_r \quad (5)$$

Here, the phases *r* are liquid bath phase (*r*=*l*) and gas phase (*r*=*g*). The term S_r is the net mass transfer to phase *r* from other interacting phases due to various reactions (described in detail in sections below).

Momentum equation

$$\frac{\partial}{\partial t}\left(\rho_r \alpha_r \mathbf{u}_r\right) + \nabla \cdot \left(\rho_r \alpha_r \mathbf{u}_r \mathbf{u}_r\right) = -\nabla \cdot \left(\alpha_r \tau_{ij,r}\right) - \alpha_r \nabla P + \alpha_r \rho_r g + M_{F,r} + MS_r' \quad (6)$$

$$\sum \alpha_r = 1 \quad (7)$$

The terms on the right hand side of the momentum equation, (equation 6), represent respectively the stress, pressure gradient, gravity, momentum exchange between the phases due to interfacial forces (only the drag force is considered here) and the net momentum transfer to phase *r* by other phases due to net mass transfer (MS_r'). Pressure is shared by both the phases. The stress term for phase *r* is described as follows:

$$\tau_{ij,r} = -\mu_{eff,r}\left(\nabla \mathbf{u}_r + (\nabla \mathbf{u}_r)^T - \frac{2}{3} I(\nabla \mathbf{u}_r)\right) \quad (8)$$

The effective viscosity for each phase, $\mu_{eff,r}$ is composed of two contributions: the molecular viscosity and the turbulent viscosity. The turbulent eddy viscosity is formulated using the *k*-*ε* turbulence model and turbulence is considered homogeneous across both phases (*k* and *ε* values are the same for each phase):

$$\mu_{T,r} = \rho_r C_\mu \frac{k^2}{\varepsilon} \quad (9)$$

The turbulence kinetic energy (*k*) and its energy dissipation rate (*ε*) are calculated from their governing transport equations (equations 10 and 11 respectively). The term τ_m in these equations (as computed by equation 14) takes into account the phasic turbulent viscosity (equation 9) and the molecular viscosity of each phase.

$$\frac{\partial \rho_m k}{\partial t} + \nabla \cdot \left(\rho_m \mathrm{u}_m k\right) = -\nabla \cdot (\Gamma_m \nabla k) + (G_m - \rho_m \varepsilon) \quad (10)$$

$$\frac{\partial \rho_m \varepsilon}{\partial t} + \nabla \cdot \left(\rho_m \mathrm{u}_m \varepsilon\right) = -\nabla \cdot (\Gamma_m \nabla \varepsilon) + \frac{\varepsilon}{k}(C_{\varepsilon 1} G_m - C_{\varepsilon 2} \rho_m \varepsilon) \quad (11)$$

where

$$\rho_m = \rho_l \alpha_l + \rho_g \alpha_g \quad (12)$$

$$u_m = u_l \alpha_l + u_g \alpha_g \quad (13)$$

$$\tau_m = \tau_l \alpha_l + \tau_g \alpha_g \quad (14)$$

The model constants used are the standard values, viz. C_μ =0.09; σ_k=1.00; σ_ε=1.00; $C_{\varepsilon 1}$=1.44, $C_{\varepsilon 2}$=1.92. The term *G* in above equation is the production of turbulence kinetic energy and described by:

$$G = \tau_m : \nabla u_m \quad (15)$$

Thermal Energy Transport

Conservation of thermal energy in the gas and liquid phases is calculated by solving for the phase static enthalpy, h_r :

$$\frac{\partial}{\partial t}(\alpha_r \rho_r h_r) + \nabla \cdot (\alpha_r \rho_r \mathbf{u}_r h_r) = \nabla \cdot (\alpha_r (\lambda_r + \lambda_r^t) \nabla T_r) + S_{h,r} + SH_{p,r} + SH_{m,r} + S_{rad,r} \quad (16)$$

where $\lambda_r + \lambda_r^t$ are the molecular and turbulent thermal conductivities, T_r is the temperature for phase *r* and source terms $S_{h,r}$, $SH_{p,r}$, $SH_{m,r}$, $S_{rad,r}$ are for energy transfer between phases, to and from particles, particle mass transfers and thermal radiation. Static enthalpy and temperature are related through the phase specific heat, Cp_r, by:

$$h_r = Cp_r T_r \quad (17)$$

Thermal radiation transport is calculated using the Discrete Transfer model of Shah (1979) and provides source terms for the phase-enthalpy and particle transport equations. A high value for the absorption coefficient is set for the liquid phase. This effectively limits radiation transport to within the gas only volumes and to/from the liquid surfaces.

Species Transport

Mass fractions of individual components (CO, N_2) in the multi-component gas phase are computed by solving each component's transport equation (equation 18) with relevant source/sink terms, while the mass fraction of H_2 in the gas phase is determined using constraint equation 19.

$$\frac{\partial \alpha_g \rho_g Y_{gi}}{\partial t} + \nabla \cdot \left(\alpha_g \rho_g \mathrm{u}_g Y_{gi}\right) = \nabla \cdot \Gamma_{gi} \alpha_g \nabla Y_{gi} + S_{gi} \quad (18)$$

$$\sum Y_{gi} = 1 \quad (19)$$

where *Y* is the mass fraction of species *i* in the *r* phase. Similarly, the mass fraction of individual components (Fe, C and slag) in the multi-component liquid phase is obtained by applying the algebraic slip model (ASM, equation 20 and 21). This is done in order to enable the separation of slag from metal. The slag is considered to be continuous in the liquid bath and its fraction is computed using constraint equation 22. The ASM enables computation of a slip velocity between metal (Fe/C) and slag, and the drift velocity of Fe/C. The drift velocity of a component is taken relative to the mixture (i.e. the liquid bath) velocity, whereas the slip velocity of a component is taken relative to the velocity of continuous medium in the mixture (i.e. slag velocity in this case).

$$\frac{\partial \alpha_l \rho_l Y_{li}}{\partial t} + \nabla \cdot \left(\alpha_l \rho_l (\mathrm{u}_l + u_{Di}) Y_{li}\right) = \nabla \cdot (\Gamma_{li} + \frac{\mu_t}{\mathrm{Sc}_t}) \alpha_l \nabla Y_{li} + S_{li} \quad (20)$$

where, u_{Di} is the drift velocity of species *i*, and is related to the slip velocity u_{Si} by equation 21.

$$u_{Di} = u_{Si} - \sum_i u_{Si} Y_{li} \quad (21)$$

$$\sum Y_{li} = 1 \quad (22)$$

Lagrangian particle tracking of ore and coal

The velocities, trajectories and temperatures of representative ore and coal particles are computed using the Lagrangian tracking approach, originally developed by Crowe *et al.* (1977), which involves solving the momentum equations based on Newton's second law (equations 23 to 25) and a particle temperature equation 26. Ore and coal particles are treated as separate phases. The interaction between the carrier fluid and particles has been treated using two-way coupling. The carrier fluid for particles can be the Eulerian gas phase or the Eulerian liquid bath phase, the appropriate phase being decided based on a critical volume fraction of these phases at the location of the particle. Particle drag and heat transfer switches from gas to liquid at this critical voidage. Equations 23 and 24 compute the particle displacement using forward Euler integration of particle velocity over the time-step. In forward integration, the particle velocity is calculated at the start of the time step and is assumed to prevail over the entire time step. At the end of the time step, the new particle velocity is computed using the particle momentum equation 25. Momentum is transferred between fluid and particles only through the inter-phase forces. In general these forces would be drag force, added mass force, pressure force, buoyancy force and Basset force. In this work, only drag and buoyancy has been considered, as they are the dominant forces.

$$\frac{dx_i}{dt} = v_i \tag{23}$$

$$x_i^n = x_i^0 + v_i^0 \partial t \tag{24}$$

$$\frac{d(m_p v_i)}{dt} = F_D + F_B \tag{25}$$

$$\frac{d(m_p C_p T_p)}{dt} = Q_C + Q_M + Q_R \tag{26}$$

The effect of turbulent dispersion on particle motion has been included for the gas phase but not the liquid phase as particle motion in the latter is dominated by the drag force. The mass, momentum and energy sources transferred by the particles to the phase in contact (gas or bath) are determined by the reactions occurring (ore reduction, coal devolatilisation and coal dissolution). Similarly, energy sources between particle and the phase in contact are computed using the Ranz and Marshall (1952) model for convective heat transfer, Q_C, and the Discrete Transfer model calculates the radiation sources, Q_R. These particle sources are applied in the control volume in which the particle is located during the time step. These sources are then applied each time the fluid coefficients are calculated.

Interfacial mass, momentum and energy exchange

The following phase-pairs interact during the simulations and exchange mass, momentum and energy:

Bath-Gas, Ore-Gas, Ore-Bath, Coal-Gas and Coal-Bath

The drag force, $M_{F,r}$, between the liquid bath and gas is computed using a user-defined drag function derived from experimental models (Schwarz, 1996). Convective heat transfer between the gas and bath, $S_{h,r}$, is calculated as:

$$S_{h,g} = -S_{h,l} = \frac{(\alpha_l \lambda_l + \alpha_g \lambda_g)\mathrm{Nu}}{\phi_B} \frac{(\alpha_l + \alpha_g)}{\phi_B} \left(T_l - T_g\right) \tag{27}$$

with the Nusselt number, Nu, calculated from the correlation of Tomiyama (1998):

$$\mathrm{Nu} = 2.0 + 0.15\mathrm{Re}^{0.8}\mathrm{Pr}_l^{0.5} \tag{28}$$

where Re is the bubble Reynolds number and $\mathrm{Pr_l}$ is the bath Prandtl number.

For ore–gas phase and ore-liquid phase interaction, the drag force coefficient is computed using the Schiller and Naumann (1935) drag model.

For a coal particle that undergoes devolatilisation or dissolution, coal particle porosity is computed and used in a modified Schiller-Naumann model in which the particle diameter remains constant (i.e. there is no swelling of the coal particle).

Convective heat transfer, Q_C, between a coal or ore particle and the fluid phase is calculated from:

$$Q_C = \pi \phi_P \lambda_r \mathrm{Nu_p} (T_r - T_P) \tag{29}$$

with the Nusselt Number, $\mathrm{Nu_p}$, given by the Ranz and Marshall (1952) correlation:

$$\mathrm{Nu_p} = 2 + 0.6\mathrm{Re_p}^{0.5}\mathrm{Pr}_r^{0.3} \tag{30}$$

where $\mathrm{Re_p}$ is the particle Reynolds number and Pr_r the Prandtl number for the fluid phase, *r*, the particle is in contact with. From Q_C the source terms, $SH_{p,r}$, for equation (16) is determined by multiplying by the number of particles in the fluid control volume.

Mass transfer that arises due to particle reactions produces source terms in the continuity equation, S_r, (equation 5) momentum equation, MS_r (equation 6) and the energy equation, $SH_{m,r}$ (equation 16). The mass transferred is dependent upon the rate of reaction of each reaction. These reactions are now discussed in more detail.

Coal devolatilisation reaction

$$\begin{array}{l} \mathrm{Coal}_{(s)} \rightarrow \mathrm{Volatiles}_{(g)} \quad + \quad \mathrm{Char}_{(s)} \\ \qquad\quad \{\mathrm{CH_4}, \mathrm{H_2O}, \mathrm{etc}\} \qquad\quad \{C + \mathrm{ash}\} \end{array} \tag{31}$$

This reaction is simplified to:

$$\begin{array}{l} \mathrm{Coal}_{(s)} \rightarrow aCH_4 + bC_{(s)} \\ \{\mathrm{cracking}\} \\ \rightarrow \quad xC_{(s)}\{\mathrm{soot}\} + yH_{2(g)} + zC_{(s)}\{\mathrm{char}\} \end{array} \tag{32}$$

Although soot will behave differently from char, it is assumed that within the bath the soot will react with oxygen to form CO. This has been assumed to also occur within the gas phase, although in reality some soot will escape with the gas into the topspace.

$$Coal_{(s)} \Rightarrow aC_{(s)} + bCO + cH_2 + dN_2 \tag{33}$$

The main aim of including devolatilisation in the bath model is to allow for the generation of large volumes of volatiles gas within the bath and to simulate the spatial distribution of this generation. Data from the literature have been used to give a simple representation of the way coal particles devolatilise. A simplified linear fit to

the Oeters and Orsten (1989) results was implemented in previous CFD models (Schwarz, 1994, Stephens *et al.* 2011).

With the inclusion of thermal effects into the model, combined with the endothermic nature of coal devolatilisation and the low heat capacity of the gas, it is possible that cooling of the particles could occur as volatiles are released. If the reaction is too fast then the particle temperature can drop to unphysical values. The model of Oeters assumes that the particle is injected directly into the liquid bath and that it heats up to close to the bath temperature before evolving volatiles. Once volatiles are released they form a gas bubble in which the particle is located. Hence the heat transfer and mass transfer to and from the particle are through gas in the bubble surrounding the particle. This would suggest that the reaction rate from Stephens *et al.* (2011) is the maximum rate and would also apply in a turbulent gas stream that was at the bath temperature.

However at lower temperatures the reaction rate would reduce. Assuming that the model from Stephens *et al.* (2011) gives the maximum rate then a reduction factor could be applied to that rate depending on particle temperature. Using an Arrhenius model and arbitrarily assuming that no reaction occurs below 500°C and the maximum rate is achieved at 1200°C, the reduction function is:

$$f(T_p) = 60e^{\frac{-6000}{T_p}} \tag{34}$$

where T_p is the particle temperature [K]. This function is plotted in Figure 3.

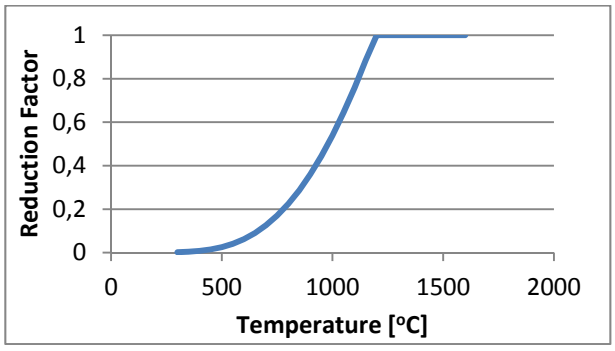

Figure 3: Reduction function, $f(T_p)$.

The overall rate of the devolatilisation reaction for each track is then given by:

$$Rate = \frac{dm}{dt} = 60e^{\frac{-6000}{T_p}} \frac{C_{coalvolatile}\, V_p\, \rho_p}{0.35\times 1.05(\emptyset_p)^{1.5}} \tag{35}$$

where V_p is the initial volume of the particle in the track.

Coal Dissolution

Coal dissolution (equation 1) is only allowed to occur between coal particles and metal. Furthermore it is assumed that it only occurs after devolatilisation is complete. In reality, some of the coal will not contact metal, but will rather react in the slag. The metal volume fraction is used to weight the reaction rate, R_{coal}, which is given by:

$$\frac{dR_{coal}}{dt} = A_{p,coal}\rho_l\chi(C_{carbon,sat} - C_{carbon})Y_{metal} \tag{36}$$

where $A_{p.coal}$ is the coal particle interfacial area, ρ_l is the liquid density, χ is the mass transfer coefficient for liquid side transport, $C_{carbon,sat}$ is the saturation carbon concentration in the bath, C_{carbon} is the carbon concentration in the vicinity of the particle and Y_{metal} is the metal mass fraction in the vicinity of the particle. The particles shrink as they dissolve, so the interfacial area is:

$$A_{p,coal} = \pi\emptyset_{p,coal}^2 \tag{37}$$

Ore Dissolution

Equation 3 describes the ore reduction and dissolution process. Here, we simplify by assuming that all the iron (Fe) produced reports to the metal phase. In reality, some ore will melt as FeOx in slag. The equation for the mass reaction rate, R_{ore} is:

$$\frac{dR_{ore}}{dt} = A_{p,ore}\rho_l\chi C_{carbon}Y_{metal}\frac{196}{36} \tag{38}$$

where $A_{P.ore}$ is the ore particle interfacial area. The particles shrink as they dissolve, so the interfacial area is again given by:

$$A_{p,ore} = \pi\emptyset_{p,ore}^2 \tag{39}$$

The stoichiometric mass coefficients in equation 3 are:

$$\mathrm{MC}_{Fe_2O_3} = \frac{160}{196};\ \mathrm{MC}_C = \frac{36}{196};\ \mathrm{MC}_{Fe} = \frac{112}{196};\ \mathrm{MC}_{CO} = \frac{84}{196}.$$

The mass transfer coefficient, χ, is estimated based on reported reaction rates measured for ore reduction by Nagasaka and Banya (1992). Table 2 summarizes the discussions above.

Table 2: Reaction physics summary.

Material	Reaction	Location	Depends on
Coal	Devolatilisation	Bath and Gas	Temperature and particle diameter. Particle diameter remains constant.
	Dissolution	Bath (Metal)	Carbon concentration in the Bath. Liquid side mass transfer control. Particle diameter reduces.
Ore	Reduction	Metal	Carbon concentration in the bath. Liquid side mass transfer control. Particle diameter reduces.

Numerical Model

The commercial code ANSYS/CFX (ANSYS, 2010) is used to solve the equations and physical models described above. ANSYS/CFX 13 uses a finite volume method to iteratively solve the above equations on an unstructured grid. Coupling between pressure, velocity and phases is handled implicitly by the CFX coupled volume fraction solver. The second order accurate "Compressive Scheme" was used to discretise advection terms in the equations to improve solution accuracy.

A second order backward Euler implicit time integration scheme was used to advance transient terms in the

equations. An initial time step of 0.0005 seconds was used to advance the solution in time for the first few time steps. Due to the highly transient nature of the flow with splashing and gas evolution an adaptive time stepping strategy was used to minimise computational time and ensure convergence at each time step. After the initial start up transient the typical time step was 0.001 seconds with on average 6 coefficient loops required at each time step to reduce the residuals below 2 x 10^{-4} RMS and to achieve the conservation target.

Density for the gas phase is calculated based on the perfect gas law and is a function of composition, pressure and temperature. The liquid bath was assumed incompressible. At wall boundaries scalable turbulent wall functions were used to capture near wall effects.

The simulations were run on quad core dual CPU, 3.6GHz Intel Westmere processors installed in CSIRO's CFD cluster. The model was run for 10 seconds of simulated time on 16 parallel partitions. Total wall time for the simulation was approximately 8 days. Further details of the numerical approach and implementation are described in ANSYS (2010).

GEOMETRY, BOUNDARY AND INITIAL CONDITIONS

The model described above was applied to the HIsmelt Research and Development Facility (HRDF) pilot plant reactor. Internal diameter of the reactor is 2.7 m in the hearth and 5.1 m in the top space with a height of roughly 6 m. To reduce the model size and run time a vertical symmetry plane is used through the centre of the lances. Model geometry is shown in Figure 4. Coal and ore particles are injected through the base of the lances with a nitrogen carrier gas at a temperature of 30°C and velocity of 80.4 ms^{-1}. The particle size distribution is accounted for using a Rosin-Rammler distribution with the coal mean diameter being 294 µm and an ore mean diameter of 1112 µm. Particles are uniformly injected from the lance exits at a rate proportional to their mass flow rate. Gas can leave the domain through a pressure boundary at the offgas outlet.

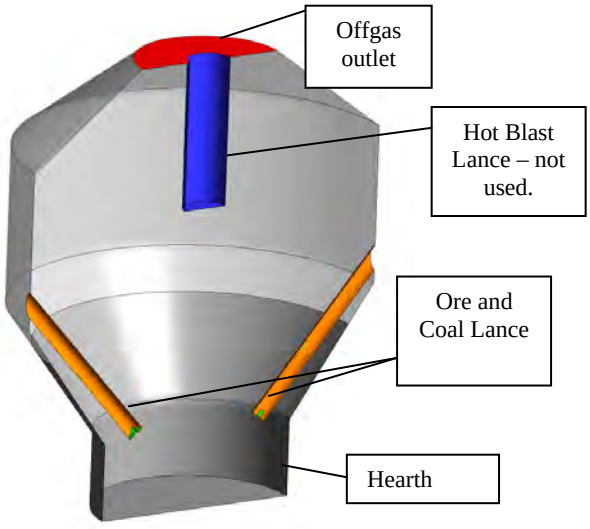

Figure 4: HIsmelt SRV geometry.

The mesh for the domain consists of over 45,000 nodes and 255,000 tetrahedral elements. An indication of the mesh resolution is shown in Figure 5 for the symmetry plane and shows the refinement used to capture the steep gradients at the lance exits.

Initial conditions for the simulation set the gas and bath temperatures at 1437°C, the metal height is 530 mm and slag depth above the metal is 1189 mm. The bath is assumed quiescent with no gas bubbles or cavities and contains no particles.

RESULTS

The model described above was run for 10 seconds of real time and the predicted gas distributions at four time instants are plotted in Figure 6. Gas injection and more significantly gas generation from the particles induces complex flow behaviour such as splashing and formation of a fountain in the top space of the vessel. Such behaviour is consistent with previous iso-thermal model results such as Stephens *et al.* (2011).

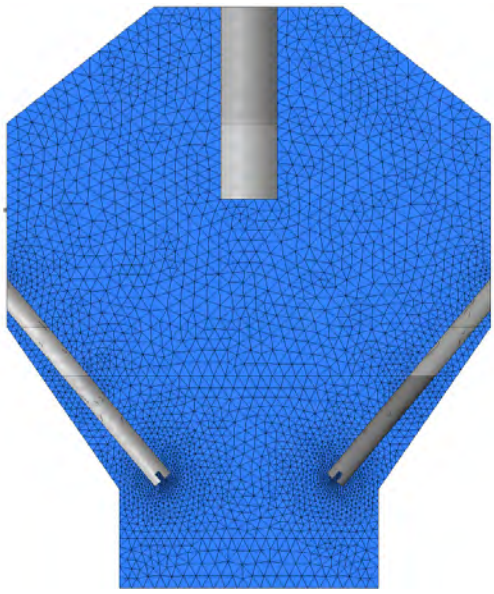

Figure 5: Symmetry plane mesh.

In this work we have extended the previous work by including heat transfer, and have predicted gas temperature distributions that are at the same time plotted in Figure 7. Black contour lines for a gas volume fraction of 0.8 are superimposed over the temperature plots. Particles and carrier gas enter the vessel at 30 °C and gas is heated rapidly to the bath temperature. However cavities with gas temperatures below 500 °C occur directly above the lances and a cool jet below 100 °C is predicted for a couple of lance diameters downstream of the lance tips. As shown by the liquid bath temperature plots in Figure 8, bath temperature remains nearly constant with only drops entrained into the gas cavities near the lance and in the top space experiencing some cooling.

Temperature of typical coal particles is plotted in Figure 9 up to a time of 9.14 seconds. Figure 9a shows how coal particles larger than 200 µm in the gas phase penetrate a significant distance into the bath and generally do not experience a rapid rise in temperature. Smaller coal particles, in Figure 9b, only partially penetrate the bath; with many being entrained by gas plumes into the top space where they undergoing heating. Many particles contact the bath and in the model are reborn into the liquid phase.

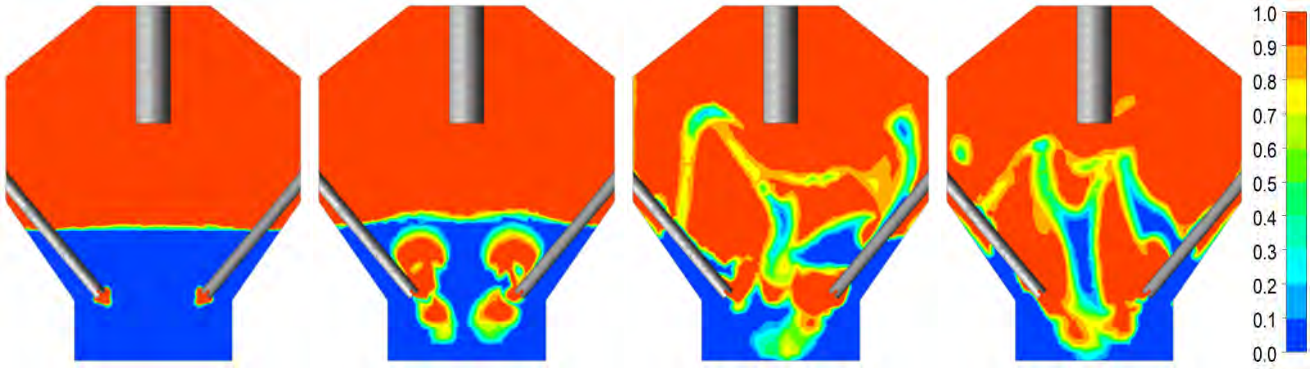

t= 0.046 [s] t =0.47 [s] t = 2.4 [s] t = 9.14 [s]

Figure 6: Gas volume fraction at various times.

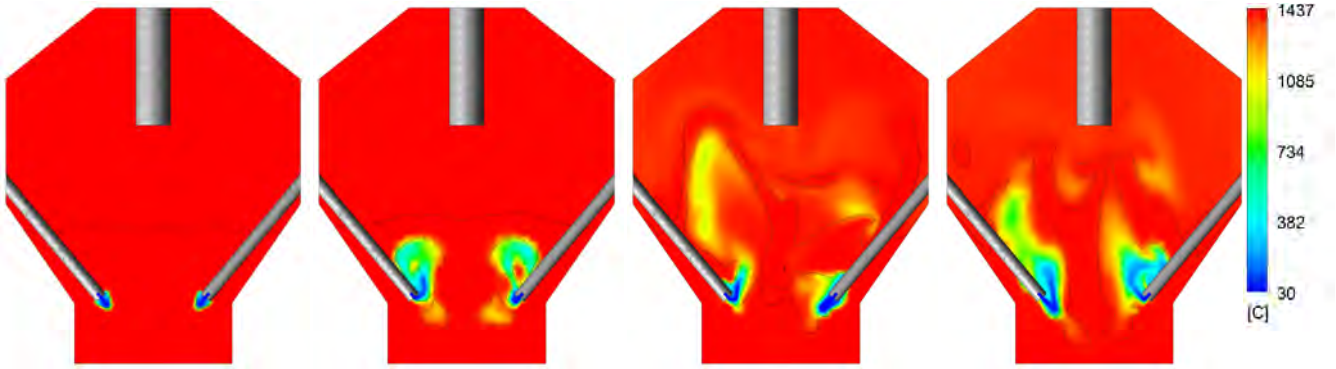

t = 0.046 [s] t =0.47 [s] t = 2.4 [s] t = 9.14 [s]

Figure 7: Gas temperature at various times.

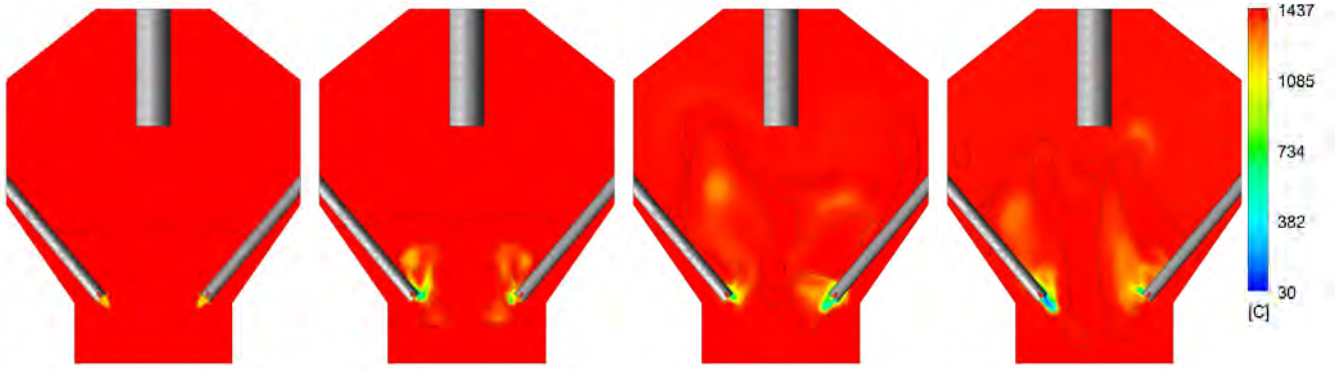

t = 0.046 [s] t =0.47 [s] t = 2.4 [s] t = 9.14 [s]

Figure 8: Bath temperature at various times.

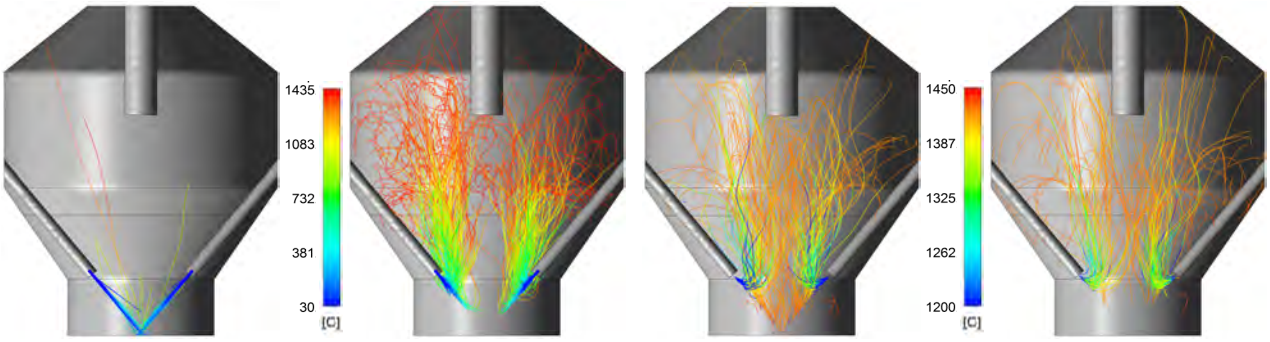

(a) >200 µm in gas (b) ≤200 µm in gas (c) >200 µm in bath (d) ≤200 µm in bath

Figure 9: Coal particle temperatures up to a time of 9.14 [s].

Temperatures for coal particles in the liquid are shown in Figure 9(c) and (d). Note the different temperature scales used for particles in the gas and liquid phases. It is also apparent that once particles contact the liquid bath they undergo rapid heating; this is for both small and large particles.

Temperatures of the larger diameter ore particles are plotted in Figure 10. With a mean diameter of 1112 µm ore particles do not experience a large temperature rise until they enter the liquid bath. They also penetrate into the liquid bath without being entrained into the top space with the gas.

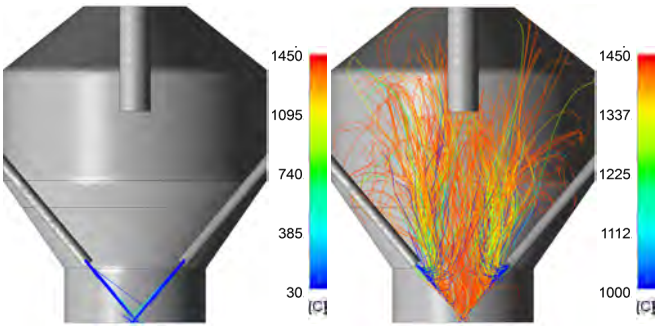

(a) Ore in gas (b) Ore in bath

Figure 10: Ore particle temperatures to a time of 9.14 [s].

Heating of the coal particles results in devolatilisation and the release of volatiles; the change in coal volatile mass fraction is plotted in Figure 11 for the same particle groups shown in Figure 9. Large particles in the gas phase undergo little volatile release due to the slow heating rate, see Figure 11a; but once they enter the bath, as shown in Figure 11c, they rapidly evolve their volatiles. Smaller particles in the gas phase undergo devolatilisation more rapidly than the larger particles in the gas, as shown in Figure 11b, but not as fast as large particles in the bath phase. When small particles contact and enter the bath they undergo rapid devolatilisation, Figure 11d, with most of the volatiles being released near the lance tip.

Rapid devolatilisation of the coal produces large gas source terms that are primarily carbon monoxide and hydrogen. Plots of the CO and H_2 mass fractions in the gas phase are shown in Figures 12 and 13. In Figure 6 at 0.47 seconds a gas cavity has formed below the lance with a region of liquid between the cavity and lance tip. An analysis of results at 25 ms intervals shows the cavity is formed by coal particles penetrating the liquid bath and devolatilising within the liquid. This can also be seen by the high CO and H_2 concentrations in Figures 12 and 13 at 0.47 seconds.

Model Validation

Given the nature of the HIsmelt process (i.e. high temperature, molten splash, heterogeneous reactions) model validation will always be problematic. In addition, thermal transients in the process (such as bath temperature) occur over longer time scales than can be currently simulated (due to the complexity of the model). Model validation has relied on gaining confidence in various aspects of the two-phase model during development by comparing with small scale water, iron and tin models (e.g. Schwarz 1996). Plant data is also used where possible to verify model predictions. For

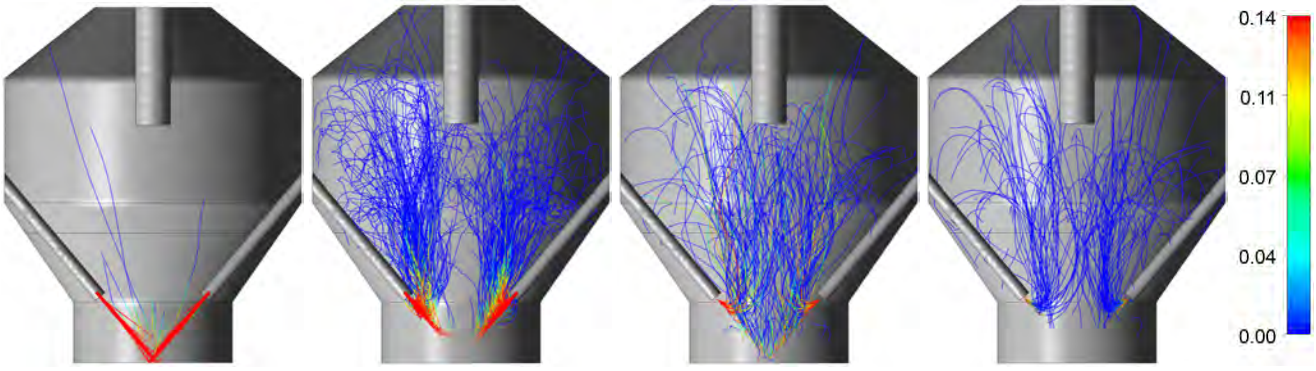

(a) >200 µm in gas (b) ≤200 µm in gas (c) >200 µm in bath (d) ≤200 µm in bath

Figure 11: Coal particle volatile mass fraction to a time of 9.14 [s].

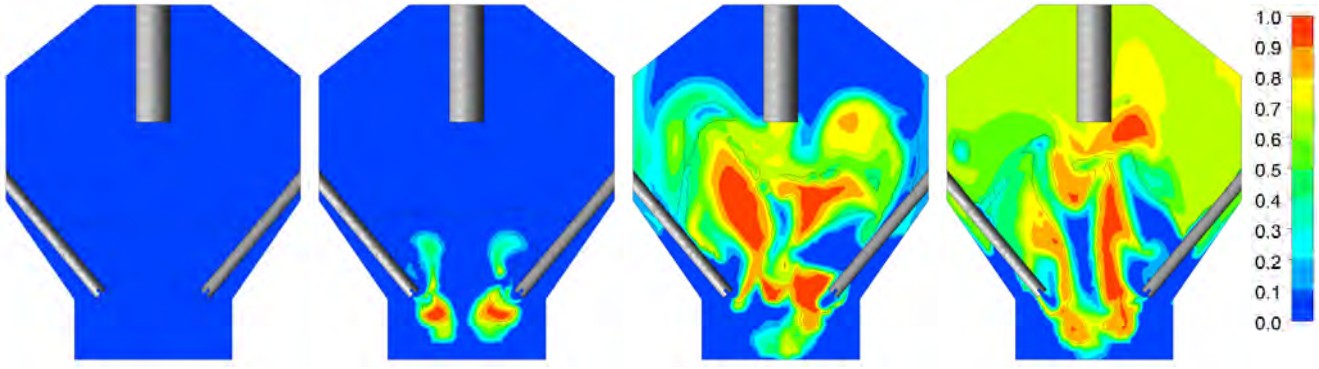

t = 0.046 [s] t =0.47 [s] t = 2.4 [s] t = 9.14 [s]

Figure 12: Carbon monoxide mass fraction at various times.

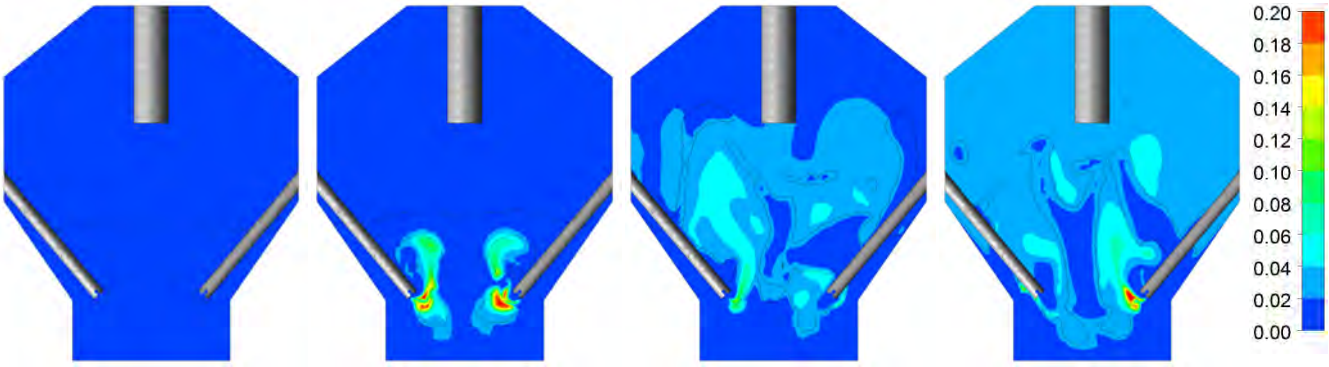

Figure 13: Hydrogen mass fraction at various times.

example, Figures 9(a) and 10(a) indicate that feed particles penetrate to the bottom of the bath. This is corroborated by wear of the refractory bricks at the centre of the hearth floor found during operation of the HRDF plant.

CONCLUSION

Multiphase fluid dynamics and heat transfer within the HIsmelt vessel are critical to plant operation and performance. Understanding these processes is critical to scale-up and further development of the HIsmelt process. A previously developed isothermal model of the bath has been extended to include heat transfer processes for both convection and radiation so as to allow the prediction of temperature distributions and particle heating rates.

Model results show that bath temperature is relatively constant and that cooler gas cavities exist near and above the lance tips. Coal particles undergo rapid heating once they enter the liquid bath, which causes rapid devolatilisation leading to the formation of gas cavities below the liquid surface. Particles in the gas smaller than 200 µm in diameter were found to increase in temperature and undergo devolatilisation. Larger coal particles tended to only devolatilise once they contracted the liquid bath. This work indicates that, while adding to computational cost, inclusion of thermal effects can be important for particle heating rates and gas generation within the bath and subsequent bath dynamics.

ACKNOWLEDGMENTS

The authors would like to thank HIsmelt Corporation for permission to publish this work, and in particular Dr Rod Dry for his long-standing support and technical inputs to the modelling effort.

REFERENCES

ANSYS Workbench / Fluent 13.0, ANSYS Inc., USA. 2010.

CROWE, C. T., SHARMA, M. P. and STOCK, D. E., (1977), "The Particle-Source-in-Cell (PSI-CELL) Model for Gas-Droplet Flows", *J. Fluids Eng.*, **99**, 325-332.

DAVIS, M., and DRY, R., (2012), "CFD modelling in the development and scale-up of the HIsmelt process", 9th *Int. Conference on CFD in the Mineral and Process Industries*, CSIRO, Melbourne, Australia, 10-12 Dec.

DAVIS, M., DRY, R., and SCHWARZ, M.P., (2003), "Flow Simulation of the HIsmelt Process", *3rd Int. Conference on CFD in the Mineral and Process Industries*, CSIRO, Melbourne, Australia, 10-12 Dec.

NAGASAKA, T. and BANYA, S., (1992), "Rate of Reduction of Liquid Iron Oxide", *Tetsu-to-Hagane*, **78**, 1753-1767.

OETERS F., and ORSTEN S., (1989), "Degassing of coal particles injected into iron melts", *Steel Research*, **60**, 145-150.

RANZ, W.E. and MARSHALL, W.R., (1952), "Evaporation from drops", *Chem. Eng. Prog.* **48**, 141-146.

SCHILLER, L. and NAUMANN, Z., (1935), "A Drag Correlation", *Z. Ver. Deutsch. Ing.*, **77**, 318.

SCHWARZ, M.P., (1994), "The role of Computational Fluid Dynamics in process modeling", *Proc. of 6th AusIMM Extractive Metallurgy Conference*, pages 31-36, Aus.IMM, 1994.

SCHWARZ, M.P., (1996), "Simulation of Gas Injection into Liquid Melts", *Applied Mathematical Modelling*, **20**, 1996, 41-51.

SCHWARZ, M.P. and TAYLOR, I. F., (1998), "CFD and Physical Modelling of Slag-Metal Contacting in a Smelter", *4th World Conference on Applied Fluid Mechanics*, Freiburg, Germany: WUA-CFD, 4:1-4:15.

SHAH, N.G., (1979), "A New Method of Computation of Radiant Heat Transfer in Combustion Chambers", *PhD thesis*, (Imperial College of Science and Technology, London).

STEPHENS, D., TABIB, M., DAVIS, M., and SCHWARZ, M.P., (2011), "CFD Simulation of Bath Dynamics in the HIsmelt Smelt Reduction Vessel for Iron Production", *8th Int. Conference on CFD in Oil & Gas, Metallurgical and Process Industries*, SINTEF/NTNU, Trondheim, Norway, 21-23 June.

TOMIYAMA, A., (1998), "Struggle with computational bubble dynamics". Third International Conference on Multiphase Flow, Lyon, France. June 8-12.

10th International Conference on CFD in Oil & Gas, Metallurgical and Process Industries
SINTEF, Trondheim, Norway *CFD 2014*
17-19 June 2014

MODELLING OF THE FERROSILICON FURNACE: EFFECT OF BOUNDARY CONDITIONS AND SiO BURST

Balram PANJWANI [1]*, **Jan Erik OLSEN**[1†], **Bernd WITTGENS**[1‡]
[1]SINTEF Materials and Chemistry, 7465 Trondheim, NORWAY

*E-mail: balram.panjwani@sintef.no
† E-mail: jan.e.olsen@sintef.no
‡ E-mail: bernd.wittgens@sintef.no

ABSTRACT

A by-product from the ferrosilicon process is process gas which escapes into the furnace hood were it reacts with air. The process gas mainly consists of CO with some SiO and moisture. Modeling the gas behavior inside the furnace hood is challenging due to the complex interaction between flow, reactions, radiation and turbulence. One of the issues is the selection of proper boundary conditions, especially, the boundary condition used for the charge surface through which the process gas is released, which strictly is neither a wall surface nor a mass flux boundary. Traditionally, this boundary condition is modeled as a mass flux boundary, without considering the effect of roughness due to uneven distribution of charge material. In present study, effect of accounting charge surface as a rough wall on the flow distribution is discussed. The results obtained from this study is compared with a simulation, where charge surface is modelled as a mass inlet boundary condition. Another issue is the boundary condition accounting for SiO burst. It is observed that process gas is frequently released in local bursts typically with a high concentration of SiO. This is believed to promote local hot spots, which favor NO_X formation. Bursts of SiO are modeled and results show that both the strength of the burst and its location play a significant role in the NO_X production.

Keywords: Ferrosilicon, Blowing, burst, SiO2 dust, Combustion, Charge surface.

INTRODUCTION

Ferrosilicon is produced in submerged arc furnaces (SAF) where ore (silica) and carbon (coke, coal, etc.) are mixed inside a furnace. Both ore and carbon react when high voltage electric energy is supplied through electrodes, and this process is known as a reduction process. The reduction process produces alloys and an energy rich off-gas inside the reduction zone, which is beneath the charge surface and close to the electrode tip. The alloys, which are in liquid phase, sink to the bottom and this molten metal is collected through a tapping hole. The energy rich process gas rises upward from the reduction zone and escapes through the charge surface into a furnace hood. Simultaneously, air is sucked into the hood through various open areas on the furnace walls due to the pressure drop. The air and process gas reacts inside the furnace hood and produces an off-gas potentially containing harmful substances. In a ferrosilicon furnace, the process gas emerging from the charge surface mainly consists of CO with some SiO, water vapour, and volatiles. Reactions taking place between process gas and air in the furnace hood create temperature sufficiently high for formation of thermal NO_X. Release of process gas from the charge surface is non-uniform not only due to the transient and inhomogeneous reduction process but also due to inhomogeneous porosity distribution of charge material beneath the charge surface. Occasionally, the process gas (CO and SiO) bursts through the charge surface. These bursts mainly consist of high concentration of SiO. The reaction of SiO with air is highly exothermic resulting in local hot pockets inside the furnace hood, which subsequently leads to increase formation of NO_X. From industrial experience the strength of the jets or bursts and the amount of NO_X formation are strongly correlated to each other. The high temperature bursts are triggered by avalanches in the charge. The charge avalanches causes outburst of large quantities of combustible gases, like CO/SiO, that rise from pockets of poorly carbonized charge material (Grådahl *et al.*, 2007). Blowing is another extreme situation, where SiO rich gas from around the electrode tip is released through a gas channel in the charge. Then large quantities of SiO are burnt in air to silica dust (SiO_2). The observed correlation between NO_X and silica is also valid under blowing: blowing results in both high NO_X and silica formation. Compared to the avalanche phenomenon, which is always short in duration, the blowing phenomenon can last much longer. A boundary condition accounting for SiO bursts is presented and its' impact on NO_X Formation is also discussed.

Another challenge when modeling the combustion inside the furnace hoods is choice of boundary condition for the charge surface due to the non-uniform distribution of charge material (ore and carbon) on the surface. Traditionally, the charge surface is modeled as a mass flux boundary condition with no roughness effects accounted for. Alternatively, the charge surface can be modeled as a wall with roughness. However, a wall has no inherent inflow of fluid, which is required for the charge surface. While modeling the charge surface as

a wall boundary condition, a model that is valid for the range from smooth to fully rough walls is required. However, with the standard turbulence model to describe the near wall zone is not accurate and therefore special treatment is required closer to the inner wall regime. One of the common approaches is to use a wall function proposed by Launder and Spalding (Launder and Spalding, 1974). In this approach, the continuity and momentum equations along with the turbulence model equations are only solved in the outer region of the boundary layer. The inner region of the boundary layer is resolved with a predefined wall function. There have been many studies in the development of the wall function applicable for both smooth and rough walls (Jiménez, 2004). In this paper, a law of wall suitable for rough-wall surfaces is reviewed. While modeling the charge surface as a wall boundary condition the release of process gas from the charge surface need to be done explicitly. The most appropriate approach is to use source term for the mass, momentum, species and energy equations. These source terms will ensure that the correct amount of process gas with correct momentum and energy is released from the charge surface. Metal industries in Norway are committed toward the improvement of furnace operation, and their aim is to lower NO_X levels and other pollutants and to achieve this, a better understanding of the flow phenomena inside the furnace hood and especially close to the charge surface is needed. Major aim of the present study is to gain more understanding of the flow phenomena taking place inside the furnace hood with help of CFD. A steady state CFD model is developed using the commercial software ANSYS FLUENT (ANSYS, 2011). The major objectives of the present research work is to address

1. How the surface roughness of the charge surface affects the flow distribution?
2. How do SiO bursts affect the temperature and NO_X formation?
3. Does the location of burst have the impact on the NO_X formation?

CFD MODEL AND BOUNDARY CONDITIONS

A steady state CFD model solving for continuity, momentum, energy, species transport and radiation equations is developed using a general purpose CFD tool ANSYS FLUENT (ANSYS, 2011). The Radiation is modeled through Discrete Ordinance (DO) model, and the turbulence is modeled with RNG k-ε turbulence model, The near wall behavior is modelled with the standard wall functions. For rough walls appropriate roughness height and roughness constant are chosen. The process gas with a certain magnitude of velocity and temperature is escaped through the charge surface. It is rather easy to set the flow parameters of process gas at the charge surface using mass flux boundary condition, however, setting the process gas flow parameters at the charge surface with wall boundary condition is not very straightforward. FLUENT specific user defined functions (UDF) are employed to model the flow phenomena close to the charge surface. UDF for the source term in the continuity, momentum, energy and species transport equations were incorporated. The value of the source term was non-zero at the first grid cell of charge surface and zero for the rest of computational domain. The spatial discretization scheme was second order accurate. The pressure interpolation scheme was standard and the pressure gradient term was discretized using Green-Gauss cell based approach. The pressure velocity coupling was based on the SIMPLE algorithm.

Combustion Model and Reaction Mechanism

In the present study Eddy Dissipation Concept model (EDC) was used for turbulence chemistry interaction (Magnussen and Hjertager, 1977). The EDC model is derived from turbulent energy cascade theory, where turbulent kinetic energy cascades from the larger eddies to smaller eddies. The cascading process continues until eddies are sufficiently small and they can't transfer energy further down. The EDC model assumes that the chemical reaction occurs on these smaller dissipative eddies, whose length and time scales are of the same order as the Kolmogorov length scale. Reaction within the fine eddies is assumed to occur as a constant pressure Perfectly Stirred Reactor (PSR) (GRAN and MAGNUSSEN, 1996a,b), where reactions proceed over the time scale, governed by the Arrhenius rates of Equation.

Table 1: Reduced reaction scheme with kinetic parameters in Kelvin, cal/mol, cm^3

Reaction	Ar	N	Er
$2CO + O_2 \rightarrow 2CO_2$	2.24E+18	0.00	4776
$2SiO + O_2 \rightarrow 2SiO2$	1.00E+18	0.00	0.24

The gas species accounted in the CFD model is CO, SiO and H2O originating from the furnace crater, O_2 and N_2 from surrounding air and CO_2 and SiO_2 which are products of the reactions. In the present study SiO2 is modeled as a gas phase, however heat of condensation from gas phase (SiO2) to solid phase (SiO2) is accounted in energy equation. Generally, there is an extensive reaction scheme governing the combustion process, accounting for detailed kinetics that lead to the larger CPU cost. Therefore, a simplified or reduced scheme shown in the Table 1 has been investigated. NO_X formation is estimated using post processing approach available with FLUENT (ANSYS, 2011) but without considering the fluctuation in temperature and species.

Furnace Geometry and Computational Domain

The modeled geometry is the pilot scale furnace designed and developed at SINTEF/NTNU. The pilot furnace is a kind of scaled version of the actual ferroalloys furnace; however, there are some noticeable differences. The pilot furnace has one electrode in the middle but the actual furnace consists of three electrodes. Furthermore, the height to diameter ratio of the pilot furnace is larger than height to diameter ratio of the actual furnace. Despite these differences, the processes such as reduction of ore and resulting process gas formation inside the pilot furnace are exactly

similar to the actual furnace. The pilot furnace can be operated with both AC and DC power supply. The furnace hood is connected to an off gas system, and equipment for monitoring composition and temperature of the gas is installed at the exhaust. A sketch of the furnace is shown in Figure 1. The original pilot furnace is asymmetric due to an offset in the exhaust, which makes impossible to investigate this geometry through 2D axis-symmetric approach, and therefore the geometry has to be modeled in 3D, which indeed results in higher CPU cost. 3D CFD validations of the pilot furnace have been performed under various conditions in previous work (Panjwani and Olsen, 2013).

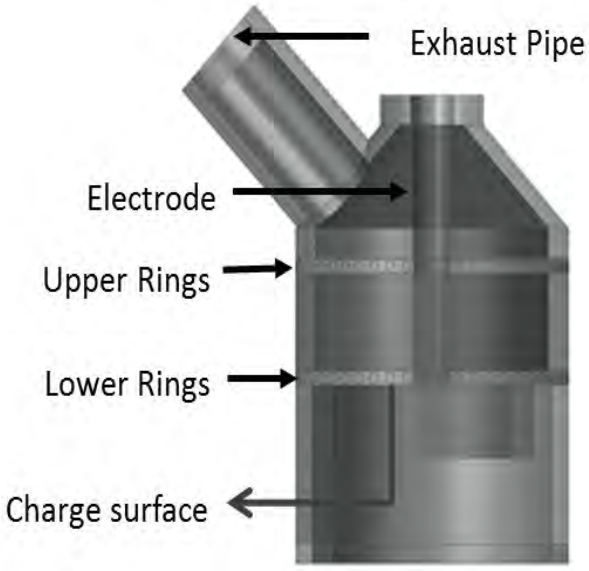

Figure 1: 3D schematic of the geometry

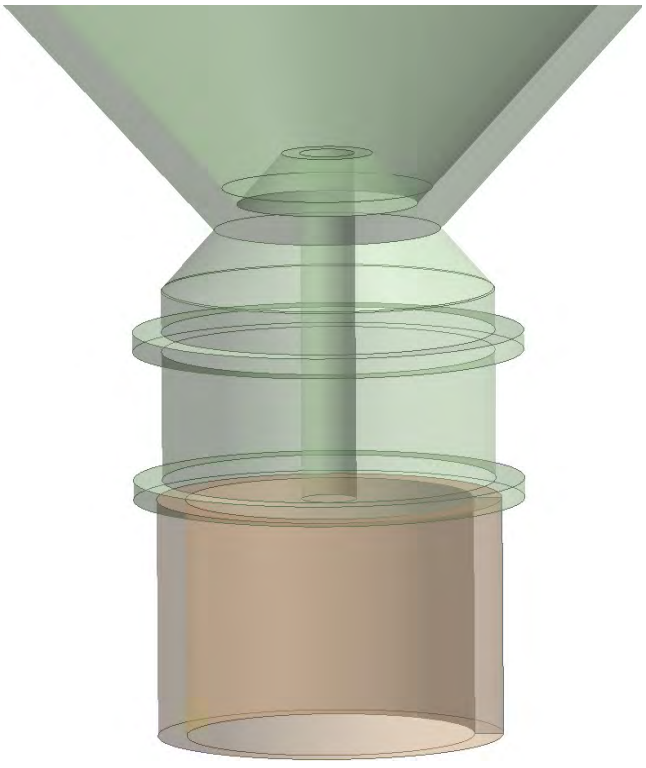

Figure 2: Schematic of the modified axis-symmetric geometry

In the present study, a modified pilot furnace, which is devised from original pilot furnace is proposed by modifying the exhaust pipe as shown in Figure 2.

This modification will allow 2D CFD simulations of the pilot furnace while preserving the underline physics of the ferrosilicon furnace. The furnace computational domain is divided into two domains, furnace domain (see Figure 2) and surrounding domain. The surrounding domain is a cylindrical volume around the furnace hood and it is a part of the computational domain. The surrounding domain is provided for an appropriate distribution of air flow through different openings on the furnace.

Most of the boundary conditions used for furnace modeling are difficult to measure, and are thus subject for qualified estimation based on experience. An important boundary condition is the amount of process gas escaping through the charge surface into the furnace hood. The metallurgical processes below the charge surface are responsible for process gas formation. These complex processes are not considered in the model. Therefore the amount of process gas is a priori unknown to the model. The only known parameters are the mass flow through the off-gas channel, offgas temperature and its composition. The mass flow and temperature of process gas escaping through the charge surface is thus estimated by tuning these values such that the measured mass flow and temperature in the off-gas channel is matched. Measuring the composition of off-gas and temperature at the off-gas channel is straightforward. For calculating the gas composition at the charge surface an elemental mass balance is performed. The composition of the process gas escaping through the charge surface is estimated from the measured composition in the off-gas channel and the composition of air from the surrounding.

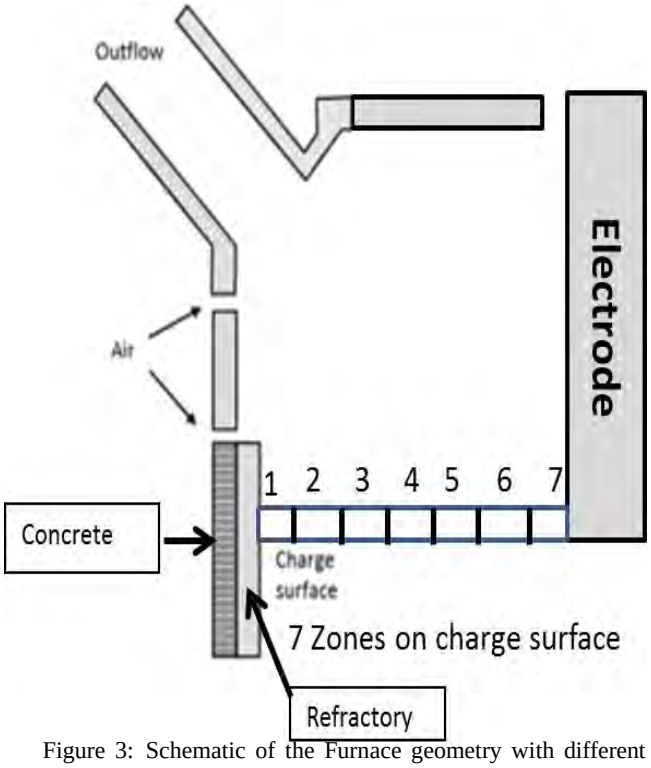

Figure 3: Schematic of the Furnace geometry with different zones and solid material

Since the process gas introduces molecules containing C and Si, the measured amounts of CO, CO_2 and SiO_2 in the off-gas will give the amount of CO and SiO in the process gas. Generally, a mass flux boundary is used at the charge surface.

The escaping of the process gas is non-uniform throughout the charge surface. Therefore the charge surface have been divided into seven zones (see Figure 3), which make easier to set different input values at different zones. The electrode is modeled as solid zone with a fixed power supply. On the wall boundaries depending on the type of the wall, a suitable boundary condition either convective or adiabatic is applied. The amount of air and its temperature being sucked into the furnace hood is supplied at the surrounding exterior surface through mass flux boundary condition. The mass flow rate through the surrounding was 1 kg/s and total amount of process gas was 0.08 kg/s. At the off-gas outlet, a pressure outlet boundary condition is employed. The specified outlet gauge pressure was 0 Pascal. The solid zones such as refractory, concrete and steel shown in Figure 2 are modeled explicitly.

CFD simulations were continued until all the residuals were below pre-specified values. In addition to that area averaged temperature at the offgas outlet surface was monitored. Our observation shows that even though the residuals for the governing equations were below the predefined value but the average temperature at outlet was not constant. Therefore, all the simulations were continued until both criteria were satisfied.

Roughness Modeling

The near-wall region consists of three main regimes: the laminar layer or linear sublayer, the buffer layer and the logarithmic layer. The laminar law holds in the linear sublayer, which is valid up to y^+=5. The logarithmic law holds in the log layer and it is valid from y^+=30 to y^+=500 - 1000. Nikuradse (Nikuradse, 1933) proposed the modification of the log law for rough surfaces by conducting extensive experiments on flow inside the rough pipe. According to Nikuradse (Nikuradse, 1933) the mean velocity distribution near rough walls has the same slope (1/κ) as smooth pipe but a different intercept. The law of the wall for mean velocity modified for roughness has following form (Cebeci and Bradshaw, 1977; Nikuradse, 1933):

$$\frac{U}{u^*} = \frac{1}{\kappa}\ln\left(\frac{\rho u^* y}{\mu}\right) + B - \Delta B \qquad (1)$$

ΔB depends, in general, on the type (uniform sand, rivets, threads, ribs, mesh-wire, etc.) and size of the roughness. For the fully rough regime, Cebeci and Bradshaw (Cebeci and Bradshaw, 1977) reported the following analytic fit to the sand-grain roughness data of Nikuradse (Nikuradse, 1933).

$$\Delta B = \frac{1}{\kappa}\ln f_r \qquad (2)$$

where f_r is a roughness function that quantifies the shift of the intercept due to roughness effects. There is no universal roughness function valid for all types of roughness. The roughness function is a function of $K^+ = \rho K_S u^*/\mu$, but takes different forms depending on the K^+ value. Where K_S is the physical roughness height and $u^* = C^{1/4}k^{1/2}$. Based on the measurements three distinct regimes have been identified hydro dynamically smooth ($K^+ \leq 2.25$), transitional ($2.25 < K^+ \leq 90$) and fully rough ($K^+ > 90$) According to the data, roughness effects are negligible in the hydro- dynamically smooth regime, but become increasingly important in the transitional regime, and take full effect in the fully rough regime. In FLUENT, the whole roughness regime is subdivided into the three regimes, and the formulas proposed by Cebeci and Bradshaw (Cebeci and Bradshaw, 1977) based on Nikuradse's (Nikuradse, 1933) data are adopted to compute ΔB for each regime.

RESULTS AND DISCUSSIONS

In total eight steady state simulations were performed to understand the effect of burst on temperature and NO_X, appropriateness of boundary condition for charge surface, and effect of charge surface roughness on the mixing and rate of reaction closer to the charge surface. Before going into the further discussions on the effect of burst and boundary condition, we would like to discuss about velocity distribution inside the pilot furnace. Since, the velocity distribution inside the furnace hood obtained from CFD was quite similar to each other for all the simulation, therefore only one velocity vector is plotted for discussion. The velocity vector plot colored with O2 concentration for the pilot furnace is shown in Figure 4.

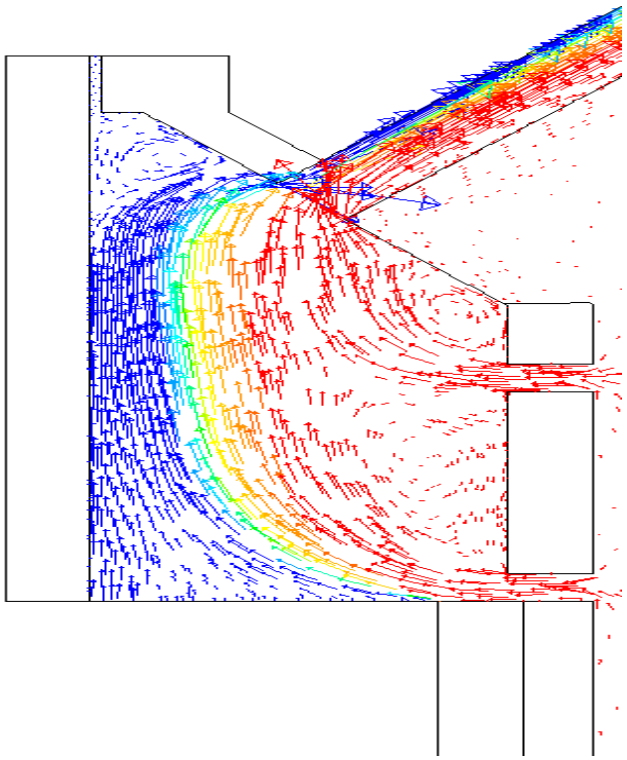

Figure 4: Vector plots for velocity distribution colored with O_2 mass fraction (max (red color)=0.23 and min (blue color)=0.0

It can be seen from vector plot that the air from the surrounding domain enters into the furnace through upper and lower rings/openings. The respective amount

of air entering through different openings on furnace depends mainly on the air mass flow rate through surroundings and the complex reaction processes taking place inside the furnace hood. The air entering through the lower ring/opening is parallel to the charge surface and it interacts with the process gas escaping through the charge surface. The rate of mixing depends on the air velocity magnitude and its direction and also on the roughness of the charge surface.

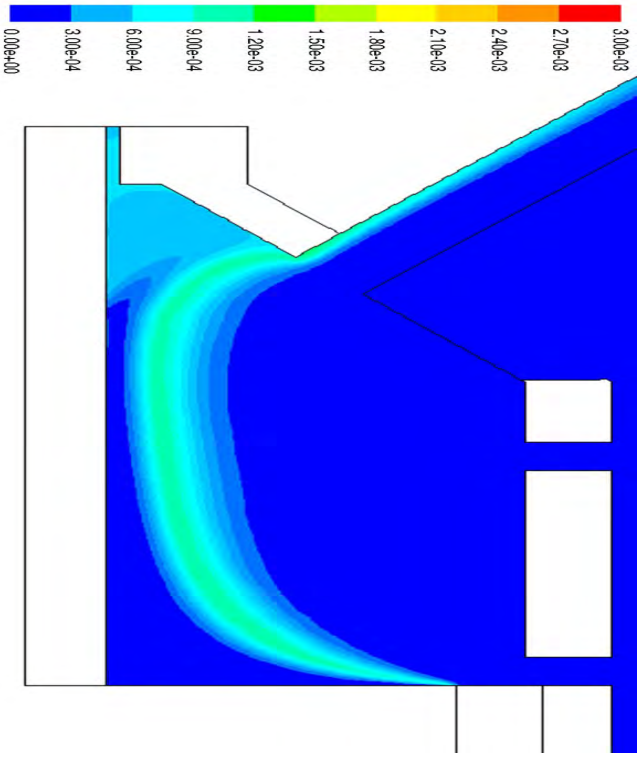

Figure 5: Contour plot of SiO_2 mass fraction (Case-1)

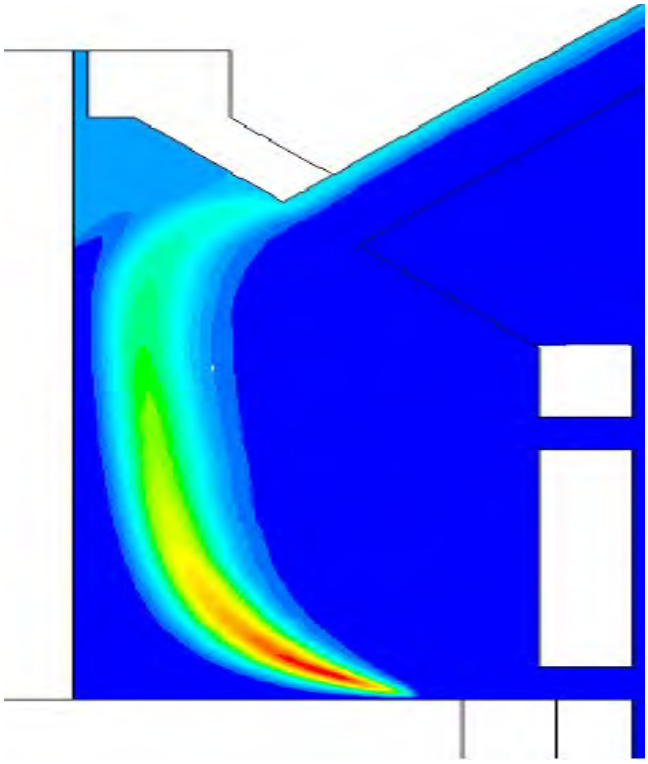

Figure 6: Contour plot of SiO_2 mass fraction (Case-2)

The flow around the roughened surface resembles as flow around the bluff bodies, and turbulence intensity behind the roughened surface depends on the roughness height and incoming velocity and its direction. Similarly, surface with higher roughness height will create large turbulence leading to the more mixing. It can also be seen (see Figure 4) that the air entering into furnace hood changes its direction from horizontal to the vertical due to the offgas location and buoyancy forces. Consequently, the air is not able to penetrate in the middle of the furnace hood.

Process gas from Burst

Occurrences of SiO burst have been observed in the real operation of ferrosilicon furnace. The burst causes a sudden release of SiO/CO jets through the charge surface. Influence of SiO burst on the temperature, SiO_2 species concentration and NOx formation is depicted through two CFD simulations. In Case-1, SiO was released uniformly throughout the charge surface and in Case-2, the same amount of SiO was released far from the electrode in the localized area on the charge surface. Formation rate of SiO_2 species concentration is much faster than the CO_2 gas formation rate due to the higher reaction rate of SiO with O_2 compare to the CO reaction rate with O_2.

Figure 5 and 6 show the SiO_2 distribution of Case-1 and Case-2 respectively. A large amount of SiO_2 concentration is clearly visible at the localized SiO release area (see Figure 6) when SiO is released in a concentrated way. However, SiO_2 concentration is diffused when SiO is released uniformly (see Figure 5). All the contour plots for SiO_2 distribution have been plotted on the same color bar and this color bar is shown in Figure 5.

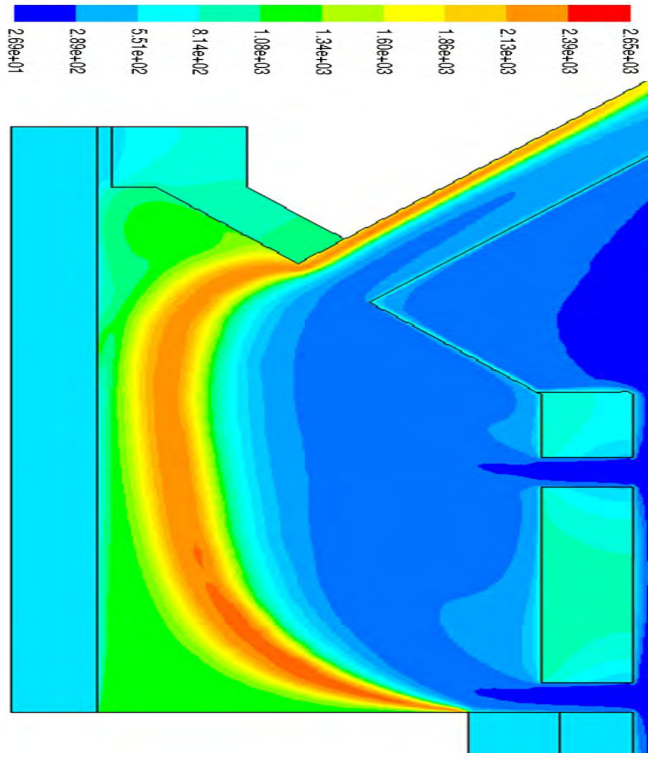

Figure 7: Contour plot of Temperature distribution ◦C (Case-1)

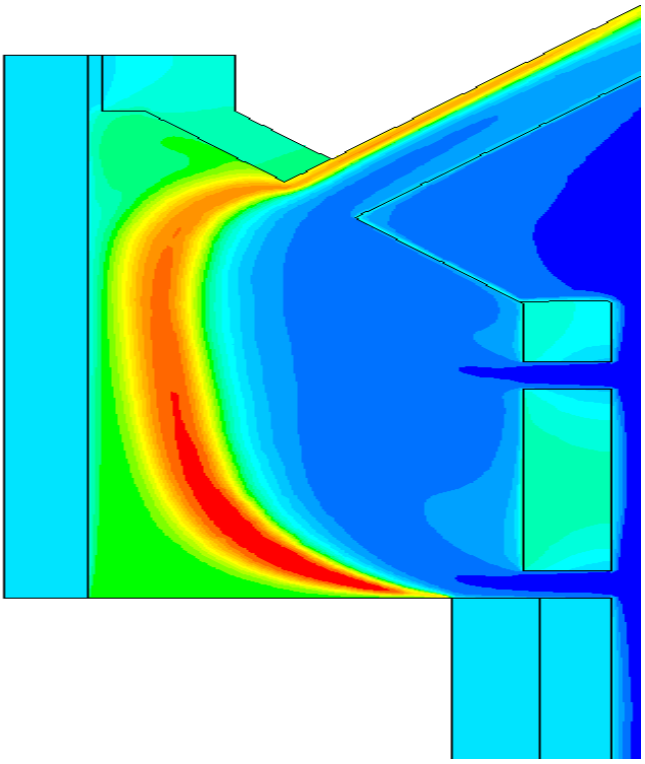

Figure 8: Contour plot of Temperature distribution ◦C (Case-2)

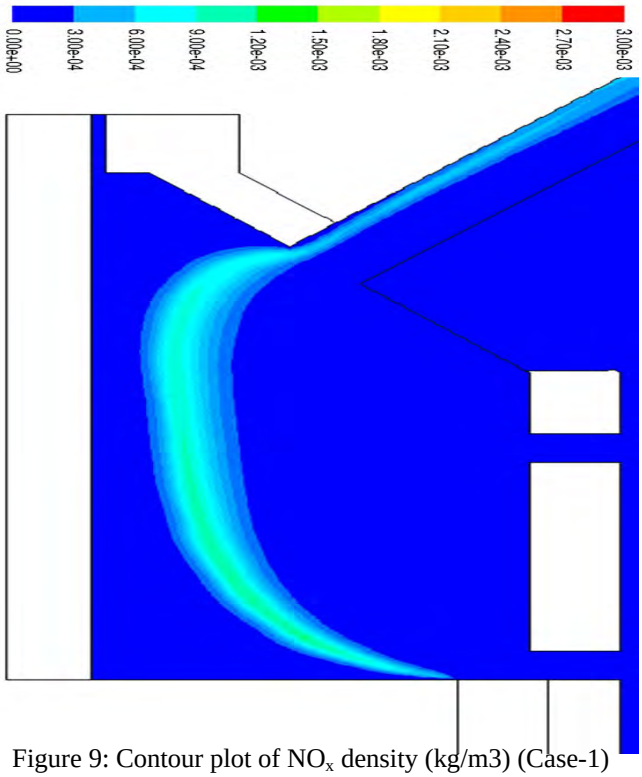

Figure 9: Contour plot of NO_x density (kg/m3) (Case-1)

A common color bar for temperature, applicable for all the temperature contour plots, is shown in Figure 7. Similarly, a common color bar for NOx density, applicable for all the NOx density contour plots, is shown in Figure 9. Distribution of NO_x density for Case-1 and Case-2 is shown in Figure 9 and 10 respectively. Total amount of NO_x was 2.16 kg/hr when SiO was released uniformly from the charge surface, whereas the amount of NO_x was 2.7 kg/hr when SiO was released in concentrated manner. It can be concluded from this study that the formation of burst leads to the higher NO_x formation even though the average SiO_2 formation is same in both the operation. Normally, the formation of burst will be very irregular and it is very difficult to predict the location of the burst. However, the most likely location of the burst formation is close to the electrodes. One more CFD simulation, Case-3, was performed to understand the effect of location of SiO burst on flow behavior. In Case-3, it was assumed that the SiO burst occur close to the electrode. It has been observed from velocity vector plot the air does not penetrate in the middle of furnace hood (see Figure 4) and there is not enough air close to the electrode. Therefore, in a limited amount of air supply there is less possibility of the SiO reaction near to the electrode and closer to the charge surface. In this situation most of the SiO reacts above the charge surface but closer to the exhaust pipe, where concentration of air is higher (see Figure 11).

It can be concluded from the results obtained from Case-2 and Case-3 that not only the location of burst but also the availability of air affects the NO_x formation. In present study only the reaction of SiO with O_2 is considered. It is not very clear whether SiO reacts with other species such as H_2O, CO and CO_2.

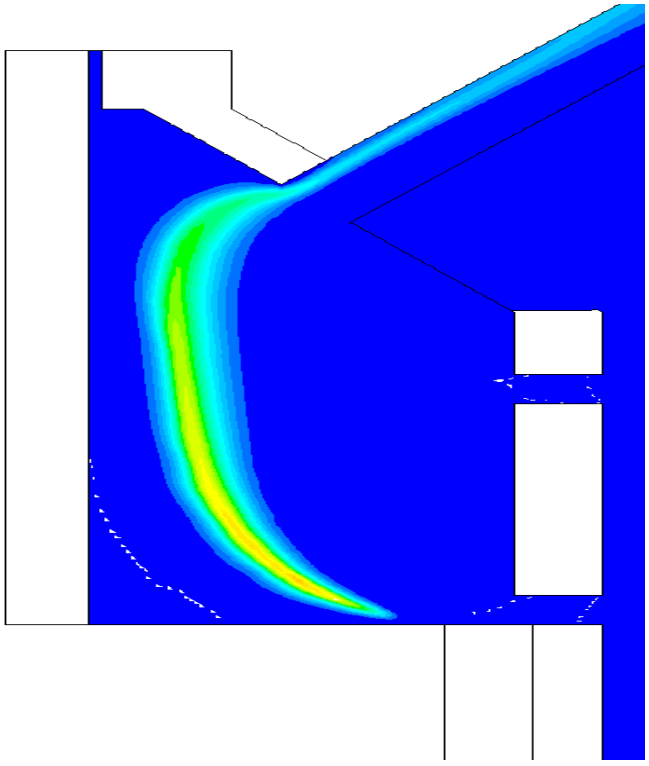

Figure 10: Contour plot of NO_x density (kg/m3) (Case-2)

Previous measurements have shown that the SiO_2 species concentration correlate well with the NOx formation. Increase in the SiO_2 concentration leads to increase in the NO_x. In order to understand this effect one more CFD simulation, Case-4, is carried out. The Case-4 is similar to the Case-2, except SiO release rate

is five times larger as compared to the Case-2. The simulation parameters of Case-4 were the same as Case-2. Figure 12 shows the SiO_2 mass fraction of Case-4, it can be seen that an increase in SiO concentration leads to the increased concentration of SiO_2. This increase in SiO_2 concentration also leads to the increase in temperature and subsequent NO_x formation as shown in Figure 13. The studies shows that total amount of NO_x increases up to 6.5 kg/hr from 2.7 kg/hr by increasing the SiO mass fraction by five times.

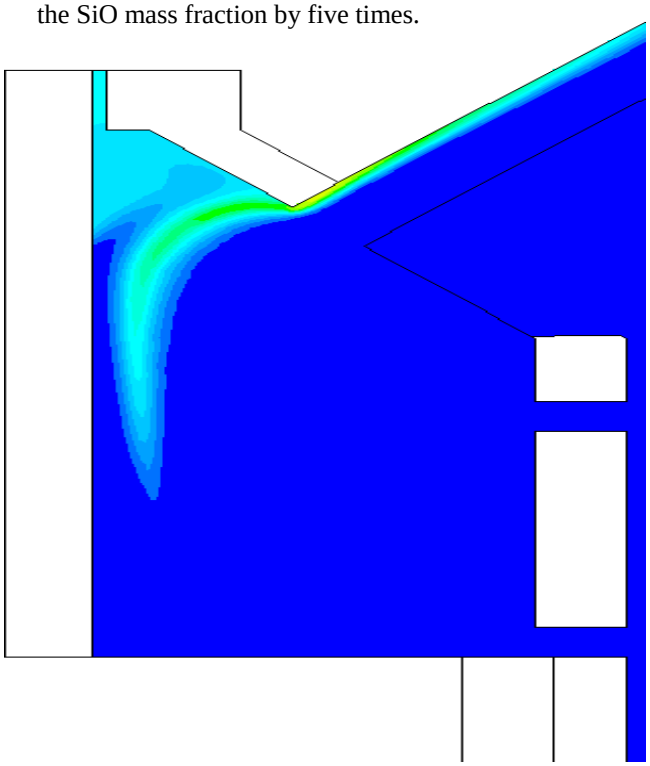

Figure 11: Contour plot of SiO_2 mass fraction (Case-3)

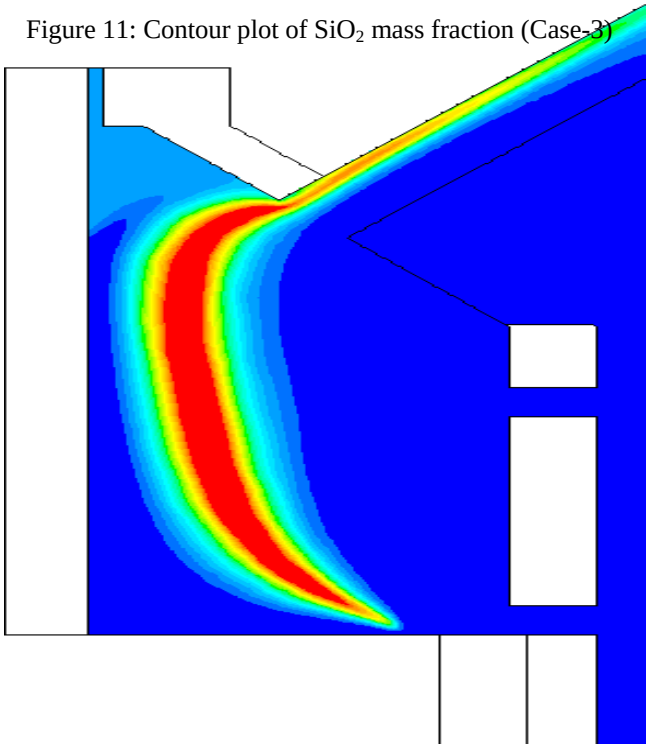

Figure 12: Contour plot of SiO_2 mass fraction (Case-4)

Effect of boundary condition

Two CFD simulations: Case-5 and Case-6 were carried out, Case-5 corresponds to the situation where mass flux boundary condition was applied on the charge surface, whereas Case-6 refers to the situation where wall boundary condition was applied on the charge surface. Otherwise, all other boundary conditions, chosen models and numerical schemes are same in both the cases.

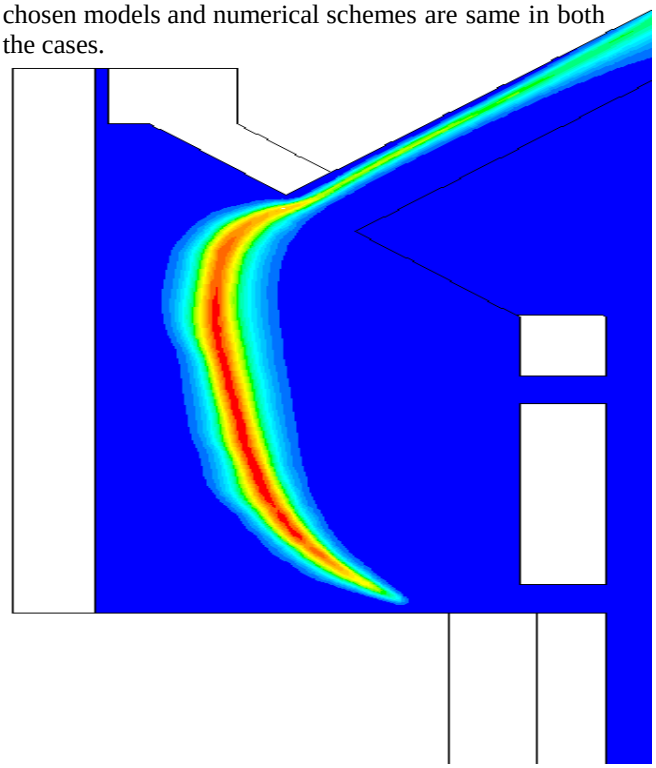

Figure 13: Contour plot of NO_x density (kg/m^3) (Case-4)

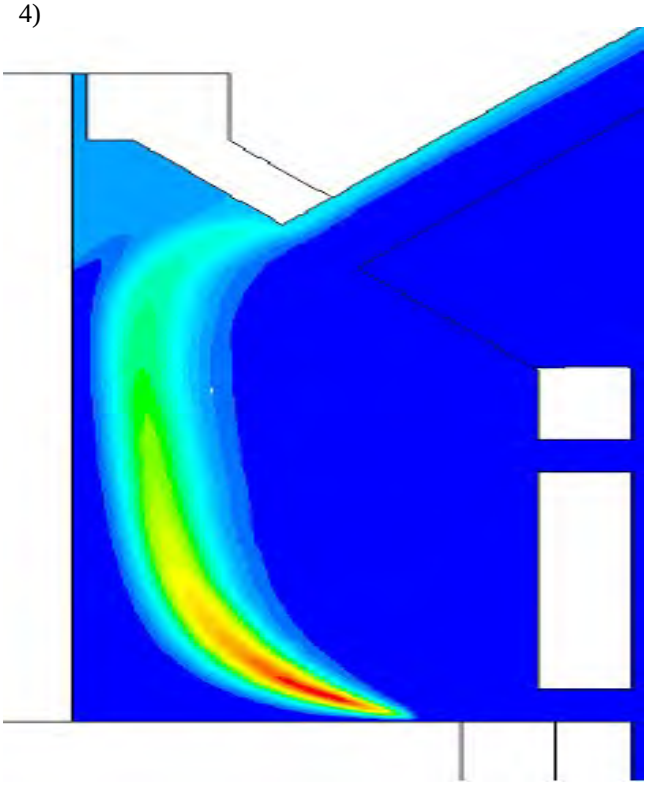

Figure 14: Contour plot of SiO_2 mass fraction (Case-5)

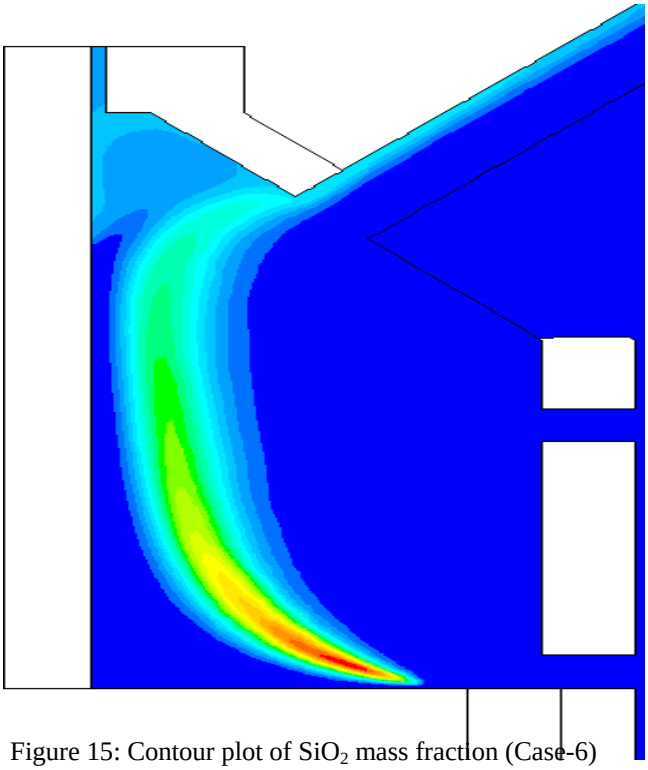

Figure 15: Contour plot of SiO_2 mass fraction (Case-6)

In Case-6, the roughness effects are not considered because an aim of this simulation (Case-6) was to find the appropriateness of the wall boundary condition for the charge surface in a place of mass flux boundary condition.

Figure 14 and 15 shows the SiO_2 mass fraction of Case- 5 and Case-6 respectively. It can be seen that there is not any significant difference between SiO_2 distribution obtained from both simulations. Although the results obtained from both the boundary conditions are similar, applicability of the wall boundary condition poses a challenge. In addition, one of the biggest challenges is to calculate the source terms for momentum and energy equation from the species mass source.

One of the biggest advantages offered by mass flux boundary is that all the flow variables of the charge surface can be set very conveniently. As it is mentioned that a main purpose of performing simulation with wall boundary condition is to account for the surface roughness of the charge surface. The wall roughness influences the mixing between process gas emerging from the charge surface and incoming air flow from lower opening. In ferrosilicon furnace, at what extent roughness affects the mixing is not very clear. Now, there is an open question whether accounting roughness, which improves physics close to the wall but introduces complexity in modeling the charge surface, overweight the simplification offered by the mass flux boundary condition. To answer this question two more CFD simulation, with and without charge surface roughness, are performed. FLUENT specific wall roughness model was chosen. The roughness height K_s was 4 mm and roughness constant C_s was 0.5. Present study showed that there was not any significant differences between the flow field of smooth and rough charge surface cases while examining the contour plots for both cases. To illustrate this, a radial velocity distribution for both cases is plotted and shown in Figure 16. Difference in velocity can hardly be noticed in the radial velocity profiles. A similar behavior was also observed in the axial velocity profile (not shown here). To illustrate the effect of the roughness on skin friction, the skin friction coefficients of the charge surface wall is plotted for both rough and smooth cases (see Figure 17).

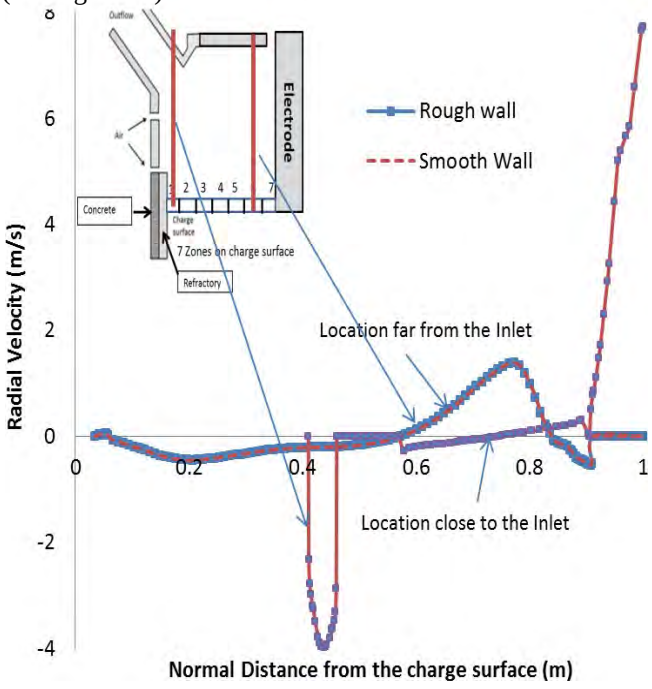

Figure 16: Radial Velocity profiles for smooth and rough charge surface

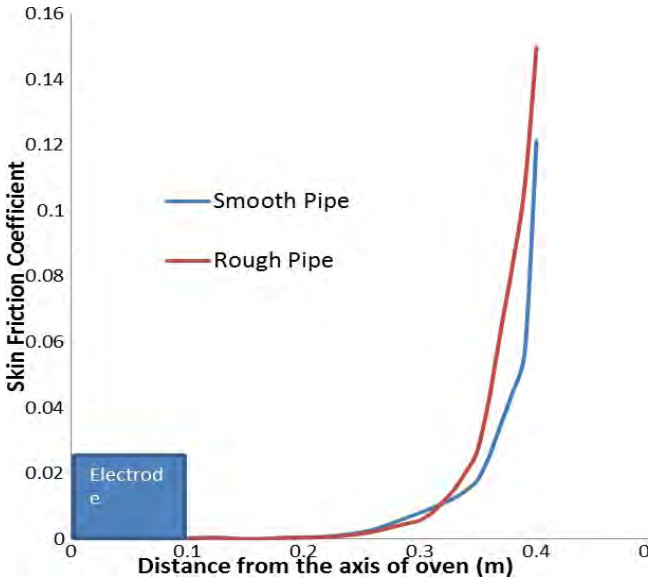

Figure 17: Skin friction coefficients for smooth and rough charge surface

A noticeable difference in the skin friction coefficient can be seen at the location close to the inlet, however far from the inlet the skin friction coefficient is negligible. The reason for this behavior can be understood by carefully examining the velocity vectors (see Figure 4). It can be seen that the incoming air from

the surrounding domain is parallel to the charge surface. Therefore higher value of skin friction coefficient is observed at the location close to the inlet (far from the electrode), However, due to the upward pressure gradients inside the furnace the direction of flow becomes normal to the charge surface at a location slightly far from opening and this leads to reduction in skin friction coefficient. From present study, it is very difficult to identify the role of charge surface roughness on turbulent mixing and reaction. Furthermore, applicability of the wall roughness models is questionable under strong lateral pressure gradient cases. The impact of wall roughness on mixing and subsequent reaction can be well understood through an explicit modeling of charge surface roughness.

CONCLUSIONS

A steady state CFD model solving for governing equation is developed using ANSYS FLUENT. Two approaches: wall boundary condition and mass flux boundary condition for modeling the charge surface is presented. Studies showed that both approaches give a similar result but using a wall boundary condition is a challenge. Furthermore, simplified approaches for modeling the SiO jets have been discussed in this study. Study showed that the concentrated SiO generates local zones of higher temperature, which are responsible for NOx formation. In addition to that, location of the SiO jets and local distribution of air supply play a major role in the NOx formation.

REFERENCES

ANSYS (2011). ANSYS FLUENT Theory Guide, V 13.

CEBECI, T. and BRADSHAW, P. (1977). *Momentum Transfer in Boundary Layers, ISBN:978-0070103009*. Hemisphere-McGraw-Hill, New York.

GRAN, I.R. and MAGNUSSEN, B.F. (1996a). "A numerical study of a bluff-body stabilized diffusion flame. part 1. influence of turbulence modeling and boundary conditions". *Combustion Science and Technology*, **119(1-6)**, 171–190.

GRAN, I.R. and MAGNUSSEN, B.F. (1996b). "A numerical study of a bluff-body stabilized diffusion flame. part 2. influence of combustion modeling and finite-rate chemistry". *Combustion Science and Technology*, **119(1-6)**, 191–217.

GRåDAHL, S. *et al.* (2007). "Reduction of emissions from ferroalloy furnaces". *INFACON XI, India*, 479–488.

JIMéNEZ, J. (2004). "Turbulent flows over rough walls".*Annual Review of Fluid Mechanics*, **36(1)**, 173–196.

LAUNDER, B. and SPALDING, D. (1974). "The numerical computation of turbulent flows". *Computer Methods in Applied Mechanics and Engineering*, **3(2)**, 269 – 289.

MAGNUSSEN, B. and HJERTAGER, B. (1977). "On mathematical modeling of turbulent combustion with special emphasis on soot formation and combustion". *Symposium (International) on Combustion*, **16(1)**, 719 – 729.

NIKURADSE, J. (1933). "Laws of flow in rough pipe" Tech. Rep. TECHNICAL MEMORANDUM1292/Forschung Arb. Ing.-Wes. No. 361.

PANJWANI, B. and OLSEN, J.E. (2013). "Combustionand mechanisms for NO_x formation in ferrosilicon electric arc furnaces". *European Combustion Meeting, ECM, Lund University, Sweden*.

MULTI-SCALE MODELING OF HYDROCARBON INJECTION INTO THE BLAST FURNACE RACEWAY

C. MAIER[1]*, **C. JORDAN**[1], **C. FEILMAYR**[2], **C. THALER**[2], **M. HARASEK**[1]

[1]Vienna University of Technology, 1060 Vienna, AUSTRIA

[2]voestalpine Stahl GmbH, 4020 Linz, Austria

* E-mail: christian.maier@tuwien.ac.at

ABSTRACT

Injection of alternative reducing agents via lances in the tuyères of blast furnaces is widely applied to reduce the consumption of metallurgical coke. Besides liquid hydrocarbons and pulverized coal the injection of recycled waste plastics is possible, offering the opportunity to chemically reuse waste material and also utilize the energy contained in such remnants.

In this work CFD models were developed and implemented that capture the multiphase nature of reducing agent injections, accounting for homogenoeus and heterogeneous reactions of materials in charge. The model is applied to the raceway zone of the blast furnace. Various geometry setups are investigated and discussed aiming at increasing the knowledge on impact of these parameters on the conditions in the blast furnace.

Keywords: CFD, multiphase heat and mass transfer, multiscale, blast furnace, direct injection.

INTRODUCTION

The majority of liquid raw iron is produced via the blast furnace route, traditionally utilizing metallurgical coke as the main reducing agent. Aiming at a reduction of primary resources, using alternative reducing agents such as liquid hydrocarbons, natural gas and waste plastics contributes to the reduction of coke rates. In the blast furnace these agents also deliver the heat necessary for melting processes as well as endothermic reduction reactions.

To optimize the utilization of the input materials, thorough examination of the impact of fuel injection is necessary. However, due to the extreme conditions in the blast furnace, the application of experimental techniques is very limited. A promising alternative is to conduct numerical experiments applying the methods of computational fluid dynamics. In this work, models are developed to study the process that takes place on multiple scales and aspects, e.g. in terms of (Pirker, 2014):

- length scales: wide range from microscopic length scales where heterogeneous chemical reactions take place on defects in the atomic structure towards global flow phenomena in the blast furnace shaft
- time scales: variation from very fast processes and high velocities in the zone of hot blast injection to comparatively low velocities of coke bed movement
- multiple phases: appearance of solid, liquid and gas phases and intense interactions

The blast furnace studied is operated by voestalpine Stahl GmbH in Linz, Austria. This furnace is arranged with equipment allowing for the utilization of a wide range of alternative reducing agents including natural gas, processed waste plastics, heavy fuel oil and tar etc. Currently, a facility for the injection of pulverized coals is installed. A schematic illustration of this blast furnace is given in figure 1.

To successfully model the utilization of feed materials in the blast furnace it is necessary to apply considerable simplifications considering e.g. the representation of the various phases and chemical reactions in order to limit the computational effort to affordable levels. An important aspect is also the definition of sound boundary conditions to properly describe the conditions at the edges of the simulation domain and reliably compute thermophysical properties of involved material streams.

MODEL DESCRIPTION

CFD-simulations were carried out using the framework of the multi-purpose solver ANSYS FLUENT® v6.3.23 (FLUENT, 2007). The modeling capabilities of the solver were extended to include the description of multiple phases such

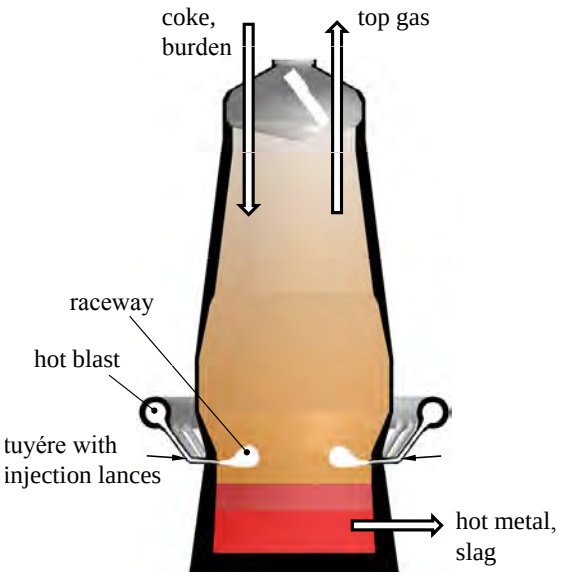

Figure 1: Blast furnace scheme.

as solid coke, gases, injected liquid hydrocarbons and plastic particles, accounting for heterogeneous heat and mass transfer phenomena. This was done by compiling user-defined subroutines into the code to implement the functionality necessary to describe processes in the raceway of blast furnaces. Non-equilibrium between the slowly descending bed of metallurgical coke and counter-currently ascending gases is considered by solving separate sets of conservation equations applying a multi-grid method (Maier *et al.*, 2012b, 2013b).

Simulation of coke bed movement

The flow of solids charged to the blast furnace has considerable influence on the operating characteristics as the loading of iron ore and coke on top of the bed and the bulk flow in shaft, raceway and hearth zone determine the operational stability to a great extent (Dong *et al.*, 2007; Zaïmi *et al.*, 2000). While the burden move further downwards coke is partially gasified and iron ores are reduced. The ore is molten in the cohesive zone. Below this region coke remains as the only solid material, allowing for liquid raw iron and slag to move downwards, countercurrently to hot blast moving towards the top of the furnace. The flow of solids in a blast furnace is mainly driven by melting of iron ore and conversion of coke in the raceway zone.

For the simulation of the flow of solid matter several approaches of problem formulations are available, including e.g. discrete elements methods (DEM), Euler-granular models or viscous flow models (Dong *et al.*, 2007).

Simulation setups applying discrete elements methods rely on the computation of the movement of individual particles by integrating Newton's law of motion for every single discrete particle. This offers the possibility to evaluate particle trajectories and interaction forces from first principles. However, in industrial apparatuses the number of particles is very large, therefore a tremendous computational effort is to be expected (Hilton and Cleary, 2012).

The so-called Euler-granular method is commonly implemented for flow simulation of gas and granular solids (Wen and Bi, 2011). Solid and fluid media are treated as continuous, fully interpenetrating with separate conservation equations. This approach makes use of the kinetic theory of gases to describe inter-phase exchange coefficients between gas or liquid and granular materials and requires a time-resolved solution procedure.

Application of viscous flow models for moving beds of particles is based on the representation of the bed as a continuous, single-phase fluid with modified viscosity (Nogami and Yagi, 2004; Zhang *et al.*, 1998). Therein, friction between particles is described by introducing a fictive solids viscosity that can be used in the Navier-Stokes equations. This approach offers the big advantage that the flow field of solid matter can be calculated using a finite volume solver. Furthermore, computations can be performed applying steady-state solvers, avoiding computationally very demanding time-discretization of the conservation equations.

The currently implemented model treats the bed of coke applying continuum fluid mechanics, including the ability to describe the driving forces for coke movement (i.e. coke utilization by oxidation and gasification reactions, momentum transfer from hot blast). Various authors state the possibility to model the movement of a bed of solids as a viscous fluid with properties of *Bingham media* (Nogami and Yagi, 2004; Schatz, 2000; Chen *et al.*, 1993).

In this model viscous properties are described by two parameters: yield viscosity μ_0 and yield stress τ_0. These parameters were determined experimentally for various solid matters. Parameters for coal particles were used in the present study ($\mu_0 = 1230\,\mathrm{Pas}$, $\tau_0 = 1.14\,\mathrm{Pa}$) (Nogami and Yagi, 2004).

As coke particles are usually larger than the length scale of roughness of the furnace refractory lining, the typically applied no-slip boundary condition for solid velocities is not valid (Zhang *et al.*, 1998). Therefore, in the simulation of coke flow a slip boundary is applied at rigid walls.

Hot blast injection, raceway cavity

In the lower region of the blast furnace oxygen-enriched air, preheated to high temperatures is injected at velocities of up to $200\,\mathrm{m/s}$ via tuyères. Due to the high momentum of the gas jet and consumption of coke via heterogeneous reactions, a cavity is formed adjacent to each tuyère. In the core of this structure the void fraction of the coke bed approaches unity, leaving space for alternative reducing agents injected via lances in the tuyère. The size and shape of the cavity determines the travelling distances of injected materials from the injection lance tip to the impaction position on the coke bed and therefore the time available for gasification and combustion reactions.

In the current model framework, to limit computational efforts to reasonable levels, the formation of the raceway zone is not computed explicitly during the solution process but given as a boundary condition. The cavity is implemented by defining a porosity profile in the coke bed, its shape is taken from from literature sources (Zhou, 2008). The size of the raceway cavity is calculated depending on the actual blast furnace operating conditions considering rates and properties of injected hot blast as well as geometry issues (i.e. tuyère diameter, height of the coke bed in the furnace shaft etc.) applying a one-dimensional model (Gupta and Rudolph, 2006). This model accounts for the impact of blast momentum, hearth diameter, coke particle properties as well as height and void fraction of the coke bed in the blast furnace on raceway formation. Particle friction was identified as an important factor. For the blast furnace the decreasing part of the hysteresis curve of the raceway formation process was reported to be the determining step. The parameters used to compute the raceway size are summarized in table 1.

Table 1: Properties of blast furnace coke particles, applied for the computation of raceway size using the model of Gupta and Rudolph (2006).

property	value	
coke particle density	1100	$\mathrm{kg/m^3}$
particle size	25	mm
particle shape factor	0.7	–
angle of particle-particle friction	43.3	°
coke bed porosity	0.5	–
upward facing fraction of raceway	0.8	–
coke bed height (max. fill level)	26	m
hearth diameter	12	m

The impact of hot blast velocity on the raceway size at typical operating conditions as calculated applying this model is shown in figure 2. In the case of a constant blast rate, blast momentum increases with decreasing tuyère diameter, therefore the penetration depth of hot blast is enhanced and cavity volume is estimated to increase by a factor of approx. 2.8 as the tuyère diameter is decreased from 160 to 130 mm.

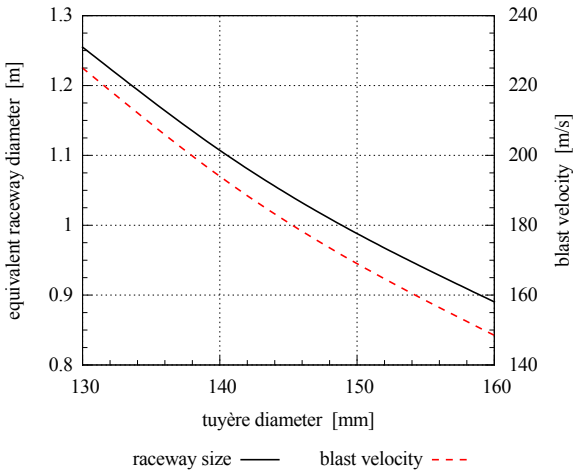

Figure 2: Variation of raceway size with respect to tuyère diameter. Hot blast rate per tuyère: 9900 Nm^3/h at 1220 °C, operating pressure 4.2 bar_g, oxygen enrichment to 27.4 $\%_{v/v}$ O_2.

Measurements of the coke bed voidage at stopped blast furnaces and hot model experiments showed that the porosity varied between approx. 0.3 near the boundary of the raceway cavity and 0.5 further away (Gupta and Rudolph, 2006). Therefore, the porosity in far-field of the raceway was implemented as $\varepsilon = 0.5$. The resulting porosity distribution in the computational domain, highlighting the raceway cavity, is shown in figure 3.

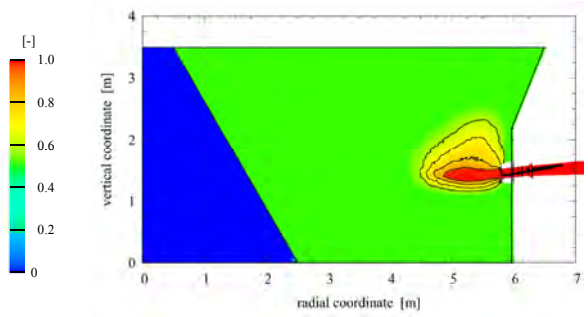

Figure 3: Porosity field in the blast furnace.

Injection of alternative reducing agents

The injection of liquid hydrocarbons and plastic particles is modeled applying tracking schemes in a Lagrangian frame of reference. Heating rates are computed accounting for contributions from laminar and turbulent convective transfer as well as radiation. The release of mass from the liquid fuel to the gas phase is computed applying a multicomponent evaporation model based on temperature dependent saturation pressures of mixture components.

At conditions in a blast furnace raceway, injected waste plastic particles exhibit non-isothermal behavior (Maier *et al.*, 2013a). This results from very high heat transfer rates due to high relative velocities and intense radiation interaction. As the thermal conductivity of injected plastic particles is rather low, thermolysis takes place near the particle surface while the core temperature remains constant.

In the simulation setup user-defined routines were hooked to the solver to properly model the release of alternative reducing agents to the gas phase.

Homogeneous reactions

Rates of homogeneous gas-phase reactions are calculated considering reactant mixing on finest scales of turbulent eddies in a set of global reactions. The considered reactions are (for detailed discussion of reaction rates please refer to (Jordan *et al.*, 2008a,b)):

$$CH_4 + 2O_2 \longrightarrow CO_2 + 2H_2O \quad \text{(R 1)}$$

$$2CO + O_2 \longleftrightarrow 2CO_2 \quad \text{(R 2)}$$

$$2H_2 + O_2 \longrightarrow 2H_2O \quad \text{(R 3)}$$

$$CO + H_2O \longleftrightarrow CO_2 + H_2 \quad \text{(R 4)}$$

$$CH_4 \longleftrightarrow C_s + 2H_2 \quad \text{(R 5)}$$

Cracking of hydrocarbon vapor to form smaller gaseous constituents as well as combustion is modeled in the gaseous regime:

$$C_{19}H_{30} + 17O_2 \longrightarrow 19CO + 15H_2O \quad \text{(R 6)}$$

$$C_{19}H_{30} + 6O_2 \longrightarrow H_2 + 7CH_4 + 12CO \quad \text{(R 7)}$$

$$C_{19}H_{30} \longrightarrow C_s + 3H_2 + 6CH_4 \quad \text{(R 8)}$$

Heterogeneous reactions

Heterogeneous reactions of coke with gas mixture components are evaluated considering major reaction routes such as oxidation, steam and CO_2 gasification and methanation (reactions R 9-R 12; kinetic expressions for reaction rates are given in table 2):

$$CH_xO_y(s) + (\frac{x}{4} - \frac{y}{2})O_2 \xrightarrow{k_{O_2}} CO_2 + \frac{x}{2}H_2O \quad \text{(R 9)}$$

$$CH_xO_y(s) + CO_2 \xrightarrow{k_{CO_2}} 2CO + yH_2 + (\frac{x}{2} - y)H_2O \quad \text{(R 10)}$$

$$CH_xO_y(s) + (1-y)H_2O \xrightarrow{k_{H_2O}} CO + (1 + \frac{x}{2} - y)H_2 \quad \text{(R 11)}$$

$$CH_xO_y(s) + (2 + y - \frac{x}{2})H_2 \xrightarrow{k_{H_2}} CH_4 + yH_2O \quad \text{(R 12)}$$

Table 2: Kinetic rate expressions for heterogeneous reactions.

	rate expression	reference
R 9	$k_{O_2} = 3.8 \cdot 10^7 \cdot e^{-\frac{150500}{R \cdot T_{coke}}}$	(Rumpel, 2000)
R 10	$k_{CO_2} = 2.7 \cdot 10^5 \cdot e^{-\frac{185200}{R \cdot T_{coke}}}$	(Rumpel, 2000)
R 11	$k_{H_2O} = 3.42 \cdot T_{coke} \cdot e^{-\frac{129700}{R \cdot T_{coke}}}$	(Tepper, 2005)
R 12	$k_{H_2} = 0.00342 \cdot T_{coke} \cdot e^{-\frac{129700}{R \cdot T_{coke}}}$	(Tepper, 2005)

Rates of reactions are computed resolving educt species transport on a particulate scale, accounting for boundary layer diffusion, diffusion in the porous coke structure and intrinsic reaction kinetics (see fig. 4).

The thickness of the particle boundary layer strongly depends on local gas flow conditions, particle properties and coke bed voidage and is calculated with respect to local turbulence and gas phase properties. The diffusive transport processes are considered as a series of resistances to the actual chemical reaction (for a detailed description of the reaction model please refer to (Maier *et al.*, 2012b)). This approach allows for the computation of effective reaction kinetics for wide temperature ranges.

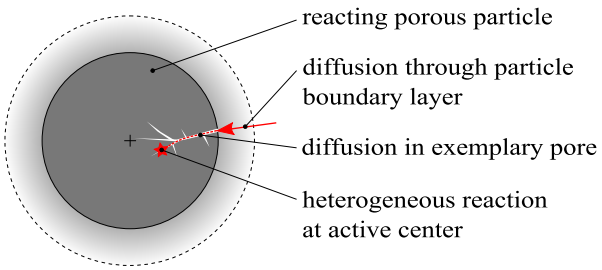

Figure 4: Schematic illustration of educt species diffusion from gas bulk flow towards the actual reaction site.

Rates of CO_2-gasification of metallurgical coke as a function of temperature at various gas-solid relative velocities are shown in figure 5. In this chart, pressure and species concentrations are similar to conditions at the boundary of a blast furnace raceway. At moderate temperatures, the overall rate of CO_2 gasification is limited by reaction kinetics. As temperatures increase, rate of reaction kinetics rise in the order of e^T, while the dependence of diffusive transport on temperature is represented by a power-law. Consequently, at high temperatures reactant concentrations in the porous coke particles decline, resulting in a limitation of the overall reaction rate.

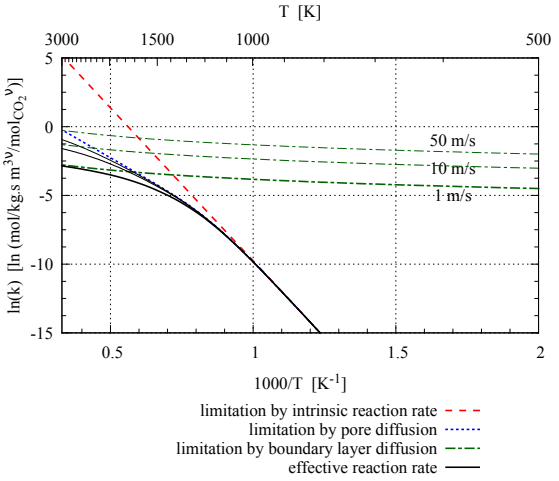

Figure 5: Heterogeneous CO_2 gasification of metallurgical coke. Conditions: gas velocities 1 m/s, 10 m/s and 50 m/s, p = 5.1 bar, coke particle size 21 mm, coke bed voidage = 0.8, gas mixture: 10 %$_{v/v}$ H_2O, 16.8 %$_{v/v}$ CO_2, 5.7 %$_{v/v}$ O_2, balance N_2.

The heat of reactions are computed from standard state enthalpy differences at local temperatures using polynomial expressions available for thermophysical properties (Lemmon *et al.*, 2014). The standard enthalpy of formation of solid coke was estimated from the tabulated values of gas species involved in the combustion reaction using the lower heat of combustion of coke given from experimental examination.
The model was implemented stepwise towards full model complexity, each module was validated by comparison of simulation results with experimental data, starting from simple processes involving heterogeneous heat transfer towards cases with homogeneous reactions and finally arriving at setups with heterogenous coke utilization (Maier *et al.*, 2012a,b, 2013a,b).

Geometry setup

The considered simulation domain consists of a segment of the blast furnace including one tuyère element (see fig. 6). Periodic boundary conditions are applied to the vertical cutting planes to properly link corresponding data structures on either side.

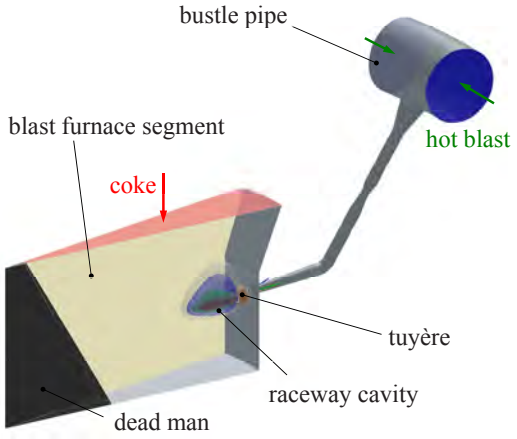

Figure 6: Overview of the simulation domain.

The geometry includes a detailed description of the tuyère and lances for injection of alternative reducing agents (fig. 7).

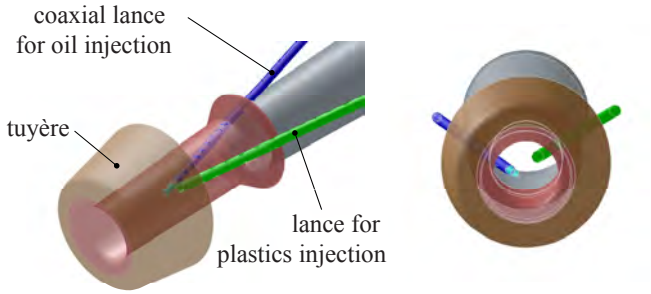

Figure 7: Geometry of simulation domain, detail: Tuyère and lances for injection. Left: isometric, right: front view.

RESULTS

In the next sections simulation results for the full blast furnace geometry are discussed. Basic operating conditions of the furnace are summarized in table 3. In the parametric study conditions are varied, these are explained in the according subsections. The strategy is set up such that the effect of one specific parameter is studied at a time by variation, while keeping the remaining variables at base conditions.

Table 3: Blast furnace baseline operating conditions.

hot metal production rate	360 t_{hm}/h
number of tuyères	32
tuyère diameter	140 mm
hot blast rate	316000 Nm^3/h
hot blast temperature	1220 °C
hot blast O_2 concentration	27.4 %$_{v/v}$
operating pressure	4.2 bar_g
liquid hydrocarbons rate	55.1 kg/t_{hm}
plastics rate	68.3 kg/t_{hm}

Baseline simulation results

In the base case, hot blast is injected at velocities of 194 $^{m}/_{s}$. First the gas follows the direction of the tuyère centerline. As the boundary of the raceway is reached, the void fraction of the coke bed decreases, therefore increasing pressure drop is exerted to the gas flow. As a consequence, the flow direction changes towards the gradient of the porosity profile, gases leave the raceway cavity in a radial direction (see fig. 8).

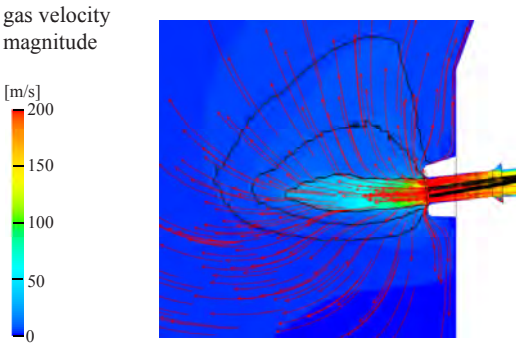

Figure 8: Gas flow field near the tuyère opening: Path-lines of gas flow and contours of velocity magnitude.

Due to inter-phase momentum transfer, coke particles are accelerated towards the center of the blast furnace. This is especially the case for material that enters the raceway cavity from top, falling into the gas jet. During the short time of flight these particles are not fully consumed by heterogeneous reactions, resulting in a circulating movement of coke particles in the zone near the tuyère opening (fig. 9). This behavior was also reported from experimental observation of operating blast furnaces using optical techniques (Kase *et al.*, 1982).

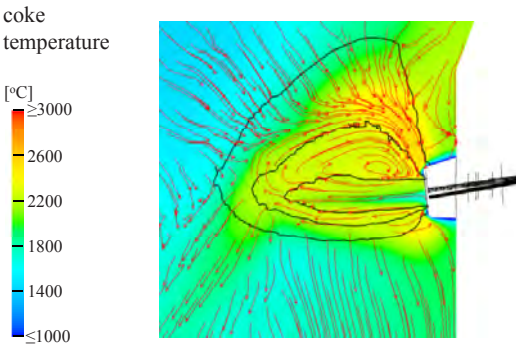

Figure 9: Coke flow and temperature field near the tuyère opening: Path-lines of coke flow and contours of coke temperature.

Liquid hydrocarbons that are utilized in the blast furnace under consideration consist of a mixture of heavy fuel oil and crude tar from coke production. Due to fierce conditions at fluid atomization, a fine droplet spray is achieved with a mean droplet diameter in the range of 100 μm. A fine spray is desired as it contributes to fast release of droplet mass to the gas phase and therefore efficient fuel utilization. The oil spray is readily evaporated just within the raceway cavity after residence times in the range of 10 ms (see droplet tracks in figure 10).
Waste plastics for injection are fed at much larger size classes (average particle diameter: 7 mm, see also fig. 11). Naturally this leads to longer residence times in the range of several seconds. This means that during time of flight particles pass the raceway zone and reach the boundary of the raceway cavity. In the simulations plastic particles are modeled to mechanically interact with the coke bed (note particle tracks in fig. 12). This behavior was also found in operating blast furnaces by investigation using high-speed imaging of the tuyère zone. The probability of reflection and/or impaction was evaluated based on the local level of coke bed porosity.

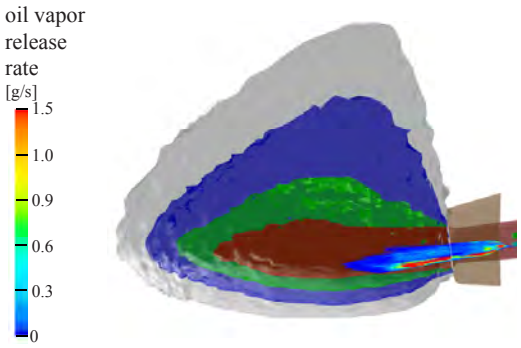

Figure 10: Trajectories of injected liquid hydrocarbons, colored by evaporation rate.

Figure 11: Processed waste plastics for injection into the furnace.

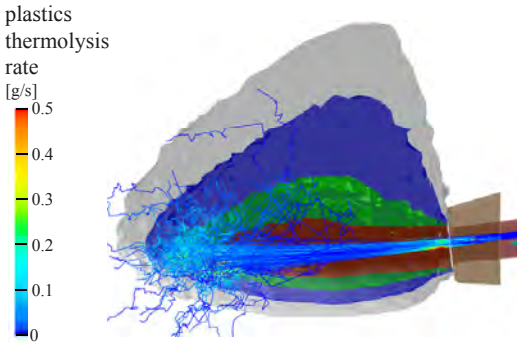

Figure 12: Trajectories of injected waste plastics, colored by thermolysis rate.

Right in front of the tuyère good mixing due to high turbulence intensity contributes to the rate of heterogeneous coke reactions as well as homogeneous reactions consuming pyrolysis products from gasification of injected alternative reducing agents. Oxygen contained in the hot blast is consumed fast, accordingly combustion products as well as heat of reactions are released in this zone. Consequently, in this zone coke temperatures reach maximal values to be expected in the blast furnace. Figure 13 shows the profile of gas species concentrations and temperature on a radial coordinate on tuyère level, also highlighting tuyère opening and

shape of the raceway cavity.
At the conditions present in a blast furnace, equilibria of Boudouard as well as water-gas reaction (reactions R 10 and R 11) are shifted to the right side, accordingly CO_2 and H_2O react with coke, releasing CO and H_2. These gases are utilized in the furnace for indirect reduction of iron oxides to raw iron. The heat required for these endothermic reactions is delivered by the reaction of injected materials and coke with oxygen introduced with the hot blast.

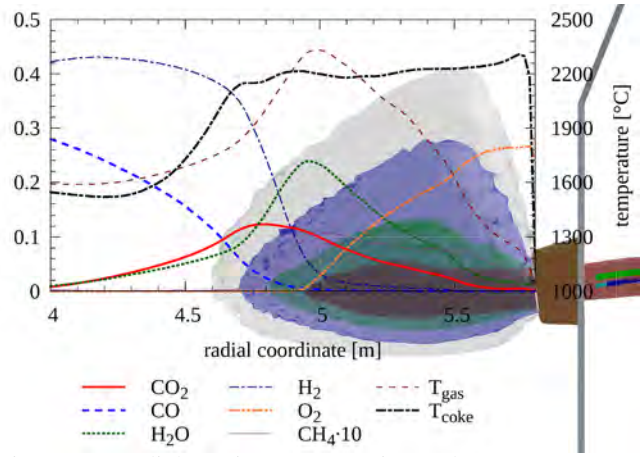

Figure 13: Radial species concentration and temperature profiles in the blast furnace on tuyère level.

The hurtling movement of coke particles in the raceway cavity also contributes to fuel utilization as heat is transferred convectively from zones with elevated temperatures (e.g. raceway boundary) towards the raceway core.

Tuyère diameter variation

To obtain stable furnace operation and successful feed utilization, deep penetration of hot blast into the coke bed is desired. As mentioned above, the diameter of the tuyères directly correlates to the hot blast momentum and consequently to the size of the raceway cavity. The effect of the inner diameter of the tuyères on heterogeneous coke reactions and utilization of injected alternative reducing agents was studied by conducting simulation runs with varying tuyère geometry while the hot blast rate was kept constant at the value given in table 3.

Table 4: Tuyère diameter variation.

case ID	tuyère diameter	raceway volume
case 1	140 mm	0.71 m^3
case 2	150 mm	0.51 m^3
case 3	160 mm	0.37 m^3

As summarized in table 4, in the range of parameter variation the volume of the raceway cavity increases by a factor of approx. 1.9. Accordingly, the residence time of hot blast and therefore the time available for combustion of injected fuels increases together with mixing intensity, resulting in a shift of gas-phase species concentration profiles. In terms of coke bed void fraction, oxygen is consumed in regions further away from the raceway core, the CO_2-peak is shifted accordingly (see fig. 14).
The situation for the conversion of steam to H_2 via heterogeneous reactions is quite similar, as shown in figure 15. However, in the case with smallest raceway zone, case3, the

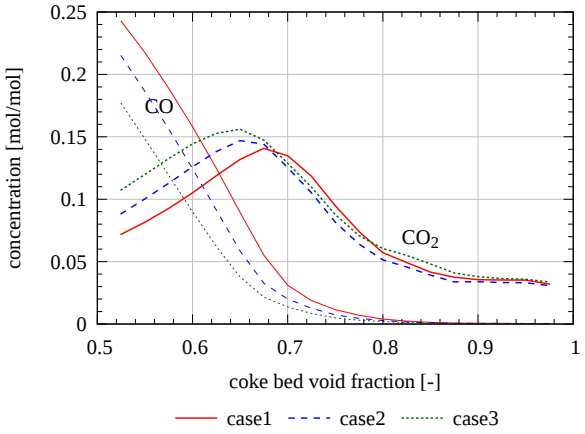

Figure 14: Tuyère diameter variation: CO and CO_2 concentration vs. coke bed void fraction.

boundary of the raceway is located closest to the tuyère opening. In this setup a part of the injected fuel oil spray is evaporated near the raceway boundary, causing a shift of the location of steam release with respect to the coke bed void fraction.
The volume of the raceway cavity is larger if a smaller tuyère is installed, as expected a deeper penetration of hot blast into coke bed is achieved, see e.g. coke utilization by heterogeneous water-gas shift reaction in figure 16.

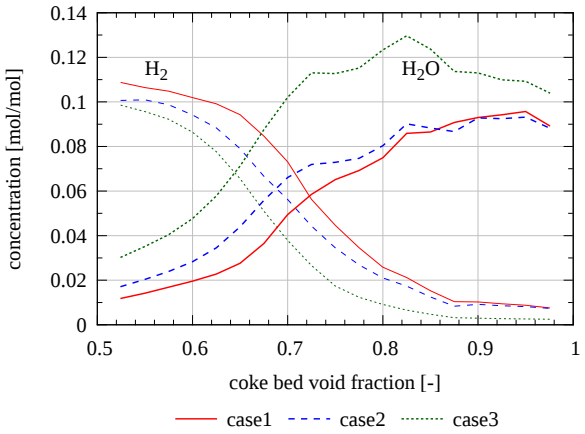

Figure 15: Tuyère diameter variation: H_2/H_2O concentration vs. cokebed void fraction.

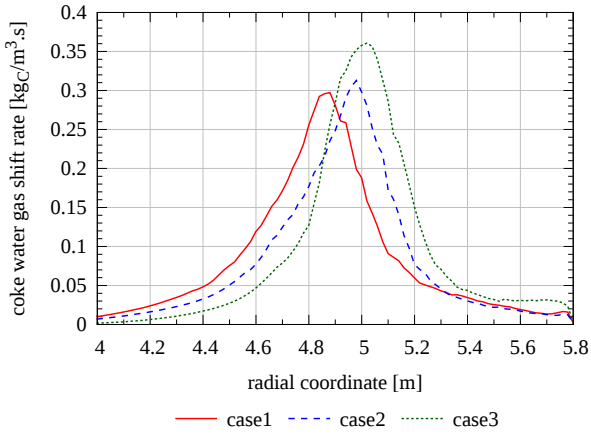

Figure 16: Tuyère diameter variation: Radial profile of coke consumption by steam gasification on tuyère level.

Lance tip position

The position of release of alternative reducing agents is determined by the position of lance tips. In the baseline setup, the lances for injection do not overlap each other (see fig. 7). Two additional geometry setups with deeper inserted lances as outlined in figure 17 were studied.

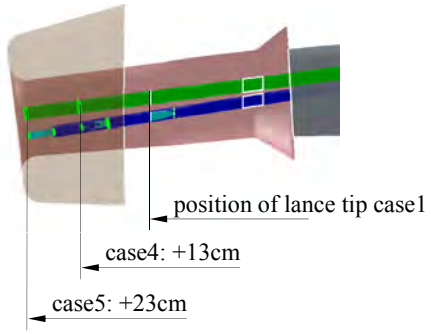

Figure 17: Sideview of tuyère and lances, highlighting range of lance tip position variation.

As expected as the lance tips are shifted towards the opening of the tuyère, the release of fuel oil vapor to the gas phase is transferred into the raceway cavity (fig. 18). In case 1 lance tips feature the largest distance to the tuyère opening. In this setup approx. 70 % of the fuel oil is evaporated within the tuyère, the remains is released in the core of the raceway cavity. In case 4 oil vapor release is already moved towards the coke bed but still gasification is completed in the region with void fractions of $90-100\,\%$, while for case 5 already some oil gasification takes place in the boundary of the raceway zone.

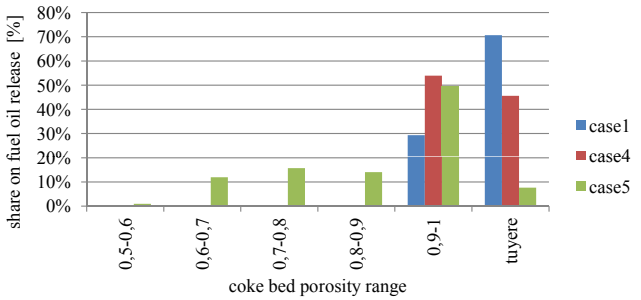

Figure 18: Location of fuel oil release, lance length variation.

Energy necessary to evaporate the fuel droplets is provided by radiation (far-field energy transfer) as well as locally from the gas phase by convective and conductive heat transfer. Therefore, at the point of fuel oil release a cooling impact is exerted on the gas flow until the combustion of volatiles overbalances this effect and temperature levels increase. In the blast furnace tuyères are installed with water-cooling systems to prevent materials from damage due to overheating. The cooling effect from oil pyrolysis influences the heat transferred via the inner surface of the tuyère and therefore the cooling duty, as summarized in table 5.

The location of the release of the oil spray also has an impact on the mean droplet residence times as the gas-temperatures in the surroundings of the spray vary. In case 5 the evaporating spray reaches very hot regions located near the boundary of the raceway cavity, therefore computed mean residence times are reduced significantly (table 5).

Due to the large particle sizes of injected waste plastics, lance length has only a minor impact on the position of plastics pyrolysis as compared to fuel oil release (fig. 19). However,

Table 5: Variation of lance tip position: Heat transfer via inner wall of tuyère, oil droplet and plastics residence times.

case ID	heat transfer rate	time to oil evaporation	time to plastics gasification
case 1	203 kW	4.36 ms	1.54 s
case 4	206 kW	3.20 ms	1.50 s
case 5	210 kW	2.10 ms	1.42 s

due to variation in gas-particle temperature differences plastics residence times vary in the range of 8 %.

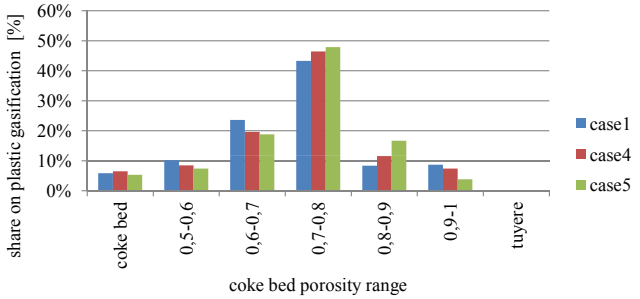

Figure 19: Location of plastics thermolysis, lance length variation.

CONCLUSIONS

A steady-state CFD model for alternative reducing agents injection into the raceway of ironmaking blast furnaces focussing on the utilization of feed materials by homogeneous and heterogeneous reactions was developed. In a parametric study the tuyère geometry was varied in terms of inner diameter and length of lances for injection. A smaller tuyère diameter contributes to increased penetration depth of hot blast into the coke bed, however at the cost of increased pressure drop of hot blast introduction. The position of the lance tip for injection of liquid hydrocarbons strongly influences estimated droplet residence times as well as the zone where oil evaporation takes place, also affecting the cooling duty of the tuyères.

The model will be applied to further operating conditions including e.g. oxygen enrichment levels, hot blast temperature and hot metal production rates. Future work will also include the extension of the model setup by a module for simulation of pulverized coal injection.

REFERENCES

CHEN, J. *et al.* (1993). "Modeling of solid flow in moving beds". *ISIJ International*, **33(6)**, 664–671.

DONG, X. *et al.* (2007). "Modelling of multiphase flow in a blast furnace: Recent developments and future work". *ISIJ International*, **47(11)**, 1553–1570.

FLUENT (2007). *http://www.fluent.com/*. FLUENT Inc.

GUPTA, G.S. and RUDOLPH, V. (2006). "Comparison of blast furnace raceway size with theory". *ISIJ International*, **46(2)**, 195–201.

HILTON, J. and CLEARY, P. (2012). "Raceway formation in laterally gas-driven particle beds". *Chemical Engineering Science*, **80**, 306–316.

JORDAN, C. *et al.* (2008a). "CFD simulation of heat transfer and high temperature conversion of plastic particles after injection into blast furnace raceway". *Proceedings of CHT-08, ICHMT International Symposium on advances in computational heat transfer*, ISBN: 978-1-56700-253-9. Marrakech, Morocco.

JORDAN, C. *et al.* (2008b). "Die Bildung von H_2 und CO durch Eindüsung von gasförmigen, flüssigen und festen Einsatzstoffen in den Hochofen". Tech. Rep. TU-ThVT-1662-2008011, Technische Universität Wien.

KASE, M. *et al.* (1982). "Analysis of coke behaviour in raceway using endoscope and high-speed camera". *Transactions of the Iron and Steel Institute of Japan*, **22(10)**, 811–819.

LEMMON, E. *et al.* (2014). *Thermophysical Properties of Fluid Systems in NIST Chemistry WebBook*. 69. National Institute of Standards and Technology.

MAIER, C. *et al.* (2012a). "Development and validation of a CFD-model for heterogeneous transfer phenomena in blast furnace processes". *5th International Conference from Scientific Computing to Computational Engineering IC-SCCE*, ISBN: 978-960-98941-9-7, 162–169. Athens, Greece.

MAIER, C. *et al.* (2012b). "Implementation and validation of a three-dimensional multiphase-CFD-model for blast furnace processes". *Chemical Engineering Transactions*, **29**, 925–930.

MAIER, C. *et al.* (2013a). "CFD-simulation of the blast furnace process: Injection of heavy oil and plastic particles into the raceway". *AISTech, The Iron and Steel Technology Conference and Exposition*, ISBN: 978-1-935117-32-2, 595–607. Pittsburgh, PA, USA. Session ID: 4041.

MAIER, C. *et al.* (2013b). "Investigation of alternative reducing agent injection into the raceway of blast furnaces using CFD". *Chemical Engineering Transactions*, **35**, 1345–1350.

NOGAMI, H. and YAGI, J.I. (2004). "An application of Bingham model to viscous fluid modeling of solid flow in moving bed". *ISIJ International*, **44(11)**, 1826–1834.

PIRKER, S. (2014). "Simulation - a corporate research topic in K1-Met". *K1-MET Scientific Exchange Day 2014*. Leoben, Austria. www.k1-met.at; 10.03.2014.

RUMPEL, S. (2000). *Die autotherme Wirbelschichtpyrolyse zur Erzeugung heizwertreicher Stützbrennstoffe*. Ph.D. thesis, Institut für Technische Chemie, Universität Karlsruhe.

SCHATZ, A. (2000). *Lump Ore, Pellets and Dead Men*. Ph.D. thesis, Johannes Kepler Universität Linz, A-4040 Linz.

TEPPER, H. (2005). *Zur Vergasung von Rest- und Abfallholz in Wirbelschichtreaktoren für dezentrale Energieversorgungsanlagen*. Ph.D. thesis, Otto-von-Guericke-Universität Magdeburg.

WEN, L. and BI, X.T. (2011). "Simulation of cavity formation hysteresis in the presence of granular compaction". *Chemical Engineering Science*, **66**, 674–681.

ZAÏMI, S.A. *et al.* (2000). "Validation of a blast furnace solid flow model using reliable 3-d experimental results". *ISIJ International*, **40(4)**, 332–341.

ZHANG, S.J. *et al.* (1998). "Modelling of the solids flow in a blast furnace". *ISIJ International*, **38**, 1311–1319.

ZHOU, C.Q. (2008). "CFD modeling for high rate pulverized coal injection (PCI) into the blast furnace". Tech. Rep. DE-FC36-97ID13554, Purdue University - Calumet, Dept. of Mechanical Engineering, Hammond, Indiana 46321, USA.

PREDICTION OF MASS TRANSFER BETWEEN LIQUID STEEL AND SLAG AT CONTINUOUS CASTING MOULD

Pascal GARDIN[1*], Ségolène GAUTHIER[1], Stéphane VINCENT[2]

[1] ArcelorMittal Global R&D, 57283 Maizières-lès-Metz, FRANCE

[2] I2M, Trèfle department, 33607 Pessac, FRANCE

* E-mail: pascal.gardin@arcelormittal.com

ABSTRACT

For the prediction of steel desulphurization and dephosphorization or the evolution of slag composition at continuous casting mould, mass transfer between two immiscible fluids in a turbulent situation should be calculated.

For this purpose, two possibilities are offered for the simulation. The first one consists in the calculation of the local chemical equilibrium with the simultaneous prediction of the species transport, but the cost is that very fine mesh should be used. The second is based on the assessment of the mass transfer coefficient from hydrodynamic calculations and further use of thermodynamic code fed with interface area and transfer coefficients. On a computing time point of view, this second method is more affordable for 3D configurations than the first one, but it is less accurate. Literature survey indicates that it is possible to obtain a realistic evaluation of the mass transfer coefficient from hydrodynamic calculations, under the condition of very precise description of the flow near the interface.

The paper explains the reasons for the different simplifications which were made to predict the mass transfer between liquid steel and slag, gives indication on interest and limitation of the coupling between fluid dynamics and thermodynamics to get the local and time dependent evolution of chemical composition in the two phases. The modelling to predict the mass transfer coefficient is also described and compared to correlation proposed in the literature. Finally, a correlation is proposed to get mass transfer coefficient up to Schmidt number = 1000.

Keywords: *CFD, Pragmatic industrial modelling, Multiphase Heat and Mass transfer, Casting, Slag.*

NOMENCLATURE

Greek Symbols

Λ Integral length scale of turbulence, [m].
δ_s Thickness of species boundary layer, [m].
δ_m Thickness of momentum boundary layer, [m].
μ Dynamic viscosity, [kg/m.s].
β Mass transfer coefficient, [m/s].
Δz Cell thickness near interface, [m].

Latin Symbols

C Non-dimensional concentration.
D Mass diffusivity, [m^2/s].
H Half height of the channel, [m].
Sc Schmidt number.
u* Friction velocity at interface, [m/s].
u_{max} Maximum velocity in the phase, [m/s].

Sub/superscripts

G Gas phase.
i Interface.
ls Liquid steel.
sl Slag.
∞ Far from interface.

.

INTRODUCTION

All along the steel refining route and casting, the liquid steel is rarely exposed to the ambient atmosphere. It is often covered with a thermal insulation: the slag. This is the case in a continuous casting mould, which is the reactor largely used to solidify steel. Figure 1 gives a schematic diagram of the operation and the various phases present in a mould:

▪ the liquid steel, also carrying argon bubbles and micro-particles coming from an endogenous precipitation in the liquid steel, is introduced through a nozzle into the mould (typical section of 1800 * 220 mm^2), the value of the Reynolds number at the outlet nozzle is in the order of 70000, which produces a high degree of turbulence in the mould and at the interface between liquid metal-slag; the argon bubbles limit the clogging phenomena inside the nozzle and strongly disturb the liquid steel / slag interface when crossing.

▪ the flux powder is deposited continuously on the upper surface and at about 1000 °C, it liquefies over a thickness of a few millimetres to form the liquid slag.

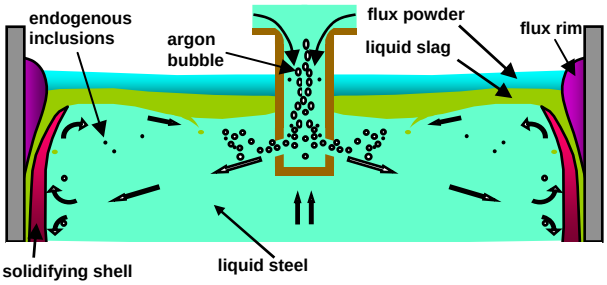

Figure 1: Different phases in a continuous casting mould, Pericleous (2008).

In a mould, the liquid slag has another specific function: it is entrained between the mould and the solidifying skin and facilitates lubrication. In the latter case, it is important to control the composition of the slag, to guarantee its good viscosity and its ability to lubricate.
Another characteristic is that the slag should not be fragmented; if slag droplets are suspended in the liquid steel, they can be entrapped by the solidifying shell and produce surface defects on the final product. It is currently one of the major defects in our steel plants.

New steels grades (such as Advanced High-Strength Steel) contain alloying elements that can affect the slag behaviour; for example, depending on the aluminium mass fraction inside the liquid steel, Al_2O_3 content of the slag can vary between 3-4 % and 30-35 %, which deeply affects its viscosity (multiplied by 5), Shahbazian et al. (2002), and its thermal conductivity, modifying the extraction of the heat flux through the mould. Robustness issues of the process are then encountered; if the viscosity increases, the quality of the lubrication is degraded, which leads to a rupture of the slag film and a direct contact of the molten steel with the mould: if a sticking takes place, it may be impossible to extract continuously the steel from the mould and the process should be stopped and the mould replaced.

Process control means that mass transfer should be controlled to have insight into the chemical evolution of the slag. In this context, we have to control the dynamic behaviour of the interface between liquid steel and slag and detect if interface fragmentation will occur or not, since it will affect interfacial area for mass transfer and steel quality if slag droplets are entrapped by the solidifying shell. Several mechanisms are involved in the fragmentation, which is already the subject of dedicated studies, Hagemann (2013), Real-Ramirez (2011). Figure 2 shows a typical interface behaviour observed in a water model. Part of the flow coming from the nozzle is deviated towards the interface and, above a critical water velocity, the interface is strongly distorted and can be fragmented. Another mechanism can be observed: the creation of a drainage cone which can produce small droplets of the upper phase in the lower one when it breaks.

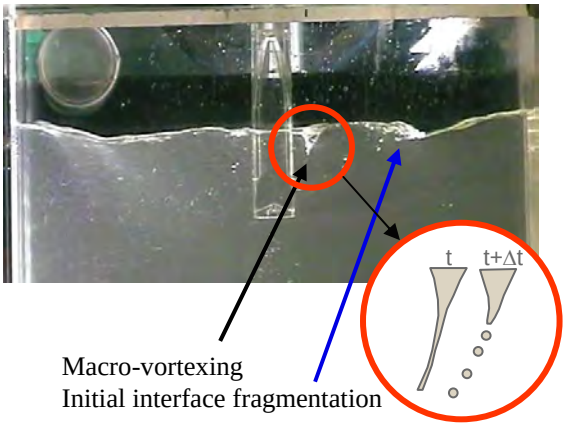

Figure 2: Typical behaviour of interface.

Mass transfer across a turbulent interface has already been investigated. In the steelmaking community, KTH teams have published some papers showing the evolution of slag compositions interacting with the liquid metal, Jonsson (1998), Andersson (2002), Doostmohammadi (2010).
However, as soon as CFD and thermodynamics are coupled, it is difficult to understand in details the numerical procedure for the coupling and there is a too brief discussion on different topics: dependence of the result to the mesh size and treatment of the interfacial turbulence (on the basis of RANS turbulence models). Although the method is qualitatively interesting, further investigations are necessary.

To get the mass transfer coefficient, different teams proposed interesting papers based on CFD calculations. In the case of a plane interface between water and liquid Calmet (1998) has shown the relevance of using a LES turbulence model to describe the interface with and without shear stress, and to identify the coefficient of mass transfer up to Schmidt number 200. More recently, Figueroa-Espinoza (2010) extended the method to predict the mass transfer between a bubble with a variable shape, using a mesh conforming to the shape of the bubble, for values of the Schmidt number up to 500.

Banerjee (2004) also took into account the deformation of the interface and made calculations for Schmidt numbers up to 10-20; he proposed the promising “surface divergence” model for deriving the mass transfer coefficient.

EVOLUTION OF CHEMICAL COMPOSITION

The objective is to get the time evolution of the steel and slag compositions. We have to calculate the flow, the local composition and advection/diffusion of the different chemical species, but also the chemical reactions between steel and slag. Ansys-Fluent™ predicts the flow of liquid steel and slag phases with the Volume Of Fluid model, each phase being constituted of a mix of several species. An in-house code is used for the thermodynamics calculations. Because

precipitation and chemical compositions in liquid or solid steel are very specific, ArcelorMittal R&D developed its own code, called CEQCSI, for Chemical EQuilibrium Calculation for the Steel Industry. It allows the calculation of local compositions and precipitations of different oxides (SiO_2 -TiO_2 - Ti_2O_3 - Cr_2O_3 - Al_2O_3 - Fe_2O_3-CrO - FeO -MgO - MnO - CaO…) and slag-metal reactions, Lehmann (2008).

By means of User Defined Functions that can be addressed in Ansys-Fluent ™, we can detect the cells where slag and steel are both present; mass fraction of the different species at time t are sent to Ceqcsi which makes the calculations for the new equilibrium composition in each phase and then gives the resulting source terms for each species to Ansys-Fluent™. Advection/diffusion takes place during Δt and new composition is calculated in the entire domain at t+Δt by Ceqcsi. With this iterative procedure, it is possible to have the time evolution of the chemical composition in each phase.

We initiated calculations in 2D. The geometry of the top region is displayed on Figure 3. The height is 1500 mm and width is 800 mm. Initial slag thickness is 50 mm. The number of cells, for the initial calculations is 21600. VOF-PLIC method is used to predict the interface and realisable k-ε is selected for turbulence modelling. Turbulence damping at interface is considered by means of a source term in the ε transport equation, Gardin (2011). Because slag is consumed to lubricate the mould, we impose slag inlet along the horizontal top line (Velocity inlet (1)) and slag is extracted by the two vertical segments (Velocity inlet (2)) with the composition of adjacent cells and negative velocity to get outlet conditions. Slag can be consumed or created due to the composition adjustment calculated by Ceqcsi; it means that slag volume, and by consequence steel volume, can change with time according to the chemical equilibrium with steel. The consequence is also that thermodynamics should be coupled with fluid flow calculations at each time step: unfortunately, freezing the steel/slag interface for further thermodynamics calculations is not possible and transient calculations should be performed.

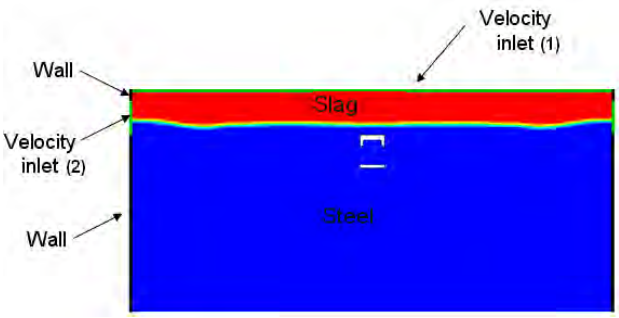

Figure 3: Top region of the calculation domain with boundary conditions.

Figure 4 illustrates the 2D velocity field that we obtained. The slag movement is mainly due to momentum transfer from liquid steel to slag at interface. The impact of slag injection by the top on slag movement is very small.

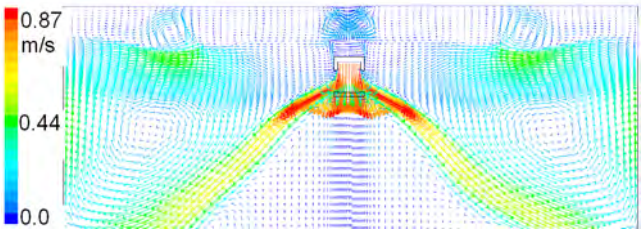

Figure 4: Typical velocity field in steel and slag.

The coupling between Ansys-Fluent™ and Ceqcsi was applied with the composition of steel and slag as it is expressed in Table 1 at t=0 s.

Table 1: Initial steel and slag compositions.

species	Steel %wt	Slag %wt
Fe	98.8273	
Al	0.031	
Mn	/	
Si	/	
Ca	/	
S	/	
O	0.0005	
SiO_2		38
Al_2O_3		9
Fe_2O_3		/
FeO		/
MnO		/
MgO		/
CaO		27
CaF_2		/

As we can see on Figure 5, Al distribution in the mould is heterogeneous after 113 s of calculation, especially near the interface. Al is transported towards the interface and there is a progressive Al consumption to form Al_2O_3 in the slag; in consequence, there is a progressive decrease of Al concentration as the flow transports Al along the interface towards the centre of the mould.

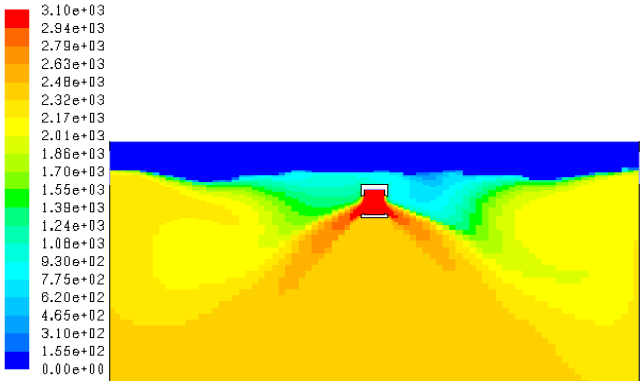

Figure 5: Mass fraction of Al (ppm) at t=113 s – time step for CEQCSI call: 0.05 s.

The Al distribution in liquid steel should be related to the alumina distribution in the slag (Figure 6) which also displays important variations; it is observed low

Al_2O_3 concentration in low velocity regions: mixing by advection/diffusion is too slow with the consequence of slag viscosity heterogeneously distributed.

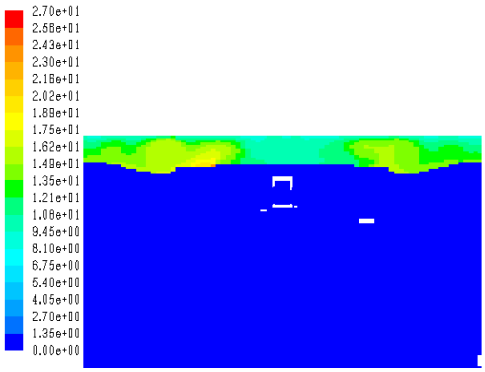

Figure 6: Mass fraction of Al_2O_3 (ppm) at t=113 s – time step for CEQCSI call: 0.05 s.

Analysis of the influence of the mesh size near the interface was realized. Initial mesh which was used for the previous results is displayed on Figure 7. Then, cells are successively divided by 2 and 4 in the region containing the interface. Cell thickness is respectively 4, 2 and 1 mm.

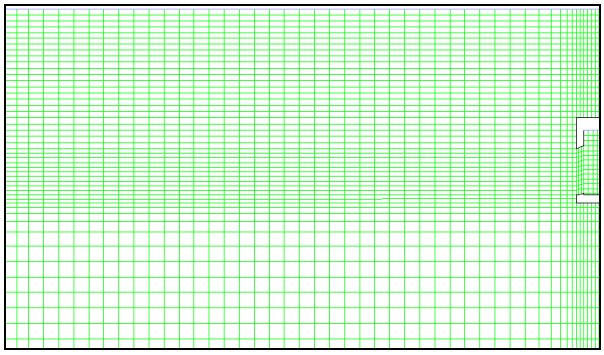

Figure 7: Initial mesh – half geometry is considered

The time step between two successive Ceqcsi calls is maintained constant to 0.05s and mean Al_2O_3 content in the slag is drawn for the three cases. Figure 8 clearly shows that results are strongly mesh dependent and that stationary concentration is more rapidly obtained for large mesh. If time step to call Ceqcsi is decreased, other calculations show that Al_2O_3 evolution is quicker than with 0.05s. At this stage, we conclude that results are mesh and time-step dependent.

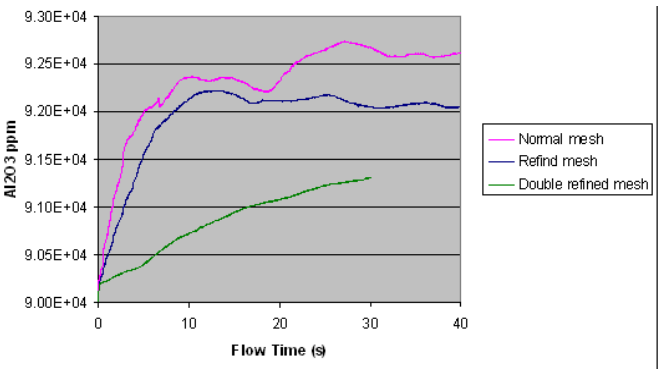

Figure 8: Mean Al_2O_3 content in slag – time step for CEQCSI call: 0.05 s.

The main idea to determine the adequate Ceqcsi time step call consists in adjusting it with the species renewal time of the cell. If we keep in mind that the species renewal in a cell is limited by the vertical diffusion, then we should have:

$(\Delta z)^2/\Delta t=D$ and Δt is the renewal time.

Δt can be identified to the Ceqcsi time step call. Table 2 gives the Δt values when diffusion length is imposed to be the cell thickness.

Table 2: Adaptation of time step to call the thermodynamics model.

Cell thickness (mm)	4	2	1
Diffusivity (m^2/s)	$4\ 10^{-5}$	$2\ 10^{-5}$	10^{-5}
Time step for Ceqcsi call (s)	0.4	0.2	0.1
Diffusion length $(D\Delta t)^{0.5}$ (mm)	4	2	1

Figure 9 shows that the superimposition of the curves is much better than previously. But, if we consider a realistic species diffusivity $D \sim 3.0\ 10^{-9} m^2/s$, the Ceqcsi time step should be 1h30 when Δz is 4 mm: it is not possible to have calculations for such long time and the numerical diffusions should overcome the molecular one. If cell thickness is 100 µm, then Δt is 3 s, which is a realistic value on the CFD point of view, with the insurmountable drawback of huge number of cells for an industrial application.

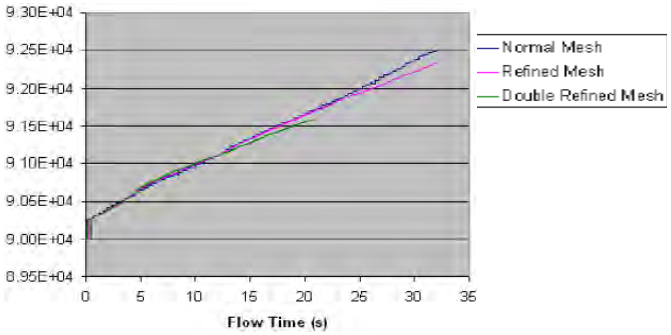

Figure 9: Mean Al_2O_3 content in slag - results independent of mesh size.

At this moment, these calculations are possible on a qualitative point of view, using much larger species diffusivity than real ones, with cell thickness larger than 1 mm. Some trends will be obtained but the time evolution will be much quicker than what it should be. Nevertheless, the information we get is sufficient to classify the mutual influence of steel grades and initial slag composition on the slag viscosity. On an engineering point of view, the coupling between CFD and thermodynamics can be fruitfully used.

To get more realistic values of the time evolution of slag composition, another method should be used, which will be explained now.

CAN WE USE CORRELATIONS BASED ON FLOW AND FLUID PROPERTIES TO EXTRACT THE MASS TRANSFER CEFFCIENT?

As it was already investigated by Calmet (1998) or Banerjee (2004), CFD can provide some valuable correlations to get the mass transfer coefficient β. For instance, the following relation can be considered (valid for Sc < 100):

$$\beta\, Sc^{0.5} / u^* \sim 0.108 - 0.158$$

$$u^* = \sqrt{\frac{\tau_i}{\rho}} \quad \text{is the friction velocity} \qquad (1)$$

where $\tau_i = \mu\left(\frac{\partial \bar{u}}{\partial n}\right)_i$ is the interface shear stress

or this one which was proposed by Banerjee, known as "surface-divergence" correlation:

$$\beta \approx Sc^{-1/2} u^* \mathrm{Re}_t^{-1/2} \left[\left(\frac{\partial u}{\partial x} + \frac{\partial v}{\partial y}\right)^2\right]_i^{1/4} \qquad (2)$$

where $Re_t = \Lambda u_{max}/\nu$ (the integral length scale of turbulence Λ is assimilated here to the height of liquid steel phase H or slag when slag is considered) and (x, y) plane is the interface plane.

When β and the interfacial area are known, Ceqcsi can calculate the time evolution of the slag composition. Interfacial area can be determined by VOF-PLIC method, see Figure 10, as soon as interface deformation is not too complex.

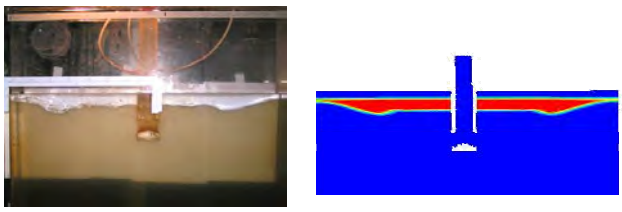

Visualisation of the interface shape

3D calculations with Ansys-Fluent

Figure 10: Schematic diagram of geometry.

But equation (1) or (2) cannot be used directly in our case since species Sc is around 1000 (value depending on species) and out of the validity range. A specific study should be carried out to extend the correlation up to Sc~1000-2000. The method consists in performing two kinds of calculations:

1- a scalar value is imposed at the interface and scalar profile is drawn at different positions and times; the profile is then used to identify the mass transfer coefficient, as it was explained by Haroun (2008).

2- based on a sufficient number of previous calculations, scaling laws are built: for instance $\beta_L \sim Sc^{-n}$ or $\beta_L \sim u^{*m}$ (n=-1/2 and m=1 for equation (1)).

Preliminary calculations were realised with Ansys-Fluent™ but, unfortunately, we did not manage to respect the interfacial shear stress continuity across a flat interface, even for very thin cells around 10 µm thickness. It was the reason why we decided to switch to another CFD code: Thetis.

Thetis is developed at Institut de Mécanique et d'Ingénierie de Bordeaux, Trèfle department. It is devoted to the prediction of multiphase flow in laminar or turbulent situation and special emphasis is given to accurate description of interface tracking based on VOF method, see Vincent (2010).

A first set of calculations was realised in the case of a channel flow with two counter-current stratified fluids: liquid in the bottom and gas at the top. The momentum source is a pressure gradient in both fluids. Intensive CFD work was already realised by Fulgosi (2003) and Adjoua (2010): their work is considered as reference to test Thetis reliability. In Thetis, mesh refinement in the interface region is adapted to get at minimum 3 cells in the viscous sub-region. Dynamic LES turbulence model is used, without adaptation of the subgrid scale model at the interface. A very good agreement with results published by Adjoua was obtained (Figure 11) and interface shear stress continuity was respected.

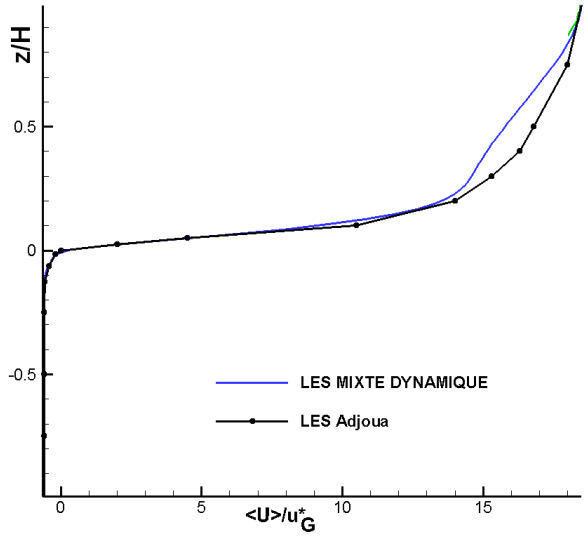

Figure 11: Dimensionless vertical coordinate according to mean velocity - comparison between LES model of Thetis and LES of Adjoua.

Since the good behaviour of Thetis was established, a second configuration was studied. It is still a channel flow but with liquid steel at the bottom and slag at the top.

The momentum source is a pressure gradient in the liquid steel phase and slag is entrained by the shear stress exerted at the interface (as it is in a real mould). The fluid properties are given in Table 3.

Table 3: Fluid properties.

	Steel	Slag
Density – kg/m^3	7000	2500
Viscosity – Pa.s	0.00539	0.0539
Interface tension	1.2 N/m	

The boundary conditions are periodic in the streamwise and spanwise directions whereas symmetry conditions are imposed in the direction normal to the interface. The initial velocity guess is chosen as a fluctuating instantaneous field coming from the simulations of Adjoua after the turbulence was developed. The maximum liquid steel velocity is selected to be 0.3 m/s (close to what is measured in real continuous casting mould near the interface) and the height of the channel filled with liquid steel is 0.009576 m. Reynolds number is then 3730.

The mesh in the interface region is depending on Schmidt number, according to $\delta_s \approx \delta_m \, Sc^{-1/3}$. If Sc=1000, species boundary layer is 10 times lower than momentum one and much more cells are necessary to describe the species behaviour.

It is important to control that we have shear stress continuity across interface (see Table 4, transient calculations), which makes possible the calculation of the friction velocity on both sides of the interface.

Table 4: Shear stress and friction velocity at interface at different times.

	$\tau_{i,ls}$ (Pa)	$\tau_{i,sl}$ (Pa)	u^*_{ls} (m/s)	u^*_{sl} (m/s)
t=1.4s	0.46	0.48	0.0081	0.014
t=4s	0.23	0.26	0.0057	0.01
t=6s	0.22	0.22	0.0055	0.0092

Figure 11 displays the concentration field at time t=4 s, when the concentration at the interface is imposed to be 1, and makes explicit the need to refine the mesh depending on Schmidt number.

The interface is totally flat and aligned with the cells, which is very important to have negligible numerical diffusion. We checked that, in the case of laminar flow with very large Sc (>10^7), the species diffusion in the vertical direction is totally negligible.

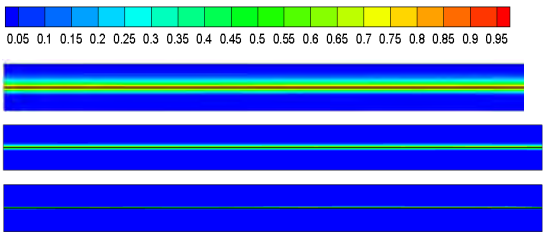

Figure 11: Mean species concentration at t=4 s, for Sc=10 (top), 100 (middle), 1000 (bottom).

Vertical concentration profiles are extracted, Figure 12. Z=0 corresponds to interface position, z < 0 is steel and z > 0 is slag. Due to the fluid properties, diffusion is not symmetrical, with deeper diffusion when species diffusivity is higher, as it is the case for slag compared to steel.

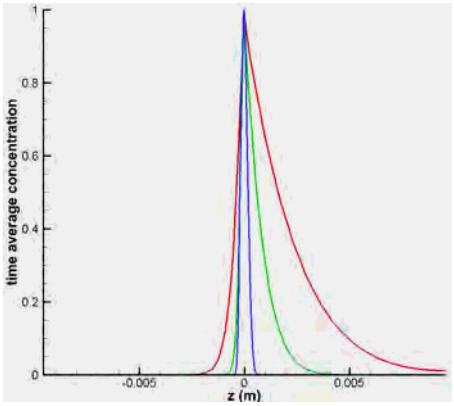

Figure 12: Vertical concentration profile at t=4 s, for Sc=10 (red), Sc=100 (green), Sc=1000 (blue).

The curves can be used to get the mass transfer coefficient, according to equation (3):

$$\beta = \frac{D\left(\frac{\partial C}{\partial z}\right)_i}{(C_i - C_\infty)} \qquad (3)$$

Table 5 summarises the results. Higher mass transfer coefficient is confirmed at the slag side. Those values are referenced as “Steel-simulation” on Figure 13.

Table 5: Mass transfer coefficients, t=4 s.

	Mass transfer coefficient, steel side ($m.s^{-1}$)	Mass transfer coefficient, slag side, ($m.s^{-1}$)
Sc=10	4.94E-05	4.23E-04
Sc=100	1.16E-05	1.33E-04
Sc=1000	1.37E-06	2.81E-05

Then, mass transfers obtained with species diffusion were compared to the ones obtained using correlation, for instance equation (2) proposed by Banerjee.

Mass transfer coefficients obtained with (2) are referenced as “Steel-SD” in Figure 13.

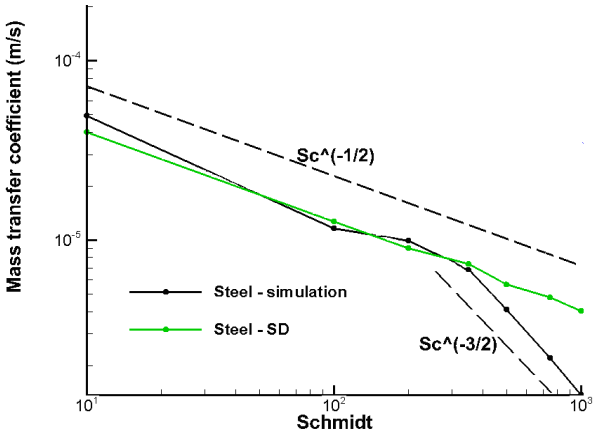

Figure 13: Dependence of mass transfer on Schmidt number, liquid steel side.

The main conclusions when we compare the two methods are:

▪up to Sc 200-300, the two methods give similar results; it is very encouraging to note that the species diffusion method also provides the $Sc^{-1/2}$ scaling law.
▪for large Sc (> 400), which is our situation for steelmaking systems, we deviate from $Sc^{-1/2}$ scaling law and have $Sc^{-3/2}$; this new result needs to be investigated in more details to understand why the scaling law is depending on Sc with a rupture around Sc=350; there are significant effects on a practical point of view, since low mass transfer coefficient is very detrimental for our process productivity.
▪standard correlations cannot be used but should be adapted for high Sc number; the species diffusion method proposed here is probably the good method to enlarge the validity range of the correlations, since the numerical diffusion is negligible; but we have to keep in mind that LES results should be compared to DNS to better assess the LES reliability near interface when typical length scales for species diffusion are much smaller than the viscous sublayer.

Further calculations were realised, with different interface frictions and Schmidt numbers. Then, a fitting function was built for both liquid steel and slag. Comparison is drawn on Figure 14 (u^*_{ls}=0.0057 m/s, u^*_{sl}=0.0103 m/s).

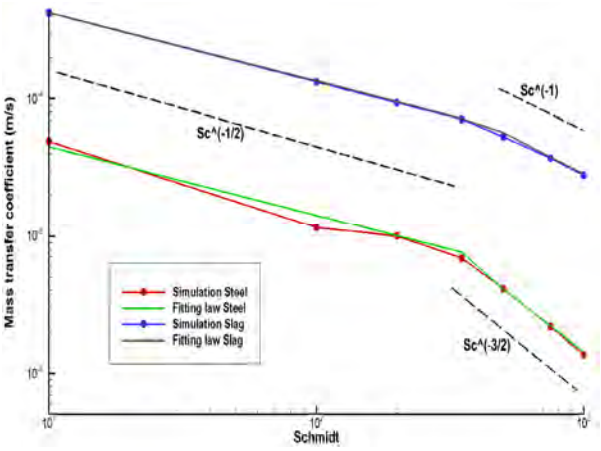

Figure 14: Dependence of mass transfer on Schmidt number, liquid steel and slag sides.

Below are the expressions of the fitting functions:

$$\beta_{ls} = u^*_{ls}\left(B_{ls}Sc^{-1/2} + E_{ls}Sc^{-3/2}\right)$$

$$\beta_{sl} = u^*_{sl}\left(B_{sl}Sc^{-1/2} + E_{sl}Sc^{-1}\right)$$

With :

$$B_{ls} = 0.025 I_{0\text{–}350}$$

$$E_{ls} = 8 I_{350\text{-}1000}$$

$$B_{sl} = 0.13 I_{0\text{–}350}$$

$$E_{sl} = 5 I_{350\text{-}1000}$$

$I_{0\text{-}350}$, $I_{350\text{-}1000}$ are the characteristic Heavyside functions being equal to 1 on the interval and 0 elsewhere.

In the near future, we will have to consolidate those correlations and understand why they are slightly different in liquid steel and slag.

When the correlations are applied in the case of continuous casting mould, the shear stress between liquid steel and slag can be approximated using the assumption of flat free surface with no-slip boundary condition. Then the shear stress is in the range 1-10 Pa and mass transfer in the liquid steel side is approximately 10^{-5} m/s (much smaller than in the slag side), which is coherent with values taken by Chaubal (1992).

CONCLUSIONS

Coupling between fluid dynamics and thermodynamics was realised to predict chemical composition of both liquid steel and slag. To get rid of mesh size dependence, it was proposed to align the time step call to thermodynamic software with the typical diffusion time across the cell near the interface. This coupling can provide qualitative information on chemical evolution but is not suitable for quantitative prediction.

Improvement of the modelling is based on the prediction of the mass transfer coefficient β. Scalar diffusion method was used to calculate β for different Schmidt numbers. Classical dependence $\beta / u^* \sim Sc^{-1/2}$ was predicted, but the scaling law was changed when Sc > 350. A correlation was proposed for both liquid steel and slag, to be applied in the range 10 < Sc < 1000. Further work will be necessary to test the correlations but the order of magnitude is compatible with values already published.

REFERENCES

ADJOUA, S., (2010), “Développement d'une méthode de simulation de films cisaillés par un courant gazeux”, *Thesis report, Toulouse University*.

ANDERSSON, M., HALLBERG, M., JONSSON, L., JÖNSSON, P., (2002), “Slag-metal reactions during ladle treatment with focus on desulphurisation”, *Ironmaking & Steelmaking*, **29(3)**, 224-232.

BANERJEE, S., LAKEHAL, D., M. FULGOSI, M., (2004), “Surface divergence models for scalar exchange between turbulent streams”, *International Journal of Multiphase Flow*, **30**, 963-977.

CALMET, I., MAGNAUDET, J., (1998), “High-Schmidt number mass transfer through turbulent gas-liquid interfaces”, *International Journal of Heat and Fluid Flow,* **19**, 522-532.

CHAUBAL, P., BOMMARAJU, R., (1992), “Development and use of a model to predict in-mould slag composition during the continuous casting of steel”, *Steelmaking Conference Proceedings,* 665-675.

DOOSTMOHAMMADI, H., ANDERSSON, M., KARASEV, A., JÖNSSON, P.G., (2010), “Use of Computational Thermodynamic Calculations in Studying the Slag/Steel Equilibrium during Vacuum Degassing”, *steel research international*, **81(1)**, 31-39.

FIGUEROA-ESPINOZA, B., LEGENDRE, D., (2010), “Mass or heat transfer from spheroidal gas bubbles rising through a stationary liquid”, *Chemical Engineering Science*, **65**, 6296-6309.

FULGOSI, M., LAKEHAL, D., BANERJEE, S., DE ANGELIS, V., (2003), "Direct numerical simulation of turbulence in a sheared air–water flow with a deformable interface", *J. Fluid. Mech.*, **282**, 319-345.

GARDIN, P., SIMONNET, M., GAUTHIER, S., (2011), "Inclusion elimination in steelmaking ladle", *8th International Conference on CFD in Oil & Gas, Metallurgical and Process Industries, Trondheim.*

HAGEMANN, R., SCHWARZE, R., HELLERAND, H.P., SCHELLER, P.R., (2013), "Model Investigations on the Stability of the Steel-Slag Interface in Continuous-Casting Process", *Metallurgical and Materials Transactions B*, **44B**, 80-90.

HAROUN, Y., (2008), "Etude du transfert de masse réactif Gaz-Liquide le long de plans corrugués par simulation numérique avec suivi d'interface", *Thesis, University of Toulouse.*

JONSSON, L., SICHEN, D., JONSSON, P., (1998), "A New Approach to Model Sulphur Refining in a Gas-stirred Ladle- A Coupled CFD and Thermodynamic Model", *ISIJ International*, **38(3)**, 260-267.

LEHMANN, J., (2008), "Application of ArcelorMittal Maizières thermodynamic models to liquid steel elaboration", *Revue de Métallurgie*, **105 (11)**, 539-550.

PERICLEOUS, K., DJAMBAZOV, G., DOMGIN, J.F., GARDIN, P., (2008), "Dynamic modelling and validation of the metal/flux interface in continuous casting", *6th European Conference on Continuous Casting 2008, Riccione.*

REAL-RAMIREZ, C.A., GONZALEZ-TREJO, J.I., (2011), "Analysis of three-dimensional vortexes below the free surface in a continuous casting mold", *International Journal of Minerals, Metallurgy, and Materials*, 2011, **18(4)**, 397-407.

SHAHBAZIAN, F., SICHEN, D., SEETHARAMAN, S., (2002), "The effect of addition of Al2O3 on the viscosity of CaO–FeO–SiO2–CaF2 slags", *ISIJ International*, **42(2),** 155–162.

VINCENT, S., BALMIGÈRE, G., CALTAGIRONE, J.P., MEILLOT, E., (2010), "Eulerian-Lagrangian multiscale methods for solving scalar equations – Application to incompressible two-phase flows", *J. Comput. Phys.*, **229**, 73-106.

Chapter 6: Oil & Gas Applications

In the oil and gas industry there are enormous possibilities to apply CFD. There is a great variety in processes and relevant phenomena which can be studied by CFD. These include pipeline transport, process optimization, oil spill tracking, wave loads on rigs and vessels, launching of rescue vessels and more. Many of these processes are governed by multiphase interactions since oil, water and/or gas often are found together in the systems of interest. Some phenomena can also be studied by single phase considerations, e.g. cooling of subsea equipment. To assess oil and gas phenomena complex models are often required, but some degree of pragmatism is also needed to create appropriate modelling tools. The models need to capture the governing physics with a sufficient accuracy at an acceptable computational cost.

The oil and gas industry have applied CFD for decades in their R&D and engineering activities. Computational capacity, numerical algorithms and knowledge on relevant physics have made great progress over these decades. This results in better and more accurate CFD models. This progress is exemplified by the papers seen in this chapter on applications of CFD to the oil and gas industry. Subjects covered include oil-water separation, cooling of subsea equipment, modelling of gas blowouts and modelling of multiphase interfaces.

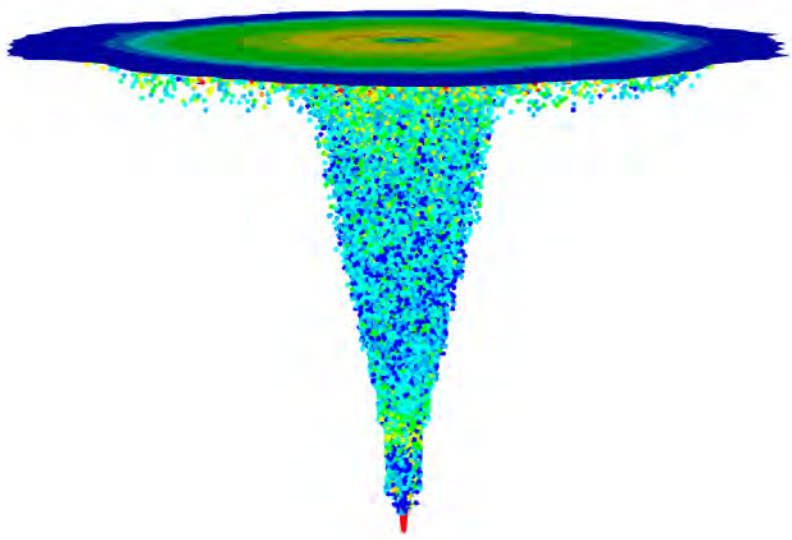

CFD MODELING OF OIL-WATER SEPARATION EFFICIENCY IN THREE-PHASE SEPARATORS

Lanre OSHINOWO*, Ehab ELSAADAWY and Regis VILAGINES
Saudi Aramco Research and Development Center, Dhahran, SAUDI ARABIA
* E-mail: oshinoom@aramco.com

ABSTRACT

Variations in oil properties or water content influence the rate of crude oil-water separation. This presents a challenge for separator operations when conditions change as fields mature, and for the design of new internals to improve separation efficiency. Computational fluid dynamics (CFD) is being used to predict separator vessel hydrodynamics and previous studies of three-phase separators have characterized the dispersed phase with a single droplet size and constant phase properties. Modelling the evolving droplet size during separation is a critical requirement to developing a realistic separator model. Emulsion rheology is also an important phenomena typically overlooked in modeling oil-water separation. In this study, a transient Eulerian multiphase approach coupled with the population balance is used to predict the gas, oil and water separation behavior in three-phase horizontal gas-oil-water gravity separators. Here, the secondary water phase is divided into multiple velocity groups and a number of bins describe the droplet distribution within each velocity group. By considering the dispersed phase fraction in the water-in-oil emulsion rheology and incorporating this into the interphase interaction, a high viscosity emulsion is formed at the interface between the oil and water phases, known as the dense packed layer or zone (DPZ). The resulting DPZ is known to have an effect on oil-water separation efficiency. Experimental data was obtained from a high-pressure pilot scale three-phase separator rig and includes phase flow rates into and out of the vessel and vertical water fraction profiles at two locations in the separator. The data was compared to the CFD predictions of separation efficiency, phase distribution and DPZ thickness in the separator.

Keywords: Emulsion, gravity separation, three-phase, separator, oil, multiphase, population balance, CFD.

NOMENCLATURE

a Coalescence rate, [m^3/s].
c_1, c_2, c_3 Coalescence rate empirical constants, [-].
B Interfacial force constant, [N.m^2].
B Birth rate, [1/s].
C_D Droplet drag coefficient, [-].
d Droplet diameter, [m].
D Death rate, [1/s].
f Drag function, [-].
f Friction factor, [-].
f_i Discrete bin fractions, [-].
$\vec{g}$ Gravitational acceleration, [m/s^2].
g Breakage frequency, [1/s].
h Collision frequency of droplets of volume V and V', [1/s].
$h_{w,l}$ Interface and liquid level, [m].
$\bar{\bar{I}}$ Unit tensor, [-].
k_B Boltzmann constant, [J/K].
K Loss coefficient, [-].
K_{ij} Mean interphase momentum exchange, [kg/m^3.s].
m Mass transfer rate, [kg/s].
M Number of bins per phase/velocity group, [-].
N Number of velocity groups, [-].
p Pressure, [Pa].
Pe Peclet number, [-].
Q Volumetric flow rate, [m^3/s].
Re Reynolds number, [-].
S population balance equation source term, [1/m^3].
T Temperature, [K].
u, v, w Components of velocity, [m/s].
V Droplet volume, [m^3].
x, y, z Coordinates, [m].

Greek Symbols
α Phase fraction, [-].
$\beta(V|V')$ probability density function of droplets breaking from volume V' to V, [-].
λ Coalescence efficiency of a binary droplet pair, [-].
μ Viscosity, [kg/m.s].
ρ Mass density, [kg/m^3].
σ Interfacial tension, [N/m].
τ Particle relaxation time, [s].

Sub/superscripts
g, w, o Gas, Water, Oil.
c Continuous phase.
d Dispersed phase.
l Liquid.
m Mixture.
i, j, k Indices i, j, k.

INTRODUCTION

The separation of gas, oil and water by gravity is found throughout oil and gas production operations. The multiphase separator is the first unit in the production line between the production manifold and the pipeline transport. In offshore production, the multiphase flow is separated into the requisite streams top-sides while onshore, the Gas-Oil Separation Plants (GOSP) handle the separation. Horizontal gravity separators are high-aspect ratio cylindrical vessels with a relatively short entrance region for disengagement of gas and liquid. To improve the efficiency of separation while reducing the overall vessel dimensions, various types of "internals" – plate, vane or cyclonic momentum breakers at the vessel inlet, coalescing plates, solid and perforated baffle plates, flow

straighteners, foam breakers, weirs, mist eliminators, electrocoalescers – are all used to promote gas-liquid and liquid-liquid separation. Computational fluid dynamics (CFD) has long been recognized as a promising tool in design, sizing and retrofit studies of multiphase separators. In the CFD work by Hansen and co-workers, the three-phase separator was modeled by considering different two-phase regions of the separator: a freeboard region with dispersed liquid droplets in gas, and the liquid bath with water or oil droplets dispersed in oil or water (Hansen *et al*., 1991, Hansen and Rørtveit, 2005). The emulsion viscosity was modeled by changing the continuous phase oil viscosity with the local water volume fraction. Another approach has been to model the oil-water emulsion as a mixture using the volume of fluid model and determine the water separation efficiency by tracking a droplet distribution with an uncoupled Lagrangian dilute-phase particle tracking model (Laleh *et al*., 2012). The presumption of dilute flow may be valid for droplets dispersed in the gas phase but not in the liquid phase. The water phase accumulates and the dilute conditions become dense phase conditions in regions of the separator, making the dilute Lagrangian approach inappropriate for modelling the oil-water phase separation. The Eulerian multiphase modelling approach is the most appropriate to describe complex phase rheology, phase separation and inversion in oil-water emulsions that exist in continuous and batch separators (Hallanger *et al*., 1996). Phases are treated as interpenetrating continua in the Eulerian multiphase approach and phase volume fractions add up to one in each cell of the computational domain. A momentum transport equation is solved for each phase in addition to a continuity equation. Interphase interaction forces, like drag and lift, are modeled using momentum exchange coefficients. Several recent studies applied Eulerian multiphase models but the dispersed water phase was modeled with a constant droplet diameter (Vilagines and Akhras, 2010, Kharoua *et al*., 2012). While these studies and others have shown that CFD helps to elucidate the macroscopic parameters, such as, flow patterns, pressure drop, and phase residence time, CFD has been unable to predict separation performance accurately (Laleh *et al.*, 2012, Frising *et al*, 2006). The main reasons for these shortcomings have been a lack of a comprehensive treatment of the oil-water emulsion rheology and the poly-disperse nature of the multiple phases. It is widely recognized that the dispersed phase size distribution in liquid-liquid dispersions influences the separation kinetics in gravity separation (Henscke *et al*., 2002). The size distribution evolves with transport through the separation vessels due to varying shear, turbulence, and due to the effects of surface active agents naturally present or injected upstream of the GOSPs. In this study, a CFD methodology to model GOSPs is presented. The population balance model is used here to predict the evolving droplet size distribution in the oil emulsion and its viscosity varies with water content. Experimental data were obtained from a pilot-scale high-pressure, three-phase horizontal gravity separator, and compared to the CFD model results.

EXPERIMENTAL

The experimental data obtained for the CFD model study was obtained from a pilot scale, high-pressure, horizontal, three-phase gas-oil-water separator flow loop at the IFP Energies Nouvelles site in Solaize, France (Pagnier *et al.*, 2008). The closed flow loop, as illustrated in Figure 1, consists of feed tank for the oil and water and a gas compression system. The flow loop has instrumentation to quantify the flows in and out of the separator vessel. The mass flow rate, pressure and temperature for each phase are controlled. The temperature control is achieved using separate heat exchangers for cooling and for heating. The oil and water phases are mixed in a Y-branch followed by two static vane mixers, one upstream and the other downstream of the heat exchangers. The gas is introduced after the second liquid static mixer. The three-

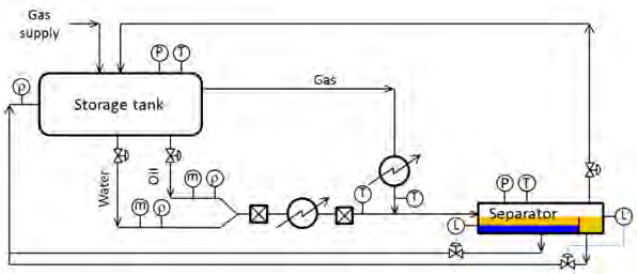

Figure 1. Pilot-scale, high-pressure, horizontal, three-phase gas-oil-water separator flow loop at the IFPEN (Pagnier, et al. 2008)

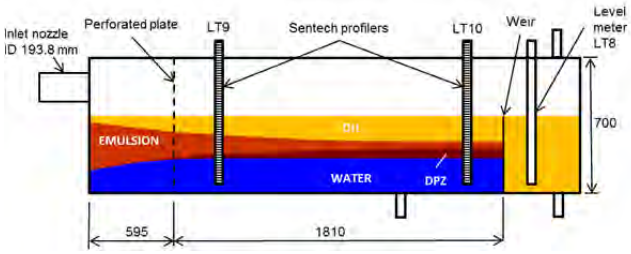

Figure 2: Schematic of the high-pressure, three-phase, pilot separator (ID 700mm, Length 3000mm).

phase flow then travels approximately 15 m through a 3-inch (ID 73.66 mm) line to the multiphase separator vessel. The separator vessel is 700 mm in diameter and 3000 mm in length and is illustrated in Figure 2. The separator inlet is an 8-inch diameter nozzle (ID 193.8 mm) while 2-inch (ID 47.3 mm) nozzles are used for the gas, oil and water outlets. A perforated plate, located 595 mm from the inlet flange, separates the entry region from the settling zone in the vessel that extends 1810 mm to the weir. The perforated plate is 10 mm thick with 13 mm holes arranged in a triangular pattern with a 54% open area. The weir height is 400 mm from the vessel bottom. The evolution of the separating water phase is measured *in-situ* in the separator using two commercially-available electrical capacitance profilers (Schuller *et al.*, 2004). The two profilers, LT9 and LT10 (Figure 2), are mounted vertically just downstream of the perforated plate (750 mm from inlet flange) and upstream of the weir (2250 mm from inlet flange), respectively. The profilers determine the spatial distribution of the water phase and the interface boundaries between the water and emulsion, emulsion and oil, oil and gas. The profilers consist of a linear array of elements with each element having a single capacitance electrode. The elements are typically spaced every 10 mm and give a measurement related to permittivity that is calibrated to the water/brine volume fraction. It is then possible to ascertain the height of the water-emulsion and oil-gas interface from the maximum and minimum permittivity measurements. The dense packed zone (DPZ) forms in the emulsion layer above the water interface. In this zone, the water fraction typically exceeds the inlet water fraction. The height of the DPZ is interpreted from an inflexion in the water fraction profile, measured from the LT10 profiler as illustrated in Figure 3, typically corresponding to water fraction in excess of the inlet value. A water fraction of 0.1 defines the boundary between the emulsion and the oil layers. The oil/liquid level in the vessel is measured by the level transmitter LT8 and controlled by the valve on the oil outlet line. Alternatively, the liquid level is controlled by the weir. The water-emulsion interface level is controlled using the water outlet control valve, based on the interface level measurement from the LT10 profiler. The oil and water discharged from the separator are circulated back to the feed tank where the phases separate and return to the flow loop. The oil-water feed tank volume is 10 m^3 while the separator vessel has a capacity of approximately 1 m^3. The oil used is a Saudi Arabian light crude oil with an API gravity

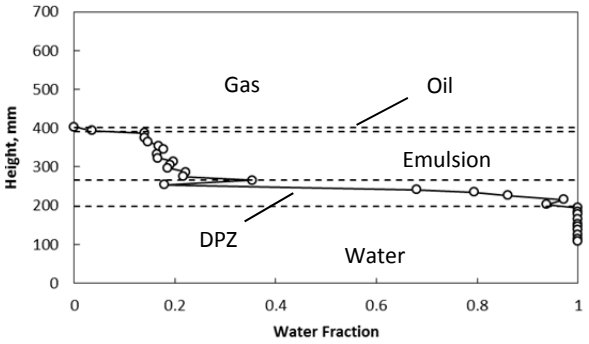

Figure 3. Measured water fraction obtained at the LT10 capacitance probe showing the dense packed emulsion zone.

of 35. The water is a brine mixture with 50 g/L NaCl. A demulsifier is added to the aqueous phase in a dosage of 50 ppm Clariant PT 4688. The gas phase is a mixture consisting of 97.8% methane, 1.1% nitrogen, 0.8% ethane, 0.2% propane, and 0.1% carbon dioxide. The operating temperature and pressure are 45°C and 24 bar, respectively. The experimental conditions selected for this paper are listed in Table 1.

Table 1. Experimental Conditions.

Oil Flowrate Q_o	m^3/h	3.40
Water Flowrate Q_w	m^3/h	1.50
Liquid Flow Q_l	m^3/h	4.9
Gas Flowrate Q_g	Am^3/h	13.95
Gas Fraction $Q_g/(Q_l+Q_g)$	-	0.74
Water Cut Q_w/Q_l	-	0.31
Water Level h_w	mm	199
Liquid Level h_l	mm	405*

** Level controlled by weir.*

MODEL DESCRIPTION

An Eulerian-Eulerian multiphase method was used to model the characteristics of the multiphase dispersion encountered in gravity separators. The liquid-dispersions found in gravity separation can be characterized as dense with the volume fraction ranging from zero to 100%. With the dispersion of gas bubbles and water droplets in the continuous oil phase, the oil phase is considered in this work to be the primary phase while the gas and water phases are considered secondary phases. The poly-dispersity of the secondary-phase water droplet population is modeled with the population balance method.

Multi-fluid Multiphase Model

The conservation equations are derived by ensemble averaging the local instantaneous balance for each phase. The continuity equation for phase *j* is

$$\frac{\partial}{\partial t}\left(\alpha_j\rho_j\right)+\nabla\cdot\left(\alpha_j\rho_j\vec{v}_j\right)=\sum_{i=1}^{n}\left(\dot{m}_{ij}-\dot{m}_{ji}\right) \quad (1)$$

where α_j, ρ_j and $\vec{v}_j$ are the phase volume fraction, density and velocity, and $\dot{m}$ is the mass transferred between phases. The momentum balance for phase *j* is

$$\frac{\partial}{\partial t}\left(\alpha_j\rho_j\vec{v}_j\right)+\nabla\cdot\left(\alpha_j\rho_j\vec{v}_j\vec{v}_j\right)=-\alpha_j\nabla p+\nabla\cdot \alpha_j\mu_j\left[\left(\nabla\vec{v}_j+\nabla\vec{v}_j^{T}\right)-\tfrac{2}{3}\nabla\cdot\vec{v}_j\bar{\bar{I}}\right]+\sum_{i=1}^{n}\left(K_{ij}\left(\vec{v}_i-\vec{v}_j\right)+\dot{m}_{ij}\vec{v}_{ij}-\dot{m}_{ji}\vec{v}_{ji}\right)+\alpha_j\rho_j\vec{g} \quad (2)$$

where p is pressure, μ is viscosity, $\bar{\bar{I}}$ is the unit tensor, and $K_{ij}\left(=K_{ji}\right)$ is the mean interphase momentum exchange coefficient and can be written in general form as:

$$K_{ij}=\frac{\alpha_i\alpha_j\rho_j f}{\tau_i} \quad (3)$$

The terms f and τ_i are the drag function and particle relaxation time, respectively, expressed as

$$f=\frac{C_D Re}{24} \quad (4)$$

and,

$$\tau_i=\frac{\rho_j d_i^2}{18\mu_m} \quad (5)$$

where d_i is the Sauter mean diameter coupling the momentum equations to the population balance equation. For settling or rising droplets, the drag originates from viscous surface shear and the pressure distribution, or form drag, around the droplet. For dilute dispersions, the droplets can settle or rise without interacting with neighbor droplets. For small droplets in the viscous regime, the Stokes law determines the terminal velocity in dilute or unhindered conditions. In the dense dispersions found in oil-water batch and continuous gravity separation, the drag function must include the influence of neighbor droplets and hindered settling. The Schiller-Naumann correlation for drag coefficient C_D is modified for hindered settling in dense suspensions using a mixture or emulsion Reynolds number Re_m based on the emulsion viscosity μ_m described later:

$$C_D=\frac{24}{Re_m}\left(1+0.15Re_m^{0.687}\right) \quad (6)$$

$$Re_m=\frac{\rho_c|u_d-u_c|d_d}{\mu_m} \quad (7)$$

where subscripts *c* and *d* refer to the continuous and dispersed phases, respectively. The drag force is the only contribution to the interphase interaction that was considered. Other forces including virtual mass force, transverse lift force, or wall lubrication force were not considered given droplet Reynolds numbers of the order 0.01 for water-in-oil dispersions relevant to crude oil separation. The turbulent dispersion force – that contributes to diffusion in dispersed flows – was not considered here. The mixture or emulsion viscosity depends on the viscosities of the dispersed and continuous phases, the concentration of the dispersed phase, the shear field, the droplet size distribution, temperature, and the emulsion stability. The interfacial stability is dependent on many non-hydrodynamic factors including the crude oil heavy fraction, solids, temperature, droplet size and distribution, pH, salinity, and composition (Kokal, 2005, Sanfeld and Steinchen, 2008). Brinkman derived the following equation for emulsion viscosity for suspensions of hard spheres (Brinkman, 1952):

$$\mu_m=\mu_c(1-\alpha_d)^{-2.5} \quad (8)$$

Krieger and Dougherty extended Brinkman's correlation by including the contribution of the maximum packing value (Krieger and Dougherty, 1959):

$$\mu_m=\mu_c\left(1-\frac{\alpha_d}{\alpha^*}\right)^{-2.5\alpha^*} \quad (9)$$

where α^* is the packing concentration of 0.64 for hard spheres in non-equilibrium reaching the limit of 0.74 for a hexagonal close packed structure. With increased pressure, droplets can deform and the maximum packing value α^* could approach unity. Ishii and Zuber extended the Krieger-Dougherty correlation by including a viscosity factor in the exponent (Ishii and Zuber, 1979):

$$\mu_m=\mu_c\left(1-\frac{\alpha_d}{\alpha^*}\right)^{-2.5\alpha^*\mu_*} \quad (10)$$

$$\mu_*=\left(\frac{\mu_d+0.4\mu_c}{\mu_d+\mu_c}\right) \quad (11)$$

Mills derived the following equation for the apparent shear viscosity of a concentrated suspension of hard spheres in a Newtonian fluid based on a free cell model (Mills, 1985):

$$\mu_m=\mu_c\frac{1-\alpha_d}{(1-\alpha_d/\alpha^*)^2} \quad (12)$$

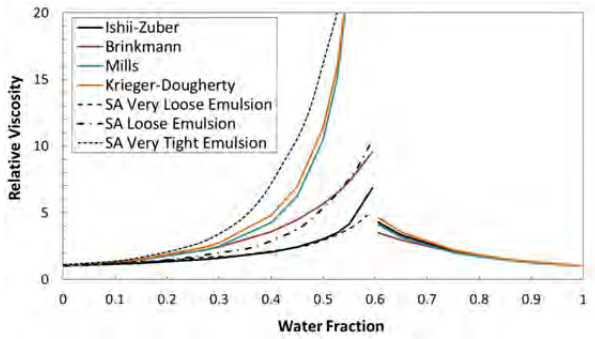

Figure 4. Relative viscosity (μ_m/μ_c) for Arab Light crude (API ~ 35) and brine (50 g/L) at 45°C. (Arabian crude emulsions from Kokal, 2005).

The emulsion viscosity equations are plotted in Figure 4 for a Saudi Arabian Light crude oil emulsion at 45°C with phase inversion at 60% water. In crude oil emulsions, the emulsion viscosity can be of the order 10 to 100 more than the continuous phase viscosity (Marsden and Mad, 1975). For comparison are the emulsion viscosity curves for very loose and very tight Arabian crude emulsions (Kokal, 2005). The terms "loose" and "tight" refer to the relative stability of the emulsion.

Population Balance Model

A population balance equation is coupled with the turbulent multiphase momentum equations conveniently describing the water droplet size distribution (Ramkrishna, 2000). The general population balance equation is written as a continuity statement of the droplet number density function:

$$\frac{\partial}{\partial t}[n(V,t)] + \nabla \cdot [\vec{v} n(V,t)] = S(V,t) \qquad (12)$$

The spatial location of the particle is an "external coordinate" in the particle state vector, while the droplet volume V is an "internal coordinate" of the population distribution. The source term $S(V,t)$ for breakage b and coalescence c due to birth (B) and death (D) rates is further expanded as:

$$S(V,t) = B_b(V,t) - D_b(V,t) + B_c(V,t) - D_c(V,t) \qquad (13)$$

The closure of Equation (12) requires a derivation of the source terms in Equation (13) above.

Breakage and Coalescence Kernels

The breakage rate kernel is the product of the breakage frequency $g(V')$ and the probability density function (PDF) $\beta(V|V')$ of droplets breaking from volume V' to V. The birth rate of droplets of volume V due to breakage is

$$B_b = \int_{\Omega_V} p\, g(V')\, \beta(V|V')\, n(V')\, dV' \qquad (14)$$

where $g(V')\, n(V')\, dV'$ droplets of volume V' break per unit time, producing for p child droplets, $p\, g(V')\, n(V')$ droplets of which a fraction $\beta(V|V')dV$ represents droplets of volume V (Luo and Svendsen, 1996). The breakage PDF $\beta(V|V')$ is also referred to as the daughter size distribution function where the fragments or daughter droplet mass must equal the original droplet mass. The death rate of droplets due to breakage is

$$D_b = g(V)n(V) \qquad (15)$$

There are several different models for determining the breakage frequency and the breakage PDF to compute the breakage rate of the droplets. The coalescence kernel $a(V-V',V')$ is a product of the collision frequency $h(V-V',V')$ between droplets of volume V and V', and the coalescence efficiency $\lambda(V-V',V')$. The coalescence efficiency is the probability that droplets of volume V will coalesce with droplets of volume V'. The birth rate of droplets due to coalescence is

$$B_c = \frac{1}{2}\int_0^V a(V-V',V')\; n(V-V')n(V')\, dV' \qquad (16)$$

The death rate of droplets due to coalescence is

$$D_c = \frac{1}{2}\int_0^V a(V,V')\; n(V)n(V')\, dV' \qquad (17)$$

In the three-phase or two-phase separator settling zone, the complex oil-water emulsion evolves primarily due to droplet coalescence while other phenomena including breakage, dissolution, aggregation, and flocculation occur to a lesser. Droplet breakage is more important at the separator entrance region where the multiphase flow is highly turbulent. Along with droplet breakage and mass transfer, coalescence influences the evolution of the droplet size distribution in liquid-liquid emulsions. Grimes (2012) developed a coalescence rate kernel in the context of batch gravity separation of oil-water emulsions. Droplet pair collisions are considered to depend on both Brownian and gravitational coalescence (Simons *et al.*, 1986). The collision frequency is (Grimes 2012):

$$h(d_k,d_j) = c_1 \frac{k_B T}{6\mu}\frac{(d_k+d_j)^2}{d_k d_j}\left[1 + Pe + 4.496 Pe^{\frac{1}{3}}\right] \qquad (18)$$

Where b_1 is an empirical fitting parameter and Pe is the sphere pair Peclet number,

$$Pe = \frac{\pi}{12}\frac{(\rho_d-\rho_c)\vec{g}}{k_B T}(1-\alpha)^{c_2} d_k d_j \left|d_k^2 - d_j^2\right| \qquad (19)$$

The coalescence efficiency is expressed as the ratio of coalescence time and the contact time:

$$\lambda(d_k,d_j) = \exp\left[-\frac{1.046}{c_3}\frac{\mu(\rho_d-\rho_c)\vec{g}}{\sigma^{3/2}B^{1/2}}\left[\frac{d_k d_j}{2(d_k+d_j)}\right]^{9/2}\right] \qquad (20)$$

The empirical constant b_2 influences the hindered settling contribution to the collision frequency, based on the Richardson-Zaki hindered settling correlation, while b_3 is used to adjust the coalescence time. The coalescence efficiency is also dependent on an interfacial force constant B, which can be related to the surfactant concentration (Grimes, 2012; Kralova *et al.*, 2011). Generally, there are recognized weaknesses with coalescence kernels, including: the derivation of the collision frequency based on the kinetic theory of gases, the lack of history to capture the cumulative effects during the coalescence process, and other empiricism (Liao and Lucas, 2010). The kernels are relatively simplistic given the complexity of the system and the phenomena.

Population Balance Equation Solution Method

To model separation of the dispersed water phase from the oil phase, the solution to the population balance cannot be based on a shared velocity field since droplets of different sizes will rise or settle at different velocities. The droplet size distribution can range over two to three orders of magnitude or more, and the distribution can be mono- or multi-modal. Multivariate methods incorporating several velocity classes are required to model this tight coupling between the droplet size distribution and the secondary phase velocity distribution. There are a number of multivariate methods described in the literature but the Inhomogeneous Discrete Method (IDM) (Frank *et al.*, 2005, Sanyal *et al.*, 2013) will be used in this work. The population balance equation is written for the IDM in terms of volume fraction of particle or droplet size i and solved here for all discrete bin fractions f_i :

$$\frac{\partial}{\partial t}(\rho\alpha f_i) + \nabla\cdot(\rho\alpha f_i v_i) = \rho V_i\left(B_{c,i} - D_{c,i}\right) \qquad (21)$$

where ρ is the density of the secondary phase. The secondary phase is divided into N velocity groups or phases, each with M bins per phase for a total of $N \times M$ bins. The sum of

coalescence mass sources for all phases is zero, while each phase or bin could have a non-zero net mass source. Each bin is advected by phase velocity u_i and $\alpha f_i (= \alpha_i)$ is the volume fraction of bin i, defined for secondary phase 0 to $N-1$ as

$$\alpha_i = N_i V_i \tag{22}$$

$$N_i(t) = \int_{V_i}^{V_{i+1}} n(V,t)dV \tag{23}$$

The droplet coalescence birth and death rates are

$$B_{c,i} = \sum_{k=1}^{N}\sum_{j=1}^{N} \alpha_{kj} N_k N_j x_{kj} \xi_{kj} \tag{24}$$

$$D_{c,i} = \sum_{j=1}^{N} \alpha_{ij} N_i N_j \tag{25}$$

where the coalescence rate $\alpha_{ij} = a(V_i, V_j)$ and

$$\xi_{kj} = \begin{cases} 1 & \text{for } V_i < V_c < V_{i+1}, \text{ where } i \le N-1 \\ 0 & \text{otherwise} \end{cases} \tag{26}$$

V_c is the particle volume resulting from the coalescence of droplets k and j defined as

$$V_c = \left[x_{kj} V_i + (1 - x_{kj}) V_{i+1}\right] \tag{27}$$

and

$$x_{kj} = \frac{V_c - V_{i+1}}{V_i - V_{i+1}} \tag{28}$$

Numerical Setup and Boundary Conditions

Model

A carefully constructed mesh consisting predominantly of hexahedral cells was built on a 180° symmetrical geometry using the cut-cell method (Figure 5). The resulting 1.4 million cell mesh consists of 8 mm cells in the bulk of the vessel and 4 mm cells in the outlet nozzles. Mesh refinement was applied at the walls.

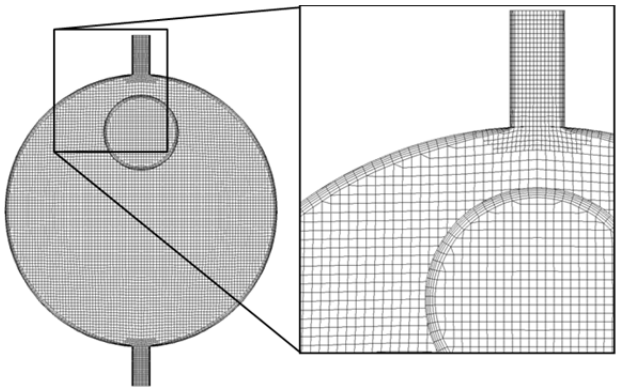

Figure 5. End-view of mesh showing details at the walls and the outlet nozzles.

Initial Droplet Size Distribution

In the pipe approaching the separator inlet, droplet size distribution evolves due to varying shear, and turbulence, the effects of surface-active agents naturally present, and the demulsifier. At the entrance to the separator, the complex oil-water emulsion continues to evolve due to breakage and coalescence. In the settling zone, coalescence processes are dominant and breakage, dissolution, aggregation, and flocculation occur to a lesser extent. In the absence of droplet size measurements at the separator inlet, the initial droplet diameter distribution is determined from the maximum stable droplet size d_{max} (Hinze, 1955)

$$d_{max} = \frac{0.725}{\left(\frac{\rho_l}{\sigma}\right)^{3/5} \epsilon^{2/5}} \tag{29}$$

where the mean turbulent energy dissipation per unit mass ϵ is

$$\epsilon = f \frac{v_m^3}{2D} \tag{30}$$

and the friction factor f is

$$f = F_2 + \frac{(F_1 - F_2)}{\left(1 + \left(Re_m/t\right)^c\right)^d} \tag{31}$$

where $F_1 = a_1 Re_m^{b_1}$ and $F_2 = a_2 Re_m^{b_2}$ (Garcia, *et al.* 2007). The parameters a_1, a_2, b_1, b_2, c, d and t are dependent on the flow regime. The minimum droplet size is determined from (Vielma, *et al.* 2008)

$$d_{min} = 8\frac{\sigma}{g\rho_l v_l^2} \tag{32}$$

The mean droplet diameter is

$$d_{mean} = 0.4 d_{max} \tag{33}$$

Using a 39−bin cumulative volume fraction distribution for water droplets dispersed in an Arabian Light crude oil (API > 35) with added demulsifier, each bin is assigned a droplet size based on a Rosin-Rammler distribution:

$$d_{i_0} = d_{mean}[-ln(1-\alpha_i)]^{1/n} \tag{34}$$

where α_i is the $i-th$ bin fraction and the spread parameter n is 2. Figure 6 shows the cumulative droplet size distribution at the separator inlet.

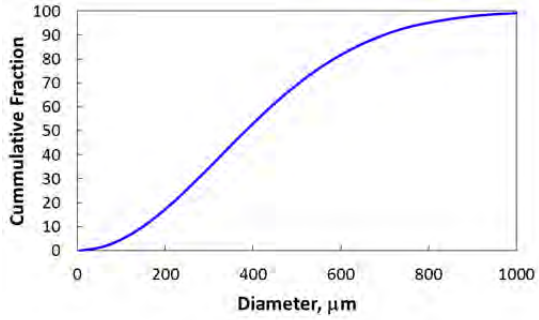

Figure 6. Cumulative droplet size distributions at the separator inlet.

Inlet Velocity Boundary Conditions

The inlet phase distributions are based on the incoming flow regime. For the experimental conditions modeled, the flow regime in the 3" pipe is stratified or intermittent elongated bubble based on three-phase gas-oil-water studies (Keskin *et al.*, 2007). The transition to the 8" nozzle will alter the flow regime to a separated or stratified flow regime. Though still developing through the reduction from the pipe to the nozzle, the larger cross-section will allow the gas to disengage and the flow regime will tend to stratified flow. A uniform velocity condition for each phase is assumed and the distribution of oil and water is considered fully mixed at the velocity inlet boundary. The inlet phase distribution is applied at the boundary using a user-defined function.

Perforated Plate

The perforated plate, described in the experimental section, is modeled as a porous media (cell zone). The inertial resistance of the porous media is based on the product of the loss coefficient K and the local kinematic head and applied as a momentum source in the z-direction for the porous cell zone. The loss coefficient K is not constant but varies with the local Reynolds number as shown in Figure 7. A user-defined function reads and interpolates a table of $\log(K)$ as a function of the $\log(Re)$ to return a value for K at the local Re based on the local approach velocity. A high loss coefficient value of 100,000 is applied in the transverse directions of the perforated plate cell zone.

Outlet Pressure Conditions

If the liquid outlet boundary pressure P_{outlet} is initially set assuming separated phases (A in Figure 8 below), the water interface will drop until a steady-state distribution of water-in-oil (w/o) emulsion is reached (B). Since the w/o concentration distribution is not known *a priori*, the outlet pressure (P_{outlet}) is initially estimated based on

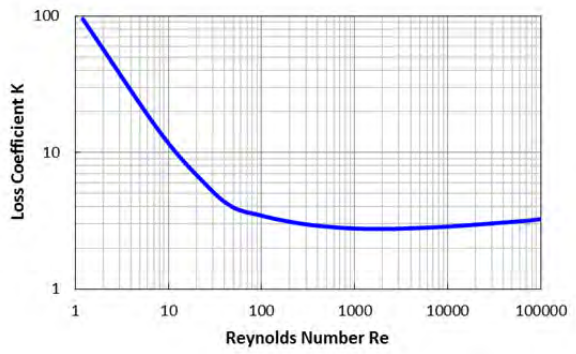

Figure 7. Perforated plate loss coefficient as a function of the perforation Reynolds number.

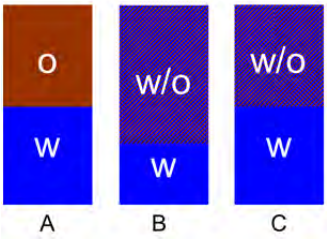

Figure 8. Illustration of the vertical column of oil (O), emulsion (w/o) and water (W) layers in the separator vessel.

$$P_{outlet} = \rho_{w/o} g h'_{w/o} + \rho_w g h_w \qquad (35)$$

and adjusted during the calculations in response to the interface level set point h_w. The interface level is determined from the average height of an iso-surface of water fraction of value 0.9 created at the intersection with an axial plane at the LT9 and LT10 locations. The outlet pressure adjustment is executed manually or automatically. Here, an automatic interface level control is applied using a Proportional-Integral-Derivative (PID) controller algorithm to efficiently manage the simulation over long run-times. The outlet pressure is controlled to the set point of water-emulsion interface height (See Table 1).

Solution

The three-phase system was modeled with the Eulerian multiphase model in ANSYS FLUENT 14.5 (ANSYS Inc., 2012). A transient solution was obtained for each run with a fixed time-step of 0.5 seconds. The primary phase is the oil phase with water and gas as secondary phases. Dispersed gas bubbles have a constant diameter of 2 mm. The Inhomogeneous Discrete Model is used and three secondary phases discretize the water phase with two bins per phase. The droplet diameter range for each phase is determined from the droplet size distribution in Figure 6. An initial value for each of the six bin fractions is specified at the inlet boundary according to the droplet size distribution. The Grimes coalescence kernel described earlier is implemented in the population balance model through a user-defined function. From Figure 4, the Ishii-Zuber and Mills correlations are shown to bound the viscosity of the relevant emulsions. The application of the emulsion viscosity in the interphase momentum exchange term (Equation (3)) is applied through user-defined functions. Three viscosity relationships are evaluated: mixture-averaged viscosity, Ishii-Zuber and Mills. The turbulence is modeled using the Realizable $k-\varepsilon$ mixture turbulence model. The solution methods are phase-coupled SIMPLE for pressure-velocity coupling, second-order upwind discretization for momentum and turbulence, QUICK discretization for the volume fraction equation. The solution is initialized with a zero velocity field and an idealized phase distribution – gas in the freeboard, inlet water fraction in the emulsion phase and clear water layer.

RESULTS

Flow Field

Figure 9 shows the liquid phase pathlines in the separator. The red pathlines are based on the oil phase velocity field, while the blue pathlines are computed from the secondary water phase with the largest diameters. All cases show the typical engineering assumption of a uniform plug flow in the separator is not achieved. The inlet section upstream of the perforated plate shows significant recirculation and mixing. At the lower emulsion viscosities (mixture and Ishii-Zuber) there is good segregation of the pathlines, while at the higher emulsion viscosity (Mills) there is less separation illustrated by increased mixing of the pathlines throughout the settling section. The pathlines curve upwards approaching the weir. The higher viscosity emulsion layer thickness increases along the settling zone upstream of the weir, displacing the oil layer and increasing the water concentration towards the liquid level. Figure 10 plots the vertical profiles of the time-averaged oil-phase axial velocity at the LT9 and LT10 locations shows the velocity field is significantly influenced by the emulsion rheology. The dense emulsion layer causes the oil to accelerate near the free surface.

Oil Distribution

Figure 11 shows the oil distribution in the mid-plane of the separator. The inlet region upstream of the perforated plate shows mixing of the oil-emulsion layer. In the settling zone between the perforated plate and the weir, there is a gradual vertical gradient of water. The mixture-averaged viscosity uses the Schiller-Naumann drag law, which assumes the droplets are settling in a quiescent environment. The interface

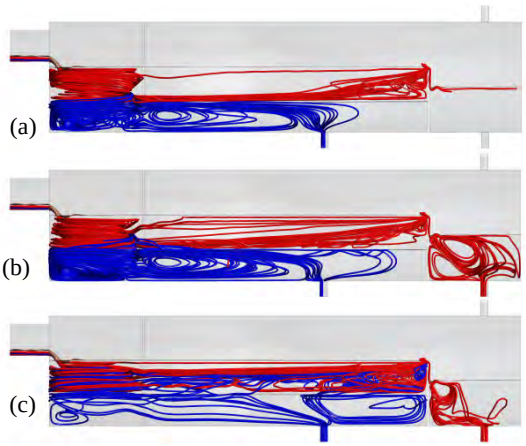

Figure 9. Pathlines of oil (red) and water (blue) on the time-averaged flow field: (a) Mixture-averaged viscosity, (b) Ishii-Zuber viscosity, (c) Mills viscosity.

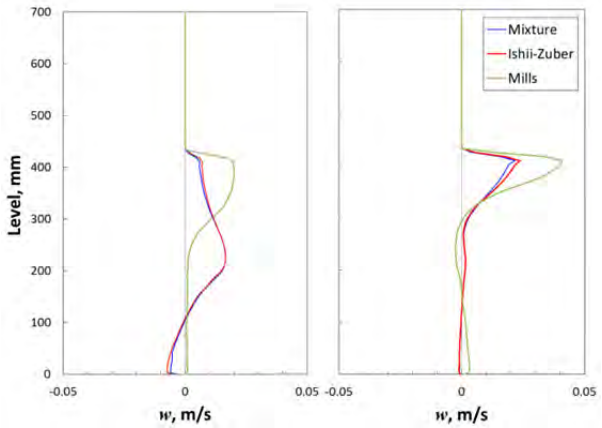

Figure 10. Vertical profiles of the oil axial velocity (time-averaged) at the LT9 and LT10 locations.

layer remains relatively constant throughout the vessel except around the perforated plate. With the higher emulsion viscosity of the Mills relationship (Figure 11(c)), there is a region of low oil and high water concentration above the water layer representative of a dense emulsion layer. The dense emulsion layer increases in thickness toward the end of the settling zone. As the relative viscosity of the emulsion increases, the settling rate slows relative to the coalescence rate allowing water to accumulate. Figure 12 shows the oil distribution in the vessel cross-section at two axial locations corresponding to the LT9 and LT10 level profilers.

Water Fraction

Figure 13 shows the water distribution in the mid-plane of the separator. The water phase gradually separates from the oil with the mixture viscosity and the Ishii-Zuber emulsion viscosity, while the Mills emulsion viscosity shows slow phase separation. Approaching the weir, the water fraction increases near the liquid level. Figure 14 shows the water distribution at the cross-section corresponding to the LT9 and LT10 profiler locations. Plotting the vertical water fraction distribution at the LT10 probe location in Figure 15 shows a distinct water-emulsion interface for each case. With the increased emulsion viscosity with the Mills relationship, a region of higher water fraction is established above the water interface. The water fraction is around 0.53 corresponding to the numerical limit on the relative viscosity of 20.

Relative Viscosity Distribution

Figure 16 shows the relative viscosity distribution in the

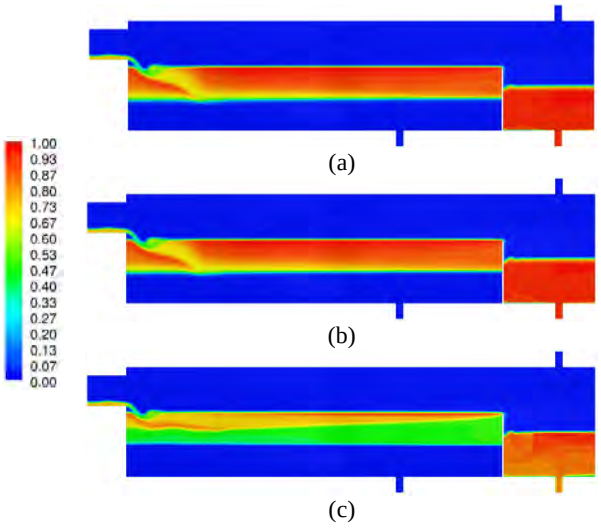

Figure 11. Time-averaged oil fraction distribution: (a) Mixture-averaged viscosity, (b) Ishii-Zuber viscosity, (c) Mills viscosity.

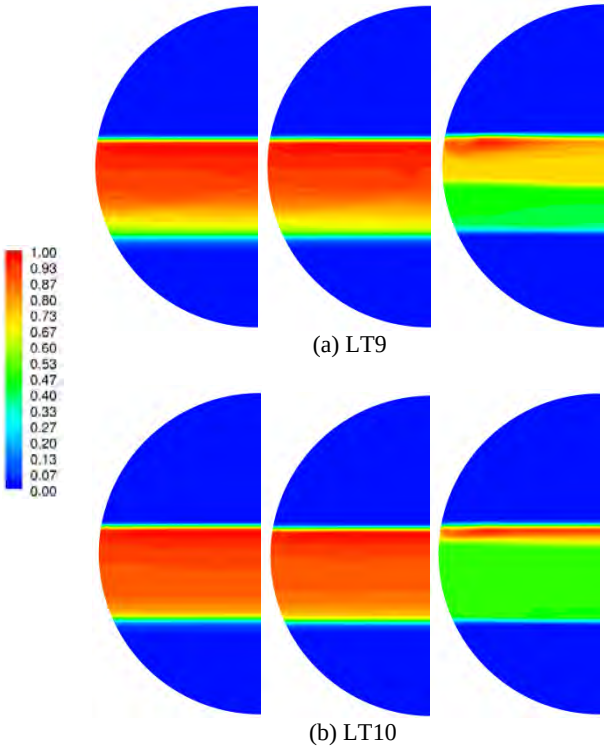

Figure 12. Time-averaged oil fraction distribution at cross-sections LT9 and LT10 (from left to right): Mixture-averaged viscosity, Ishii-Zuber viscosity, and Mills viscosity.

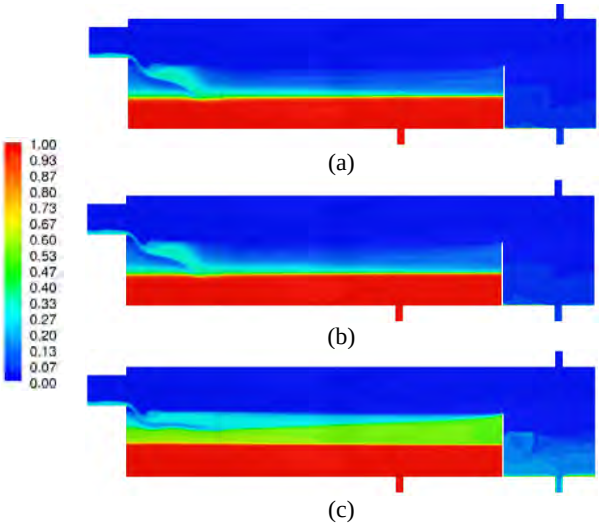

Figure 13. Time-averaged water fraction distribution: (a) Mixture-averaged viscosity, (b) Ishii-Zuber viscosity, (c) Mills viscosity.

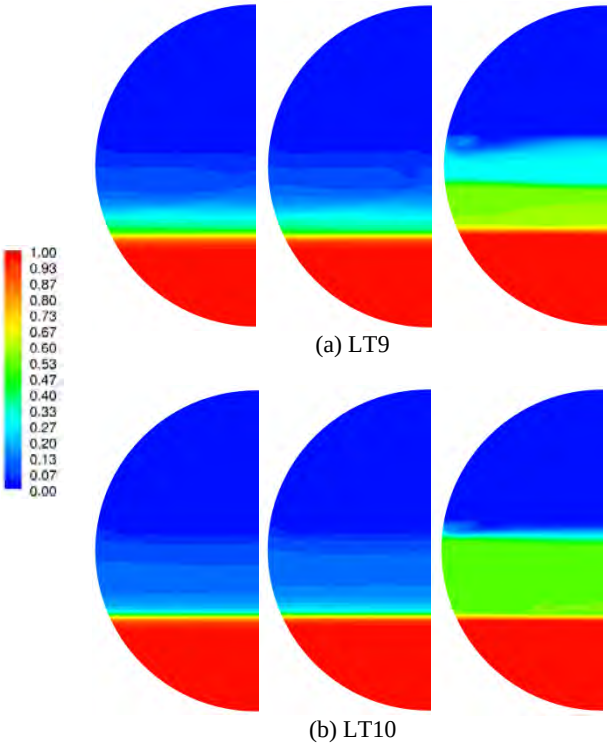

Figure 14. Time-averaged water fraction distribution at cross-sections LT9 and LT10 (from left to right): Mixture-averaged viscosity, Ishii-Zuber viscosity, and Mills viscosity.

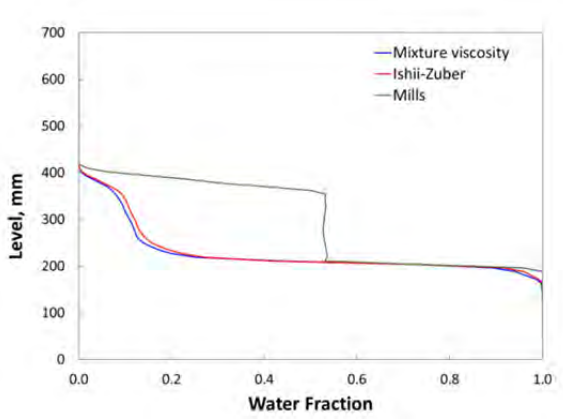

Figure 15. Time-averaged water fraction profiles at LT10 for different emulsion viscosity correlations.

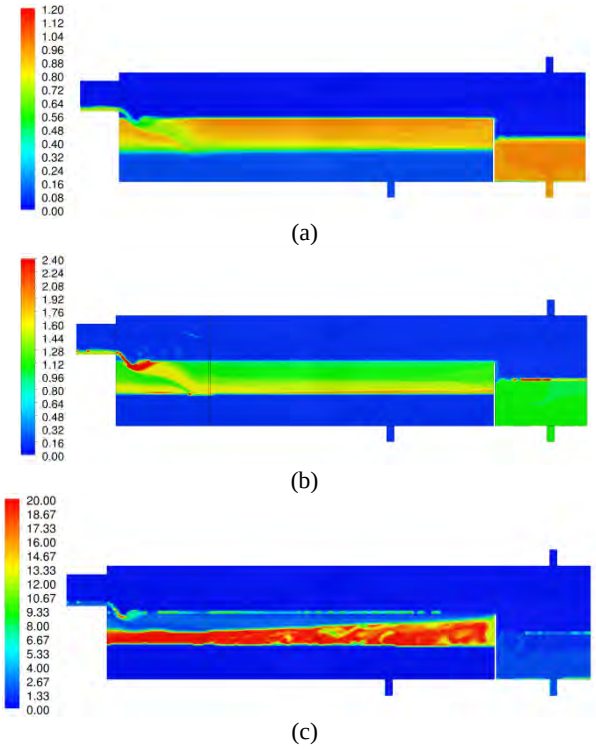

Figure 16. Time-averaged relative viscosity distribution: (a) Mixture-averaged viscosity, (b) Ishii-Zuber viscosity, (c) Mills viscosity.

separator mid-plane. There is an increase in the emulsion viscosity corresponding to the dense emulsion layer above the water interface when an emulsion viscosity relationship is used. The Ishii-Zuber emulsion viscosity is 1.5 times the oil viscosity at the inlet water fraction of 0.27. The Mills emulsion viscosity is 2.2 times at the same water fraction increasing rapidly approaching infinity at the close packing limit of 0.64. The emulsion viscosity relationships show that the hindered settling behavior of the destabilizing emulsion can be reproduced. For this case of an Arab Light crude emulsion with brine (50 g/L) at 45°C, the emulsion viscosity predicted by the Mills relationship is excessive. A rheological characterization is needed to determine the unique viscosity relationship for specific crude oil-water emulsions.

Droplet Diameter Distribution

Figure 17 shows the average water droplet diameter of the three secondary water phases in the vessel cross-section at two axial locations corresponding to the LT9 and LT10 level profilers. As expected, the droplet diameter increases with retention time and water fraction. The larger droplets settle to the interface quickly resulting in a higher droplet diameter above the interface compared with the downstream LT10 location.

Emulsion Layer and Dense-Packed Zone

As the water droplets settle to the water interface in the settling zone, the droplets increase in diameter due to coalescence. The relative viscosity of the emulsion increases slowing separation as the droplets accumulate faster than they coalesce. The region above water interface with higher water concentration is the dense packed zone or DPZ where the water fraction is between the inlet emulsion and unity. Figure 18 compares the water, emulsion and oil layers at the LT9 capacitance profilers to the different CFD predictions with the different emulsion viscosity models. Figure 19 shows the water, emulsion, DPZ and oil layers at the LT10 profiler. While the comparison is qualitative based on how the interface boundaries are determined experimentally, the mixture and Ishii-Zuber reasonably reproduce the DPZ thickness while the Mills relationship over-predicts the DPZ thickness. The emulsion layer thickness is over-estimated by the three emulsion viscosity models suggesting that the water droplets are much larger either from higher coalescence rates or larger droplet sizes entering the separator. Larger droplets will increase the emulsion destabilization rates compared with the model predictions. The water fraction distribution is just one piece of a dataset that must include droplet size and viscosity measurements in order to fully validate the CFD predictions of droplet distribution and emulsion rheology.

Separation Efficiency

The efficiency of water separation from the oil is

$$Separation\ Efficiency, \% = \frac{Q_w|_{Inlet} - Q_w|_{oil\ Outlet}}{Q_w|_{Inlet}} \times 100\%$$

Figure 20 compares the experimentally determined separation efficiency to the different emulsion models. The separation efficiency decreased with the increase in emulsion viscosity showing that the DPZ retards emulsion destabilization. The mixture and Ishii-Zuber emulsion viscosity models under-

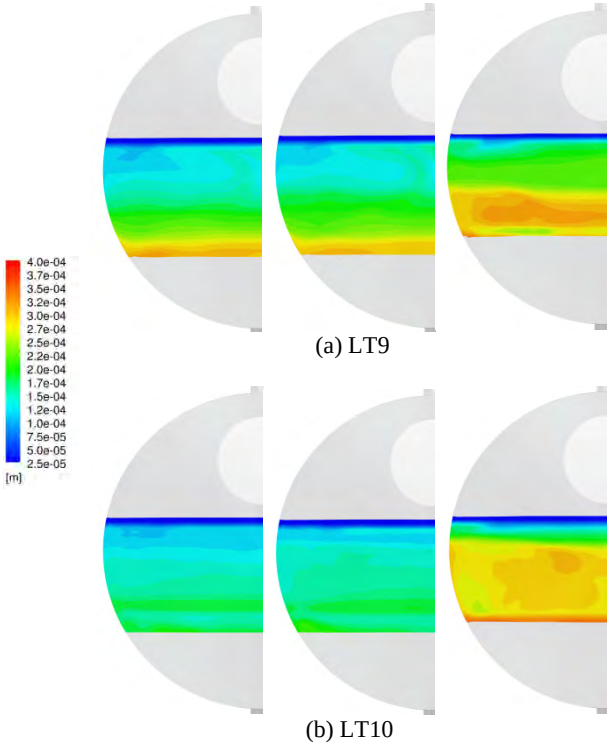

Figure 17. Time-averaged droplet diameter (in m) distribution at cross-sections LT9 and LT10 (from left to right): Mixture-averaged viscosity, Ishii-Zuber viscosity, and Mills viscosity.

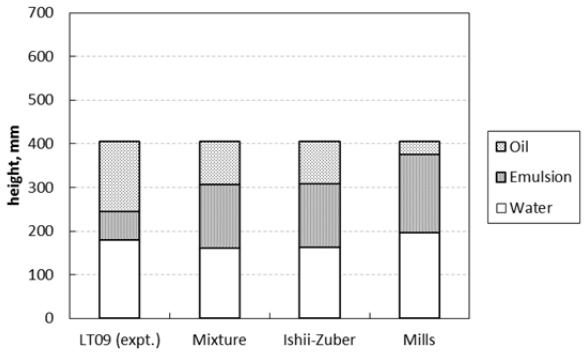

Figure 18. Oil, Emulsion and Water distribution at location LT9.

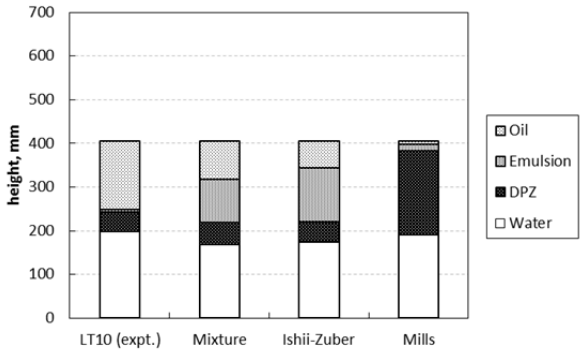

Figure 19. Oil, Emulsion, DPZ and Water distribution at location LT10.

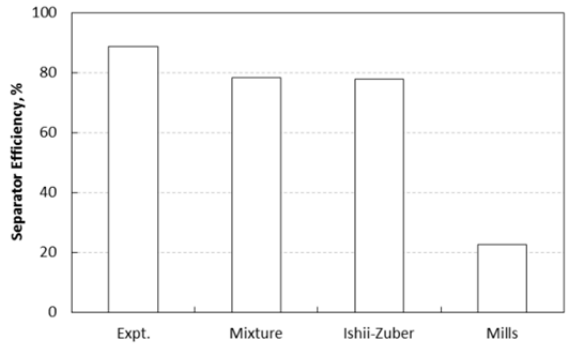

Figure 20. Comparison of experimental and predicted separation efficiency.

predict the separation efficiency. The predicted separation efficiency is influenced the emulsion viscosity relationship, and by other model inputs including the inlet droplet size distribution and the coalescence kernel parameters.

CONCLUSION

In this work, a detailed simulation of a pilot-scale high-pressure three-phase separator has been successfully carried out using the Eulerian multiphase model in ANSYS FLUENT to predict oil-water separation efficiency. The inhomogeneous population balance model was used to describe the evolving droplet size distribution in the polydisperse water phase. Simulations and experiments were performed within the domain of a separator vessel of diameter of 700 *mm* and length of 3000 *mm*. The treatment of the emulsion rheology was implemented through the inter-phase interaction terms between the oil phase and each of the secondary water phases. While there is uncertainty in the experimental water fraction, good agreement of the vertical distributions of the water phase is achieved at different locations in the separator. More detailed experimental data is required to validate the CFD models. The inlet multiphase flow must be adequately characterized for phase and droplet size distribution. Droplet coalescence and breakage should be incorporated and be specifically defined for the horizontal multiphase separator configuration. The CFD methodology presented here is a step toward predicting the dense emulsion layer thickness above the water interface, the evolution of the droplets size distribution through the separator, and the oil-water separation efficiency. More study is needed to include a more accurate description of the emulsion rheology and the coalescence and breakage mechanisms, while taking in to consideration the complexity of crude oil inhomogeneity, pH, salinity, asphaltene content or impurities in the water, and the surface-active compounds added to the produced fluids.

ACKNOWLEDGEMENTS

The authors acknowledge the Saudi Arabian Oil Company (Saudi Aramco) for supporting and granting permission to present and publish this article. The authors also acknowledge IFPEN for conducting the experiments and to TOTAL for their role in coordinating the experimental program. The authors would also like to acknowledge ANSYS for their support on the PID controller user-defined function and Scheme file.

REFERENCES

ANSYS Inc. *ANSYS FLUENT™ Theory Guide.* Canonsburg, PA: ANSYS Inc, 2012.

BRINKMAN, H.C. "The viscosity of concentrated suspensions and solutions." *J. Chem. Phys.* 20 (1952): 571.

FRANK, T., P.J. ZWART, J-M. SHI, E. KREPPER, D. LUCAS, and U. ROHDE. "Inhomogeneous MUSIG Model - a Population Balance Approach for Polydispersed Bubbly Flows." *International Conference on Nuclear Energy for New Europe, September 5-8.* Bled, Slovenia, 2005.

FRISING, T., NOIK, C., and DALMAZZONE, C. "The Liquid/Liquid Sedimentation Process; From Droplet Coalescence to Technologically Enhanced Water/Oil Emulsion Gravity Separators: A Review." *Journal of Dispersion Science and Technology* 27 (2006). 1035-1057.

GARCIA, F., J.M. GARCIA, R. GARCIA, and D.D. JOSEPH. "Friction factor improved correlations for laminar and turbulent gas-liquid flow in horizontal pipelines." *International Journal of Multiphase Flow* 33 (2007): 1320-1336.

GRIMES, B.A. "Population Balance Model for Batch Gravity Separation of Crude Oil and Water Emulsions. Part I: Model Formulation." *Journal of Dispersion Science and Technology* 33 (2012): 578-590.

HALLANGER, A., F. SOENSTABOE, and T. KNUTSEN. "A Simulation Model for Three-Phase Gravity Separators (SPE 36644)." *SPE Annual Technical Conference and Exhibition, 6-9 October 1996.* Denver, Colorado, USA: Society of Petroleum Engineers, 1996. 695-706.

HANSEN, E.W.M., and G.J. RØRTVEIT. "Numerical Simulation of Fluid Mechanisms and Separation Behavior in Offshore Gravity Separators." Chap. 16 in *Emulsions and Emulsion Stability*, edited by J. Sjöblom, 593-605. CRC Press, 2005.

HANSEN, E.W.M., et al. "Fluid Flow Modeling of Gravity Separators." *5th International Conference on Multi-Phase Production.* Cannes, 1991.

HENSCKE, M., L.H. SCHLIEPER, and A. PFENNIG. "Determination of a Coalescence Parameter from batch-

Settling Experiments." *Chemical Engineering Science* 85 (2002): 369-378.

HINZE, J.O. "Fundamentals of the hydrodynamic mechanism of splitting in dispersion processes." *AIChE J.* 1, no. 3 (1955): 289-295.

ISHII, M., and N. ZUBER. "Drag Coefficient and Relative Velocity in Bubbly, Droplet or Particulate Flows." *AIChE J.* 25 (1979): 843-855.

KESKIN, C., H.-Q. ZHANG, and C. SARICA. "Identification and Classification of New Three-Phase Gas/Oil/Water Flow Patterns." *SPE Annual Technical Conference and Exhibition, 11-14 November*. Anaheim, California, U.S.A.: Society of Petroleum Engineers, 2007.

KHAROUA, N., L. KHEZZAR, and H. SAADAWI. "Application of CFD to Debottleneck Production Separators in a Major Oil Field in the Middle East (SPE 158201)." *SPE Annual Technical Conference and Exhibition, 8-10 October*. San Antonio, Texas, USA: Society of Petroleum Engineers, 2012.

KOKAL, S. "Crude-Oil Emulsions: A State of the Art Review." *SPE Production & Facilities* (Society of Petroluem Engineers) 20, no. 1 (2005): 5-13.

KRALOVA, I., SJÖBLOM, G. ØYE, S. SIMON, B. GRIMES, AND K. PASO. "Heavy Crude Oils/Particle Stabilized Emulsions." *Advances in Colloid and Interface Science* 169 (2011): 106-127.

KRIEGER, I.M., and I.M. DOUGHERTY. "A mechanism for non-Newtonian flow in suspensions of rigid spheres." *Trans. Soc. Rheol.* 3 (1959): 137.

LALEH, A.P., W.Y. SVRCEK, and W.D. MONNERY. "Design and CFD Studies of Multiphase Separators - A Review." *The Canadian Journal of Chemical Engineering* 90 (2012): 1547-1560.

LIAO, Y., and D. LUCAS. "A literature review on mechanisms and models for the coalescence process of fluid particles." *Chemical Engineering Science* 65 (2010): 2851-2864.

LUO, H., and H.F. SVENDSEN. "Theoretical Model for Drop and Bubble Breakage in Turbulent Dispersions." *AIChE J.* 42, no. 5 (1996): 1225-1233.

MARSDEN, S., and M. MAD. "Stability Of Concentrated Crude Oil-In-Water Emulsions As A Function Of Shear Rate, Temperature And Oil Concentration." *26th Annual Technical Meeting of the Petroleum Society of CIM, June 11-13*. Banff, Alberta, Canada: PETROLEUM SOCIETY OF CIM, 1975.

MILLS, P. "Non-Newtonian behaviour of flocculated suspensions." *J. Physique Lett.* 46 (1985): 301-309.

PAGNIER, P., C. NOIK, P. MAUREL, A. RICORDEAU, and J.-L. A. VOLLE. "Multiphase Loop Tests for Subsea Separation-Unit Development." *Paper SPE 115963 presented at SPE Annual Technical Conference and Exhibition.* Denver, Colorado, USA, 21-24 September: Society of Petroleum Engineers, 2008.

RAMKRISHNA, D. *Population Balances: theory and Applications to Particulate Systems in Engineering.* eBook: Academic Press, 2000.

SANFELD, A., and A. STEINCHEN. "Emulsion stability, from dilute to dense emulsions - Role of drops deformation." *Advances in Colloid and Interface Science* 140 (2008): 1-65.

SANYAL, J., S. OZARKAR, and F. LIU. "A Comprehensive CFD Strategy for the Simulation of Dense, Polydisperse Granular Flow in Fluidized Bed Reactors." *8th International Conference on Multiphase Flow (ICMF 2013), May 26 - 31*. Jeju, Korea, 2013.

SCHULLER, R.B., T. GUNDERSEN, M. HALLERAKER, and B. ENGEBRETSEN. "Measurement of water concentration in oil/water dispersions with a circular single-electrode capacitance probe." *Instrumentation and Measurement, IEEE Transactions* 53, no. 5 (2004): 1378-1383.

SIMONS, S., M.M.R. WILLIAMS, and J.S. CASSELL. "A kernel for combined Brownian and gravitational coagulation." *Journal of Aerosol Science* 17, no. 5 (1986): 789-793.

VIELMA, M., S. ATMACA, C. SARICA, and H. ZHANG. "Characterization of Oil/Water flows in horizontal pipes." *SPE Projects, Facilities & construction*, 2008: 1 - 21.

VILAGINES, R.D., and A.R. AKHRAS. "Three-phase Flows Simulation for Improving Design of Gravity Separation Vessels (134090)." *SPE Annual Technical Conference and Exhibition, 19-22 September 2010.* Florence, Italy: Society of Petroleum Engineers, 2010.

GOVERNING PHYSICS OF SHALLOW AND DEEP SUBSEA GAS RELEASE

Jan Erik OLSEN & Paal SKJETNE

SINTEF Materials and Chemistry, 7465 Trondheim, NORWAY

* E-mail: jan.e.olsen@sintef.no

ABSTRACT

A modelling concept for studying the resulting bubble plume from a subsea gas release is presented. Simulation results show good consistency with available experimental data. The modelling concept is applied to assess the importance of different physics and mechanisms assumed to influence the behaviour of the bubble plume. It is shown that buoyancy, drag, turbulent dispersion and gas dissolution are the governing mechanisms, and that gas dissolution is important for deep releases.

Keywords: subsea, gas release, Lagrangian, parcel, HSE, bubble plume, CFD

NOMENCLATURE

Greek Symbols

α Volume fraction [ ]
ρ Mass density [kg/m^3].
μ Dynamic viscosity [kg/m s]

Latin Symbols

C_D Drag coefficient[ ]
c Concentration [kg/m^3]
d Diameter [m]
$\boldsymbol{F}$ Force [N]
G Drag correction [ ]
k Mass transfer coefficient [m/s]
$\dot{m}$ Mass transfer rate [kg/s]
P Pressure, [Pa]
$\boldsymbol{u}$ Velocity, [m/s]

Sub/superscripts

B Buoyancy
b Bubbles
D Drag
i Species index
L Lift
l Liquid
PG Pressure gradient
sol Solubility
TD Turbuelent dispersion
VM Virtual mass

INTRODUCTION

Subsea gas release is caused by well blowouts, pipeline failures and other, and poses a threat to the safety of people and assets operating offshore. In order to perform risk assessments it is important to understand the quantitative impact of the gas release. Since realistic experiments are prohibitively expensive and potentially dangerous, quantitative models have been identified as interesting research tools.

Traditional integral methods (Fanneløp and Sjøen 1980) provide a good representation of the rising bubble plume if the model coefficients are tuned properly. However, the method yields limited results for the surface characteristics, which is a limitation since this is where the plume will interact with offshore structures, floating installations and ships. Multiphase computational fluid dynamics (CFD) provides greater generality since it is more fundamental and can, in principle, provide information on both the bubble plume and the surface behaviour. The computational cost of such models is significantly higher than the traditional integral models. However, it has been demonstrated that a 3D transient multiphase CFD model can be applied to the study of the ocean plume and the free surface behaviour (Cloete, Olsen et al. 2009).

A variety of forces and mechanisms influences the rising bubble plume. The significance of these mechanisms varies with gas rate and release depth. Some can be neglected and some must be accounted for. The study presented in this paper assesses the importance of the different mechanisms, and clarifies the governing physics of subsea gas release. Instinctively there is a suspicion that the governing physics might be different in a shallow and deep release. It is difficult to clearly define a shallow and deep release. Here it is linked to the length scales typical for offshore operations. We have chosen 30 meters to represent a *shallow* release and 300 meters to represent a *deep* release.

MODEL DESCRIPTION

An Eulerian-Lagrangian modelling concept has been developed to study subsea gas release. It is based on an Eulerian mixture model with interface tracking of the

ocean surface separating the ocean and atmosphere which constitutes two Eulerian phases, and Lagrangian tracking of the dispersed bubbles in the ocean. The Eulerian method with interface tracking is a VOF (volume of fluid) method, and the Lagrangian tracking method is a discrete phase model, i.e DPM. This is also known as a coupled DPM-VOF model (Cloete, Olsen et al. 2009).

The discrete phase model tracks the bubbles as parcels. Each parcel may consist of several bubbles. All bubbles within the same parcel share the same properties, i.e. equal density, diameter and more. This reduces the computational cost considerably since billions of bubbles can be represented by a reasonable amount of parcels. Without this feature, it would not have been feasible to study subsea gas release with Lagrangian bubble tracking. The bubble motion is governed by Newton's second law of motion stating that bubble acceleration equals the sum of all forces acting on the bubbles:

$$\frac{d\boldsymbol{u}_b}{dt} = \boldsymbol{F}_B + \boldsymbol{F}_D + \boldsymbol{F}_L + \boldsymbol{F}_{VM} + \boldsymbol{F}_{PG} + \boldsymbol{F}_{TD} \qquad (1)$$

Here we have listed contributions from buoyancy ($\boldsymbol{F}_B$), drag ($\boldsymbol{F}_D$), lift ($\boldsymbol{F}_L$), virtual mass ($\boldsymbol{F}_{VM}$), pressure gradient ($\boldsymbol{F}_{PG}$) and turbulent dispersion ($\boldsymbol{F}_{TD}$). These are the forces known to influence bubbles in a bubble plume. Note that these forces are normalized with bubble mass. In addition mass transfer due to dissolution of gas into the ocean is believed to have an important effect on the fate of bubbles resulting from the gas release. Gas dissolution is accounted for by the following expression for mass transfer rate

$$\dot{m}_i = -\pi\, d_b^2\, k_i \left(c_i^{sol} - c_i^l\right) \qquad (2)$$

where d_b is bubble diameter, k_i is mass transfer coefficient, c_i^{sol} is solubility concentration and c_i^l is bulk concentration of species *i*. We will limit this study to release of methane. The solubility data for methane of Lekvam & Bishnoi (1997) and the expression for mass transfer coefficient of Zhang & Zu (2003) are applied. The bubble size is modelled by a transport equation which is governed by turbulence (break-up and coalescence) (Cloete, Olsen et al. 2009).

The continuous phases , i.e. water and atmosphere, are mathematically described by the VOF model as mentioned above. Their motion is coupled to the bubble motion through the drag force which is implemented as an exchange term in the momentum equations. A standard k-ε model was initially assigned to the modelling concept (Cloete, Olsen et al. 2009). As in many implementations of the k-ε model the interphase between water and atmosphere is not recognized as boundary. In reality the ocean surface dampens turbulence since eddies can not be sustained over this interface. Due to this an enhanced implementation of the k-ε model has been developed. It includes a source term in the ε-equation which dampens turbulence at the surface and an additional source term in both equations due to the added buoyancy of density variations of a gas over large pressure variations (Pan, Johansen et al. 2013).

The modelling concept is implemented in the commercial software ANSYS/Fluent 14.5 via several user defined functions. The model has been compared against data from a series of controlled experiments where gas was released in a rectangular basin with a depth of 7 meters and a surface area of 6 x 9 meters (Engebretsen, Northug et al. 1997). Air was released at the bottom at 3 different gas rates, of which the middle gas rate of 170 Nl/sec had the most complete set of results presented. Thus we have compared results from model simulations and experiments at this gas rate.

In Figure 1 we see the water velocity close to the water surface as a function of height above basin floor. Results from simulation performed with the standard and enhanced k-ε model are seen. Close to the surface the enhanced model has significantly better consistency with the experimental results than the standard model. Further down into the water, there is less discrepancy between the models. This is as expected since the enhancement primarily applies to the surface region. Figure 2 shows the velocity profiles at different elevations above the basin floor for both modelling and experimental results. Only data for the enhanced k-ε model are shown since the standard model produced almost equal results. We see a good agreement between model and experiments for the velocity profiles at the lower elevations (1.75 and 3.80 m). There is some discrepancy at the highest elevation (5.88 m). This is believed to be caused by an error in the flow measurements. Höntzsch turbine flow meters were applied. They are optimized for mono-directional flow, but for the bending flow close to the surface they will overpredict the flow velocity.

In these release scenarios gas dissolution has no effect due to the shallow depth and short residence time of the bubbles. The implemented model for mass transfer and gas dissolution have however been validated against experiments with good consistency in a separate study (Skjetne and Olsen 2012).

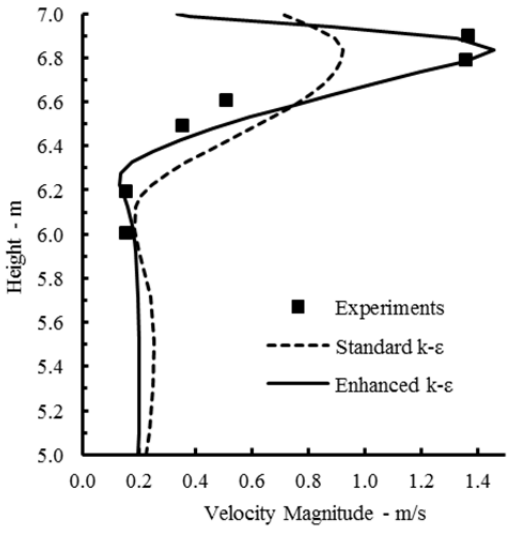

Figure 1**:** Velocity magnitudes near water surface for a gas rate of 170 Nl/s as a function of height above basin floor at a location 1.75 meters from plume centre. Models are compared with experiments.

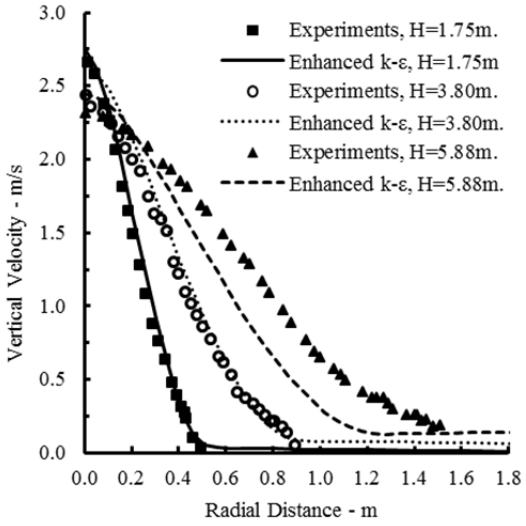

Figure 2: Plume velocity at 3 different elevations for a gas rate of 170 Nl/s. Model and experiments are compared.

SENSITIVITY ASSESSMENT

In the following we present results on sensitivity analyses on different physics assumed to affect the behaviour of a subsea gas release. Since buoyancy is the driving force of the plume, it always has to be accounted for. Drag forces are responsible for the coupling between the dispersed bubble phase and the continuous water phase and should thus not be neglected. The lift force has previously been shown to have a negligible effect on the bubble plumes associated with a subsea gas release (Olsen and Cloete 2009). Thus sensitivity to buoyancy, drag and lift will not be considered here. The effect of other forces and mechanisms are assessed in the following. In the assessment we will primarily focus on the vertical velocity along the centreline from ocean floor to ocean surface (i.e. plume axis).

Gas Expansion

Gas density is a function of pressure and temperature. The density increases with increasing pressure (i.e. depth). Thus the gas expands as the bubbles rise towards the surface. For low pressure this can be expressed by the ideal gas law, but the true density variation is more complex. Here we have applied the ideal gas law due its simplicity. In reality the true density deviates from the ideal gas laws at greater depths, but for a sensitivity analysis we assume that it is a valid assumption.

The effect of gas expansion can be assessed by comparing simulation results between expanding gas and gas with constant density. However, it is difficult to know which constant density to compare against. Here we have compared against bottom density (maximum), top density (minimum) and average density. In Figure 3 we see the effect of different density specifications on the vertical liquid velocity along the plume axis for a release from 30 meter at 10 kg/s. The results are taken after quasi steady state is reached. The height above the ocean floor (y-axis) is normalized with respect to ocean depth. This might exceed the value of 1 if the release is strong enough to sustain a fountain. We see that the velocity based on minimum and maximum densities deviate significantly from the velocity based on density from the ideal gas law. The average density is on average equivalent to the ideal gas law. However, it will give bad estimates of velocities close to the release zone. Note how the constant density approximations seem to decelerate the flow compared to an expanding gas. This tells us that gas expansion has an accelerating effect on the flow which is explained by the increasing buoyancy as gas density decreases during the ascent of the bubbles. In Figure 4 we see the same comparison for a release from 300 meter at 100 kg/s. The trend is the same as for the release from 30 meter, but not as pronounced. There are two reasons for a less pronounced effect of gas expansion. First there is significantly more gas dissolution at higher gas rates leaving less gas to expand. Secondly most gas expansion occurs close to the surface, and the surface region is less dominating in a deep release compared to a shallow release. Still the rise velocity is significantly affected by gas expansion. In addition other indicators such as total gas dissolution, plume spreading and more is affected when neglecting gas expansion (not shown here). Thus gas expansion needs to be accounted for.

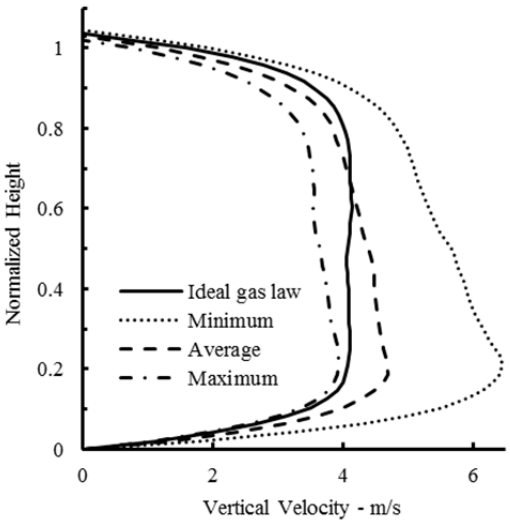

Figure 3: Effect of gas density on vertical velocity for a release from 30m at 10 kg/s.

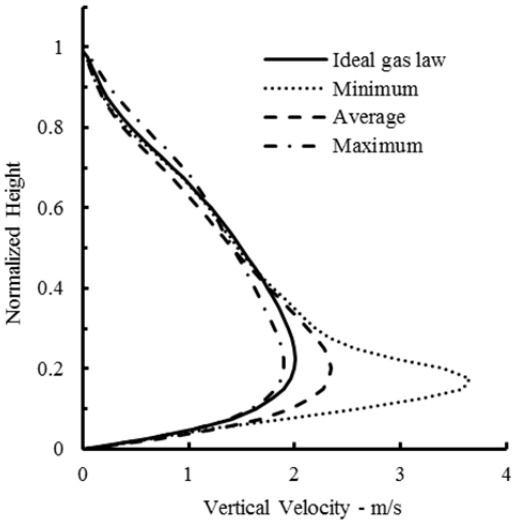

Figure 4: Effect of gas density on vertical velocity for a release from 300m at 100 kg/s.

Turbulent Dispersion

Turbulent dispersion is dispersion of bubbles, droplets and particles due to turbulence. In principle it is a drag force based on the fluctuating contribution to the instantaneous velocity. The standard drag force only accounts for the mean contribution, whereas the particle in reality is exposed to the instantaneous velocity. There are several models describing turbulent dispersion. We apply the random walk model (Gosman and Ioannides 1983) which is frequently used in Lagrangian tracking.

In Figure 5 we see how the vertical velocity varies from ocean floor to surface along the vertical centreline from the release point. Figure 5 shows results from simulations were turbulent dispersion has been neglected and accounted for. The results clearly demonstrate that there is a significant effect of the turbulent dispersion. Turbulent dispersion yields a lower vertical velocity due to lateral dispersion of bubbles. This is also illustrated in Figure 6 where we see that turbulent dispersion is responsible for the widening of the plume and hence the so-called *plume angle*. It is quite clear that turbulent dispersion can not be neglected.

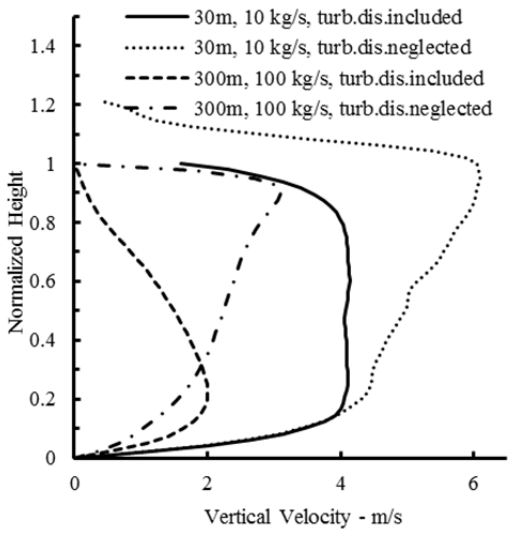

Figure 5: Effect of turbulent dispersion on vertical velocity.

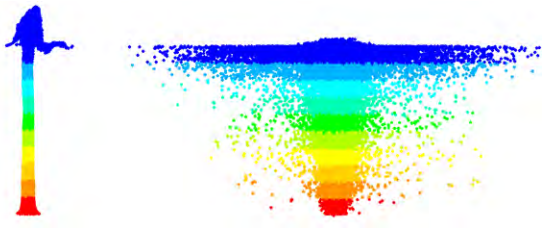

Figure 6: Plume shape coloured by gas density for simulation with neglected (left) and included (right) turbulent dispersion.

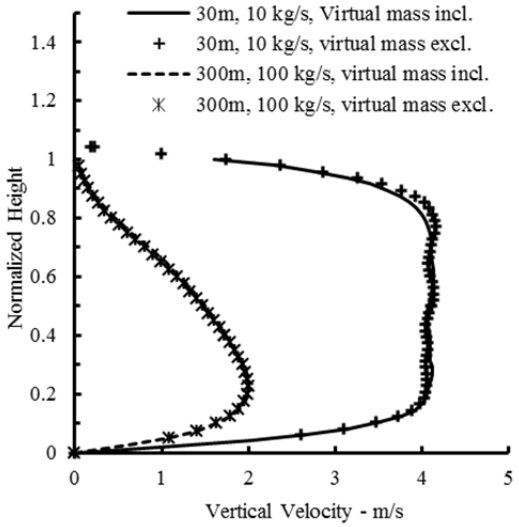

Figure 7: Effect of virtual mass on vertical velocity.

Virtual Mass

The virtual mass force is the force required to accelerate the fluid surrounding the particle. It is expressed by

$$\boldsymbol{F}_{VM} = \frac{1}{2}\frac{\rho_l}{\rho_b}\left(\frac{D\boldsymbol{u}_l}{Dt} - \frac{d\boldsymbol{u}_b}{dt}\right) \qquad (3)$$

Simulations including and neglecting the virtual mass force have been performed. The resulting vertical velocity along the plume axis is shown in Figure 7 for both shallow and deep release. We see that the virtual mass force has very little influence on the results, and it could be neglected.

Pressure Gradient Force

The pressure gradient force is the hydrodynamic force acting on the bubbles due to the pressure gradient in the surrounding liquid. Mathematically it is expressed by

$$\boldsymbol{F}_{PG} = \frac{\rho_l}{\rho_b}\boldsymbol{u}_b \nabla \boldsymbol{u}_l \qquad (4)$$

Results from simulations including and excluding the pressure gradient force are seen in Figure 8 and Figure 9. They show that the effect of the pressure gradient force can be neglected with respect to the vertical velocity along the plume centre axis.

The pressure gradient force could in principle have a more pronounced effect closer to surface as its nature typically affects a bending flow which is present at the surface. The horizontal velocity profile along the ocean surface was thus also assessed. The effect of the pressure gradient force was not detectable.

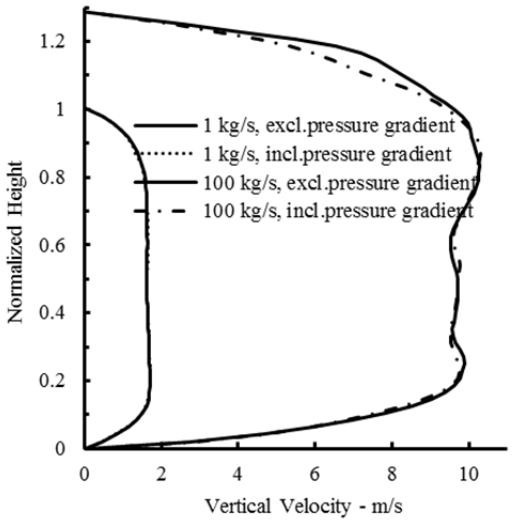

Figure 8: Effect of pressure gradient force on vertical velocity for release from 30 meter.

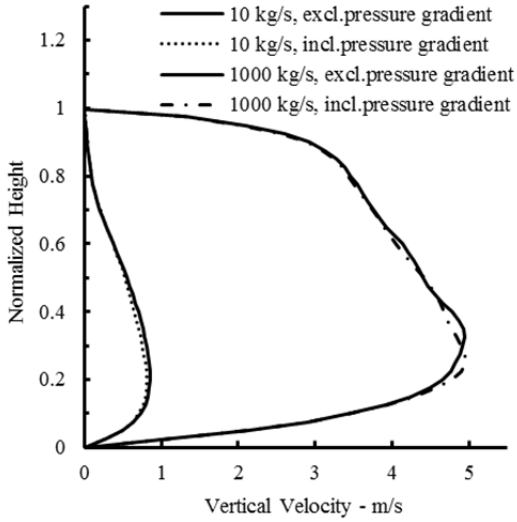

Figure 9: Effect of pressure gradient force on vertical velocity for release from 300 meter.

Gas Dissolution

Gas dissolution transfers mass from bubbles to the ocean and reduces the buoyant potential of the bubble plume. Thus gas dissolution will decrease the amount of gas reaching the surface and reduce the vertical velocity. Gas dissolution increases with residence time and is thus expected to have a greater impact on a deep release than on a shallow release. According to Eq.(2) will also bubble size have a significant impact on gas dissolution. This is illustrated by Figure 10. The figure shows the lifetime of a methane bubble exposed to gas dissolution at a depth of 30 or 300 meters as a function of bubble size. The data is based on the assumptions of single bubbles with a slip velocity of 0.3 m/s and thus represents a minimum lifetime. There is some variation with depth due to variations in solubility and methane density. We see that the lifetime varies significantly with bubble size. A bubble with a diameter of 1mm has a typical lifetime of 1 minute, whereas a bubble with a diameter of 5 mm can survive for 7-8 minutes. Thus estimating the bubble size accurately is vital for estimating the gas dissolution accurately.

Simulations with gas releases from 30 and 300 meter show that gas dissolution is significant when gas is released from 300 meters and almost neglectable when gas is released from 30 meters. This is indicated by the simulation results shown in Table 1.The table show that the rise time (i.e. time for first gas to reach the surface) correlates strongly with the release depth and to some extent with the release rate which was also shown by Bettelini and Fanneløp (1993). The rise time is affected by the inertia of the water column which needs to be accelerated by the first gas. The bubbles following the first gas will thus travel faster to the surface and obtain a lower residence time than the first bubbles. The mean residence time when a quasi-steady state is reached is shown in Table 1. It confirms that the quasi-steady state residence time is shorter than the rise time, and that the residence time and rise time has a similar dependence on release depth and release rate.

Since gas dissolution is a transient process, the amount of dissolution obviously depends on the residence time. This is supported by the data in Table 1 which is illustrated by Figure 11. We see that gas dissolution increases with residence time, but naturally levels out when there is no more gas to dissolve. Due to this correlation, there is a big difference in gas dissolution from a shallow and deep release.

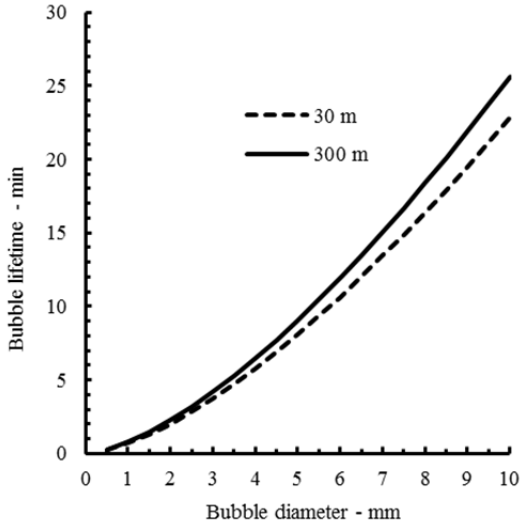

Figure 10: Effect of gas dissolution on vertical velocity for release from 30 meter.

Table 1: Global parameters for shallow and deep gas release.

	30 m.		300 m.	
	1 kg/s	10 kg/s	10 kg/s	100 kg/s
Rise time - s	18.7	8.1	502.3	169.3
Mean residence time - s	18.2	9.6	369.8	170.1
Surface flux - kg/s	0.93	9.97	0.12	19.2
Relative gas dissolution - %	6.7	0.3	98.8	80.8
Surface radius - m	16.9	18.2	69.8	128.5

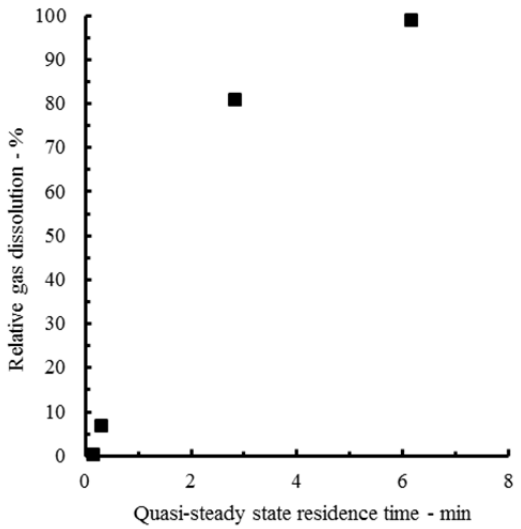

Figure 11: Correlation between residence time and gas dissolution.

CONCLUSION

An assessment of relevant physics and mechanism governing the fate of shallow and deep subsea gas releases have been conducted by mathematical simulations with an Eulerian-Lagrangian transient 3D modelling concept as described above. Buoyancy is the driving force of the gas release, while drag is the interaction force between gas bubbles and water which sets the water in motion. Since these are governing mechanisms, they have to be accounted, and thus their importance has not been assessed in this assessment. The assessment was carried out on releases from 30 meters and 300 meters and it shows that gas expansion and turbulent dispersion are also of great importance. These effects can not be neglected. Exemptions can only be made for very shallow releases (depth < 2m) were gas expansion can be neglected and for releases with very low gas rates where turbulence and turbulent dispersion has no effect. The assessment shows that the pressure gradient force and virtual mass force are insignificant. Previous studies also show that lift forces have little effect.

Gas dissolution is important for bubbles residing sufficiently long in the water column. Residence time increases with release depth and decreases with gas rate. The effect of gas dissolution also strongly depends on bubble size. Thus the effect of gas dissolution cannot be assessed by residence time alone. The simulation examples shown in this paper support that gas dissolution is significant for a deep release (300 meter) whereas the effect is small in a shallow release (30 meter).

ACKNOWLEDGEMENT

This study was performed in the SURE joint industry project funded by BP, Gassco, Shell, Statoil, Total, DNV LG, Safetec, Wild Well Control and PSA (Petroleum Safety Authorities).

REFERENCES

Bettelini, M. S. G. and T. K. Fanneløp (1993). "Underwater plume from an instantaneously started source." Applied Ocean Research **15**: 195-206.

Cloete, S., J. E. Olsen and P. Skjetne (2009). "CFD modeling of plume and free surface behavior resulting from a sub-sea gas release." Applied Ocean Research **31**(3): 220-225.

Engebretsen, T., T. Northug, K. Sjøen and T. K. Fanneløp (1997). Surface Flow and Gas Dispersion from a Subsea Release of Natural Gas. 7th int. offshore and polar engineering conference, Honolulu, International Society of Offshore and Polar Engineers.

Fanneløp, T. K. and K. Sjøen (1980). "Hydrodynamics of Underwater Blowouts." AIAA(Paper No. 80-0219).

Gosman, A. D. and E. Ioannides (1983). "Aspects of computer simulation of liquid-fuelled combustors." J.Energy **7**: 482-490.

Lekvam, K. and P. R. Bishnoi (1997). "Dissolution of methane in water at low temperatures and intermediate pressures." Fluid Phase Equilibria **131**(1-2): 297-309.

Olsen, J. E. and S. Cloete (2009). Coupled DPM and VOF model for analyses of gas stirred ladles at higher gas rates. Seventh International Conference on CFD in the Minerals and Process Industries, Melbourne, CSIRO.

Pan, Q. Q., S. T. Johansen, L. Sætran and M. Reed (2013). An enhanced k-epsilon model for bubble plumes. 8th International Conference on Multiphase Flow (ICMF), Jeju, Korea.

Skjetne, P. and J. E. Olsen (2012). "A parcel based modelling concept for studying subsea gas release and the effect of gas dissolution." Progress in Computational Fluid Dynamics **12**(2-3): 187-195.

Zhang, Y. and Z. Xu (2003). "Kinetics of convective crystal dissolution and melting, with applications to methane hydrate dissolution and dissociation in seawater." Earth and Planetary Science Letters **213**: 133-148.

COOL-DOWN SIMULATIONS OF SUBSEA EQUIPMENT

Atle JENSEN[12*], Stig GRAFSRØNNINGEN[1]

[1] FMC Technologies, 1386 Asker, NORWAY

[2] Dep. of mathematics, Univ. of Oslo, 0316 Oslo, NORWAY

* E-mail: atle.jensen@fmcti.com

ABSTRACT

Experiments and numerical conjugate heat transfer simulations are performed on a simple T-pipe geometry. The T-pipe geometry is partially insulated and mimics subsea equipment which is subject to cool-down after a production shut-down. During flowing conditions the flow is turbulent before closing down and cool-down starts. After some time after shut-down the flow becomes near stagnant in parts of the geometry whereas it remains turbulent in the vertical section for a long time after shut-down due to large buoyant forces. Velocities were measured with particle image velocimetry (PIV), whereas temperature was measured using resistance temperature detectors (RTD's) and thermocouples. A particular focus is on the effect of using Reynolds-averaged Navier–Stokes (RANS) turbulence models on a buoyant flow which is laminar, transitional and turbulent within a single fluid domain.

Keywords: CFD, turbulence, natural convection, PIV.

NOMENCLATURE

Greek Symbols

ρ Mass density, [kg/m^3].
μ Dynamic viscosity, [kg/ms].
ν Kinematic viscosity, [m^2/s].
β Coefficient of thermal expansion, [1/K].
α Thermal diffusivity, [m^2/s].
σ Stefan-Boltzmann constant, [W/m^{2}K^4].
ε Emissivity, [-].
ε Turbulent dissipation rate, [m^2/s^3].
δ Kronceker Delta, [-].
ω Turbulence eddy frequency, [1/s].

Latin Symbols

L Characteristic length, [m].
p Pressure, [Pa].
u Velocity, [m/s].
g Gravitational acceleration [m/s^2].
h Heat transfer coefficient [W/m^{2}K].
k Thermal conductivity, [W/mK].
k Turbulent kinetic energy [m^2/s^2].
T Temperature, [°C].

Sub/superscripts

G Gas.
i Index i – spatial direction x.
j Index j – spatial direction y.
s Surface.
∞ Ambient.
t Turbulent.

INTRODUCTION

In subsea oil and gas industry, thermal insulation of equipment is often used as a method to slow down cool-down, and to facilitate shut-down procedures. Great effort is spent on predicting the thermal behaviour of hydrocarbon production systems in order to identify and prevent hydrate formation in the production fluid during normal production, and during planned or unplanned shut downs.

Subsea equipment generally cannot be fully insulated for different reasons; avoid overheating of electronic components, facilitate remotely operated underwater vehicle (ROV) access, clearance, and various other reasons. The uninsulated parts of the subsea equipment create cold-spots which may have a severe effect on the thermal performance. Detailed thermal analyses are required to assess the effect of these cold-spots and to make sure the equipment is adequately insulated. An increasingly large fraction of the detailed thermal analyses within the subsea industry nowadays are conjugate heat transfer computational fluid dynamics (CFD) simulations.

Engineering flows are generally turbulent and laminar flows are seldom encountered. One exception is natural convection, i.e. buoyancy driven flow. During cool-down of subsea equipment, laminar, transitional and turbulent flow may occur simultaneously within the same domain. RANS-turbulence models, which is the only feasible level of turbulence treatment in CFD for engineering purposes on full scale equipment, are developed for high Reynolds number flow and are generally unable to predict the correct solution if the actual flow is laminar or transitional.

CFD simulations are often used in the design process of the insulation on subsea equipment in the subsea industry. However, the accuracy and uncertainty of the

simulations are seldom reported, nor are the results verified against experimental data. The use of mainstay engineering CFD approaches introduces an uncertainty due to the inadequacy of the RANS-models to capture laminar to turbulent transitions and relaminarizations.

An assessment of the effect of using turbulence models on such transitional flows has been performed in order to shed some light on the uncertainty of thermal CFD cool-down simulations.

Only a few papers have investigated the thermal performance of straight vertical or horizontal dead legs in order to understand the convective behavior of the fluid. Habib et al. (2005) conducted an experimental and numerical study of the effect of dead leg geometry and average flow velocity on oil/water separation in dead legs. The length of the dead leg was varied and a fluid mix of 90% oil and 10% water was considered. They concluded that the size of the stagnant fluid region increased with increased length to diameter ratio and decreased with increased inlet velocity. Asteriadou et al. (2009) presents several CFD models of a flow in a T-piece configuration. The computational models were validated by experiments. The flows varied from laminar to turbulent. The authors report that finer mesh and enhanced wall functions application with mesh refinement did not seem to have a positive impact on the solution.

A handful of papers were found on cool-down, numerical modelling and experiments. Taxy and Lebreton (2004) conducted CFD simulations and full scale insulation tests. They concluded that numerical simulations helped to understand the phenomenology observed during different tests and were the key element to determine the correct action to implement in the insulation design. In Moe et al. (2005) the temperature development in two simple geometries and one gate valve were tested in a laboratory and analyzed with CFD. They found excellent agreement in some of the cases and concluded that CFD is a suitable tool for cool-down simulations. Furthermore, they also claimed that CFD would provide valuable input to finite element analysis (FEA) simulations to correct for the convective heat transfer. A full scale cool-down test of an X-Tree was used to verify the design and numerical models in Aarnes et al. (2005). CFD and FEA agreed very well with the test results in the main part of the X-Tree system.

Mme et al. (2008) presented results from both experiments and numerical modeling of a cool-down in a pipe with a cold spot. The inclination of the pipe was varied and it was found that the heat transfer was most efficient when the inclination was close to horizontal. CFD with a k-ε model was used to simulate the cool-down. The heat flow by the simulations was reported to be under-predicted up to 25%. In a recent paper by Lu et al. (2011), CFD and FEA were validated against controlled experiments. A coated 24 inch steel pipe was welded onto a production tree and elbow. The test assembly was placed in fresh water and temperatures were measured with thermocouples. Measurements were conducted in steady-state and during cool-down. The discrepancy was 5% between CFD and experiments for both cases. FEA gave similar results compared to the experiments.

This article presents results from conjugate heat transfer cool-down CFD simulations with comparison against cool-down experiments with a particular focus on the effect of using RANS turbulence-models on a buoyant flow which is laminar, transitional, and turbulent, within a single fluid domain.

EXPERIMENTS

For validation of the CFD model, experiments were conducted at the Hydrodynamics laboratory, University of Oslo. An idealized geometry in transparent material (Plexiglass) was chosen to give access to optical measurement techniques but also the possibility for more quantitative analysis, e.g. observations.

Experimental setup and techniques

A large diameter (ID 6") horizontal pipe (3m long header) with a vertical branch (1m) mounted together was used in the experiments (shown in Figures 1 and 2). The vertical dead-leg must be long to be able to generate flow with Rayleigh numbers ($Ra = \frac{g\beta\Delta TL^3}{\nu\alpha}$) encountered in subsea equipment. The characteristic length scale used in the Rayleigh number is the free vertical length, i.e. the length of the dead-leg in the dead-leg, and the diameter in the header region.

Water was used as test media and circulated until the required temperature was met and steady state conditions were reached (stage 1 - steady state). The flow rate was 1300 kg/h with an accuracy of +/- 0.5%. The inlet temperature was 45°C and the ambient temperature was 21°C.

A set of valves were mounted on each side of the test rig to be able to enclose the flow (state 2 - cool-down). The header was insulated with Glava (40mm) and installed horizontally on a table covered with Styrofoam to avoid heat transfer to and from the table.

Fluid velocities and external/internal temperatures were measured with high accuracy using PIV, flow meters, PT100 RTD sensors and thermocouples. PIV has seen an increase in popularity over the last two decades, much caused by the developments in camera and laser technology. This method is using pattern matching techniques to be able to track the motion of passive particles which are added to the flow. A sequence of images is used in the post-processing to find the temporal variation of the velocity in a flow. Kinematics and dynamics can be found using various processing techniques. The PT100 sensors were measuring the water temperature, whereas the thermocouples were measuring the wall temperature at different positions in the interior and exterior. The accuracy of PIV is very high if the experiments are carefully executed, the error is expected to be around 1%.

The vertical pipe (dead-leg) is not insulated, thus, from a modeling point of view, the external boundary conditions between the pipe geometry and the air (a heat transfer coefficient in conjunction with an ambient temperature and the radiative heat loss) is very important. Contradictory to for fully insulated equipment the value of the heat transfer coefficient will potentially influence the results to a great extent. However, the header is insulated to be able to simulate more realistic subsea conditions, i.e. equipment which is partially insulated.

During stage 2 (cool-down) the internal and external temperatures were measured together with velocity fields. The temperatures were sampled continuously, but the velocity fields were acquired every five minutes. The velocity field results presented herein is the average of several experiments.

Water temperature was measured at 7 different locations using RTD's inserted 50 mm into the header and dead-leg. The locations of the sensor locations/measuring points are listed in Table 1. The location of the RTD's can also be seen in Figure 1 and a different view with coordinate system in Figure 2.

Table 1: Internal sensor locations.

Sensor name	Location		
	X [m]	Y [m]	Z [m]
PT1	0	0.0225	-0.977
PT2	0	0.0225	-0.377
PT3	0	0.0225	0.396
PT4	0	0.0225	0.996
PT5	0	0.397	0.023
PT6	0	0.797	0.023
PT7	-0.059	0.950	0

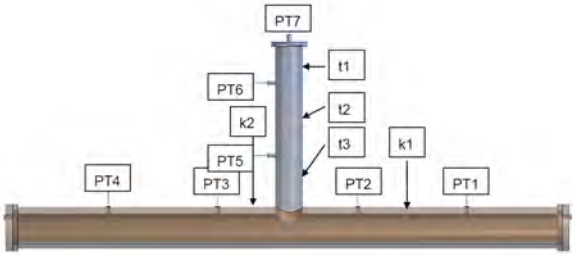

Figure 1: Side view of CFD-model with insulation and sensor locations.

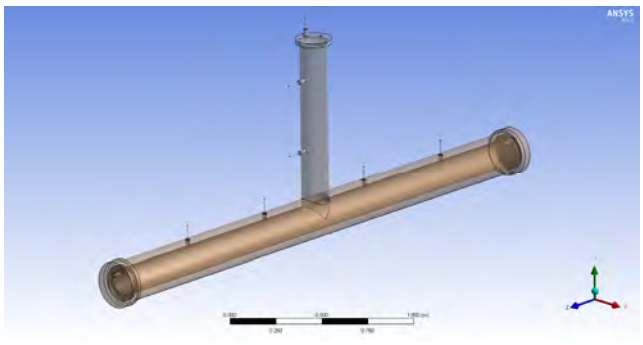

Figure 2: Perspective view showing the orientation of the coordinate system.

Type-t and type-k thermocouples were used to measure the external temperature of the test-geometry. For redundancy three sensors were used to measure the external temperatures at each location. The results from these sensors are not presented.

CFD SIMULATIONS

A side view of a CFD-model of the experimental setup is shown in Figure 1. The model contains the Plexiglas geometry, the insulation, and sensors. The RTD's used to measure the internal fluid temperatures are large and intrusive and may influence the results if not accounted for. Hence, a simplified version of the sensor was included in the CFD-model. The simulations were run using ANSYS CFX v.14.5.

The CFD-simulations were run in two stages; the first to mimic the production phase in a subsea system, i.e. flow through the geometry before a planned or unplanned shut-down. The second stage emulates the shut-down phase, i.e. from the initial valve closure and the subsequent cool-down. The second stage uses the results from the first stage as an initial condition.

The heat transfer from the test geometry to the ambient air is governed by radiation and convection. The radiative heat transfer was modeled assuming black body radiation, i.e. the heat loss due to radiation is modeled as

$$q_{rad} = \epsilon\sigma({T_s}^4 - {T_\infty}^4) \quad (1)$$

where ε is the emissivity of the body, σ is the Stefan-Boltzmann constant, T_s is the surface temperature, and T_∞ is the ambient temperature. The external Nusselt number ($Nu = \frac{hL}{k}$) due to convective heat transfer on the dead-leg was computed using the following empirical correlation

$$\overline{Nu} = [0.825 + \frac{0.387Ra^{1/6}}{[1+(\frac{0.492}{\mathrm{Pr}})^{9/16}]^{8/27}}]^2 \quad (2)$$

, where $Pr = \frac{\nu}{\alpha}$ (Prandtl number). This equation is valid for vertical walls, and vertical cylinders under certain conditions. A similar correlation (other constants) was used to compute the Nusselt number for the header, see Incropera (2007).

During stage 1 the flow in the geometry is a combination of forced, mixed and natural convection. The flow in the header is dominated by forced convection, whereas both forced and natural convection is of importance in the lower part of the dead-leg. In the upper part of the dead-leg natural convection is of sole importance. Similar effects are expected for actual subsea equipment as well.

During stage 2, after the circulation has stopped and the isolation valves are closed, a convective pattern inside the geometry develops due to the thermal differences in the system. The level of mixing in the header during stage 1 and stage 2 depends on the flow pattern. If the flow is turbulent, the mixing between the header and dead-leg regions is large whereas it is limited if the flow is laminar. Whether a flow is laminar or turbulent is given by local conditions.

Turbulence is generated by mean velocity shear and coupled turbulent velocity and temperature fluctuations, whereas it is suppressed by thermal stratifications and turbulent shear. Mean shear dominates production of turbulent kinetic energy, hence for a vertical pipe, given that the Rayleigh number is large enough, the turbulence will be generated in the shear region close to the wall. For intermediate Rayleigh numbers such a configuration may lead to intermittent flow, where intermittent alludes to a flow which spatially and temporally is turbulent.

Simulations with different turbulence models were conducted to determine the effect of the various RANS turbulence models;

- *k-ω*
  - Two-equation model – first moment closure model
- *SST*
  - Two-equation model – first moment closure model
- *RSM-ω*
  - Reynolds Stress model – second moment closure model
- *k-ε*
  - Two-equation model – first moment closure model

Historically the *k-ε* model has been the mainstay turbulence model within engineering, and still is within some communities. Turbulence models are generally developed based on assumptions of high Reynolds number flow, which does not fit the nature of turbulent natural convection flow very well.
The near wall mesh in turbulent simulations is generally very important to accurately calculate the wall shear and heat fluxes. RANS-models often use wall functions to predict the near wall physics as the near wall mesh requirements may become prohibitively stringent for high Reynolds number flow. The wall functions use models to account for the near wall physics without having to resolve the innermost region of the boundary layer with the computational grid. Wall functions are based on functions which describe the viscous sub-layer and the buffer layer found in high Reynolds number flow. However, the near wall physics found in turbulent natural convection does not resemble that of the forced flow; hence wall functions cannot be used to accurately predict turbulent natural convection.

Some of the turbulence models available in CFX (*ω*-based models, both single moment and second moment closures) and other CFD-packages use a low-Reynolds number formulation in innermost part of the boundary layer. In order to exploit the low-Reynolds number formulation a near wall mesh resolution of $y^+ < 1$ is required to avoid the use of wall functions.

The *ε*-based turbulence models, both first moment closures and second moment closures generally rely on wall functions even though the near wall mesh is $y^+ < 1$. It should be noted that it is generally recommended to avoid very fine near wall mesh resolutions ($y^+ > 30$) when using the *k-ε* model as this combination is known to produce strange results. A $y^+ > 30$ cannot be guaranteed even for rather coarse near wall meshes for such geometries due to near stagnant flow in some regions. The *ε*-based turbulence models do not switch to a low-Reynolds number formulation close to walls for fine meshes. This makes the *ε*-based turbulence models unsuited for turbulent natural convection flows. A simulation using the widely used *k-ε* model is included to assess the effect of using this model even though it is anticipated that the results are poor. The results observed herein for the *k-ε* model may to a certain extent be attributed to a too fine near wall mesh.

Barakos and Mitsoulis (1994) investigated natural convection in a square cavity for a wide range of Rayleigh numbers numerically using turbulence models with and without wall functions. Their results show that the predicted Nusselt number deviates significantly from the experimental data when wall functions are used. The predicted Nusselt number is twice that of the experimental data for large Rayleigh numbers, whereas results from simulations without wall functions compare well with the experimental data.

The *k-ω* turbulence model is known to produce good results for natural convection in enclosures and lid-driven cavities. However, all the single moment closures use a single scalar to describe the turbulence which leads to the inherent assumption that the turbulence is isotropic, which for buoyant turbulent flows is not the case. Furthermore, the single moment closures rely on the Boussinesq-approximation to relate Reynolds stresses to the mean shear $-\overline{u_i u_j} = 2\nu_t S_{ij} - 2/3k\delta_{ij}$. Here $\overline{u_i u_j}$ is Reynolds stresses, ν_t is turbulent eddy viscosity, S_{ij} is the rate of strain tensor, and k is turbulent kinetic energy. This assumption leads further to an inherent equilibrium between the Reynolds stresses and mean shear, which is generally not valid for buoyant turbulent flows. Nevertheless, even though single moment closures does not have the best prerequisites to accurately model this type of flow, simulations using single moment closure models are

included here to see if they are able to produce adequate results or not.

Simulations with three different meshes using the *k-ω* model were conducted to determine which mesh level that was required to obtain mesh independent results. All meshes were made of a combination of tetrahedrons, hexagons and prisms. Conformal mesh was used for nearly the entire model. On curved interphases such as for the inner pipe wall it is important to use a conformal mesh. If a non-conformal mesh is used it is vital that the mesh resolution is fine enough so that the surface area on both sides of the interphase is accurately predicted. On the interphase the heat flux is conserved, if the surface area on each side of the interphase is different, the heat flux will not be conserved. A non-conformal coarse surface (interphase) mesh may significantly influence the results in a conjugate heat transfer simulation. Sweep mesh was used on the piping where possible. The mesh in a part of the geometry is shown in Figure 3.

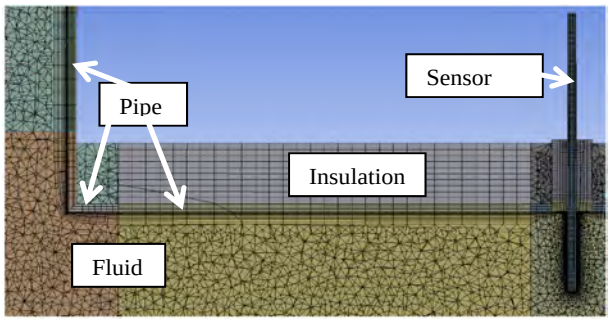

Figure 3: Fine mesh - note that the domains have been decomposed to ease the meshing process, hence the same domain may have different colors in this figure.

Key mesh sizes for the coarse, intermediate, and fine mesh are listed in Table 2.

Table 2: Mesh sizes

	Coarse	Intermediate	Fine
Total number of nodes	0.42M	1.10M	1.54M
Radial cell count insulation	2	6	10
Radial cell count uninsulated piping	2	5	8
Radial cell count insulated piping	2	3	5
Circumferential cell count on piping	40	40	60
First layer height piping	2e-3 [m]	2e-4 [m]	2e-4 [m]
Number of layers piping	7	12	12
Body sizing on piping (where applicable)	5e-3 [m]	5e-3 [m]	4e-3 [m]
Body sizing on insulation (where applicable)	1e-2 [m]	5e-3 [m]	5e-3 [m]
Body sizing on fluid	1.5e-2 [m]	7e-3 [m]	7e-3 [m]

The mesh convergence tests showed that the intermediate and fine mesh produced near identical results, but that there were minor differences, hence the fine mesh was used for the rest of the simulations. Results from the mesh convergence test are shown in Figure 4 and Figure 5. Note that the difference in internal temperature between the intermediate and fine mesh hardly is discernible here. The differences in internal wall temperatures were larger. The wall temperatures in the dead-leg (both internally and externally) for the intermediate and fine mesh differed to some extent, hence it is concluded that the fine mesh is required (results not shown here).

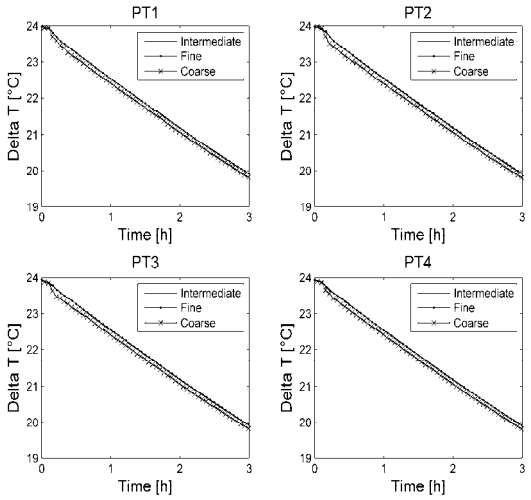

Figure 4: Mesh convergence - temperature data during cool-down

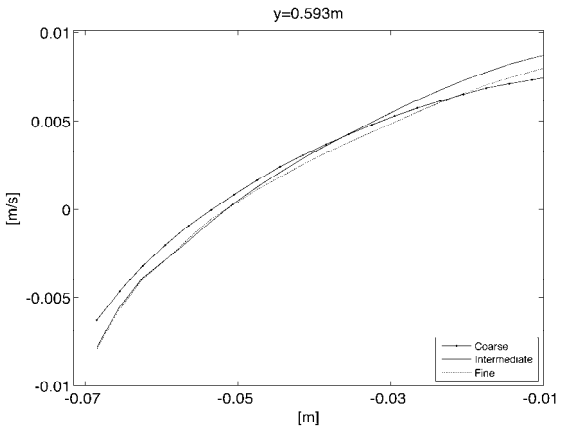

Figure 5: Mesh convergence - velocity profile after 45 minutes cool-down

The CFD simulations were run with a time step of maximum 1 s or a RMS CFL-number of 5, whichever was the most stringent.

RESULTS

The temperature excess ΔT with error bars is shown in Figure 6 and Figure 7 for all internal temperature sensors during three hours of cool-down. The comparisons show good agreement between the simulations (using the fine mesh) and experiments. Here the results from simulations with the *k-ω* model are shown together with the simulation without any turbulence model and the experimental data. The results show that there is good agreement between the CFD

simulations and the experimental data, but that the CFD simulations generally over estimates the temperature in the dead-leg region during both steady-state and cool-down.

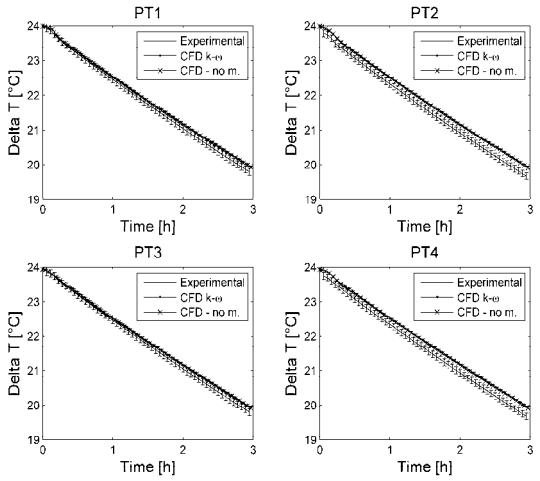

Figure 6: Experimental vs. CFD; PT1 - PT4 (internal sensors in the header)

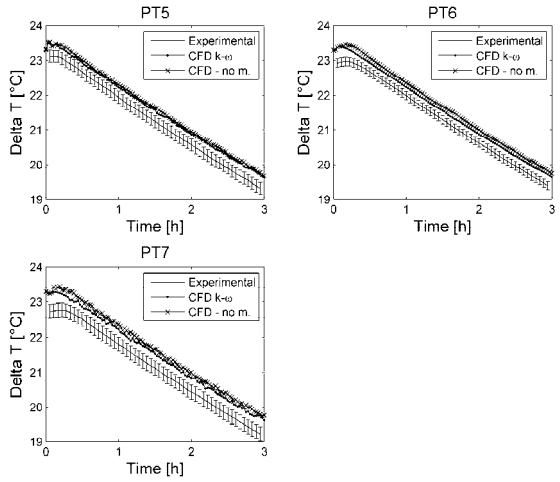

Figure 7: Experimental vs. CFD; PT5 - PT7 (internal sensors in the dead-leg)

A comparison between velocity profiles from CFD for the fine mesh and experiments are given in Figure 8 to Figure 10. Close to the wall in the dead-leg the production of turbulent kinetic energy is large, thus the flow is most likely fully turbulent here during the first part of the cool-down period. In the middle of the dead-leg, there is less mean shear; hence there is less production of turbulent kinetic energy. Turbulent kinetic energy is to some extent transported from the shear region to the middle of the pipe, but due to the limited amount of production the turbulence level in this region is smaller. As the insulated geometry cools down the driving force for the buoyant flow, the temperature excess ΔT, is smaller, hence the velocities also slow down. These two effects lead to a state where the flow close to the wall is turbulent, whereas the flow in the middle of the dead-leg is laminar. As mentioned earlier, this is a type of flow RANS-models cannot be expected to predict accurately.

After approximately two hours, see Figure 10, the production of turbulence in the shear zone is reduced and a laminar model is describing the velocity profiles better.

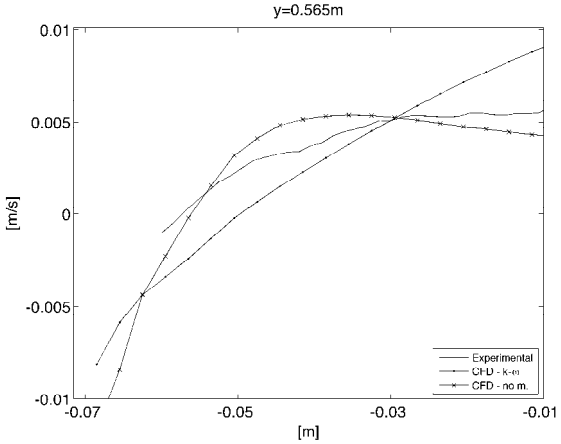

Figure 8: Vertical velocity at y=0.565m; CFD vs. exp - 15 min.

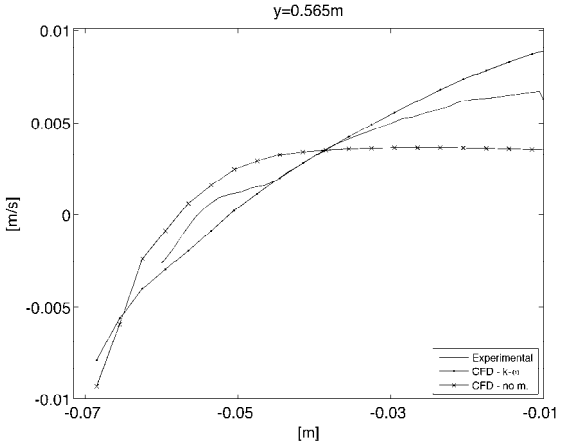

Figure 9: Vertical velocity at y=0.565m; CFD vs. exp - 60 min.

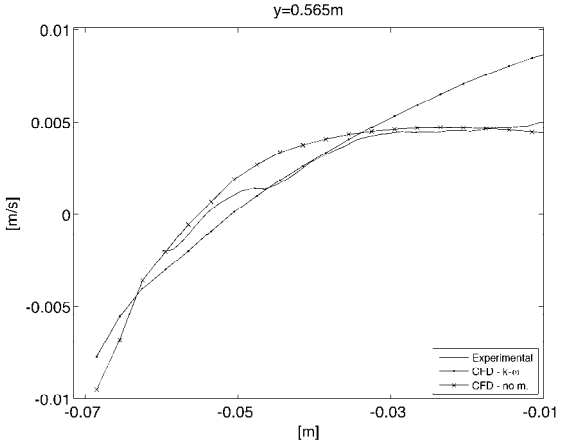

Figure 10: Vertical velocity at y=0.565; CFD vs. exp - 135 min.

Results from simulations with various turbulence models are shown in Figure 11 and Figure 12. The fine mesh was chosen and from the figures it is clear that the choice of model is important for accurate prediction of the velocity. The results show that there is virtually no difference between the *k*-ω, SST, and RSM-ω models in this case. Even though the RSM-ω model includes more physics compared to the two other models, it does not

predict the velocity field better than the simpler two-equation models.

As previously shown, the *k-ω* model compares satisfactorily with the tests for the first 100 minutes of the cool-down close to the wall. However, when the flow is laminar the *k-ω* fails in reproducing the velocity profiles. Then, a laminar model can be used. It can be seen from the results that the *k-ε* fails at all times. The reason for this is because this model uses wall functions, and then the near wall physics is not resolved nor accurately predicted. A RANS turbulence model that is able to simulate accurately the whole time period is not available. In this case, more sophisticated methods of treating turbulence are required, such as Direct Numerical Simulations (DNS) or Large Eddy Simulation (LES). LES with dynamic models such as the dynamic Smagorinsky-model have the prerequisite to predict this type of flow better than RANS-models. However, LES comes with a highly elevated computational cost compared to the RANS-simulations.

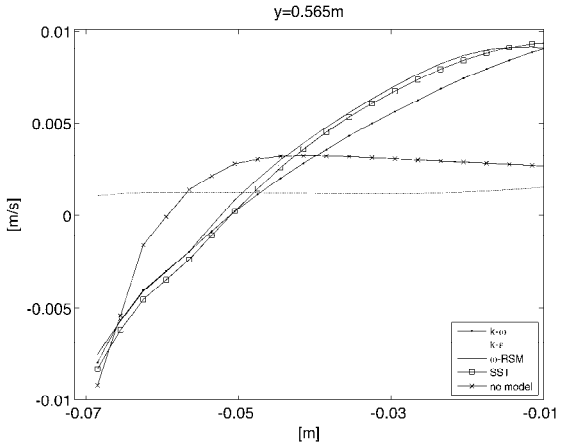

Figure 11: Mean velocity at y=0.565m for different numerical models. The x-axis denotes the horizontal position in the dead-leg - 30min.

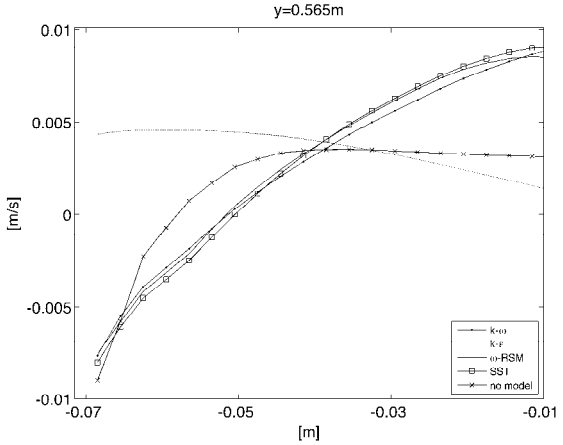

Figure 12: Mean velocity at y=0.565m for different numerical models. The x-axis denotes the horizontal position in the dead-leg - 120min.

CONCLUSION

A thorough comparison between results from CFD simulations and experimental tests of a simplified geometry resembling actual subsea equipment cool-down is conducted.

The choice of turbulence models and mesh refinement is discussed.

There are large discrepancies between results from the different turbulence models and also when the mesh size is varied. However, the results of the velocity profiles from *k-ω*, *ω-RSM* and *SST* are almost identical. The results clearly show the inadequacy of the often used standard of *k-ε* model for such problems. The reason for this is that the standard *k-ε* model uses wall functions that approximate the near wall physics which again is used to compute the wall shear and wall heat flux.

Even though the turbulence generated by buoyancy is anisotropic the results show that for this type of simulations an isotropic turbulence model can be used, e.g. the *k-ω* turbulence model. The anisotropy is weak compared to other effects. Furthermore the results show that in this case the Boussinesq-approximation may be used, the enforced equilibrium between Reynolds stresses and mean shear does not introduce any additional errors.

A mesh convergence test was carried out to determine the mesh level required for such type of geometries. The velocity fields proved rather insensitive to the mesh test, but the effect was clearly seen on the temperature field, particularly on the wall temperatures. It is concluded that when CFD simulations of subsea equipment cool-down are carried out, it is more important to conduct simulations on a proper mesh compared to choosing sophisticated turbulence models. (This is contradictory to what is often done in engineering, it is quicker and easier to change turbulence model rather than to re-mesh the model).

For this case the overall goal is to be able to estimate the temperature during cool-down. The choice of turbulence model is less important, but the quality and size of the mesh should get most of the attention.

Based on visual observations and a comparison between the CFD and experimental data it is concluded that the flow field after about 60 minutes is laminar, particularly in the middle of the dead-leg. Hence, no turbulence model should be used to predict the flow. However, in real life, for design simulations of thermal insulation on subsea equipment the actual flow field inside the geometries during a cool-down is unknown. One may make an estimate based on the expected Rayleigh number, but in practice, it is very difficult to accurately determine the type of flow. The CFD simulations have shown that the thermal field is generally insensitive to choice of turbulence models vs. no-model for this type of geometry. Hence, if it is uncertain whether the flow is turbulent or laminar, a turbulent simulation using the *k-ω* model will most likely produce adequate results for insulated equipment.

The results presented in this report are performed for the given pipe dimensions and flow rates. These results are not easily scalable, but methodology and mesh strategy are valid and carefully investigated and may be used for simulations of subsea equipment.

REFERENCES

AARNES, K.A., LESGENT, J. and HÜBERT, J.C., (2005), "Thermal Design of a Dalia SPS Deepwater Christmas Tree – Verified by Use of Full-Scale Testing and Numerical Simulations", *Offshore Technology Conference*, Houston, Texas, USA.

ASTERIADOU, K., HASTINGS, A.P.M., BIRD, M.R. and MELROSE, J., (2009), "Exploring CFD Solutions for Coexisting Flow Regimes in a T-Piece", *Chem. Eng. Technol*,, **32**, 948-955.

HABIB, M.A., BADR, H.M., SAID, S.A.M., MOKHEIMER, E.M.A., HUSSAINI, I. and AL-SANAA, M., (2005), "Characteristics of flow field and water concentration in a horizontal deadleg", *Heat and Mass Transfer*, **41**, 315-326.

BARAKOS, G. and MITSOULIS, E., (1994), "Natural convection flow in a square cavity Revisited: laminar and turbulent models with Wall functions", *International Journal for Numerical Methods in Fluids*, **18**, 695-719.

INCROPERA, F.P., DEWITT, D.P., BERGMAN, T.L. and LAVINE, A.S, (2007), "*Fundamentals of Heat and Mass Transfer* (6th ed.)", Hoboken: John Wiley & Sons.

LU, Y., MAROTTA, E. and SKEELS, B., (2011), "CFD Thermal Analysis of Subsea Equipment and Experimental Validation ", *Offshore Technology Conference, Houston, Texas, USA.*

MME, U., JOHANSEN, S.T., SARKAR, S., MOE, R., GOLDZAL, A. and LADAM, Y., (2008), "Flow and heat transfer in pipe caused by localised cold spot", *Progress in Computational Fluid Dynamics*, **9**, 409-416.

MOE, R., SØRBYE, S., SKOGEN, K. and LOFSEIK, C., (2005), "A comparison of experimental data and CFD predicted cool down in subsea equipment", *Fourth International Conference on CFD in the Oil and Gas, Metallurgical & Process Industries*, Tronheim, Norway, 6-8 June.

TAXY, S., and LEBRETON, E., (2004), "Use of Computational Fluid Dynamics to Investigate the Impact of Cold Spots on Subsea Insulation Performance", *Offshore Technology Conference*, Houston, Texas, USA.

LATTICE BOLTZMANN SIMULATIONS APPLIED TO UNDERSTANDING THE STABILITY OF MULTIPHASE FLUID INTERFACES

Gerald G PEREIRA*
CSIRO, Computational Modelling Group, Clayton 3169, AUSTRALIA

* E-mail: Gerald.Pereira@csiro.au

ABSTRACT

Multiphase flow occurs in a multitude of industrial and technological situations ranging from oil and minerals recovery to microfluidics and nanofluidics. In all these cases we are interested in modelling the flow of two immiscible phases through a complex geometrical domain. In the past few years, the Lattice Boltzmann method has been developed to model fluid flow both for single phase flow and two (or more) phases. In this study we consider the flow of a less viscous phase into a more viscous fluid (say water into oil) and focus on the stability of the interface. In particular it is known the interface becomes unstable leading to fingers of the less viscous phase jetting through the more viscous phase which has deleterious effects on oil recovery. We use the LB method to model this flow for a variety of fluid geometries.

Keywords: Multiphase, interface stability, oil and gas.

NOMENCLATURE

Greek Symbols

ρ LB particle density, [dimensionless].
μ LB dynamic viscosity, [dimensionless].
ν LB Kinematic viscosity, [dimensionless].

Latin Symbols

f LB distribution function, [dimensionless].
P LB pressure, [dimensionless].
$\boldsymbol{r}$ LB lattice position, [dimensionless].
$\boldsymbol{u}$ LB velocity, [dimensionless].
$\boldsymbol{e}$ LB discrete velocity vectors, [dimensionless].
F LB force, [dimensionless].
g LB weights, [dimensionless].
c_s LB speed of sound, [dimensionless].
w LB weights, [dimensionless].

Sub/superscripts

k multiphase component.
i LB velocity direction.

INTRODUCTION

Understanding immiscible multiphase flow is vital in a vast array of industries such as oil recovery, mining, and technologies such as micro or nanofluidics. In our work we have been most interested in applications in the oil and gas industries where initially the rock or *porous medium* is filled with a wetting (oil phase). A second, non-wetting phase (i.e. water) is then injected to displace the wetting phase. Since the two phases are immiscible a well defined interface exists between the two phases.

One of the most important quantities to determine the capability of a porous medium to produce oil is the permeability. When there are two (or more) phases present relative permeability curves are determined. In this case, as the second phase is injected instabilities in the interface between the two fluids can cause trapping of the initial phase by the injected phase. As such the relative permeability of the initial phase falls rapidly, even though there may be a large amount of that phase still present in the porous medium.

Although relative permeabilities can be measured experimentally this can be quite difficult and time and/or money consuming. Alternatively , if one can obtain a digital model (such as from computed tomography X-ray scans or CT scans) of the rock at the pore level then this data may be imported into suitable numerical solvers so as to solve for the transport properties in the porous medium. There are a number of numerical methods which may, in principal, solve for the flow field in a real porous media. For example, in the past network models (Blunt, 2001; Pereira, 1999) have been used to determine relative permeability curves. In this case the complex topology of the porous medium is approximated by an equivalent network of interconnected pores and throats. The pores hold most of the fluid while the throats are where most of the pressure drops occur. Pores are approximated as spheres (or some similar regular geometry) while the throats are approximated by long, thin cylinders. Although relative permeability curves can be calculated with this method, the biggest problem is to accurately represent the complex topological microstructure with much simpler network models. Invariably, this leads to over-simplifications of the porous medium which then lead to results which are not representative of the real medium.

Alternatively, one can directly apply the numerical CFD solver to the CT data and solve for the (steady-state) flow field. Using techniques such as finite element methods or Smoothed Particle Hydrodynamics one requires a suitable boundary mesh between the void space and solid domain of the porous medium. Because

this is a highly irregular surface, this is typically very difficult. A relatively recent CFD method that overcomes many of the problems with the methods mentioned above is the Lattice Boltzmann (LB) method (Succi, 2001). This method is based on the Boltzmann transport equation which considers the microscopic motion of distributions of particles. In the LB method the velocity space is discretised (and limited) to a small subset of possibilities, which enables a solution on a suitable simplified lattice. However, the exact pore space that is present in the digital data is modelled, i.e. the resolution of the numerical model is at the same scale as the digital data with no approximations.

The LB method is now quite commonly used to compute flow fields for single phase flow (Pan and Miller, 2006). However, its application to immiscible multiphase flow is much more in its infancy. The main question to address is how to capture the effect of surface tension which causes the separation of the two phases? There have been a number of different attempts at representing the effect of surface tension. These include a colour gradient model (Gunstensen and Rothmann, 1992) a thermodynamic, free energy model (Swift *et al*, 1995) a mean-field theory model (He *et al*, 1998) and a microscopic interaction model based on attractive and/or repulsive potentials between neighbouring particles (Shan and Chen, 1993). The methods by Swift *et al* (1995) and He *et al* (1998) were developed to naturally model a change of phase whereas the other two methods are isothermal and so specifically model the two-phase (immiscible) region of phase space. In this study we adopt the so called *Shan-Chen model* (Shan and Chen, 1993) to model surface tension. However, we implement an enhanced version of this model, so to reduce a numerical artefact - the so-called *spurious currents*.

In the next section we introduce this model and extract macroscopic parameters such as surface tension and contact angles from it. We then apply it to sample porous media such as packed beds and carbonate samples.

MODEL DESCRIPTION

The LB model is a mesoscopic numerical method used to study incompressible fluid dynamics. Its main advantages over more conventional CFD techniques (which directly solve the Navier-Stokes equations) are its programming simplicity, computational efficiency and inherent parallelism due to a large amount of local computations. In addition, as mentioned in the Introduction, it naturally deals with complex porous media if suitable digital information is provided. Details of this method, applied to single phase flow, are available (Succi, 2001; Chen and Doolen, 1998) and thus we shall only focus here on the LB method applied to immiscible, multiphase flow.

In the LB method distributions of fluid particles are propagated on a discrete lattice. At each time-step the fluid particles undergo a two-step process where particles are propagated to adjacent lattice nodes (called "*streaming*") and then collided with other particles which converge on a specific node (called "*collision*"). Solid boundaries are treated in the streaming step whereby a bounce-back boundary condition is implemented (i.e. any fluid particles which stream into a solid site are simply reversed). More complex and accurate boundary conditions such as half-way bounce-back or linear interpolation boundary conditions are also possible. In the collision step particle distributions relax towards a given equilibrium distribution - a Maxwellian distribution. Then macroscopic properties such as fluid density, fluid velocity and the stress tensor can be derived from the particle distributions. If we are dealing with only a single fluid, one set of particle distributions is defined, i.e. $f(\boldsymbol{r}, \boldsymbol{u}, t)$ which denotes the distribution of particles travelling with a particular velocity $\boldsymbol{u}$ at time t at lattice node $\boldsymbol{r}$. We will only consider a three dimensional (3D) model in this paper so that we implement the common D3Q19 model which indicates that there are 18 possible vectors, $\boldsymbol{e}_i$, in which particles may move in addition to the null vector. These 18 possibilities are the vectors ($\pm$1, 0, 0), (0,$\pm$1,0), (0,0,$\pm$1), ($\pm$1,$\pm$1,0), ($\pm$1,0,$\pm$1), (0,$\pm$1,$\pm$1).

For n phases we now define n sets of distributions functions, which represent each immiscible phase - $f^1(\boldsymbol{r},\boldsymbol{u},t)$ ... $f^n(\boldsymbol{r},\boldsymbol{u},t)$. For each phase we solve the LB equation at node i. So for the k^{th} phase (where $k \in 1,...n$) we need to solve the LB equation:

$$f_i^k(\boldsymbol{r}+\boldsymbol{e}_i\Delta t, t+\Delta t) - f_i^k(\boldsymbol{r},t) = -\frac{1}{\tau_k}\left[f_i^k(\boldsymbol{r},t) - f_i^{k,eq}(\boldsymbol{r},t)\right]. \quad (1)$$

The term $f_i^{k,eq}$ is the equilibrium Maxwell distribution given by

$$f_i^k = w_i\rho_k\left[1+\frac{\boldsymbol{e}_i\bullet\boldsymbol{u}_k^{eq}}{c_s^2}+\frac{(\boldsymbol{e}_i\bullet\boldsymbol{u}_k^{eq})^2}{2c_s^4}-\frac{\boldsymbol{u}_k^{eq}\bullet\boldsymbol{u}_k^{eq}}{2c_s^2}\right], \quad (2)$$

where w_i are weights which are defined for the given D3Q19 model. In Eq.(1), τ_k represents a relaxation time for phase k and it can be shown to be related to kinematic viscosity via $\nu_k = c_s^2(\tau_k - 1/2)$ where c_s is the sound speed and c_s^2 equals 1/3.

The relationship to macroscopic parameters such as density and velocity of the k^{th} phase are given by

$$\rho_k = \sum_i f_i^k \quad \text{and} \quad \rho_k\boldsymbol{u}_k = \sum_i f_i^k\boldsymbol{e}_i. \quad (3)$$

The Shan-Chen model (Shan and Chen, 1993) (also referred to sometimes as the *pseudo-potential* model) employs nearest neighbour inter-particle potentials to model the interactions between components. In a sense this follows physical reality at the microscopic level where molecules interact via short-range Lennard-Jones type potentials. In the Shan-Chen model lattice nodes which have a separation of less than or equal to $2^{1/2}$ units are coupled together.

In the Shan-Chen model, the interaction potential between components is accommodated via a force, F_k which is introduced through the velocity $\boldsymbol{u}_k^{eq}$ in Eq.(2). This velocity is defined as (Shan and Chen, 1993)

$$\rho_k\boldsymbol{u}_k^{eq} = \rho_k\boldsymbol{u}' + \tau_k\boldsymbol{F}_k. \quad (4)$$

In this equation $\boldsymbol{u}'$ is a combined velocity and to satisfy momentum conservation must be

$$\boldsymbol{u}' = \frac{\sum_k \tau_k^{-1} \rho_k \boldsymbol{u}_k}{\sum_k \tau_k^{-1} \rho_k} \quad . \qquad (5)$$

The fluid-fluid interaction for phase k at lattice node $\boldsymbol{r}$ is then given by

$$\boldsymbol{F}_k(\boldsymbol{r}) = \rho_k(\boldsymbol{r}) c_s^2 \sum_{k \neq k'} g_{kk'} \sum_i w(|\boldsymbol{e}_i|^2) \times \rho_{k'}(\boldsymbol{r} + \boldsymbol{e}_i)\boldsymbol{e}_i \ , \qquad (6)$$

where $g_{kk'}$ is the interaction potential (or coupling parameter) between dissimilar components. The weights w depend on the separation between interacting nodes with $w(1)=1/6$ and $w(2)=1/12$. Note, we assume the coupling is zero for similar components. The pressure in this model is given by the equation of state

$$P = c_s^2 \sum_k \rho_k + 3 \sum_{kk'} g_{kk'} \rho_k \rho_{k'} \ . \qquad (7)$$

One of the issues with this nearest neighbour implementation is that it leads to large spurious currents which are a numerical artefact. These numerical artefacts, if not reduced to a minimum, will lead to large numerical instabilities. Thus we shall attempt to reduce these numerical instabilities in two ways. Firstly, it has been found (Porter *et al*, 2012) extending the range of the pseudo-potential leads to a significant reduction (up to 1000 times) of these spurious currents. The range of pseudo-potential can in principal go to infinity but this of course comes at a computational cost. We have implemented here both 6th order (including all neighbours less than or equal to 2 units away) and 8th order (including all neighbours less than or equal to $8^{1/2}$ units away) pseudo-potentials. This increases the number of neighbours to be sampled from 18 (Shan-Chen) to 32 (6^{th} order) to 64 (8^{th} order), but greatly enhances the numerical stability of the method. Weights, which are required in Eq. (6), for the additional neighbour pairs have been given by Sbragaglia *et al* (2007). Secondly, a slightly different form of the LB evolution (Eq.1) is used which employs an explicit force in the LB equation. This forcing term is defined by He *et al* (1998)

$$\Im_i^k = \frac{F_k \bullet (\boldsymbol{e}_i - \boldsymbol{u}^{eq})}{\rho_k c_s^2} f_i^{k,eq} \ , \qquad (8)$$

where now $\boldsymbol{u}^{eq} = \boldsymbol{u}'$ and $\Im_i^k$ is suitably added to Eq.(1). The phase velocities are modified in this case to $\rho_k \boldsymbol{u}_k = \sum_i f_i^k \boldsymbol{e}_i + \boldsymbol{F}_k/2$.

Relationship to macroscopic surface tension

The Shan-Chen model yields an interface between two immiscible phases via microscopic parameters g_{12}, g_{s1} and g_{s2}. (The subscript s refers to a solid surface so that g_{s1} is the interaction between solid surface and phase 1.) They need to be related to macroscopic surface tension and contact angle measurements. To do this we use the Young-Laplace equation

$$\Delta P = \frac{2\gamma}{R}, \qquad (9)$$

where γ is the macroscopic surface tension and R is a droplet radius.

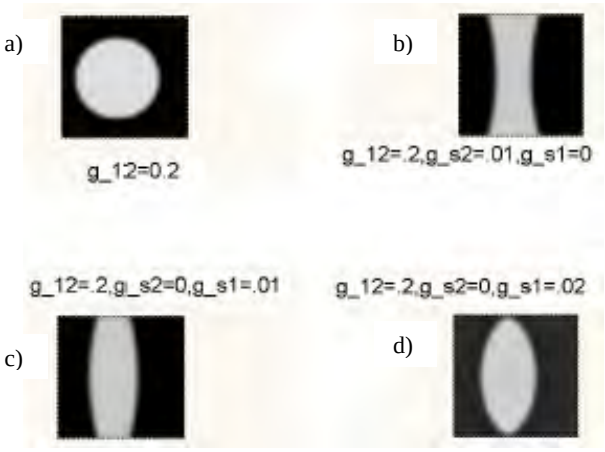

Figure 1. Droplets created using the Shan-Chen model (a) In the bulk, (b) wetting droplet (light shade) between two hard, flat surfaces (c) non-wetting droplet between surfaces and (d) different contact angle non-wetting drop between two surfaces.

To obtain γ we begin with a number of different sized cubical droplets. These quickly relax to spheres of different radius (see Fig. 1a) and then we measure the pressure difference between the interior and exterior of the droplet using Eq. (7). This plot is shown in Fig. 2 and the surface tension is extracted from the gradient. To convert this surface tension to physical (SI) units we need to suitably scale it with physical values of mass and time. Properties such as length and mass can be easily related to physical case of interest. However, time is more difficult. A time scale can be extracted by relating the physical viscosity and LB viscosity.

We can also model different contact angles of droplets on hard surfaces as shown in Fig.1b, c and d. This is done by varying the surface-droplet parameters g_{s1} and g_{s2}. In Fig. 1b these parameters are set to $g_{s1} = 0.01$ and $g_{s2} = 0.0$ resulting in a wetting droplet (the light shade corresponds to the droplet). In Figs. 1c and 1d we change these parameters to $g_{s1} = 0.0$ and $g_{s2} = 0.01$ (for c) and $g_{s1} = 0.0$ and $g_{s2} = 0.02$ (for d) resulting in different non-wetting contact angles. A relationship relating the contact to the interaction (coupling) constants has been given by Huang *et al* (2007):

$$\cos\theta = \frac{2(g_{s1} - g_{s2})}{g_{12}(\rho_1 - \rho_2)}, \qquad (10)$$

where ρ_1 and ρ_2 are densities of fluid 1 and 2, respectively.

It is well know that the Shan-Chen model gives surface tensions which can depend on the viscosity ratio between fluids. This can be overcome by using multi-relaxation time (MRT) schemes (D'Humieres *et al*, 2002). However, for the present study we implement a single relaxation time (SRT) scheme.

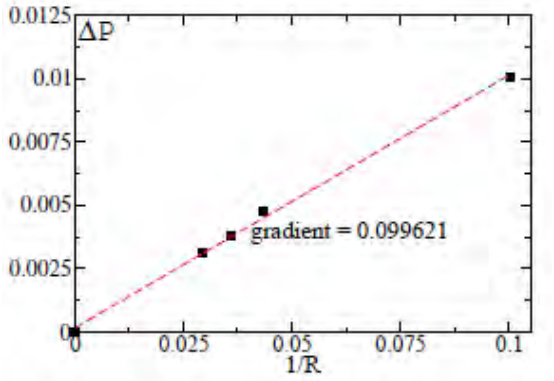

Figure 2. Young-Laplace law for g_{12} = 0.2. We plot the pressure difference between the interior and exterior of the droplet versus the inverse radius of the droplet. Black squares represent the LB results while the dashed line is a best fit line which passes through the origin and the squares.

IMMISCIBLE FLUID DISPLACEMENT

We next apply the LB model to flow in a square capillary or tube. The tube is initially filled with a wetting fluid and a second non-wetting fluid is injected to displace the wetting fluid. This can be achieved in one of two ways - either with an inlet and outlet pressure difference or with a body force (such as gravity) on the whole fluid. The pressure boundary conditions are implemented by prescribing densities (via the distribution functions) on the inlet and outlet (Zou and He, 1997). Body forces can be included by adding them to the force in Eq. (4). A number of different viscosity ratios have been implemented in the following simulations. Generally, we only obtain numerically stable simulations for viscosity ratios between 1 and 5. The non-wetting fluid has the lower viscosity so as to mimic the (practical) case of a water-oil flood.

Capillary pressure

When a non-wetting fluid displaces a wetting fluid in a capillary tube it must overcome the capillary pressure given by $2\gamma\cos\theta/R$ where $2R$ is the tube cross-sectional diameter. So for a given pressure difference between the inlet and outlet the non-wetting fluid will only enter the tube with a diameter greater than $2\gamma\cos\theta/\Delta P$. To test that the model captures this correctly we ran a number of simulations with a narrow, rectangular throat joining the inlet and outlet reservoirs. (The inlet is at the left edge of Fig. 3 and outlet is at the right edge of this figure. The invading fluid is the A-phase which is red.) For each simulation the throat width is constant (at 20 LB units) but the pressure gradient is successively decreased. In Figs. 3a-3d we show the results where we have decreased the pressure difference between the inlet and outlet from 10^{-2} LB units (Fig. 3a) to 5.8 X 10^{-3} (Fig. 3b) to 5.1 X 10^{-3} (Fig. 3c) and finally 4.4 X 10^{-3} (Fig. 3d).

In Fig.3a the invading, non-wetting fluid (red) rapidly invades the narrow throat before entering the outlet reservoir and increasing in size as a non-wetting bubble. In Fig.3b the invading fluid can overcome the capillary threshold pressure but by Fig. 3c this is not possible. We thus estimate the threshold capillary pressure is between 5.1 X 10^{-3} and 5.8 X 10^{-3} LB units. Additional simulations in between these two values have been carried out and it appears that the threshold pressure is very near 5.1 X 10^{-3} LB units. Note in Figs. 3c and 3d the meniscus in the left-hand (inlet) reservoir cannot fill the corners as the pressure in the A-phase (red region) is not large enough to fill the small corner. In both these cases, even though we ran the simulation for as long as possible, the A-phase never filled the narrow throat or the corner regions.

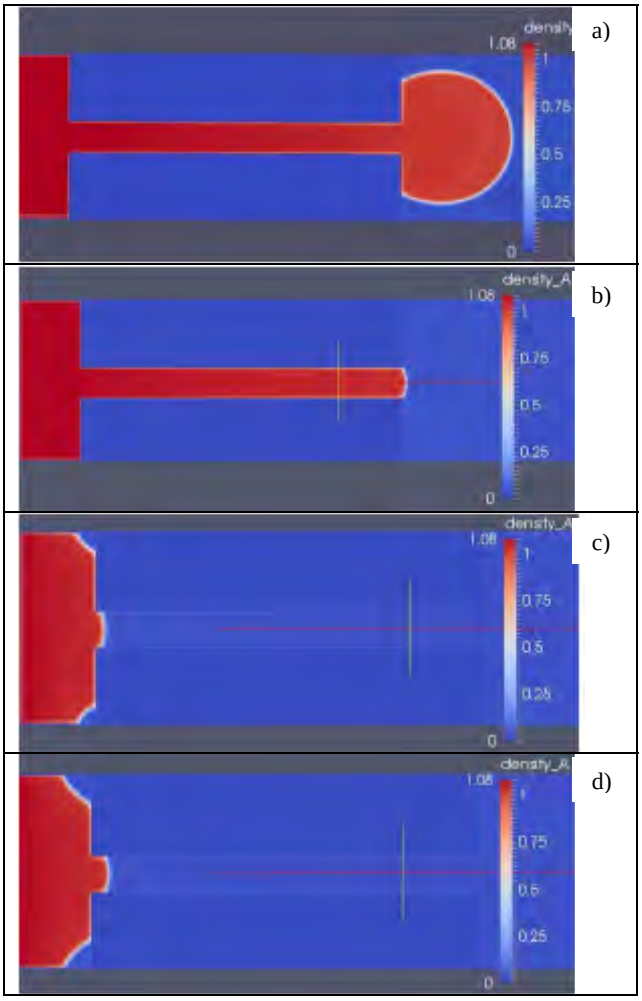

Figure 3. LB simulations of a non-wetting fluid (red) invading a rectangular pore throat which is 20 LB units wide. a) A pressure difference of 10^{-2} LB units between inlet (left side) and outlet (right side) has been applied. b) Pressure difference of 5.8 X 10^{-3}, c) pressure difference of 5.1 X 10^{-3} and d) pressure difference of 4.4 X 10^{-3}. For the last two cases, the meniscus remains at the entrance of the narrow throat for the duration of the simulations (which were allowed to run for as long as practically possible).

Porous media

The aim of this work is to be able to model multiphase flow in a real porous medium. Previously we have done this for single phase flow in carbonate rocks using CT scan digital data (Liu *et al*, 2014). Multiphase flow poses a much larger numerical problem due to surface tension which causes the two phases to remain demixed. Applying the present model directly to CT data is a serious problem for a number of reasons. Firstly, the

complex and irregular pore space can lead to extremely narrow throats and hence extremely high pressures. The multiphase LB algorithm becomes numerically unstable very quickly and the solution cannot be achieved. Secondly, the multiphase method requires one to solve for up to *n* distribution functions which can mean an exorbitantly large amount of compute time and memory. Thirdly the complex 3D topology of real porous media makes it extremely difficult to visualize and (hence) understand the flow transport paths.

For the reasons just mentioned, initially, we implement a much simpler porous medium and then build to more complex cases. These are pseudo 3D models. We previously (Pereira, 1999) used these types of model to understand the rules for three-phase displacement (i.e., displacement of oil and water by a third phase such as gas). Although they are an over-simplification of a real porous medium, they are extremely useful in developing new numerical models since they allow us to follow the pore-scale fluid flow.

The sample porous medium we use is a rectangular domain (in the *x* and *y* directions) with a small thickness (in the third direction, *z*). The length of the sample in the *x* direction is slightly greater than in the *y* direction. Solid spheres are placed in a two-dimensional, hexagonal pattern in the rectangular domain. The spheres have a variable diameter selected from a uniform distribution between 4 and 10 LB units. The centres of the spheres coincide with the mid-plane in the *z*-direction. Figure 4 shows the sample porous medium with the inlet placed along the bottom edge and the outlet along the top edge. Solid spheres are a dark blue colour, the invading fluid (non-wetting) is red and the defending fluid (wetting) is a lighter shade of blue. In this case we wish to simulate a gravity flood so that we drive the fluid with a body force of 10^{-5} LB units. Solid boundary conditions are imposed on the left-hand and right-hand side-walls. The *x* dimension is 160 LB units and the *y* dimension is 120 LB units. The *z* direction thickness is only 6 LB units but we have periodic boundary conditions in this direction. We use a viscosity of 0.166 LB units for the non-wetting phase and 0.5 LB units for the wetting phase, giving a viscosity ratio of 3.

Figure 4b displays the flow at an intermediate time during the primary drainage flood. In the bottom left corner and the central region (near the inlet) there exist clusters of relatively large spheres. Thus the gap between these spheres is quite small and hence the capillary pressure required to invade these regions is large. As a result the invading fluid preferably floods the right hand side of the domain and the left central region. Thus two main fingers develop, which is typical of *viscous fingering*. As the flood proceeds the finger on the left side of the domain has the path of least resistance and hence rapidly reaches the outlet (Fig. 4c). The other finger, on the right side of the domain, has reached around 2/3 of the distance between inlet and outlet. It is clear from this simulation the interface between the non-wetting phase and wetting phase is unstable leading to viscous fingers which leave behind vast unexplored regions of the B-phase (blue), before reaching the outlet.

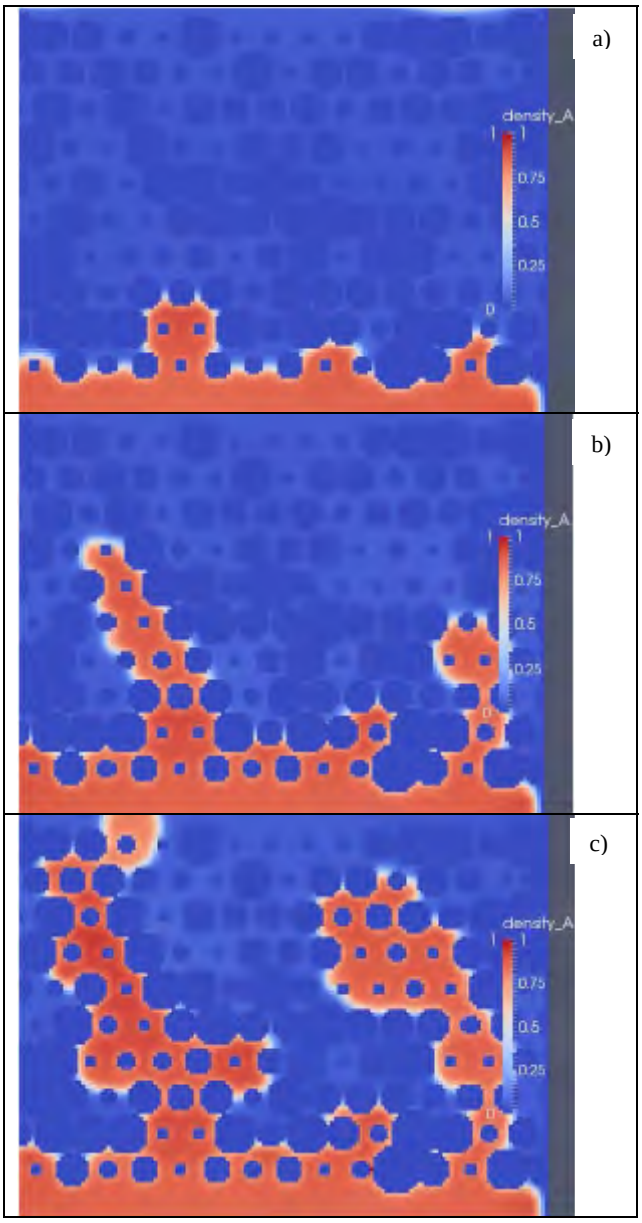

Figure 4. Two-phase immiscible displacement for a sample of packed spheres. A slice in the *x*-*y* plane is shown. The A-phase (red) is the non-wetting/invading fluid while the B-phase (blue) is the wetting/defending fluid. The dark blue spheres are solid. Fluid is driven by a constant body force of 10^{-5} LB units. a) Early configuration, b) intermediate configuration where non-wetting fluid preferentially fingers through domain and c) breakthrough configuration where non-wetting fluid has fingered through on two sides of the domain leaving behind regions of wetting fluid.

Carbonate Sample: The previous simulation has shown the present method yields a physically realistic realisation of a gravity driven flood in a packed bed. We now would like to apply it to a real rock sample. At the moment we do not have the computer memory and speed to complete a full 3D flood. So instead we apply the technique to a pseudo 3D geometry. We have obtained CT data of real carbonate rocks (Liu *et al*, 2014) and taken a slice of this data. That is a slice of dimension 400 voxels by 400 voxels and thickness of 6

voxels. Each voxel corresponds to a cube of edge length 2.9μm, so that the sample simulated is essentially 1.35mm^2 (with thickness in third dimension negligible). The porosity of this sample is high at around 55%.

One of the advantages of the LB method can be readily seen from Fig. 5, in that we simply input the CT data into our LB code. No pre-processing of the boundaries between solid and pore regions needs to be made, as in some other methods (Pereira *et al*, 2011). The flood in this case is driven by a body force of 10^{-5} LB units and solid boundary conditions are applied on the left and right-hand side walls. The same viscosities as for the packed bed case are used.

As in the packed bed case, the interface between non-wetting and wetting phases is unstable and leads to viscous fingers developing. These fingers rapidly invade the sample leaving behind unexplored regions of wetting phase. This will have significant implications on the overall recovery and relative permeability curves.

In principal, we can calculate relative permeability curves for this primary drainage flood using a single phase, multiple-relaxation time, LB method as we have previously done (Liu *et al*, 2014). At various stages during the flood, the configuration of each phase is input into the single phase code and permeabilities are calculated. In a realistic (three-dimensional) domain, one obtains non-zero permeabilities for each phase during the flood. However, in this simplified scenario, as soon the invading phase spans the width of the sample porous medium (e.g., see Fig. 4c) the defending phase permeability drops to zero. So the relative permeability curves become almost trivial. As such we do not display them for these cases.

CONCLUSIONS

The present work describes a numerical model for the complex process of multiphase flow in porous media. While we have focussed on applications in oil recovery, where the porous medium can have a highly irregular, random topology we also would like to apply this to other technological applications such as in micro or nano-fluidics. The present model is based on the Shan-Chen method but with an increased range of interaction which leads to an enhanced numerical stability of the algorithm. It has been shown to properly describe the behaviour of immiscible fluids leading to bubbles and droplets (either wetting or non-wetting) on solid substrates.

We have proceeded to apply the method to model immiscible flooding of porous media, which included packed beds and real rock samples. Both cases led to viscous fingering which results when the invading phase has a smaller viscosity than the defending phase and for comparatively large body forces. By varying these parameters (viscosity ratios and body forces) we would expect to recover other regimes of capillary fingering and stable displacement.

In spite of the encouraging results from this work, there still remain a few issues that remain to be addressed. These are:

- Implementation of a multi-relaxation time (MRT) scheme, yielding surface tensions which are independent of viscosity.
- Capability to deal with much larger three-dimensional domains, so as to model a real porous medium. This requires parallelisation of the present code.

These issues will be addressed in the future and results reported elsewhere.

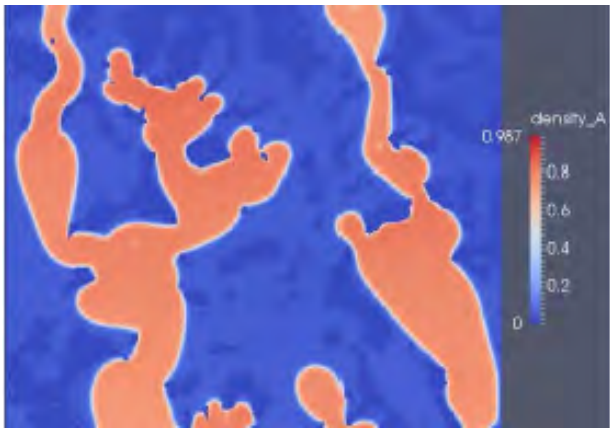

Figure 5. Breakthrough configuration in a carbonate sample. The invading (non-wetting) phase is red while the defending (wetting) phase is light blue. The solid regions are dark blue.

REFERENCES

BLUNT, M.J. (2001). "Flow in porous media - pore network models and multiphase flow". *Curr. Opin. Coll. Int Sci.*, **6**, 197-207.

CHEN, S. and DOOLEN, G.D. (1998). "Lattice Boltzmann method for fluid flows". *Ann. Rev. Fluid Mech.*, **30**, 329-364.

D'HUMIERES, D., GINZBURG, I., KRAFCZYK, M., LALLEMAND, P. and LUO, L.-S. (2002). "Multiple-relaxation-time lattice Boltzmann models in three dimensions". *Phil. Trans. R. Soc. Lond. A*, **360**, 437 - 451.

GUNSTENSEN, A.K. and ROTHMANN, D.H. (1992). "Lattice Boltzmann studies of immiscible two phase flow through porous media". *J. Geophys. Res*., **98**, 6431 - 6441.

HE, X., CHEN, S. and DOOLEN, G. (1998). "A novel thermal model for the lattice Boltzmann method in the incompressible limit". *J. Comput. Phys*., **146**, 282 - 300.

HUANG, H., THORNE, D.T., SCHAPP, M.G. and SUKOP, M.C. (2007). "Proposed approximation for contact angles in Shan-and-Chen-type multicomponent multiphase lattice Boltzmann models". *Phys. Rev. E*, **76**, 066701(1 - 6).

LIU, J., PEREIRA, G.G. and REGENAUER-LEIB, K. (2014). "From characterisation of pore structures to simulations of pore-scale fluid flow and the upscaling of permeability using microtomography: A case study of heterogeneous carbonates". *J. Geochem. Exp*., **144**, 84 -96.

PAN, C.X., LUO, L.S. and MILLER, C.T. (2006). “An evaluation of lattice Boltzmann schemes for porous medium flow simulations”. *Comp. and Fluids*, **35**, 898--909.

PEREIRA, G.G. (1999). “Numerical pore-scale modelling of three-phase fluid flow: Comparison between simulation and experiment”. *Phys. Rev. E*, **59**, 4229 - 4238.

PEREIRA, G.G., PRAKASH, M. and CLEARY, P. (2011). “SPH modelling of fluid at the grain level in a porous medium”. *App. Math. Modell.*, **35**, 166 - 175.

PORTER, M.L., E.T.COON, E.T., KANG, Q., MOULTON, J. and CAREY, J.W. (2012). “Multicomponent inter-particle potential lattice Boltzmann model for fluids with large viscosity ratios”. *Phys. Rev. E*, **86**, 036701(1 - 8).

SBRAGAGLIA, M., BENZI, R., BIFERALE, L., SUCCI, S., SUGIYAMA, S. and TOSCHI, F. (2007). “Generalized lattice Boltzmann method with multirange pseudopotential”. *Phys. Rev. E*, **75**, 026702(1 - 13).

SHAN, X. and CHEN, H. (1993). “Lattice Boltzmann model for simulating multiple phases and components”. *Phys. Rev. E, 47*, 1815 - 1819.

SUCCI, S. (2001). “The Lattice Boltzmann Equation for Fluid Dynamics and Beyond”. Oxford, UK.

SWIFT, M.R., OSBORN, W.R. and YOEMANS, J. (1995). “Lattice Boltzmann simulation of non-ideal fluids”. *Phys. Rev. Lett.*, **75**, 830 - 833.

ZOU, Q. and HE, X. (1997). “On pressure and velocity boundary conditions for the lattice Boltzmann BGK model”. *Phys. Fluids*, **9**, 1591 - 1598.

Chapter 7: Pipeflow

Multiphase flows in pipes are seen in numerous industrial, agricultural and municipal applications. Examples range from transport of oil and gas, to irrigation systems and transport of municipal waste water. If we look closer at the oil and gas applications, these systems are truly multiphase as the transport deals with oil, gas and water being the primary fluids. In addition sand particles, leftover drilling muds, and steel particles to milling (cutting operations) must be transported. On top of that, particles such as wax, hydrates, asphaltenes and inorganic scale may precipitate from the fluids, depending on composition, temperature and pressure. The hydrodynamics of such reactive flows, having at least three fluid phases and multiple solid phases, is of extreme complexity, and currently there are no prediction tools available which from first principles can predict accurately the behavior of such systems. However, we see that the evolution of CFD models is developing fast in subdomains of this large and complex research field.

Seen from an industrial perspective the need is fast, but accurate prediction tools which preferably should be able to predict much faster than real time. In the first place models should be able to compute pressure drop, liquid accumulation and temperature evolution for any length of a pipeline. The only methods which allow such fast predictions are the 1D pipe flow models. Unfortunately, such computationally fast models will have to rely on quite rough empirical or semi empirical relations which only can be obtained from experiments or multidimensional flow modeling.

From this perspective it is clear that Computational Fluid Dynamics has no role in predicting pipeline systems as such, but is critical for understanding the ways flows may behave under different conditions. Performing experiments in large diameter pipelines are very costly, and by development of better CFD models it will be possible to reduce number of experiments and extend an experimentally obtained database by numerical experiments. As CFD offers multidimensional resolution of the flow many important properties of a flow may be computed which at the same time may be very difficult or nearly impossible to measure.

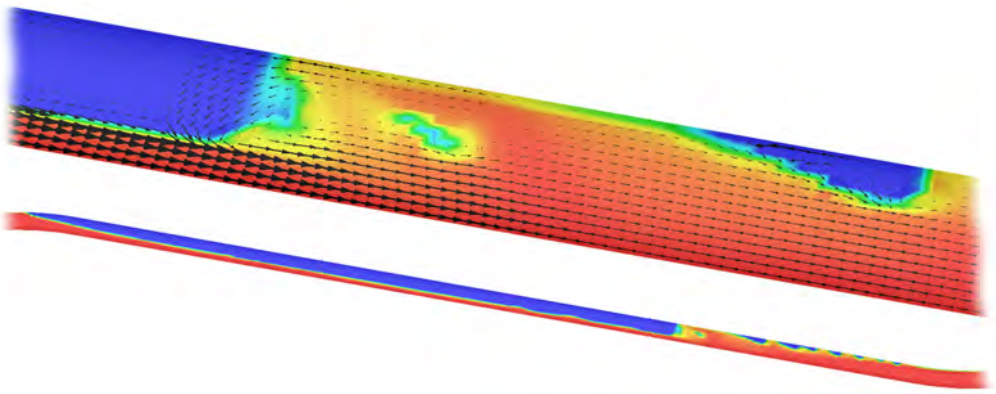

CFD MODELLING OF GAS ENTRAINMENT AT A PROPAGATING SLUG FRONT

Jinsong HUA[1]*, Jørgen NORDBØ [2] and Martin FOSS [1]

[1] Institute for Energy Technology, PO Box 40, NO-2027 Kjeller, NORWAY

[2] NTNU Department of Chemical Engineering, 7491 Trondheim, NORWAY

* E-mail: jinsong.hua@ife.no

ABSTRACT

Slug flow is encountered frequently during multiphase fluid transport in pipes. The gas entrainment process at a slug front significantly affects the hydrodynamic behaviour of slug flows. Due to the complexity of the flow physics and the dynamic coupling of the affecting factors, the mechanism by which these factors contribute to the gas entrainment process is not clearly understood. Typical factors affecting the gas entrainment are pipe inclination, Taylor bubble propagation and liquid film. Current experiments are not able to clarify the effect of these factors on the flow characteristics of slugs. Hence, a computational fluid dynamics based numerical method is applied in this paper to simulate the gas entrainment process at the slug front. The objective is to investigate the factors affecting the gas entrainment. A 2D numerical model is created using a commercial CFD package Star-CCM+. To capture the dynamic behaviour of liquid-gas interface at the slug front, the volume of fluid (VOF) model with relatively fine mesh and small time step is used. The simulation results show that the turbulent kinetic energy at the slug front is closely related to the gas entrainment rate. The effects of pipe inclination, Taylor bubble propagation and liquid film flow parameters on the turbulent kinetic energy generation and gas entrainment process at the slug front are also discussed.

Keywords: CFD, slug flow, gas entrainment, two-phase flow, VOF method.

NOMENCLATURE

Greek Symbols

α Gas volume fraction, [-].
ε Dissipation rate of turbulent kinetic energy, [m^2/s^3].
θ Pipe inclination, [degree].
κ Interface curvature, [1/m].
μ Dynamic viscosity, [kg/m/s].
ρ Mass density, [kg/m^3].
σ Surface tension coefficient, [N/m].
Φ Gas shedding flux, [m/s].

Latin Symbols

C_μ, C_1 and C_2 Turbulence model constants, [-].
C_0 Velocity distribution coefficient, [-].
D Pipe diameter, [m].
$\boldsymbol{F}_{ST}$ Surface tension force distributed in volume, [N/m^3].
g Gravity acceleration, [m/s^2].
G_k Turbulent kinetic energy production term, [$kg/m/s^3$].
H_f Liquid holdup, [-].
k Turbulent kinetic energy, [m^2/s^2].
L Pipe length, [m].
$\mathbf{n}$ Interface unit normal vector, [-].
p Pressure, [Pa].
R_{LC} Liquid recirculating rate in bubble wake zone, [-].
S_{ij} Mean rate-of-strain tensor [1/s]
t time, [s].
$\mathbf{u}$ Velocity, [m/s].
U_m Mixture velocity, [m/s].
U_d Drift velocity, [m/s].

Sub/superscripts

b Taylor bubble.
f Liquid film.
G Gas phase.
L Liquid Phase.
R Moving reference frame.
s slug front or slug body.
t Turbulence.
w Pipe wall or Taylor bubble wake.

INTRODUCTION

Gas-liquid slug flow is encountered frequently in long distance pipelines over a wide range of gas and liquid flow rates and pipe inclinations. The two-phase slug flow is described by alternating elongated large bubbles (also known as Taylor bubbles) moving above liquid films and liquid slugs containing small bubbles. The small gas bubbles in the liquid slugs originate from the gas entrainment process occurring on the dynamic gas-liquid interface between the tail of the elongated gas bubble and the front of liquid slug. Propagation and dispersion of small bubbles into the liquid slug change the hydrodynamic characteristics (e.g. pressure drop) of the aerated liquid slug significantly. The accuracy of pressure drop predictions in long pipelines depends

strongly upon accuracy in estimating the small gas bubble concentration (or the liquid holdup) in the liquid slug. Slug liquid holdup is required for the closure of most slug flow models, including those of Kokal and Stanislav (1989) and Taitel and Barnea (1990). A slug liquid holdup model, empirical or mechanic, is thus an essential part of any slug flow model. The development of an improved liquid holdup model should therefore be based on a detailed understanding of the gas entrainment process at the slug front.

The flow complexity of the gas entrainment process at the propagating slug introduces significant challenges and difficulties for accurate measurement in experiments. This hinders the exploration of flow physics and quantification of the flow parameters. First of all, the gas entrainment process involves dynamic interaction between the elongated bubble tail and the propagating slug front. It is challenging for the current multiphase flow measurement techniques to track and measure the fluid flow parameters close to the dynamic liquid-gas interface. It is also challenging to track the volume changes of the elongated bubble with an irregular tail and the gas content in the liquid slug. Secondly, the fluid flow at the slug front is highly turbulent. The turbulence eddy at the slug front interacts with the liquid-gas interface, creating waves and perturbations on the interface. Thirdly, multi-scale sized bubbles are involved in the gas entrainment process. The elongated bubble has the largest scale of the bubbles involved. Due to the shear flow between the liquid film and the slug front, the rolling waves are formed on the liquid-gas interface, and the tail of the elongated bubble is broken up into medium sized bubbles. They are shed into the slug front or the wake region of the elongated bubble. In this region the bubbles are broken up into smaller bubbles due to the strong turbulence eddies. The presence of gas bubbles also modifies the turbulence structure at the slug front. Some of the smaller bubbles are dispersed further into the downstream liquid slug body. In spite of these challenges, research efforts have been put on experimental studies of the gas entrainment process. The experimental results have been used to develop some fundamental mechanistic models or empirical formulations for predicting gas entrainment rate and void fraction in liquid slug.

The early research efforts on the gas entrainment process focused on the development of purely empirical correlations for predicting slug liquid holdup based on experimental statistical data. Gregory et al. (1978) proposed a simple correlation to predict slug liquid holdup as a function of mixture velocity only. The correlation was based on experimental data obtained from two horizontal 0.0258 m and 0.0512 m pipe diameter flow loops using air/oil system. Since the correlation neglected the effect of fluid properties and pipe geometric parameters such as pipe inclination, the correlation gave inaccurate predictions compared to data from other flow loops under different conditions. The correlation was improved by Malnes (1982) taking into account the physical properties of fluid such as surface tension and liquid density. The correlation of Gregory et al. is widely used due to its simplicity and reasonable accuracy.

Andreussi and Bendiksen (1989) investigated the effects of pipe diameter, inclination angle and fluid physical properties on slug liquid holdup for air/water flows in horizontal and near horizontal pipes. A semi-correlation was proposed to account for the effects of these parameters. Experimental data by Nydal and Andreussi (1991) showed that the gas entrainment is approximately proportional to the relative velocity between the slug front and the liquid film and to the interface length scale. Further statistical study of Nydal et al. (1992) revealed that slug liquid holdup is a weak function of liquid superficial velocity and pipe diameter in horizontal pipes. The liquid viscosity effect on slug liquid holdup was investigated experimentally by Nadler and Mewes (1995) using three different fluid systems, air/light oil, air/heavy oil and air/water. The experimental results showed that the slug liquid holdup increases significantly with increasing liquid viscosity, which indicates a reduced gas entrainment rate at the slug front. It was also observed that the slug liquid holdup differs significantly between the air/oil system and air/water system. This is attributed to the difference in surface tension and liquid density.

Based on the available experimental data over a wide range of two-phase slug flow conditions, improved correlations were developed taking into account better understanding of the slug flow physics. Gomez et al. (2000) developed a correlation to predict the void fraction in liquid slugs in pipes from horizontal to vertical. The experimental data they used included 283 data points collected from six different slug flow studies covering a wide range of pipe diameters, fluid properties and inclination angels. The correlation treats the liquid slug holdup as a function of the inclination angle and the slug Reynolds number. The slug Reynolds number lumps the effect of mixture velocity, liquid viscosity, pipe diameter. Abdul-Majeed (2000) proposed another correlation for estimating slug liquid holdup in horizontal and slightly inclined pipes. It was based on a large data bank consisting of 423 data point from different laboratories. The correlation performed satisfactorily when validated against the horizontal data. However, it performed poorly when validated against the data for inclined pipes.

The exercise on developing empirical correlations indicated that the validity of correlations depends strongly on the range of experimental data set used. The correlations cannot be extended to new flow conditions, which is a strong limitation of the empirical correlations as a predictive tool. Another approach for predicting the gas entrainment and liquid holdup in slugs is to develop a unified mechanistic model, which includes the gas entrainment mechanism. Based on the unit cell model proposed by Dukler and Hubbard (1975), Taitel and Barnea (1990, 1998) developed a slug tracking flow model predicting the evolution of slugs in a pipeline. Brauner and Ullmann (2004) proposed a unified approach to predict slug void fraction in horizontal, inclined and vertical slug flows. Slug aeration is

attributed to a recurrent bubble entrainment from the Taylor bubble tail. The gas entrainment rate is determined based on an energy balance between the rate of turbulent kinetic energy production and the rate of bubble surface energy production. The gas entrainment model of Brauner and Ullmann (2004) was incorporated into the slug flow model of Issa et al. (2006) that improves the slug void fraction prediction at moderate and high mixture velocity.

Zhang et al. (2003) developed a unified mechanistic model to predict slug liquid holdup based on the balance between turbulent kinetic energy of the liquid phase and surface free energy of dispersed, spherical gas bubbles. The turbulent kinetic energy is estimated using the shear stress at the pipe wall and the momentum exchange between the liquid slug and the liquid film in a slug unit. Al-Safran (2009) proposed a new correlation for predicting slug liquid holdup in horizontal pipes using an independent, mechanistic, dimensionless variable. The variable is the momentum transfer rate between the slug body and the liquid film. The correlation was developed using 410 horizontal experimental data points with a wide range of fluid physical properties, pipe size scale, operational and geometrical conditions. It was claimed that the performance of this correlation is much better than other correlations.

As indicated in the development of the mechanistic models (Taitel and Barnea 1998; Zhang et al. 2003; Brauner and Ullmann 2004) and the one-dimensional two-fluid model (Issa et al. 2006) for slug flows, many assumptions, simplifications and empirical correlations are required for closure of the governing equations. This affects the model accuracy and model extension to other flow conditions. The first principal numerical simulation based on computational fluid dynamics provides another approach to simulate slug flows using constitutive correlations that are less empirical. Yan and Che (2011) investigated hydrodynamic characteristics like velocity field, volume fraction distribution of dispersed small bubbles, wall shear stress and mass transfer coefficient in the gas-liquid upward slug flow in a vertical pipe. Hua et al. (2012) reported the validation study of using VOF method to simulate the propagation of a single elongated bubble in inclined pipes. The numerical predictions agree well with experiments.

In this paper, a CFD modelling approach based on the volume of fluid (VOF) method was applied to simulate the gas entrainment process at a propagating slug front. To capture the dynamic liquid-gas interface, a fine resolution mesh and a small time step size are required. Due to the high requirement of computational resources, a 2D model is used in this study. A moving reference attached to the gas bubble is implemented to allow the slug front to be located near the centre of the computational domain during the long simulation time. This was done to incorporate the propagation of slug front and elongated bubble. The focus of this study is on understanding the mechanism of gas entrainment at slug front and influencing factors. They include Taylor bubble traveling speed, pipe inclination and liquid film velocity and thickness. The gas entrainment process can also be affected by other factors such as surface tension and fluid properties. Since the CFD simulations are computationally expensive and the simulation time is long, this limited the number of numerical tests. The simulations provide new insights about the flow physics of gas entrainment process, which may enable development of better correlations and mechanistic models.

NUMERICAL MODEL DESCRIPTION

Problem Description

A schematic diagram of a slug unit of gas-liquid slug flow in an inclined pipe is shown in Figure 1. The diameter of pipe is set to D, and the inclination angle to horizontal is set to θ. The gas and liquid mixture flow upwards along the pipe with superficial velocities of U_{SG} and U_{SL} for the liquid and gas phases respectively. The mixture velocity for the slug flow is $U_m = U_{SL} + U_{SG}$. The propagating speed of the elongated bubble along the pipe is U_b. The liquid film under the Taylor bubble has a liquid holdup of H_f, and an upward flowing speed of U_f. The liquid slug front velocity is U_s. Normally, the slug front velocity is faster than the liquid film velocity ($U_s > U_f$), the highly turbulent flow at the liquid-gas interface may break the Taylor bubble tail into small bubbles. The bubbles are entrained into the slug front at a flux of Φ_{Ge}. Some of the relatively large bubbles in the Taylor bubble wake can be carried back to the liquid-gas interface by the recirculating liquid flow and merge with the Taylor bubble. The flux for this process is Φ_{Gb}.

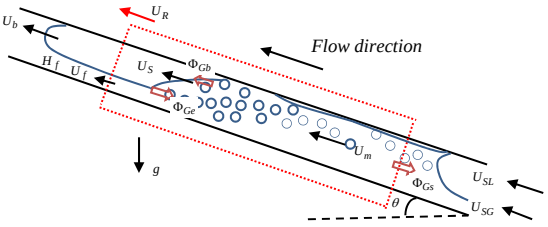

Figure 1: Schematic diagram of a slug unit propagating upward an in inclined pipe.

If the slug flow reaches its fully developed status, the Taylor bubble may reach a quasi-steady state. This means that there is no significant change in the Taylor bubble size. Under this situation the net gas volume shedding rate from the Taylor bubble tail to the slug front ($\Phi_{Ge} - \Phi_{Gb}$) is approximately equal to the gas flux entering into the nose of the tailing Taylor bubble (Φ_{Gs}). The traveling speeds of the Taylor bubble and the slug front are approximately equal ($U_b \approx U_s$).

CFD Model

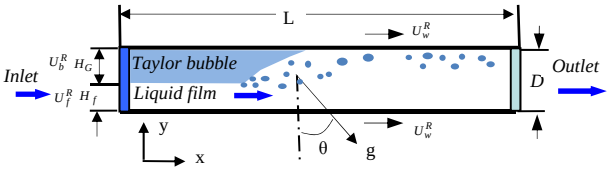

Figure 2: Schematic diagram of the CFD model for gas entrainment process at propagating slug front.

A CFD model partially covering the Taylor bubble, the liquid film and the slug body, as indicated by the dot-lines in Figure 1, is built for studying the gas entrainment process. To achieve a better focus on the dynamic gas-liquid interface between the Taylor bubble and the slug, a moving reference frame with the same moving speed with the Taylor bubble ($U_R = U_b$) along the pipe is applied. The schematic diagram of the CFD model is shown in Figure 2. The diameter of pipe is set to $D = 0.1\ m$. The ratio of pipe length to diameter is L/D=20. An air-water fluid system is set in the model.

The pipe wall is moving in the opposite direction of the Taylor bubble travelling velocity: $U_w^R = U_b$. No-slip condition is applied on the pipe wall. Flow inlet boundary condition is specified on the left end of the pipe, and outflow boundary condition on the right end of the pipe where the reference pressure is set to zero. The inlet velocity of the liquid film layer is assumed to be $U_f^R = U_b - U_f$ in the moving reference frame. Liquid holdup for the Taylor bubble section is assumed to be H_f. The corresponding liquid film thickness is $(H_f \cdot D)$ for the flow inlet boundary. Since the reference frame is moving with the Taylor bubble, the inlet velocity for the gas phase layer is set to zero ($U_G^R = 0$). The pipe inclination angle (θ) is set by specifying the direction of the gravitational acceleration inside the computational domain.

Mathematical Formulations

The dynamics of the gas-liquid interface inside the computational domain is tracked using a volume of fluid method. A phase volume fraction function (α) is used to identify the liquid phase ($\alpha = 0$) and gas phase ($\alpha = 1$). The two-phase fluid system is treated as a fluid mixture with variable properties (density ρ and viscosity μ), which is weighted by the fluid properties of each phase and its volume fraction,

$$\rho = \rho_G \cdot \alpha + \rho_L \cdot (1-\alpha) \quad (1)$$

$$\mu = \mu_G \cdot \alpha + \mu_L \cdot (1-\alpha) \quad (2)$$

It is reasonable to assume both the gas and liquid phases are incompressible under the specified flow conditions in the present study. The Navier-Stokes equations for single phase flow can be extended for the fluid mixture of two-phase flow.

The continuity equation for the fluid mixture reads

$$\nabla \cdot (\mathbf{u}) = 0 \quad (3)$$

And the momentum equation can be expressed as

$$\frac{\partial \rho \mathbf{u}}{\partial t} + \nabla \cdot (\rho \mathbf{u}\mathbf{u}) = -\nabla p + \nabla \cdot (\mu_e \nabla \mathbf{u}) + \mathbf{F}_{ST} + (\rho - \rho_L)\mathbf{g} \quad (4)$$

where μ_e is the effective viscosity, consisting of laminar mixture viscosity and turbulent viscosity $\mu_e = \mu + \mu_t$. $\boldsymbol{F}_{ST}$ stands for the surface tension force, which can be calculated as

$$\boldsymbol{F}_{ST} = \sigma \cdot \kappa \cdot \nabla \alpha \ . \quad (5)$$

Here, σ is the surface tension coefficient, and κ is the interface curvature, which is calculated by the divergence of the interface normal ($\boldsymbol{n}$),

$$\kappa = \nabla \cdot \boldsymbol{n} \ \text{ and } \ \boldsymbol{n} = \frac{\nabla \alpha}{|\nabla \alpha|} \quad (6)$$

The dynamic evolution of the volume fraction function is governed by the conservation of gas phase,

$$\frac{\partial \alpha}{\partial t} + \nabla \cdot (\boldsymbol{u}\alpha) = 0 \ . \quad (7)$$

To close the above governing equations, turbulent viscosity (μ_t) is required for the momentum equation. Hence, a standard k-ε turbulence model is solved. Two governing equations for turbulent kinetic energy (k) and dissipation rate (ε) are expressed as

$$\frac{\partial \rho k}{\partial t} + \nabla \cdot (\rho \boldsymbol{u} k) = \nabla \cdot \left[\frac{\mu + \mu_t}{\sigma_k} (\nabla k) \right] + (G_k - \rho\varepsilon) \quad (8)$$

$$\frac{\partial \rho \varepsilon}{\partial t} + \nabla \cdot (\rho \boldsymbol{u} \varepsilon) = \nabla \cdot \left[\frac{\mu + \mu_t}{\sigma_\varepsilon} (\nabla \varepsilon) \right] + \frac{\varepsilon}{k} (C_1 G_k - C_2 \rho\varepsilon) \quad (9)$$

where G_k is the turbulent kinetic energy production term. σ_k and σ_ε are the turbulent Prandtl numbers for turbulent kinetic energy and dissipation. C_1 and C_2 are the model constants. The turbulent viscosity (μ_t) can be calculated as

$$\mu_t = \rho C_\mu k^2 / \varepsilon \ . \quad (10)$$

The turbulent kinetic energy production can be estimated as

$$G_k = 2\mu_t S_{ij} S_{ij} \ \text{ and } \ S_{ij} = \frac{1}{2}\left(\frac{\partial u_j}{\partial x_i} + \frac{\partial u_i}{\partial x_j} \right) \quad (11)$$

Model Implementation

The commercial CFD package Star-CCM+ is used as the base numerical tool for implementing the proposed CFD model and solving the governing equations. A uniform square mesh is applied to the CFD model. After some numerical tests on the model sensitivity to mesh grid size and time step size, it is found both of them should be small enough to capture the dynamic liquid-gas interface with acceptable phase volume conservation. The mesh with 100 grids along the diameter and 2000 grids along the axis is a suitable choice for the present study. Therefore, the grid size is at the order of one millimetre. Such fine mesh makes the CFD model capture the sharp interface of the Taylor bubbles reasonably well, but it is still not fine enough to capture the interface for the small dispersed bubbles. A constant time-step size is set to 1.0×10^{-4} s in the simulations, and a second order temporal discretization scheme is applied. The initial Taylor bubble is assumed to be of rectangular shape with length of $(5 \cdot D)$ and width of $[(1 - H_f) \cdot D]$ located in the upper left part of the model.

RESULTS AND DISCUSSION

In the proposed CFD model, an air-water system with constant densities and viscosities ($\rho_G = 1.18\ kg/m^3$, $\rho_L = 997\ kg/m^3$, $\mu_G = 1.85 \times 10^{-5}\ Pa\ s$, $\mu_L = 0.88 \times 10^{-3}\ Pa\ s$) and the interfacial tension coefficient ($\sigma = 0.074\ N/m$) is applied. The pipe diameter is set to $D = 0.1\ m$. The simulation can then be specified by the following four parameters; (1) pipe wall velocity (U_w^R); (2) liquid holdup (H_f) for the section of the Taylor bubble; (3) liquid film velocity (U_f^R); (4) pipe inclination (θ). These four flow parameters are varied one by one to study their effects on the gas entrainment process at the slug front. The simulation results are compared to those of a base reference case.

Base Reference Simulation Case

The flow condition for the base reference case is defined by the following settings:

$U_w^R = 1.5\ m/s$; $U_f^R = 1.0\ m/s$; $H_f = 0.4$; $\theta = 10°$

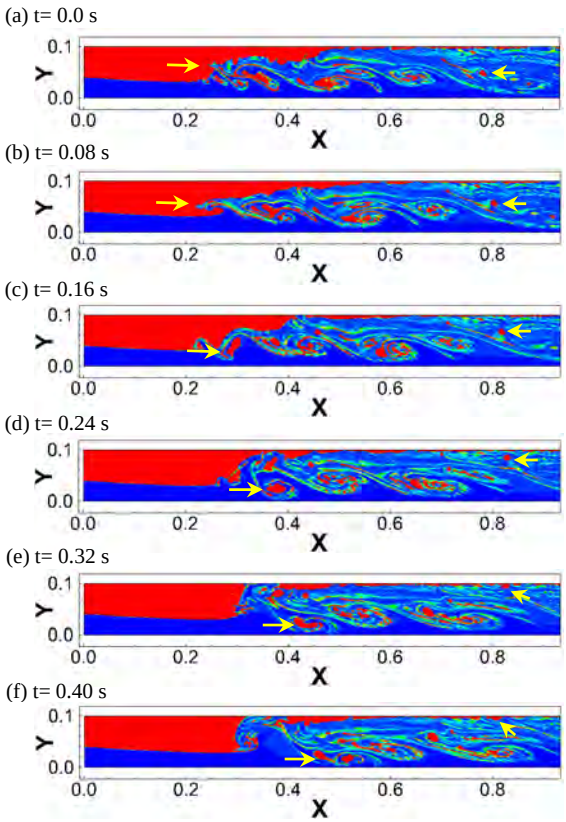

Figure 3: Temporal variation of phase distribution predicted by the CFD model during the gas entrainment process. The red colour stands for the gas phase, and the blue colour stands for the liquid phase.

Figure 3 and Figure 4 show the temporal variation of void fraction and velocity field at every 0.08s over a short period of 0.4s. The starting point (t= 0.0 s) begins at the time point 6s after the simulation is started from the initial state. The red colour represents the gas phase with void fraction higher than 0.2, while the blue colour stands for the liquid phase with void fraction of zero. As highlighted by the long yellow arrows shown in Figures 3 and 4, the fragmentation process of a large gas bubble from the Taylor bubble tail and its entrainment into the slug is highlighted. As shown in Figure 4(a), a liquid jet is initiated from the liquid-gas interface due to the interaction between the liquid film and the recirculating liquid flow at the slug front. The liquid jet protrudes into the Taylor bubble as shown in Figures 3(b) and 4(b). Due to gravity, the liquid jet tip moves downward and impinges on the liquid film under the Taylor bubble. A small amount of gas is trapped between the protruded liquid jet and the liquid film as shown in Figure 3(c), and a new strong circulating vortex is formed at slug front due to the shearing flow between the liquid film and slug front as shown in Figure 4(c). Under the effect of the circulating vortex, the entrained gas bubble is shed into the lower part of pipe as shown in Figures 4(d), and small bubbles are pinched off around the large bubble as shown in Figure 3(d). The large entrained bubble is stretched further by the vortex as shown in Figure 3(e) and finally it is broken up into two smaller bubbles as shown in Figures 3(f) and 4(f). These small bubbles will be dispersed further into the slug body.

As shown in Figure 4, there are about four vortexes between the slug front and the developed slug body. The region from the slug front to the developed slug body is also known as the Taylor bubble wake zone. It has been reported from experiments that the wake zone length is about four to seven pipe diameters.

As the flow develops further into the slug body, the strength of the circulating vortexes becomes weaker. Some of the dispersed bubbles in the wake zone with relatively large size start to rise upward due to buoyancy as indicated by the short yellow arrows in Figures 3 and 4. Finally they will reach the top pipe wall, forming a thin gas layer, which is also known as Taylor bubble tail. Due to the effect of circulating vortexes, the gas layer moves toward the Taylor bubble or slug front. Hence, the characteristics of the dynamic Taylor bubble tail is determined by the balance of the decaying rate of circulating vortexes in the wake zone and the dispersed bubble size. After the wake zone, the small bubbles are dispersed further into the slug body together with the liquid flow.

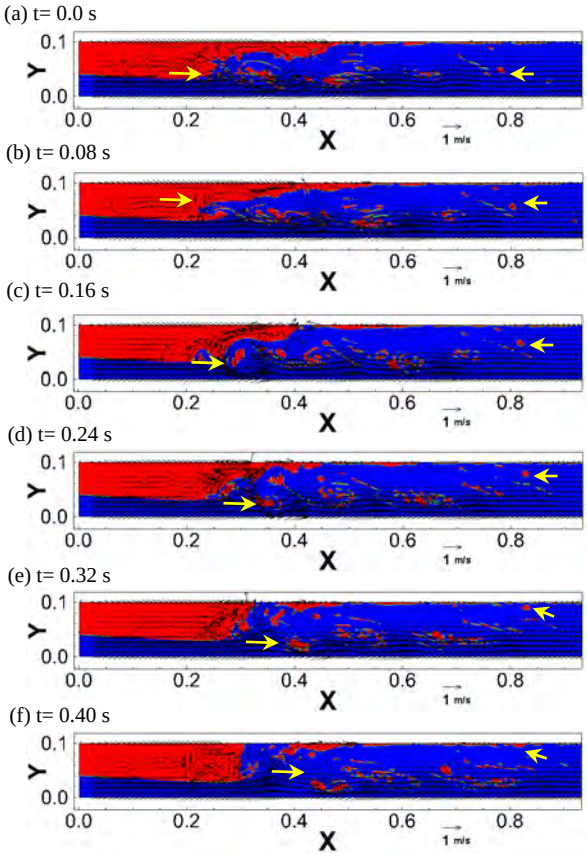

Figure 4: Temporal variation of velocity field (vector) predicted by the CFD model during the gas entrainment process. The red colour stands for the gas phase, and the blue colour stands for the liquid phase.

To estimate the gas entrainment rate, it is important to measure the dynamic change of the Taylor bubble volume and the shedding rate of gas phase out of the slug body. This is shown in Figure 5. As the simulation

is conducted in a 2D CFD model, the area covered by gas phase in the model is used to indicate the physical gas volume. The total gas volume decreases steadily with time at a shedding rate of $\dot{V}_G = -1.14 \times 10^{-3}\, m^2/s$. As suggested in (Nydal and Andreussi 1991), it is better to express the gas phase shedding flux using the shedding velocity $\Phi_{Gs} = \frac{-\dot{V}_G}{D} = 1.14 \times 10^{-2}\, m/s$. Due to the complex dynamic behaviour at the slug front, the Taylor bubble volume fluctuates significantly due to gas entrainment, breakup and coalescence with the tailing small bubbles. In a time averaging view, the Taylor volume also decreases with time at a rate of $\dot{V}_b = -1.33 \times 10^{-3}\, m^2/s$. The corresponding gas entrainment velocity is expressed as $\Phi_{Ge} = \frac{-\dot{V}_b}{D} = 1.33 \times 10^{-2}\, m/s$. A mean gas shedding flux $\Phi_G = (\Phi_{Ge} + \Phi_{Gs})/2$ is used to quantify the gas entrainment rate in this study.

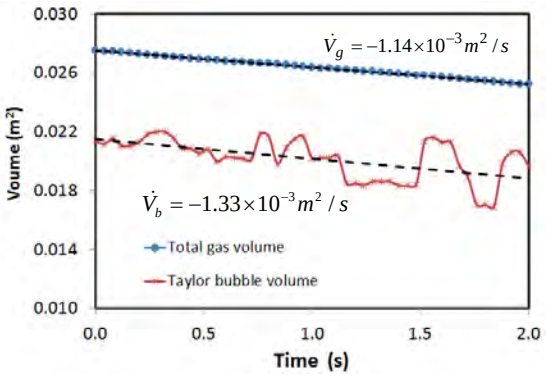

Figure 5: Temporal variation of total gas phase volume and Taylor bubble volume predicted by the 2D CFD model.

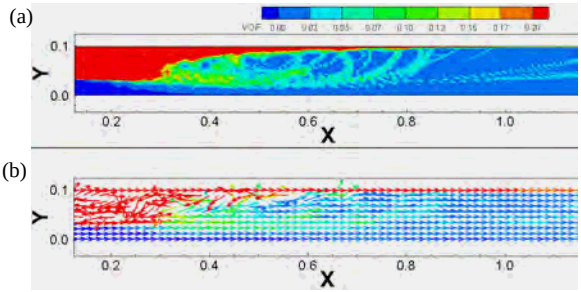

Figure 6: Time averaged variable field of (a) gas volume fraction and (b) fluid flow direction.

Due to the highly dynamic features of liquid-gas interface at the slug front, it is difficult to extract useful and quantified information from the temporal fields of phase distribution and velocity. Instead, we average the temporal variable fields over a longer period of time, about 2 s. Figure 6(a) shows the time averaged field of gas volume fraction. The region of red colour shows the time–averaged Taylor bubble shape. The region with medium gas volume fraction stands for the bubble wake zone. The developed slug body is shown by the blue region. The time averaged velocity field shown in Figure 6(b) illustrates the direction vector of fluid flow, which is coloured by the gas volume fraction. It clearly shows that the fluids near the gas-liquid interface front flows towards the Taylor bubble. This is a result of the strong circulating vortexes at the slug front and wake zone. Hence, the definition of liquid circulation rate proposed by Hua et al. (2012) is used to quantify the strength of circulating flow, $R_L = (U_{LD} - U_L)/U_{LD}$, where U_L is the net liquid flux and U_{LD} is the flux of liquid flowing towards the downstream.

The variation of liquid circulation rate along the pipe axis is shown in Figure 7. The liquid circulation rate is nonzero at the slug front and wake zone. The highest peak of recirculation rate corresponds to the slug front, where the gas is entrained by a strong circulating vortex. The region with nonzero circulation rate in the downstream of the slug front corresponds to the wake zone. The liquid circulation rates of the liquid film under the Taylor bubble and the developed slug body are approximately zero. Hence, the distribution of liquid circulation rate can be used as an indicator for different flow regions in slug flow.

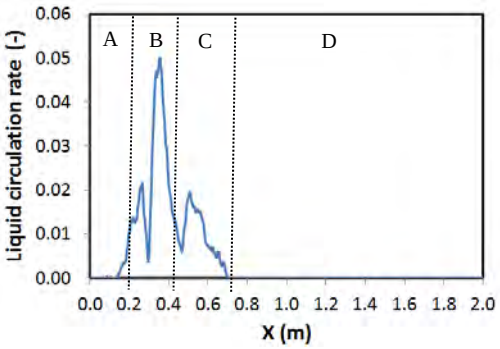

Figure 7: Variation of liquid circulation rate along the pipe axis and the corresponding regions: A for liquid film; B for slug front; C for wake zone; and D for developed slug body.

As illustrated in the simulation results, the gas entrainment process is related to the instability of liquid-gas interfaces and flow velocity fluctuation. Actually, the flow velocity fluctuation can be characterised by the turbulent kinetic energy. Figure 8 shows the variation of sectional averaged turbulent kinetic energy along the pipe axis. The turbulent kinetic energy is increasing in the liquid film, and reaches the highest value at the slug front. The turbulent kinetic energy decays downstream the slug front, and reaches a medium steady value at the wake zone. After the wake zone, the turbulent kinetic energy decays in the developed slug body.

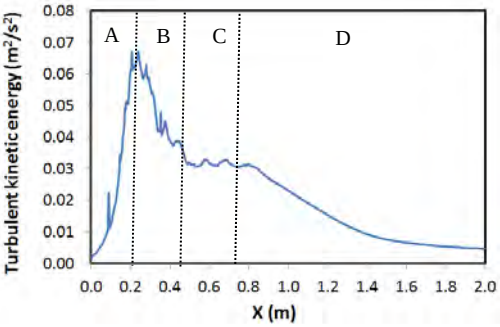

Figure 8: Variation of sectional averaged turbulent kinetic energy along pipe axis for different zones: A for liquid film; B for slug front; C for wake zone; and D for developed slug body.

The pressure drop along the pipe axis due to flow friction is shown in Figure 9. The effect of hydrostatic

pressure is subtracted from the static pressure calculated in the CFD simulation. A low pressure region is formed after the Taylor bubble, which is travelling faster than the liquid. This low pressure induces significant acceleration of the slug front, which generates liquid jets. The interaction of liquid jets and liquid film is a mechanism for gas entrainment.

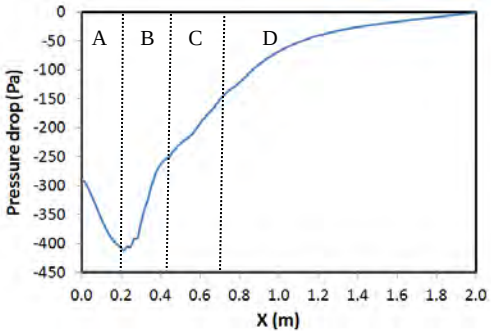

Figure 9: Variation of pressure drop along pipe axis for different zones: A for liquid film; B for slug front; C for wake zone; and D for developed slug body.

From the results of the base reference simulation case, it can be concluded that the gas entrainment process is caused by the interaction between the turbulent slug front and the liquid film. The fluid acceleration at the slug front is attributed to the pressure gradient caused by the low pressure zone created by the travelling Taylor bubble. Hence, the gas entrainment rate is affected by the turbulent kinetic energy at the slug front and the pressure drop. As we know, both the turbulent kinetic energy and the pressure drop along the pipe can be affected by flow conditions such as pipe inclination, Taylor bubble travelling speed, liquid film thickness and liquid film velocity.

Effect of Pipe Inclination (θ)

The effect of pipe inclination on the distribution of pressure drop and turbulent kinetic energy along the pipe axis is shown in Figure 10. Here, only pipe inclination angle is changed, while other parameters are kept constant. As shown in Figure 10(a), the overall pressure drop due to friction is not significantly affected by varying the pipe inclination. However, the pressure jump over the slug front increases significantly with inclination angle. The turbulent kinetic energy distribution along the pipe shown in Figure 10(b) indicates that the turbulent kinetic energy inside the whole slug body increases with the pipe inclination. At small pipe inclination, the high turbulent kinetic energy region is created at the slug front. As the pipe inclination increases, the high turbulent kinetic energy region shifts from the slug front to the slug wake zone. The gas shedding velocity (Φ_G), void fractions in the wake zone (α_w) and developed slug body (α_s) for different pipe inclinations are listed in Table 1. The gas entrainment rate increases with the pipe inclination.

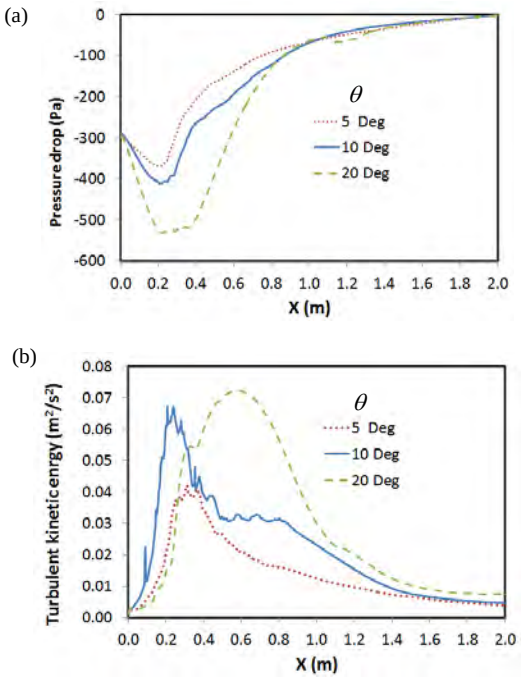

Figure 10: Variation of (a) pressure drop and (b) turbulent kinetic energy along pipe axis under different pipe inclination angle of 5º, 10º and 20º.

Table 1: Variation of gas shedding velocity and void fractions under different pipe inclinations.

θ	5º	10°	20º
Φ_G (m/s)	7.50E-3	1.24E-3	1.28E-2
α_w	1.40E-1	1.12E-1	9.59E-2
α_s	2.09E-2	2.57E-2	3.79E-2

Effect of Taylor Bubble Propagating Speed

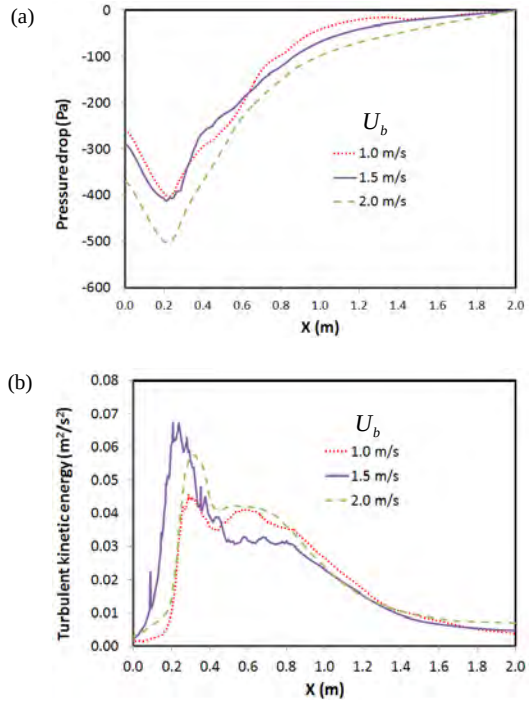

Figure 11: Variation of (a) pressure drop and (b) turbulent kinetic energy along pipe axis under different Taylor bubble travelling speed of 1.0 m/s, 1.5 m/s and 2.0 m/s.

The Taylor bubble propagating speed is used to set the pipe wall velocity in the CFD model with moving reference frame. As shown in Figure 11(a), the overall pressure drop due to friction increases with the Taylor bubble travelling speed. However, the local pressure gradient at the slug front is related to the local turbulent kinetic energy. The data shows that the highest turbulent kinetic energy at the slug front is seen when the Taylor bubble velocity is 1.5 m/s, as shown in Figure 11(b).

Table 2: Variation of gas shedding velocity and void fractions under different Taylor bubble travelling speeds.

U_b (m/s)	1.0	1.5	2.0
Φ_G (m/s)	8.46E-3	1.24E-2	1.35E-2
α_w	1.66E-1	1.12E-1	2.16E-1
α_s	3.44E-2	2.57E-2	2.71E-2

The gas shedding velocity (Φ_G), void fractions in the wake zone (α_w) and developed slug body (α_s) for different Taylor bubble travelling speeds are listed in Table 2. The gas entrainment rate increases with the Taylor bubble travelling speed.

Effect of Liquid Film Thickness (h_f)

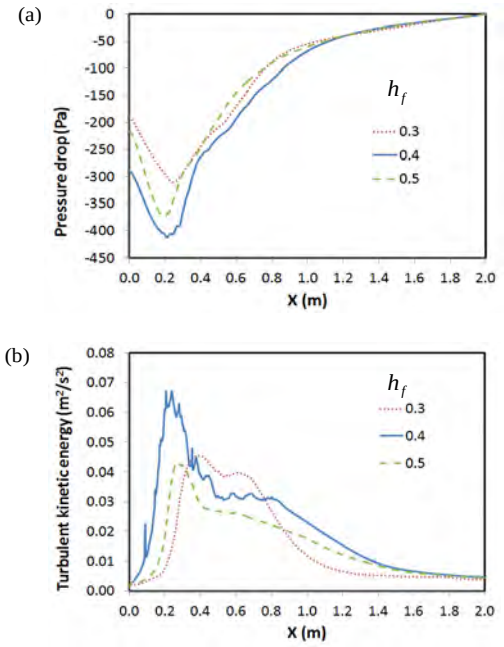

Figure 12: Variation of (a) pressure drop and (b) turbulent kinetic energy along pipe axis under different liquid film thickness.

The effects of liquid film thickness (i.e. liquid holdup under Taylor bubble) on the distribution of pressure drop and turbulent kinetic energy along the pipe axis are shown in Figure 12. When the liquid film has a medium liquid holdup, the interaction between the slug front and the liquid film is at its highest. A high turbulent kinetic energy at the slug front is seen for this situation as shown in Figure 12(b). When the liquid film is thinner, it has less momentum to interact with slug front. On the other hand, when the liquid film is thicker, the liquid slug front does not have enough momentum to affect the flow status in liquid film. The momentum exchange between the liquid film and slug front is higher when their individual momentums are similar. This creates strong disorder in the flow and generates high turbulent kinetic energy. The pressure drop shown in Figure 12(a) also shows that the liquid film with a medium thickness has the highest overall pressure drop.

Table 3: Variation of gas shedding velocity and void fraction under different liquid film thicknesses.

h_f	0.3	0.4	0.5
Φ_G (m/s)	5.08E-3	1.24E-2	1.12E-2
α_w	2.00E-1	1.12E-1	1.89E-1
α_s	2.23E-2	2.57E-2	2.31E-2

The gas shedding velocity (Φ_G), void fractions in the wake zone (α_w) and developed slug body (α_s) for different liquid film thicknesses (or liquid holdup) are listed in Table 3. The case with a medium liquid film has the highest gas entrainment rate.

Effect of Liquid Film Velocity

The effect of liquid film velocity on the gas entrainment process is also illustrated by the variation in pressure drop and turbulent kinetic energy at the slug front as shown in Figure 13. Clearly, the shearing between liquid film and slug front increases with increasing liquid film velocity. The high shearing rate at the slug front will lead to higher turbulent mixing and produce higher turbulent kinetic energy as shown in Figure 13(b). The highly turbulent flow at the slug front induces extra friction from the pipe wall, and increases the pressure drop at slug front. This is shown in Figure 13(a).

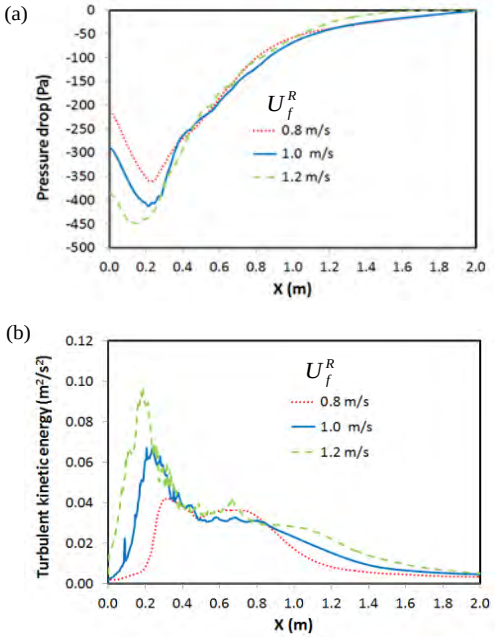

Figure 13: Variation of (a) pressure drop and (b) turbulent kinetic energy along pipe axis under different liquid film velocity.

Table 4: Variation of gas shedding velocity and void fraction under different liquid film velocities.

U_f^R (m/s)	0.8	1.0	1.2
Φ_G (m/s)	6.11E-3	1.24E-2	1.27E-2
α_w	1.74E-1	1.12E-1	2.18E-1
α_s	2.10E-2	2.57E-2	3.28E-2

The gas shedding velocity (Φ_G), void fractions in the wake zone (α_w) and developed slug body (α_s) for different liquid film velocities are listed in Table 4. The gas entrainment rate increases with the liquid film velocity.

CONCLUSION

A CFD model has been applied to simulate the gas entrainment process at a propagating slug front. To capture the dynamic gas-liquid interface, a 2D VOF CFD model with fine mesh (about $1\,mm$) and small time step size (about $1.0 \times 10^{-4}\,s$) is implemented using the commercial CFD package Star-CCM+. In addition, to simulate the propagating slug front, the numerical model is implemented using a moving reference frame attached the Taylor bubble. The gas entrainment rate is obtained by monitoring the decrease of total gas volume or the shrinkage of Taylor bubble volume.

From the flow field and phase volume fraction distribution results, it can be concluded that the amount of gas entrained is determined by the interaction between the liquid film under Taylor bubble and the circulating vortex flow at the slug front. The interaction strength can be characterised by the turbulent kinetic energy at the slug front. This can be affected by many factors such as pipe inclination, Taylor bubble travelling speed, liquid film thickness and liquid film velocity. The parameter sensitivity studies outline the mechanism of action by these factors on the gas entrainment process. High pipe inclination will cause high pressure drop at the slug front and higher liquid acceleration. High Taylor bubble travelling speed will result in lower pressure in the bubble wake zone, which leads to higher pressure drop at the slug front. A medium liquid film thickness has the highest momentum exchange rate between the liquid film and the slug front. High or low liquid film thickness reduces the momentum exchange. Increasing the liquid film velocity will result in high shearing at slug front, which induce high momentum exchange. In general, highly turbulent fluctuations at the slug front will lead to high gas entrainment.

A limited number of simulations have been finished to study the gas entrainment at a propagating slug under different flow conditions. The simulation results are qualitatively reasonable. It is still challenging to interpret the simulation results quantitatively at the present stage. The accuracy of the simulation results can be affected by the numerical models adopted in this study. For example, the simplification as a 2D model has strong effects on the accuracy of turbulence model and multiphase flow model, which always have 3D structure in nature. The k-epsilon turbulence model is not the best candidate model for such complex multiphase flows, but it produces stable numerical results with reasonable accuracy. The gas entrainment process can also be affected by other factors (e.g. surface tension coefficient, fluid properties) which are not considered in this paper. All these factors can be included in future research tasks. The simulation results presented in this paper describe gas entrainment process reasonably well, and provide new insight for developing and improving the mechanistic model for gas entrainment in slug flows.

ACKNOWLEDGEMENT

The authors would like to thank the support from the FACE center - a research cooperation between IFE, NTNU and SINTEF, funded by The Research Council of Norway, and by the following industrial partners: Statoil ASA, GE Oil&Gas, Schlumberger, FMC technologies, CD-adapco, and Shell Technology Norway AS.

REFERENCES

ABDUL-MAJEED, G.H., (2000), "Liquid slug holdup in horizontal and slightly inclined two-phase slug flow". *J. Petr. Sci. Eng.*, **27**, 27-32.

AL-SAFRAN, E., (2009), "Prediction of slug liquid holdup in horizontal pipes", *J. Energy Resour. Technol.*, **131**, 023001-1 - 023001-8.

ANDREUSSI, P. and BENDIKSEN, K., (1989), "An investigation of void fraction in slugs for horizontal and inclined gas-liquid slug flow", *Int. J. Multiphase Flow*, **15**, 937-946.

BRAUNER, N., and ULLMANN, A., (2004), "Modelling of gas entrainment from Taylor bubbles. Part A: Slug flow", Int. J. Multiphase Flow, **30**, 239-272.

DUKLER, A. and HUBBARD, M., (1975), "A model for gas-liquid slug flow in horizontal and near horizontal tubes", *Ind. Eng. Chem. Fundam.*, **14**, 337-347.

GOMEZ, L.E., SHOHAM, O. and TAITEL, Y., (2000), "Prediction of slug liquid holdup horizontal to upward vertical flow", *Int. J. Multiphase Flow*, **26**, 517-521.

GREGORY, G., NICHOLSON, M. and AZIZ, K. (1978), "Correlation of the liquid volume fraction in the slug for horizontal gas-liquid slug flow", *Int. J. Multiphase Flow*, **4**, 33-39.

HUA, J., LANGSHOLT, M. and LAWRENCE, C., (2012) "Numerical simulation of single elongated bubble propagation in inclined pipes", *Prog. in Comput. Fluid Dynamics*, **12**, 131–139.

ISSA, R.I., BONIZZI, M. and BARBEAU S., (2006), "Improved closure models for gas entrainment and interfacial shear for slug flow modelling in horizontal pipes", *Int. J. Multiphase Flow*, **32**, 1287-1293.

KOKAL, S. and STANISLAV, J., (1989), "An experimental study of two-phase flow in slightly inclined pipes-II: liquid holdup and pressure drop", *Chem. Eng. Sci.*, **56**, 681-693.

MALNES, D., (1982), "Slug flow in vertical, horizontal and inclined pipes", Institute for Energy Technology, Kjeller Norway, Report No. IFE/KR/E-83-002 V.

NADLER, M., and MEWES, D., (1995), "Effect of the liquid viscosity on phase distribution in horizontal gas-liquid slug flows", *Int. J. Multiphase Flow*, **21**, 253-266.

NYDAL, O. and ANDREUSSI, P., (1991), "Gas entrainment in long liquid slug advancing in a near horizontal pipe", *Int. J. Multiphase Flow*, **17**, 179-189.

NYDAL, O., PINTUS, S. and ANDREUSSI, P., (1992), "Statistical characterization of slug flow in horizontal pipes", *Int. J. Multiphase Flow*, **18**, 439-453.

TAITEL, Y. and BARNEA, D., (1990), "Two-phase slug flow", *Adv. Heat Transfer*, **20,** 83-132.

TAITEL, Y. and BARNEA, D., (1998), "Effect of gas compressibility on a gas slug tracking model", *Chem. Eng. Sci.*, **53**, 2089-2097.

YAN, K. and CHE, D., (2011), "Hydrodynamic and mass transfer characteristics of slug flow in a vertical pipe with and without dispersed small bubbles". *Int. J. Multiphase Flow*, **37**, 299–325.

ZHANG, H.Q., WANG, Q., SARICA, C., BRILL, J.P., (2003). "A unified mechanistic model for slug liquid holdup and transition between slug and dispersed bubble flows", *Int. J. Multiphase Flow*, **29**, 97–107.

CFD SIMULATIONS OF THE TWO-PHASE FLOW OF DIFFERENT MIXTURES IN A CLOSED SYSTEM FLOW WHEEL

José F. ROCA R.[1*], **João N.E. CARNEIRO**[1], **José E.S. OLIVEIRA**[1], **Sjur MO**[2], **Martin FOSSEN**[3], **Stein T. JOHANSEN**[2]

[1]Instituto SINTEF do Brasil, 22251-050 Rio de Janeiro, BRAZIL

[2]SINTEF Materials and Chemistry, 7465 Trondheim, NORWAY

[3]SINTEF Petroleum Research, 7465 Trondheim, NORWAY

[*] E-mail: jose.roca@sintefbrasil.org.br

ABSTRACT

The objective of this work is to study the behaviour of mixtures involving air/water and oil/water at low pressures and oil/ high CO_2-content gas at high pressures in a closed system 'Wheel Flow Loop'. Such apparatus has been used in different contexts before, e.g. to evaluate the mixture apparent viscosity of different emulsions or the hydrate behaviour under realistic conditions of pressure and temperature. Typically, torque and rotation velocity measurements are used to estimate the overall wall shear stresses. Only in a few cases, there exists the possibility to visualize the interface between phases through a (sapphire) window. Furthermore, secondary flow present in such curved configurations may have an effect on pressure loss depending on ratio of pipe diameter and curvature radius and flow regime. Consequently, more detailed information on the flow and phase distribution in the wheel is very relevant to understand the underlying physics in the wheel and aid data interpretation.

In this paper, two-phase flow in the Wheel Flow Loop geometry is simulated numerically, by means of a classic Volume of Fluid (VOF) approach and a coupled 'VOF' / Eulerian-Eulerian approach. Thus, 3D flow calculations using ANSYS® Fluent's VOF are critically compared with a Quasi-3D (Q3D) approach from LedaFlow®. Additionally, both numerical results have been compared with experimental data obtained in the SINTEF Multiphase Flow Laboratory at Tiller in Norway for different mixtures showing reasonable agreement. Torque/velocity output data has received special attention.

Experiments have evidenced hysteretic behaviour when an increasing-decreasing stepwise angular velocity is imposed to the wheel. Both this phenomenon and the carry-over starting point have been successfully reproduced by the CFD calculations.

Keywords: Wheel flow loop, CO_2-rich mixture, two-phase flow, Quasi-3D.

NOMENCLATURE

Greek Symbols

ℓ	Turbulent length scale, [m]
λ	Friction factor, $[-]$
μ	Dynamic viscosity, $[\mathrm{Pa}\cdot\mathrm{s}]$
ρ	Mass density, $[\mathrm{kg/m^3}]$
θ	Polar coordinate (angle), $[^\circ]$
τ^{wall}	Wall shear stress, [Pa]

Latin Symbols

a	Pipe radius, [m]
A^{wall}	Wall area, $[\mathrm{m}^2]$
d	Pipe diameter, [m]
De	Dean number ($\mathrm{De} = \mathrm{Re}\sqrt{\frac{a}{R}}$), $[-]$
GOR	Gas-oil ratio, $[\mathrm{m^3/m^3}]$
k	Turbulent kinetic energy, $[\mathrm{m^2/s^2}]$
LSI	Large Scale Interface
N_X	Number of x-cells, $[-]$
N_Y	Number of y-cells, $[-]$
$Q3D$	Quasi-3D
r	Polar coordinate (radius), [m]
R	Wheel radius, [m]
Re	Reynolds number ($\mathrm{Re} = \frac{\rho U_0^{\mathrm{wall}} d}{\mu}$), $[-]$
$\mathrm{Re_c}$	Critical Reynolds number, $[-]$
t	Time, [s]
T	Torque, $[\mathrm{N}\cdot\mathrm{m}]$
U^{wall}	Wall velocity of the wheel, $[\mathrm{m/s}]$
x	Streamwise coordinate, [m]
y	Transversal coordinate, [m]

Sub/superscripts

i	x-index (streamwise)
j	y-index (transversal)

INTRODUCTION

During petroleum production gas, oil and water may flow simultaneously in pipes, forming complex mixtures which are often difficult to characterize under realistic conditions. A closed system wheel flow loop has been used by different authors (e.g. Urdahl et al., 1997; Johnsen et al., 2001; Johnsen and Rønningsen, 2003) as an approach to estimate the apparent viscosity of mixtures under different water cuts, realistic pressure - temperature conditions and Reynolds numbers as usually observed in the field. These are not straightforward to be reproduced, e.g. in standard rheometers. The idea behind such setting is that the wheel may, in some respect, resemble a pressurized infinite loop, being relatively easy to operate with reduced costs. This, and the possibility to place the wheel inside a climate chamber has also driven the use as a tool to study flow assurance problems, e.g. related to hydrates, including the performance of inhibitors (Rasch et al., 2001). An example of a wheel flow loop is shown in Figure 1.

Recently, the production and transport of hydrocarbon mixtures with high CO_2 content have received special attention (Zain et al., 2001; Almeida et al., 2010). The presence of CO_2 in unusual amounts may compromise mechanical integrity due to pipeline corrosion while influencing other issues related to flow assurance such as excessive Joule - Thomson cooling, wax deposition, inorganic scaling, among others. Experiments for such mixtures in flowing systems are very expensive and rarely found. Thus, the wheel setup has been also evaluated here for systems containing significant CO_2 content.

In one of the early works on flows in curved pipes, Mori and Nakayama (1964) studied the effect of curvature on secondary flows. Over a wide range of laminar- and turbulent regimes, they noted that fluid is driven to the outer wall by centrifugal forces creating vortices in the cross section as shown in Figure 2. In addition, they noticed that secondary flows create an extra flow resistance which depends on the ratio of the wheel to the pipe radii R/a affecting pressure drop for different regimes. Figure 3 depicts the friction factor λ as function of a wide range of Reynolds numbers Re. It was observed that the curvature effects is higher at laminar regimes than for turbulent flow. In fact, the diminution of curvature effect is even more evident at higher $\mathrm{Re} \sim 10^4$. Furthermore, the critical Reynolds number Re_c, at which transition to turbulent flow occurs, increases as radii ratio R/a diminishes, i.e. when curvature effect augments.

White and Bond (1971) pointed out the advantage of using a small scale hollow shaped wheel for the estimation of friction factors of fluids containing high molecular weight species where shear degradation of the molecules can occur under conditions of high local shear stresses (e.g. in pumps or valves), otherwise present in standard flow loop configurations.

In the work of Urdahl et al.(1997) a closed wheel flow loop is used to evaluate the effective viscosity of live oil. The imposed rotation produces a relative velocity between fluid and pipe wall resembling transportation of the fluid in a pipe. They found that, at constant temperature, viscosity increases with higher velocities when mixing between oil- and water phase takes place. Johnsen et al.(2001) used also a rotating wheel to calculate the apparent viscosity of emulsion through measurements of torque at a wide range of tangential velocities ranging from 0.7 m/s to 3.0 m/s. They compared the results with data obtained from viscometers and traditional flow loops, finding reasonable agreement with emulsion of $50\% - 60\%$ water cut.

Johnsen and Rønningsen (2003) applied the wheel shaped loop to study water-in-oil emulsions with several live North Sea oils with saturation pressures up to 100 bar and water cuts up to 90%. The method is shown to provide useful estimates of emulsion viscosity for live oils.

Visualization of the flow in these types of experiments is usually limited. In this context, the present work is an attempt to better understand the flow phenomena inside the wheel through detailed CFD computations and comparison of Torque measurements. During the last decade SINTEF, ConocoPhillips, and Total have developed LedaFlow, a multiphase numerical tool in order to predict multiphase flow phenomena in pipelines. This tool has been extended to handle the rotating wheel geometry using the quasi-3D (Q3D) approach. The Q3D approach compromises speed and accuracy by averaging the flow over transversal slices and is described in more detail below. This approach will also be compared to full 3D simulations carried out using a

Figure 1: Wheel Flow Loop located at the Tiller Laboratory, SINTEF Norway.

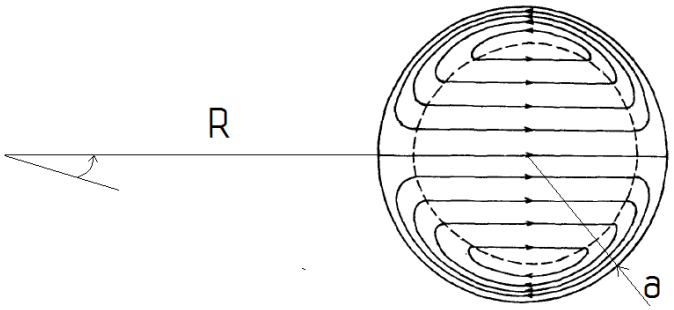

Figure 2: Secondary flow at large Dean number ($\mathrm{De} = \mathrm{Re}\sqrt{\frac{a}{R}}$), Mori and Nakayama (1964).

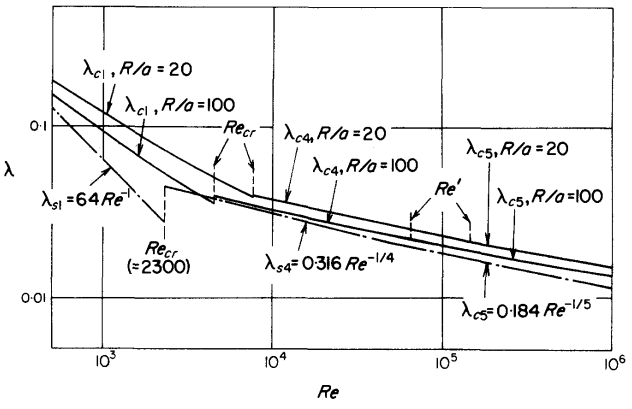

Figure 3: Friction factor as a function of Reynolds number Re for different R/a, Mori and Nakayama (1966).

commercial CFD software, as explained later on.

MODEL DESCRIPTION

Quasi-3D model (Q3D)

The model and numerical method, together with some applications have been described previously in Laux et al. (2007; 2008b; 2008a), Ashrafian et al. (2011) and Mo et al. (2014). The model is based on a multi-field concept where mass and momentum equations are formed for all fields in question. This means that for 3-phase flows we normally deal with 9 fields and for 2-phase flow with 4 fields. In our case the mass and momentum equations for each phase are obtained by merging all the fields of a phase into a common transport equation. This process introduces simplifications of the physics but also reduces the solver requirements since the number of equations is reduced. The turbulence is modeled using a $k-\ell$ model where k is the turbulent kinetic energy and ℓ is a turbulent length scale (Laux et al. 2007). Transport equations for turbulent kinetic energy is solved for each phase while the turbulent length scales are solved by a Poisson equation, using a length scale boundary condition at the walls and the large scale interfaces. The sizes of the dispersed fields (bubbles and droplets) are represented by evolution equations for the Sauter mean diameter. The large scale interfaces (LSIs) are reconstructed from the predicted phase volume fractions without solving an own transport equation for fraction functions. At each side of the LSI the model behaves as an Euler-Euler model with a continuous phase containing possible dispersed phases. At the LSI the momentum exchange between the continuous fluids (phases) is computed from standard wall functions for rough walls, see e.g. Ashrafian and Johansen (2007). The roughness of the large scale interface is computed by a Charnock model (1955). The same type of wall functions are used to represent the wall boundary conditions (wall friction).

Finally, the model is simplified by assuming small variation over the slices. This allows slice averaging the equations over the transversal dimension (z) of the pipe, as illustrated in Figure 4, thereby reducing the spatial dimensionality. This is important in order to reduce computational time significantly without sacrificing too much of the physics. In addition the model allows for vertical pipe bends. The bends are composed of bend segments with constant radius of curvature. This approach is therefore very well adapted to handle the wheel geometry. In each of the bent segments we use local spherical coordinates, which after the slice averaging is reduced to 2D polar coordinates. The numerical methods applied in this work have been explained previously in Laux et al. (2007). The temporal discretization is first order implicit Euler, while the spatial discretization is using the total variation diminishing (TVD) compliant third order scheme ACUTER (Meese, 1998).

Wheel

The simulation domain is sketched in Figure 5. The geometry has the shape of a wheel with radii ratio $R/a = 40$. For our cases the wheel is filled with two fluids. The wheel and fluids are initially at rest. When the simulation is started the wall velocity is either ramped up or set instantaneously to a given rotation velocity $U^{\text{wall}}(r) = (r/R)U_0^{\text{wall}}$. During the simulations the wall shear stress is directly calculated. The torque is then given by:

$$T = \int dA^{\text{wall}} \tau^{\text{wall}}(r,\theta) r \tag{1}$$

where $dA^{wall} = dA^{\text{wall}}(r,\theta)$ is the differential wall area. For Q3D the total torque at a given time is then calculated based on the wall shear stress for each slice as:

$$T = \sum_{i=1}^{N_X} \sum_{j=1}^{N_Y} \tau_{j,i}^{\text{wall}} A_{j,i}^{\text{wall}} (R - a + y_j) \tag{2}$$

where (j,i) is cell index across and along the pipe respectively and N_Y, N_X is the number of cells in the given directions. Also $\tau_{j,i}^{\text{wall}}$ is the shear stress and $A_{j,i}^{wall}$ is the slice wall area (two sides) for the given Q3D slice.
If the wheel radius R is large compared to the pipe radius a the following approximation can be used:

$$T \approx 2\pi a R^2 \int_0^{2\pi} \tau_{\text{1D}}^{\text{wall}}(\theta) d\theta \tag{3}$$

Using 1D-collapsed Q3D variables (cross-sectionally averaged) we get:

$$T \approx R \sum_{i=1}^{N_X} \tau_{\text{1D},i}^{\text{wall}} A_{\text{1D},i}^{\text{wall}} \tag{4}$$

where $\tau_{\text{1D},i}^{\text{wall}}$ is the 1D collapsed wall shear stress in 1D-cell i and $A_{\text{1D},i}^{\text{wall}}$ is the wall area for this 1D-cell.

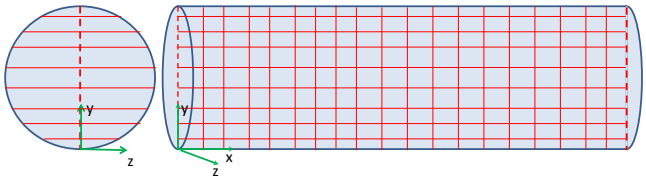

Figure 4: Grid layout of a pipe. The model equations and predicted field quantities are averaged over the slices seen in left part of the figure.

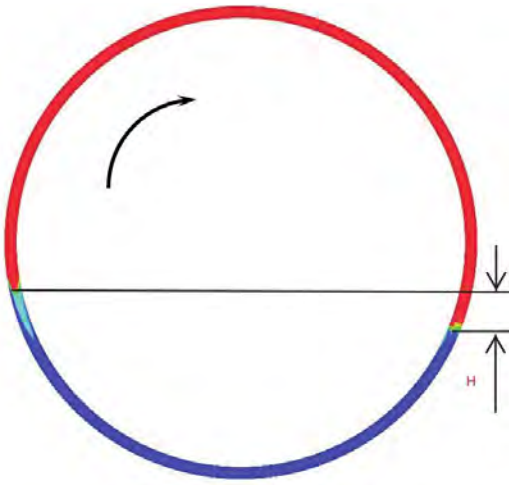

Figure 5: Sketch of a $R = 1$ m radius wheel made of $d = 5$ cm diameter pipe. Here the wheel is filled with approximately $(40\%, 60\%)$ of heavy 'blue' and light 'red' phases respectively.

Fluent's VOF model (3D)

Fluent 14.5 was used to simulate the full 3D wheel geometry. We employed the compressive volume of fluid method (VOF) to simulate the two-phase flow phenomena. The VOF method uses a color function, F, to capture the phase fractions and identify the free surface position. The color function is defined as a step function which represents the volume fraction of one of the fluids within each cell. When F is equal to 0 or 1 the cell is away from the interface and the cell is fully filled with one phase, while for values between 0 and 1 the cell is filled with both phases and therefore the cell contains a free surface. VOF belongs to the so called one-fluid family of methods, where a single momentum equation is solved for the domain and the resulting velocity field is shared among the phases. Additionally, in cases where the interface is clearly defined (segregated array of phases – as seen in Fig. 5) good predictions are expected. On the other hand, in the case that dispersions are formed, the VOF model does not perform well. In that case, as will be shown later, coupling with an Euler-Euler approach is desired. Due to Re $\sim 10^4$ in several cases, the turbulence needs to be considered, and modeled by means of the Reynolds Averaged Navier-Stokes equation and the realizable k-ε model. The latter solves two additional transport equations for the turbulent kinetic energy and the dissipation rate. A complete description of the method and the governing equations can be found in Fluent Theory Guide by ANSYS, Inc (2013).

Experimental setup

The Wheel Flow Loop consists of a 5.25 cm inner diameter stainless steel pipe bent into a 1 m radius wheel shaped loop which gives a total volume of 13.4 *litres*. The wheel used in the current tests can be operated at 250 bar of pressure and is placed inside a climate chamber for temperature control from -5 to $+60$ °C. Furthermore, the wheel has a shorter section consisting of a sapphire pipe for visual observations of phenomena inside the wheel. There is a video camera attached to the wheel which follows it during rotation and thus can capture videos from all positions.

The wheel is instrumented with temperature sensor PT100, pressure sensor and a Shaft Type Reaction Torque Transducer from Sensotec with a range up to 135 N.m. Additionally, filling of the wheel is done by high pressure pumps outside the wheel chamber and all components, liquids and gases, are filled by weight with an accuracy of ± 5 g. As will be shown later, experiments using different mixtures were performed: air/water, oil/water and oil/gas with significant CO_2 content. For CO_2 cases, the amounts filled of each compound are given in Table 1.

Table 1: Mass composition of CO_2 experiment

Compound	Amount [g]	Mass fraction [%]
CO_2	676	8%
CH_4	965	12%
Oil	6479	80%

At 60 °C this gave a pressure of 250 bar. The wheel was rotated at various velocities ranging from 0.05 m/s to 2 m/s as for the 3D and Q3D simulations. Experiments were performed at temperatures ranging from 25 °C to 55 °C with steps of 10 °C between. The other experiments were run at approximately standard conditions.

RESULTS

In this work several cases involving the three different mixtures have been selected for comparison of experimental data with numerical results obtained by the classic VOF method and our Q3D approach. The properties of air, water and oil are listed in Table 2. Additionally, different meshes of our wheel were generated for Fluent's VOF and LedaFlow-Q3D simulations.

Table 2: Fluid properties at $P = 1$ bar and $T \approx 20$ °C

	Air	Water	Oil
Density [kg/m^3]	1.2	1000	800
Viscosity [Pa.s]	1.9E-5	1.0E-3	3.2E-3

Some numerical simulations using Fluent were performed with two different meshes. The coarse mesh is composed of $\approx$ 80000 cells while the refined mesh has a total of $\approx$ 230000 cells. The difference in the calculated torque on the two meshes was less than 2%. The coarse mesh provides sufficiently accurate results with less computational effort; therefore the coarse mesh was adopted for the subsequent simulations. The Q3D approach used less cells, approximately 5000.

As seen in Figure 6, the steady-state is reached for both simulations ($t > 12$ s) even though initial conditions are quite different. For instance, at the beginning Fluent imposes *instantaneously* full velocity generating a high torque to spin the wheel.

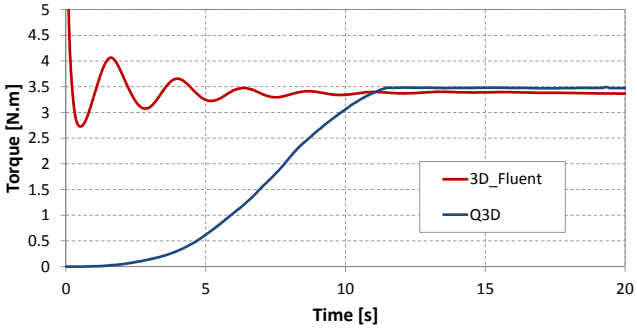

Figure 6: Transient evolution of torque for Fluent and Q3D.

In Q3D the wall velocity was slowly increased in order to help convergence, unlike the Fluent's VOF which did not evidence any problem related to convergence when using a step velocity.

It should be noted that, for calibration purposes, a constant offset was applied to ensure that experimental torque vanishes at zero velocity for all mixtures. For instance, an offset 0.49 N.m was applied in air/water mixture, while 0.37 N.m in oil/water mixture. Furthermore, due to uncertainties and current limited understanding of experimental torque oscillations, we try to focus on the comparison of qualitative flow behaviour in the Wheel. As further work, improvement of raw data treatment, as well as Wheel balancing, will be assessed, since in some cases standard deviation can reach

up to 1.75 N.m.

Air and water mixture $\alpha_W = 40\%$

The first mixture is composed of 60% air and 40% water. Here different velocities are imposed and torque measured for each velocity. The height H shown in Figure 5 will balance the torque needed to rotate the wheel and is correlated to wall shear stress. Visual comparison between LedaFlow-Q3D and Fluent's VOF showed that H values are very similar.

For none of the cases, carry-over was predicted and main contribution of torque is due to water phase. Figure 7 shows that numerical results are below experimental data with a maximum difference around 1.2 N.m at 2 m/s. Furthermore, Fluent's VOF and LedaFlow-Q3D presented very similar results in cases where the interface is clearly identified, evidencing the prediction capabilities of both tools, although Q3D uses significantly less cells. Regarding computational effort, Fluent's VOF took 4.5 hours over 6 cores, while LedaFlow-Q3D spent approximately 2 hours over 2 cores in order to simulate 20 seconds.

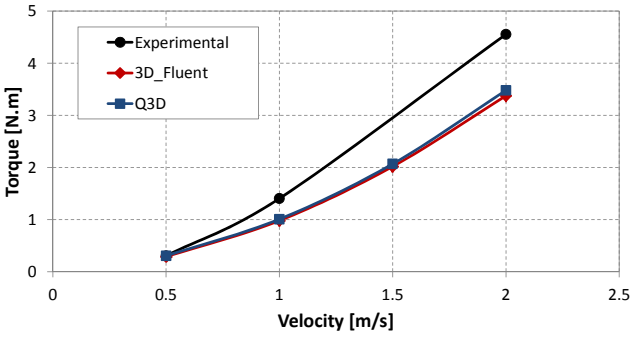

Figure 7: Torque versus velocity for air-water mixture.

Oil and water mixture $\alpha_W = 50\%$

Oil and water composes the second mixture, filling the wheel evenly. Due to small difference between densities, one phase carries the other, generating emulsions when velocity is above 1 m/s.

According to Figure 8, torque also increases with velocity and is still underestimated. For instance, at the maximum velocity 1 m/s the Q3D result is 0.7 N.m below experimental, while the difference between Fluent's VOF and experimental results is 0.8 N.m.

CO_2 mixtures $\alpha_{CH_4-CO_2} = 22.2\%$

The molar composition of gas in the third mixture is 15.3% CO_2, 61.3% CH_4 among other components (mass composition is detailed in Table 1), with $GOR = 220\ \mathrm{m^3/m^3}$. An increasing-decreasing stepwise rotation velocity is imposed to the wheel at different pressure-temperature conditions as seen in Figure 9. Comparison between lab data and numerical results of torque versus wheel velocity is presented in Figures 10 and 11. Notice that error bars represent the standard deviation around the mean torque value indicating a transient effect due to changes in the velocity, evidencing oscillations in torque for some points. However, points with small deviation do not show bars.

Experimentally, it is observed that torque increases with velocity until a certain velocity is reached and liquid starts to be carried over, causing a sudden drop in torque. When deceleration begins, lower torque values are measured and hysteresis is clearly evidenced.

Q3D results showed that hysteretic behaviour is predicted

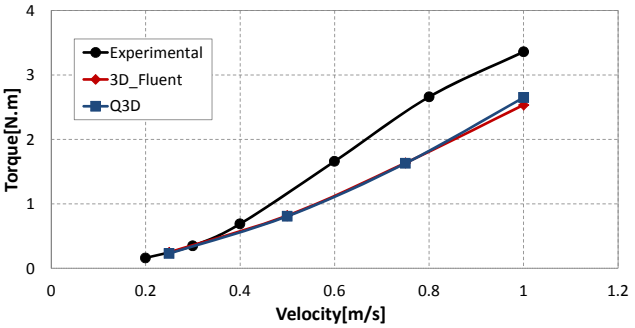

Figure 8: Torque versus velocity for oil-water mixture.

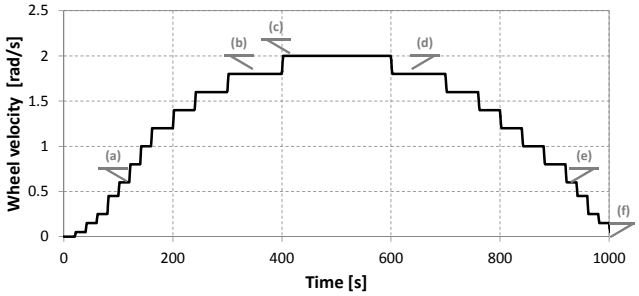

Figure 9: Stepwise velocity imposed to the wheel.

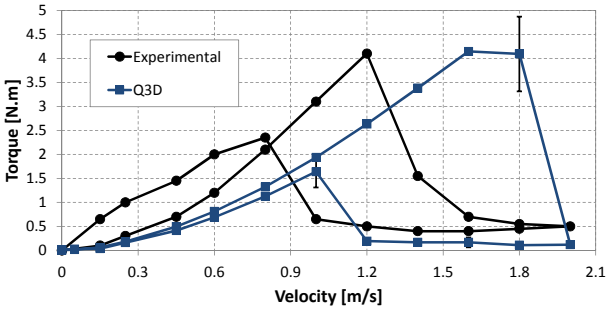

Figure 10: Torque versus velocity for CO_2 mixture at $P = 182.4$ bar and $T = 15.3\ ^\circ$C.

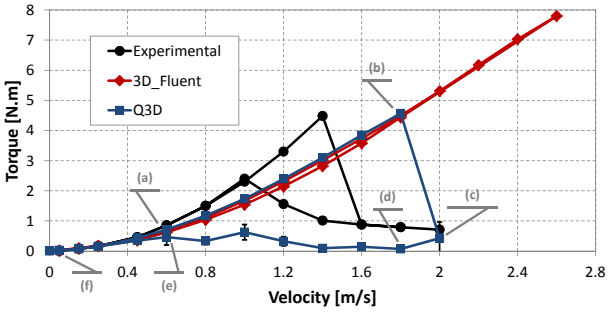

Figure 11: Torque versus velocity for CO_2 mixture at $P = 250$ bar and $T = 60\ ^\circ$C.

qualitatively when the particle size equation is solved (i.e. VOF coupled with an Euler-Euler approach with dynamic of particle size) and coalescence time is increased to delay formation of larger bubbles which separate out of the liquid phase. Moreover, Figure 10 shows in detail that the predicted velocity needed to cause torque drop differs in 0.6 m/s from experimental, whereas in Figure 11, the difference is 0.4 m/s. Thus, the numerical model underestimates the torque needed for a given velocity and carry over starts at higher velocity than observed in experiments.

On the other hand, as expected the results obtained with Fluent's VOF did not present the abrupt drop in torque and hysteretic behaviour, because the dynamics of particle size is not modelled in VOF.

Figure 12 shows phase distribution at different times. Notice that each snapshot is related to Figures 9 and 11 showing how the wheel velocity evolves and the associated average torque for each velocity. When the wheel accelerates, liquid is carried over through the gas cap region and fine bubbles progressively entrains the liquid front. After $t = 402$ s the interface completely vanished (the gas phase is fully dispersed in the liquid) causing a torque drop as shown at $t = 650$ s. Then, as wheel velocity decreases, bubbles start to coalesce and eventually the gas cap is restored, generating a small torque recovery.

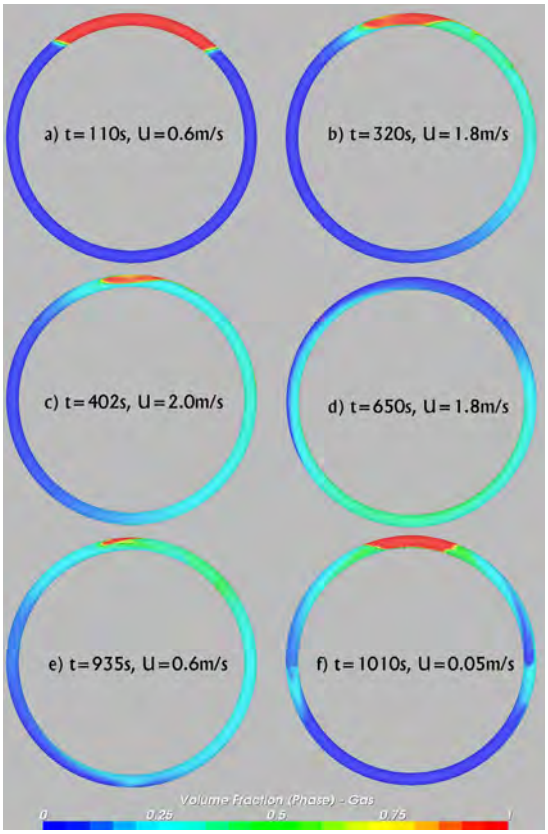

Figure 12: Results from Q3D approach for a CO_2 mixture at different velocities – clockwise direction ($P = 250$ bar and $T = 60\,^{\circ}$C).

CONCLUSION

The conclusions are:

1. Numerical results using LedaFlow-Q3D approach and Fluent's VOF were compared with lab data for three different mixtures. Predictions are generally below experimental data in all cases. Qualitatively, both VOF and Q3D are able to reproduce the torque dependence on wheel velocity. And, Q3D is able to predict the drop in torque for high velocities.

2. In cases where the interface is defined and phases segregated, there is a close agreement between Fluent's VOF and LedaFlow-Q3D results.

3. Relative error between VOF and Q3D is below 4% and may be considered insignificant when taking into account that Q3D simulations were faster and used less cells. The minor importance of secondary flow (3D effect) for the radii ratio $R/a = 40$ and flow regime may explain the close agreement.

4. Dynamic treatment of dispersed phase particle size is a critical element to reproduce the hysteresis on torque.

Current work is focused on mitigating the difference between experimental and numerical results. In particular, the large oscillations in torque measurements need to be further understood. Finally, a coupled VOF-Multi Fluid approach in Fluent, including droplet size modeling, will be compared to the Q3D results.

ACKNOWLEDGEMENT

The financial support to the Leda Project, the long-time contributions from the Leda Technical Advisory Committee, as well as permission to publish, by Total, ConocoPhillips, and SINTEF are all gratefully acknowledged. Our colleagues Ernst Meese, Runar Holdahl, and Jørn Kjølås (SINTEF), Wouter Dijkhuizen and Dadan Darmana (Kongsberg Oil & Gas Technologies), Harald Laux (OSRAM Opto Semiconductors GmbH, Regensburg), and Alain Line (INSA, Toulouse) are acknowledged for their contributions to the development.

REFERENCES

ALMEIDA, A.S. *et al.* (2010). "CCGS opportunities in the Santos basin pre-salt development". Society of Petroleum Engineers, Rio de Janeiro, Brazil.

ANSYS (2013). "14.5 Fluent Theory Guide". *ANSYS, Inc.*

ASHRAFIAN, A. and JOHANSEN, S. (2007). "Wall boundary conditions for rough walls". *Progress in Computational Fluid Dynamics*, **7(2-4)**, 230–236.

ASHRAFIAN, A. *et al.* (2011). "Multidimensional modeling of stratified wavy three-phase flows". *Rio Pipeline Conference & Exposition, Sep. 20-22*.

CHARNOCK, H. (1955). "Wind stress on a water surface". *Quart. J. Roy. Meteor. Soc*, **81**, 639–640.

JOHNSEN, E.E. *et al.* (2001). "A simplified experimental approach for measuring viscosity for water-in-crude-oil emulsions under flowing conditions". *J. Dispersion Science and Technology*, **22**, 33–39.

JOHNSEN, E. and RØNNINGSEN, H. (2003). "Viscosity of 'live' water-in-crude-oil emulsions: experimental work

and validation of correlations". *J. Petroleum Science and Engineering*, **38**, 23–36.

LAUX, H. *et al.* (2007). "Simulation of multiphase flows composed of large scale interfaces and dispersed fields". *Proc. Int. Conf. Multiphase Flows, Leipzig, July 9-13th*.

LAUX, H. *et al.* (2008a). "Multi-dimensional simulations of slug and slug-like flows in inclined pipes and channels". *6th North American BHRG Conference on Multiphase Technology*. Banff, Canada.

LAUX, H. *et al.* (2008b). "Multidimensional simulations of multiphase flow for improved design and management of production and processing operation". *2008 Offshore Technology Conference*. Houston, Texas, U.S.A. OTC-19434.

MEESE, E.A. (1998). *Finite volume methods for the incompressible Navier–Stokes equations on unstructured grids*. Ph.D. thesis, NTNU.

MO, S. *et al.* (2014). "Quasi-3d modelling of two-phase slug flow in pipes". *The Journal of Computational Multiphase Flows*, **6**, 1–12.

MORI, Y. and NAKAYAMA, W. (1964). "Study on forced convective heat transfer in curved pipes (1st report, laminar region)". *Int. J. Heat Mass Transfer*, **8**, 67–82.

MORI, Y. and NAKAYAMA, W. (1966). "Study on forced convective heat transfer in curved pipes (2nd report, turbulent region)". *Int. J. Heat Mass Transfer*, **10**, 37–59.

RASCH, A. *et al.* (2001). "Evaluation of a low dosage hydrate inhibitor in hydrocarbon fluid systems at high subcooling". *Presented at 10th International Conference Multiphase '01*, 13–15. Cannes, France.

URDAHL, O. *et al.* (1997). "Viscosity measurements of water-in-crude-oil emulsions under flowing conditions: A theoretical and practical approach". *Colloids and Surface A: Physicochemical and Engineering Aspects*, **123**, 623–634.

WHITE, D. and BOND, J. (1971). "A low shear rate turbulent flow apparatus". *Applied Scientific Research*, **23**, 368–372.

ZAIN, Z. *et al.* (2001). "Evaluation of CO2 gas injection for major oil production fields in malaysia - experimental approach case study: Dulang field". Presented at SPE Asia Pacific Improved Oil Recovery Conference, Kuala Lumpur, Malaysia.

10th International Conference on CFD in Oil & Gas, Metallurgical and Process Industries
SINTEF, Trondheim, Norway CFD 2014
17-19 June 2014

MODELLING OF PARTICLE TRANSPORT AND BED-FORMATION IN PIPELINES

C. Narayanan*, S. Gupta, D. Lakehal

ASCOMP GmbH, Zurich, SWITZERLAND
*Corresponding author, E-mail address: chidu@ascomp.ch

Keywords: Two-phase flow, Eulerian-Lagrangian method, black powder, four-way coupling, VLES, LES

ABSTRACT

Particle transport and bed formation in gas and condensate pipelines could occur under various flow regimes, from dilute flows to high mass-loading conditions, to conditions where particle beds form in the pipeline. Proper modelling requires a comprehensive approach that can handle all the different regimes. A range of complex phenomena have to be accounted for, including turbulence of the carrier phase, particle-turbulence and particle-wall interactions, surface roughness effects, particle-particle interactions, particle agglomeration, deposition, saltation and re-suspension. We present here recent results of TransAT's particle transport predictions to conditions of one-way, two-way and four-way particle-flow coupling, spanning the three flow regimes evoked: (i) dilute suspensions, (ii) high mass-loading conditions, and (iii) particle beds in the pipeline.

INTRODUCTION

In dense particle-beds systems, the flow behaves in a very subtle way, with complex physical mechanisms taking place near the wall, where the particles accumulate. A number of simplified analytical solutions to determine the conditions of particle-bed removal in pipes and channels have indeed been proposed, but with limited success due to the simplifications implied. Today, intensive research is devoted to understand the conditions for dense particle-bed formation and removal, in hydrocarbon and in other related areas, but the difficulties encountered in measurements and flow visualization have hindered this progress.

In particle-laden pipelines, the particles tend to be transported through the pipeline by gas flow under specific conditions. The velocity required to move the particles could in some cases be estimated based on the pipeline diameter, gas pressure, and particle size and density (Tsochatzidis and Maroulis, 2007; Smart, 2007). Deposition of black powder will occur if there are solids in the pipeline fluid and the velocity is not high enough to drag the particles along by viscous flow forces. Sediment deposits can lead to blockage of the line, especially during pigging, while flowing powder can damage compressors, plug filters and damage user equipment. In extreme cases, the piping could be half full of black powder, causing shutdown of the compressor and up to 60 tons of black powder could subsequently be removed from the piping. Similarly, promising oil extraction techniques such as hydraulic fracturing involve transporting a proppant, such as sand, into rock fractures to keep them open and facilitate oil flow.

There are various incentives to explore the use of advanced prediction methods for this class of flows, featuring Lagrangian particle tracking spanning one to four-way particle-flow coupling, instead of average Euler-Euler formulations, Large Eddy Simulation (LES) instead of RANS, and transient rather than steady-state simulations. The current study which falls in this spirit presents a hierarchical modelling framework for the particle transport regimes mentioned above including validation and application of the model to select practical figures-of-merit (pressure drop in particle laden flows in pipes, and particle bed-formation and prediction of critical velocity of transport in pipes).

The modelling focuses on the statistical representation of particle-particle interactions close to the close-packing limit (collision stress) and particle-wall interactions, including the effect of statistical roughness. In terms of turbulence modelling, unsteady simulations will be used. Given the limitations of the RANS approach, LES and Very Large Eddy Simulation (VLES) methods will be emphasized, which have the ability to provide better flow unsteadiness needed to lift up the particles and move the deposited bed. The results were obtained with the CMFD code TransAT. The main issues and limitations will be discussed in the paper.

THE PHYSICAL MODEL IN Trans*AT*

The Numerical Approach

The CMFD code TransAT© (2014) is a multi-physics, finite-volume solver for the multi-fluid, Navier-Stokes equations. It uses structured multi-block meshes, and uses both the body-fitted coordinates (BFC) and immersed surface techniques (IST) for mesh generation. The solver is pressure based corrected for low-Mach number compressible flows. High-order schemes can be employed; up to 2^{nd}-order schemes in space and 5^{th} order Runge-Kutta scheme in time. Multiphase flows with or without phase change can be tackled using interface tracking for both laminar and turbulent flows (Level Set and Phase Field), the phase averaged mixture model, and

the Lagrangian particle tracking, including with heat transfer.

Turbulence Simulation (LES vs. VLES)

The basic idea of VLES (Johansen et al. 2004) is to combine RANS and LES for a specific flow, where the size of the most important scales can be identified. Here the flow is decomposed into a resolved and a subscale part, the latter being independent of the grid (in contrast to the sub-grid scale modelling in LES), but is dependent on the flow, and thus the flow characteristic length scale. Larger scales than this cut-off scale are resolved, while the rest are modelled, though with more refined statistical turbulence models than zero-equation ones, because turbulence sub-scales are neither isotropic nor independent of the boundary conditions, as speculated in LES. The approach assumes that the Kolmogorov equilibrium spectrum applies to the sub-filter.

Lagrangian modelling for dilute systems

In this formulation, individual particles are tracked in a Lagrangian way within an Eulerian flow field. One-way coupling refers to the particle cloud not affecting the carrier phase, because the field is dilute. In contrast, two-way coupling refers to the scenario where the flow and turbulence are affected by the presence of particles (mildly charged but still in the dilute regime). In the one- and two-way coupling cases, the carrier phase is solved in the Eulerian way, i.e. solving for the continuity and momentum equations:

$$\nabla \cdot \boldsymbol{u} = 0 \tag{1}$$

$$\partial_t(\rho \boldsymbol{u}) + \nabla \cdot (\rho \boldsymbol{u}\boldsymbol{u}) - \nabla \cdot \boldsymbol{\tau} = -\nabla p + \boldsymbol{F}_b + \boldsymbol{F}_{fp} \tag{2}$$

This set of transport equations is then combined with the Lagrangian particle equation of motion:

$$d_t(v_{p_i}) = -f_d \frac{9\mu}{2\rho_p d_p^2}\left(u_{p_i} - u_i[x_p(t)]\right) \qquad f_d = 1 + 0.15 Re_p^{2/3} \tag{3}$$

where $\boldsymbol{u}$ is the velocity of the carrier phase, $\boldsymbol{u}_{p_i}$ is the velocity of the carrier phase at the particle location $\boldsymbol{x}_{p_i}$, $\boldsymbol{v}_{p_i}$ is the particle velocity, $\boldsymbol{\tau}$ is the viscous stress and p the pressure. The source terms in Eq. (2) denote body force $\boldsymbol{F}_b$, and the rate of momentum exchange per volume between the fluid and particle phases, $\boldsymbol{F}_{fp}$. The coupling between the fluid and the particles is achieved by projecting the force acting on each particle onto the flow grid:

$$F_{fp} = \sum_{i=1}^{N_p} \frac{\rho_p V_p}{\rho_m V_m} R_{rc} f_i W(x_i, x_m) \tag{4}$$

where *i* stands for the particle index, N_p for the total number of particles in the flow, f_i for the force acting on a single particle centered at $\boldsymbol{x}_i$, R_{rc} for the ratio between the actual number of particles in the flow and the number of computational particles, and W for the projection weight of the force onto the grid node $\boldsymbol{x}_m$, which is calculated based on the distance of the particle from those nodes to which the particle force is attributed. V_m is the fluid volume surrounding each grid node, and V_p is the volume of a single particle (Narayanan and Lakehal, 2006).

Lagrangian modelling for dense systems

The Eulerian-Lagrangian formulation for dense particle systems featuring mild-to-high volume fractions (α > 5%) in incompressible flow conditions is implemented in TransAT as follows (Eulerian mass and momentum conservation equations for the fluid phase and Lagrangian particle equation of motion):

$$\partial_t(\alpha_f \rho) + \nabla \cdot (\alpha_f \rho \boldsymbol{u}) = 0 \tag{5}$$

$$\partial_t(\alpha_f \rho \boldsymbol{u}) + \nabla \cdot (\alpha_f \rho \boldsymbol{u}\boldsymbol{u}) = -\nabla p + \nabla \cdot \boldsymbol{\tau} + \boldsymbol{F}_b + \boldsymbol{F}_{fp} - \boldsymbol{F}_{coll} \tag{6}$$

where α_f is the volume fraction of fluid ($\alpha_f + \alpha_p = 1$), $\boldsymbol{u}$ is the velocity of the carrier phase, $\boldsymbol{u}_{\mathrm{p}}$ is the velocity of the carrier phase at the particle location, v_p is the particle velocity, Π is the sum of viscous stress σ and pressure p, τ is the turbulent stress tensor (depending whether RANS, V-LES or LES is employed).

In this dense particle context, the Lagrangian particle equation of motion (Eq. (3)) should have an additional source term $\boldsymbol{F}_{coll}$ denoting the inter-particle stress force. The inter-phase drag model in (Eq. (3)) is set according to Gidaspow (1986). The particle volume fraction is defined from the particle distribution function (ϕ) as

$$\alpha_p = \iiint \phi V_p dV_p d\rho_p du_p \tag{7}$$

The inter-phase momentum transfer function per volume in the fluid momentum equation (Eq. (2)) is

$$F_p = \iiint \phi V_p [A] dV_p d\rho_p du_p; \tag{8}$$

with A standing for the particle acceleration due to aerodynamic drag (1st term in the RHS of Eq. 3), i.e. excluding body forces and inter-particle stress forces (2nd and 3rd terms, respectively). The pressure gradient induced force perceived by the solids is not accounted for. The fluid-independent force $\boldsymbol{F}_{coll}$ is made dependent on the gradient of the so-called inter-particle stress, π, using

$$\boldsymbol{F}_{coll} = \nabla \pi / \rho_p \alpha_p \tag{9}$$

Collisions between particles are estimated by the isotropic part of the inter-particle stress (its off-diagonal elements are neglected.) In most of the models available in the literature π is modelled as a continuum stress (Harris & Crighton, 1994), viz.

$$\boldsymbol{\pi} = \frac{P_s \alpha_p^{\beta(=2-5)}}{max[\alpha_{cp} - \alpha_p; \varepsilon(1-\alpha_p)]} \tag{10}$$

The constant P_s has units of pressure, α_{cp} is the particle volume fraction at close packing, and the constant β is set according to Auzerais *et al.* (1988). The original expression by Harris & Crighton (1994) was modified to remove the singularity at close pack by adding the expression in the denominator (Snider, 2001); ε is a small number on the order of 10^{-7}. Due to the sharp increase of the collision pressure, near close packing, the collision force (Eq. (9)) acts in a direction so as to push particles away from close packing. In practice the particle volume fraction can locally exceed the close packing limit marginally.

ONE-WAY COUPLING: DROPLET DEPOSITION IN A PIPE

Problem setup and modeling

The example discussed here was simulated using TransAT in the context of analyzing pipeline transport of natural gas and condensates. The objective is to predict the situation illustrated in Figure 1 (Brown et al., 2008), where liquid can be entrained under strong interfacial shearing conditions in the form of droplets from the liquid layer sitting at the bottom of the pipe. These should ultimately deposit on to the walls of the tube forming a film or redeposit back onto the pool itself. The core region consists of a mixture of gas and entrained liquid droplets. In the present study, it is assumed that entrainment of liquid droplets from the film on the upper surface of the pipe is negligible; an assumption consistent with experimental observations in relatively large diameter pipes (Brown et al., 2008).

A 3D body-fitted grid containing 500.000 cells well clustered near the pipe wall was generated. Two turbulence prediction strategies were employed: URANS and LES. The reason for this comparison is to identify the predictive performance of the models in reproducing the interaction between turbulence and the particles. The Lagrangian approach (1-3) under one-way conditions were employed to track the particles together with a particle-wall interaction model. The Langevin model for particle dispersion was used for RANS (Lakehal, 2002). In the LES, periodic boundary conditions along the pipe were employed to sustain turbulence; of course the pipe was shortened in length compared to RANS ($L = 2\pi D$).

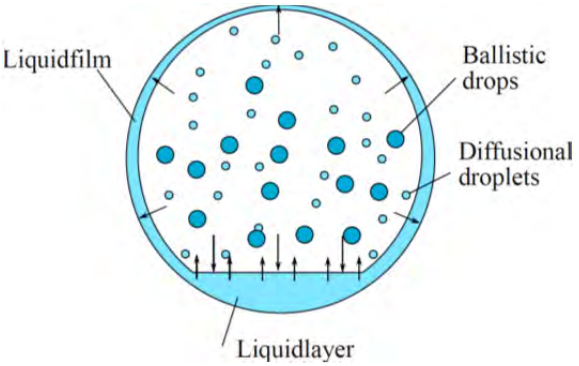

Figure 1: Schematic of the droplet entrainment model (extracted from Brown et al., 2008).

The WALE sub-grid scale model has been used for the unresolved flow scales only (not for particles). About 3000 droplets were injected, with a Gaussian size distribution around a 50 μm mean particle diameter, including: Range 1: D_p=1-48 μm; Range 2: D_p=49-85 μm ; Range 3: D_p=86-123 μm ; Range 4: D_p =124-161 μm ; Range 5: D_p =162-200 μm. Simulations were run on a 64 processor parallel cluster using the MPI protocol.

Discussion of the results

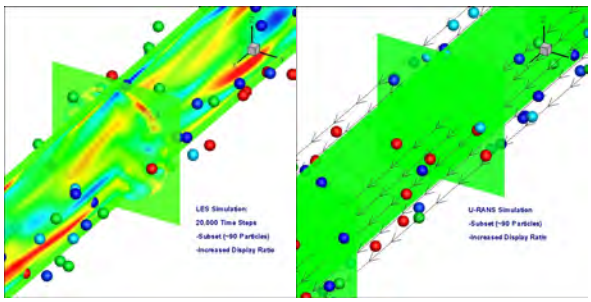

Figure 2: Snapshots of the flow in a gas pipe showing particle interaction with turbulence: left (LES); right (RANS).

The results depicted in Fig. 2 show a clear difference between URANS and LES. While the LES (left panel) depicts a clear turbulence dispersive effect on the particles, drifting some to the wall region, the URANS results (right panel) deliver a steady path of the particles with the mean flow. This is an important result, suggesting that albeit detailed 3D simulations, the results are sensitive to turbulence modeling.

The droplets population remaining in the gas core has been thoroughly studied by Lecoeur et al. (2013), and plotted as a function of two parameters (axial distance travelled in the pipe and the size of the droplets) for both RANS and LES. The results obtained show important discrepancies between the two approaches: (i) the droplet size has a more important effect in LES than in RANS: while in LES larger droplets tend to deposit faster than the smaller ones due to their ballistic nature (free-flight mechanism), in RANS, however, it seems that the smallest droplets do deposit faster than the large ones.

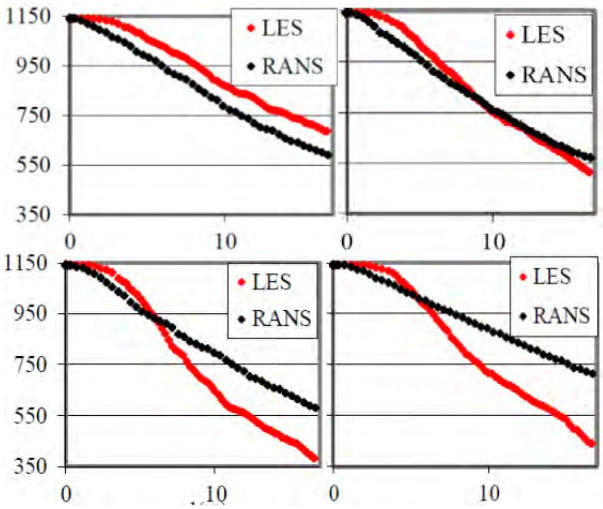

Figure 3: Cumulative number of droplets remaining in the pipe core for selected ranges of droplet sizes. (Upper panels) Range 1 (D=1-48 μm) and 2 (D=49-85 μm). (Lower panels): Range 3 (D=86-123 μm) and 5 (D=162-200 μm).

It was also found that the RANS-predicted deposition rate of droplets is rather monotone (see Fig. 4, black lines) and almost at equal rate or speed in the range 10-160 μm; differences start to be perceived for heavier droplets of diameter larger than 160 μm (see Fig. 3, black line in the 4th panel). The variation in the rate of droplet deposition is better depicted using LES, since particles of different sizes react differently to the various resolved eddies.

Looking closely at Figure 3 reveals more details about the rate of droplet deposition in the pipe. The number of droplets remaining in the gas core is shown there as a function of the axial distance travelled in the pipe, for all droplet-size ranges (10-48μm; 49-85μm; 86-123μm and 162-200μm). Smaller droplets (Range 1) tend to deposit faster in RANS than in LES; a tendency that changes gradually to Range 2 droplets that deposit equally be it with RANS or LES, to the extreme situation where ballistic droplets (Range 3 & 4) deposit much faster in LES than in RANS. Simply, LES is capable to distinguish between diffusional and free-flight deposition mechanisms (Botto et al., 2003).

TWO-WAY COUPLING: HEAVY-LOADED PARTICULATE FLOW IN A PIPE

Problem setup and modeling

The distribution of particles in a highly-loaded rough-wall channel was validated against experiments of Lain et al. (2002). The setup is a 2D channel of height 3.5cm and length 6m. The particles have a diameter of 130μm and a density of 2450 kg/m^3. The void fraction of the inflow fluid is set to a very small number (~0.001) so as to turn on the two-way coupling module. The mean inflow velocity was set to 20m/s in the x-direction with a standard deviation of 1.6m/s in x- and y-directions. The initial angular velocity of the particles was set to 1000 s^{-1}. A grid size of 125x34 was used. The simulations were run using the two-way coupling model and a Langevin forcing to account for the effects of turbulence on the particles. Further, since the pressure-drop in the channel is strongly affected by wall roughness, its effect on particles should be modelled, too. We use the model proposed by Sommerfeld and Huber (1999), which assumes that the particle impact angle is composed of the trajectory angle with respect to the wall and a stochastic component to account for wall roughness, $\alpha' = \alpha + \gamma\xi$, where ξ is a Gaussian random variable with zero mean and a standard deviation of one, and γ is a model constant. The particle wall restitution and friction coefficients are calculated using the expressions in Lain and Sommerfeld (2008).

Discussion of the results

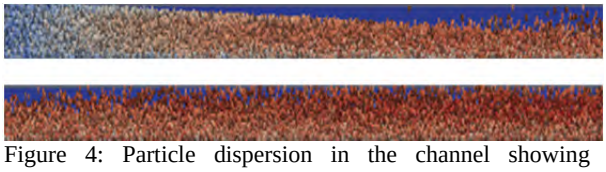

Figure 4: Particle dispersion in the channel showing re-suspension after a tendency for settling (two parts of the channel).

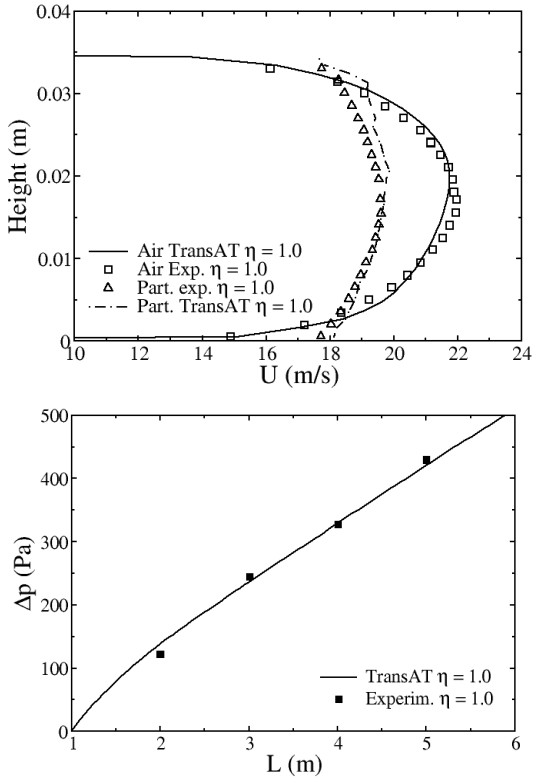

Figure 5: (upper panel) velocity profiles, and (lower panel) pressure drop in the pipe with wall roughness gradient of 1.5°, for a mass-loading of 1.0. : Exp. vs. TransAT

As seen in Fig. 4, as the simulation proceeds in time, a particle tends to move towards the bottom of the channel before re-suspension occurs thanks to the roughness model. The results in Fig. 5 (upper panel) show excellent agreement between the fluid and particle velocity profiles measured experimentally and those simulated by TransAT. The symmetry of the particle profile (like the fluid one) reflects the perfect dispersion of the particles in the channel, due to their systematic re-suspension caused by wall roughness. The lower panel of Fig. 5 shows that the simulation accurately predicts the pressure drop along the channel (the results are shown for a wall roughness gradient of 1.5 and a mass loading of 1).

FOUR-WAY COUPLING

Validation: Particle suspension sedimentation

This 3D problem was proposed by Snider (2001) as a case to validate his model. A well-mixed suspension of sand particles and air is left to settle to close pack solely due to the effect of gravity. The calculation parameters are given below. Particles are initially motionless and are uniformly, randomly distributed. The initial fluctuation in volume fraction is 0.3 on average as shown in Fig. 6. The heavy, large-size particles fall by the action of gravity in a 0.3m deep container filled with a lighter fluid (density ratio of 1/1000). The problem has an analytical solution to the evolution of the upper mixture interface between suspended particles and clarified fluid given by $h = gt^2/2$.

Particle radius	300 μm
Particle density	2500 kg/m^3
Fluid density	1.093 kg/m^3
Fluid viscosity	1.95e-5 kg/ms
Initial particle volume fraction	0.3
Size of container	13.8^{2}x30 cm^3
Comp. Grid	15x15x41

Table 1. Fluid flow conditions and parameters

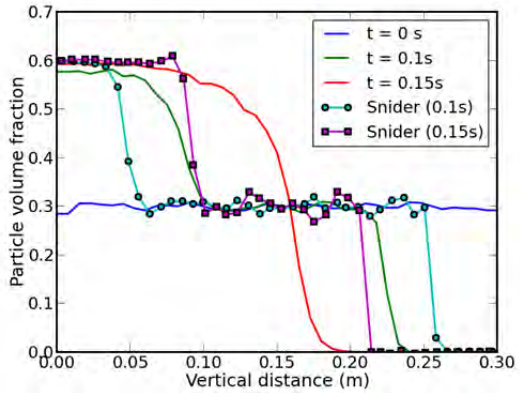

Figure 6: Volume fraction at times during sedimentation

Figure 6 shows the particle volume fractions, including comparison with the original data of Snider (2001). The interface between clarified fluid and mixture at 0.1s and 0.15s matches reasonably with Snider's (2001) data and with the analytical value of 0.25m and 0.19m from the bottom. Figure 7 shows that at 0.15s particles reach close packing at the bottom of the domain and at 0.2s no further settling has occurred. Figure 8 shows the particle distributions during settling at four instants (0.1, 0.15, 0.185 and 0.2s). The present four-way coupling solution, with the particle normal stress model as presented here and as implemented in TransAT, gives a natural settling to close pack.

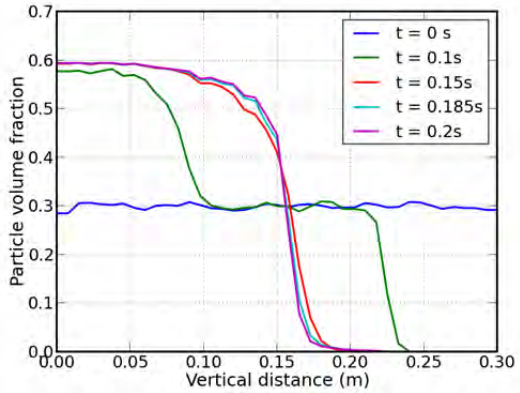

Figure 7: Volume fraction at times during sedimentation

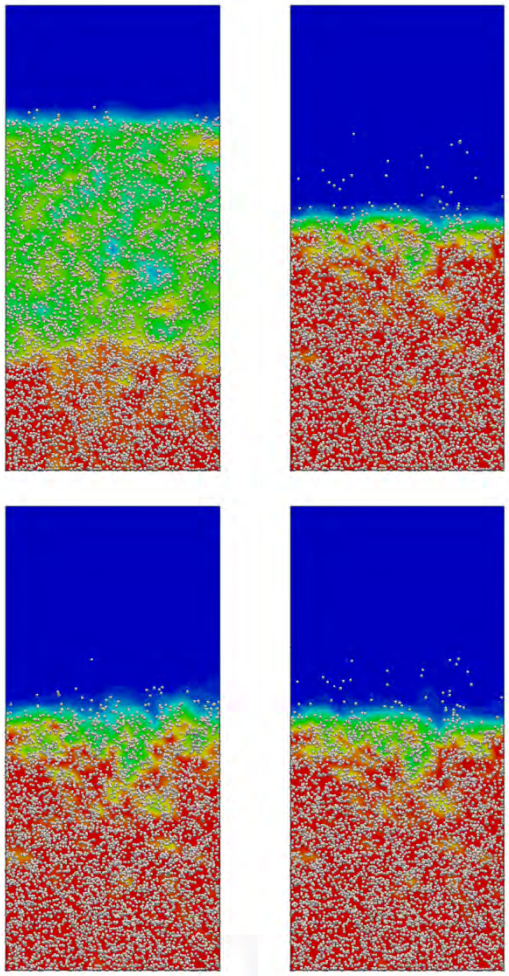

Figure 8: Particle volume-fraction distribution α_p (Red=0.6; Blue=0) at 0.1, 0.15, 0.185 and 0.2s.

Sand-particle transport in a pipeline

Danielson (2007) proposes a model to predict the critical velocity of bed formation for particle transport in pipes, based on the assumption that there is a critical slip velocity between the sand and the fluid that remains constant over a wide range of flow velocities. Sand transported in (near) horizontal pipes will drop out of the carrier flow and form a stable, stationary bed at below critical velocities. The bed height develops to an extent such that the velocity of the fluid above the bed equals the critical velocity. When the velocity reaches a critical value, sand is transported in a thin layer along the top of the bed. A steady state is reached such that the sand eroded from the top of the bed is replaced by new sand from the upstream. At higher velocities, the sand bed breaks up into slow moving dunes and further increase in velocity results in sand transported as a moving bed at the bottom of the pipe. If the velocity is above the critical velocity, sand is entrained in the fluid flow:

$$U_c = \mathrm{K}\ \vartheta^{-1/9}\, d^{-1/9}\, [gD(s-1)]^{5/9} \qquad (11)$$

where K is a model constant equal to 0.23 based on SINTEF data (Danielson 2007) and ϑ is the fluid viscosity. The sand transport simulation is made here in two-dimensions with conditions given in Danielson (2007). Particles with diameter of 250, 350 and

450 μm are simulated for fluid velocities of 0.78, 1.2 and 1.6 m/s. The particle volume fraction at the inlet is 0.1. The channel length is 0.3m and height is 0.01 m, and is covered by 12 cells in the cross flow direction.

Figure 9 shows a set of results at four time instants; each set gathers results of the cases with fluid velocities of 0.78, 1.2 and 1.6 m/s, respectively. As the simulation proceeds in time a particle bed starts to form at the bottom of the channel and the inelastic wall reflection results in a non-homogeneous particle distribution along the height of the channel. There is a slowdown of fluid in regions of higher particle volume fractions at the bottom of the channel, and acceleration of the fluid in regions of lower particle volume fraction at the top of the channel. This is well captured due to the four-way coupling between particles and fluid momentum equations. The critical velocity predicted by Eq. (11) for a 3D pipe flow under these conditions is 4 m/s. For the simulation with inlet velocity of 0.78 m/s (first panel in each set), a stable bed is predicted with the fluid velocity at the top of the bed equilibrating to ~ 3m/s. Note that this is lower than the correlation most probably due to the fact that in the channel case, there is less wall friction (only at the bottom wall) than in a pipe. When the fluid velocity is increased (2nd and 3rd panels in each set), it can be seen in the images that the bed height indeed diminishes such that the flow velocity at the top of the bed is again approximately 3m/s. Further validation of the model for 3D pipes is necessary.

Conclusions

The paper presents a simulation campaign of flows laden with solid particles of different size, under different flow conditions. Particle transport predictions were performed to conditions of one-way, two-way and four-way particle-flow coupling, spanning three flow regimes: (i) dilute suspensions, (ii) high mass-loading conditions, and (iii) suspension sedimentation and particle bed formation in pipelines.

REFERENCES

F.M. Auzerais, R. Jackson, W.B. Russel, The resolution of shocks and the effects of compressible sediments in transient settling, *J. Fluid Mech*. 195, 437 (1988).

L. Botto, C. Narayanan, M. Fulgosi, D. Lakehal, Effect of near-wall turbulence enhancement on the mechanisms of particle deposition, *International Journal Of Multiphase Flow*, 31:8. 940 (2005).

L. Brown, G. Hewitt, B. Hu, C.P. Thomson, P. Verdin, Predictions of droplet distribution in low liquid loading, stratified flow in a large diameter pipeline, In Proc. BHR Conf. Cannes, France, May 2008.

T.J. Danielson, Sand transport in Multiphase pipelines, *OTC 18691*, Proc. Offshore Tech. Conf. Texas USA, 2007.

D. Gidaspow, Hydrodynamics of fluidization and heat transfer supercomputer modeling, *Appl. Mech. Rev.* 39, 1, (1986).

S.E. Harris, D.G. Crighton, Solutions, solitary waves and voidage disturbances in gas-fluidized beds, *J. Fluid Mech*. 266, 243 (1994).

S.T. Johansen, J. Wu, W. Shyy, 2004. Filtered-based unsteady RANS computations. *Int. Journal of Heat and Fluid Flow*, 25, 10-21, (2004).

S. Lain, M. Sommerfeld, J. Kissin, Experimental studies and modelling of four-way coupling in particle-laden horizontal channel flow, *Int. Journal of Heat and Fluid Flow*, 23, 647-656, (2002).

S. Lain, M. Sommerfeld, Euler/Lagrange computations of pneumatic conveying in a horizontal channel with different wall roughness, *Powder Technology*, 184, 76-88 (2008).

D. Lakehal, On the modelling of multiphase turbulent flows for environmental and hydrodynamic applications, International Journal of Multiphase Flow, 28:5. 823-863 (2002).

N. Lecoeur, C. Narayanan and G. Hewitt, The role of turbulence modeling in the simulation of droplet transport in annular flow, Proc. ICMF 2013, Jeju, Korea, 2013.

C. Narayanan, D. Lakehal, Particle transport and flow modification in planar temporally evolving laminar mixing layers. I.Particle transport under one-way coupling, *Physics of Fluids*, Part 1, 18: 9. 093302 (2006).

J. Smart, Determining the Velocity Required to Keep Solids Moving in Pipelines, *The Journal of Pipeline Engineering*, 6 No. 1 (2007).

D. M. Snider, An Incompressible Three-Dimensional Multiphase Particle-in-Cell Model for Dense Particle Flows, *JCP*, 170, 523–549, (2001).

M. Sommerfeld, N. Huber, Experimental analysis and modelling of particle–wall collision, *Int. J. Multiphase Flow, 25*, 1457–1489 (1999).

TransAT User Manual, (2010). www.ascomp.ch/transat.

N.A. Tsochatzidis, K.E. Maroulis, Methods help remove black powder from gas pipelines, *Oil & Gas Journal*, 03 (2007).

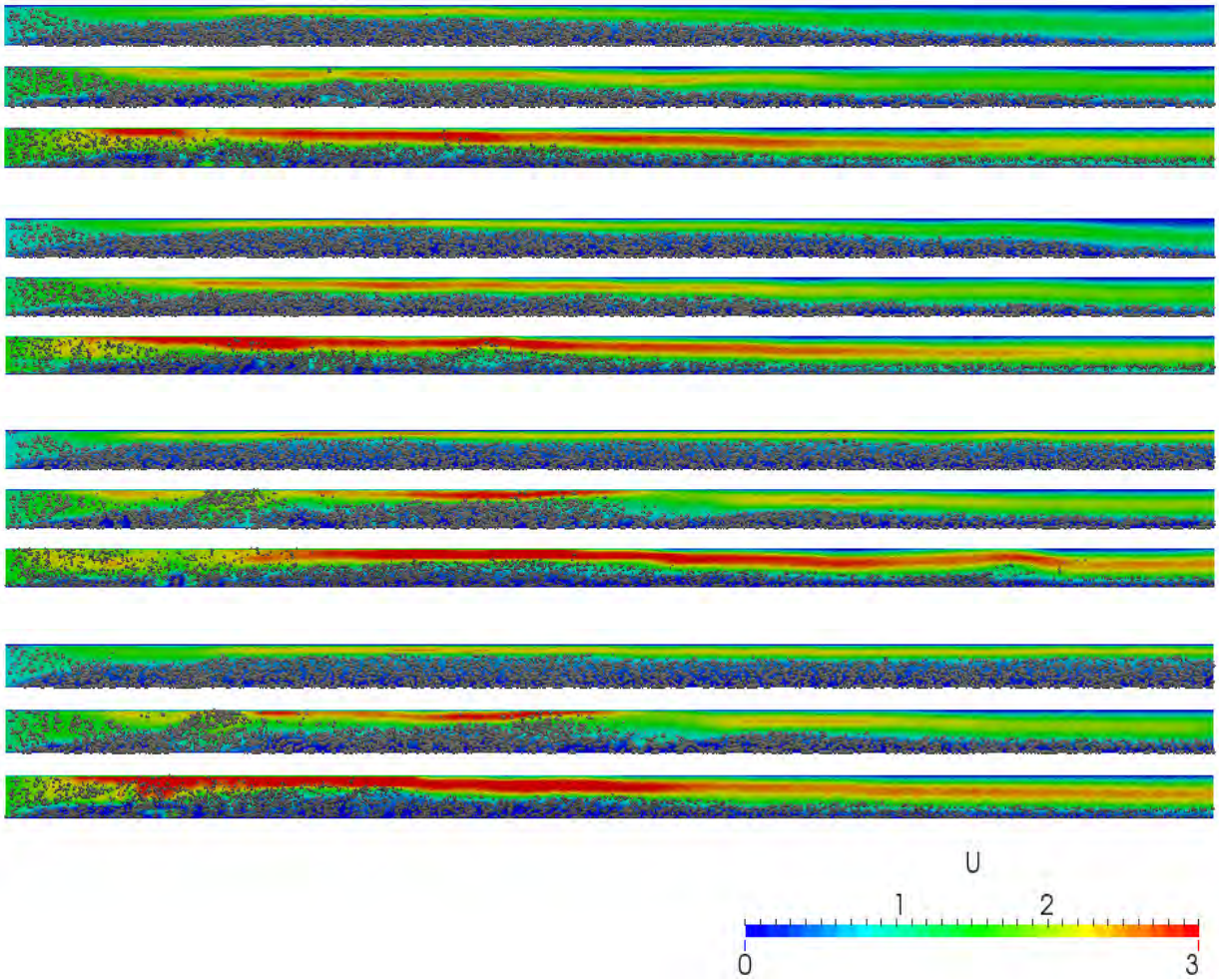

Figure 9: Particle distribution in the channel at 4 instants. Each set of panels refers to different inflow conditions (upper panel: 0.78m/s, middle panel: 1.2m/s, and lower panel: 1.6m/s). The last two time instants show the formation of a stable particle bed for the lowest inflow velocity case.

Simulation of two-phase viscous oil flow

Stein Tore JOHANSEN[1,3]*, Sjur MO[1], Jørn KJØLAAS[2], Christian BREKKEN[2] and Ivar ESKERUD SMITH[2]
[1]SINTEF Materials and Chemistry, 7465 Trondheim, NORWAY
[2]SINTEF Petroleum, 7465 Trondheim, NORWAY
[3]NTNU, Energy & Process Engineering, 7491 Trondheim, NORWAY

* E-mail: Stein.T.Johansen@sintef.no

ABSTRACT

Multiphase flows of heavy oils and other fluids with high apparent viscosity is a particular industrial challenge. Main challenges here is that interfacial waves, atomization at the large scale gas–liquid interface as well as bubble entrainment and separation all are significantly modified by high fluid viscosity. In addition the viscous liquid may behave as laminar while gas and other low viscosity liquids show turbulent behaviour. Accordingly, correct modelling of the turbulence, including correct transitional behaviour between turbulent and laminar flow becomes of great importance.

In this paper we have investigated two phase flows of gas at a rather high density and viscous oil. Experiments have been performed at the SINTEF Multiphase Flow Laboratory at Tiller, Trondheim. The experimental section was horizontal, with a pipe inner diameter of 69 mm. Pressure drop - and liquid hold-up time series, as well as video-documentation of the flow, were recorded.

The experiments have been analysed and simulated by the Quasi-3D flow model which has been developed in the LedaFlow development project. The results show that flow regimes are well predicted, as well as liquid fractions (hold-up) and pressure drops. Furthermore, some cases have been identified where the Quasi-3D concept is challenged and where the full 3D effects need special attention and modelling.

In the paper we describe the experiments in more details, discuss the general challenges on viscous flow modelling, present the special features of our Quasi-3D flow model and compare predictions to the experimental results. Finally we discuss the perspectives of multidimensional modelling as a virtual laboratory for multiphase pipe flows comprising viscous liquids.

Keywords: Two phase pipe flow, viscous fluid, turbulence, laminar-turbulence transition, Quasi-3D modelling

NOMENCLATURE

Greek Symbols

α	Volume fraction	[-]
ε	Wall roughness	[m]
ε_m	Turbulent dissipation for phase m	[m^2/s^3]
κ	Von Karman Constant (≈ 0.4)	
μ_m	Molecular viscosity for phase m	[Pa·s]
μ_m^T	Turbulent viscosity for phase m	[Pa·s]
ρ_m	Density for phase m	[kg/m^3]
θ	Pipe inclination	[°]

Latin Symbols

D	Pipe diameter	[m]
Fr	Froude number ($Fr = v_{drift} \Big/ \sqrt{gD}$)	
v_{drift}	Drift velocity, $v_{drift} = U_g - U_o$	[m/s]
g	Gravity (9.81 m/s^2)	[m/s^2]
k_m	Turbulent kinetic energy for phase *m*	[m^2/s^2]
ℓ	Turbulent length scale	[m]
L	Pipe length	[m]
R	Pipe radius	[m]
Re_g	Gas Reynolds number ($\mathrm{Re}_g = \frac{\rho_g U_{sg} D}{\mu_g}$)	
Re_l	Liquid Reynolds number ($\mathrm{Re}_l = \frac{\rho_l U_{sl} D}{\mu_l}$)	
U_k	Stream wise velocity for phase k	[m/s]
U_{sk}	Stream wise superficial velocity for phase k ($U_{sk} = \alpha_k U_k$)	[m/s]
x	Axial distance	[m]
y	Transversal distance	[m]
$\Delta x, \Delta y$	Mesh spacing	[m]

Sub/superscripts

g gas
l liquid
crit critical

INTRODUCTION

Multiphase flows containing viscous fluids appear in many oil and gas applications. Heavy oil contains large molecules and precipitates which result in a viscosity which often is strongly temperature dependent and in some cases may lead to non-Newtonian behaviour. By heating such fluids they may be transported easily as long as the temperature is kept high. However, in some cases heating and excessive insulation is very expensive and it is desirable to transport the fluids at approximately ambient temperature. Evaluation of the feasibility of such transport would rely on accurate flow models.

A special challenge here is that an oil phase at high viscosity may flow as laminar while the remaining phases (gas, water) may show turbulent behaviour. In addition, the interface structures, drainage of liquid wall films, entrainment processes and phase separation are all significantly modified by a high liquid viscosity.

Another challenge is that availability of high quality experimental data from multiphase flow in pipes larger than 2 inches is extremely scarce (Zhang et al., 2012). However, for pipe diameters less than 2 inches surface tension and wall wetting effects play a more significant role than in larger and industrial size pipes. Of the few experiments with somewhat larger pipe diameters we find Gokcal (Gokcal, 2005, Gokcal, 2008), who performed experiments in a 19 m long horizontal flow loop with inner diameter 50.8 mm. He used air and a viscous oil, where the oil viscosity varied from about 180 to 600 cP.

In a literature review (Zhang et al., 2012) it was commented that more experiments and physical models are needed in order to have appropriate understanding and good 1D model predictions. Improving the understanding of such gas/liquid flow is a major motivation of this paper.
In the paper we will discuss the capability of a multidimensional Quasi-3D model (Laux et al., 2007, Mo et al., 2012, Mo et al., 2013b, Mo et al., 2013a) in predicting this type of viscous two phase gas/liquid flows. Detailed experimental data, to be used to understand the physics and benchmark the model, has been recorded at the SINTEF Multiphase Flow facility at Tiller, outside Trondheim. This is further explained in the next section.

EXPERIMENTS

In the experiments we apply a horizontal pipe with 69 mm ID, and a test section which is 51.4 m. As the experimental loop is indoor, the fluid temperature was monitored and was kept quite constant, with less than 0.1 °C variations during one experiment. The fluid temperature in the test section varied between 18 and 23 °C between experiments. The experimental setup has been documented by (Eskerud Smith et al., 2011). In addition to the instrumentation (broad band gamma densitometers, pressure sensors) we have applied a traversing gamma densitometer. This instrument can record a statistically averaged liquid distribution across the pipe cross section.
From a larger set of two-phase experiments a subset was selected. These data is characterized by a gas/liquid density ratio of approximately 0.05 and a gas/liquid viscosity ratio of approximately 1.5e-4. The surface tension was measured to 0.02 N/m. The oil viscosity itself was in the range of 0.08 – 0.11 Pa·s, which is approximately 100 times more viscous than water. The experimental matrix with summarized overall experimental results is found in Table 1.

Table 1 Experimental matrix with measured liquid holdup and pressure drop.

Exp. ID	Re_liq	Re_gas	Liquid holdup [-]	Pressure gradient [Pa/m]
he10671	6.15E+02	1.03E+05	**0.82**	-506
he10643	6.12E+02	2.16E+05	**0.63**	-672
he11011	4.71E+02	4.32E+05	**0.63**	-746
he11013	4.92E+02	6.47E+05	**0.52**	-944
he10656	5.93E+02	8.64E+05	**0.44**	-1012
he10619	5.83E+02	1.08E+06	**0.39**	-1235
he10627	5.97E+02	1.30E+06	**0.30**	-1684
he11014	5.07E+02	1.51E+06	**0.29**	-1997
he11015	5.06E+02	1.73E+06	**0.24**	-2081
he11016	5.11E+02	1.94E+06	**0.20**	-2227

The Reynolds numbers in the table are based on the superficial velocity. We see that for an approximately constant liquid Reynolds number (Re_l) the liquid fraction decreases significantly with increased gas Reynolds number (Re_g). As a consequence, the liquid phase velocity has increased by a factor of approximately 4 for the highest gas flow rate. Hence, as the gas Reynolds number increases the liquid will pass through the transition from laminar to turbulent liquid flow. This is a result of an increasing liquid Reynolds number based on the hydraulic diameter and phase velocity of the liquid. At the same time the pressure drop increases strongly with increasing gas flow rate.
More details about the experimental results are given in the result section, after introducing the flow model.

MODEL DESCRIPTION

Model basis

The flow model is based on a 3D and 3-phase formulation, where the equations are derived based on volume averaging and ensemble averaging of the Navier-Stokes equations. Conceptually, the model is based on the following elements (Laux et al., 2007). A multi-fluid Eulerian model allowing two types of dispersed fields[1] in each of the three continuous fluids.

[1] Each phase can appear as different fields. For a 3-phase situation each phase may be continuous or dispersed in each of the other continuous phases.

i) The flow domain consists of several zones, each with a well-defined continuous fluid, separated by Large Scale Interfaces (LSIs)
ii) Between the zones local boundary conditions are applied (interface fluxes)
iii) A field based turbulence model with wall functions for LSIs and solid walls.
iv) Evolution models for droplet- and bubble sizes
v) By adding together the field-based equations for each phase, phase based mass-, momentum-, and turbulence equations are obtained

At the LSIs we use the concept of wall functions, where the shear stresses from both sides of the interface are approximated by the wall functions for rough walls (Ashrafian and Johansen, 2007). The same wall functions are used to calculate the added turbulence production in LSI cells. The effect of non-resolved waves is modelled by a density corrected Charnock model (Charnock, 1955). The use of wall functions at the LSIs is supported by e.g. (Bye and Wolff, 2007) studying the air-sea interface.

The turbulence is modelled using a $k-\ell$ model where k is the turbulent kinetic energy and ℓ is a turbulent mixing length scale based on flow domain geometry. The length scale is solved from a Poisson equation where the length scale at solid walls and LSIs are related to roughness and given as boundary conditions:

$$\nabla^2 \ell = -\frac{\kappa}{R} \qquad (1)$$

Here κ is the von Karman constant and R is the pipe radius. The length scale in cells near walls and LSIs are given by algebraic relations. The turbulent kinetic energy equations are solved for each phase by applying wall laws at solid walls and the LSIs. The turbulent viscosity for phase m is given by:

$$\mu_m^T = \rho_m \ell \left(0.35 k_m\right)^{1/2} \qquad (2)$$

where ρ_m is density and k_m is turbulent kinetic energy for phase m. The turbulent dissipation rate for phase m is:

$$\varepsilon_m = \frac{\left(0.35 k_m\right)^{3/2}}{\ell} \qquad (3)$$

The resulting model gives the volume fractions and velocity (momentum) for the phases in the flow. In order to apply local boundary conditions inside the flow as described above we need to identify the LSIs. This is done based on an evaluation of the predicted phase volume fraction, based on the assumption that there is a critical volume fraction which controls phase inversion. In this work a phase is assumed continuous if the local volume fraction in a computational cell is above a critical volume fraction $\alpha_{crit} = 0.5$. Based on a relatively simple reconstruction algorithm, the interface is reconstructed such that the local boundary conditions can be applied. Presently, the effects of surface tension on the motion of the LSI are not included. This simplification is valid as long as we use relatively coarse grids and do not want to resolve capillary waves. This model framework has the capability to handle any 3-phase (or less) multiphase flow as long as the flow can be described by 9 fields – 3 continuous fields with 2 dispersed fields in each. As this model is directed towards applications such as predictions of multiphase flows in pipelines the target is to simulate reasonably long sections of pipes for considerable flow-times. This restriction demands simplifications in order to be able to obtain results in a reasonable CPU time. Weeks or months of computer time on parallel machines would not be acceptable for most industrial applications. The simplification we have introduced is the Quasi-3D (Q3D) approximation. By slicing the pipe in one direction, normal to the pipe axis, (usually the vertical direction), as demonstrated in Figure 1, the flow can be resolved on a 2-dimensional mesh, but still keeping important aspects from the 3D pipe geometry.

The full 3D model equations are then averaged over the transversal distance to create slice averaged model equations. In this process the 3D structures are homogenized and the flow becomes represented by slice averaged fields. One result is that the wall fluxes, such as shear stresses, becomes source terms in what we call Quasi-3D (Q3D) model equations (for details, see (Laux et al., 2007)). It should be noted that the length scale equation (1) is solved using the 2D Laplacian in the x-y plane (Figure 1).

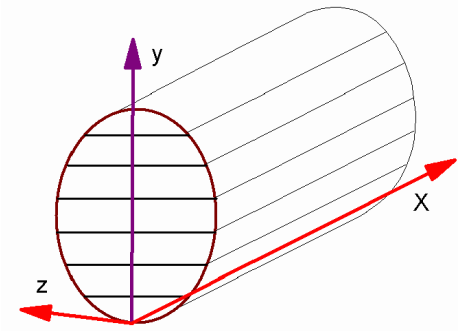

Figure 1 Quasi 3D grid cells, showing one axial (x-direction) and seven vertical cells (y-direction). The z-direction is averaged over to get Q3D equations.

The numerical solution is performed on a staggered Cartesian mesh, where the discrete mass, pressure and momentum equations are solved by an extended phase-coupled SIMPLE method (for details, see e.g. (Patankar, 1980)). The implicit solver uses first order-time discretization and up to third-order in space for convective terms (Laux et al., 2007).

The Quasi 3D model description is expected to perform well in horizontal stratified and hydrodynamic slug flows where the large scale interface is dominantly horizontal at a given axial position x, as seen in Figure 1 and demonstrated in previous papers (Laux et al., 2008a, Laux et al., 2008b, Laux et al., 2007).

The applicability of the Q3D approximation to horizontal gas liquid flows with high liquid viscosity

will be discussed next. We note that the model has not included a field for the thin liquid film which is drained by gravity after passage of waves or slugs. Adding such a field with separate momentum- and mass conservation equations may be necessary in the case when the liquid is extremely viscous.

Simulations

Based on the 10 flow situations, represented by Table 1, 10 flow cases were defined. The length of the simulated domain was 20 meters, with diameter 69 mm. The applied grid comprised 20 (transversal) x 1000 (axial) grid points. Thus, the grid aspect ratio is 5.8.

The simulations were run for 60 seconds real time, and data from the last 30 seconds were applied to calculate statistics from the simulations. The total simulation time spanned from approximately 4 to 30 times the fluid residence time in the flow domain. By further inspection of the data it was verified that the last 30 seconds should give a good representation of the capability of the model. At the flow inlet the flow was in all cases assumed stratified (liquid fraction of 0.4), with no dispersed droplets and bubbles. The inlet turbulent energy was set to 0.001 m^2/s^2. The model has several physical constants related to the bubble- and droplet transport models (Mo et al., 2013b), which are given in Table 2. Wave roughness is characterized by the Charnock constant (used default value of 10) and the dispersed phase concentrations at the Large Scale Interface are set to 0.3.

Table 2 Model constants for the size of dispersed fields (Mo et al., 2013b).

	C1	C2	C3	C4
Bubbles	10	0.1	1.00E-05	0.1
Droplets	0.02	0.002	1.00E-06	0.1

RESULTS

Pressure drop and liquid holdup

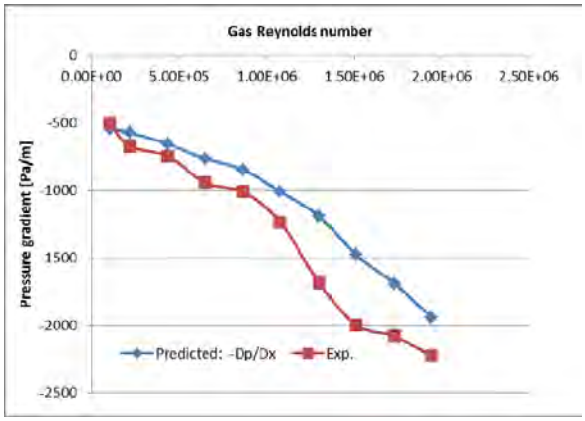

Figure 2 Predicted- and experimental pressure gradient versus gas Reynolds number.

The time averaged pressure drop was calculated over the last 50% of the pipe length. The predicted and experimental pressure drops are compared in Figure 2. We see that for the lowest velocity the model and experiments compare well. With increased flow velocity we see a consistent under-prediction of the pressure drop, not exceeding 30%. The under-prediction is quite systematic, but with a good qualitative trend.

The liquid holdup was calculated at a position 95% of the pipe length from the inlet. The results are shown in Figure 3, where we see that holdup is well reproduced for the entire velocity range. For the lowest gas Reynolds numbers we see some under-prediction of the liquid holdup. This can also be seen as an over-prediction of the gas velocity. The overall comparison is very good, both qualitative and quantitative.

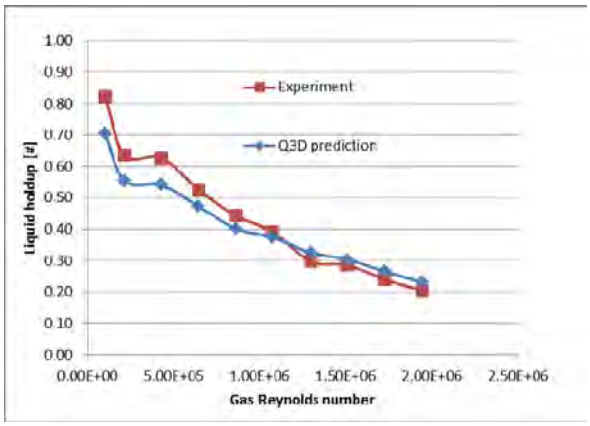

Figure 3 Predicted- and experimental liquid holdup versus gas Reynolds number.

Dynamic performance of the liquid holdup

The liquid holdup (fraction) was measured dynamically with a broad band gamma densitometer. In Figure 4 we see the comparison between the predicted- and experimental time traces of the liquid holdup, for all the cases, and where the ID codes refer to Table 1. We see that the two cases with lowest gas velocity have a typical slug type time trace. This is reproduced by the model, but the variations in the liquid fraction are larger in the predictions than in the experiments. In other words, the bubbles in the experiments are shallower than in the model.

With increasing gas velocities (moving upwards in the figure) the flow becomes more stratified, with lower amplitude in the liquid holdup oscillations. These trends are by large captured by the model. However, from the figure we have an indication that the Q3D model produces more large scale waves than observed in the experiment. We may note that for both experiments and simulations the data sampling interval is 0.1 sec. In the high gas velocity cases, such as he100671, the liquid velocity is approximately 5 m/s and only waves larger than 0.5 m are possible to resolve by the gamma densitometer (due to time averaging). However, the Q3D model reports the instantaneous results on the 20 mm grid. A better comparison would be to smooth the prediction results in the same manner as the gamma densitometer works. Then the simulation results would look smoother for the high flow rate cases.

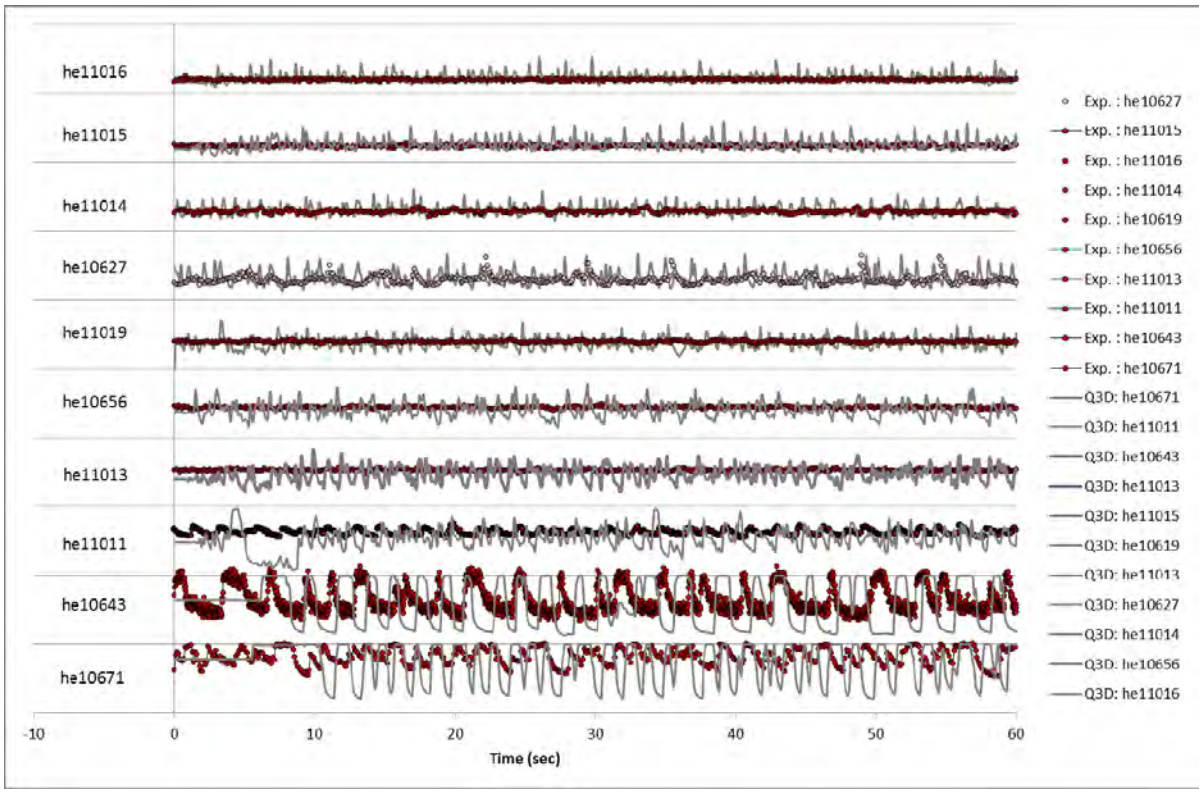

Figure 4 Predicted- versus experimental time traces of the liquid holdup for all 10 cases studied. The ID codes refer to Table 1. The gas velocity increases from bottom to top.

Flow structures and statistics

In Figure 5 to Figure 14 we show snap shots of the liquid distribution (red colour) for the different gas Reynolds numbers. Note that the diameter is increased by a factor four in the figures for visibility. Regions with yellow colour indicate high amounts (∼25%) of dispersed gas entrained into the liquid. Case IDs are defined in Table 1, and the gas velocity increases by increasing figure number. In addition the figures show the comparison between the experimental and predicted vertical distribution of the liquid. Note that for the experiments (blue lines) the scatter around the average liquid fraction is a combination of the variations on the physical volume fraction and the nature of the narrow band gamma instrument. The predicted profiles are extracted from position 95% of the pipe length (19 m).

What we see from the figures is that for the two lower gas flow rate cases (he10671 and he10643) the flow regime is slug flow. However, the predicted liquid profile does not agree well with the experimental liquid distribution in Figure 5, verifying that the predicted spreading of the large bubbles over the pipe cross section is not in accordance with the experiments. A main explanation for this is that our model is slice-averaged over the width of the pipe. The additional dispersion due to different velocities in the cross section is not included in the model. In turbulent flows this approximation is very good. However, in the present two cases the liquid is laminar and the reduced dispersion due to the dimension reduction has clearly some impact on the prediction. Still, both predicted pressure drop and holdup must be seen as acceptable.

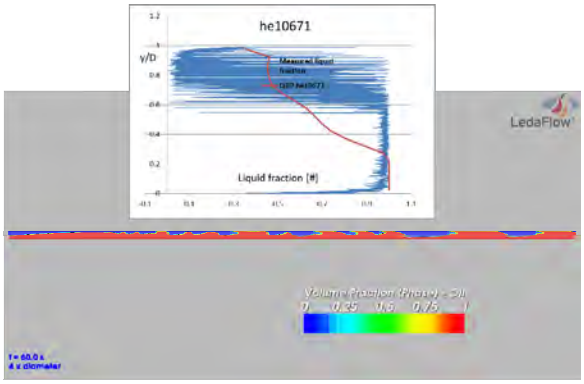

Figure 5 Case he10671: Snap shot of oil fraction. Insert shows predicted versus experimental ensemble averaged profile of vertical liquid holdup distribution.

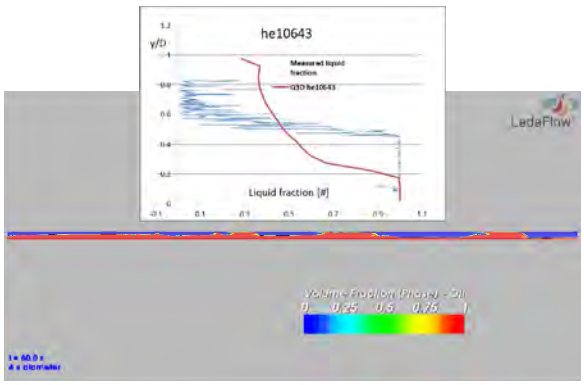

Figure 6 Case he10643: Snap shot of oil fraction. Insert shows predicted versus experimental ensemble averaged profile of vertical liquid holdup distribution.

For the cases he11011 to he10619 (Figure 7 to Figure 10) we see that our model is producing more waves than what can be supported from the traversing gamma holdup profiles. The reason for the relatively poor qualitative prediction of the liquid distribution seen in a case like he11013 is not clear. In an almost parallel experiment (he10648, not shown here) the predicted profile is much closer to the experiments. At the moment we do not have a good explanation why the experimental flow is much more stable than in the simulation. One possibility is that the effective friction at the Large Scale interface (LSI) is not accurate for this flow range, impacting the interface stability. At the same time the overall interface friction must be rather well reproduced due to the good prediction of liquid holdup. Understanding the combined role of droplet momentum exchange, wall and interface friction will need further investigations.

From case he10627 (Figure 11) and onwards (until Figure 12), we see that distribution of the liquid over the pipe cross section is rather well reproduced. For the three largest gas Reynolds numbers the comparison is very good. It is interesting to note that for these flow cases we have significant amounts of entrained bubbles (shown by the yellow regions).

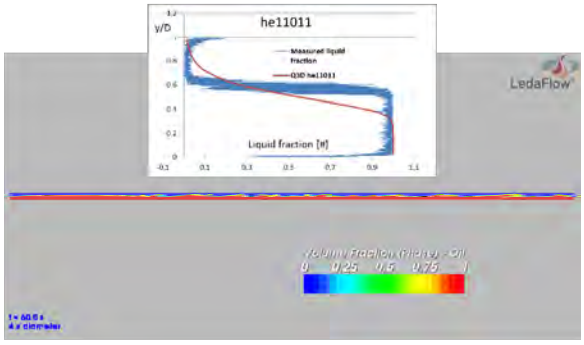

Figure 7 Case he11011: Snap shot of oil fraction. Insert shows predicted versus experimental ensemble averaged profile of vertical liquid holdup distribution.

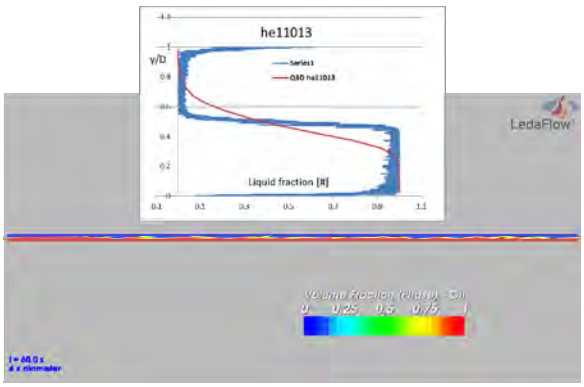

Figure 8 Case he11013: Snap shot of oil fraction. Insert shows predicted versus experimental ensemble averaged profile of vertical liquid holdup distribution.

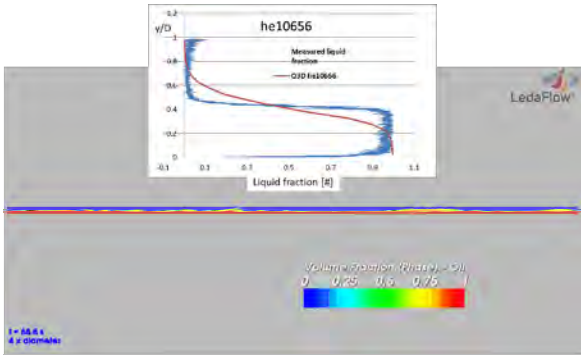

Figure 9 Case he10656: Snap shot of oil fraction. Insert shows predicted versus experimental ensemble averaged profile of vertical liquid holdup distribution.

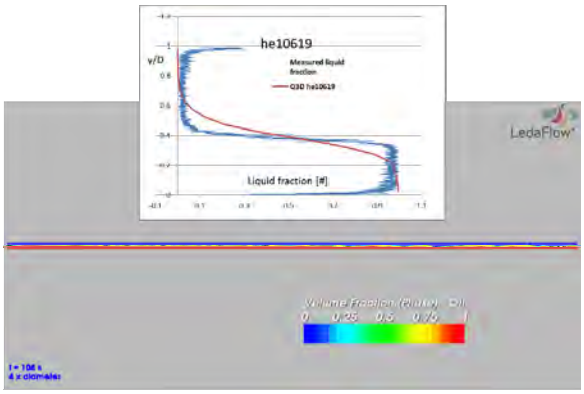

Figure 10 Case he10619: Snap shot of oil fraction. Insert shows predicted versus experimental ensemble averaged profile of vertical liquid holdup distribution.

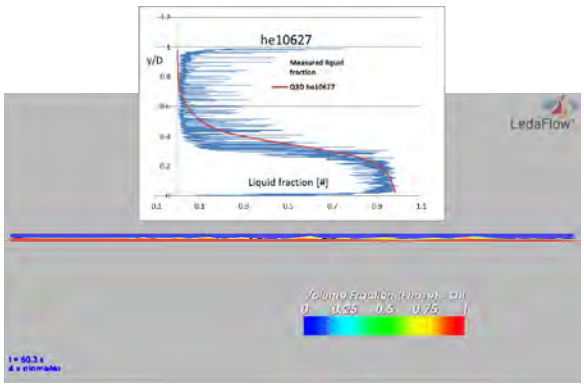

Figure 11 Case he10627: Snap shot of oil fraction. Insert shows predicted versus experimental ensemble averaged profile of vertical liquid holdup distribution.

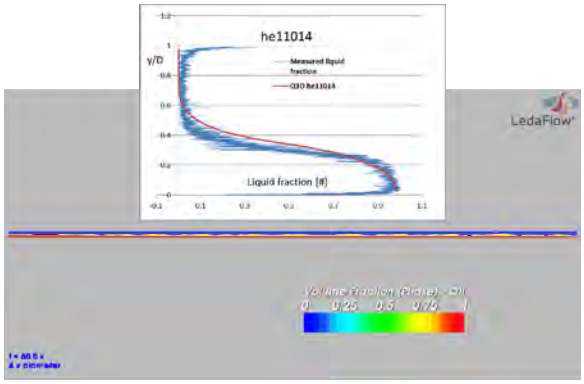

Figure 12 Case he11014: Snap shot of oil fraction. Insert shows predicted versus experimental ensemble averaged profile of vertical liquid holdup distribution.

Grid dependency

Introductory simulations with 15 and 20 grid points over the pipe cross section indicated that some improvements of the resolution of waves were achieved by going to 20 cells. The axial grid was tested at 500, 1000 and 2000 grid points. The 500 axial grid points led to suppression of waves. One case (he11014) was run using 2000 axial points. The predicted vertical profiles of the liquid holdup could not visually be distinguished from the case using 1000 point.

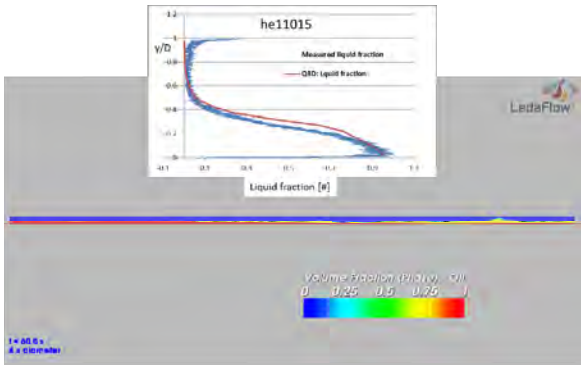

Figure 13 Case he11015: Snap shot of oil fraction. Insert shows predicted versus experimental ensemble averaged profile of vertical liquid holdup distribution.

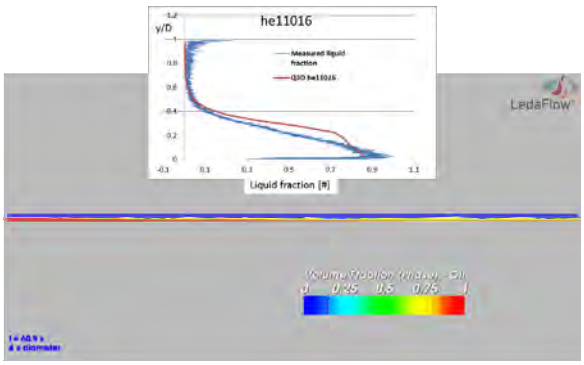

Figure 14 Case he11016: Snap shot of oil fraction. Insert shows predicted versus experimental ensemble averaged profile of vertical liquid holdup distribution.

Developed flow

The length needed to develop the flow depends on several physical phenomena, especially the entrainment and coalescence and separation of entrained bubbles. The development length will in general be longer at higher velocities since bubble coalescence time scales can be quite long. In general, the flow has been developed to a quite developed state, as seen in Figure 15. What we see here is representative for all the simulations. By doubling the length of the flow domain only marginal improvements can be expected.

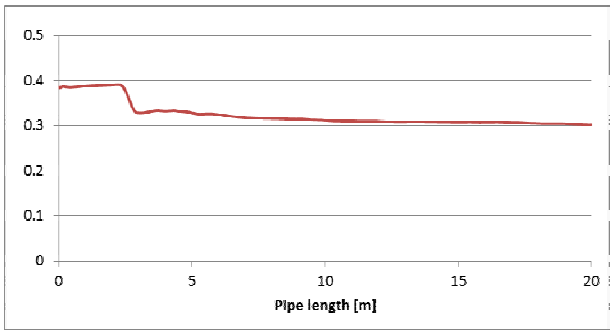

Figure 15 Time averaged liquid holdup versus length of simulated pipe (Case he11014).

CONCLUSIONS

Horizontal two-phase gas-liquid flow with a highly viscous liquid was simulated using a Quasi-3D flow model. Even if the model is reduced from 3D to 2D the prediction power of the model is good. The liquid holdup is very well predicted while the pressure drop shows a systematic under-prediction. Parts of this under-prediction may be due to an increased effective viscosity due to entrained micro-bubbles in the oil phase. Still the qualitative change in liquid holdup and pressure drop versus gas flow rate is very well reproduced, and the gas Reynolds number for transition between slug-flow and stratified flow is predicted accurately.

From liquid holdup time traces and comparisons with the traversing gamma experiments it was found that during slug flow the bubble shape is not correctly reproduced by the model. This is a result of the

predominantly laminar flow in the liquid and strong variation in the liquid velocity within one computational cell (slice). In order to account for this effect a Taylor type dispersion mechanism must be included in the model. Even if the bubble propagation was not correctly predicted the quantitative prediction of pressure drop and liquid fraction was both better than $\pm 15\%$.

For the higher gas flow rates ($Re_g > 10^6$) it was found that the Q3D model predicts very well both the quantitative and qualitative flow behaviour.

It should be noted that the model was run without trying to improve on the model coefficients. With this in mind, it is clear that the Q3D model is capable of predicting viscous gas-liquid two-phase flows. Based on our findings we realize that the Q3D model has a significant potential to become a numerical laboratory for interpretation and extension of experimental data, and can in addition serve as a means to deduce closure laws for simplified 1D models.

A natural extension of this work is to investigate the performance of the Q3D model for inclined and vertical two-phase flows, and as a further step extend the investigation to three-phase flows. Already now we realize that access to high quality experiments including cross-sectional profiles will be crucial for such a development.

ACKNOWLEDGEMENTS

The financial support to the Leda Project, the long-time contributions from the Leda Technical Advisory Committee, as well as permission to publish, by Total, ConocoPhillips, and SINTEF are all gratefully acknowledged. Our colleagues Ernst Meese, and Runar Holdahl (SINTEF), Wouter Dijkhuizen and Dadan Darmana (Kongsberg Oil & Gas Technologies), Harald Laux (OSRAM Opto Semiconductors GmbH, Regensburg), and Alain Line (INSA, Toulouse) are acknowledged for their contributions to the development.

REFERENCES

ASHRAFIAN, A. & JOHANSEN, S. T. 2007. Wall boundary conditions for rough walls. *Progress in Computational Fluid Dynamics,* 7**,** 230-236.

BYE, J. A. T. & WOLFF, J.-O. 2007. Charnock dynamics: a model for the velocity structure in the wave boundary layer of the air-sea interface. *Ocean Dynamics,* 58**,** 31-42.

CHARNOCK, H. 1955. Wind stress on a water surface. *Quart J Roy Meteor Soc,* 81**,** 639-40.

ESKERUD SMITH, I., KRAMPA, F. N., FOSSEN, M., BREKKEN, C. & UNANDER , T. E. Investigation of Horizontal Two-Phase Gas-Liquid Pipe Flow Using High Viscosity Oil: Comparison with Experiments Using Low Viscosity Oil and Simulations. 2011. BHR Group 2011 Multiphase 15, 2011 Cannes, France. BHR Group.

GOKCAL, B. 2005. *Effects of high oil viscosity on two-phase oil-gas flow behavior in horizontal pipes.* Master of Science, University of Tulsa.

GOKCAL, B. 2008. *An experimental and theoretical investigation of slug flow for high oil viscosity in horizontal pipes. Ph.D. Dissertation,.* PhD, The University of Tulsa.

LAUX, H., MEESE, E., JOHANSEN, S. T., LADAM, Y., BANSAL , K. A., DANIELSON, T. J., GOLDSZAL, A. & MONSEN, J. I. 2007 Simulation of multiphase flows composed of large scale interfaces and dispersed fields. Int. Conf. Multiphase Flows, 2007 Leipzig.

LAUX, H., MEESE, E. A., MO, S., JOHANSEN, S. T., BANSAL, K. M., DANIELSON, T. J., GOLDSZAL, A. & MONSEN, J. I. Multi-dimensional simulations of slug and slug-like flows in inclined pipes and channels. OTC 2008a Houston. 21-37.

LAUX, H., MEESE, E. A., MO, S., UNANDER, T. E., JOHANSEN, S. T., BANSAL, K. M., DANIELSON, T. J., GOLDSZAL, A. & MONSEN, J. I. 2008b. Multidimensional Simulations of Multiphase Flow for Improved Design and Management of Production and Processing Operation. *2008 Offshore Technology Conference.* Houston, Texas, U.S.A: SPE.

MO, S., ASHRAFIAN, A., BARBIER, J.-C. & JOHANSEN, S. T. Quasi-3D modelling of two-phase slug flow in pipes. Ninth International Conference on CFD in the Minerals and Process Industries, CSIRO, 2012 Melbourne, Australia, 10-12 December

MO, S., ASHRAFIAN, A. & JOHANSEN, S. T. 2013a. Simulation of flow regime transitions in vertical pipe flow. *8th International Conference on Multiphase Flow, ICMF2013.* Jeju, Korea.

MO, S., ASHRAFIAN, A. & JOHANSEN, S. T. 2013b. Two phase flow prediction of fluid displacement operations. *8th International Conference on Multiphase Flow, ICMF 2013.* Jeju, Korea.

PATANKAR, S. V. 1980. *Numerical Heat Transfer and Fluid Flow*, New York, McGraw-Hill Book Company.

RØNNINGSEN, H. P. 2012. Rheology of petroleum fluids. *Annual Transactions of the Nordic Rheology Society,* 20**,** 11-18.

ZHANG, H.-Q., SARICA, C. & PEREYRA, E. 2012. Review of High-Viscosity Oil Multiphase Pipe Flow. *Energy & Fuels,* 26**,** 3979-3985.

Progress in Applied CFD

SELECTED PAPERS FROM 10TH INTERNATIONAL CONFERENCE ON COMPUTATIONAL FLUID DYNAMICS IN THE OIL & GAS, METALLURGICAL AND PROCESS INDUSTRIES

This book contains selected papers from the 10th International Conference on Computational Fluid Dynamics in the Oil & Gas, Metallurgical and Process Industries, hosted by SINTEF in Trondheim in June 2014 (CFD2014). The CFD conferences focus on the application of CFD in the oil and gas industries, metal production, power generation, chemicals and other process industries. The papers in the conference proceedings and this book demonstrate the current progress in applied CFD.

SINTEF Academic Press